DISS. ETH NO. XXXXX

RIVER DYKE FAILURE MODELING UNDER TRANSIENT WATER CONDITIONS

A dissertation submitted to

ETH ZURICH

for the degree of

Doctor of Sciences

presented by

WILMER FERNEY MORALES PEÑUELA

M.Sc., Nacional University of Colombia

born on 29.09.1980

citizen of

Republic of Colombia

accepted on the recommendation of

Prof. Dr. Sarah M. Springman

Prof. Dr. Dietmar Adam

Dr. Jacques Garnier

2013

Contents

Kurzfassung

Abstract

Knowledge of the performance of river dykes during flooding is necessary when designing governmental assistance plans aimed to reduce both casualties and material damage. This is especially relevant when floods have increased in their frequency during the last decades, together with the resulting material damage and life costs.

Most of previous attempts for analyzing dyke breaching during flooding have neglected to consider the soil mechanics component and the influence of infiltration and saturation changes on the failure mechanisms developed in the river dyke. This research project aimed to fill that gap in knowledge by analyzing, in a comprehensive manner, the effect of transient water conditions, represented by successive flood cycling, on the seepage conditions and subsequent breaching of dykes. Therefore, three key sub-projects were carried out: the analysis of the results from an overflow field test, the physical modeling of small-scaled models under an enhanced gravity field, and the numerical modeling of the flow response and the resulting stability of both the air- and water-side slopes.

The overflowing field test was carried out in a section of a dyke enclosed within a rectangular sheet-pile box along the Rhone River in Baltschieder, south west Switzerland. This formed the concluding part of another research project (Mayor, 2013), which had been devoted to the analysis of the response of a dyke to successive flood cycles.

The grass cover and a low erodability gravel on the crown of the dyke prevented the it from being eroded superficially, as was expected. An instability event on the air-side slope, followed by internal erosion, was observed instead. Laboratory tests were carried out to determine the unsaturated flow parameters of the silty sand composing the main body of the dyke. These, together with parameters estimated from empirical relationships, such as the Kozeny-Carman (Carrier, 2003) and modified Kovacs (Aubertin et al., 2003) equations, allowed numerical modeling of the experiment to be completed with success. Both the flow response and stability of the dyke were simulated to represent the response that was observed during the test.

The physical modeling was performed by testing 12 small-scale models at an increased gravity of 33-g. These represented dykes of 5 m height at prototype scale, with three different slope gradients (1:2.0, 1:2.5, 1:3.0), and included one or two protective measures (a toe filter, a cut-off wall) plus a homogeneous dyke. The goal was to analyze the effect of each protective measure on the groundwater flow during flood cycles and on the breaching mechanism that developed during an overflow event. Therefore, two cycles of floods, with a subsequent overflow were applied to all of the models. The flood cycles had a sinusoidal shape, each one with a duration of 20 days. The overflow was intended to replicate a hydrograph measured in a Swiss river during a flood in 2005.

The sand used to build the models was characterized by compiling information from previous research projects, which had used the same soil. Specific tests were performed in order to determine the mechanical (water content controlled triaxial test and suction controlled oedometer tests) and hydraulic parameters (Soil Water Retention Curve) under unsaturated conditions.

Two types of dyke breaching mechanisms were identified. If a cut-off wall was not included, water started eroding the soil surface, creating a breach throat, through which water flowed rapidly, which, in turn, increase the size of the throat. A second type of breaching mechanism was observed when a cut-off wall was placed. A breach throat started to develop in the crest of the dyke, closer to the wall, in a similar manner to that observed for the dykes without the wall. When the throat reached the cut-off wall, it could not continue increasing towards the water-side. Instead, the soil in front of the wall, i.e. on the air-side, started to be eroded, creating a narrow and shallow breach zone in the vicinity of the wall.

A numerical simulation of the unsaturated groundwater flow for all twelve dykes was carried out with commercial software based on the Finite Element Method (FEM), which allows the governing equation for flow through unsaturated porous media to be solved. Additionally, the variation in time of the stability of both air- and water-side slopes was investigated using a limit equilibrium approach.

The results from the numerical simulations matched accurately with the results obtained with the centrifuge modeling, including the prediction of local instabilities during the flood cycles for those dykes that did not include a toe filter. This was a consequence of an appropriate definition of the boundary conditions of the problem, together with an accurate estimation of the soil parameters through specific laboratory tests.

List of symbols

AEV	Air entry value
a_R	Radial acceleration
a_T	Tangential acceleration
a, b	Fit parameters for non-linear elasticity model / Forchheimer equation parameters
BBM	Barcelona Basic Model
β	Inertia resistance factor
β_0, β_1	Critical angles during dyke breaching
CSL	Critical state line
C_{ijkl}	Compliance matrix
C_c	Curvature coefficient / Compression index
C_s	Recompression index
C_u	Uniformity coefficient
c'	Effective cohesion
c'_{app}	Apparent cohesion due to an unsaturated condition
D_R	Relative density
d_{ch}	Characteristic dimension of the soil particles
$d_{effective}$	Effective diameter for the Kozeny-Carman approach
d_{10}, d_{15}, d_{30}, d_{50}, d_{60}	Sieve sizes, at which the 10, 15, 30, 50 and 60 % of the soil passes
δ_{ij}	Kronecker's delta
E	Young's modulus
$\dot{E}$	Erosion rate
EV	Envirosmart ®
e	Void ratio
e_{max}	Maximum void ratio
e_{min}	Minimum void ratio
ε	Normal strain / Electric permittivity
FEM	Finite element method
FoS	Factor of safety
F_f	Force equilibrium / Friction factor
F_m	Momentum equilibrium
ϕ^b	Friction angle with respect to change in suction
ϕ'	Effective angle of friction
ϕ'_{crit}	Angle of friction at the critical state
ϕ'_{max}	Maximum angle of friction
G_s	Specific gravity of the soil grains
g	Earth's gravity
Γ	Specific volume at p'=1 kPa
γ	Bulk unit weight of soil
γ_d	Unit dry weight of soil

$\gamma_{d\ max}$	Maximum unit dry weight of soil
γ_s	Unit weight of soil solids
γ_w	Unit weight of water
H	Water head
η	Porosity
I_p	Plasticity index
i	Hydraulic gradient
L	Length of the rods of TDR sensor
L_a	Apparent length of TDR sensor
L_o	Offset of TDR sensor
λ	Slope of the NCL in the ln p' – v space
λ^*	Virgin stiffness as function of suction (hypoplastic constitutive model)
K	Intrinsic permeability
K_a	Apparent dielectric constant
k	Hydraulic conductivity
k_{app}	Apparent permeability (Forchheimer equation)
k_{sat}	Hydraulic conductivity at saturation
κ	Slope of the unload-reload line in the ln p' – v space
κ^*	Reload stiffness as function of suction (hypoplastic constitutive model)
M	Slope of the critical state line in the *p' - q* space
M_E	Confined deformation modulus
m	Mass
m_v	Coefficient of volume change
m_w	Water storage parameter
μ	Dynamic viscosity
m, n, p, α, ξ	Fitting parameters for the SWRC and hydraulic conductivity function
N	Specific volume at p'=1 kPa (hypoplastic constitutive model)
NCL	Normal consolidation line
n	Gravity level
ν	Poisson's ratio / Darcy's velocity
PPT	Pore pressure transducer
p'	Effective mean or hydrostatic stress
p'_c	Preconsolidation stress
p*	Mean net stress
Q	Water flux
Q_f	Applied boundary flux
q	Deviator stress
θ	Volumetric water content
θ_{res}	Residual volumetric water content
θ_{sat}	Volumetric water content at saturation
Re	Reynolds' number
Re*	Boundary Reynolds number

ρ_w	Density of water
ρ_s	Density of soil solids
S	Matric suction
S_r	Degree of saturation
σ	Normal stress
σ_{vm}	von Mises stress
σ_1, σ_2, σ_3	Principal stresses
σ^*	Net stress
T	Surface tension of the fluid-air interface
TDR	Time domain reflectometry
TM	Tensiometer
τ	Shear stress
τ_0	Shear stress of the water flow
$\tau*$	Dimensionless shear stress
U	Potential energy
USCS	Unified Soil Classification System
u_a	Air pressure
u_w	Pore water pressure
u^*	Shear velocity of water flow
V	Volume
v	Specific volume
WEV	Water entry value
w	Gravimetric water content
w_L	Liquid limit
w_{opt}	Optimal water content
w_P	Plastic limit
Ω	Wetting angle
ω	Angular velocity
χ	Effective stress parameter for unsaturated soils
ψ	Dilatancy / Matric suction

1 Introduction

1.1 Motivation

Knowledge of dyke-performance during flooding is necessary when designing governmental assistance plans. These plans help to reduce both casualties and material damage. For instance, floods in Europe have increased in their frequency during the last decades, together with the resulting material damage and life costs. Hoyois & Guha-Sapir (2003) report an increase from eight floods in 1978 to 38 in June 2002 (Figure 1.1). This is not exclusively a European problem. Gautam & van der Hoek (2003) reported that floods in more than 80 countries killed almost 3000 people and caused hardships for more than 17 million worldwide during 2002.

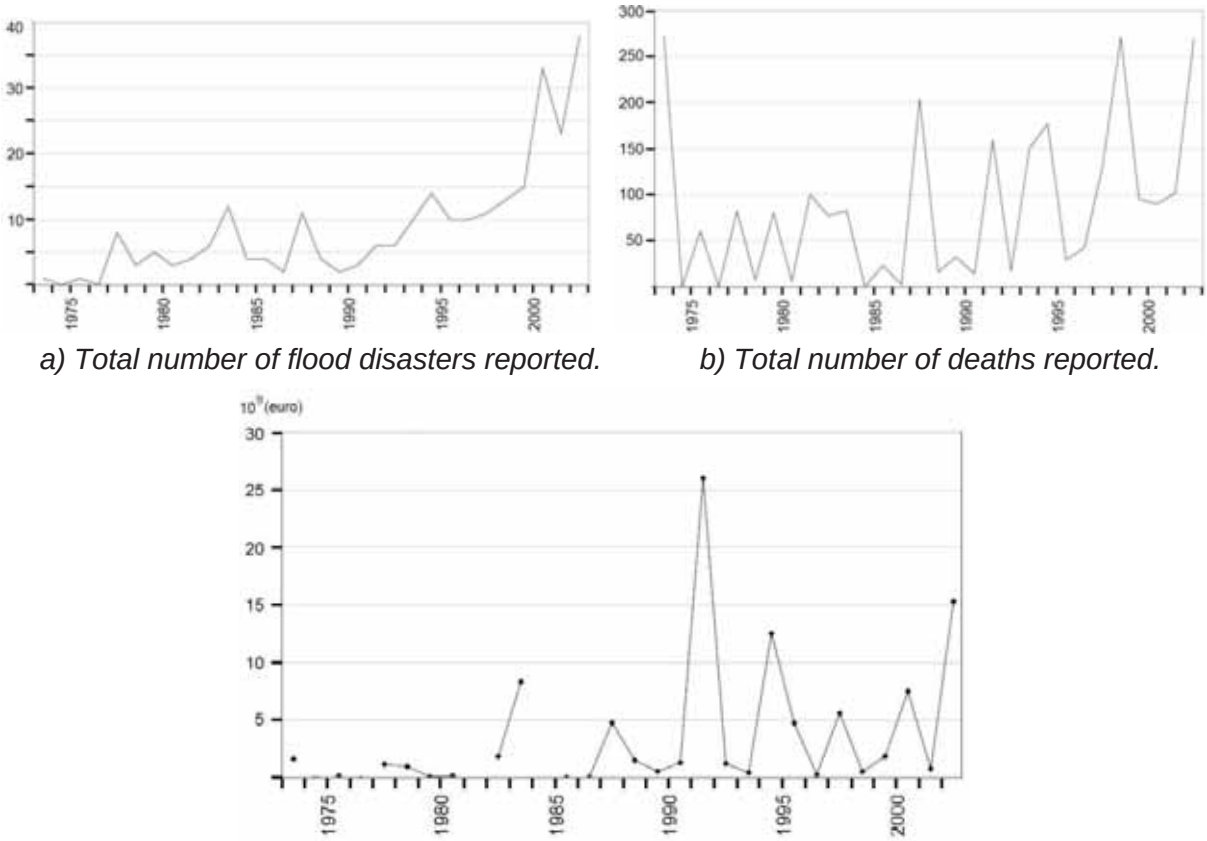

a) Total number of flood disasters reported. *b) Total number of deaths reported.*

c) Total cost of damage reported.

Figure 1.1: Floods in the European Macro-Region (after Hoyois & Guha-Sapir, 2003).

Switzerland is also affected by this situation. According to (Bezzola et al., 2008) and Mayor (2009), although only two significant flooding events occurred during a period of about 100 years (1875-1977), several floods have occurred during the last 36 years (1977, 1978, 1987, 1993, 2000, 2002, 2005 and 2007) affecting several areas across the country and causing significant damage and losses.

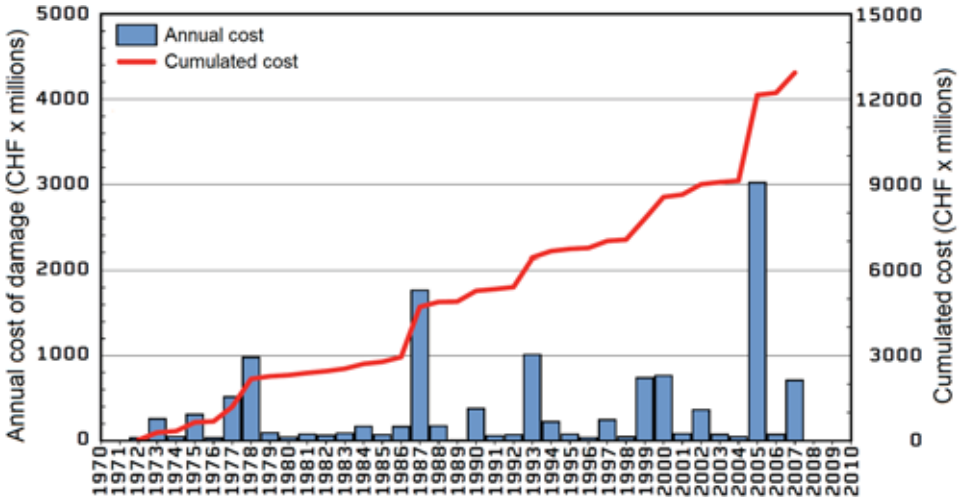

Figure 1.2: Annual cost due to floods in Switzerland since 1970 (after Bezzola et al., 2008).

Disse & Engel (2001) assert that changes in climate directly affect the occurrence and severity of floods. UVEK (2008), after analyzing flooding events in Switzerland, supported the idea that with the inclusion of global climate change, these events may be more frequent than previously observed. Mudelsee et al. (2004) explain that the risk of extreme river floods increases because a warmer atmosphere can carry more water.

Additionally, several attempts for analyzing dyke breaching during flooding have been performed by researchers and governmental agencies. However, most of them neglect to consider the soil mechanics component other than based on very simplified concepts. Simplistic assumptions regarding soil-structural behavior have been used instead. The most common of these assumptions is to treat the flow over an embankment as a wide weir flow. This limits the predictive capability of the analysis because bank failure is not analyzed based on principles of soil mechanics, but purely on erosion rates. This approach neglects the influence of infiltration and saturation changes on the failure mechanism in the river levee (Fäh, 2007).

These approaches also do not take into account the effect of water table fluctuations on dyke stability prior to breaching. All of the above confirms that there is a significant gap in the scientific knowledge of breaching and the failure of river dykes, which lies at the boundary of fluid and soil mechanics. Therefore, this research project was aimed to improve both process understanding and optimization of remediation strategies and design.

The increasing need for understanding the complete process generating floods is highlighted. This includes from the water source in the highlands to the breach mechanisms and development. In consequence, the Competence Center for Environment and Sustainability (CCES) funded the research project APUNCH (**A**dvanced **P**rocess **UN**derstanding and prediction of hydrological extremes and **C**omplex **H**azards), from which this research formed a part.

The project goal was to gain a comprehensive and ‘process-chain-based’ insight into the response of Alpine watersheds subjected to storm rainfall events. One of the major challenges was the combination of physical modeling, field testing and numerical simulations to ana-

lyze and predict the conditions that lead to failure of dykes (Burlando et al., 2008). The project plan was carried out by several institutes within the ETH domain (IFU, IGP, VAW and IGT at ETHZ; LHE, LAP and LCH at EPFL and WSL)[1].

The last part of the analysis chain was to investigate the triggers for dyke failure. However, the condition of the earth structure, prior to the event producing the failure of the dyke, determines its stability and behavior. Therefore, an analysis of successive flooding events before the complete failure of the dyke by overflow was studied.

The problem was analyzed following a multi-topic approach, which included a field test, and both numerical and physical modeling. Physical modeling is form of an engineering simulation in which scaled models are tested, while attempting to reproduce the behavior of a full-scale prototype. Small-scale models can be tested under increased or one gravity fields. The former have an advantage that the actual stresses are well replicated and hence appropriate shear strength will be mobilized. In this way, the stress dependent behavior of soil can be scaled in a correct manner (Allersma, 1996). The latter are relatively easy to build and test at 1-g level, however, unconservative predictions of the Ultimate Limit State (ULS) are obtained from them under some modes of kinematic constraint due to a high dilatancy angle ψ arising at low stresses in the model (Mayne et al., 2009). Since the response of embankments built with granular materials is highly stress dependent, centrifugal modeling was the more appropriate physical modeling approach in this case.

1.2 Thesis layout

The dissertation is divided into 6 chapters, with an additional reference list and 5 appendixes:

- The first chapter is this introduction, where the main motivations to carry out the research are exposed.
- Chapter 2 compiles basic information regarding soil behavior and physical modeling needed for a complete understanding of the rest of the thesis.
- Chapter 3 describes the analysis of the information from a field test, in which a section of a dyke on the Rhone River was subjected to overflow.
- Chapter 4 is dedicated to the physical modeling with small-scale models tested under an enhanced gravity field. Detailed information is given regarding scaling factors of hydraulic processes as well as the testing plan and the analysis of the results.

[1] ETHZ: Swiss Federal Institute of Technology, Zürich.
EPFL: Swiss Federal Institute of Technology, Lausanne.
IFU: Institute of Environmental Engineering.
IGP: Institute of Geodesy and Photogrammetry.
VAW: Laboratory of Hydraulics, Hydrology and Glaciology.
IGT: Institute for Geotechnical Engineering.
LHE: Environmental Hydraulics Laboratory.
LAP: Processor Architecture Laboratory.
LCH: Hydraulic Constructions Laboratory.
WSL: Swiss Federal Institute for Forest, Snow and Landscape Research.

- Chapter 5 presents the results of numerical simulations. These were carried out with the same geometries and boundary conditions as for the centrifuge tests, and the comparison between both types of modeling is done.
- Finally, some conclusions and outlook are given in Chapter 6.

2 Literature review

Failure of dykes can be studied through physical and numerical modeling. The former includes field and laboratory tests, whereas the latter is focused on computational analyses. In all cases, understanding the behavior of both soil and the geotechnical structure is required in order to assess the results from the modeling and to propose protection measures.

Basic reference information and previous research work done is reviewed in this chapter. This includes the mechanisms that might lead to instability of a dyke. A description of the mechanical behavior of unsaturated soils is given, as it is likely to occur in dykes during the rise and fall of river levels. This includes the formulation of the effective stresses to take the matric suction into account. Similarly, an explanation of the formulation of groundwater flow in the framework of unsaturated soils is presented, together with the techniques to determine the main variables for flow analysis (matric suction and volumetric water content), and their relationship, known as the Soil Water Retention Curve, which determines the flow characteristics in an unsaturated porous media.

A review of the full-scale tests performed for other research projects is presented. These were found to be relevant for the understanding of the dyke breaching mechanism. Analogously, a review is given regarding relevant previous research carried out on small-scale models tested under enhanced gravity conditions. Alongside this, an explanation about the relevant centrifuge modeling and testing techniques is given. The principles of the methods used for the numerical modeling of the problem is discussed at the end of the chapter together with some conclusions and implications pertinent to this research project.

2.1 Dyke breaching mechanisms

Dyke breaching is a complex scenario that must be fully understood and taken into account during the design phase. According to TAW (1998), a distinction has to be made between failure and collapse. The former occurs when one or more of the functions of the protective system are not fulfilled, whereas the latter refers to the loss of strength or large scale changes in geometry. In some cases, failure might occur without collapse, which implies the structure may still fulfill its protective role, at least during the current crisis. For instance, water may flow over the flood defense and inundate the hinterland, without the defense collapsing completely.

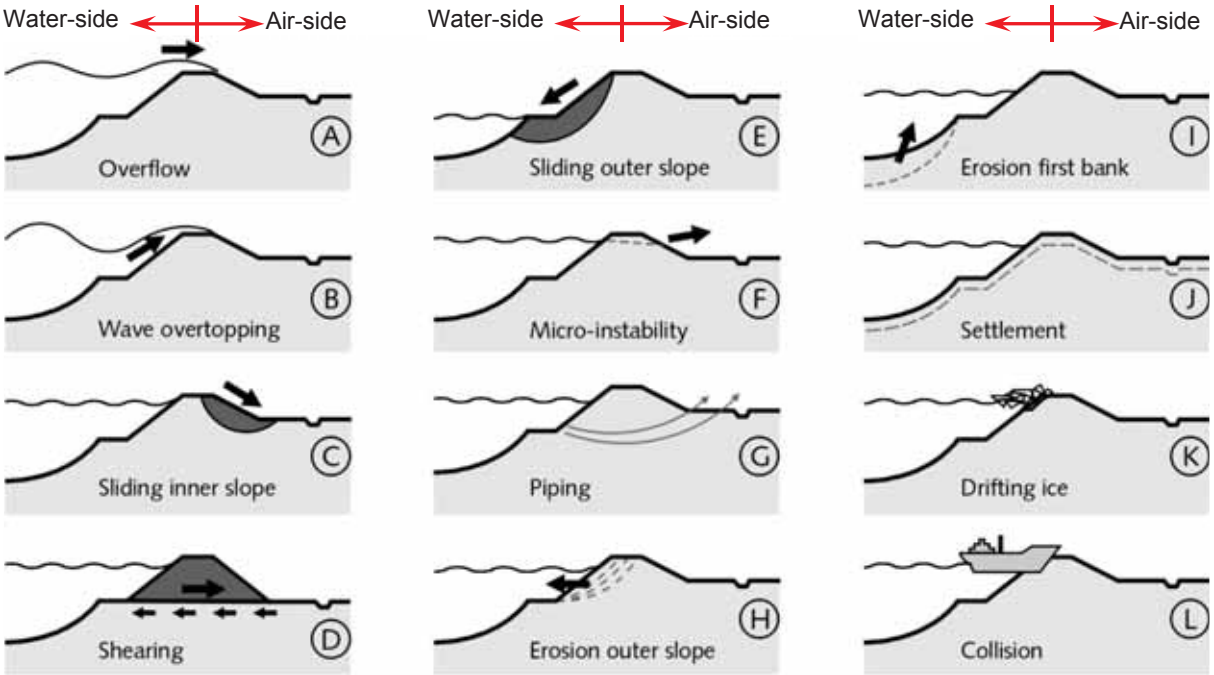

Figure 2.1: Failure mechanisms of dykes (after TAW, 1998).

A failure mechanism refers to the manner in which the water retaining capacity is lessened. Figure 2.1 illustrates the main failure mechanisms that a dyke might experience. These are described by TAW (1998) as:

- Inundation of the dyke ring area through a combination of high water level and wave overtopping, without collapse of the defense structure (A).
- Erosion of the water-side slope by the force of the flowing water, and by a combination of high water level and wave overtopping (B).
- Instability (sliding) of the air-side slope, due to either infiltration of the overflowing water in a combination of high water level and wave overtopping, or water pressure against the defense and increased water pressure in the subsoil (C).
- Shearing of a soil body, also by water pressure against the defense and increased water pressure in the subsoil (D).
- Sliding of the water-side slope in the case of a rapid fall in the water level after high water (E).
- Instability of the water / air-side slope by existing seepage water through the soil body analogous to failure mechanism C, but at lower water levels (F).
- Piping, as a consequence of seepage flow through the subsoil, so that the erosion starts at the toe of the dyke and soil is liquefied (sand boils) (G).
- Erosion of the water-side slope or the toe and foreshore by current or wave movement (H, I).
- Large-scale settlements and distortions of the soil body (J).
- Mechanical threats, such as impact from ice and shipping (K, L).

Although there are several types of failure that might occur to a dyke, this thesis will only focus on the failure due to overflow (A) as a consequence of an increase in the water level, without taking waves into consideration.

2.1.1 Erosion and piping processes

Chen et al. (1987) report that the Waterways Experiment Station of the Corps of Engineers (WES) found that low embankments constructed of well compacted fine grained or well-graded granular material with fines can withstand some overflow depths for limited periods. Seepage through relatively clean rockfill is detrimental to stability and can lead to shallow slides, which progress downslope soon after being exposed to this flow process.

Additionally, Chen et al. (1987) indicate that two of the most important factors influencing the durability of the embankment are the effects of concentration of flow at abutments or low areas along the crest, and erosion resistance of the construction material at the downstream toe area. Other embankment failure modes during an overflow event, e.g. instability, internal seepage and mass bank failure, can combine to cause breaching and failure of the dyke.

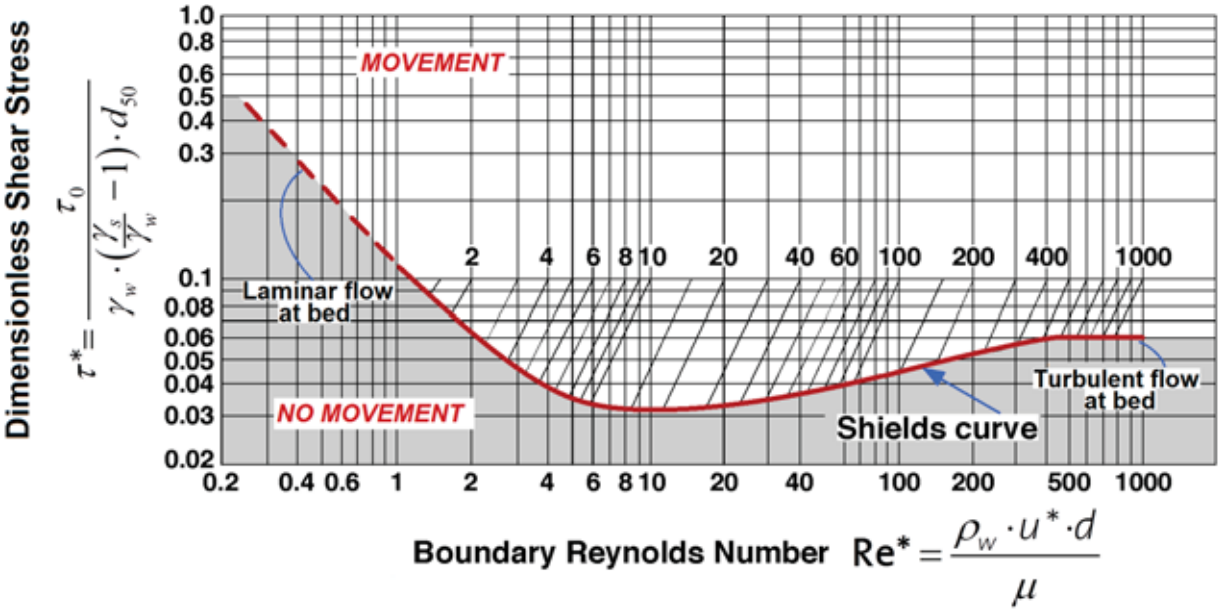

Figure 2.2: Shields diagram for dimensionless critical shear stress (modified from Henderson, 1966; U.S.A.C.o.E., 1994).

Erosion appears after the shear stress exerted by the flow exceeds the critical shear stress of the soil. Shields diagram (Figure 2.2) is usually used to evaluate whether the material will be prone to erosion. This diagram relates a dimensionless shear stress τ^* [-] with the boundary Reynolds number *Re** [-], where τ_o is the shear stress of the water flow of shear velocity u^*, ρ_w and γ_w are the density and unit weight of water, γ_s is the unit weight of the soil grains, and d_{50} is the grain size for which 50% of the grains are smaller. Shields diagram defines a threshold for the movement of particles at the bed of the flow. The particles remain stable at the bottom of the flow below the Shields curve (shaded zone in Figure 2.2). A state above

the curve implies that particles will be dragged by the flow. Briaud et al. (2008) proposed a classification system based on the erosion rate and the flow velocity (Figure 2.3).

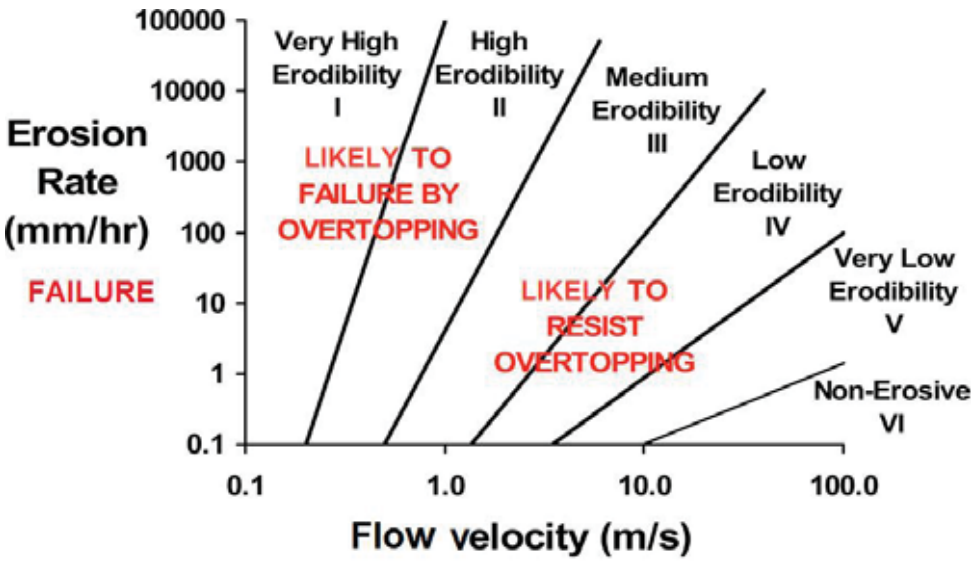

Figure 2.3: Guideline for erosion resistance during overflow (after Briaud et al., 2008).

Fujisawa et al. (2008) studied the erosion characteristics of compacted soils used for embankment materials. A soil composed of 10% clay, 12% silt, and 78% sand was used. The maximum dry density was 1970 kg/m^3 at the optimum water content of 11.0%. An erosion apparatus, similar to that proposed by Briaud et al. (2001), was used. They found that the erosion rates of the specimens decrease linearly with the increase of dry density under a constant shear stress applied by the fluid to the soil. This is highly relevant, as it indicates that strict control of the densities during construction is desirable if not essential. Grass can be also used as a protective measure against superficial erosion, as it can resist flow velocities of up to 2 m/s (Seijffert & Verheij, 1998).

According to Richards & Reddy (2007) and Fell et al. (2003), *piping* is a general term to define different erosive process taking place inside the soil matrix. These processes can be described as:

Internal erosion: a process, in which tractive forces remove soil particles, that rather than being initiated by Darcian flow at an exit point, is initiated by erosive forces of water along a pre-existing opening.

Backwards erosion: where the erosion is occurring at the exit point and progressing back into the slope, because fluid velocities may be more erosive for a given hydraulic gradient due to higher velocity flows at a soil-structure boundary.

Suffusion: gradual migration of fine materials through a coarse matrix leading to failure. This process can result in a loose framework of granular material with relatively high seepage flows that leads to collapse of the soil skeleton. Suffusion can be a much slower process than is commonly observed where internal erosion occurs along a concentrated leak. Hence,

suffusion may be related to long-term seepage problems that exhibit increasing seepage quantities over a period of years.

Fell et al. (2003) identify four phases piping processes: initiation and continuation of erosion, progression to form a pipe, and formation of a breach, as shown in Figure 2.4.

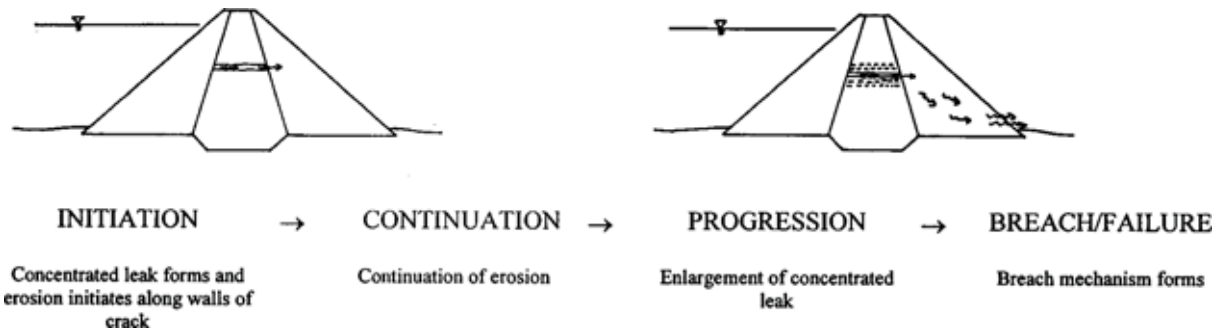

Figure 2.4: Process of evolution of piping (after Wan & Fell, 2004a).

Jones (1981) argued that piping in natural soils plays a significant role in hydrological processes, and therefore, in geomorphological development in terms of drainage channels and valley network progress. His concept is illustrated in Figure 2.5, in which pipes of diverse genesis interact with the hydrological events taking place in a valley.

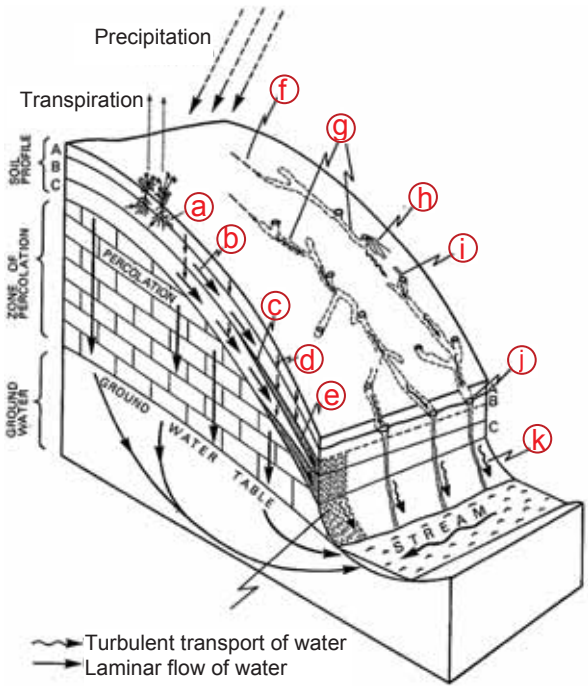

a) Moisture extraction by plant roots
b) Unsaturated flow thorough soil matrix
c) Saturated wedge of soil
d) Unsaturated flow in matrix
e) Saturated flow thorough soil matrix
f) Subsurface flow from matrix into upstream end of pipes
g) Pipes beneath surface
h) Overland flow from pipe outlet
i) Inflow through pipe “blow-hole”
j) Pipes formed at change in soil properties
k) Flow pipe from outlet

Figure 2.5: Piping as an agent of hydrological and geomorphological processes (after Jones, 1981).

The inclusion of pipes in the hydrological models is of high importance, as they portray the interaction of the different geomorphological agents in a more realistic way. Weiler & McDonnell (2004) proposed a model to take into account the influence of pipe flow on saturation patterns under rainfall events. Since the exact location of the pipes is unknown, the

model uses three parameters instead: density of pipes, height of the pipe above bedrock, and standard deviation of pipe height.

Dykes present a propensity to develop pipes due to diverse factors. Mayor & Springman (2012) assert that insufficient compacted layers of soil, roots from vegetation or animals can influence the emergence of pipes (Figure 2.6). This coincides with Mériaux et al. (2006) and FEMA (2005), which explain that the development of a root system may weaken the structure through localized loss of fill density, generating preferential seepage paths leading to internal erosion problems. This can produce a potentially dangerous increase in hydraulic seepage gradient and internal erosion problems in dykes.

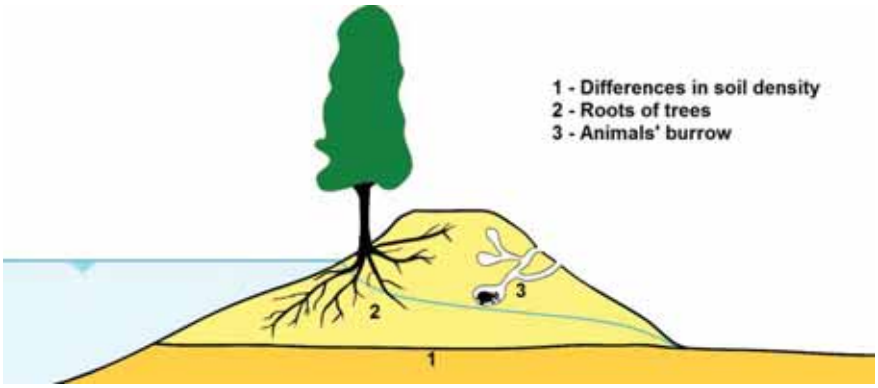

Figure 2.6: Agents acting on a dyke, which might lead to pipe emergence (after Mayor & Springman, 2012).

2.1.2 Failure mechanisms during overflow

Two types of failure development during overflow have been found. The first corresponds to a scenario in which water overflows uniformly along the entire width of the dyke's crest. In this case, failure is uniform along the width of the dyke akin, to a plane strain situation, which can be analyzed two-dimensionally. The failure takes place in four stages, as described by Chinnarasri et al. (2003) (Figure 2.7): a) initial stage with small erosion on the dyke crest, b) second stage with slope failure, shown here as a circular form, c) third stage with a wavelike-shape formed, and d) last stage, as a large wedge formed with a shallow slope.

Schmocker et al. (2010) and Schmocker (2011) show how the seepage line during overflow does not emerge on the air-side slope of small-scale plane strain models tested at 1-g in a flume (Figure 2.8). This generates an unsaturated zone between the seepage line and the water overflowing. A slope instability occurs when this zone is reduced due to both shifting of the seepage line, which is usually called the phreatic surface in soil mechanics and defines where the ground is saturated and $u_w = 0$, and infiltration from the water overflowing, most probably owing to the reduction of suction, which provides an apparent cohesion to the soil, as explained in the next section. This highlights the importance of taking the unsaturated behavior of the soil into consideration.

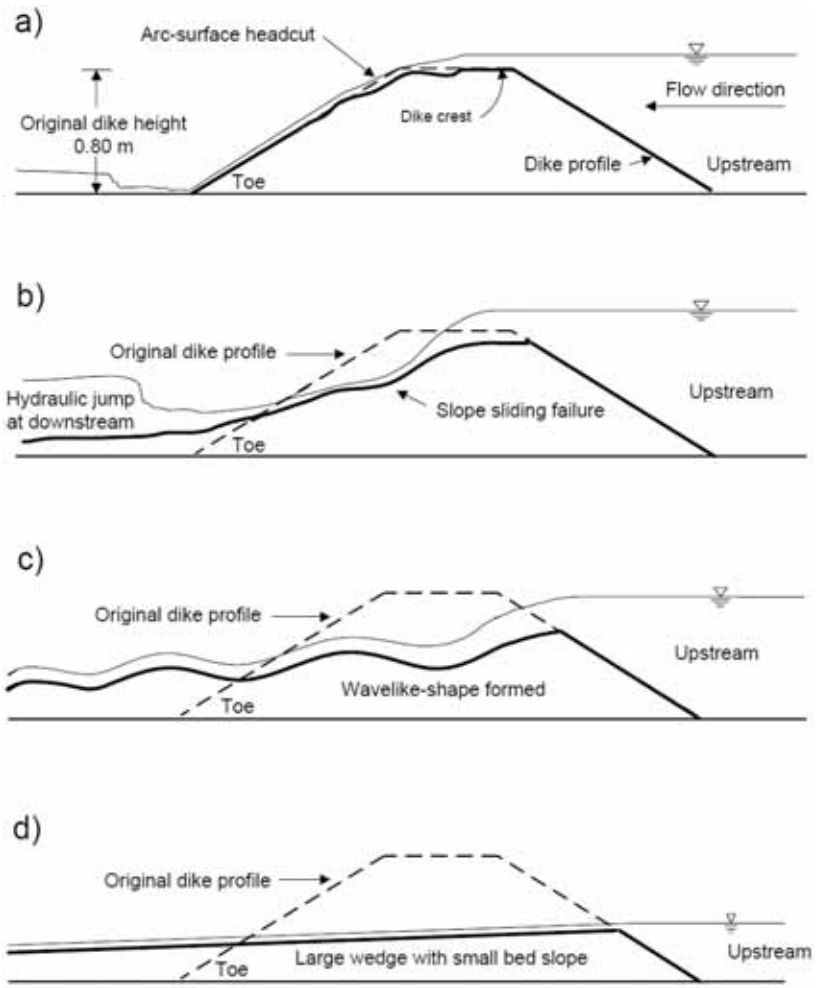

Figure 2.7: Process of dyke failure due to uniform overflow along the crest (after Chinnarasri et al., 2003).

The second type of development of the failure is when the overflowing water initially flows through a channel instead of uniformly along the crest. In this case, the problem is more complex and requires a fully three-dimensional analysis. This case is more likely to happen in reality, as the height of the dyke's crest is not uniform due to settlement from construction procedures, consolidation and creep, or even from aging effects. Water will tend to overflow first through the lower sections in the crest, therefore, these sections act as notches to confine and channel the flow during the initial stages of overflow (Figures 2.9 and 2.10).

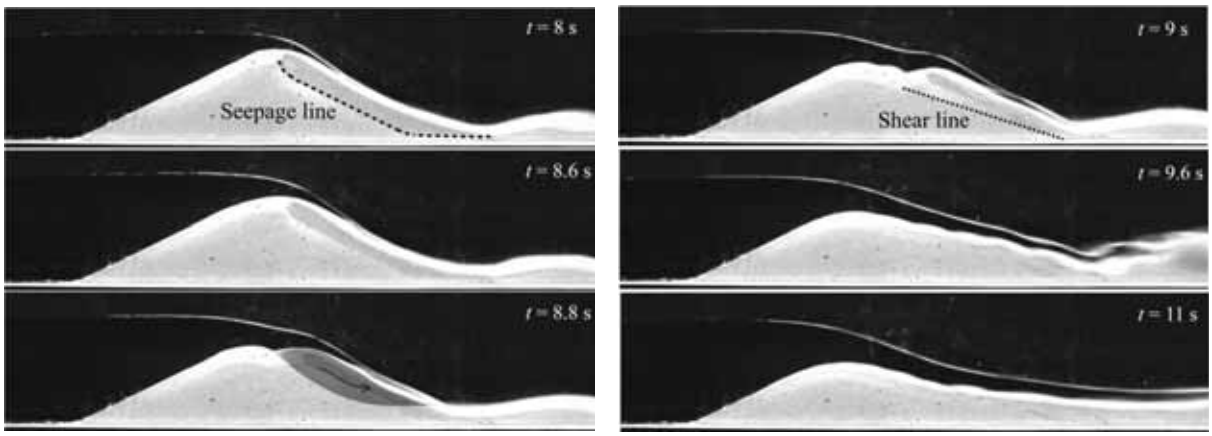

Figure 2.8: Seepage line during overflow of a model sand dyke of original height 0.2 m in a flume (after Schmocker, 2011).

Based on field tests, Visser (1998) described the breaching mechanism of a dyke built with sand in five stages (Figure 2.10):

1) Steepening of the slope angle of the channel towards the water-side from a value β (Figure 2.9) at $t = t_0$ up to a critical value β_0 at $t = t_1$.
2) Retrograde erosion of the inner slope at constant angle β_1 (Figure 2.10) for $t_1 < t < t_2$. This increases the width of the breach. The stage finishes at t_2, when the breach inflow starts to increase.
3) Lowering of the top of the dyke in the breach, with constant angle of the breach side-slopes, resulting in an increase of the width of the breach for $t_2 < t < t_3$. The dyke in the breach is completely washed out to the base of the dyke at polder level at t_3.
4) Critical flow stage, in which the breach flow is critical throughout the breach for $t_3 < t < t_4$, and the breach continues to grow laterally. The flow through the breach changes from critical to subcritical at t_4.
5) Subcritical flow stage is reached, in which the breach continues to grow, mainly laterally, due to subcritical flow in the breach for $t_4 < t < t_5$. The flow velocities in the breach become so small at t_5 that the breach erosion stops.

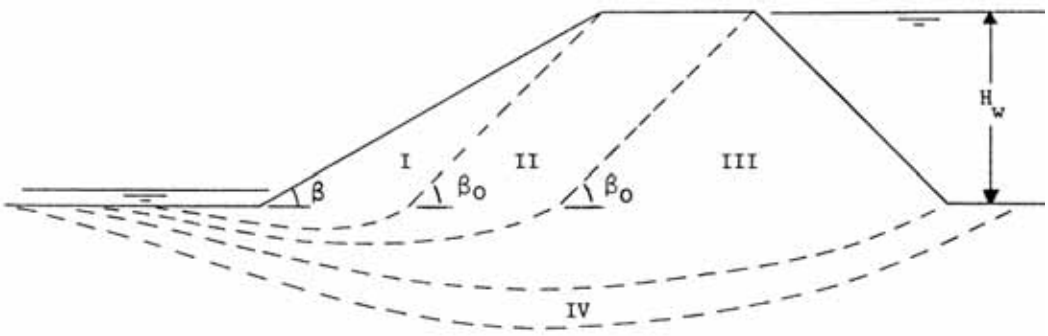

Figure 2.9: Four stages in the process of breach erosion (after Visser et al., 1990).

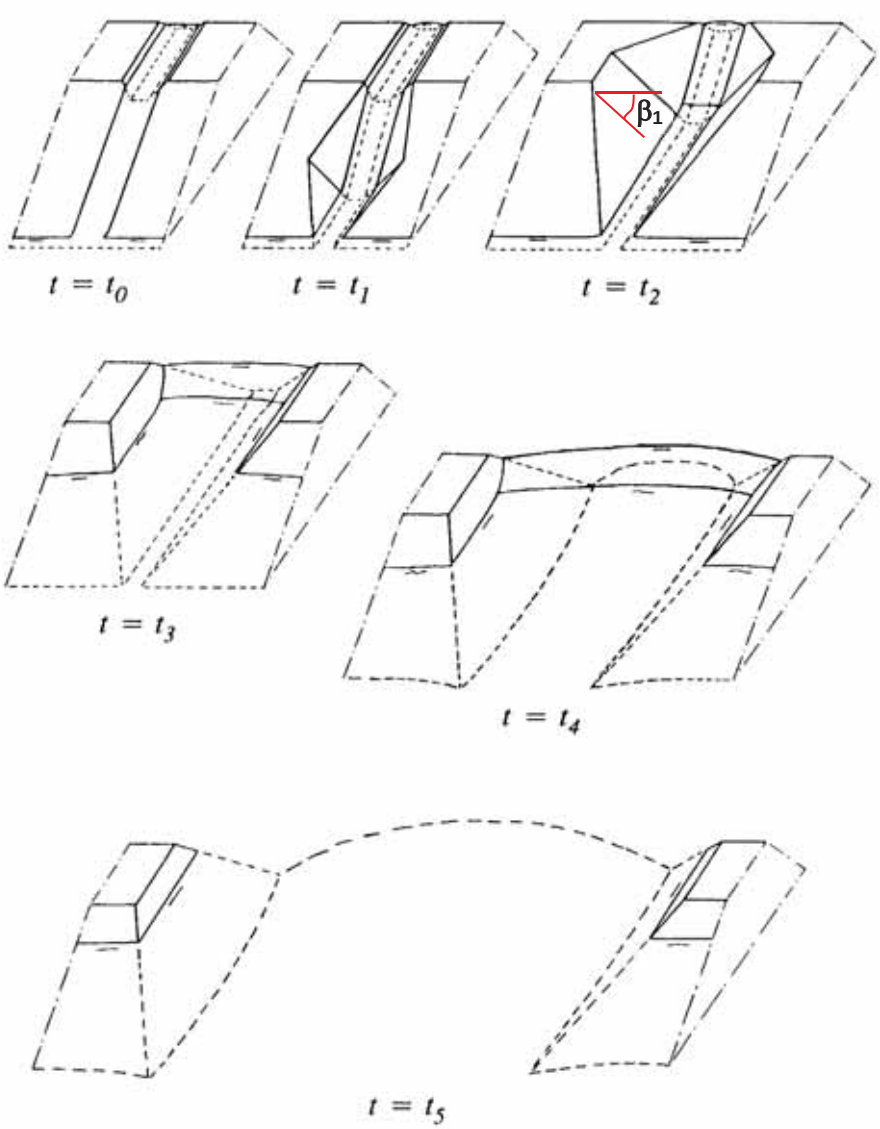

Figure 2.10: Breaching development of a sand dyke with the initial overflow focused on a channel (after Visser, 1998).

The description of these failure mechanisms is useful for risk assessment and management. However, they describe the breaching of a homogeneous dyke. Furthermore, understanding of the breaching mechanism of structures including different protection measures, such as cut-off walls, still missing. This gap in the knowledge acquires greater relevance when two or more protective measures are used in the same dyke.

2.2 Basic information about unsaturated soil mechanics

Dykes subjected to transient water conditions exhibit a varying water table across the body of the dyke. This has a consequence that some parts of the soil will be fully saturated, whereas other portions of the soil are completely dry (Figure 2.11). There is, however, an intermediate state, in which the soil is in a partially saturated condition. This soil is usually known as *unsaturated soil*, and there are several dedicated frameworks to describe its mechanical behav-

ior and flow characteristics. This section is devoted to describing the mathematical formulations to model this behavior, as they provide the basis for a better understanding of the problem.

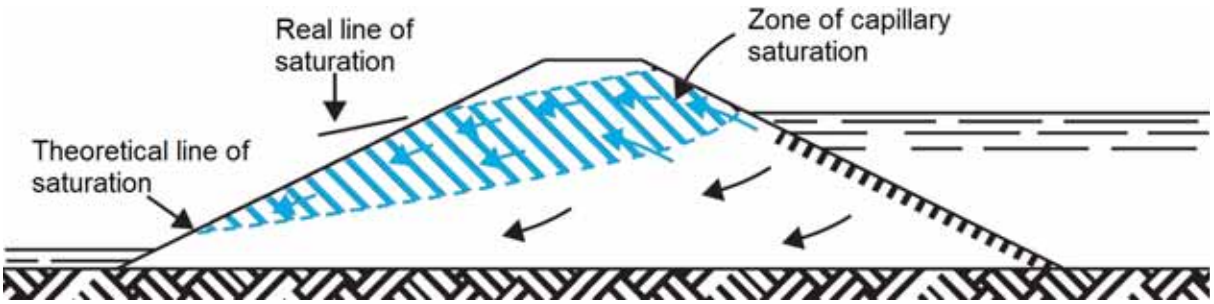

Figure 2.11: A dyke illustrating the flow of water above the theoretical phreatic line through the capillary zone (Terzaghi, 1943).

An unsaturated soil is commonly defined as a three-phase material, comprising soil solids, water, and air (Terzaghi, 1943; Fredlund & Rahardjo, 1993; Porras Ortiz, 2004). The presence of even the smallest amount of free air, e.g. occluded air bubbles, renders a soil unsaturated (Fredlund et al., 2012).

Figure 2.12 illustrates typical soil conditions, where S_r is the degree of saturation and u_w is the pore water pressure. The soil is saturated below the water table and the water pressures are positive. The zone immediately above the water table is known as the capillary zone. This zone is essentially saturated, having negative pore water pressures. The soil above the capillary zone desaturates with increasing height above the water table until it is completely dry.

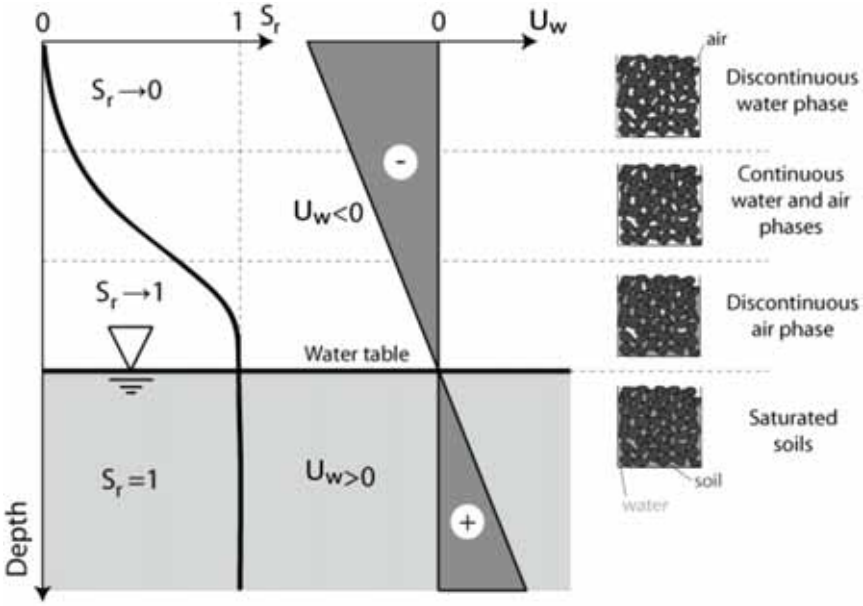

Figure 2.12: Schematic representation of the saturation phases in a soil profile with a ground water table below the surface (after Nuth, 2009).

The remaining water in an unsaturated soil is mostly found near the contact points between grains, as shown in Figure 2.13. The water interface is concave due to tension forces and the wetting angle Ω, creating menisci between the soil grains. The pressure on both sides of the water surface must be equal, as the system is in equilibrium. Inside the meniscus, the pressure is equal to the water pressure u_w, while it is equal to the gas pressure, generally air (u_a) outside the meniscus. The difference in pressure S is defined as *matric suction* (Equation 2.1).

$$\textit{Matric suction (S)} = u_a - u_w \qquad 2.1$$

One of the major characteristics of unsaturated soils is their susceptibility to volume change. Heaving and wetting collapse are the most typical problems in this respect (Fredlund & Rahardjo, 1993). Both refer to the behavior of the soil due to a wetting process at a constant mechanical load. The former implies an increase in the total volume of the soil, whereas the latter leads to a decrease. Heaving is a typical response to wetting for expansive soils, causing severe structural damage to structures and economic detriment to society (Fredlund & Rahardjo, 1993; Abed, 2008).

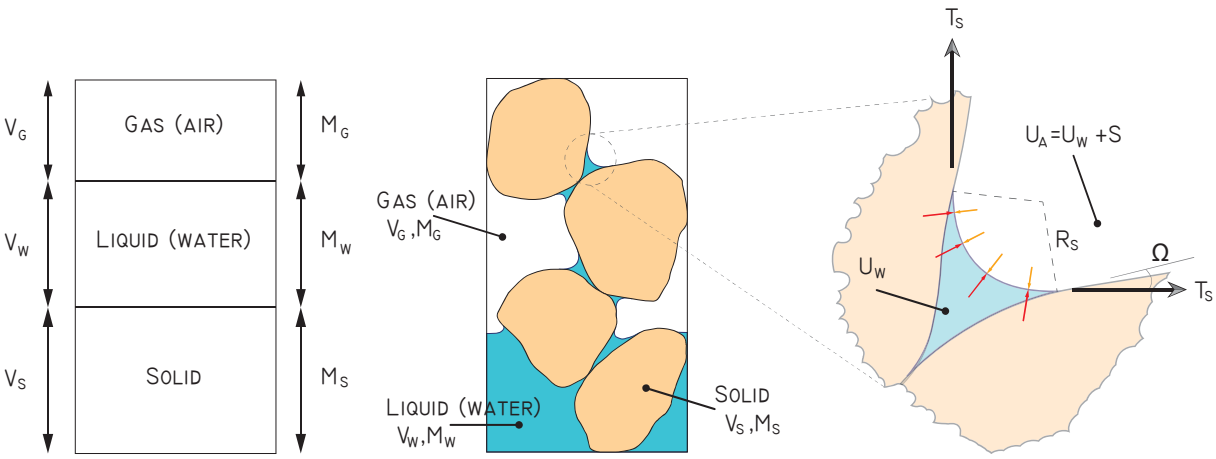

Figure 2.13: Phase diagram of an elementary volume of unsaturated soil illustrating the tension forces developed in the meniscus of water between grains (based on Fredlund & Rahardjo, 1993; Nuth, 2009).

Wetting collapse is found in soils with an open structure, which might have formed due to the natural depositional processes or the compaction method, or completely independent of either of them. A reduction in suction (wetting) for a given confining stress may induce an irrecoverable volumetric compression (collapse) (Alonso et al., 1990). This is shown in Figure 2.14a, in which, a schematic granular soil is represented by circular grains, whose open structure is maintained by the tensile forces of the water menisci. The structure collapses, after soaking the soil, causing a sudden change in the volume. The results of an oedometer test are presented in Figure 2.14b, in which collapse is seen as a vertical line at constant σ_v' in the σ_v'– e plane.

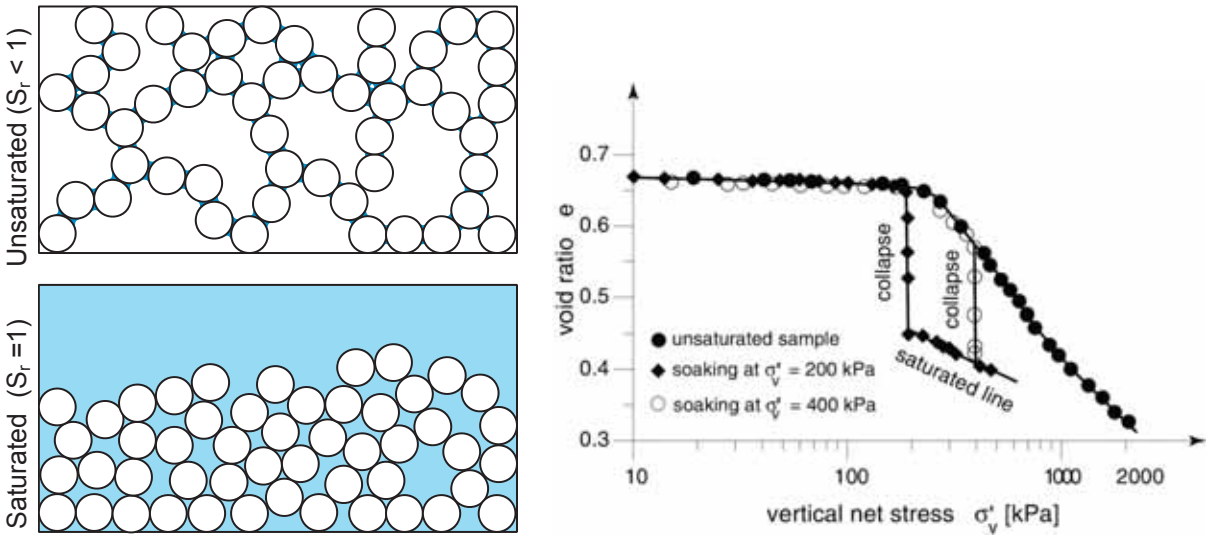

a) Schematic representation. *b) Oedometer test (after Abed, 2008).*

Figure 2.14: Wetting collapse of soils.

2.2.1 Mechanical behavior

The mechanical behavior of a soil can be represented mathematically by a constitutive model. This expression describes the relationship between stresses, strains, and state variables. The latter describe the physical conditions of the soil at some specific moment. In soils these state variables might be water pressure, void ratio, and degree of saturation. The constitutive models for unsaturated soils were built on top of the knowledge acquired and through earlier studies in soil physics (e.g. Forchheimer, 1901; Buckingham, 1907; Kozeny, 1927) during the development of models for fully saturated soils. Therefore, a brief description of the latter is given before going in detail into the former.

2.2.1.1 Constitutive modeling for saturated soils

According to Potts et al. (2002), there are three generations of constitutive models for saturated soils. The first generation covers the analysis up to the decade of the 70s, in which the use of computers and the Finite Element Method (FEM) allowed advanced models to be used. The first model was based on linear elasticity. The behavior of the soil is characterized by 2 parameters *E* (Young's modulus), and ν (Poisson's ratio). This model is represented in Equation 2.2, where ε are the strains, σ are the stresses, and *C* is a proportionality tensor known as *compliance matrix*. The main drawback is that linear elasticity does not reproduce important features of soil behavior as volume changes.

$$\varepsilon_{ij} = C_{ijkl} \cdot \sigma_{kl} \qquad 2.2$$

$$\begin{bmatrix} \varepsilon_{xx} \\ \varepsilon_{yy} \\ \varepsilon_{zz} \\ \varepsilon_{yz} \\ \varepsilon_{zx} \\ \varepsilon_{xy} \end{bmatrix} = \frac{1}{E} \begin{bmatrix} 1 & -\nu & -\nu & 0 & 0 & 0 \\ -\nu & 1 & -\nu & 0 & 0 & 0 \\ -\nu & -\nu & 1 & 0 & 0 & 0 \\ 0 & 0 & 0 & 1+\nu & 0 & 0 \\ 0 & 0 & 0 & 0 & 1+\nu & 0 \\ 0 & 0 & 0 & 0 & 0 & 1+\nu \end{bmatrix} \begin{bmatrix} \sigma_{xx} \\ \sigma_{yy} \\ \sigma_{zz} \\ \sigma_{yz} \\ \sigma_{zx} \\ \sigma_{xy} \end{bmatrix} \qquad 2.3$$

The goal of a second type of constitutive models was to include non-linearity into the elastic models. A popular model was proposed originally by Kondner (1963), which uses a hyperbola to fit the non-linear relationship between shear stress, represented by the deviator σ_1 - σ_3, and the normal strain ε. The model also requires 2 parameters *a, b* (Figure 2.15).

A third model from the first generation takes plasticity into account, and assumes the soil to be linear elastic perfectly plastic. This means that the soil behaves as a linear model until it reaches a yield stress σ_{yi}, whereupon plastic deformations are predicted without additional load being applied (Figure 2.16). The Mohr-Coulomb failure criterion (Figure 2.17) is a model of this type, in which the relation between the normal effective stress σ' and the shear stress τ is assumed to be linear. The angle of this line is the friction angle of the soil ϕ', which is an additional parameter to E and ν. This model has a shape of a conic hexagon in the principal stress space (Figure 2.17b). In both figures the cohesion intercept is set to zero.

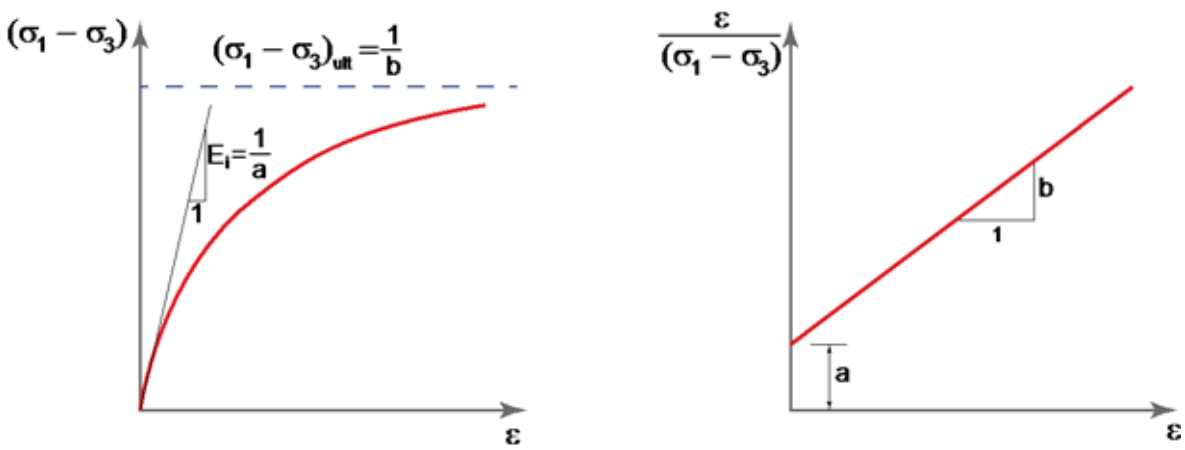

Figure 2.15: Hyperbolic linear elastic model (based on Kondner, 1963).

Figure 2.16: Stress-strain relationship for a linear elastic perfectly plastic constitutive model.

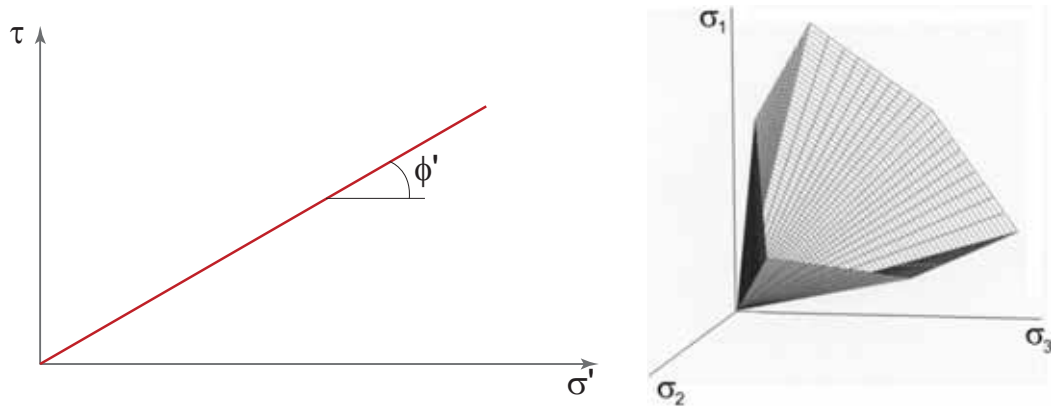

a) Normal-shear stress space. *b) Principal stresses space.*

Figure 2.17: Mohr-Coulomb constitutive model for saturated soils (adapted from Brinkgreve et al., 2011).

Although these models allow plastic deformations to be estimated, their use of associated flow rules might lead to excessive dilatancy (Potts et al., 2002). They cannot take into account the stress or deformation history. Consequently, it is not possible to differentiate between unloading and reloading paths.

These gaps led to the development of the second generation of constitutive models, which began with the inclusion of a cap to enclose the elastic compressive strain. Drucker et al. (1957) closed the fixed yield surface with a movable yield cap, as shown in Figure 2.18, where *p'* and *q* are the hydrostatic (or mean) and deviatoric stresses defined in Equations 2.4 and 2.5 for triaxial conditions.

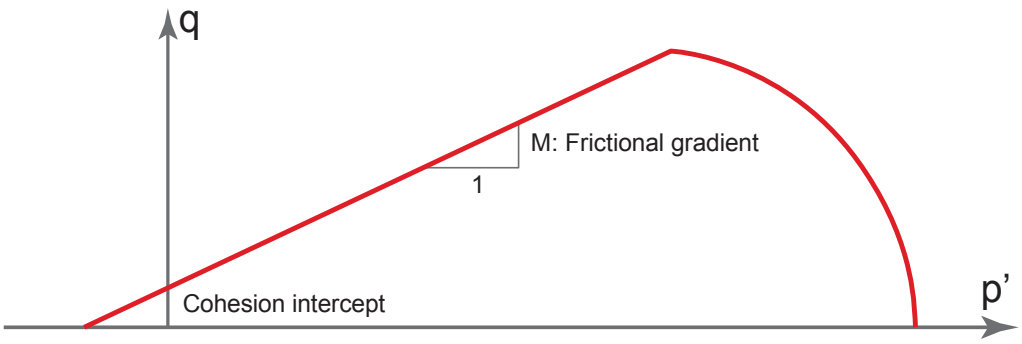

Figure 2.18: Drucker-Gibson-Henkel cone-cap model (adapted from Drucker et al., 1957).

$$p' = \frac{\sigma_1 + \sigma_2 + \sigma_3}{3} - u_w \qquad 2.4$$

$$q = \sigma_1 - \sigma_3 \qquad 2.5$$

At about the same time, Roscoe et al. (1958) presented the concept of critical state for soils, which states that if the soil is continuously distorted until it flows as a frictional fluid, it will come into a well-defined critical state and shear at constant void ratio. Roscoe & Schofield (1963) presented a model based on this concept, for which the yield locus is known as a generic Cam Clay model (e.g. Muir Wood, 2002). The yield surface f_{CC} is defined by Equation

2.6 (Figure 2.19a) for original Cam Clay. A modification to this model was presented by Roscoe & Burland (1968) and is known as Modified Cam Clay. The yield surface for this model f_{MCC} is defined by Equation 2.7, and it is an ellipse in the p' - q space (Figure 2.19b).

M is defined as the slope of the critical state line (CSL) in the p' - q space. The CSL is, in fact, a three dimensional curve in the p' - q - v space, which intercepts the top of the ellipses (Figure 2.19d). The specific volume v is defined as v = $1 + e$, where e is the void ratio. The projection of the CSL on the p' – q and $ln\ p'$ - v planes results in a straight line (Figure 2.19a-c). M is related to the effective friction angle ϕ'_{crit}, at the critical state, estimated from triaxial tests, as described by Equations 2.8 (triaxial compression) and 2.9 (triaxial extension). The preconsolidation mean isotropic effective stress p'_c defines the size of the yield surface. The interception of the elliptical yield surface with the plane p'_c – v results in a two-dimensional curve known as the Normal Consolidation Line (NCL). The CSL and the NCL are straight and parallel lines with an inclination λ in the $ln\ p'$ – v plane.

Figure 2.19c illustrates how the deformations for stress conditions inside the yield surface ($p' \leq p'_c$) are elastic and follow the unloading-reloading path (U-R) with an inclination κ (Equation 2.10). The specific volume follows the NCL when the stress conditions exceed the preconsolidation stress ($p' > p'_c$), and then the soil is normally consolidated (Equation 2.11). In the latter case, the preconsolidation stress is set as the maximum mean isotropic effective stress applied. Γ is the specific volume when the CSL is extended to a reference pressure of 1 kPa, whereas v_κ is the specific volume of the extension of a specific unloading-reloading path to a mean stress value p' = 1 kPa. Therefore, Γ is constant (and a parameter of the model), whereas v_κ changes according the stress history applied to the soil.

The advantage of these models was that they could simulate both shearing and consolidation. They could also account for the soil stress history and changes in volume due to loading-unloading-reloading cycles. However, this second generation of constitutive models failed to replicate some specific features of soil behavior observed from laboratory tests, among others, the increase of shear strength with matric suction. This led to the development of the third generation of constitutive models, which includes the modeling of unsaturated soils.

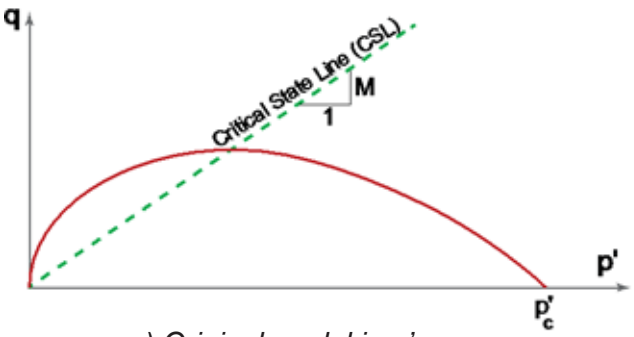

a) Original model in p'-q space.

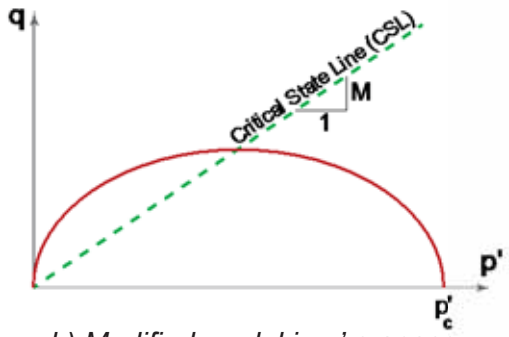

b) Modified model in p'-q space.

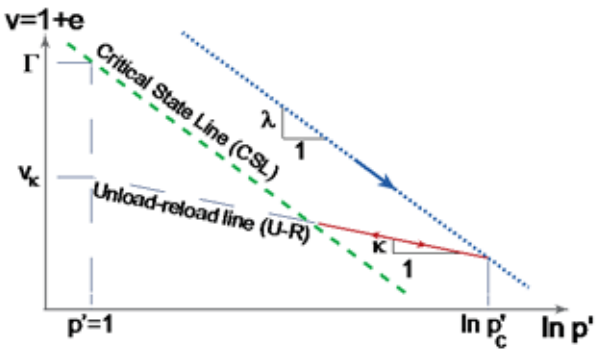

c) Model in ln p'- v space.

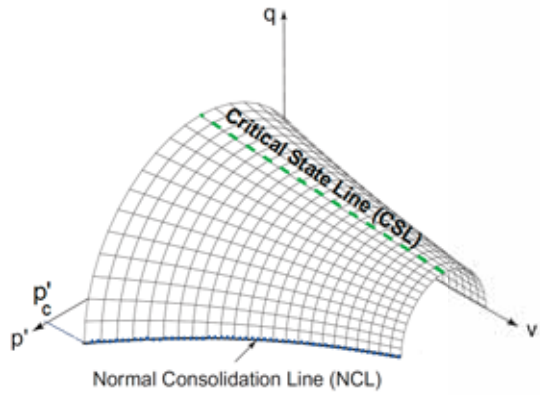

d) Modified model in p'-q-v space.

Figure 2.19: Original and modified Cam Clay models.

$$f_{CC} = q + M \cdot p' \cdot \left[\frac{p'}{p'_c} \right] \leq 0 \qquad 2.6$$

$$f_{MCC} = \left[\frac{q}{M} \right]^2 + p' \cdot \left[p' - p'_c \right] \leq 0 \qquad 2.7$$

$$M_{COMP} = \frac{6 \cdot \sin \phi'_{crit}}{3 - \sin \phi'_{crit}} \qquad 2.8$$

$$M_{EXT} = \frac{-6 \cdot \sin \phi'_{crit}}{3 + \sin \phi'_{crit}} \qquad 2.9$$

$$\mathrm{v}_{U-R} = \mathrm{v}_{\kappa} - \kappa \cdot \ln p' \qquad 2.10$$

$$\mathrm{v}_{NCL} = \Gamma - \lambda \cdot \ln p' \qquad 2.11$$

2.2.1.2 Stress variable for the constitutive modeling of unsaturated soils

The mechanical behavior of saturated soils is dependent on the effective stresses, whose general expression is given by Equation 2.12, where σ'_{ij} is the *ij* component of the effective stress tensor, σ_{ij} is the *ij* component of the total stress tensor, α is a weighting function, u_w is the pore water pressure, and δ_{ij} is Kronecker's delta ($\delta_{ii} = 1$, $\delta_{i \neq j} = 0$). In Terzaghi's effective stress definition (Terzaghi, 1925), $\alpha = 1$. A detailed description of different definitions of the effective stresses for saturated soil is found in Nuth & Laloui (2008b) and Nuth (2009).

$$\sigma'_{ij} = \sigma_{ij} - \alpha \cdot u_w \cdot \delta_{ij} \qquad 2.12$$

However, there is no consensus on which stress variable has to be used for unsaturated soils. Bishop (1959) presented an extension of Terzaghi's effective stress by exchanging the water pressure u_w for an equivalent pore pressure, which may be considered as that portion of the effective stress in a soil resulting from the pressure of all fluids in the pores (Nuth, 2009).

Defining u_a as the interstitial air pressure, and u_w as the pore water pressure, Bishop's effective stress can be expressed as Equation 2.13, where χ is called the effective stress parameter or Bishop's parameter, $(\sigma_{ij} - u_a\delta_{ij})$ is known as net stress and $(u_a - u_w)$ is the matric suction.

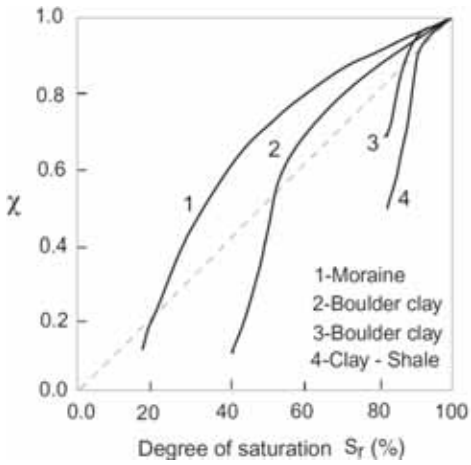

Figure 2.20: The factor χ plotted as a function of the degree of saturation S_r (after Fredlund & Rahardjo, 1993).

$$\sigma'_{ij} = \left(\sigma_{ij} - u_a \cdot \delta_{ij}\right) + \chi \cdot \left(u_a - u_w\right) \cdot \delta_{ij} \qquad 2.13$$

The parameter χ was originally thought to be related to the degree of saturation, ranging from 0 to 1, as shown in Figure 2.20. However, it was found that the parameter was different when it was determined either for volume change or for shear strength. Bishop's effective stress also seemed to have difficulties in explaining the wetting collapse condition. As a consequence, Burland (1964) proposed that the mechanical behavior of unsaturated soils should be treated by considering net stress and suction separately.

This process led to the acceptance of two independent stress measures in unsaturated soil mechanics by many researchers. Fredlund & Morgenstern (1977) concluded that any combination of the following pairs can be used to describe the stress state:

$$\begin{aligned} &(\sigma - u_a) \text{ and } (u_a - u_w) \\ &(\sigma - u_w) \text{ and } (u_a - u_w) \\ &(\sigma - u_a) \text{ and } (\sigma - u_w) \end{aligned} \qquad 2.14$$

Nevertheless, recent studies have proposed not to express the parameter χ in terms of volumetric ratios (related to the degree of saturation). For instance, Khalili & Khabbaz (1998) and Khalili et al. (2004) proposed that the parameter should be expressed in terms of the matric suction and the air entry value (AEV) (Equation 2.15).

$$\chi = \left(\frac{u_a - u_w}{AEV} \right)^{-0.55} \qquad 2.15$$

2.2.1.3 Constitutive modeling of unsaturated soils

The discussion about which stresses should be used for modeling the mechanical behavior of unsaturated soils has resulted in two frameworks for constitutive modeling: the independent stresses approach and that depending upon Bishop's generalized effective stress. The major difference is the definition of the strain–stress relationship. The elastic strains for the generalized effective stress approach can be described in the same way as for saturated soils, i.e. Equation 2.2, whereas the strains are defined in Equation 2.16 for the independent stresses approach, for which, a new tensor C^s is introduced to express the proportionality between strain and suction (Abed, 2008).

$$\dot{\varepsilon}^e_{ij} = C^e_{ijhk} \cdot \left(\dot{\sigma}'_{hk} - \dot{u}_a \delta_{hk} \right) + C^s \cdot \left(\dot{u}_a - \dot{u}_w \right) \delta_{hk} \qquad 2.16$$

The main drawback of Bishop's generalized stress is that the parameter χ usually depends on soil properties, as well as on soil states, which means that the stress space is affected by multiple influences. On the other hand, the main drawbacks of the models based on the independent stresses approach are that they require two or more yield surfaces, and often they lack a simple transition from partially to fully saturated states to recover to Terzaghi's expression (Equation 2.12) for the saturated case.

According to Gens et al. (2006), one of the first elasto-plastic models designed explicitly for describing the mechanical behavior of unsaturated soils was presented by Alonso et al. (1990) in a model known today as the Barcelona Basic Model (BBM). It is based on the independent stresses approach, and uses the first pair of stresses in Equation 2.14, in which the quantity σ - u_a is known as *net stress.* The first state parameter of the model is the mean net stress p^* defined in Equation 2.17, where σ^* are the net stresses, defined in Equation 2.18.

The second state parameter is the deviator stress q (Equation 2.5). The third parameter is the matric suction S (Equation 2.1).

$$p^* = \frac{\sigma^*_1 + \sigma^*_2 + \sigma^*_3}{3} - u_a \qquad 2.17$$

$$\sigma^*_{ij} = \sigma_{ij} - u_a \qquad 2.18$$

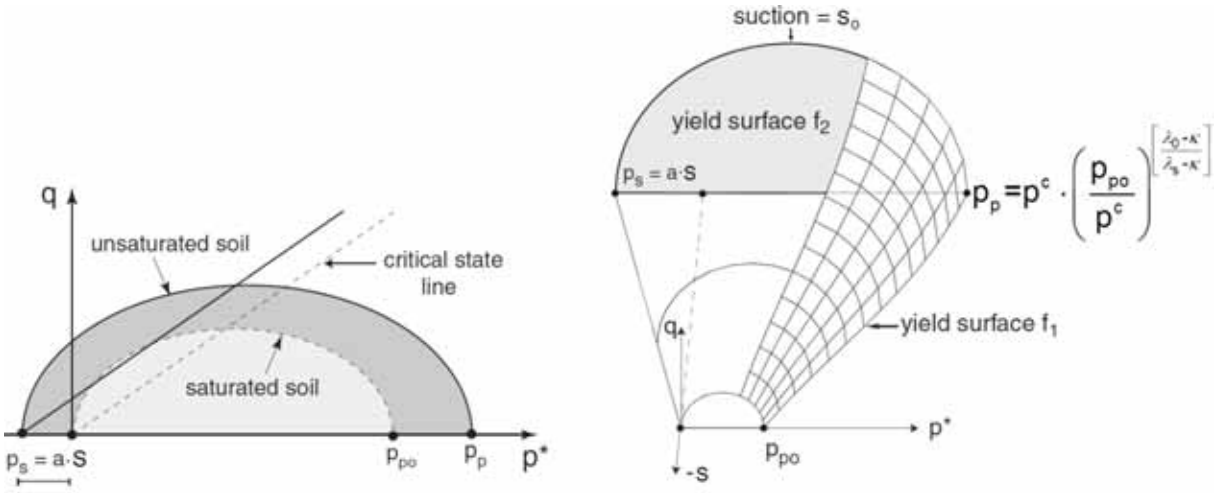

a) p - q space.* *b) p* - q - S space.*

Figure 2.21: Barcelona Basic Model (after Abed, 2008; based on the model by Alonso et al., 1990).

The model is shown in Figure 2.21. The yielding space, within the deformations are elastic, is enclosed by two yield surfaces. The first yield surface f_1 (also known as *LC: loading collapse*) is an ellipse in the p^* - q plane, which corresponds to the yield surface of the Modified Cam Clay model. The size of the ellipse increases with the matric suction to take into account both the increase in the pre-consolidation associated with increasing suction, and the wetting collapse. Additionally, the yield surface f_1 is extended by a factor p_s, which accounts for the increase in shear strength with suction due to apparent cohesion. The loading collapse yield surface can be written as:

$$f_1 = q^2 - M^2 \cdot (p^* - p_s) \cdot (p_p - p^*) \qquad 2.19$$

$$p_s = a \cdot S \qquad 2.20$$

$$a = M \cdot \frac{\tan \phi^b}{\tan \phi'} \qquad 2.21$$

Where M is the slope of the critical state line (CSL). The parameter a is defined in Equation 2.21, where ϕ^b is the friction angle with respect to change in suction (Fredlund et al., 1978), and is determined from suction controlled direct shear tests, in which the samples are sheared under a constant vertical net stress, but at different matric suctions. The slope of the straight line fitting the failure points determines the angle ϕ^b.

$$p_p = p^c \cdot \left(\frac{p_{po}}{p^c} \right)^{\left[\frac{\lambda_0 - \kappa}{\lambda_s - \kappa} \right]} \qquad 2.22$$

$$\lambda_s = \lambda_\infty - \left(\lambda_\infty - \lambda_o \right) \cdot e^{-\beta \cdot S} \qquad 2.23$$

The parameter p_p also determines the size of the ellipse and is estimated from Equation 2.22, where p^c is a reference pressure. The parameter λ_s represents the stiffness increase with suction, where λ_∞ represents soil stiffness at very high suction and β is a factor controlling the rate of stiffness increase with suction. The stiffness at no suction, i.e. saturated soil, is λ_0, which corresponds to the parameter λ in the Cam Clay models. According to Abed (2008), the best way to determine p^c and λ_∞, is by back analyzing laboratory data from suction controlled triaxial tests, and fitting them to Equations 2.22 and 2.23.

The BBM requires a second yield surface f_2 (also known as *SI: suction increase*). This is represented as a vertical plane in the p^* - q - S space (Figure 2.21b) (Equation 2.24), and it is related to the plastic volumetric strains that occur due to a suction increase. The BBM assumes that whenever the soil reaches a maximum previously attained value of the suction S_{max} irreversible strains will begin to develop (Alonso et al., 1990).

$$f_2 = S_{\max} \qquad 2.24$$

A new generation of constitutive models has been developed using Bishop's generalized stress. Most of them are formulated within the elasto-plastic framework, whereas others rely on hypoplasticity (Vaunat et al., 2000; Laloui & Nuth, 2005; Russell & Khalili, 2005; Mašín & Khalili, 2008; Nuth, 2009). The model proposed by Laloui & Nuth (2005) and Nuth (2009) is presented in Figure 2.22, as an example. This model has a yield surface, which in the p' – q plane is the same as the original Cam-Clay model (Roscoe & Schofield, 1963) (Figure 2.19a). A loading collapse (LC) curve on the p' – S plane, which can be projected vertically along the q axis, cuts the original Cam Clay (OCC) yield surface (Figure 2.22).

Sheng & Fredlund (2008) conclude that the increment p_s in BBM, and the consequent shift of the CSL (Figure 2.21a), is a simple consequence of the use of net or effective stresses in the formulation of the constitutive model, as shown in Figure 2.23, where the elastic region of those models based on Bishop's generalized stress is bounded by a line $p' = 0$ kPa.

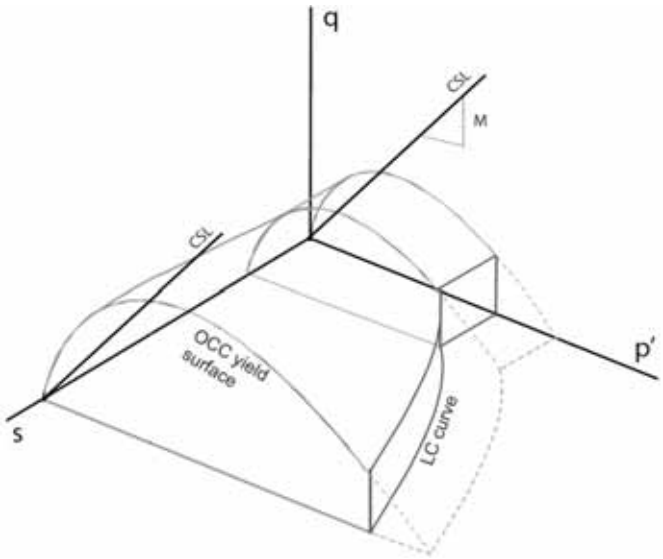

Figure 2.22: Advanced constitutive model for environmental geomechanics with unsaturated extension (ACMEG-s) proposed by Laloui & Nuth (2005).

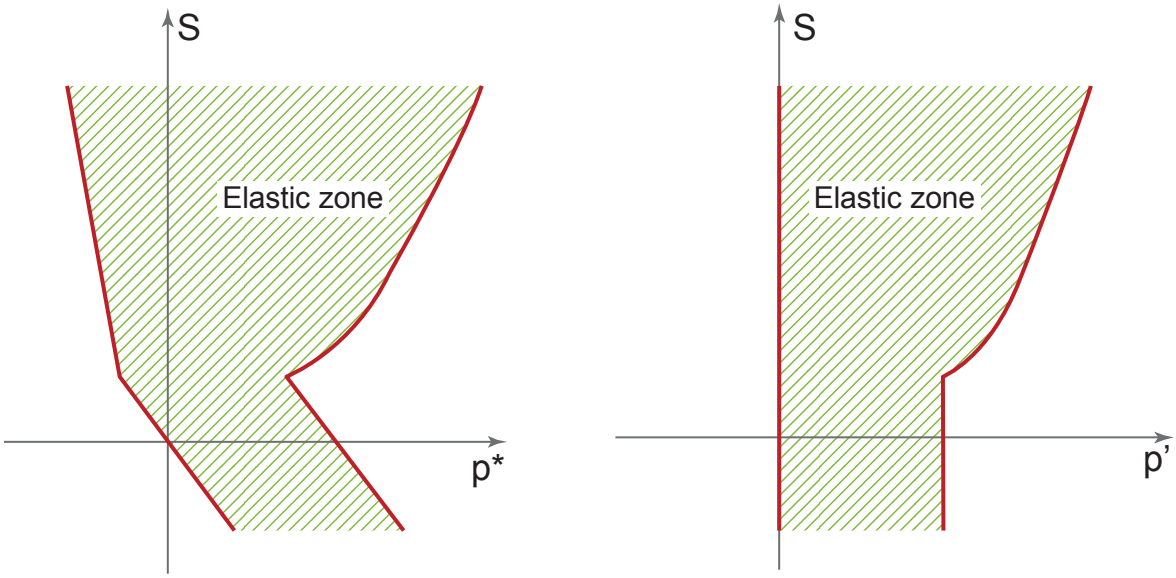

a) Mean net stress (p) vs matric suction.* *b) Effective mean stress (p') vs matric suction.*

Figure 2.23: Schematic view of loading-collapse yield surface (adapted from Sheng & Fredlund, 2008).

2.2.2 Groundwater flow behavior

2.2.2.1 Governing equation

Darcy's law, as derived from the Navier-Stokes equations, is written as shown by Equation 2.25. In these equations, ***Q*** is the vector of the volume of water crossing a unit area perpendicular to the flow per unit of time in rectangular coordinates, ***K*** is the vector of the hydraulic conductivity in rectangular coordinates**,** *p* is the pressure (either positive or negative), ρ is the liquid density, ***i*** is the unitary vector of the Cartesian coordinates, *g* is the gravity, ϕ is the

potential *gz*, where *z* is the height from a reference level, and ψ is a potential defined as $\int dp / p$. The equation can be extended to Cartesian coordinates and is given by Equation 2.26.

$$\boldsymbol{Q} = -\boldsymbol{K} \cdot \nabla \left(g \cdot \boldsymbol{i} + \frac{\nabla p}{\rho} \right) = -\boldsymbol{K} \cdot \nabla \left(\phi + \psi \right) \qquad 2.25$$

$$\boldsymbol{Q} = -\left[K_x \cdot \frac{\partial(\phi+\psi)}{\partial x} + K_y \cdot \frac{\partial(\phi+\psi)}{\partial y} + K_z \cdot \frac{\partial(\phi+\psi)}{\partial z} \right] \qquad 2.26$$

Darcy's law applies exclusively to flow in saturated porous media. However, Richards (1931) used the equation of continuity for capillary flow (Equation 2.27) to extend its use to unsaturated states by formulating a new partial differential equation for both saturated and unsaturated flow.

$$\nabla \cdot q = \rho_s \frac{\partial \theta}{\partial t} = \rho_s \frac{d\theta}{d\psi} \frac{\partial \psi}{\partial t} \qquad 2.27$$

The volumetric water content is represented by θ. Richards assumed a flow in the *z* direction, and developed the equation consequently. Here, and for sake of generality, the expression for fully three-dimensional flow is developed. Substituting Equation 2.26 into 2.27:

$$\begin{aligned} &\frac{\partial K_x}{\partial x} \frac{\partial(\phi+\psi)}{\partial x} + K_x \frac{\partial^2(\phi+\psi)}{\partial x^2} + \frac{\partial K_y}{\partial y} \frac{\partial(\phi+\psi)}{\partial y} + K_y \frac{\partial^2(\phi+\psi)}{\partial y^2} + \\ &\qquad + \frac{\partial K_z}{\partial z} \frac{\partial(\phi+\psi)}{\partial z} + K_z \frac{\partial^2(\phi+\psi)}{\partial z^2} = \rho_s \frac{d\theta}{d\psi} \frac{\partial \psi}{\partial t} \end{aligned} \qquad 2.28$$

And reorganizing terms:

$$\begin{aligned} &K_x \frac{\partial^2(\phi+\psi)}{\partial x^2} + K_y \frac{\partial^2(\phi+\psi)}{\partial y^2} + K_z \frac{\partial^2(\phi+\psi)}{\partial z^2} + \frac{\partial K_x}{\partial x} \frac{\partial(\phi+\psi)}{\partial x} + \\ &\qquad + \frac{\partial K_y}{\partial y} \frac{\partial(\phi+\psi)}{\partial y} + \frac{\partial K_z}{\partial z} \frac{\partial(\phi+\psi)}{\partial z} = \rho_s \frac{d\theta}{d\psi} \frac{\partial \psi}{\partial t} \end{aligned} \qquad 2.29$$

Splitting the derivatives of the sums:

$$\begin{aligned} &K_x \left(\cancel{\frac{\partial^2(\phi)}{\partial x^2}} + \frac{\partial^2(\psi)}{\partial x^2} \right) + K_y \left(\cancel{\frac{\partial^2(\phi)}{\partial y^2}} + \frac{\partial^2(\psi)}{\partial y^2} \right) + K_z \left(\cancel{\frac{\partial^2(\phi)}{\partial z^2}} + \frac{\partial^2(\psi)}{\partial z^2} \right) + \frac{\partial K_x}{\partial x} \frac{\partial(\phi)}{\partial x} + \\ &\qquad + \frac{\partial K_x}{\partial x} \frac{\partial(\psi)}{\partial x} + \frac{\partial K_y}{\partial y} \frac{\partial(\phi)}{\partial y} + \frac{\partial K_y}{\partial y} \frac{\partial(\psi)}{\partial y} + \frac{\partial K_z}{\partial z} \frac{\partial(\phi)}{\partial z} + \frac{\partial K_z}{\partial z} \frac{\partial(\psi)}{\partial z} = \rho_s \frac{d\theta}{d\psi} \frac{\partial \psi}{\partial t} \end{aligned} \qquad 2.30$$

As the function ϕ is defined as the multiplication of a scalar and a vector, its second derivatives will be null. Reorganizing terms again:

$$K_x\left(\frac{\partial^2(\psi)}{\partial x^2}\right)+K_y\left(\frac{\partial^2(\psi)}{\partial y^2}\right)+K_z\left(\frac{\partial^2(\psi)}{\partial z^2}\right)+\frac{\partial K_x}{\partial x}\frac{\partial(\psi)}{\partial x}+\frac{\partial K_y}{\partial y}\frac{\partial(\psi)}{\partial y}+\frac{\partial K_z}{\partial z}\frac{\partial(\psi)}{\partial z}+ \\ +\frac{\partial K_x}{\partial x}\frac{\partial(\phi)}{\partial x}+\frac{\partial K_y}{\partial y}\frac{\partial(\phi)}{\partial y}+\frac{\partial K_z}{\partial z}\frac{\partial(\phi)}{\partial z}=\rho_s\frac{d\theta}{d\psi}\frac{\partial\psi}{\partial t} \qquad 2.31$$

This can be rewritten as:

$$\boxed{\mathrm{K}\cdot\nabla^2\psi+\nabla\mathrm{K}\cdot\nabla\psi+\nabla\mathrm{K}\cdot\nabla\phi=\rho_s\frac{d\theta}{d\psi}\frac{\partial\psi}{\partial t}} \qquad 2.32$$

This emphasizes θ and ψ as the major state variables to analyze groundwater flow in unsaturated media. Therefore, a description of the methods required to determine them is given below. Additional information regarding the relationship $d\theta/d\psi$, commonly known as the Soil Water Retention Curve (SWRC), and the methods to determine it, is given in Sections 2.2.2.4 and 2.2.2.5. The hydraulic conductivity ***K*** can be also expressed as a function of the matric suction, as explained in Section 2.2.2.6.

2.2.2.2 Measurement of the matric suction

Matric suction can be measured either in a direct, or an indirect manner. Direct methods measure the negative pore water pressure; whereas indirect methods measure another variable and the matric suction is obtained after calibration of the sensor. A high entry value (HAE) ceramic disk is used to separate air and water pressures when direct measurements are made. Pan et al. (2010) and Fredlund et al. (2012) present a comprehensive description of the methods adopted to measure matric suction. These are summarized in Figure 2.24 and described below.

- $(u_a\text{-}u_b)$ measurement
  - Direct methods
    - Tensiometer
      - Simple (< 80 kPa)
      - Jet-fill (< 85 kPa)
      - High suction (< 1350 kPa)
      - Small-tip (< 80 kPa)
    - Axis translation (< 1500 kPa)
  - Indirect methods
    - Electrical resistance sensors (< 1500 kPa)
    - Thermal conductivity sensors (< 1500 kPa)

Figure 2.24: Summary of techniques adopted to measure the matric suction in a soil (based on Fredlund et al., 2012).

Direct methods

Simple tensiometers consist of a HAE, porous ceramic filter, connected to a pressure measuring device through a small-bore tube. The improved version, which is used in practice today, is known as a jet-fill tensiometer (Figure 2.25a), which has a water reservoir at the top.

The purpose of this reservoir is to be able to remove air bubbles by pressing a button that creates a vacuum.

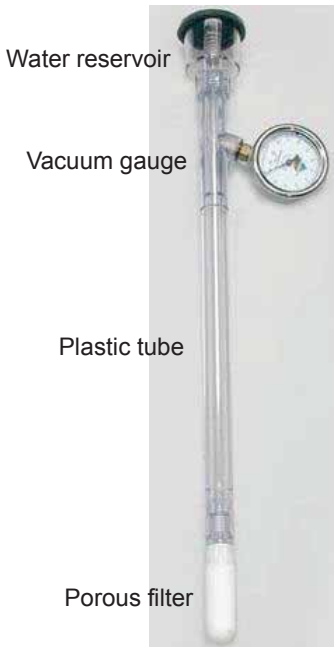

a) Jet-fill tensiometer (www.soilmoisture.com).

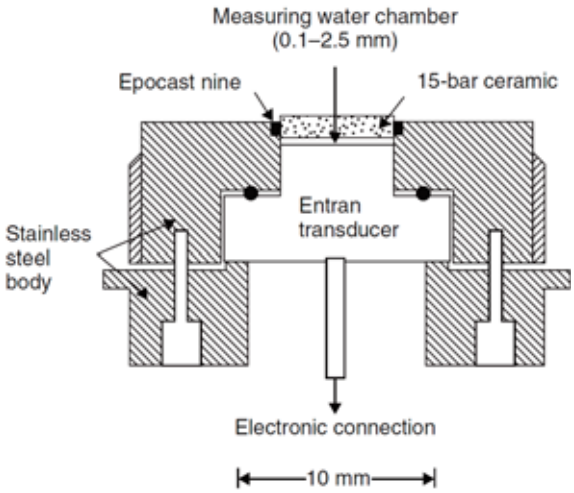

b) High suction tensiometer (after Guan, 1996).

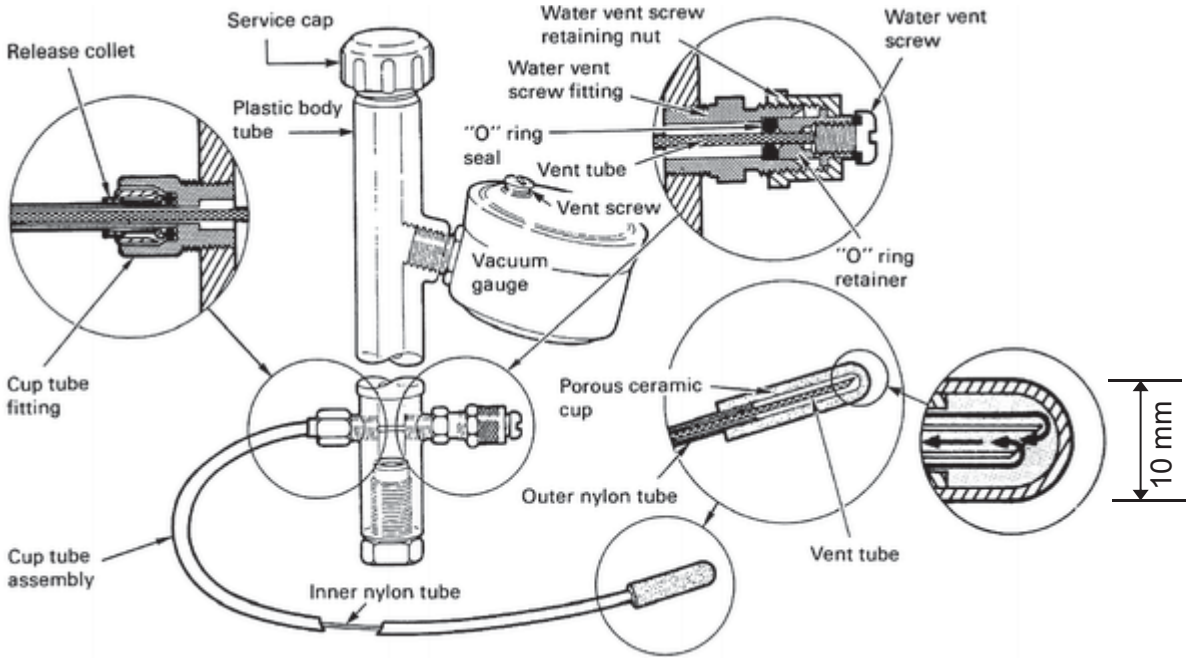

c) Small tip tensiometer (www.soilmoisture.com).

Figure 2.25: Types of tensiometers.

The high suction tensiometers (Figure 2.25b) are designed to measure suctions greater than 100 kPa and up to 1350 kPa. The ceramic filter is separated from a membrane through a water reservoir. A change in suction generates a deflection of the membrane, and this is calibrated to correspond to a suction value. These sensors are small (< 15 mm), which is an

advantage when used in small-scale models. Therefore, an extended description of these small tensiometers is given in the chapter about centrifuge modeling (cf. Section 4.2.3).

The small-tip tensiometers are similar to simple tensiometers, with the only difference being their reduced size (Figure 2.25c). They are connected to the pressure measuring device through a flexible tube instead of a stiff tube, as for simple tensiometers. These sensors have been found suitable for measuring matric suction up to 80 kPa in standard laboratory test, such as direct shear test (Askarinejad et al., 2012a; Askarinejad, 2013).

The axis-translation technique is mainly used to measure the matric suction of a soil in the laboratory (Fredlund & Rahardjo, 1993). The soil is placed inside an enclosed chamber and in contact with a saturated HAEV disk. The tendency of the water pressure in the compartment underneath the disk to become negative relative to the air pressure is counteracted by increasing the air pressure in the chamber until the pressure of the water is close to null. Then, the applied air pressure corresponds to the matric suction of the soil. This method is most often used to control suction, when investigating the mechanical and hydraulic properties of unsaturated soils for a range between 0 and 1500 kPa (Delage & Cui, 2008).

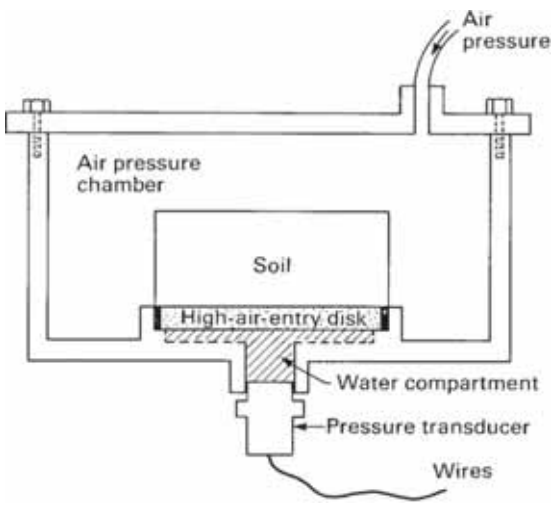

Figure 2.26: Schematic view of a laboratory setup to measure the matric suction with the use of the axis-translation technique (Fredlund & Rahardjo, 1993).

Indirect methods

Matric suction can be measured indirectly by using a porous block as a measuring sensor. It is brought to be in equilibrium with the matric suction of the soil. At this condition, both the porous block and the soil matric suctions are equal. Then the matric suction is estimated from the water content of the porous block, which is determined by measuring the electrical or thermal properties of the porous block, as these properties are a function of the water content of the porous block. Therefore, matric suction can be established through a calibration process.

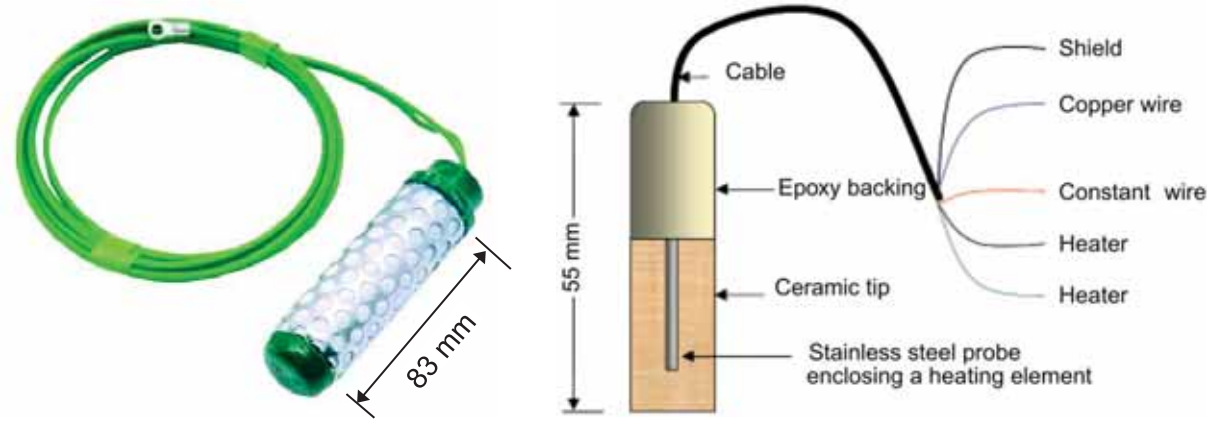

a) Electrical resistance sensor (http://www.irrometer.com).

b) Thermal conductivity sensor (after Leong et al., 2012).

Figure 2.27: Sensors for indirect measurement of matric suction.

The electrical conductivity sensor (Figure 2.27a) measures the electrical conductivity of the porous block. The electrical resistance of the block decreases, as the moisture content of the porous block increases. The main disadvantage of these sensors is that electrical resistance is highly sensitive to salts diluted in water, which modify the calibration factor. On the other hand, thermal conductivity of soils has been found not to be sensitive to the presence of diluted salts in water (Shaw & Baver, 1939). The thermal conductivity of a soil increases with increasing water content, which is, in turn, related to the matric suction. Thus, the sensors (Figure 2.27b) can be calibrated to determine the suction.

2.2.2.3 Measurement of the volumetric water content

A summary of the description by Walker (2000) of the current techniques available for measuring the volumetric water content (θ) of soils is presented in Figure 2.28. However, time domain reflectometry (TDR) and capacitance techniques are regarded as the most reliable methods for measurement of volumetric moisture content (Hanumantha-Rao & Singh, 2011). The former has been used in this research project to determine the volumetric water content of the soil in the field test and in the centrifuge modeling. Therefore, it is described in detailed below.

θ measurement
- Thermogravimetric method
- Neutron scattering method
- Gamma ray attenuation method
- Soil electrical conductivity method
  - Electrical conductivity probes
  - Electrical resistance blocks
  - Electromagnetic induction
- Tensiometer method
- Hygrometric method
- Soil dielectric method
  - Capacitance probes
  - Time domain reflectometry probes

Figure 2.28: Summary of techniques adopted to measure the volumetric water content of a soil (based on Walker, 2000).

The advantages of the TDR technique include (Walker, 2000; Hanumantha-Rao & Singh, 2011): i) the sensors can be installed at any depth and readings can be automatically and stored or transmitted, allowing easy monitoring of the soil moisture profile; ii) portability; iii) the approximately "universal" calibration curve, particularly at high soil moisture contents; and iv) the precise depth resolution when horizontally inserted sensors are used. The main disadvantages of the system include: i) the relatively small zone of influence of the TDR sensors and their sensitivity to the region immediately adjacent to the forks; ii) the sensitivity to air gaps surrounding the forks; iii) attenuation of the signal caused by salinity or highly conductive heavy clay soils; and iv) the lack of a "universal" calibration curve for heavy clay soils and at low moisture contents.

Time domain reflectometry (TDR)

The working principle of the TDR system is shown in Figure 2.29 to determine the dielectric constant, temporally, in the ground. An electromagnetic wave is propagated along the coaxial cable to a sensor, which is embedded in the soil. Part of the incident electromagnetic wave is reflected at the beginning of the sensor because of the impedance difference between the cable and the sensor. The remainder of the wave propagates through the sensor until it reaches the end of it, where the wave is reflected. The round-trip time Δt_a of the wave, from the beginning to the end of the sensor, can be measured by a sampling oscilloscope on the cable tester (Noborio, 2001).

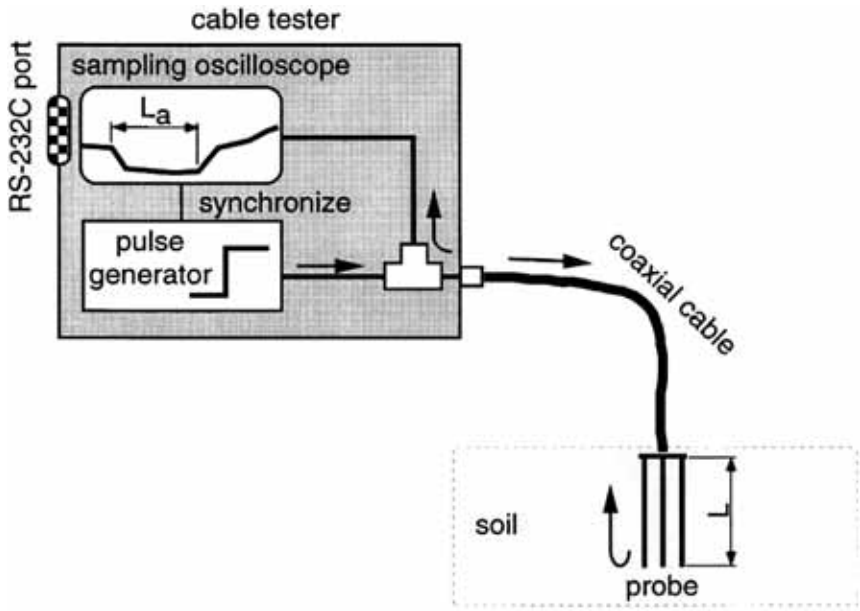

Figure 2.29: Block diagram for a TDR installed in the ground to measure water content and bulk electrical conductivity of soil. Arrows indicate directions of electromagnetic waves. L and La represent the actual sensor length and an apparent sensor length displayed on the cable tester, respectively (after Noborio, 2001).

Typical TDR sensors consist of two or three rods or forks (wires) connected to a coaxial cable (Figure 2.30). The connection is made inside a casing, generally made of epoxy. The rods are in contact with the soil over a length *L*.

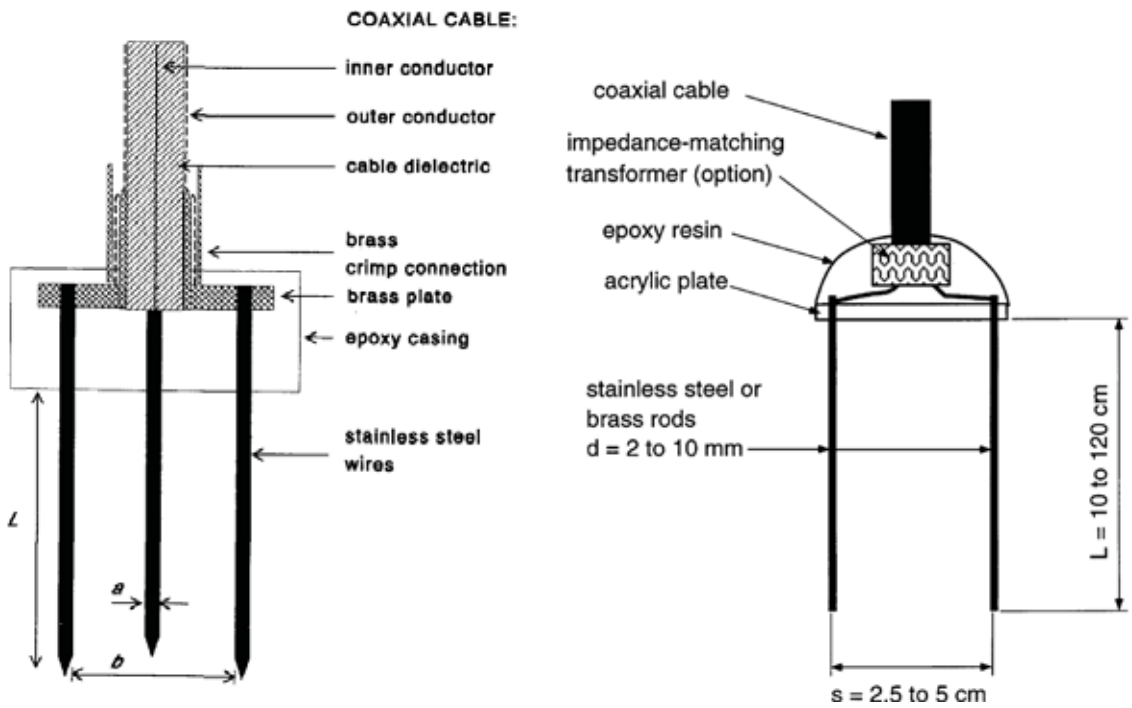

a) Triple rod coaxial sensor (after Heimovaara, 1993).

b) Double rod coaxial sensor (after Noborio, 2001).

Figure 2.30: Outline of typical TDR sensors.

Figure 2.31 is a typical waveform obtained from a sensor inserted into the soil. The point *A* represents the time at which the wave enters the epoxy casing. *B* is the point at which the wave starts traveling along the rods and *C* corresponds to the moment at which the wave is reflected from the tip of the rods. Δt_p is the total time that the wave travels in the sensor, Δt_a is the effective time that the wave travels along the rods, and Δt_o is defined as the sensor offset.

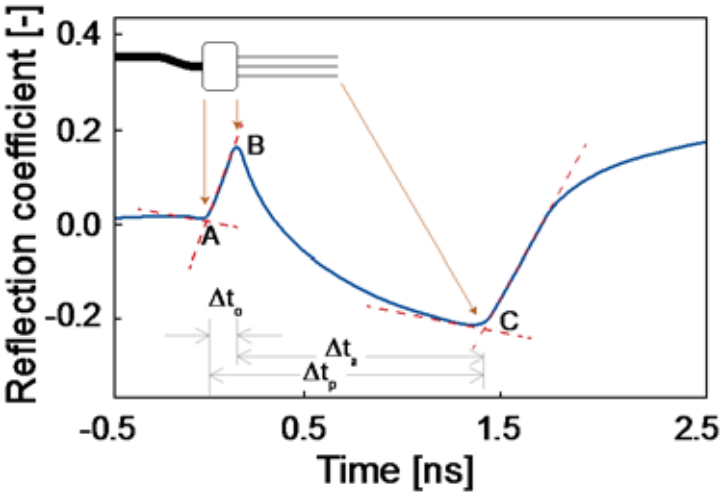

Figure 2.31: TDR waveform for a loamy sand (adapted from Heimovaara, 1993; Ekblad & Isacsson, 2007).

The evaluation of the intersection of the wave is undertaken with the double-reflection waveform analysis procedure (Heimovaara, 1993). Changes are sought in the slope of the waveform and analyzed to define the intersection points A and C.

Point *A* is not always clearly defined. The first reflection (point A in Figure 2.31) might disappear if long cables are used (Heimovaara, 1993). Also, the waveforms often did not show a clear first reflection point for different water conditions during saturation, as shown in Figure 2.32.

In a commercial TDR cable tester, the measurement is reduced to an apparent sensor length L_a displayed on the cable tester (Noborio, 2001). This apparent length (Equation 2.33) is defined from the basic time–distance expression, and assuming that v = c (Ekblad & Isacsson, 2007).

$$v = \frac{2 \cdot L}{\Delta t_a} \qquad \text{then} \qquad L_a = \frac{c \cdot \Delta t_a}{2} \qquad 2.33$$

The apparent dielectric constant (K_a) of the moist soil can be calculated according to Topp et al. (1980) and Heimovaara (1993), as indicated in Equation 2.34, where *c* is the velocity of an electromagnetic wave in free space (3×10^8 m/s), *v* is the propagation velocity in m/s and Δt_a is the elapsed time.

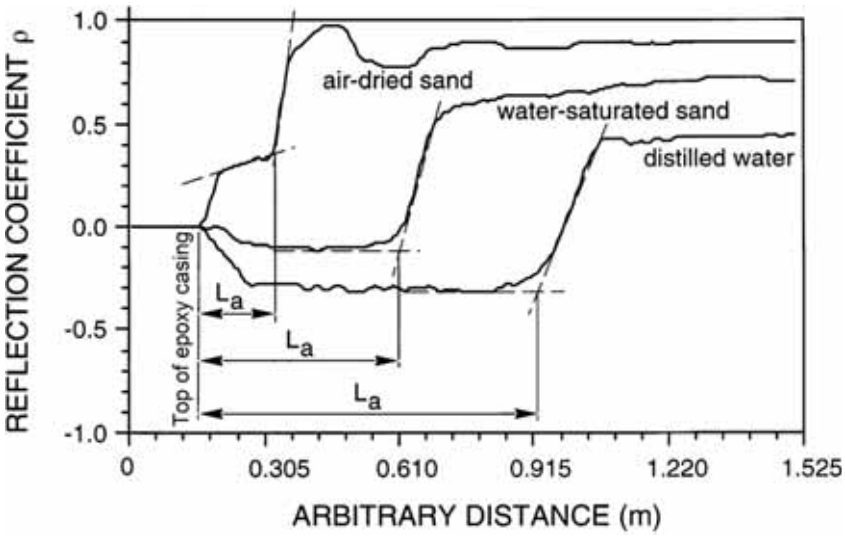

Figure 2.32: TDR waveforms for different saturation conditions (after Noborio, 2001).

$$\sqrt{K_a} = \frac{c}{v} = \frac{c \cdot \Delta t_a}{2 \cdot L} = \frac{L_a}{L} \qquad 2.34$$

Because the dielectric constant of water is much larger than for other soil constituents, determining water content by measuring an apparent dielectric constant of moist soil is feasible (Hoekstra & Delaney, 1974). Davis & Annan (1977) presented one of the early studies showing the relationships between the volumetric water content *(θ)* and the apparent dielectric constant (K_a). Nevertheless, Topp et al.'s (1980) relationship (Equation 2.35) is the most commonly used because it has been demonstrated to give good results over a large range of soils.

$$\theta = 5.30 \times 10^{-2} + 2.92 \times 10^{-2} \cdot K_a - 5.50 \times 10^{-4} \cdot K_a^{\ 2} + 4.30 \times 10^{-6} \cdot K_a^{\ 3} \qquad 2.35$$

Topp et al. (1980) found that the apparent dielectric constant K_a of soil was not strongly sensitive to temperature (10 – 36°C), soil texture (clay to sandy loam), bulk density of soil (1.14 – 1.44 mg/m^3, for non-swelling soils) and soluble salt content (moistened with salt-free water, 0.01 N $CaSO_4$, or 2000 ppm NaCl solution).

Equation 2.35 is only dependent upon soil parameter K_a, it is therefore, remarkably transferable to a wide range of different soils with a reasonable degree of accuracy (Take et al., 2007). That is a reason why it is frequently referred to as a "universal" calibration curve. However, several researchers have found that it might not represent the relationship accurately for some soils, requiring a specific calibration in each case (Heimovaara, 1993; Noborio, 2001; Ekblad & Isacsson, 2007; Take et al., 2007; Hanumantha-Rao & Singh, 2011; Askarinejad, 2013).

The effect of water flow at steady state with unit a gradient on the θ measurement was studied by Hinnell et al. (2006), who found that the TDR rods modify the water content within the sample volume of the TDR sensor. However, the water content changes caused by flow disruption are too small to have a significant impact on the measurement accuracy of the TDR

sensors. As a result, the effects of flow disruption due to the presence of the rods can be ignored for most applications of time domain reflectometry.

2.2.2.4 Soil Water Retention Curve

The relationship between matric suction and volumetric water content (or saturation) is described as the Soil Water Retention Curve (SWRC). It determines the response of the unsaturated porous media to drying and wetting cycles (Equation 2.32). An extended description of its characteristics, parameters and its estimation is given below, as the SWRC was used throughout this research project.

The term *characteristic* is frequently found in the literature instead of *retention*. This term, however, means intrinsic, implying that a unique and peculiar Water Retention Curve would exist for a given soil (Nuth & Laloui, 2008a). Experimental results show that the curve is not unique and a strong influence of the soil density on the SWRC has been found (Miao et al., 2006; Askarinejad et al., 2010; Casini et al., 2010; Morales et al., 2011; Askarinejad et al., 2012a; Zhou et al., 2012).

A SWRC is presented schematically in Figure 2.33. The main parameters shown in the graph are the Air Entry Value (AEV), defined as the matric suction at which air starts to enter the soil matrix when desaturating it along the drying path, the Water Entry Value (WEV), which is the value at which water starts to displace air in the porous medium along the wetting path (Wang et al., 2000), θ_{sat} is the volumetric water content at saturation, and θ_{res} stands for residual water content, i.e. the volumetric water content after a drying process. This value is not zero because the void structure does not allow all of the water in the voids to be displaced from the soil matrix.

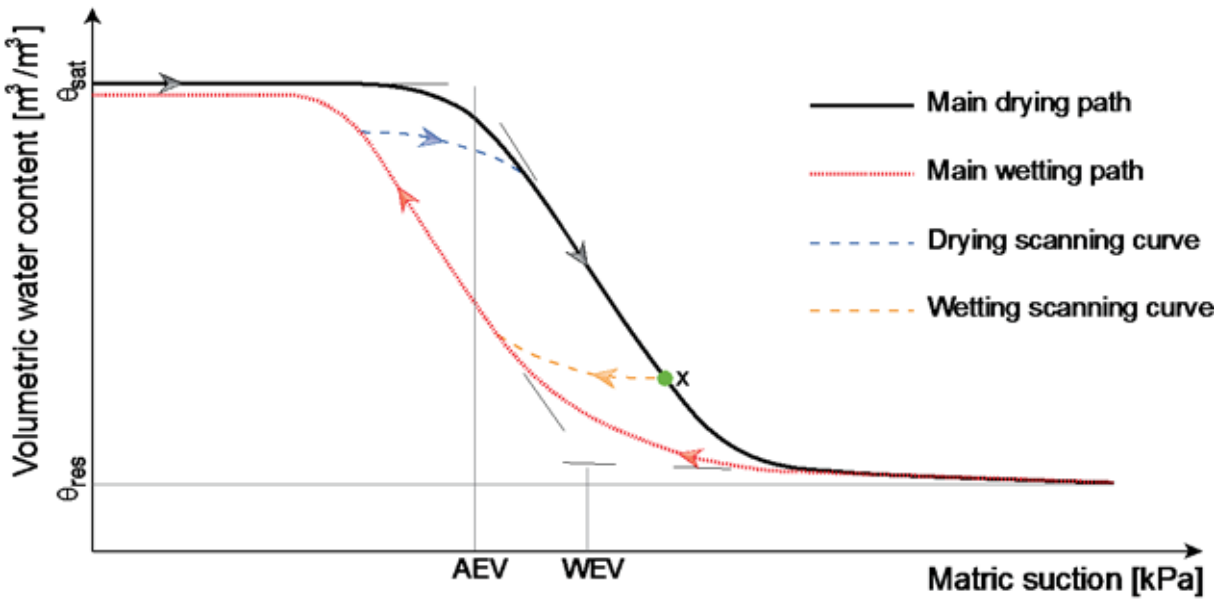

Figure 2.33: Soil water retention curve (SWRC).

The drying path follows a horizontal path until it reaches the AEV. From that point onwards, it follows a relatively steep curve in the S - θ space until it reaches the θ_{res}, whereupon the matric suction rises as the residual state is approached. The wetting process begins with a smooth curve until it reaches the WEV, and the saturation increases at a greater rate (almost parallel to the drying path) compared to the suction until the soil approaches the saturated state.

This hysteretic response is typical of a SWRC, and previous research has found that it can be attributed to 4 main causes (Maqsoud et al., 2004; Pham et al., 2005): i) irregularities in the cross-sections of the void passages, resulting in the so-called “Ink Bottle” effect, ii) different spatial connectivity of the pores during the drying or wetting process, iii) variations in the liquid–solid contact angle, being greater in an advancing meniscus than in a receding meniscus, and iv) air entrapment within the soil mass.

The soil does not reach a fully saturated state after following a wetting path. This is owing to air bubbles that remain trapped within the soil mass, thus decreasing the saturation degree. As a consequence, the θ reached is smaller than the theoretical value θ_{sat}.

When the soil is on the drying path, but a wetting process takes place before the soil attains to the residual water content (Point ‘x’ in Figure 2.33), the soil becomes more saturated with the resulting matric suction defined as following the wetting scanning curve from that point ‘x’. This is an intermediate path between the drying and wetting paths. The same applies when the soil is following a wetting path and suddenly a drying process occurs. In this case, the soil follows a drying scanning curve beginning from the point of reversal.

Recent experimental research concluded that a pronounced hysteresis on the SWRC might be also attributed to trapped air between the sample and underneath the high-air-entry (HAE) value disk of the device used to determine the SWRC, which increases at higher suctions (Mavroulidou et al., 2009). This shows the importance of performing adequate experimental procedures, which avoid interference of the testing procedure, and therefore, errors in the soil parameters obtained.

2.2.2.5 Determination of the SWRC

A summary of the methodologies that could be used to determine a specific SWRC is shown in Figure 2.34. As mentioned above, this curve is not unique, and it has to be determined for specific density conditions of the specimen. There are mainly four methodologies: determination in the laboratory, estimation from the grain size distribution only or combined with Atterberg limits, and data mining.

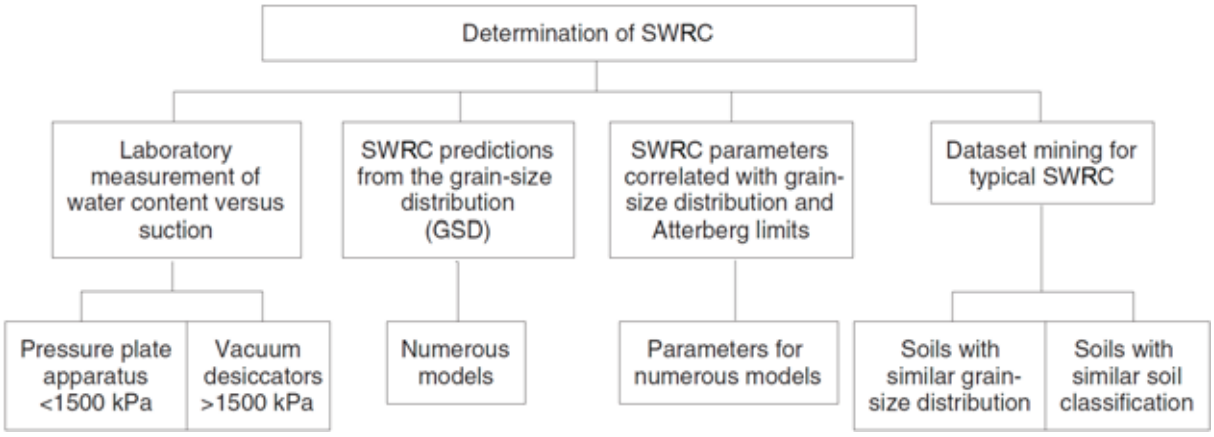

Figure 2.34: Methodologies for determination of a specific SWRC (after Fredlund et al., 2012).

Determination in the laboratory

Delage & Cui (2008) and Fredlund et al. (2012) present detailed descriptions of the procedures adopted to obtain the SWRC in the laboratory. The two main techniques are axis-translation and the osmotic method. The axis-translation technique consists of applying an air overpressure to the sample, while the water pressure is kept constant. In the osmotic method, the soil sample is placed in contact with a semi-permeable membrane behind which an aqueous solution of large-sized molecules of polyethylene glycol (PEG) is circulated. Suctions can be measured up to 1500 kPa with both techniques.

An oedometer-type pressure plate as described by Perez-Garcia et al. (2008) and Fredlund & Houston (2013), is used at ETH Zurich to determine the SWRC, which is based on the axis-translation technique. A hanging column is attached to the system to be able to apply very low air pressures (<10 kPa) to the specimen.

A sketch of the device is presented in Figure 2.35. It consists of a closed chamber, in which the air pressure may be increased using a control panel. Volume change is monitored via two graduated tubes at the sides of the device, which are connected to an HAEV disk located at the bottom of the chamber.

The test duration is determined partially by the equilibration time between readings, which is a function of the soil type and the Air Entry Value of the disk. Therefore, the manufacturer (GCTS) recommends selecting the disk according to the soil type, as shown in Table 2.1.

A fully saturated specimen of cylindrical shape of 63 mm in diameter and 20 mm height is placed inside a metallic ring and both are placed on top of, and in good contact with the HAEV disk, which has been previously saturated. A loading cap is positioned over the specimen to apply an external pressure, which simulates the overburden pressure under which the soil is located in-situ. Then the cell is hermetically closed to preserve the humidity and temperature conditions of the specimen and keep them constant. Furthermore, the test is

performed in a room with controlled humidity and temperature. Finally, the cell is connected to two lateral tubes, which are calibrated to measure the change of water volume.

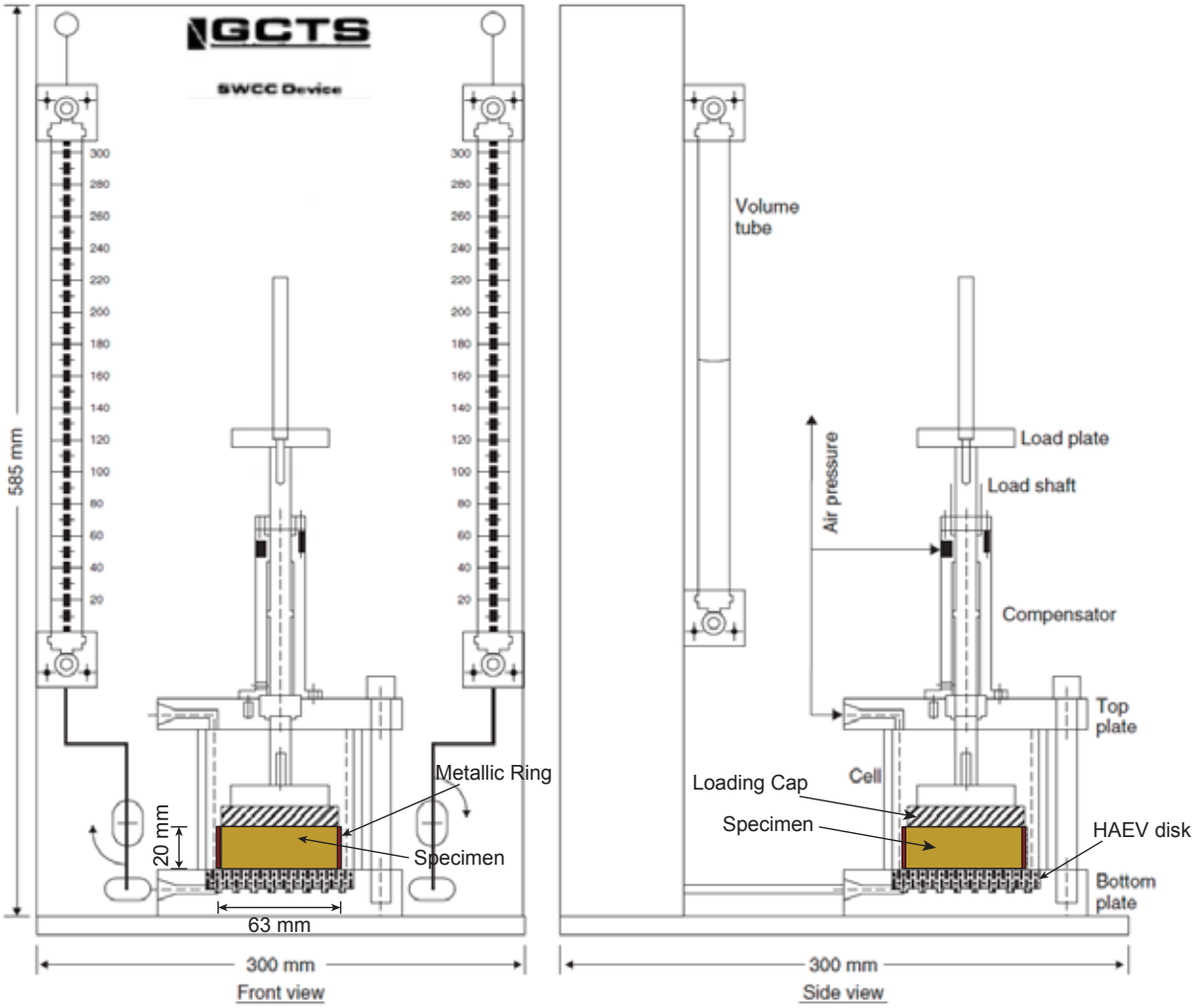

a) Front view. *b) Side view.*

Figure 2.35: Oedometer-type pressure plate to determine the SWRC at ETH Zurich (modified from www.gcts.com).

Table 2.1: Selection of the HAEV disk depending on the type of soil to be tested.

Type of Soil	AEV of the disk	Equilibration time [hours]
Sand	1 bar (100 kPa)	6
Silty Sand, Clayey Sand	3 bar (300 kPa)	6
Sandy Silt, Sandy Clay	5 bar (500 kPa)	24
Clay	15 bar (1500 kPa)	24

The test is performed as follows: air pressure is applied in the chamber, and matric suction can be calculated from Equation 2.1, as a consequence of the new matric suction applied. A volume of water is expelled from the soil and flows into the lateral tubes; this volume is measured and used to calculate the new degree of saturation and current volumetric water

content state. After equilibrium is reached, i.e. no further water volume change is observed for the air pressure u_a applied, a paired value of $S - \theta$ is obtained, and the air pressure is increased again to obtain a new pair of values. All of the paired values are plotted on a chart with volumetric water content θ vs. S, resulting in the SWRC, as shown in Figure 2.36.

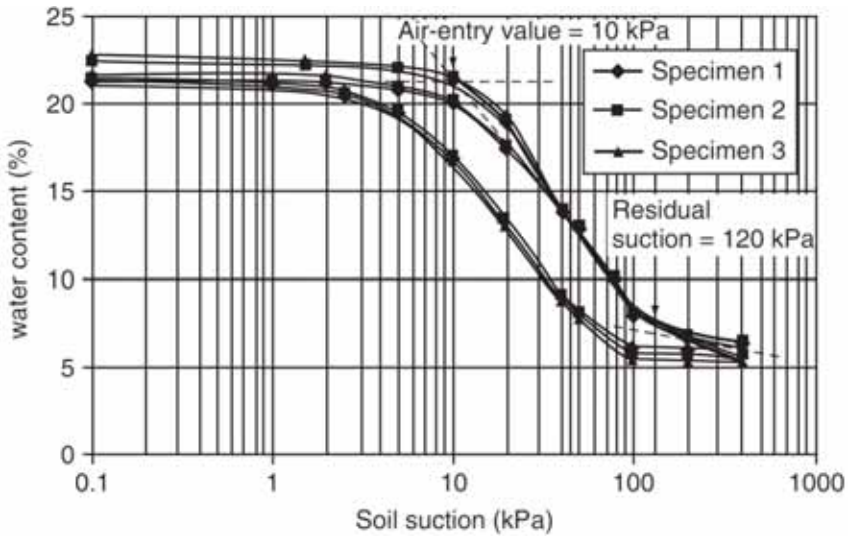

Figure 2.36: Soil water retention curve of a silt obtained with a oedometer-type pressure plate (after Fredlund et al., 2012).

Estimation based on the grain size distribution

The SWRC is strongly influenced by the size and distribution of voids in the soils and the amount of water in the voids. Various studies have been undertaken that show that the grain size distribution curve can be used to estimate the SWRC, in a sufficiently accurate way for use in engineering design (Aubertin et al., 2003; Maqsoud et al., 2004; Torres, 2011; Mayor, 2013). Fredlund et al. (2012) point out that the effects of stress history, soil fabric, confinement, and hysteresis on the SWRC are difficult to address when using estimation procedures associated with the grain size distribution curve. Notwithstanding this view, Mayor (2013) found positive results when comparing the SWRC obtained from paired measurements of suction and θ in an instrumented dyke, from laboratory tests and based on estimations from the grain size distribution.

The method by Arya & Paris (1981) is probably the most well-known of these procedures. However, recent research, e.g. (Mayor, 2013), has found that whereas the method by Arya & Paris (1981) fitted laboratory results quite well, the Modified-Kovacs method (Aubertin et al., 2003) predicts the SWRC in the field more effectively. This model has also been found to perform well for tailing materials as well as coarse and fine-grained soils (Fredlund et al., 2012).

Equations 2.36 to 2.42 present the formulation of the modified-Kovacs approach for both coarse and fine-grained soils. The model assumes that water is held by capillary forces, which are responsible for capillary saturation, S_c, and by adhesive forces, causing saturation by adhesion, S_a. Both components act simultaneously in these models, and are thus included

in measurements made to determine the SWRC (Aubertin et al., 2003). S_r is the desired saturation for a volumetric water content θ, η is the initial porosity of the soil, h_{c0} is the equivalent capillary height related to an equivalent pore diameter and the solid surface area, ρ_s is the density of the soil grains in kg/m^3, ψ is the soil suction represented as a head or length, m is a dimensionless pore-size coefficient, a_c is a dimensionless adhesion coefficient, ψ_r represents the suction at residual water content, e is the initial void ratio, ψ_n is a normalization parameter introduced to maintain consistency in the units (ψ_n = 1 cm when ψ is in cm), ψ_0 is the suction head equal to 107 cm of water corresponding to dry soil conditions, d_{10} is the diameter in cm corresponding to 10% passing on the grain size distribution, and C_u is the uniformity coefficient equal to d_{60} / d_{10}.

$$S_r = \frac{\theta}{\eta} = 1 - \langle 1 - S_a \rangle (1 - S_c) \tag{2.36}$$

$$S_c = 1 - \left[\left(\frac{h_{c0}}{\psi} \right)^2 + 1 \right]^m \exp\left[-m \cdot (h_{c0} \cdot \psi)^2 \right] \tag{2.37}$$

$$S_a = a_c \left(1 - \frac{\ln(1 + \psi / \psi_{res})}{\ln(1 + \psi_0 / \psi_{res})} \right) \frac{(h_{c0} / \psi_n)^{2/3}}{e^{1/3} (\psi / \psi_n)^{1/6}} \tag{2.38}$$

$$h_{c0}(cm) \begin{cases} \dfrac{0.75}{[1.17 \cdot \log(C_u) + 1] \cdot e \cdot d_{10}} & \text{Granular soil} \\ \dfrac{0.15 \cdot \rho_s}{e} w_L^{1.45} & \text{Plastic soil} \end{cases} \tag{2.39}$$

$$\psi_r(cm) = 0.86 \cdot \sqrt{h_{c0}} \tag{2.40}$$

$$m \begin{cases} \dfrac{1}{c_u} & \text{Granular soil} \\ 0.00003 & \text{Plastic soil} \end{cases} \tag{2.41}$$

$$a_c \begin{cases} 0.01 & \text{Granular soil} \\ 0.0007 & \text{Plastic soil} \end{cases} \tag{2.42}$$

Fitting equations

Some mathematical expressions have been developed to express the SWRC as a continuous function. This is of special interest for hydro-mechanically coupled constitutive modeling, in which the deformations modify the SWRC, owing to changes in the void ratio. This change in the SWRC influences the distribution of the pore water pressure within the soil mass, which, in turn, determines the deformations. Fredlund et al. (2012) present a summary of 13 fitting equations found in the literature, of which the most used are presented in Table 2.2. Where ψ is the soil suction represented as a head or length, *AEV* is the air entry value. α, n, ζ, and m are fitting parameters.

Table 2.2: Some fitting equations for the SWRC, including saturation degree and suction.

Reference	Equation
Gardner (1958)	$S_r = \frac{1}{1+\alpha \cdot \psi^n}$
Brooks & Corey (1964)	$S_r = \left(\frac{AEV}{\psi}\right)^{\varsigma}$
van Genuchten (1980)	$S_r = \frac{1}{\left[1+\left(\alpha \cdot \psi\right)^n\right]^m}$
Fredlund & Xing (1994)	$S_r = \frac{1}{\left\{\ln\left[\exp(1)+\left(\frac{\psi}{\alpha}\right)^n\right]^{1-1/n}\right\}^m}$

2.2.2.6 Hydraulic conductivity

The hydraulic conductivity at full saturation k_{sat} might be determined through laboratory tests such constant and falling head tests. However, estimation can be done using empirical equations, based on a specific particle size, or the complete grain size distribution. The equation by Hazen (1892) (Equation 2.43) is commonly used in engineering practice, although it was developed for loose, clean sands with a coefficient of uniformity (d_{60} /d_{10}), less than about 2 (Carrier, 2003). The formula is widely used due to its simplicity, as it only requires d_{10} (in cm), which is the particle size for which 10 % of the soil sample passing the given sieve size, and a coefficient c_H usually assumed equal to 100. k_{sat} is determined in cm/s with this equation.

$$k_{sat} = c_H \cdot d_{10}^{\ 2} \qquad 2.43$$

Kozeny (1927) presented a formula to determine k_{sat} from the complete grain size distribution. It has been modified to fit the laboratory measurements better, and now it is known as the Kozeny-Carman equation (Equation 2.44) (Carrier, 2003). In this equation k_{sat} is determined in cm/s, f_i is the fraction of particles between two sieve sizes d_1 and d_2 (in cm), e is the void ratio, and SF is a shape factor (spherical = 6.0, rounded = 6.1, worn = 6.4, sharp = 7.4, and angular = 7.7).

$$k_{sat} = 1.99 \times 10^4 \left(\frac{100\%}{\sum\left[f_i / \left(d_1^{\ 0.404} \times d_2^{\ 0.595}\right)\right]}\right)^2 \left(\frac{1}{SF^2}\right)\left(\frac{e^3}{1+e}\right) \qquad 2.44$$

According to Fredlund et al. (2012), direct experimental measurement of the function of water coefficient of permeability versus matric suction for an unsaturated soil is difficult and time consuming. Therefore, some estimation procedures have been proposed, based on a clear

linkage between the commencement of the desaturation of a soil (i.e., the AEV) and the decrease in its coefficient of permeability, as shown in Figure 2.37.

Table 2.3 summarizes some of the expressions developed, and corresponding to the fitting models for the SWRC given in Table 2.2. The fitting parameters correspond to those in Table 2.2, except for the model by Fredlund & Xing (1994), for which a new parameter *p* is introduced.

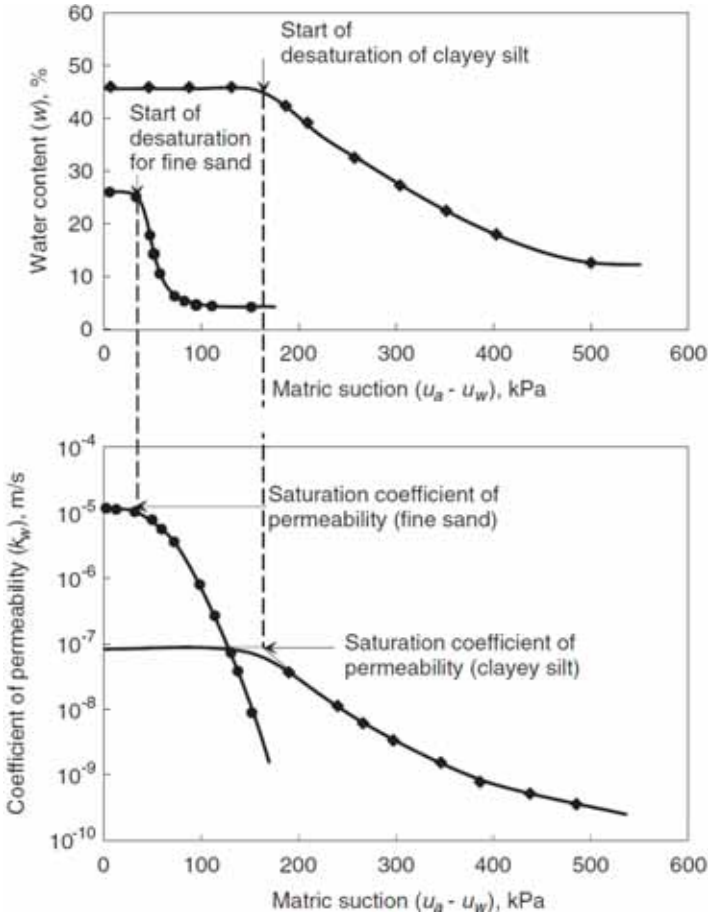

Figure 2.37: Typical water permeability function (after Fredlund et al., 2012).

Table 2.3: Some expressions to estimate the hydraulic conductivity from the fitting parameters of the SWRC given in Table 2.2.

Reference	Equation
Gardner (1958)	$k = k_{sat} \cdot \exp\left[-\alpha \cdot \left(\frac{1-\psi}{\alpha \cdot \psi}\right)^{1/n}\right]$
Brooks & Corey (1964)	$k = k_{sat} \cdot \psi^{(2+3\cdot\varsigma)}$
van Genuchten (1980)	$k = k_{sat} \cdot \left\{1-\left[1-\psi^{n/(n-1)}\right]^{1-1/n}\right\}^2$
Fredlund & Xing (1994)	$k = k_{sat} \cdot \psi^{p}$

Abed (2008) presents a comparison of the relative permeability, defined as the ratio between the hydraulic conductivity at a certain suction and the hydraulic conductivity at saturation, as fitted to the experimental data, for a sandy silt, and estimated with the equations given in Table 2.3 (Figure 2.38). For this example, the formulation by Fredlund & Xing (1994) gave the best fit, followed by van Genuchten's equation. The approximations with the formulas given by Brooks & Corey, and Gardner do not portray correctly the behavior of the experimental data.

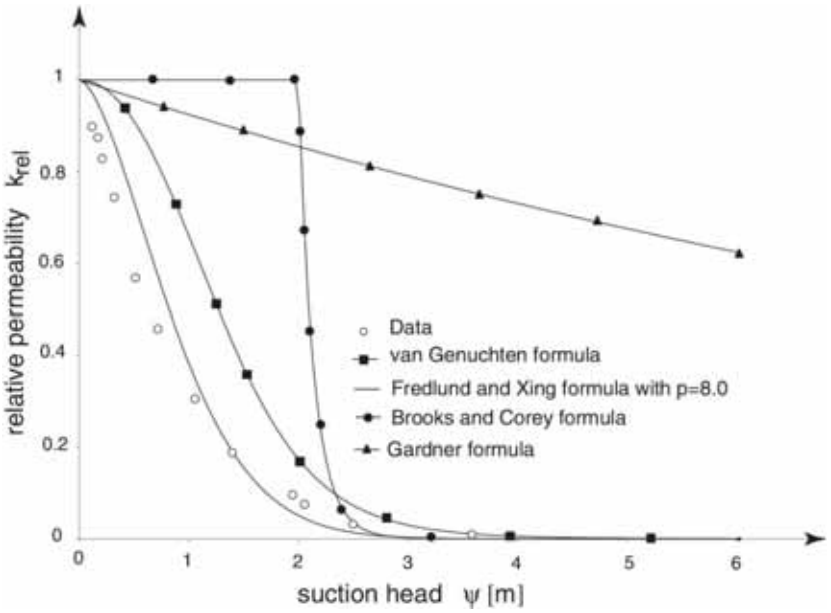

Figure 2.38: Performance of some fitting models for water relative permeability (after Abed, 2008).

2.3 Physical modeling with a geotechnical centrifuge

Different options for physical modeling of engineering structures are available, as described in a recent state of the art report by Mayne et al. (2009). These options include: 1-g with large-scale models, 1-g with small-scale models, calibration chambers, 1-g shaking tables, and small-scale models tested in centrifuge facilities.

Each type of modeling has advantages and disadvantages, which have to be considered by the modeler. For instance, with large-scale models at 1-g, the stresses are correctly represented, but there will be larger costs and they require more time for construction, whereas small-scale models at 1-g are faster and cheaper to be built, but the stress conditions are not properly represented and processes, such as capillary suction and dilatancy, might affect the results, as discussed by Springman (2000).

Small-scale models subjected to enhanced gravity conditions, on the other hand, scale the stress correctly with depth, reveal key mechanisms of soil behavior and failure mechanisms, allow different stress histories to be simulated with a shorter testing time, and lower costs when compared to full-scale models. The proper representation of stresses is a significant

issue, as it is widely recognized that soil behavior depends, among others, on the effective confining stress and stress history (Schofield, 1980).

The use of physical modeling with small-scale models tested in a geotechnical centrifuge was found to be optimal for this research project, as some of its goals were to investigate the breaching mechanism and to study the stability conditions of dykes during non-steady conditions, which causes some zones of soil to be in an unsaturated condition, which in turn, and explained above, is highly dependent on the stress history.

In the following subsections, the principles of centrifuge modeling, including the reporting and development of some general scaling factors are covered; issues arising from the techniques and facilities are evaluated; the difference between beam and drum centrifuges is explained and a description of the geotechnical centrifuge facility at ETH Zurich is given. The section is finished with a discussion about the results from previous research projects carried out on analysis of dyke behavior and breaching.

2.3.1 Principles

Assuming a semi-infinite space, as shown in Figure 2.39, the total vertical stress acting at a point *A,* located at a depth z_p, is estimated to be $\sigma_v = \gamma \cdot z_p$, where γ is the bulk unit weight of the soil. The former can be rewritten as $\sigma_v = \rho \cdot g \cdot z_p$, where ρ is the density of the soil and *g* is Earth's gravity. This becomes $\sigma_v = \rho \cdot g \cdot z_m = \rho \cdot g \cdot z_p/n$ for a model, which is *n* times smaller than the prototype. As the density is prepared in the model to maintain a constant value, the gravitational acceleration must be increased by a factor *n* to scale the stresses correctly.

Model and *prototype scales* are terms used to represent the variables for the model and the prototype, respectively. In general, the data from the tests are recorded at model scale and are converted to prototype scale by multiplying the model values by an appropriate scaling factor. Further information regarding scaling factors is given in Sections 2.3.2 and 4.1.

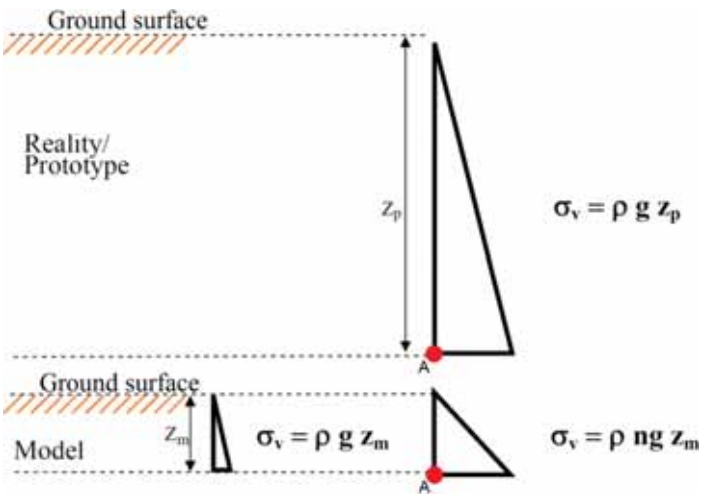

Figure 2.39: Total vertical stresses in a soil model comparing prototype (top) (index p*) with a 1-g small-scale model (bottom left) and centrifuge model (bottom right) (index* m*) (after Laue, 2002).*

An elegant solution to this shortcoming is to increase the acceleration field by rotating the small-scale model around an axis. Figure 2.40 illustrates that a mass subjected to circular motion with angular velocity ω experiences two accelerations: tangential (a_T) and radial (a_R). However, if the rotation radius r and the angular velocity ω are kept constant, then the mass does not experience a tangential acceleration, and the centrifugal acceleration is constant, and expressed by Equation 2.45.

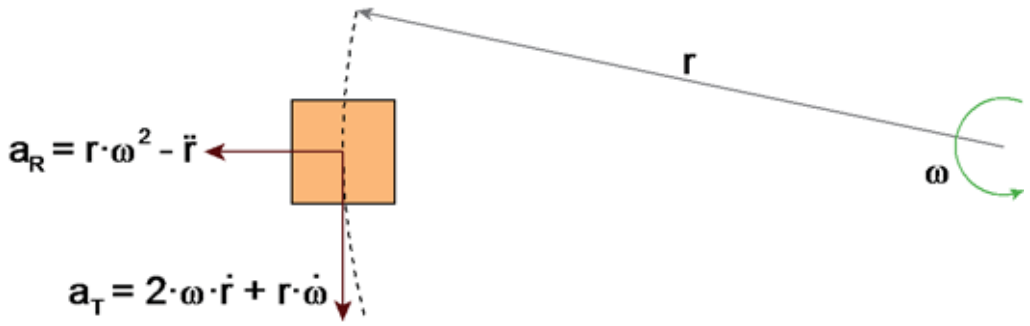

Figure 2.40: Forces experienced by a body under circular motion.

$$a_R = r \cdot \omega^2 \qquad 2.45$$

The first mention of applied centrifuge modeling in the literature appears to be that of Bucky (1931), although Phillips (1869) had already introduced scaling relationships and concluded that self-weight body forces were significant, and he proposed the exploitation of centrifugal acceleration to generate increased body forces on reduced size model (Craig, 2002). However, international attention to the technique was only paid after the work of Pokrovsky & Fedorov (1936). A significant boom in application of the technique took place during the 70s and 80s (Craig, 2002). As of today, several institutes around the world use the technique to solve a range of different engineering problems. A specialized international journal is printed, and several regional conferences (Eurofuge, Asiafuge) and an international conference are held every 4 years as well, from which, the last one was held in Zurich in 2010 (Springman et al., 2010).

Craig (1984); Taylor (1995); Lee (2002); Garnier (2005) and Mayne et al. (2009) describe the differentiation between the philosophy of centrifuge modeling and testing. On the one hand, centrifuge modeling refers to a model prepared to represent a specific prototype, for which there are some design decisions to be made. In centrifuge modeling, a clear need exists to replicate sufficiently some features of the prototype. In that way, data collected on the centrifuge model can be extrapolated through the correct scaling factors to the prototype to assess its behavior and take a decision.

Centrifuge testing, on the other hand, is used to validate or to study the behavior of a class of problems, rather than for a particular prototype. The results of a series of tests can be correlated to corroborate or predict the general behavior of the structure. In this case, the centrifuge technique is used to generate realistic stress distributions and measure the outcome in the form of deformations, and therefore, to represent an accurate description of the problem.

Centrifuge technique has some intrinsic challenges, which have to be taken into account by the modeler. Firstly, the acceleration field is non-linear, as the acceleration increases linearly with radius (Equation 2.45). This generates a variation of acceleration in the space that the model occupies. This produces an inherent error in the stresses calculated (Schofield, 1980). Taylor (1995) analyzed this problem and concluded that there is exact correspondence in stress between model and prototype at 2/3 of the model height (Figure 2.41). The maximum under and over-stress are located at 1/3 of the height and at the total height of the model, respectively. Notwithstanding, he concluded that the error is smaller than 3%, and that even for small centrifuges (r < 1.5 m), this error is acceptable and should not impact on any engineering outcomes.

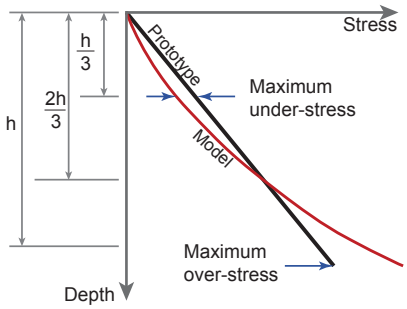

Figure 2.41: Scaling error due to inertial forces in the model (after Taylor, 1995).

A second inherent challenge is the influence of the model construction and the boundary conditions on the results of the experiments. Clay models are usually shaped or inserted in the testing container from a large block consolidated from an initial slurry, whereas sand models are usually pluviated into the containers (Phillips, 1995). The preparation of the model should ensure that models can be built with similar conditions in order to guarantee the repeatability of the tests (Chen et al., 1998). Therefore, automated systems to pluviate the sand have been developed (Garnier & Cottineau, 1988; Allard et al., 1994; Zhao et al., 2006; Detert et al., 2012).

According to van der Poel & Schenkeveld (1998), although the pluviation technique allows homogeneous sand models to be made, it has as disadvantages: i) the preparation of models in a circular container leads to relatively large boundary effects, ii) the sand has to be saturated after pluviation, which might cause lifting or internal collapse of models of loose density. Mayne et al. (2009) also warn that hopper systems that promote sand heap formation should be avoided due to the tendency for these to adopt self-organized criticality, leading to creation of heterogeneous specimens.

Another challenge refers to the boundary conditions of the models. Khoo et al. (1994) note that to simulate a plane strain condition in centrifuge experiments, the zero out-of plane normal strain and zero in-plane shear stress conditions must be fulfilled, due to the significant influence that errors in the boundary conditions might cause in the behavior. According to Phillips (1995), a plane strain model should be sufficiently wide so that wall friction is not a significant proportion of the resisting forces. He also recommends making the measurements along the centerline of the model, where the influence is smaller and that the containers for

two- and three-dimensional studies should be about twice as long as the soil depth to minimize the boundary effects.

2.3.2 General scaling factors

Geometric, kinematic and dynamic similarities are the three basic issues to be considered when using reduced scale models (Cargill & Ko, 1983). These can be seen as similarity of form, similarity of motion and similarity of forces (Chanson, 2004).

The geometric similarity is satisfied by scaling all of the geometrical lengths by a fixed ratio (prototype/model) *n.* The kinematic similarity requires that the ratios of velocities and acceleration in prototype and model should be constants. A constant ratio between forces and stresses acting in the model and prototype is necessary to achieve dynamic similarity.

Scaling of physically modeled problems in geotechnical engineering is a topic studied by many institutes. In an attempt to summarize the most accepted scaling factors, Technical Committee 2 (now TC-104) of the International Society for Soil Mechanics and Geotechnical Engineering (ISSMGE) published a report. The principal scaling rules were developed for diverse boundary value problems and analyzed by means of physical modeling at increased gravity (Garnier et al., 2007).

Table 2.4 presents a summary of some basic scaling factors that are applied for centrifuge modeling, as shown in Figure 2.39, whereby, a model *n*-times smaller than a prototype has the same stresses as in the prototype. A complete discussion regarding the scaling factors for flow problems is given in Section 4.1.

Table 2.4: Some basic scaling factors for centrifuge modeling (summarized from Schofield, 1980; Garnier et al., 2007).

Quantity	Scaling factor (model / prototype)
Acceleration	n
Linear dimension	n^{-1}
Mass, volume	n^{-3}
Density	1
Unit weight	n
Stress	1
Force	n^{-2}
Bending moment	n^{-3}
Displacement, amplitude	n
Strain	1
Time (groundwater flow)	n^{2}
Diffusion (consolidation)	n^{2}
Frequency	n^{-1}

2.3.3 Types of centrifuge facilities

There are two main types of centrifuge facility: beam and drum. The beam centrifuge (Figure 2.42) consists of two arms attached to a rotating central axis. At the end of the arm is a basket in which the model is placed, which is usually inside a rigid strongbox (Schofield, 1980). The connection between the basket and the arm has a hinge, which allows the basket to rotate in the direction of the resultant increased gravity. This is convenient, as the effect of Earth's own gravity can be taken into account, by rotating the basket at an angle, for which the axis coincides with resultant vectors of the desired gravity level, as shown in Figure 2.42.

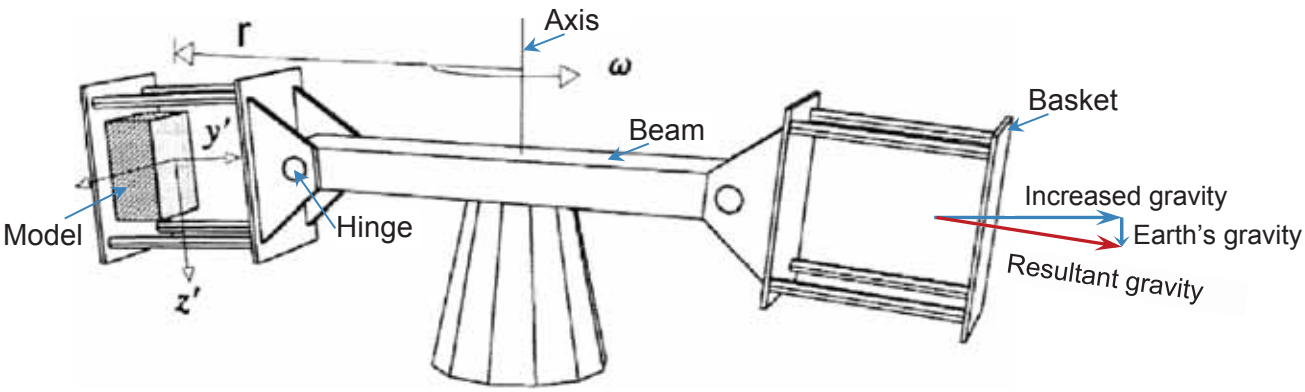

Figure 2.42: Schematic view of a beam centrifuge (adapted from Nater, 2005).

Drum centrifuges, on the other hand, consist of a rotating channel, which has the shape of an annular ring. Strongboxes can also be used, by fixing them to the channel and to rotate with it (Figure 2.43). Usually, a tool platform is placed in the center of the ring. Diverse actuation tools required for the tests (e.g. water suppliers, load applier), can be placed on this platform, which can rotate at the same angular speed as the ring or remain stationary. This allows the tool platform to be stopped and removed, while the channel continues rotating under the applied acceleration field. In this way, new actuation tools can be mounted on the tool platform to be used during the test. According to Laue (2002), this improves the flexibility of modeling in most respects and limits the number of stress cycles or excursions that the model must be exposed to between 1-g and n-g, and therefore, this represents an advantage over beam centrifuges.

Drums centrifuges are preferred to model problems that take place over a large superficial area such as slides run-out and debris flows (Bowman et al., 2006; Bowman et al., 2010; Gaudin et al., 2010), dykes along riverbanks (Kusakabe et al., 1988a), contaminant transport (Gurung et al., 1998). This advantage arises because of the larger plan area provided for the test, as the spinning channel of the drum centrifuge acts as a container itself (Kusakabe et al., 1988b; Stewart et al., 1998).

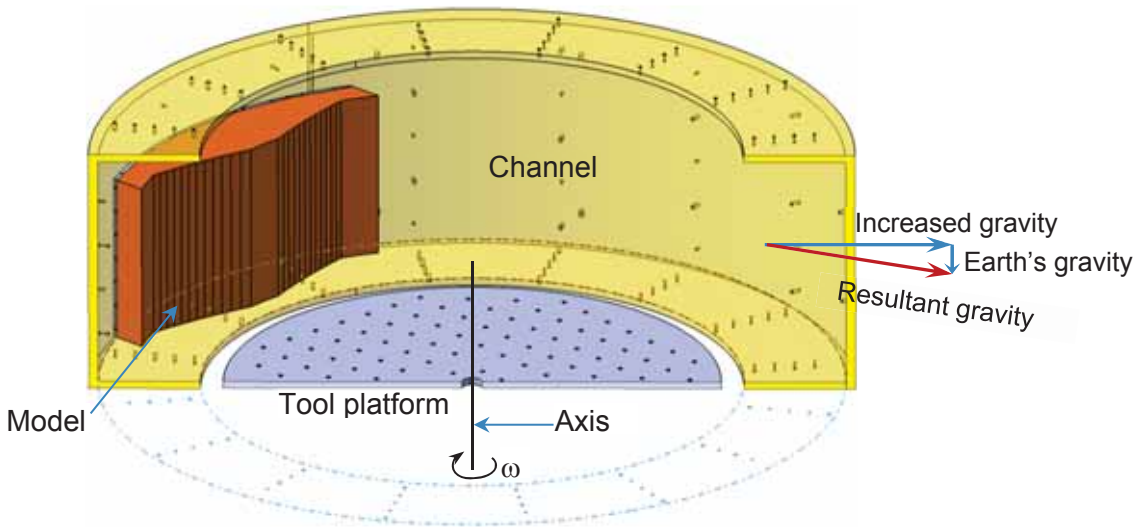

Figure 2.43: Schematic view of a drum centrifuge.

A model to be tested in a drum centrifuge can be either constructed directly inside the channel of the centrifuge or built in the laboratory inside a strongbox and fixed to the channel afterwards. The construction inside the channel is used when an extensive soil deposit is needed. Therefore, the complete channel is filled with soil, which is poured with an external device while the channel rotates. If sand is used, it must be partially saturated while the centrifuge is stopped to shape or instrument the model and place any actuators, thus the apparent cohesion provided by the capillary forces holds the model in place (Phillips, 1995). Successful attempts for in-flight model construction have been reported by Fragaszy & Cheney (1981); Kusakabe et al. (1988a); Laue (2002); Laue et al. (2002); Nater (2005) and Weber (2007).

Construction of models in the laboratory, with subsequent placement in the channel, requires the use of strongboxes. The process is shown in Figure 2.44, where the strongbox (a) is filled with the soil and the model is shaped (b). The model is then tilted through 90° (c) for its final positioning. The rotated box and model are placed in the drum channel (d) and the test begins (e).

The acceleration of 1-g owing to Earth's gravity acts parallel to the surface of the model. This represents a challenge for this type of model preparation after the strongbox and the model are tilted (Figure 2.44c), as the surface should remain stable for the time between the model is installed and the experiment begins. This is of special interest for models built with sand, for which the soil is partially saturated to obtain a temporary increased strength due to apparent cohesion.

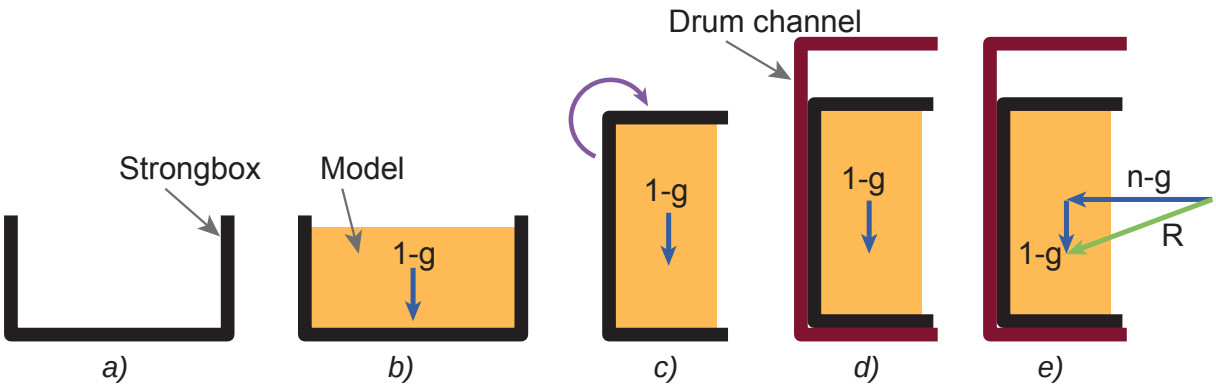

Figure 2.44: Process of model preparation outside the drum centrifuge.

2.3.4 Drum centrifuge facility at ETH Zurich

The geotechnical drum centrifuge facility at ETH Zurich is described by Springman et al. (2001). The facility consists of a preparation laboratory, the centrifuge pit, and a control room, from which the technician, the project engineer and the proof engineer supervise the progress of the test. These three roles are based on the security guidelines at Cambridge University (Schofield, 1980) to ensure safe operation of the facility.

Figure 2.45 shows a schematic view of the drum centrifuge at ETH Zurich. It consists of a main channel (1), in which the model is built or placed and a tool platform (2) where instruments (actuators) can be mounted together with the data acquisition systems. The rotation of the channel and the tool platform is given by an external (4) and an internal (5) shaft, respectively. Each of them is controlled by a motor and they can be linked to rotate together, or independently of each other. This allows the platform to be stopped during the test while the channel is still rotating, which is very useful when the instruments on the tool platform have to be changed or adjusted. A safety shield is lowered vertically to protect the stationary platform from the spinning channel in this case. Communication between the on-board computer and the control room is provided by sets of electrical slip rings (6, 10, and 13). An additional slip ring (not shown in the figure) is mounted on the tool platform over the internal shaft (5), and it allows water to flow to the model from a tap outside the centrifuge through a hose. This is explained in detail in Sections 4.2.2 and 4.2.6.

The internal ring is a channel, 2.2 m in diameter, 0.7 m high and 0.3 m deep. It can be accelerated up to 440-g with a maximum payload of 2 tons. The entire channel may be filled with soil to a maximum of 2000 kg, to create a large deposit of dimensions equivalent to greater than 100 m deep, 2.5 km long and 250 m wide. However, smaller models can be tested by using strongboxes fixed to the channel of the drum. In that way, a model can be prepared outside the centrifuge and then be placed inside at 1-g for subsequent testing at n-g, with the challenges mentioned above.

A large variety of complex problems are currently being modeled, as reported by Mayne et al. (2009); Laue et al. (2012) and Springman (2014). The facility had 2 types of strongboxes (cubic and cylindrical) at the time the work began, and a new semi-circular strongbox was

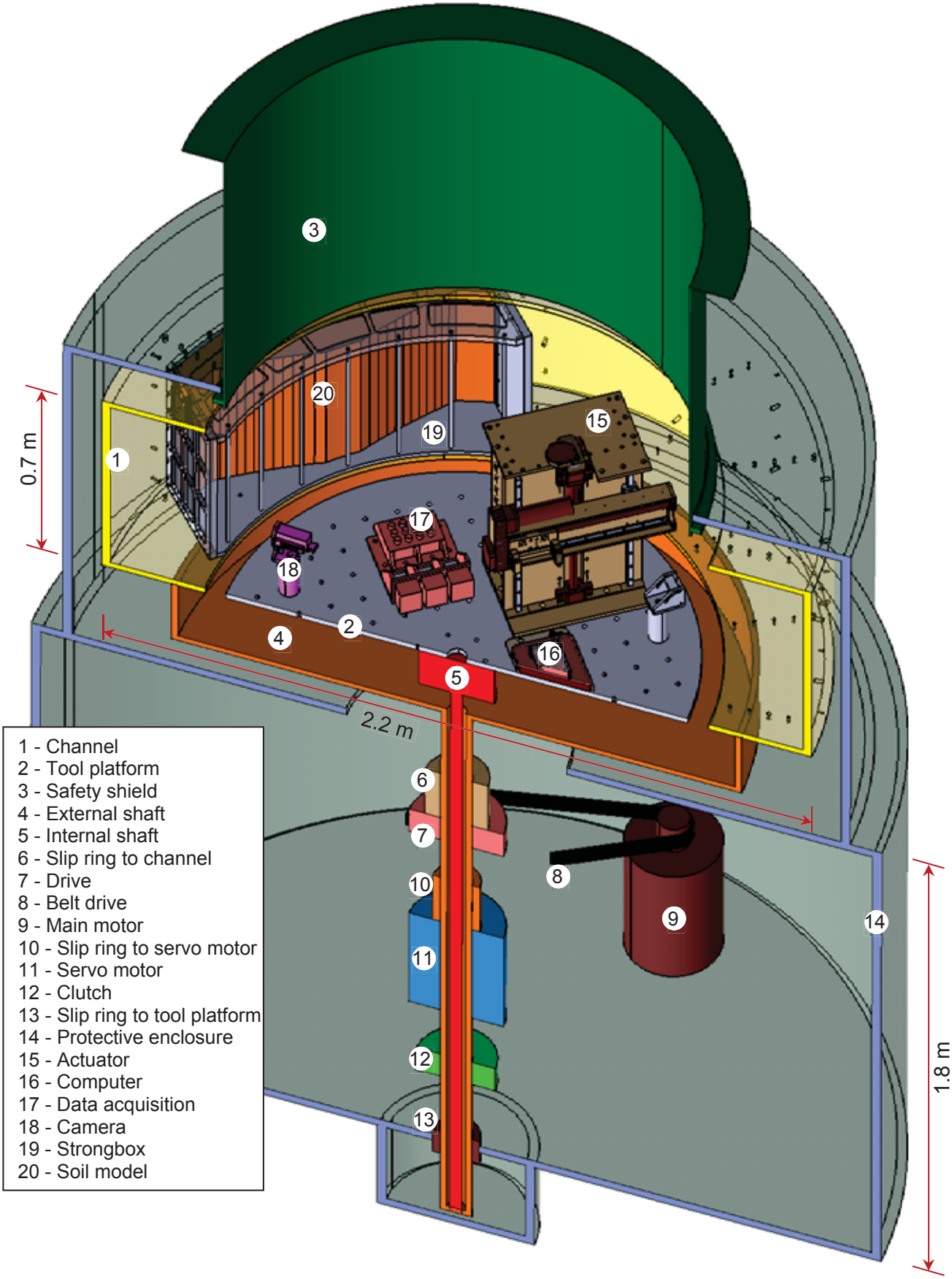

Figure 2.45: Schematic view of the geotechnical drum centrifuge at ETH Zurich.

built to allow larger models to be created. A comprehensive description of the strongbox is given in Section 4.2.1 and in Morales et al. (2012a) and Morales et al. (2012b).

2.3.5 Digital image processing

Davies & Jones (1998) describe the use of image processing techniques in centrifuge modeling as a method to obtain quantitative data of displacements and strains from a series of images taken during the experiment. The techniques can be used to obtained information in 2 or 3 dimensions. Each one of these techniques requires the use of specific conditions for the image, for instance, 3D analyses require images of the same point taken from two or more cameras simultaneously.

The two most used image processing techniques for analysis of centrifuge experiments are described in the following subsections. Particle Image Velocimetry is mainly used to obtain two-dimensional quantitative data, whereas photogrammetry is used to analyze three-dimensional problems.

2.3.5.1 Particle Image Velocimetry

Particle Image Velocimetry (PIV) is an image processing technique developed in the early 1980s to analyze flow velocities from digital images (Adrian, 1991; Gonzalez & Woods, 1992). However, White et al. (2001) argument that it might also be used for solid mechanics analyses, specifically for soil deformation measurement, as it may be considered a low-velocity flow process.

Stamhuis (2006) defines PIV in the context of application to fluid flow as “Mapping of average displacements of groups of tracer particles over a short time interval in a fluid flow by correlating sub-images of two successive images of one illuminated plane of that flow". Although this definition comes directly from PIV use in fluid mechanics, as in Adrian (1991), it describes the principle behind the process accurately.

Figure 2.46 illustrates the PIV process in a general way. First, an image (at $t = t_1$) is subdivided into several small areas called *test patches* ($I_{test}(u)$). A PIV algorithm defines a color-based pattern for each patch and seeks for that pattern over another image taken a posteriori (at $t = t_2$). The search is performed within a specific area denominated as a “search patch” ($I_{search}(u)$) by a cross-correlation technique, which is different for each piece of software. A trial displacement vector s can be drawn after the position of the test patch has been identified in the second image.

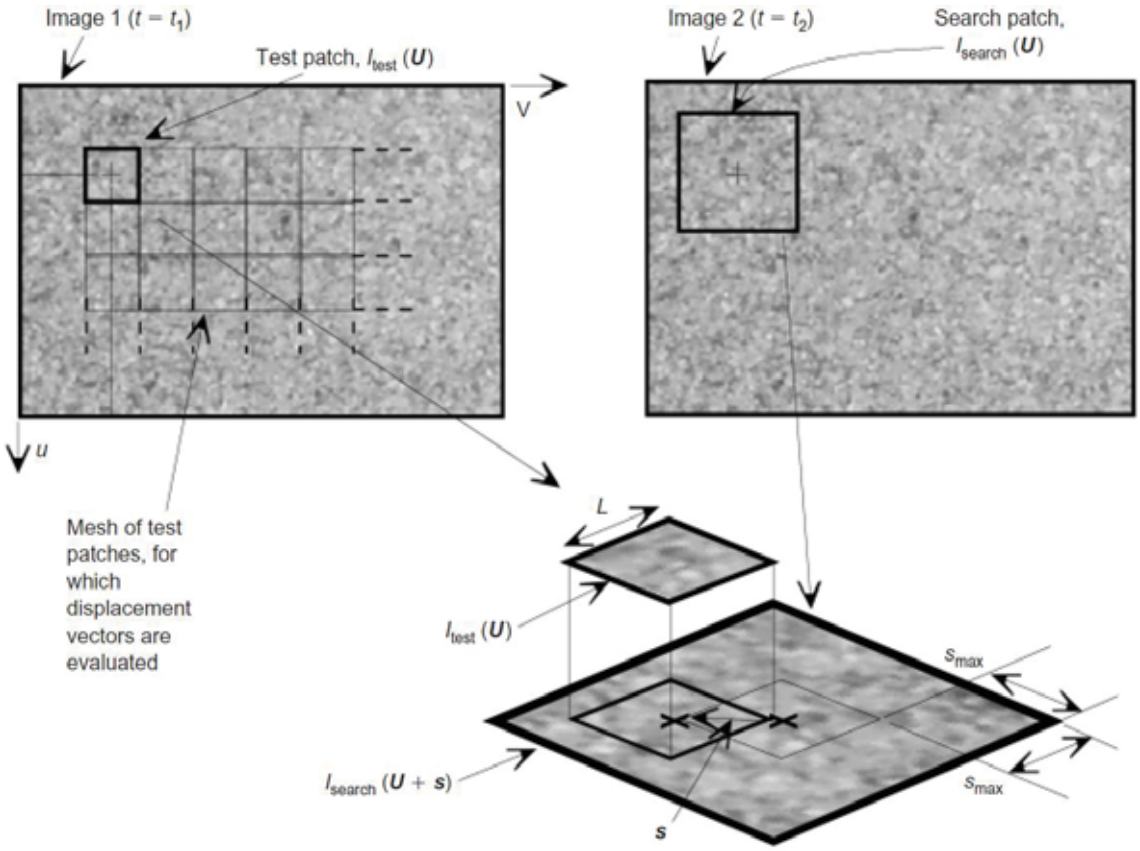

Figure 2.46: PIV analysis steps (after White et al., 2003).

Accuracy and precision of PIV analyses depend, among others, on the patch size and image contrast. White et al. (2003) analyzed the precision of the method for 5 sizes of camera sensors (CCD) by varying the test patch size, which in turn, modifies the maximum number of test patches per image (Figure 2.47). The precision is presented as a fraction of the field of view (FOV) width, which is the number of pixels of one size of the image e.g. 2500 pixels for a camera with a CCD of 6 Megapixels. The precision increases with the sizes of the CCD sensor, since better texture identification can be performed. Likewise, the precision increases with the size of the test patch, as a larger area is used to create the color-pattern to search for.

The most common software used for PIV analyses within the centrifuge testing community is *geoPIV,* which is shareware software developed by Take and White at Cambridge University. It is a Matlab® module, which implements the PIV technique in a style suited to the analysis of geotechnical tests (White & Take, 2002) and computes deformation and strain fields based on the analysis of digital photographs taken by commercial digital cameras during geotechnical centrifuge tests.

Brief descriptions regarding the use of the software can be found in White & Take (2002, 2003) and its applications for centrifuge testing are discussed, among others, by White et al. (2001); Take (2003); White et al. (2003); White et al. (2005).

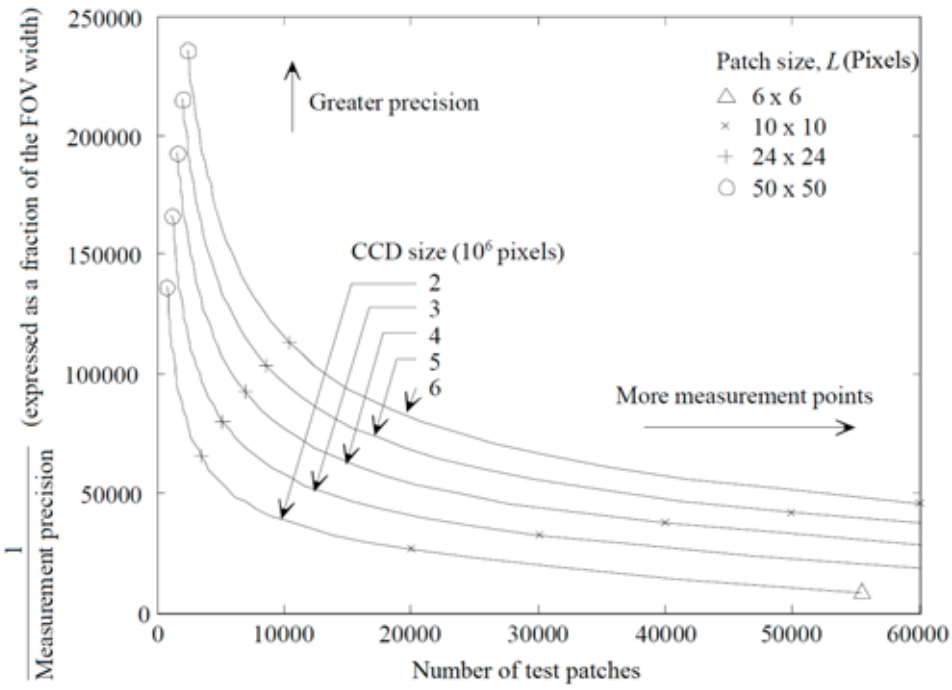

Figure 2.47: Precision against measurement array size (after White et al., 2003).

The use of this technique to analyze the results from centrifuge tests has increased significantly in recent years. Thirty-six papers referring to its use were published in the last 7th International Conference on Physical Modelling in Geotechnics held in Zurich, (Springman et al., 2010), 5 in the last Asiafuge in Mumbai, (2012) and 7 more in the last Eurofuge in Delft, (2012).

The results obtained have improved in the recent times due to the increase in resolution of the cameras used in-flight, and the automation of the tasks involved in the method, such the presented by Askarinejad & Springman (2014).

2.3.5.2 Photogrammetry

Photogrammetry is a technique used to obtain a three-dimensional visualization of an object based on two or more photographs of that object. According to Ghosh (1992), its first use can be traced back to the middle of the 19th century. Figure 2.48 shows the fundamental concept behind the technique. A point *P* with coordinates *x,y,z* is projected onto the plane of the photograph as the point intercepting the line joining the point and the focal point of the camera (projection center). This projected point has coordinates *u,v* on the plane of the photo. A set of coordinates of the projected points is obtained when the process is repeated for several points and several pictures.

A mathematical correlation can be produced from this set of coordinates to determine the position of each point in the global coordinate system, as explained by Ghosh (1992). The result of this process is known as *photogrammetric restitution,* which is the spatial representation of a three-dimensional object, based on projected points of the object on the plane of overlapping photographs.

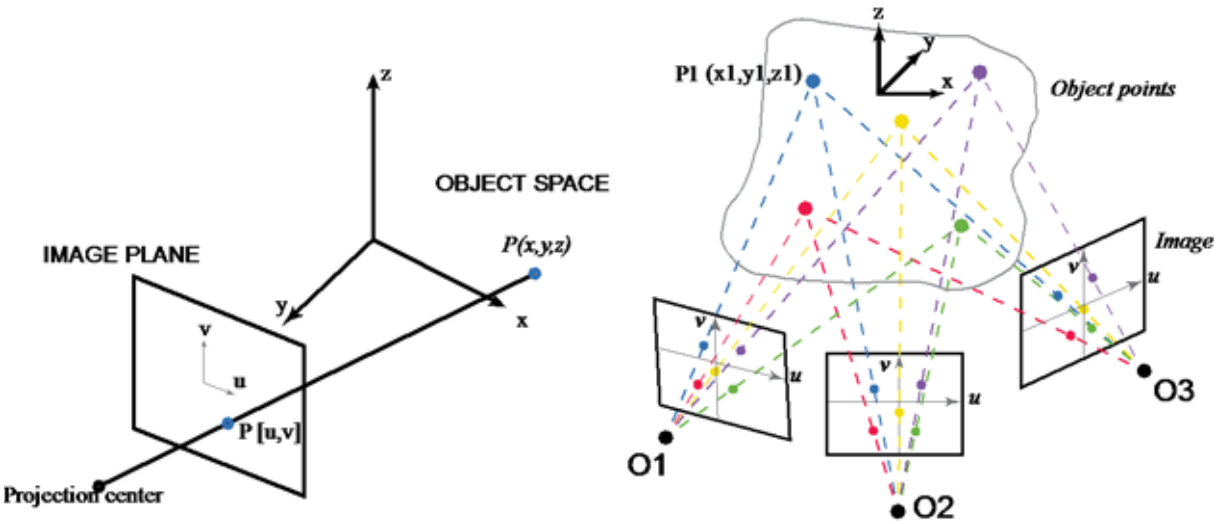

Figure 2.48: Principles of photogrammetry. Left: projection of a point in space on the plane of the photo. Right: projection of different spatial points on a set of photographs (adapted from Stanco et al., 2011).

Photogrammetry was mainly used to create terrain models based on aerial photographs. However, access to digital cameras and the increase in larger computational capacity have led to the development of a new branch in the technique called *close range photogrammetry.* The models generated can be used for precise spatial measurements, as demonstrated by Yilmazturk et al. (2008) and Sanz-Ablanedo et al. (2009).

The use of close range photogrammetry in geotechnics has increased during the last decade. Geotechnical field applications of photogrammetry include geological mapping, measurement of excavated rock surfaces, landslide monitoring and post-earthquake mapping (Cleveland & Wartman, 2006).

Thomas & Cantré (2009) describe the use of photogrammetry to analyze the deformation and rupture of clay beams and geosynthetic tubes. Complex geological processes have been analyzed with this technique, as described by Fischer & Keating (2005), who determined fault displacement distribution and lateral propagation of a monocline, and Yakar (2011), who use it to study the formation of sinkholes. Superficial erosion due to rainfall was analyzed by Rieke-Zapp & Nearing (2005) and Heng et al. (2010). The deformations of the cross section of a small-scale model of a tunnel were assessed with photogrammetry by Lee & Bassett (2006).

The first reference to the use of photogrammetry on a geotechnical centrifuge is given by Taylor et al. (1998) to measure the three-dimensional movement of the ground surface caused by a tunnel heading collapse, concluding that the quality of the measurements was comparable with conventional surveying at prototype scale. Since then, it has become a common practice at City University in London (McNamara et al., 2012).

2.3.6 Previous research on dyke behavior

Lee et al. (2010) assert that the centrifuge modeling studies of the New Orleans levees, which failed during Hurricane Katrina in 2005, exemplify the usefulness of physical modeling to explore complex fluid-embankment interactions.

A review of previous studies on dyke behavior, appraised with small-scale models under enhanced gravity, is given in this section. The section is divided into three parts: studies modeling flooding and overflow, studies involving flooding but no overflow, and studies analyzing other types of dyke failure.

2.3.6.1 Analysis of dykes exposed to flooding with a final overflow phase

Okumura et al. (1998) tested two 1/20th scale models of a dyke at 20-g. Both of them were 155 mm high (3.1 m at prototype scale). The models were built over an impermeable steel base with slope gradients of 1:1 on both the water and the air-side, owing to the small size of the strongbox (0.46 × 0.46 × 0.2 m) (Figure 2.49a). The soil used was a mixture of sand (87%), silt (2%) and clay (11%), which is classified according to the USCS as SM. The average grain size was 0.55 mm, with a maximum dry density of 1.9 kg/m^3, at an optimum water content of 12.7 %. The models were built by compacting the soil in layers to 97% of the maximum dry density, at the optimum water content.

Water was supplied from a storage tank to fill the upstream space at a constant rate (not specified). This allowed two different flooding scenarios to be tested. Firstly, a sudden overflow was simulated for one of them (0.69 days filling + 0.7 days of overflow), when the water level was originally at the bottom of the water-side. The overflow phase for the second model began after steady state flow had been applied, with the water level at 90% of the dam height.

Figure 2.49b presents a general failure mechanism for both experiments, while Figure 2.50 shows the failure mechanism for each series. Gully erosion is observed along the slope during the first stage of the overflow, and then an internal erosion process takes place at the toe of the air-side slope. The internal erosion is clearer in the first series (rapid water rise and overflow), in which it creates a vertical ridge in the scarp, whose dimension was not reported, as the erosion develops upstream. On the other hand, superficial erosion is the main characteristic for the second series (overflow after steady state). The erosion erodes the sand almost parallel to the original slope.

Although the results obtained help to understand the breaching mechanism of a dyke under an overflow event, the geometry of the model and testing conditions were not optimal. On the one hand, the modelers had to construct a dyke model with steeper slopes than is recommended by construction guidelines, such as USACoE (2000). On the other hand, the authors could not apply a defined water level, which could vary with time. This is important, as overflow is normally the final step in a chain of cyclic flooding events.

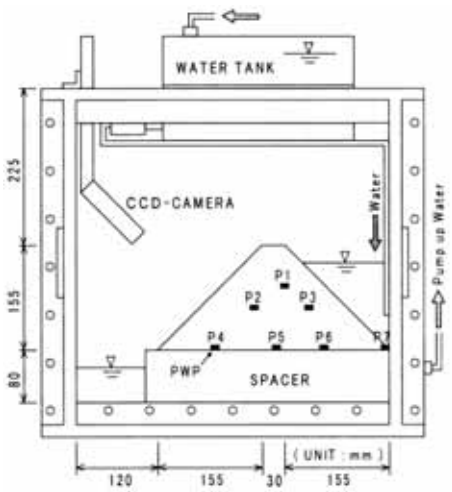

a) Model geometry.

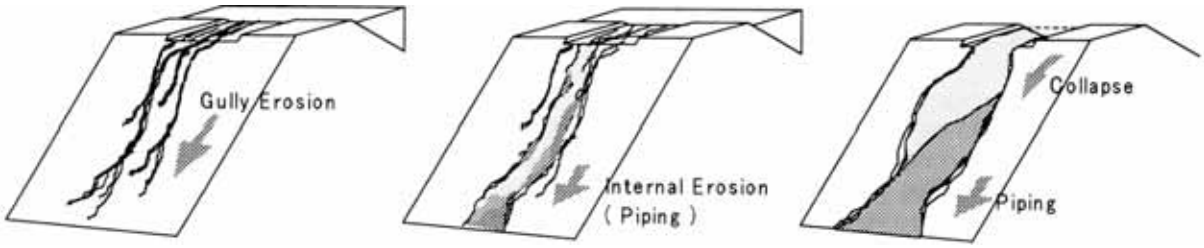

b) General failure process observed for both experiments.

Figure 2.49: Overflow test on a dyke made of silty sand (after Okumura et al., 1998).

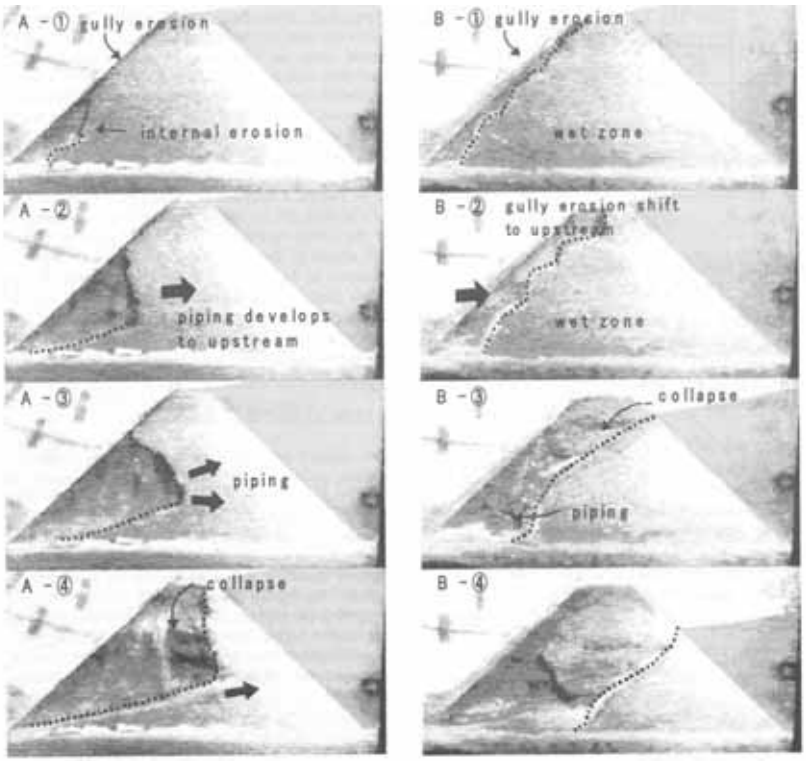

a) 0 %. *b) 90%.*

Figure 2.50: Patterns of the failure mechanism for initial water table height as % of dyke height prior to overflow (after Okumura et al., 1998).

Ko et al. (1989a, 1989b, 1989c) tested six models of a dyke, 1.8 m high at prototype scale with slope gradients 1:3.0 and 1:2.0 for the air and water-sides, respectively (Figure 2.51). The model was designed to verify the results of a full-scale test performed by Chen et al. (1987). However, only the air-side half of the dyke was modeled (Figure 2.52b) due to restrictions in the size of the container. This confirms the necessity of a modeling, which includes the complete cross section of the dyke.

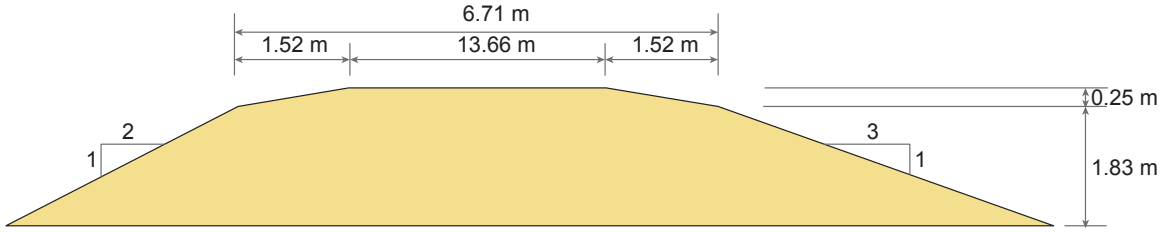

Figure 2.51: Cross section at prototype scale of the analyzed dyke with a non-erodible revetment (adapted from Ko et al., 1989b).

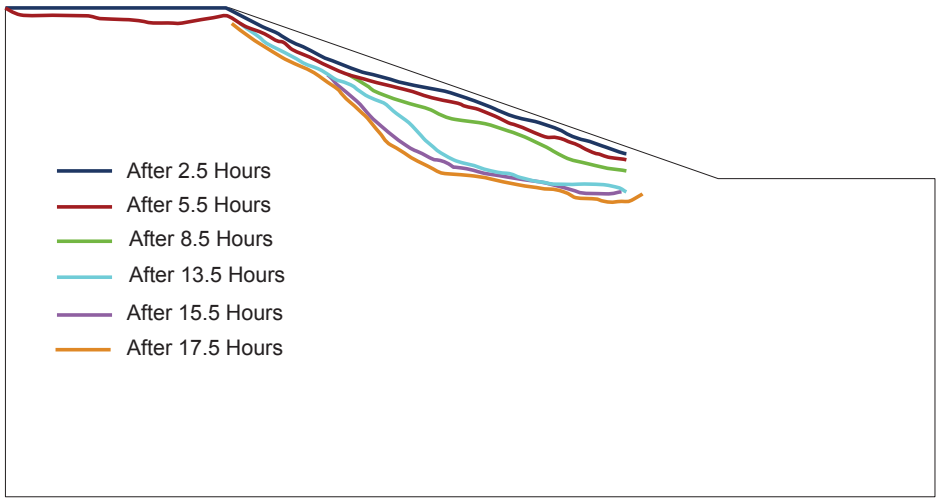

a) Full-scale test (adapted from Chen et al., 1987).

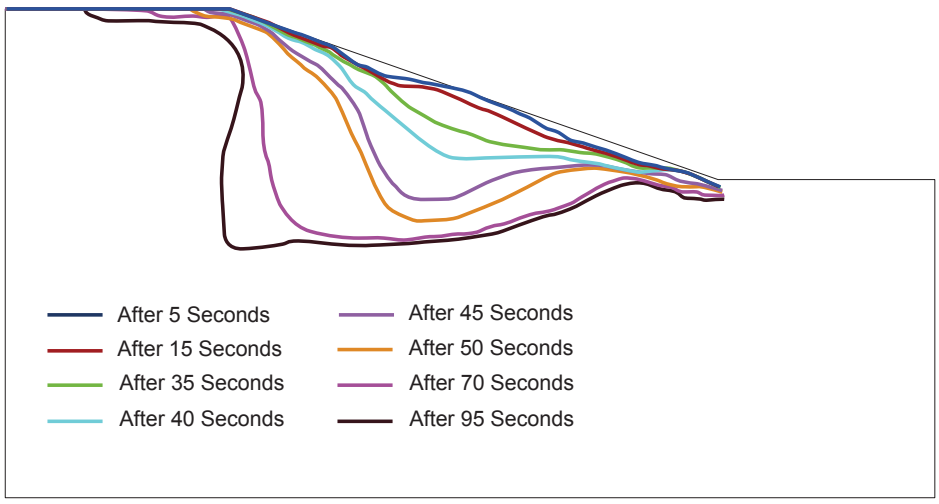

b) Small-scale test in a geotechnical centrifuge (adapted from Ko et al., 1989b).

Figure 2.52: Comparison of the erosion profiles of the air-side slope of the dyke, at different times.

The same soil was used in both field test and centrifuge experiments (37% sand, 50% silt, and 13% clay). It is classified as a both silt or clay of low plasticity (CL/ML), as it lies on the A-line of Atterberg's classification chart (w_L = 19%, I_p = 13%). The soil was mixed in an electric mixer with the appropriate quantity of water to obtain an optimum water content of 14%, and then compacted statically in the sample container in layers of 12.5 mm using a hydraulic press to a dry density of 90% of the maximum dry density (1890 kg/m^3). The surface of each layer was thoroughly scarified prior to placing the subsequent layers.

The experiment was carried out with an acceleration of 71-g. Water was applied directly on the crown of the dyke with an overflow depth of 8.5 mm, and controlled by two shut-out valves to have a fixed flow rate. This value was not reported. Photographs were taken every minute to analyze the erosion profiles and their development. These are shown in Figure 2.52 for the full and small-scale tests. The authors compared the profiles to find matches in both cases. The times of the matched profiles at model and prototype scale were used to derive a scaling factor for time and erosion rates of dyke built with clay (Equations 2.46 and 2.47), where $\dot{E}$ is the erosion rate. However, the flow patterns were not the same. Therefore, the scaling factor might not be correct.

$$\frac{\dot{E}_p}{\dot{E}_m} = n^{-1.38} \qquad 2.46$$

$$\frac{t_p}{t_m} = n^{1.38} \qquad 2.47$$

This project represents an important step to determine the scaling factors of erosion due to overflow, and the results can then be applied to dykes built with fine-grained soils. Nonetheless, and owing to physical differences in the erosion process for granular soils, the development of this process due to overflow in dykes built with sand remains less understood.

2.3.6.2 Analysis of dykes with a flood process but without an overflow phase

Cargill & Ko (1983) tested 12 models to investigate a transient flood during both water level rise and rapid drawdown of a dyke built with silty sand (SM) compacted at a water content of 10% in layers of 12.5 mm thick, although the densities were not reported. The models were 250 mm high, which at an acceleration of 50-g, represented a height of 12.5 m at prototype scale (Figure 2.53). The slopes were 2:1, so that both slopes could be modeled in the strongbox with dimensions 455 × 175 × 300 mm. The foundation soils under the dyke were also not modeled, and were therefore assumed to be impermeable. This represents a limitation of the models, as dykes can be also built on a soil with greater hydraulic conductivity, which can combine the create unsafe conditions (Mayor & Springman, 2012).

Water was provided through a hydraulic slip ring connected to a solenoid valve. The water level rose in 4 minutes (166 hours at prototype scale) until it reached 75% of the total height of the dyke, and it was then kept at that level for 8.5 minutes (354 hours at prototype scale);

finally, a rapid drawdown event was simulated by lowering the water level in 2 minutes (83 hours at prototype scale). The pore water pressures registered are shown in Figure 2.54. The pore water pressure at points 3 and 4 is dissipated faster than for the other points. This is a consequence of the double drainage path that might occur following rapid drawdown (towards water and air-side at different times in the drawdown), whereas points 1 and 2 will have only one drainage direction (towards the air-side).

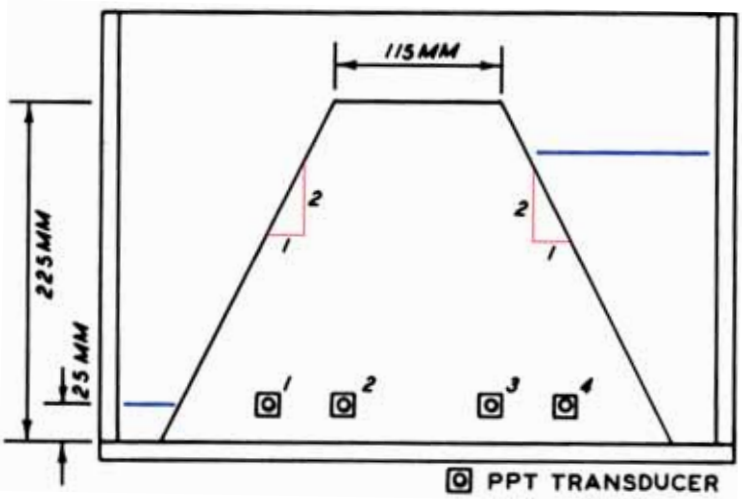

Figure 2.53: Geometry of the dyke model subjected to flood and rapid drawdown (adapted from Cargill & Ko, 1983).

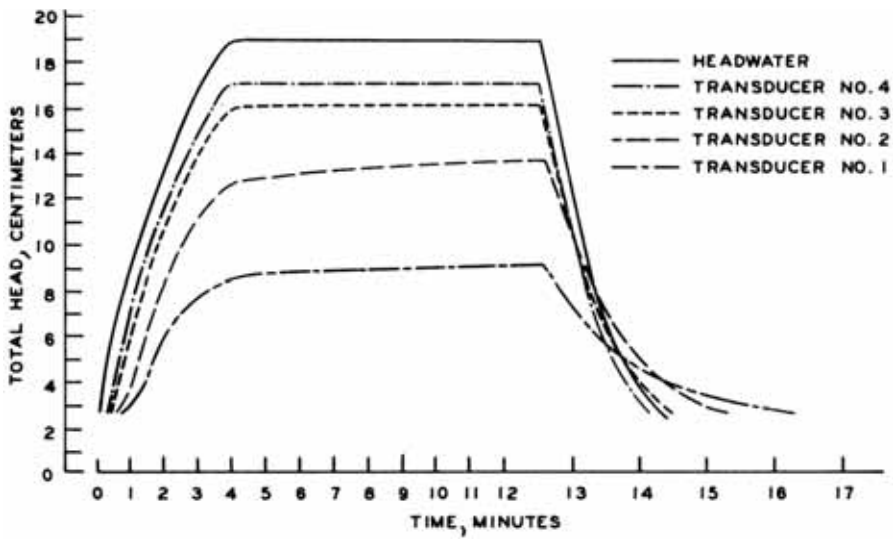

Figure 2.54: Total water head at model scale of the tests of a dyke subjected to flood and rapid drawdown (after Cargill & Ko, 1983).

The only research about dyke modeling in a drum centrifuge is reported by Kusakabe et al. (1988a). A dyke model was built around the circumference of the drum, with slope gradients of 1:1, with a height of 40 mm and tested at 40-g. This represented a dyke of 1.6 m height at prototype scale. The whole surface of the channel was filled with marine clay, which was

used to simulate an impermeable layer underneath the dyke. Loam was compacted manually at a water content of 104% to form the dyke over 3/4 of the circumference of the drum, whereas a mixture of the loam and Toyoura sand was compacted over shorter lengths in 4 mixture ratios sand/loam in terms of the weights (0, 28.5, 60, 70%) in the remaining 1/4 of the drum. A structure was placed in the middle of this dyke section (Figure 2.55a). It was made of mortar, and simulates some sluice gates. No information was reported regarding the achieved densities after compaction.

The flooding condition was simulated by pouring water directly into the water-side of the model through a vinyl tube, which was stationary while the centrifuge was spinning, although the flow rates were not reported. An overflow phase was not possible to simulate, as the crest of the dyke model was 5 mm above the depth of channel of the centrifuge rim (Figure 2.55b).

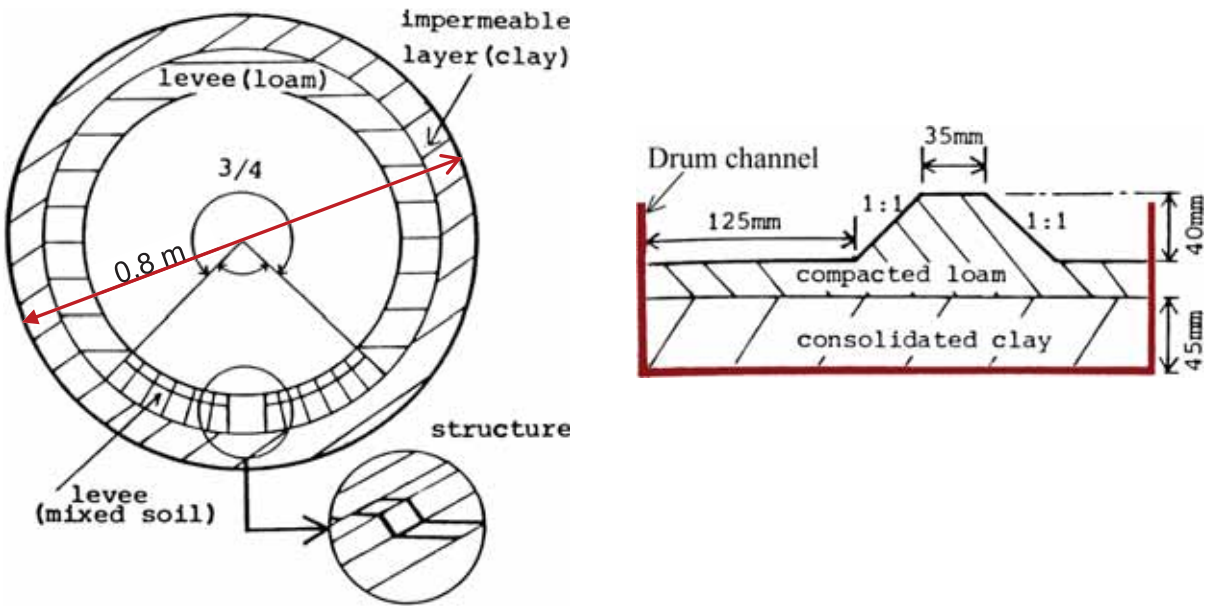

a) Plan view of the model inside the centrifuge. *b) Cross section of the model.*

Figure 2.55: Dyke modeled with 1:1 slopes around the circumference of a drum centrifuge (after Kusakabe et al., 1988a).

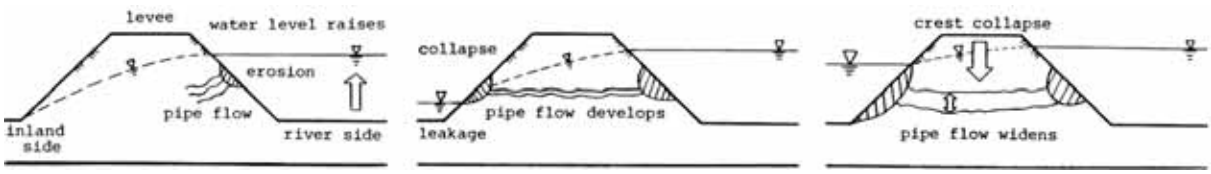

Figure 2.56: Development of the dyke failure (after Kusakabe et al., 1988a).

Figure 2.57: Sketch showing the formation of pipes (after Kusakabe et al., 1988a).

The failure mechanism observed in all the tests performed is shown in Figure 2.56. Surface erosion on the water-side slope is observed as the water level rises. Simultaneously, a pipe flow begins to develop (Figure 2.56a). A local failure is observed on the air-side slope, caused by the increase of water leakage through the pipe (Figure 2.56b). The flow pipe increases in diameter, as result of the internal erosion. This causes the collapse of the crest of the dyke. This emphasizes the importance of selecting appropriate slope angles on the water and air-sides of dykes to prevent a piping induced failure through the dyke and offers and opportunity for such investigations to be carried out.

The main difference observed for the different types of dykes, was that those dykes with a low content of sand (0, 28%) the pipes remained stable, before collapse of the crest, up to greater diameters than for those dykes with larger content of sand (60, 70%). The authors attributed this to a larger cohesion of the soils with lower content of sand, although a more modern interpretation might consider the performance of the unsaturated mixtures to rely more on suctions than any cohesion in a remolded model (Schofield, 2005).

The results obtained from this research add to the general understanding of failure processes in dykes. However, the results might be affected by the model preparation and testing procedures, because the manual compaction of the soil, without an apparent control of the achieved density might lead to looser soil layers, or concern about the compaction layers interfaces, as no scarification of each layer was reported. Additionally, the pouring of the water from a stationary point outside the spinning channel might have triggered the superficial erosion observed on the water-side slope. Furthermore, the lack of instrumentation inside the model does not contribute to the analysis of the process. Finally, an overflow phase was not possible to achieve, which would have provided a complete view of the flooding process.

Sasanakul et al. (2008); Ubilla et al. (2008); Sasanakul et al. (2010) and Steedman & Sharp (2011) modeled the dyke system that failed during the flood caused by Hurricane Katrina in 2005 (Seed et al., 2005). Five models of dykes were tested: London Avenue North and South, Orleans North and South, and 17th Street. As a result, two types of dykes were identified as being critical (Figure 2.58): those in which the swampy marsh laid on top of the sand (London Avenue and Orleans South), and those which had a clay substratum (17th Street and Orleans North). All of them had been remediated by adding a sheet pile wall, which protruded above the levee surface to provide additional flood retention capacity. Nevada sand was used in the models to represent the natural sand, kaolin to represent the soft lacustrine

clay and levee clay, and natural material from the field to represent the swampy marsh deposits.

Nevada sand was reported to have a specific gravity (G_S) of 2.67, maximum and minimum unit weitghts of 17.33 and 13.87 kN/m^3, respectively, which correspond to minimum and maximum void ratios of e_{min} = 0.511 and e_{max} = 0.887. The permeability was around 5.6 × 10^{-5} m/s and mean grain size d_{50} 0.15 mm. The sand layer was built by dry pluviation at 60% relative density, and saturated afterwards. The kaolin clay had a unit weight of 17.1 kN/m^3, at a water content of 43%. The liquid and plastic limits w_L, w_p were 60–70% and 30–35%, respectively.

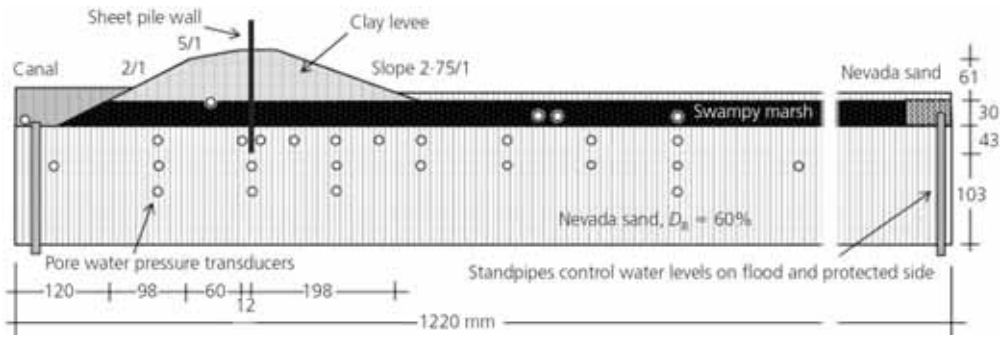

a) London Avenue South dyke model.

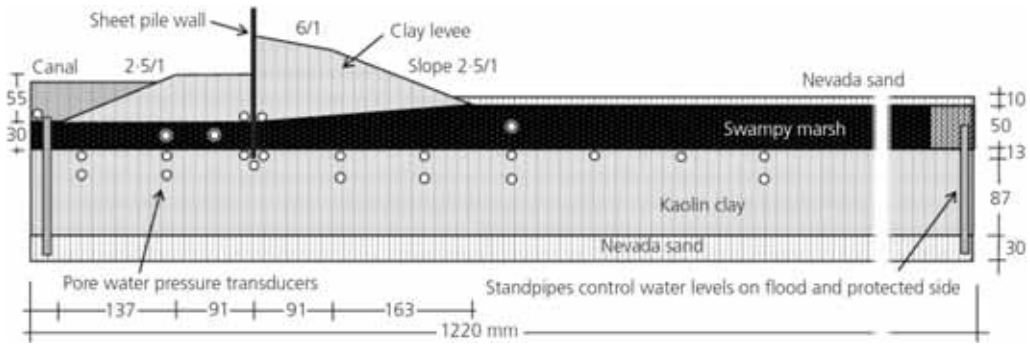

b) 17th Street dyke model.

Figure 2.58: Models of the dyke systems in New Orleans that failed during Hurricane Katrina in 2005 tested at 50-g (after Steedman & Sharp, 2011) (Dimensions in mm).

Dry powdered kaolin clay was mixed with de-aired water until a slurry mix with 100% moisture content was achieved, and the slurry was then placed in the container to be consolidated at 50-g for 15 hours (1562 days at prototype scale). After completion of the consolidation phase, the sheet pile and the peat soil were placed; the latter was cut from undisturbed blocks taken in-situ. A second consolidation phase took place during 4 hours (416 days at prototype scale). Finally, the levee sections, which were prepared in molds with consolidated slurry, were placed on top of the peat layer; adjacent to the sheet pile wall.

Water was supplied from a reservoir underneath the dyke model by a pump. The water level in the canal was imposed at 0.3 m above the crest, which was defined as the normal operation level prior to hurricane Katrina. The water level was then increased, at a constant rate (not specified), to simulate the Katrina flood.

Although two different failure mechanisms were observed in these models, both started in the same way. When the water level exceeded the dyke height and was contained inside the channel by the sheet pile, the hydrostatic water pressure was sufficient to rotate the sheet pile. As a consequence, a small crack developed at the interface between the sheet pile and the dyke, which was then filled with water. The wall was subjected to hydrostatic pressure, over a greater height, from the water filling the crack, which extended until the total lateral stress equaled the hydrostatic pore water pressure (Figure 2.59).

The difference in the subsequent failure mechanisms lay in their evolution once the wall started to be displaced. The wall started to rotate for those dykes without a clay substratum (London Avenue and Orleans South). This occurred until the wall reached failure and there was full hydraulic connection between the sand and the canal through the crack (Figure 2.60).

A different failure mechanism was observed in the models where the toe of the sheet pile wall terminated in the clay layer, as shown in Figure 2.61a-d. Following the opening of the water-filled crack (Figure 2.61b & c), a translational failure (Figure 2.61d) occurred through the clay, starting at the toe of the wall and progressing landwards (Steedman & Sharp, 2011).

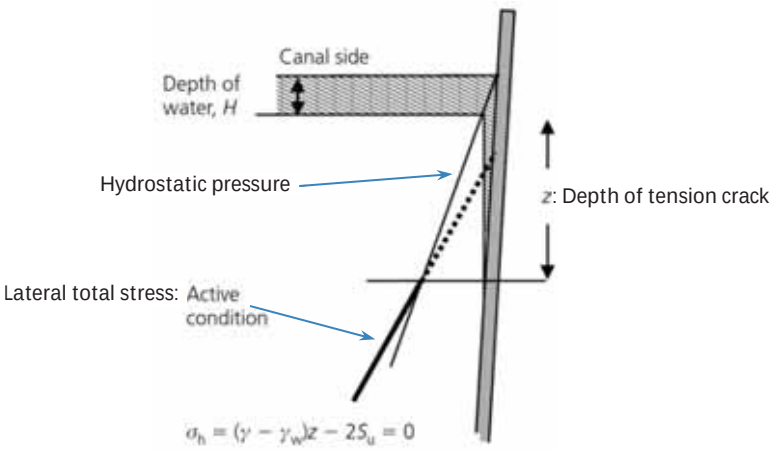

Figure 2.59: A tension crack developed due to the wall being rotated due to the raised water level (after Steedman & Sharp, 2011).

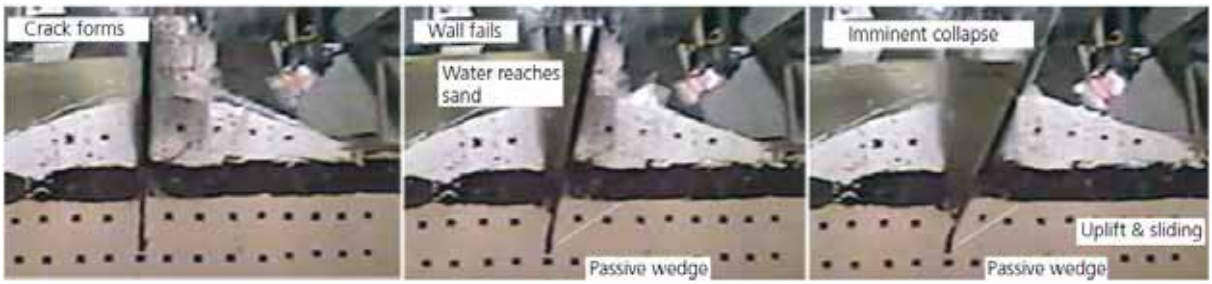

a) *b)* *c)*

Figure 2.60: Development of the failure of the London Avenue South dyke (after Steedman & Sharp, 2011).

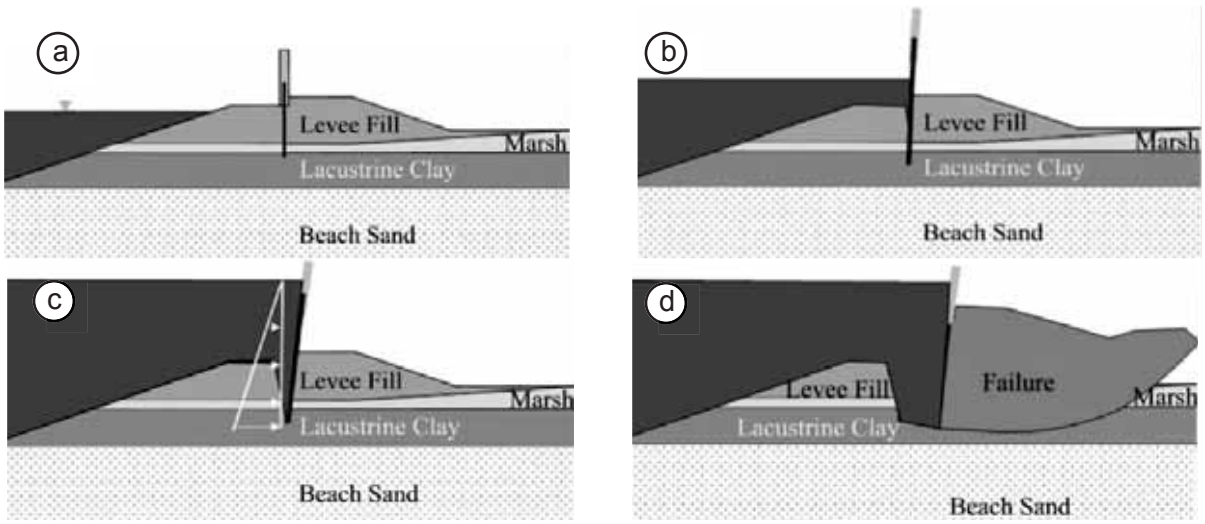

Figure 2.61: Development of the failure of the 17th Street dyke (after Sasanakul et al., 2008).

Kumar & Viswanadham (2012) analyzed the use of a geocomposite to form an internal toe drain in the dykes. They used a 1/30th scale dyke model that was 200 mm high (6 m at prototype scale). The water-side slope had a gradient of 1:1.5, while the air-side was 1:1.0 (Figure 2.62a). The soil used was a mixture of 80% fine sand with 20% commercially available kaolin, which led the authors to claim that the soil could be considered to behave as silty sand. The soil was reported to have maximum dry unit weight of 18.75 kN/m^3, at an optimum water content of 8%. Nevertheless, no information was given about the construction procedure or final densities achieved. Values for cohesion (11.9 kPa) and friction angle (27°) were interpreted from a simple drained direct shear test. The hydraulic conductivity at $\gamma_{d\,max}$ was reported to be 1.54×10^{-6} m/s.

According to the authors, the geometry of the dyke was selected such that the factor of safety at the onset of seepage would be close to 1. Two models were tested: one was a homogenous dyke (RL-1) and the other was of the same soil but with an internal drain at the interface between dyke and ground from the toe to the point under the center of the crest of the (RL-3).

A flood was simulated over four days (at prototype scale), by pumping water from a reservoir outside the model container. Inducing identical flood levels for both tests was attempted, but due to the limitation of the pump capacity in a high gravity environment, the water head slightly dipped and fluctuations in the flood level were observed (Figure 2.63).

The performance of the toe filter is shown in Figure 2.64, where a normalized pore water pressure (NPWP) is analyzed in time for point PPT3 and PPT5, i.e. close to the middle of the base, and at the toe of the dyke. This normalized value is the ratio between the measured pore pressure u_w and the external water pressure applied at the bottom of the water-side slope of the dyke, which was measured by PPT 1. The evolution of NPWP for model RL-3 is similar at both points, with an increase to a value close to 0.2, which remains constant during the rest of the test. This emphasizes that the use of the filter was effective in lowering the water table inside the dyke.

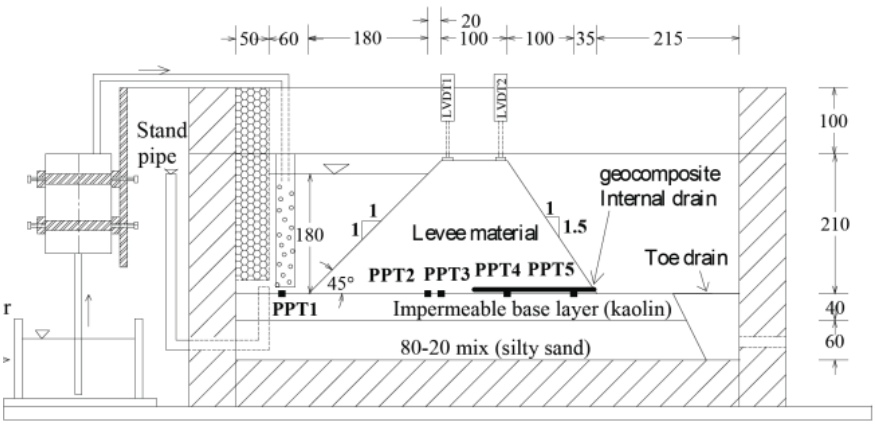

Figure 2.62: Geometry of the small-scale model of a silty sand dyke with a geocomposite as an internal drain. Model RL-1 did not feature the internal drain. (after Kumar & Viswanadham, 2012).

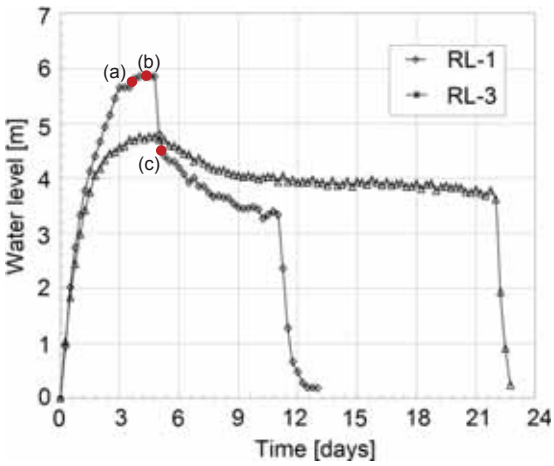

Figure 2.63: Water level imposed on models RL-1 and RL-3. (after Kumar & Viswanadham, 2012).The red points correspond to the times in Figure 2.65.

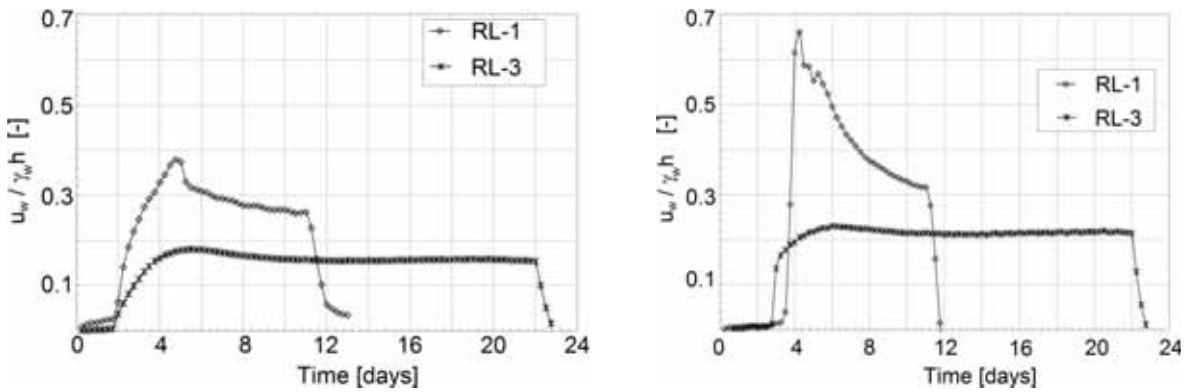

a) At PPT 3. *b) At PPT 5.*

Figure 2.64: Normalized pore water pressures at prototype scale, where $\gamma_w h$ is the measurement made by PPT 1 in Figure 2.62. (after Kumar & Viswanadham, 2012).

The NPWP of model RL-1 shows variations that correspond to the water levels imposed (Figure 2.63), with higher values at the toe of the dyke (PPT 5). This indicates that excess pore pressures were developed at this point (NPWP = 0.68). This might explain the failure

process observed on the air-side slope, in which a circular slip surface developed (Figure 2.65) just before attaining the highest possible flood level (point *a* in Figure 2.63). Although the authors do not give any explanation for this, the most plausible situation is that the excess pore water pressure reduced the effective stresses, which together with the loading applied by the steep slope, led to the instability and hence the resistance along the shear surface.

This research shows the importance of installing a toe filter to reduce the possibility of failure on the air-side slope during high water level conditions. Nonetheless, the modeling has as weakness, as most of the work reviewed above, that the model does not represent the geometry recommendations given by construction and design guidelines. This is a consequence of the reduced space available in the strongboxes used.

a) 3.85 days. *b) 4.51 days.* *c) 5.1 days.*

Figure 2.65: Development of dyke failure on the air-side slope for model RL-1 (with no toe drain) (after Kumar & Viswanadham, 2012).

2.3.6.3 Analysis of diverse features in the stability of dykes

Bezuijen & den Adel (2006) report the results of two tests performed at an increased gravity level of 80-g. The aim of the experiments was to investigate the stability of a dyke by raising the ground water flow from the center of the dyke to both slopes. According to the authors, this is a possible loading situation for a dyke in the neighborhood of a river, with a varying water level and a permeable soil layer that connects the water level in the river with the water level inside the dyke. The tests used a sand at 60% relative density, with a d_{50} = 95 µm, coefficient of uniformity C_u = 1.55, and a hydraulic conductivity of 9 $\times 10^{-5}$ m/s, at a porosity of 0.34.

The geometry of the model was the same for both tests. The dyke was 110 mm high (8.8 m at prototype scale). One test was made of homogenous sand, whereas a clay cover was placed over the sand for the second test. The thickness of this clay layer was not reported. The dyke had slopes with gradients 1:2.0 and 1:3.3 (Figure 2.66). The water inlet was located in the middle of the base of the dyke, and was connected to a tank of 100 l capacity, which was pressurized with air to increase the water table.

Figure 2.67 presents a sequence of 4 pictures taken at different hydraulic loads to the slope with a gradient of 1:2.0 (Figure 2.67a) and for the slope with a gradient of 1:3.3 (Figure

2.67b). The times at which the photos were taken were not reported by the authors. The yellow lines and the blue triangles represent the original profile of the dyke, and the water level, respectively. Soil was flushed away from the core of the homogeneous dyke material and deposited beyond the toe. Some blocks of partially saturated soil detached from the slopes were flushed away. The amount of eroded soil was greater for the steeper slope (1:2.0).

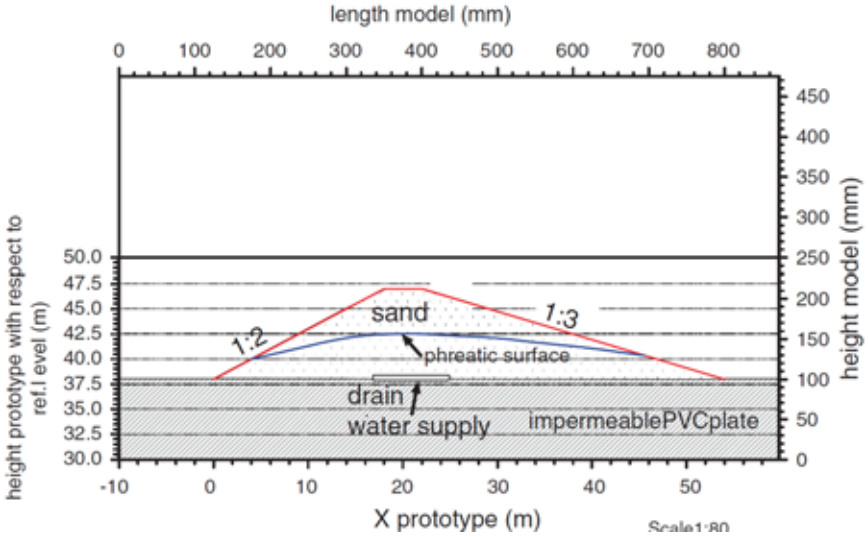

Figure 2.66: Modeling of a dyke at 80-g with a raised groundwater table in the center (after Bezuijen & den Adel, 2006).

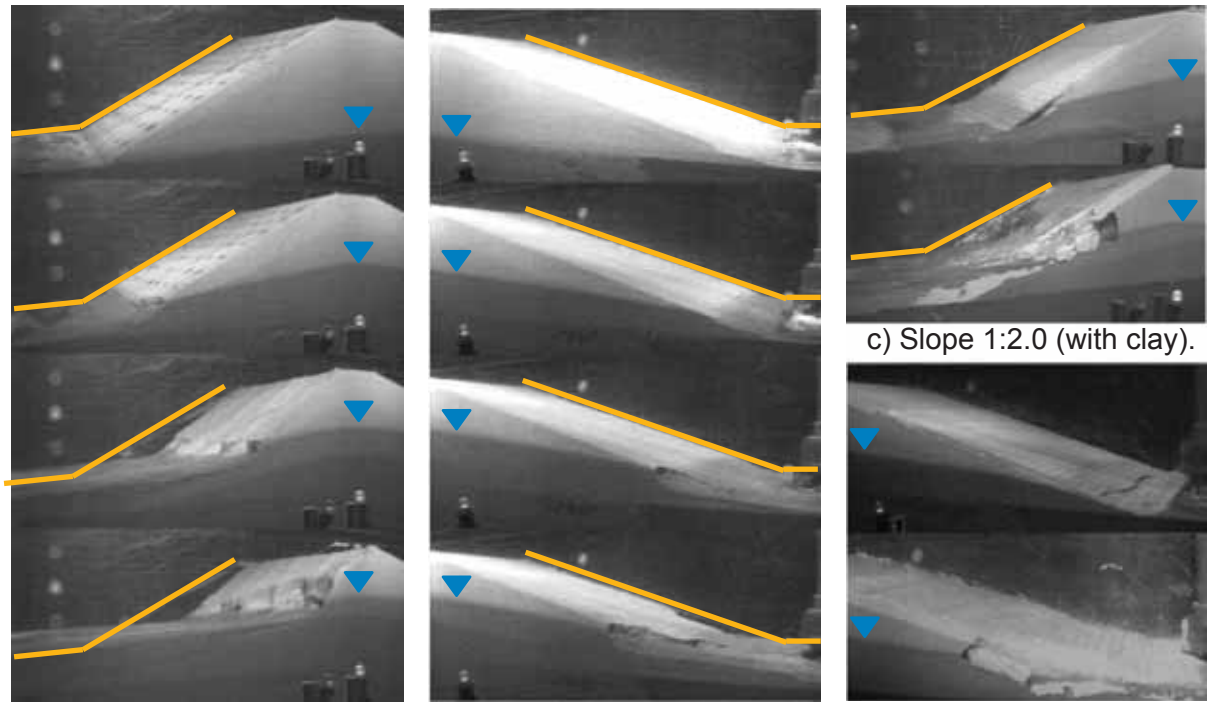

c) Slope 1:2.0 (with clay).

a) Slope 1:2.0. *b) Slope 1:3.3.* *d) Slope 1:3.3 (with clay).*

Figure 2.67: Failure mechanisms of a dyke varying the groundwater table from the center, showing the original surface (yellow) and the height of the water table (blue triangle). (after Bezuijen & den Adel, 2006).

A similar failure mechanism was seen when a cover of clay was used. The slope with a gradient of 1:2.0 experienced significant generalized damage and loss of soil volume from the toe (Figure 2.67c), whereas the progressive damage for the slope 1:3.3 was the result of failure through grains of sand being removed individually from the contact between the model and the walls of the box (Figure 2.67d).

Figure 2.68 shows the process through which a block of unsaturated sand detached from the slope. Water springs appeared on the air-side slope underneath a vertical ridge. This caused the pore pressure to increase in the soil at the ridge, with the subsequent decrease of effective stress, which led to a failure of a block of soil, creating a new ridge, and the process repeated itself.

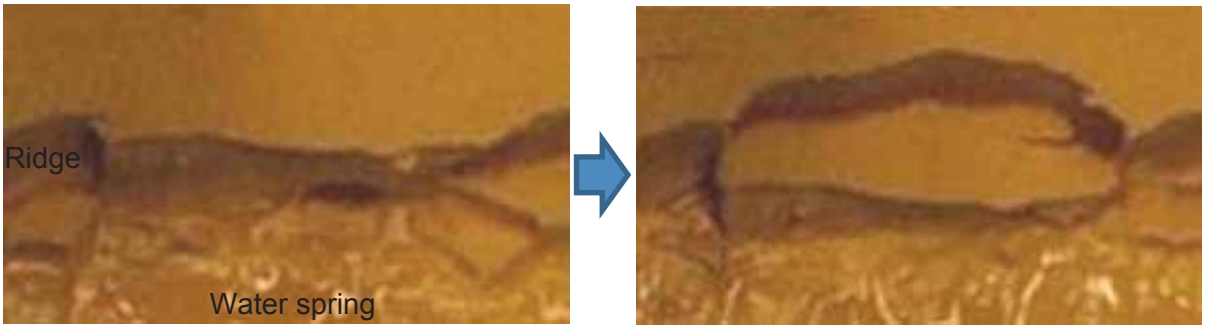

Figure 2.68: Local instability for the sand model with slope gradient 1:2.0 (after Bezuijen & den Adel, 2006).

2.4 Full-scale case studies

Data on overflowing events are scarce, and full-scale tests to study the problem are very expensive (Ko et al., 1989b). Therefore, sufficiently detailed information regarding field or full-scale test is rare and often limited. Notwithstanding these challenges, information was found from three research projects, in which full-scale models relevant to this research project was found. The first is a series of full-scale models tested in Norway, in which both types of failure overflow and internal erosion were investigated. Another series of tests in the Netherlands studied failure due to overflow. Finally, two tests about failure owing to internal erosion are reported.

Höeg et al. (2004); Vaskinn et al. (2004); Vaskinn et al. (2005) and Morris et al. (2007) report the construction of 5 full-scale embankments in the vicinity of Røssvatnet, Norway, where the Røssvassdammen dam is located (Figure 2.69). The field tests were located in a valley that was 600 m downstream from the dam, so that the inflow of the dyke could be controlled by regulating one or more of the three flood gates of the dam. However, water flow rates during the tests were not reported.

The geometrical characteristics of the dykes are listed in Table 2.5. Three dykes were built homogeneously, with one type of soil (clay, gravel, moraine), whereas two dykes had a rockfill protection layer to cover a moraine core. The height of the dykes varied between 4.5 and

6 m, with a length of 42 m for all the tests. Each dyke was built with the same slope gradient on both air and water-side, which varied between 1:1.3 and 1:2.0 and 8 pore pressure transducers were installed at the base of the dykes. No reference was given regarding the choice of these geometries, nor were results from these devices presented by the authors.

Figure 2.69: Location of the field test in Norway (www.maps.google.com; Morris et al., 2007).

The physical properties of the four soils used to build the dykes: clay, gravel, rockfill and moraine, are listed in Table 2.6. No information was reported about the construction methods, except for the dyke built with clay, which was reported to have been built in layers of 0.4 m and compacted mechanically.

Table 2.5: List of the 5 field tests carried out in Røssvatnet, Norway (after Vaskinn et al., 2004).

Test	Type of dyke	Slope gradient air-side	Slope gradient water-side	Height [m]	Width [m]	Breaching mechanism
1	Homogeneous clay	1:2.0	1:2.0	6	36	Overflow
2	Homogeneous gravel	1:1.7	1:1.7	5	36	Overflow
3	Rockfill with central moraine core	1:1.5	1:1.5	5.9	36	Overflow
4	Rockfill dam with central moraine core	1:1.5	1:1.5	6	36	Internal erosion
5	Homogeneous moraine	1:1.3	1:1.3	4.5	36	Internal erosion

Table 2.6: Properties of the four soils used the tests (adapted from Vaskinn et al., 2005).

Property		Clay	Gravel	Rockfill	Moraine
Gravimetric water content	[%]	30	7	2.6	6

d_{50}	[mm]	0.009	4.65	85	7
Porosity	[-]	0.47	0.22	0.16	0.21
Void ratio	[-]	0.89	0.28	0.19	0.27
Angle of friction	[°]	22.9	42	42	42
Cohesion	[kPa]	4.9	0.9	0	20
Dry density	[kN/m^3]	14.7	21.15	20.8	20.5

A notch of width 3 m and depth 0.5 m deep was dug in the middle section of the dyke for the first three tests. This was done to avoid erosion near the abutments of the dyke. Internal erosion was originated for test 4 and 5 by including a built-in defect during the construction of the dyke (Figure 2.70). This acted as a trigger device and consisted of a PVC pipe of diameter 200 mm, with openings on the top. The pipe was covered with homogenous sand (details of this sand were not reported). Two triggers were included for the rockfill dyke with a moraine core (test 4). The small trigger was covered with a sand layer of 1 by 1 m, whereas the sand layer around trigger number 2 was extended to the top of the dam, as shown in Figure 2.71. The trigger for test 4 started at the middle of the base of the dyke, i.e. in the moraine core, whereas it was extended along the complete base of the dyke for test 5. The pipes were closed at the downstream end by a valve at the start of the test. Sand was then flushed out by opening this valve and the internal erosion started.

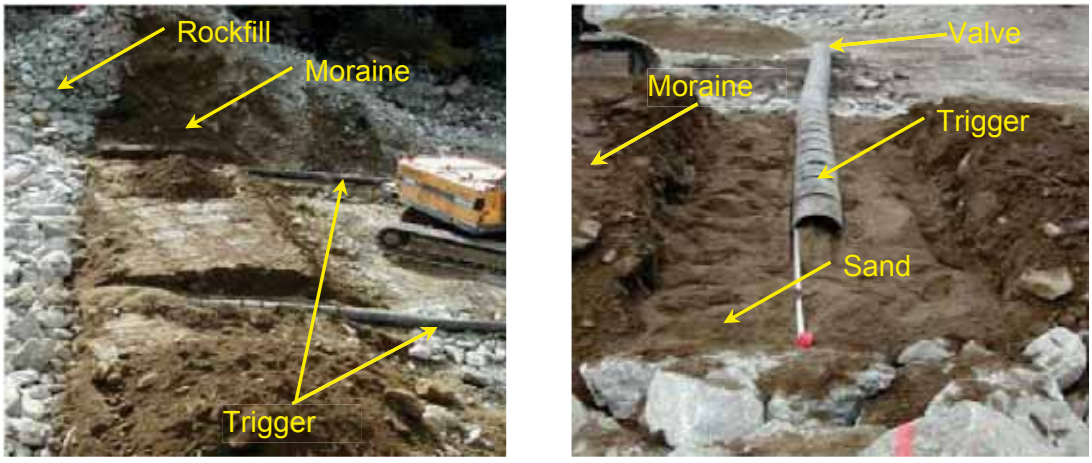

Figure 2.70: Built-in defect to induce internal erosion for tests 4 and 5 in 6 m high dykes at Røssvatnet (after Vaskinn et al., 2004).

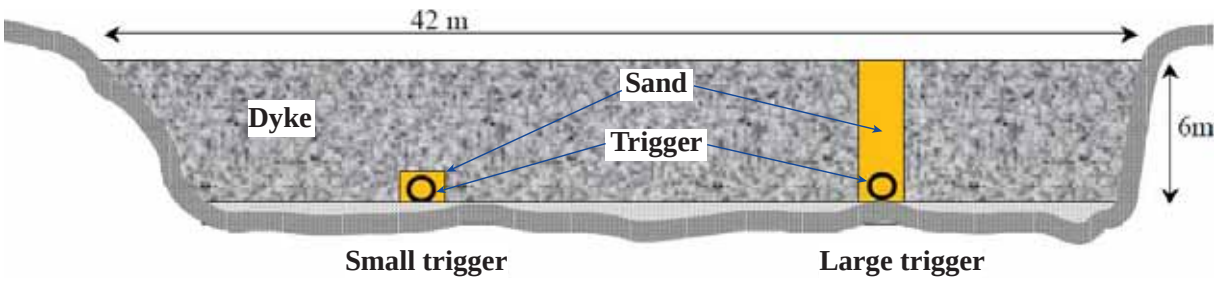

Figure 2.71: Defects included during the construction of Røssvatnet dykes No. 4 and 5 to trigger internal erosion (after Vaskinn et al., 2004).

Figure 2.72: Breaching process due to overflow of the homogeneous dyke built with clay (test 1). The time of each picture was not given (after Vaskinn et al., 2004).

The development of the breach of the homogeneous dyke built with clay (test 1) is shown in Figure 2.72, of the homogeneous dyke built with gravel (test 2) in Figure 2.73, and for the dyke built of rockfill with a moraine core (test 3) in Figure 2.74. A vertical headcut developed with the overflow in these three cases. The width of the headcut remained almost invariable and similar to the initial notch dug (3 m) until the headcut reached the base of the dyke. The breach widened rapidly from that moment until the dyke was eroded almost completely. This last phase was reported to last approximately 10 minutes, as illustrated in Figure 2.74c-d.

The breach of the homogeneous dyke built with gravel required a longer time than expected. The authors attributed this to the weather conditions at the moment of the test (Figure 2.73). It was reported that the temperature was below zero degrees Celsius on the day of the test. The authors claim that this might have had an influence, because water inside the dyke might have been frozen, bonding the granular material, responding more like a permafrost than as a purely gravelly soil.

The failure process due to internal erosion of the dyke built of rockfill and a moraine core is presented in Figure 2.75. Initially, the small trigger (Figure 2.71) was opened first and was kept open for 4 days, but no dyke failure was observed. As a consequence, the large trigger was opened. A sinkhole was reported to form rapidly on top of the dam. This evolved into a breaching process similar to that observed for the overflow tests.

Figure 2.73: Breaching process due to overflow of the homogeneous dyke built with gravel (test 2). No information about the time of each picture was given (after Vaskinn et al., 2005).

Figure 2.74: Breaching process due to overflow of the dyke built with rockfill and a moraine core (test 3), with time shown in each photograph (after Vaskinn et al., 2005).

Figure 2.75: Breaching process due to internal erosion of the dyke built with rockfill and a moraine core (test 4). No information was given about the time of pictures a), c) and d) (after Vaskinn et al., 2004).

Only the small trigger was built for test 5, but it was placed through the complete cross section of the dyke instead of only under the air-side as was the case in test 4. Opposite to that observed with the dyke in test 4, which stood 4 days with the trigger open without failure, the internal erosion of test 5 led to fast failure of the structure. The dam was completely breached only 20 minutes after opening the trigger mechanism,. The authors ascribe this to the length of the triggering device, which extended through to the toe of the water-side slope for test 5. The water pressure at that location, hence the hydraulic gradients, would be greater than in the middle section, influencing the velocity floe in the sand surrounding the triggering device, and leading to erosion through the pipe.

A similar breach mechanism for overflowed dykes was observed by Hahn et al. (2000), who tested a dyke built with the aim of increasing the knowledge regarding breach formation, as a step toward better prediction of floodwave hydrographs.

The dyke was 22 m long, 2.3 m high, with slope gradients of 1:3.0 on both air and water-sides. The dyke was divided into three sections, each one 7.3 m long (Figure 2.77). Each section was built with a different soil. Sections 1 and 2 were built with a silty sand, whereas section 3 was constructed with clay. The soil parameters for all three soils are listed in Table 2.7.

Figure 2.76: Breaching process due to internal erosion of the homogeneous dyke built with moraine (test 5). No information was given about the time of pictures c) and d) (after Vaskinn et al., 2005).

Breaching began through a notch dug on each section. Notches were trapezoidal, 0.46 m high by 1.83 m wide at the base with 1:3.0 side slopes. Inflow during testing was supplied by a canal. The inflow discharge during the test was maintained at 1 m^3/s (measured by a Parshall flume). The water level was set to 1.2 m during the 2 weeks prior to testing, and this was raised on the day of the experiment.

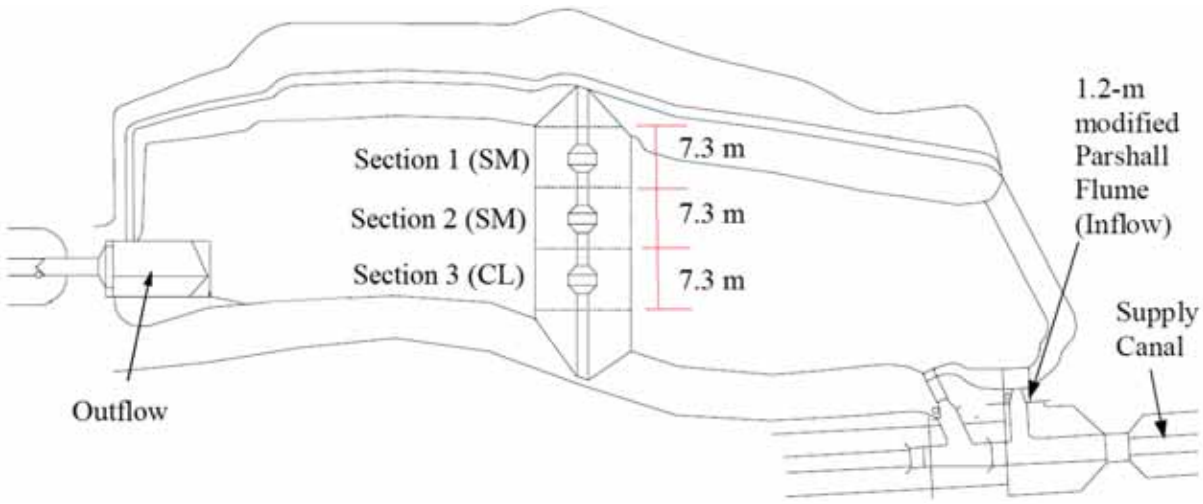

Figure 2.77: Plan view of the full-scale experiment (modified from Hahn et al., 2000).

Table 2.7: Properties of the three soils used the tests (adapted from Hahn et al., 2000).

	Section 1	Section 2	Section 3
USCS	SM	SM	CL
w_{opt} [%]	9	10.5	14
$\gamma_{d\ max}$ [kN/m^3]	18	18.2	17.5
% Sand	70	63	25
% Silt	25	31	49
% Clay	5	6	26
w_L [%]	NP	NP	34
I_p [%]	NP	NP	16
c' [kPa]	0.8	10.3	8.2
ϕ [°]	26.5	13.3	20

NP: Non plastic

Figure 2.78 illustrates the stages of the breaching process observed during all three tests, which as mentioned above, is similar to the mechanism observed by Vaskinn et al. (2005): (a) water flowed over the intact dyke; (b) some rill erosion was observed; (c) the rills deepened and a cascade was developed; (d) the cascade developed into a single upstream eroding headcut; (e) erosion of the sidewall resulted in mass failures and breach widening; (f) breach widened as the headcut advanced upstream.

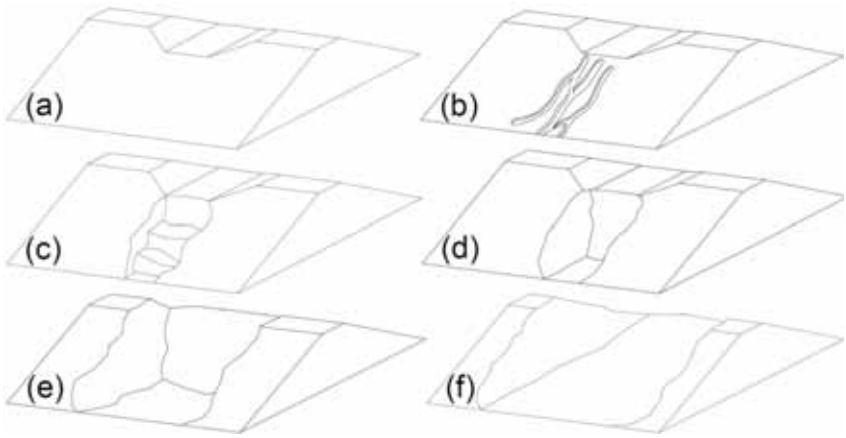

Figure 2.78: Generalized breaching process observed during overflow tests (after Hahn et al., 2000).

Figure 2.79a shows how the headcut developed almost vertically after the cascading process (at 10:45). The cross section shown in Figure 2.79b reveals how the flow initially eroded a narrow rill (12:23 and 13:52) before evolving into a U-shaped breach with lateral walls that were almost vertical. This breaching mechanism coincides with that observed by Vaskinn et al. (2004); Morris et al. (2007) and Visser et al. (1990). However, these results only represent the breaching mechanism when the flow is directed onto an initial notch, leaving space for investigating the breaching mechanism due to overflow along the complete crest of the dyke.

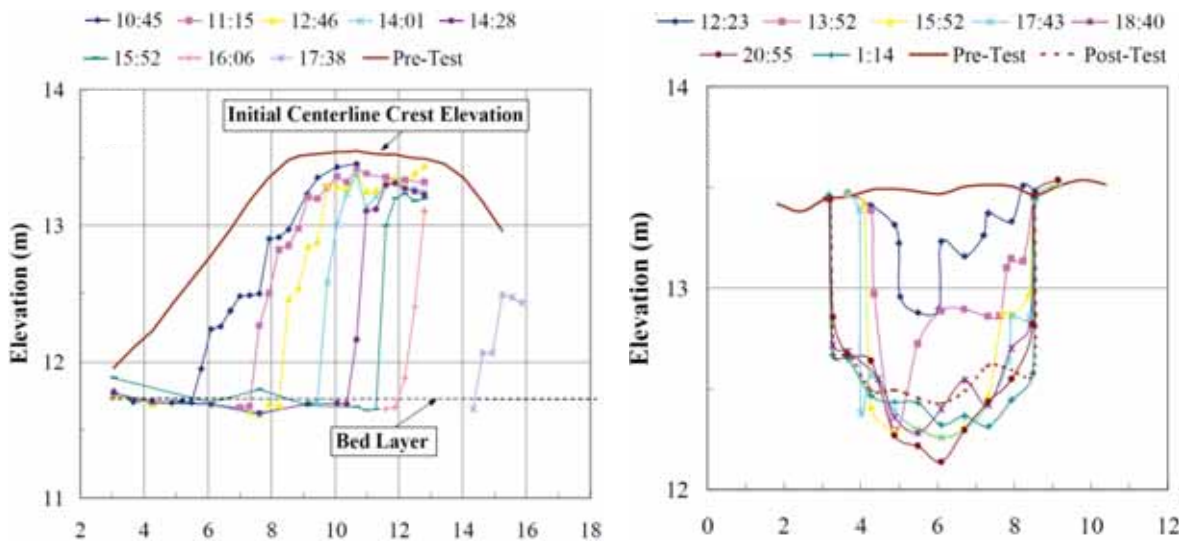

a) Along the cross section. *b) Along the crest.*

Figure 2.79: Evolution of the breach profile of the overflow test of the dyke section built with clay, with water supplied from the right (adapted from Hahn et al., 2000).

de Vries et al. (2010); van Beek et al. (2010) and Bezuijen et al. (2012) describe a series of full-scale tests at IJkdijk, in the Netherlands. The aim of the experiments was to analyze piping mechanisms of erodible dyke foundations.

Two basins were created (30 × 15 m) and filled with two different sands: a fine sand with a d_{50} = 150 μm, and a medium sand with d_{50} = 210 μm. The dry sand was applied in layers and compacted to a relative density of 50%, and then it was saturated. The dyke was built by compacting lumps of clay. The dyke was 3.5 m high, 15 m wide, and had slope gradients of 1:2 on both sides (Figure 2.80). No further information was provided about the soil properties or compaction methodology.

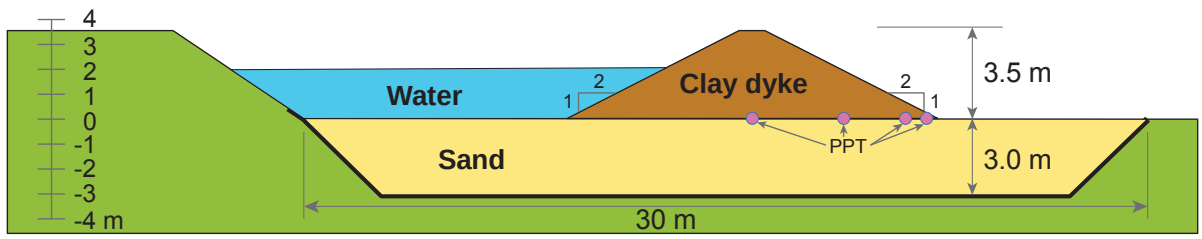

Figure 2.80: Cross section of the full-scale models built at IJkdijk, NL, for investigation of failure due to internal erosion (adapted from de Vries et al., 2010).

The authors recognized four stages in the development failure due to internal erosion: seepage, retrograde erosion, widening of the pipe and failure. *Seepage* underneath the levee was observed during the first steps of increasing the hydraulic head, but without transport of sand. This phase was followed by *retrograde erosion* when the hydraulic gradient was between 0.007 and 0.09, which was manifested by spots of sand appearing at the toe of the air-side slope but without boiling or forming sand craters. Some sand craters were reported at hydraulic gradients of 0.11-0.14. Sand grains were, however, not deposited at or over the rim

of the crater. This occurred when the hydraulic gradient was increased and the amount of transported sand increased with time (Figure 2.81a).

The *widening of the pipe* started when the pipe reached the water-side. The channel was enlarged from the water-side towards the air-side side. The sand, eroded as a result of the widening and deepening of the channel, was pushed forward, clogging the pipe temporally (Figure 2.81b). A different process occurred for both tests after the widening of the channel reached the air-side: the dyke deformed for the test with medium sand closing the pipe, and causing the sand transport to decrease (Figure 2.81c), whereas the flow and sand transport increased until the levee failed for the test with fine sand (Figure 2.81d). The latter process started with a large increase in turbulent flow and sand transport (mud flow), affecting a large area. Cracks appeared in the dyke and parts of the toe of the levee were eroded, which caused the erosion to increase.

a) *Sand and water transport during the phase of retrograde erosion.*

b) *Sand and water transport during the phase of widening of the pipe.*

c) *Water and sand flowing through the closed pipe due to deformation of the dyke (medium sand).*

d) *Final condition of the dyke after failure (fine sand).*

Figure 2.81: Failure phases of the IJkdijk dykes built on top of medium and fine sand (after de Vries et al., 2010; Bezuijen et al., 2012).

Pore pressure transducers were placed in 4 rows of 16 transducers each. These rows were placed at 0.2 m, 1.2 m, 3.8 m and 7.6 m from the downstream toe of the levee (Figure 2.80).

The goal for the monitoring of pore water pressure was to verify its use as an indication of pipe formation.

The authors claimed that there was potential for the pore water pressure measurements to be used as an early warning system for piping. For that reason, they presented contour plots of hydraulic gradients during pipe formation (t = 54.4 hours) and close to the end of the progressive erosion phase (t = 100 hours), as shown in Figure 2.82.

Full-scale experiments about the dyke response under variable water conditions were reviewed. Although data from the instruments installed was not available, the breaching mechanisms could be analyzed. These show the importance of taking into account the soil conditions at the moment of the breach event. For example, the temperature of the soil might cause the soil to respond more as permafrost. In the same way, full-scale tests help testing novel techniques for warning system.

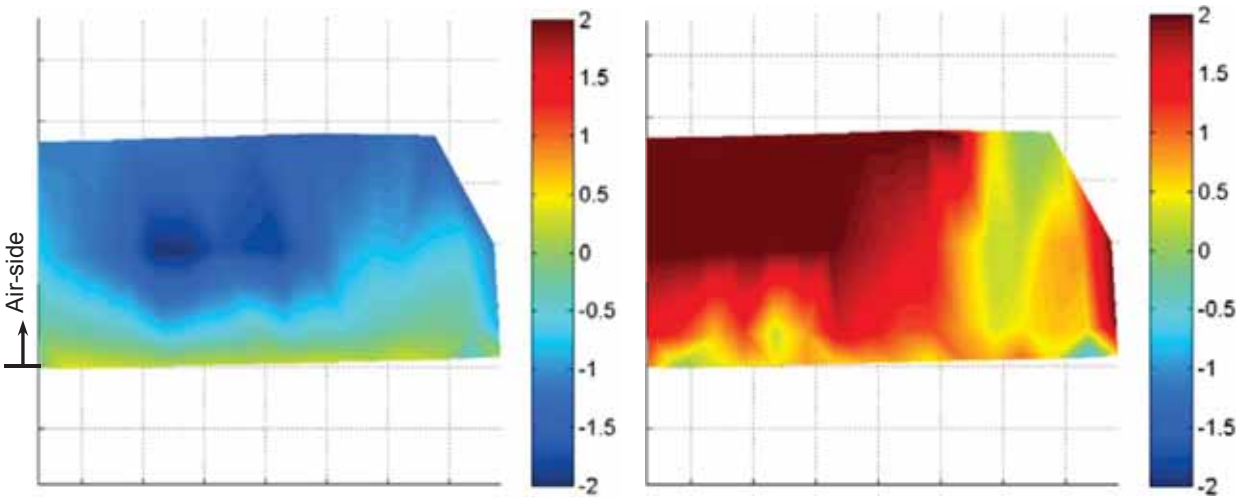

a) After 54.4 hours. *b) After 100 hours.*

Figure 2.82: Hydraulic gradient on the base the dyke on top of a foundation built with fine sand (in plan view) (after de Vries et al., 2010).

2.5 Numerical modeling

Numerical modeling is a technique used to solve engineering problems, for which the Ordinary Differential Equation (ODE) governing the problem does not have an analytical solution. Most of the numerical techniques discretize the area (2D problems) or volume (3D problems) into elements, at which the ODE is solved in an approximate way by applying some boundary condition. This is known as a Boundary Value Problem (BVP). According to Potts (2003), their ability to reflect field conditions accurately essentially depends on the ability of the geotechnical engineer to assign appropriate boundary conditions. This requires experience and engineering judgment. Therefore, the modeler should know the approximate answer before beginning with the numerical method (Muir Wood, 2012).

This section describes the reference information of the method used in this research project to model the groundwater flow and the stability of the dyke numerically. The basic concepts

are described, on which the software is based. An example found in the literature is reviewed at the end at the end of this section.

2.5.1 Groundwater flow modeling

According to Barbour & Krahn (2004), four phases should be fulfilled during the process of performing a numerical simulation of a geotechnical problem: 1) *observation and development of a conceptual model*. General information, including soil properties is gathered during this phase, and the geological conditions are defined; 2) *definition of the theoretical description (model) of the problem*. The key material and general behaviors will need to be understood in this phase. The ODEs governing the problem have to be defined as well; 3) *development and verification of the numerical model*. The BVP is defined at this stage. The geometry (domain) is chosen within which the solution of the ODE equations will be sought. The solution will be subjected to a set of boundary conditions applied to the domain, and to a set of material properties specified within the domain. The method of solution, e.g. finite difference and finite element techniques, has to be selected; 4) *Interpretation, calibration, and validation against the physical reality*. Once a mathematical solution is obtained, the results must be carefully interpreted and checked against the physical reality. Response patterns should be compared instead of just the specific numbers. If the numbers are similar but the pattern (spatial and temporal variation) is completely wrong, it is likely that something is wrong with the model. If the numbers are different but the patterns are similar, the process has been established correct, although the parameters may require calibration.

Finite difference method (FDM), finite element method (FEM), boundary element method (BEM), finite volume method (FVM), and particle tracking models are the most popular methods to solve groundwater flow problems (Bear et al., 1992). However, approaches based on finite difference and finite element methods are the most widely used (Potts, 2003).

The software GeoStudio ® (Krahn, 2012a) was chosen for this research project to solve the BVP of transient flow through unsaturated porous media numerically, and to investigate the stability of the slopes of the dyke. In consequence, a description of the basic concepts used by the software will be given next.

2.5.1.1 Flow modeling with SEEP/W

SEEP-W is a module of GeoStudio ® that allows two-dimensional problems of groundwater flow to be simulated. It solves Equation 2.48, which is an ODE derived by Lam et al. (1987) based on Richards equation (Equation 2.32) to analyze two-dimensional unsaturated transient flow with a finite element scheme. H is the total flow head, k_x, k_y are the hydraulic conductivity in the x and y-directions, Q_f is an applied boundary flux, θ is the volumetric water content, t is the time, γ_w is the unit weight of water, and m_w is the storage term, and is the slope of the SWRC (Figure 2.83). Since the SWRC is modeled only by its slope, hysteretic behavior cannot be represented.

$$\frac{\partial}{\partial x}\left(k_x \frac{\partial H}{\partial x}\right)+\frac{\partial}{\partial y}\left(k_y \frac{\partial H}{\partial y}\right)+Q_f = m_w \gamma_w \frac{\partial H}{\partial t} \qquad 2.48$$

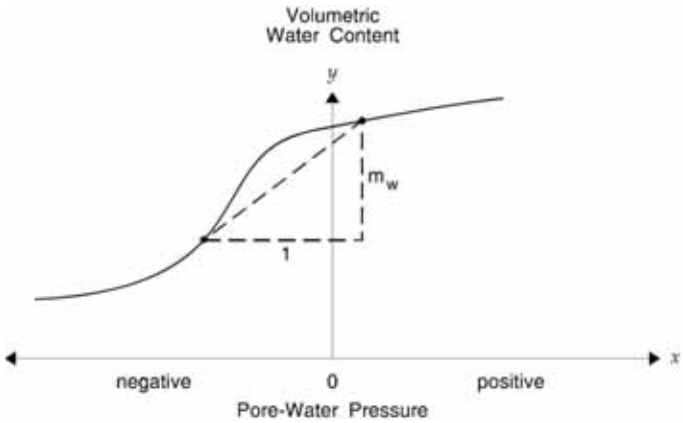

Figure 2.83: Storage term m_w (after Krahn, 2012b).

Applying the Galerkin method of weighted residuals (Zienkiewicz et al., 2005) to Equation 2.48, the two-dimensional seepage equation for a finite element is derived as Equation 2.49, where $[B]$ is the gradient matrix, $[C]$ is the hydraulic conductivity matrix of the element, $\{H\}$ is the vector of total head, $\langle N \rangle$ is the vector of the interpolating function of the element, *q* is the unit flux across the edge of an element, λ is storage term for a transient seepage equal to $m_w \gamma_w$. *t* is the time, *A* is a designation for summation over the area of an element, and *l* a designation for summation over the edge of an element. This equation can be re-written as Equation 2.50, where $[K]$ is the characteristic matrix of the element, $[M]$ is the mass matrix of the element, and $\{Q\}$ is the applied flux vector.

$$\int_A \left([B]^T [C][B]\right) dA\{H\} + \int_A \left(\lambda \langle N \rangle^T \langle N \rangle\right) dA\{H\}, t = q \int_L \left(\langle N \rangle^T\right) dL \qquad 2.49$$

$$[K]\{H\} + [M]\{H\}, t = \{Q\} \qquad 2.50$$

SEEP/W uses the backward difference method to integrate Equation 2.50 in time. This is an implicit method that approximates the derivative using information from previous time steps already computed (Zienkiewicz et al., 2005). The spatial integration is performed by Gaussian integration, which estimates the integral of a function as the summation of the multiplication of the value of the function at some sampling points called *Gauss points,* and a weighting value. The type of elements available at the moment is listed in Table 2.8.

Table 2.8: Type of elements available in SEEP/W.

Type of element	Gauss points
4-noded quadrilateral	4
8-noded quadrilateral	4
3-noded triangle	1
6-noded triangle	3

2.5.1.2 Slope stability analysis with SLOPE/W

SLOPE/W is the module of GeoStudio that can be used to evaluate the safety factor of geotechnical structures. It is based on the General Limit Equilibrium formulation (GLE) (Fredlund & Krahn, 1977).

The soil mass, for which a failure surface is assumed, is discretized in vertical slices, as shown in Figure 2.84. Seven forces act on each slice: the weight of the slice *W,* the normal and tangent forces at the base of the slice *N, T,* the normal interslice forces E_R, E_L, and the shear interslice forces X_R, X_L. Loads can also be applied to the surface. The difference between the different limit equilibrium methods e.g. Bishop simplified (Bishop, 1955), Janbu (Janbu, 1954) and others, depends on which equations of statics are included and satisfied, as well as on which interslice forces are included, and finally, the relationship assumed between the interslice shear and normal forces.

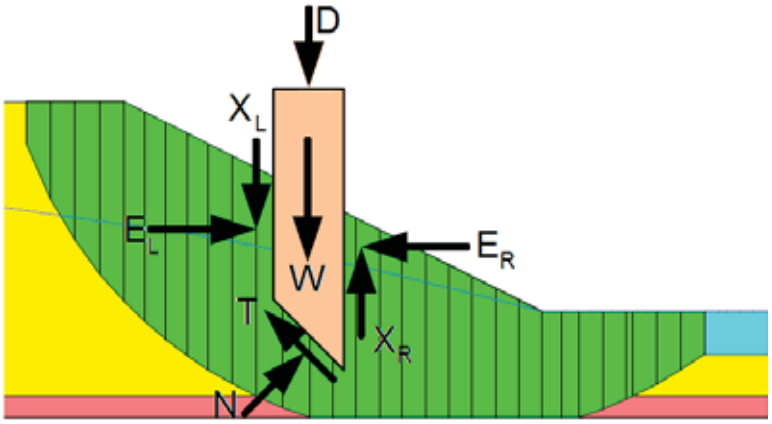

Figure 2.84: Slice discretization and slice forces in a sliding mass (after Krahn, 2012c).

GLE is based on two equations for factors of safety and allows for a range of interslice shear-normal force conditions. One equation gives the factor of safety with respect to moment equilibrium F_m (Equation 2.51), while the other equation gives the factor of safety with respect to horizontal force equilibrium F_f (Equation 2.52). In these equations, *c'* is the effective cohesion, ϕ' is the effective angle of friction, *u* is the pore water pressure, *N* is the normal force at the base of the slice of weight *W.* The concentrated point load is denoted as *D*, α is inclination of the base of the slice, and β, *R, x, f, d,* ω are geometric parameters.

$$F_m = \frac{\sum\left(c' \cdot \beta \cdot R + (N - u \cdot \beta) R \cdot \tan\phi'\right)}{\sum W \cdot x - \sum N \cdot f \pm \sum D \cdot d} \qquad 2.51$$

$$F_f = \frac{\sum\left(c' \cdot \beta \cdot \cos\alpha + (N - u \cdot \beta) \cdot \tan\phi' \cdot \cos\alpha\right)}{\sum N \cdot \cos\alpha - \sum D \cdot \cos\omega} \qquad 2.52$$

The normal force *N* at the base of each slice is obtained as the summation of vertical forces acting on the slice, and can be expressed, as shown in Equation 2.53, where X_R and X_L are

the interslice shear forces at each side of the slide. F is equivalent to F_m if Equation 2.53 is replaced in Equation 2.51, and equivalent to F_f if replaced in Equation 2.52.

GLE handles the relationship between the normal interslice force E and the shear interslice forces X as expressed in Equation 2.54, where $f(x)$ is a function that illustrates the distribution of the interslice forces with distance x. λ is a percentage of $f(x)$. The GLE methodology varies λ until $F_m = F_f$.

$$N = \frac{W + \left(X_R - X_L\right) - \left(\dfrac{c' \cdot \beta \cdot \sin\alpha + u \cdot \beta \cdot \sin\alpha \cdot \tan\phi'}{F}\right)}{\cos\alpha + \dfrac{\sin\alpha \cdot \tan\phi'}{F}} \qquad 2.53$$

$$X = E \cdot \lambda \cdot f(x) \qquad 2.54$$

Figure 2.85 presents an example of how GLE relates the different limit equilibrium analyses. Both factors of safety F_m and F_f are plotted as a function of the parameter λ. The simplified Bishop method satisfies only the moment equilibrium equation and neglect any interslice forces ($\lambda = 0$), the Janbu method satisfies the force equilibrium while neglects any interslice forces, whereas the method by Morgenstern & Price (1965) fulfills both equations ($\lambda \neq 0$).

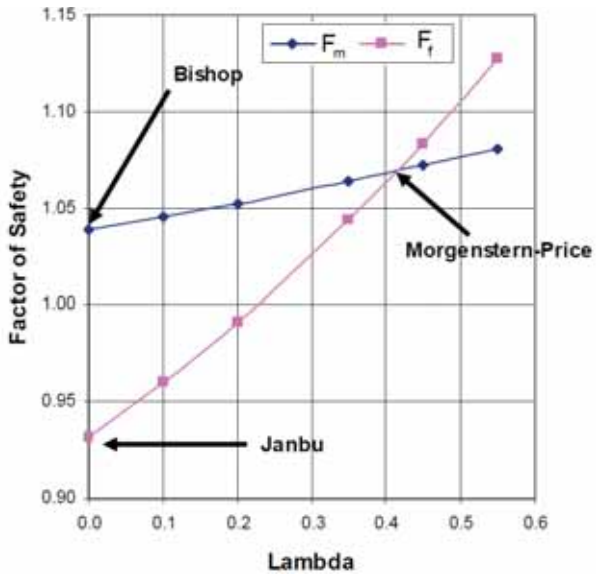

Figure 2.85: Comparison of three limit equilibrium methods under the GLE formulation (Krahn, 2012c).

2.5.2 Previous research on numerical simulation of groundwater flow

The results from a relevant previous research project are discussed next. Kumar & Viswanadham (2012) modeled numerically two dykes at prototype scale of the models they tested under enhanced gravity (cf. Section 2.3.6.2). One homogeneous dyke was built with silty sand, and the other dyke included a toe filter. Transient analyses of the groundwater

flow were carried out with SEEP/W, whereas a slope stability analysis was performed for each time step using SLOPE/W, with the simplified Bishop limit equilibrium method.

Identical soil properties were assigned ($\gamma = 18.75$ kN/m^3, c' = 11.9 kPa, ϕ' = 27°, and k_{sat} = 1.54 $\times$ 10^{-6} m/s), except for the hydraulic properties of the geotextile used as a toe filter, which were scaled-up corresponding to 30-g (acceleration level during the centrifuge tests). The water levels applied were exactly the same as those measured during the centrifuge experiments (Figure 2.63). The SWRC of the soil was reported to have been estimated from the grain size distribution. However, the method followed for that purpose was not reported.

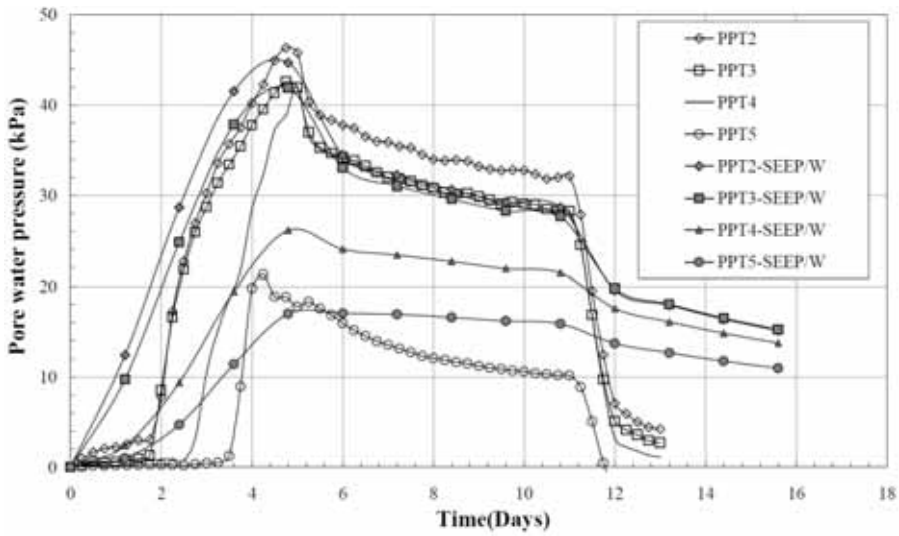

a) Homogenous dyke (RL-1).

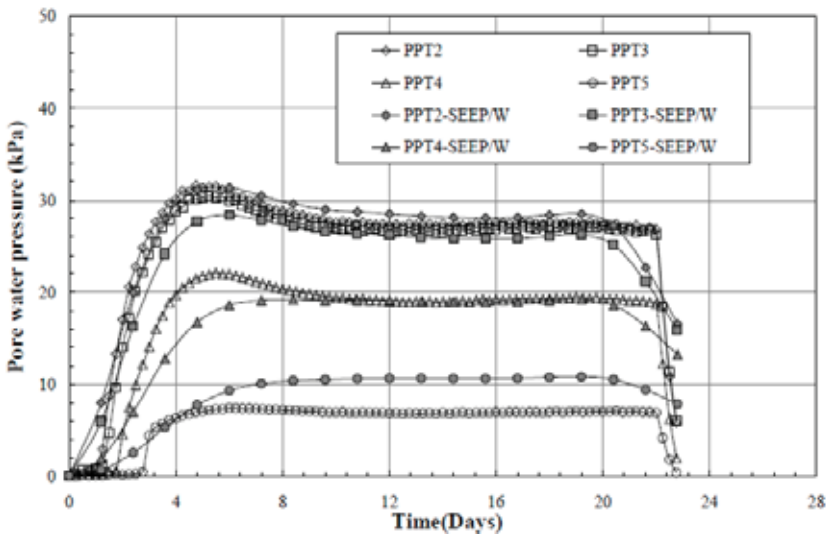

b) Dyke with a toe filter (RL-3).

Figure 2.86: Comparison of the results from the transient numerical analyses of groundwater flow with the obtained from small-scale models tested at enhanced gravity. The location of the points is shown in Figure 2.62 (after Kumar & Viswanadham, 2012).

The comparison of the pore water pressures simulated to those obtained in the experiments is presented in Figure 2.86. In reality, a delay of about 2 days after the initiation of the flooding occurred before the pore water pressures built up at the bottom of the dyke. The authors attributed this delay to unsaturated-saturated properties of the soil, or a thin coating of bentonite on the water-side. Nevertheless, the coincidence of patterns and values is high, especially for the pore pressure transducers placed and modeled in the middle of the dyke. This shows how diverse modeling methodologies can be used together in order to understand a complex geotechnical problem.

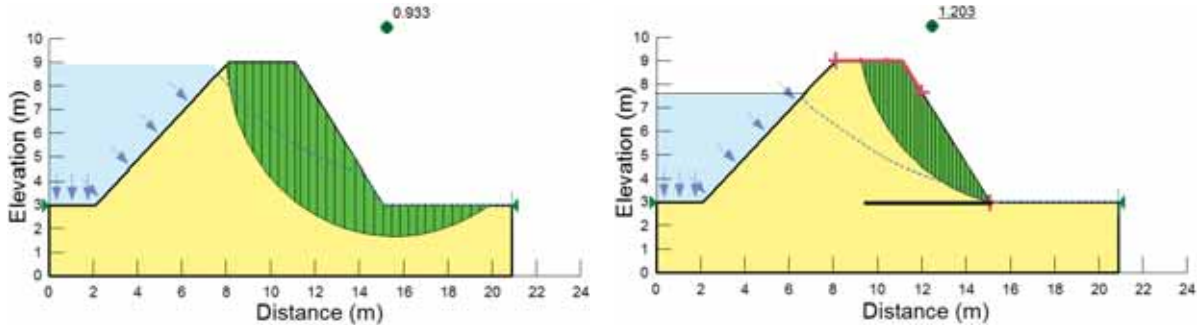

a) Homogenous dyke (RL-1). *b) Dyke with a toe filter (RL-3).*

Figure 2.87: Critical slip surfaces for both dykes at the maximum water levels simulated (after Kumar & Viswanadham, 2012).

The minimum factor of safety at the maximum water levels was reported to be 0.933 for the homogenous dyke (RL-1) (Figure 2.87a), and 1.203 for the dyke with the toe filter (RL-3) (Figure 2.87a). These results explain the failure observed on the air-side slope of the homogenous dyke (Figure 2.65), which was not experienced by the dyke with the toe filter. Since the water level in model RL-3 did not reach the crest of the dyke, as it did for model RL-1, as a consequence of the failure in the water pumping system in the centrifuge experiment, it would have been desirable that the authors had performed a further analysis to investigate the effect of a higher water level on the dyke with toe filter. Additionally, no information was given regarding the inclusion of increased shear strength due to the unsaturated conditions of the soil, which will have an effect on the results of stability analyses.

2.6 Summary and open questions

Basic information required to carry out more advanced modeling of river dyke failure, when subjected to transient water conditions, has been compiled and explained, together with results from other relevant research projects for this work.

The information covers different topics that will be used in the next chapters, such as understanding the soil as an unsaturated material that behaves in a different manner to saturated soils, which is the main assumption in current geotechnical practice.

In the following chapters some characteristics of dyke failure will be investigated that are still not completely understood: 1) the influence of protective measures (a cut-off wall, a toe filter and its combination) on the flow behavior during cyclic flooding events followed by an over-

flow, 2) analysis of the failure mechanism of the dyke when these protective measure are used, 3) analysis of the problem with small-scale models that allow the complete geometry of the dyke to be modeled without cutting off parts of the slopes, or creating models with steep slopes due to restriction from the size of the containers.

3 Overflow field test

As part of an applied research project, a section of a dyke on the Rhone River was isolated within a sheet pile box. The location of the field test is shown in Figure 3.1, together with an aerial view of the test cell. The dyke's response to extensive and repeated river floods was monitored. This, and some more specific goals of the experiment are documented by Mayor et al. (2008); Springman & Mayor (2009).

The test was carried out as the concluding phase of another research project (Mayor, 2013). The analysis of the results and the numerical modeling are the contributions of this work to this field experiment.

a) Geographical location (after Mayor et al., 2008).

b) Aerial view showing the Rhone valley and the test cell (Photographs by S.M. Springman).

Figure 3.1: Location and aerial view of the test cell.

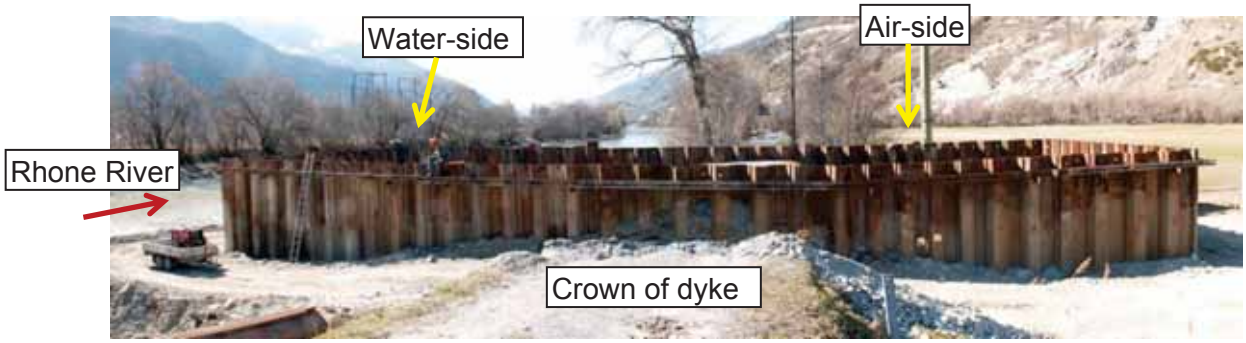

a) View from outside the cell (adapted from Springman & Mayor, 2009).

.

b) View of the air-side slope from inside the cell (photograph by P.A. Mayor on 10.06.2008).

c) Water pumping system (photographs by P.A. Mayor and VAW[2] on 10.06.2008).

Figure 3.2: Detailed view of the test cell.

A pumping system on the water-side of the cell allowed a specially defined temporal series of water heights to be applied to the dyke (Mayor et al., 2008) (Figure 3.4c). This feature, together with the sheet pile wall enclosure, allowed the water level to be increased above the

[2] Laboratory of Hydraulics, Hydrology and Glaciology. ETH Zurich. (www.vaw.ethz.ch)

crown of the dyke, converting the test cell into a suitable space for performing an overflow or breaching test.

A new goal was then added to the experiment: to analyze the dyke behavior during a breaching process due to overflow. This test was carried out on 10.06.2008, with duration of 8 hours and 12 min (07:40 to 15:52) in cooperation with researchers from VAW and it determined the end of the experiment that had been initiated on 13.04.2007.

3.1 Experiment layout

The experiment was performed in a rectangular cell built with Larssen 25 sheet piles. Each section of sheet pile has a U shape of length 500 × 210 mm (Figure 3.3). The dimensions of the cell were 23.84 × 12.5 × 11 m (length × width × height). Figure 3.4 presents a plan and section view of the cell, including the measurement devices and boreholes.

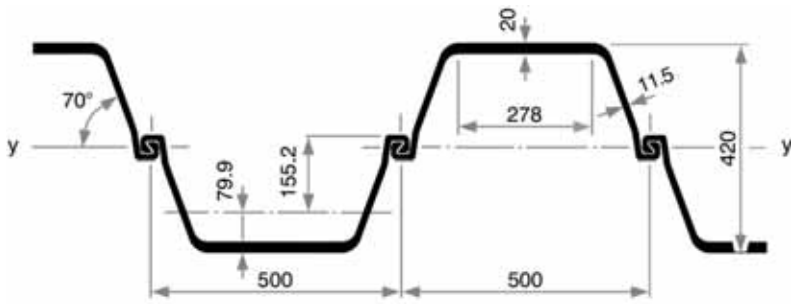

Figure 3.3: Dimensions of the sheet pile Larssen 25 (taken from http://tk-steelcom.com.au).

An arbitrary coordinate system is defined and indicated in the figure. The *X* coordinate is perpendicular to the river flow, whereas the *Y* coordinate is parallel to it. The elevation above the sea level (masl) is used to reference key points in the cell. The coordinates of the reference points A, B, C, D, E and F are given in Table 3.1.

Table 3.1: Coordinates of the test cell in the defined coordinate system.

Point*	X-Coordinate [m]	Y-Coordinate [m]	Height [masl]
A	11.42	0	645.85
B	11.42	12.5	645.85
C	35.26	12.5	645.85
D	35.26	0	645.85
E	11.42	0	634.85
F	35.26	0	634.85

* cf. Figure 3.4.

Figure 3.5 shows the profile obtained from a survey campaign (Mayor, 2013). Three cross sections were measured: one in the middle of the cell (Y = 6.25 m) and two sections located 3m up and downstream (Y = 3.25 m and Y = 9.25 m). The differences between these three sections are small. Therefore, the profile of the cross section is assumed to be constant throughout the cell and corresponding to that measured at the centerline (Y = 6.25 m).

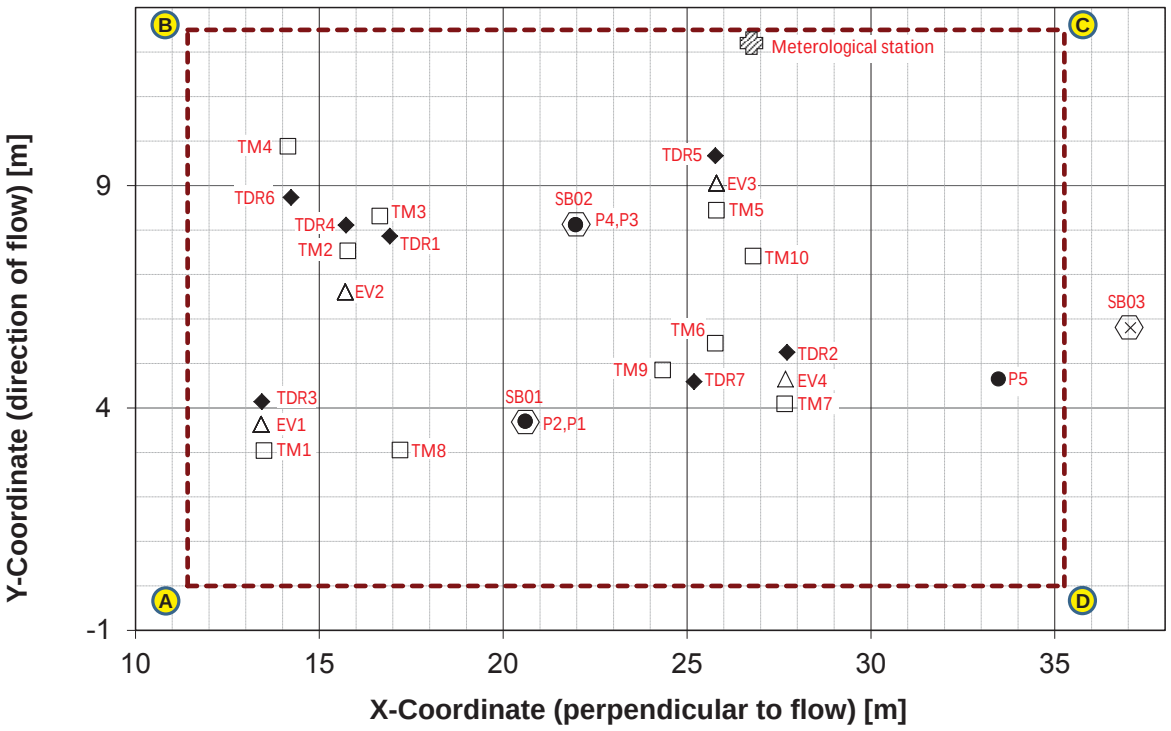

a) Plan View.

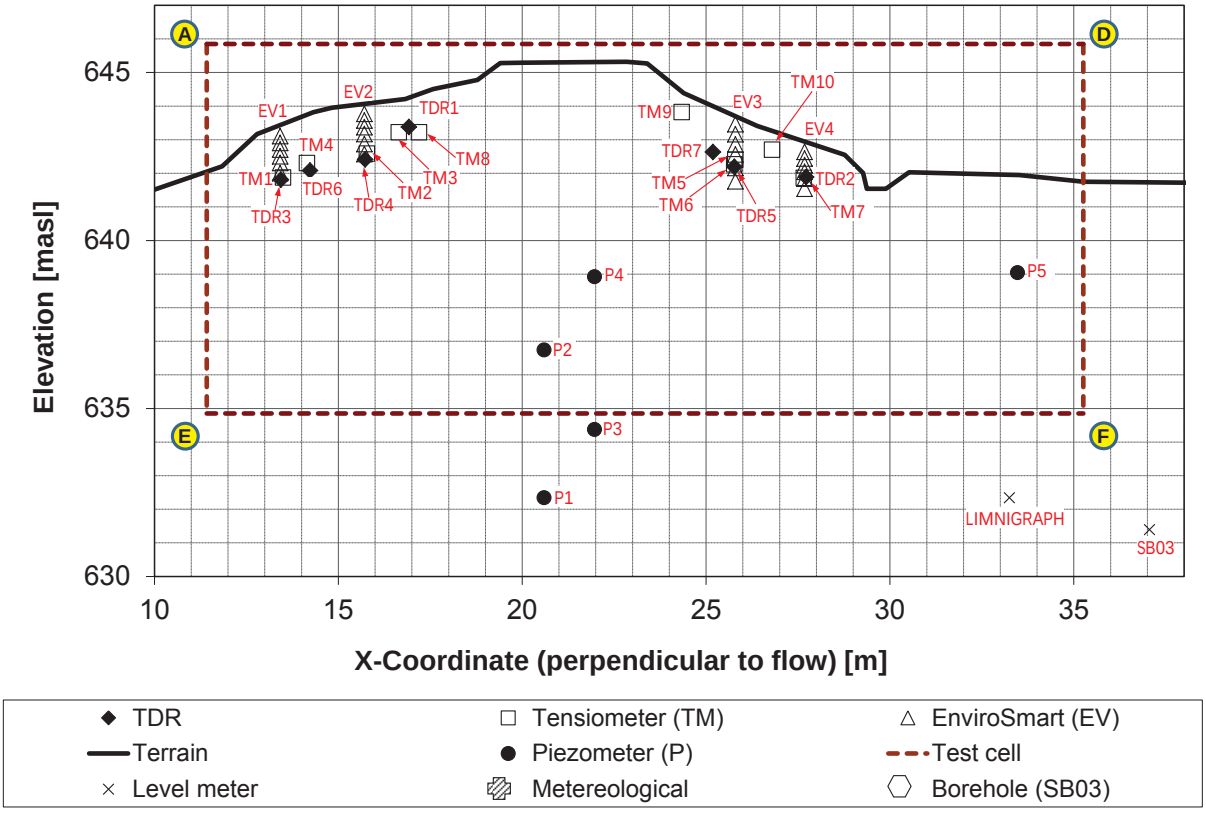

b) Cross section.

Figure 3.4: Layout of the test cell including location of instrumentation and boreholes.

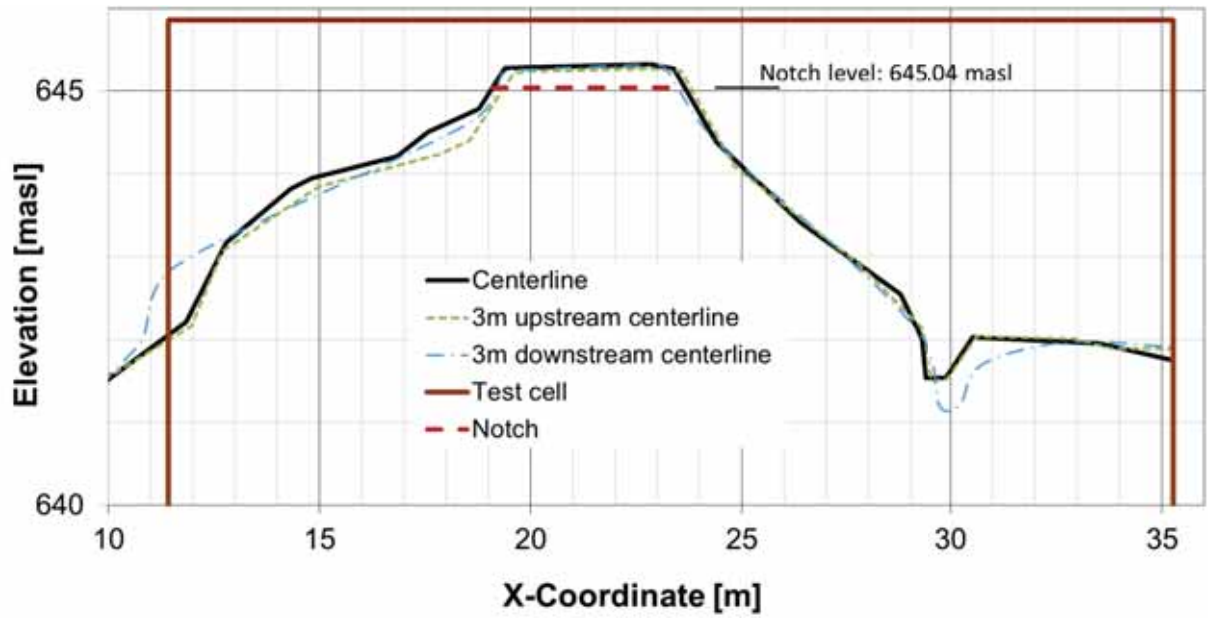

Figure 3.5: Survey for three sections inside the test cell (adapted from Mayor, 2013).

Figure 3.6: View of the air-side slope from inside the test cell (photograph by P.A. Mayor on 09.06.2008).

Several measuring devices and a metereological station were located inside the cell. The metereological station included a rain gauge. The detailed information about the location of the devices, which is related to the arbitrary coordinate system adopted, is presented in Table 3.2. The monitored variables are volumetric water content, negative water pressure (suction), temperature (water and air), water level and rainfall amount. Data from all the devices

were collected every ten minutes and stored in a data logger for later downloading with a laptop.

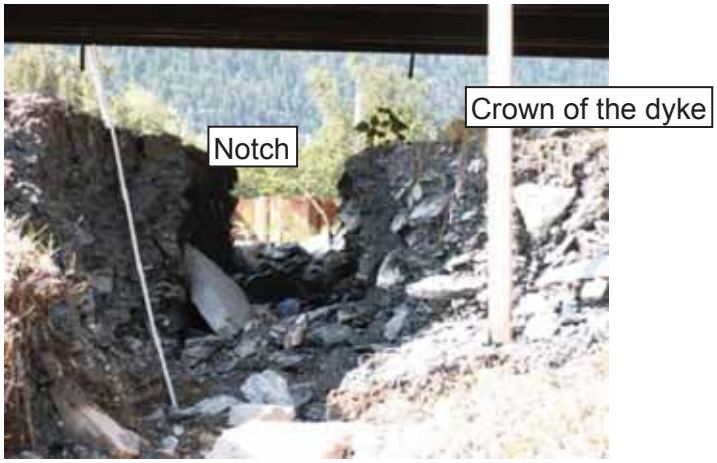

Figure 3.7: Notch excavated in the crown of the dyke in the middle of the enclosed test section: gravel with large platey stone fragments at 0.50 m depth. (photograph by P.A. Mayor on 11.06.2008).

It was planned to install EnviroSmart, TDR and tensiometer devices in the center just beneath the dyke's crown (X=21.5), but the drilling device was not able to pass through a stiff layer at approximately 0.7 m below the surface. When the initial notch for the overflow test was dug (cf. Section 3.2.2.2), a soil layer consisting mainly of densely packed large stone fragments was found at that depth (Figure 3.7), which explains the difficulty experienced in installing the devices along the centerline near the crown.

Table 3.2: Location of the measuring devices for the Baltschieder test cell (adapted from Mayor, 2013).

Device	Symbol	X-coordinate [m]	Y-coordinate [m]	Elevation [masl]
TDR 1	TDR1	16.92	7.86	643.38
TDR 2	TDR2	27.72	5.25	641.89
TDR 3	TDR3	13.44	4.14	641.81
TDR 4	TDR4	15.73	8.11	642.41
TDR 5	TDR5	25.77	9.67	642.19
TDR 6	TDR6	14.23	8.73	642.08
TDR 7	TDR7	25.19	4.59	642.63
Tensiometer 1	TM1	13.50	3.04	641.87
Tensiometer 2	TM2	15.78	7.53	642.58
Tensiometer 3	TM3	16.65	8.31	643.22
Tensiometer 4	TM4	14.15	9.88	642.30
Tensiometer 5	TM5	25.80	8.44	642.40
Tensiometer 6	TM6	25.77	5.45	642.26
Tensiometer 7	TM7	27.66	4.09	641.86
Tensiometer 8	TM8	17.20	3.05	643.22
Tensiometer 9	TM9	24.34	4.85	643.82
Tensiometer 10	TM10	26.80	7.41	642.70
EnviroSmart 1.1	EV1	13.42	3.63	643.11
EnviroSmart 1.2	EV1	13.42	3.63	642.91
EnviroSmart 1.3	EV1	13.42	3.63	642.71
EnviroSmart 1.4	EV1	13.42	3.63	642.51
EnviroSmart 1.5	EV1	13.42	3.63	642.31
EnviroSmart 1.6	EV1	13.42	3.63	642.01
EnviroSmart 2.1	EV2	15.71	6.61	643.77
EnviroSmart 2.2	EV2	15.71	6.61	643.57
EnviroSmart 2.3	EV2	15.71	6.61	643.37
EnviroSmart 2.4	EV2	15.71	6.61	643.17
EnviroSmart 2.5	EV2	15.71	6.61	642.87
EnviroSmart 2.6	EV2	15.71	6.61	642.57
EnviroSmart 3.1	EV3	25.80	9.05	643.46
EnviroSmart 3.2	EV3	25.80	9.05	643.16
EnviroSmart 3.3	EV3	25.80	9.05	642.86
EnviroSmart 3.4	EV3	25.80	9.05	642.56
EnviroSmart 3.5	EV3	25.80	9.05	642.16
EnviroSmart 3.6	EV3	25.80	9.05	641.76
EnviroSmart 4.1	EV4	27.68	4.65	642.64
EnviroSmart 4.2	EV4	27.68	4.65	642.44
EnviroSmart 4.3	EV4	27.68	4.65	642.24
EnviroSmart 4.4	EV4	27.68	4.65	642.04
EnviroSmart 4.5	EV4	27.68	4.65	641.84
EnviroSmart 4.6	EV4	27.68	4.65	641.54
Piezometer 1	P1	20.60	3.70	632.34
Piezometer 2	P2	20.60	3.70	636.74
Piezometer 3	P3	21.97	8.12	634.37
Piezometer 4	P4	21.97	8.12	638.92
Piezometer 5	P5	33.47	4.65	639.04
Level meter 1	-	33.25	-10.80	632.34
Level meter 2 (SB03)	-	37.06	5.80	631.39
Meteorological station	-	25.75	12.50	644.00

3.2 Overflowing process

3.2.1 Record of activities

The experiment was carried out on Monday 10.06.2008 between 07:40 CET and 15:52 CET. Table 3.3 provides a detailed description of the main events observed. The test is analyzed in seven main phases, which are explained in detail in the following sections:

1. Initial state prior to the experiment.

2. Preparation of the dyke for the overflow test.

3. Increase of water level on the water-side.

4. Artificial raining on the air-side.

5. Initial symmetrical overflow.

   (a) General slope instability.
   (b) Internal erosion processes.

6. Temporary lowering of water level to allow water to be drained from the air-side trench.

7. Asymmetrical overflow.

Table 3.3: Timetable of the activities carried out for the field experiment in Baltschieder on 10.06.2008.

0740-1200	**INCREASING THE WATER LEVEL OVER WATER-SIDE OF THE DYKE TO 645.04 masl (Level of the notch)**
1142-1207	**ARTIFICIAL RAINING**
1142	Start of artificial raining at 40 mm/hour
1207	End of artificial raining
1215-1353	**FIRST STAGE OF FLOW (SYMMETRICAL FLOW PATH)**
1200	Start pumping water
1219	Start of flow over the dry surface of the dyke at 645.23 masl
1219-1225	Flow over the shoulders of the dyke. More bags with sand where placed on the water-side of the crest
1302-1318	General failure of the air-side slope
1302	First observable deformations on the centerline of the slope
1303	Appearance of cracks at the shoulder of the crown on the air-side of the dyke
1303-1305	Growth in the length and width of the cracks
1306-1318	Slump of soil mass, mainly on the right side of the air-side slope
1318-1343	Internal erosion
1318	Appearance of the soil volcano at the bottom of the slope (left side)
1318-1343	Noticeable settlement under the left 'channel' together with the appearance of piping volcanoes at the bottom of the slope and at the middle height and the intersection with the sheet pile wall
1345	Stop pumping water into the upstream compartment of the test cell to allow the water to be drained from the trench on the air-side
1353	Water stops flowing over the surface

1353-1433	**INTERVAL**
1411-1412	Appearance of settlements in many localized places. They seem to form underground pipes
1420-1421	Idem
1429-1430	Idem
1430	Taking samples of the fine piped material
1432	Taking samples of the eroded material
1433-1552	**SECOND STAGE OF FLOW (SINGLE BRANCH FLOW PATH)**
1433	Start pumping water
1438	Start of flow over the dry surface of the dyke (semi-symmetrical path flow)
1439-1451	Development of one branch flow
1439-1448	Some deformations of the surface are visible above the underground pipe
1450	Visually it seems that there was a reduction of flow but this was not the case, and the right hand branch of the flow started to disappear
1451	A constriction of the flow is evident as well as the disappearance of the right hand branch of surface flow
1451-1552	Flow of water evidently follows a single branch directly over the 'natural channel' formed as a consequence of the piping.
1515-1519	A blockage in the notch was retired manually increasing the width of inlet on the upstream side; However, it did not influence the flow path
1543	Stop pumping water into the upstream compartment of the test cell
1552	Water stops flowing over the surface

3.2.2 Detailed description of each phase

3.2.2.1 Initial state prior to the experiment

The enclosed dyke section was subjected to several cycles of raising and lowering the water level since the cell was installed in 2007 (Mayor, 2013). Figure 3.9 shows the variation of the water level during the last nine days before the breaching experiment. A constant water level of 642.86 masl was imposed from 01.06.2008 to 05.06.2008. The water level was increased up to 644.96 masl at 06:40 and maintained at that height for almost 24 hours before a further test was carried out to raise the water level to the level of the notch. The water level was decreased at a constant rate from 645.05 masl to 642.86 masl during the following 30 hours

Figure 3.8: Initial state of the air-side dyke (photograph by VAW on 9.06.2008 at 15:18).

The water level was set to 644.82 masl on 09.06.2008. The raise of water level was carried out in several steps in the period between 06:40 and 15:40. Finally, water level reached 644.82 masl, which was maintained until 10.06.2008 at 7:40.

Figure 3.10 shows the measurements for piezometric head during the last nine days before the experiment. A raise of the water level of about 2.09 m, from 642.86 to 644.95 masl (05.06.2008), is reflected by a small increment of 0.29 m rise in the water table, from 640.23 to 640.52 masl (piezometers 4 and 5). This indicates that the piezometric head in the ground below the dyke is determined by regional conditions rather than by the water level in the river. Mayor (2013) noticed the same response and suggested that this might be a consequence of a layer of fine graded material on the riverbed acting as a low permeability barrier between the river and the underlying material.

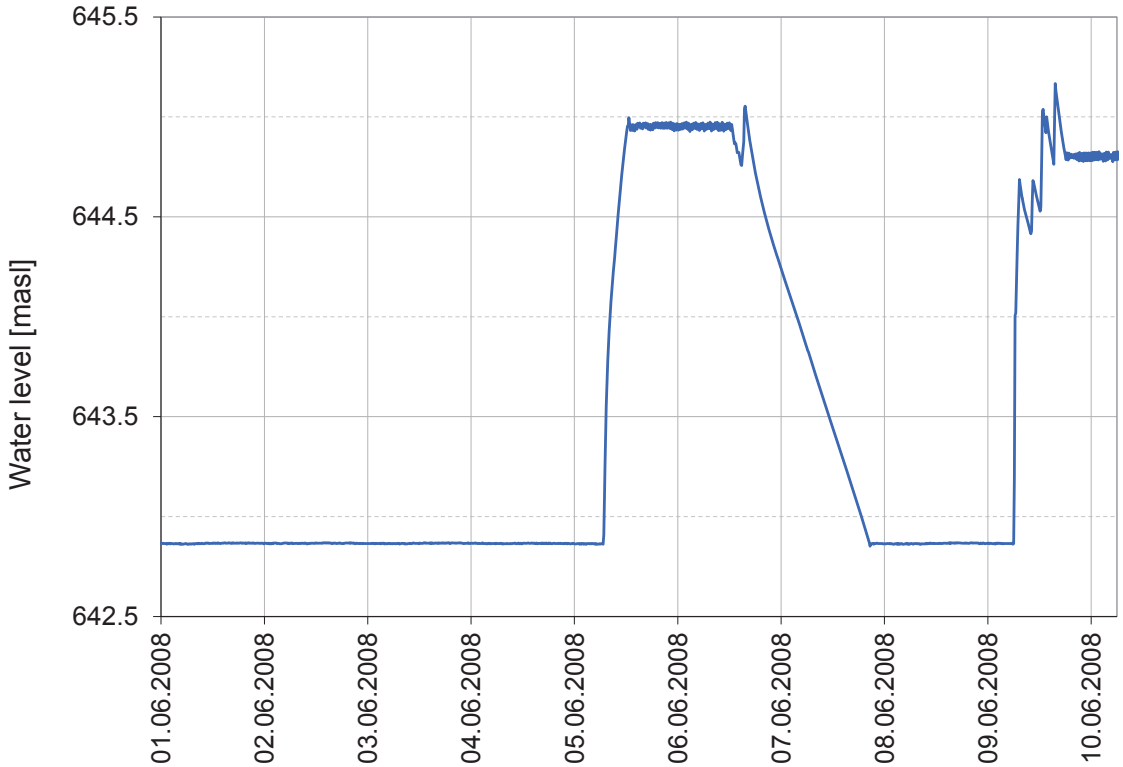

Figure 3.9: Water level over 9 days before the breaching experiment on 10.06.2008.

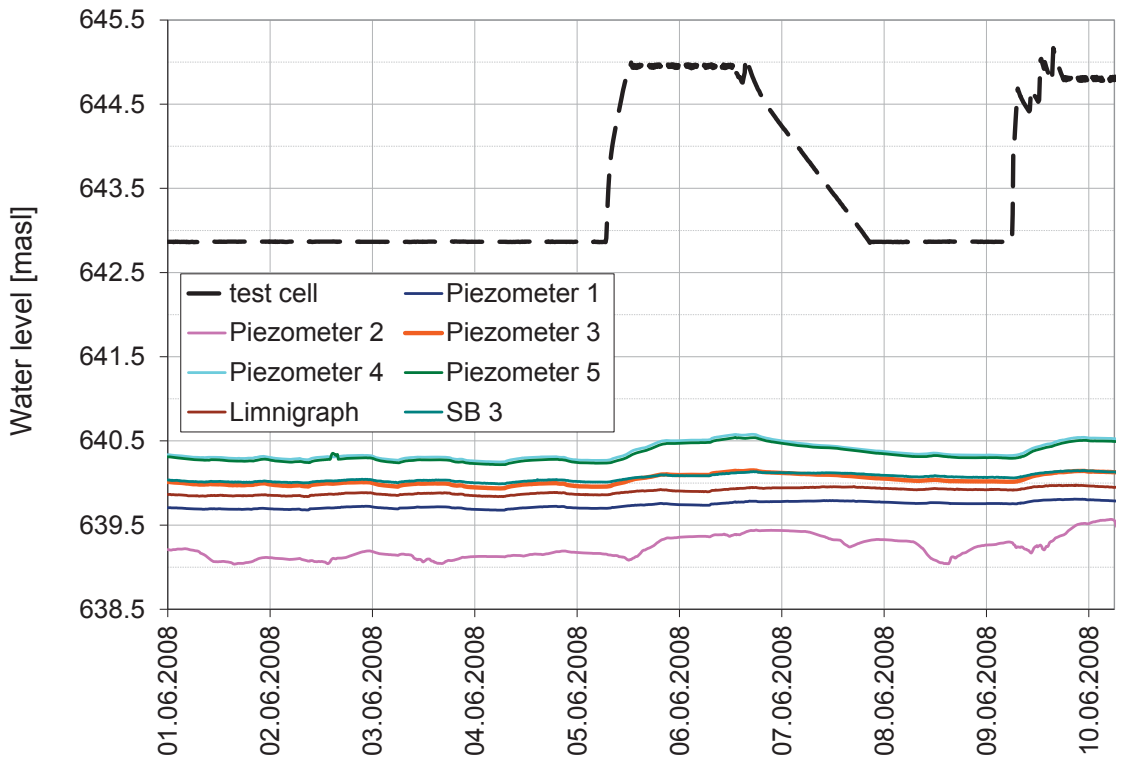

Figure 3.10: Piezometric water heads during 9 days before the breaching experiment on 10.06.2008.

The lag in the reaction, i.e. the time elapsed between increasing the water level and a reaction from the sensors, is larger for those devices at which the change of the magnitude of piezometric head is lower. The response and measured values of piezometers 4 and 5 is identical. Therefore, they seem to be a single line in Figure 3.10, indicating that both devices are, most probably, located in the same stratum. A similar explanation could apply for piezometer 3 and the water level located at SB03. It was expected that piezometer 2, being located above piezometer 1, would show higher values. However, the water head measured by piezometer 2 is more irregular than the others and its values are lower than for piezometer 1. This suggests that piezometer 2 is located in a stratum completely different from the others, probably a trapped lens of more permeable soil.

Figures 3.11 to 3.16 illustrate the volumetric water content measured by TDR and EnviroSmart (EV) devices for nine days before the overflow test took place. Figure 3.17 shows the pore water pressures measured for the same period.

The results from the TDR (Figure 3.11) and EnviroSmart (Figures 3.13 to 3.16) devices illustrate that all the devices had a gradual decrease in the volumetric water content during the period of time in which the water level was held at a constant height of 642.6 masl (01.06.2008 - 05.06.2008). This implies a desaturation process in the soil due to the groundwater flow regime.

Figure 3.12 presents the lag in the reaction of TDRs when the water level is raised. TDRs located on the water-side (1, 3, 4 and 6) responded to the change in the water level with a lag of approximately 50 minutes (0.83 hours). TDRs 2, 5 and 7, which are located in the air-side, exhibited longer lags in time of 9, 5.5 and 3.66 hours, respectively. These indicate that the dyke was saturated from top to bottom, as TDR 7 was located above TDR 5, and this above TDR 2.

The volumetric water content had an exponential decay after the water level was lowered. The first devices to react were TDRs 7, 5 and 2, as they were located on the air-side. Their values decayed close to 0.2 m^3/m^3. From the devices on the water-side, the first to react was TDR 1, which had also an exponential decay to 0.16 m^3/m^3. The other TDR devices (3, 4, and 6) required more time to start draining. Their decay was not exponential as for the others TDRs but rather linear, and they values were above 0.3 m^3/m^3 in all 3 cases.

All gauges composing the EnviroSmart devices on the water-side (EV 1 and 2) presented a fast reaction to the raise of the water level, and the same type of exponential decays when the water level was lowered. Notwithstanding, another behavior was observed for the devices on the air-side (EV 3 and 4). The upper gauges of the devices (EV 3.1, 3.2, 4.1, 4.2, 4.3) show long delays for reacting to the change of water level. This indicates that those gauges were located in another stratum of soil with lower permeability, which retarded the water flow and the change of the volumetric water content. This was confirmed after the experiment, when a layer of soil corresponding to a fill was found near to the surface of the air-side slope.

The measurements from tensiometer devices (Figure 3.17) showed an increase in the suctions during the period from 01.06.2008 to 05.06.2008. This increase in suction coincided with the decrease of the volumetric water content. The devices on the air-side (TM 5, 6, 7, 9 and 10) require more time to react, in a similar way to that observed for the water content. The velocity of decay, once the water level was decreased, was not equal for all sensors, thus the tensiometers on the air-side present a fast decay, whereas the sensors on the water-side measured an exponential decay, similar to that observed for the water content.

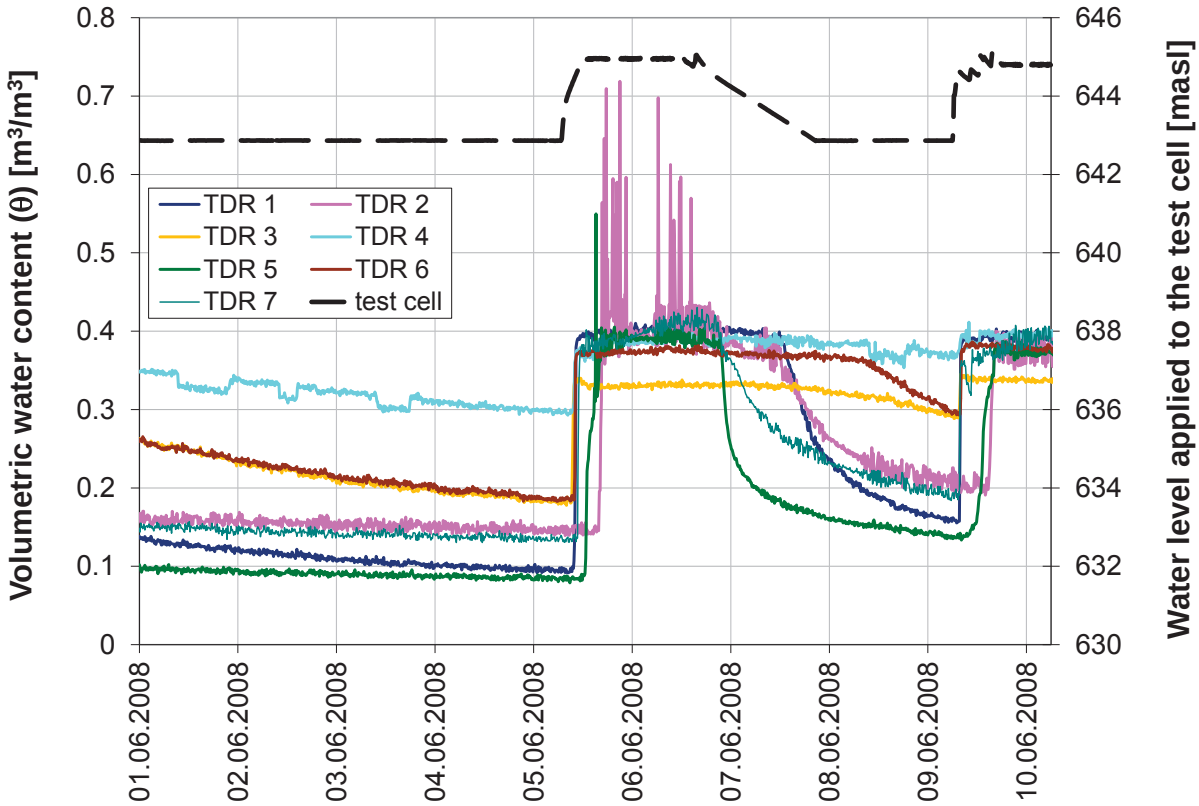

Figure 3.11: Volumetric water content measured by TDR devices over 9 days before the breaching experiment on 10.06.2008.

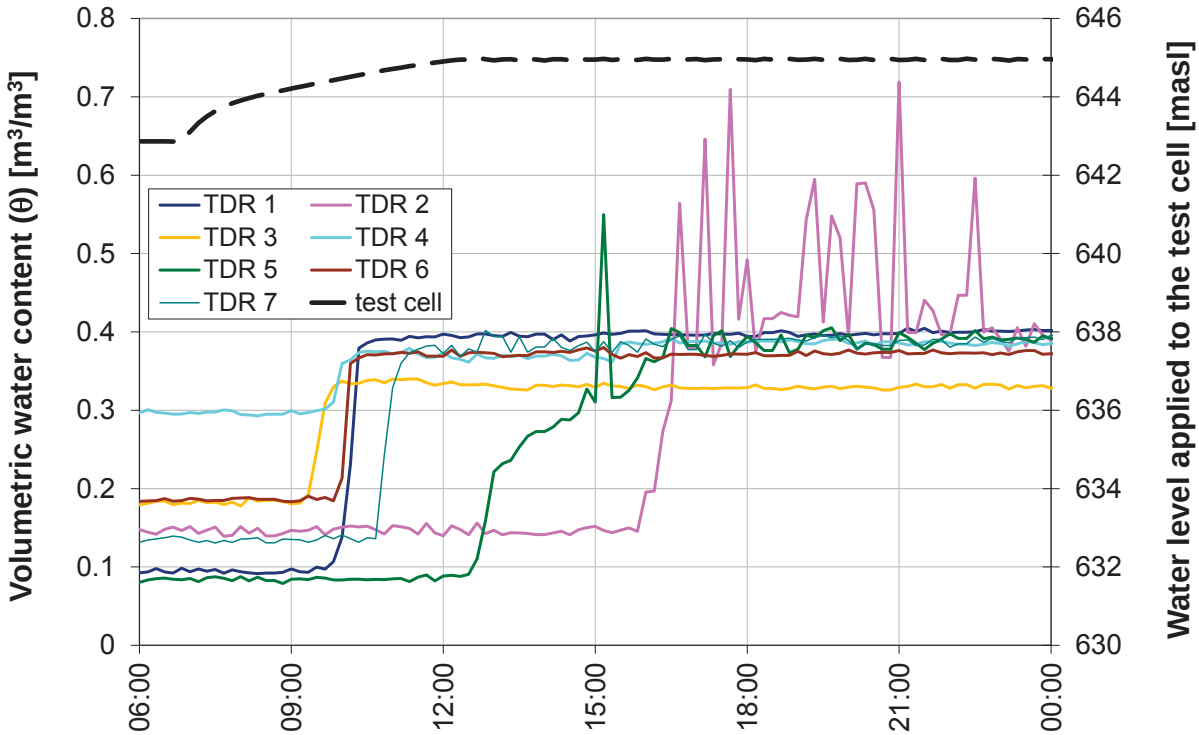

Figure 3.12: Detail of the lag in time in the measurement of volumetric water content by TDR devices on 05.06.2008.

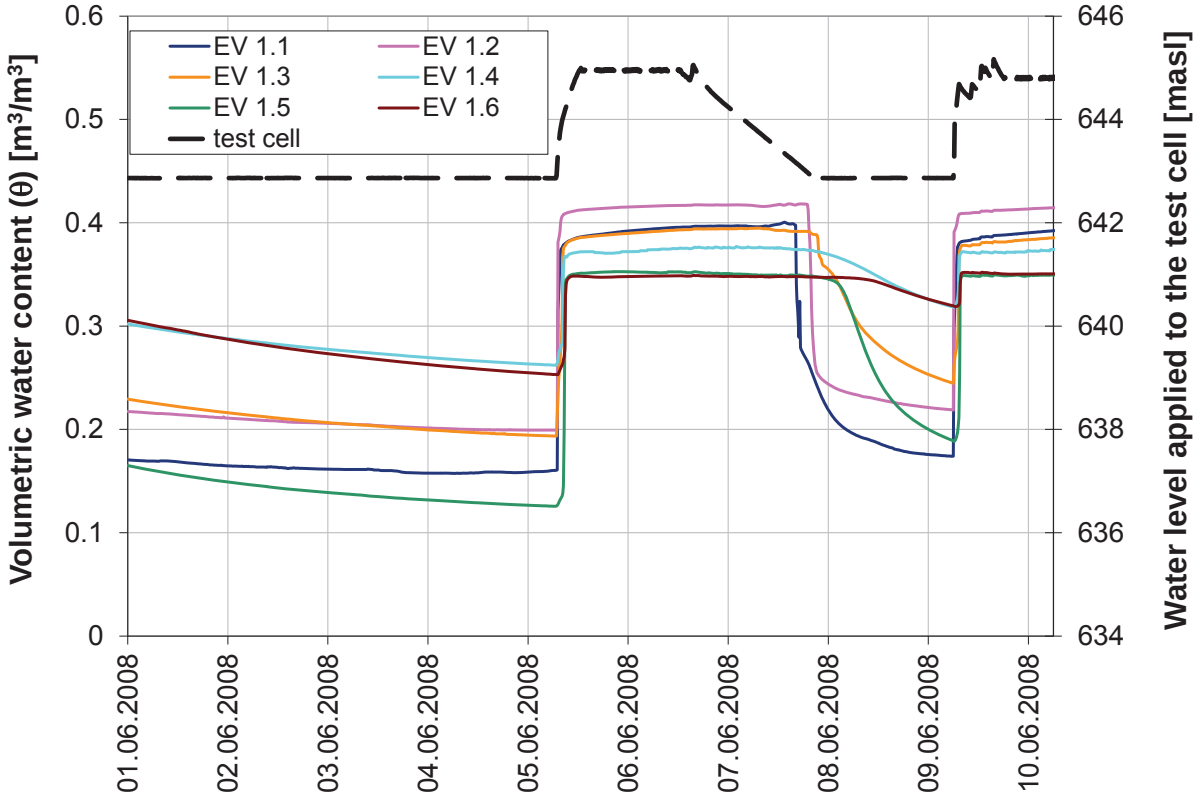

Figure 3.13: Volumetric water content measured by EnviroSmart 1 (X=13.42 m ; Y=3.63 m) over 9 days before the breaching experiment on 10.06.2008.

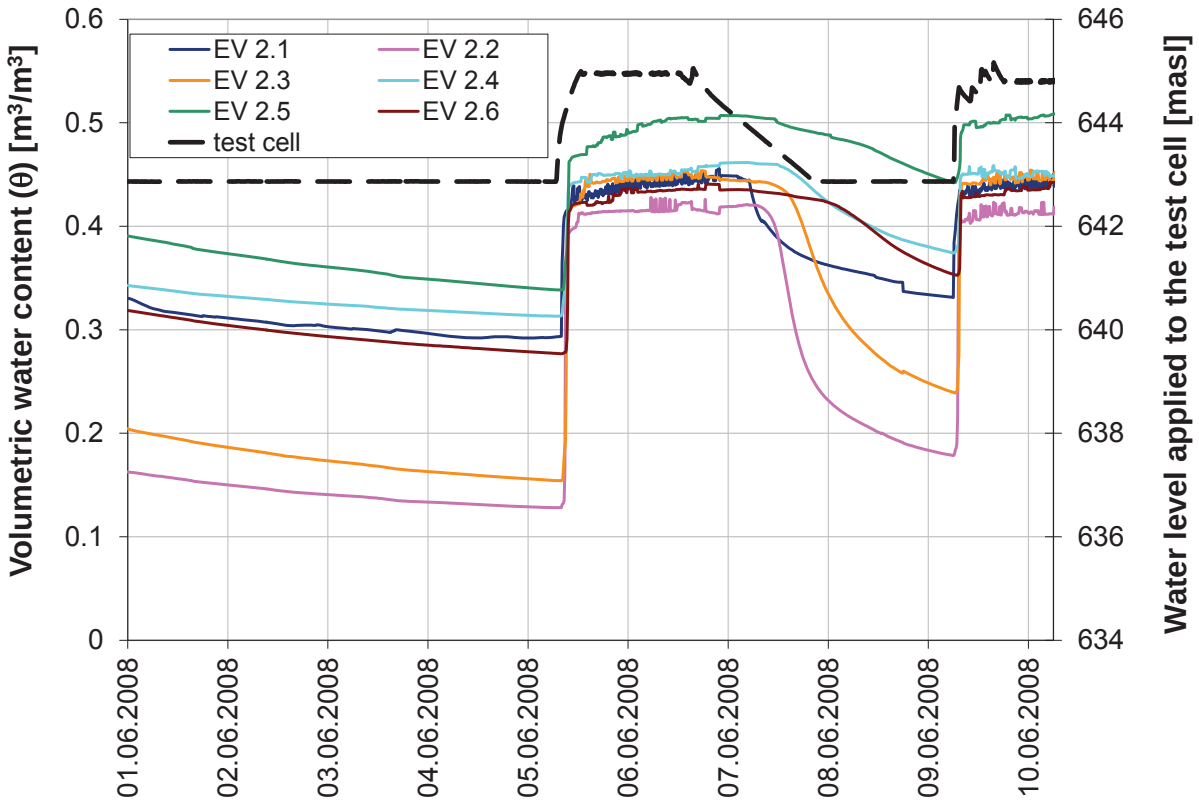

Figure 3.14: Volumetric water content measured by EnviroSmart 2 (X=15.71 m ; Y=6.61 m) over 9 days before the breaching experiment on 10.06.2008.

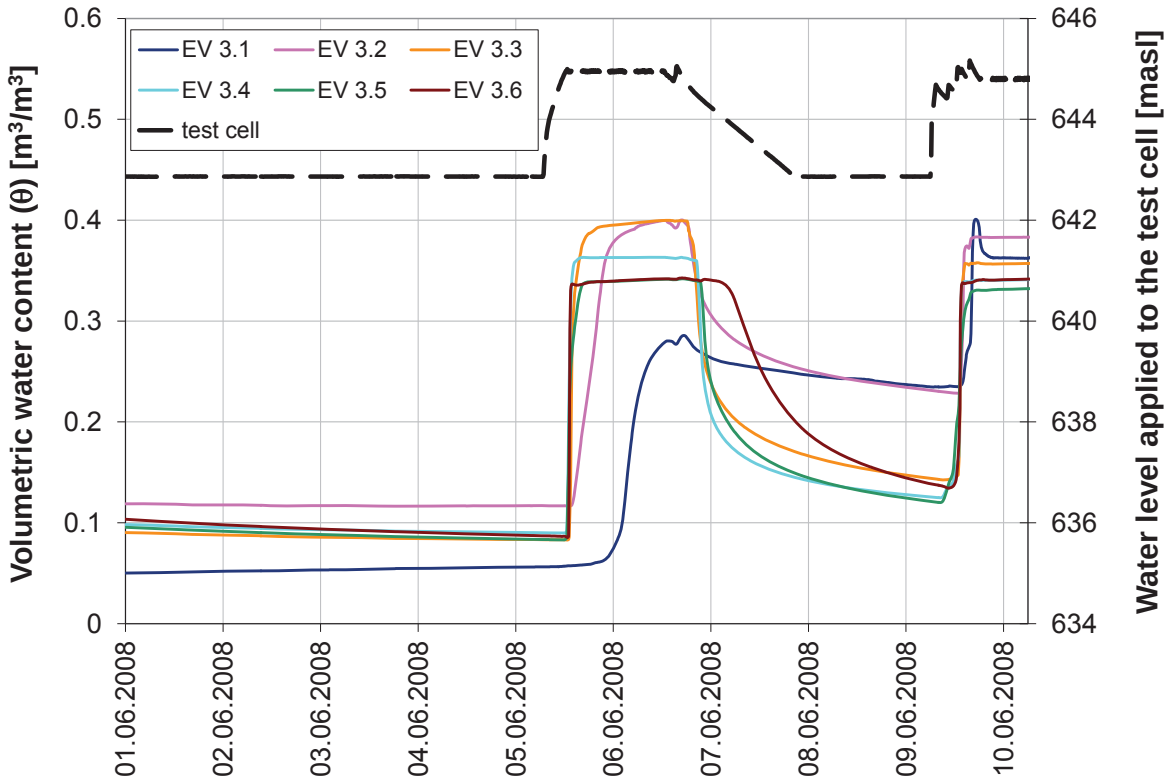

Figure 3.15: Volumetric water content measured by EnviroSmart 3 (X=25.80 m ; Y=9.05 m) over 9 days before the breaching experiment on 10.06.2008.

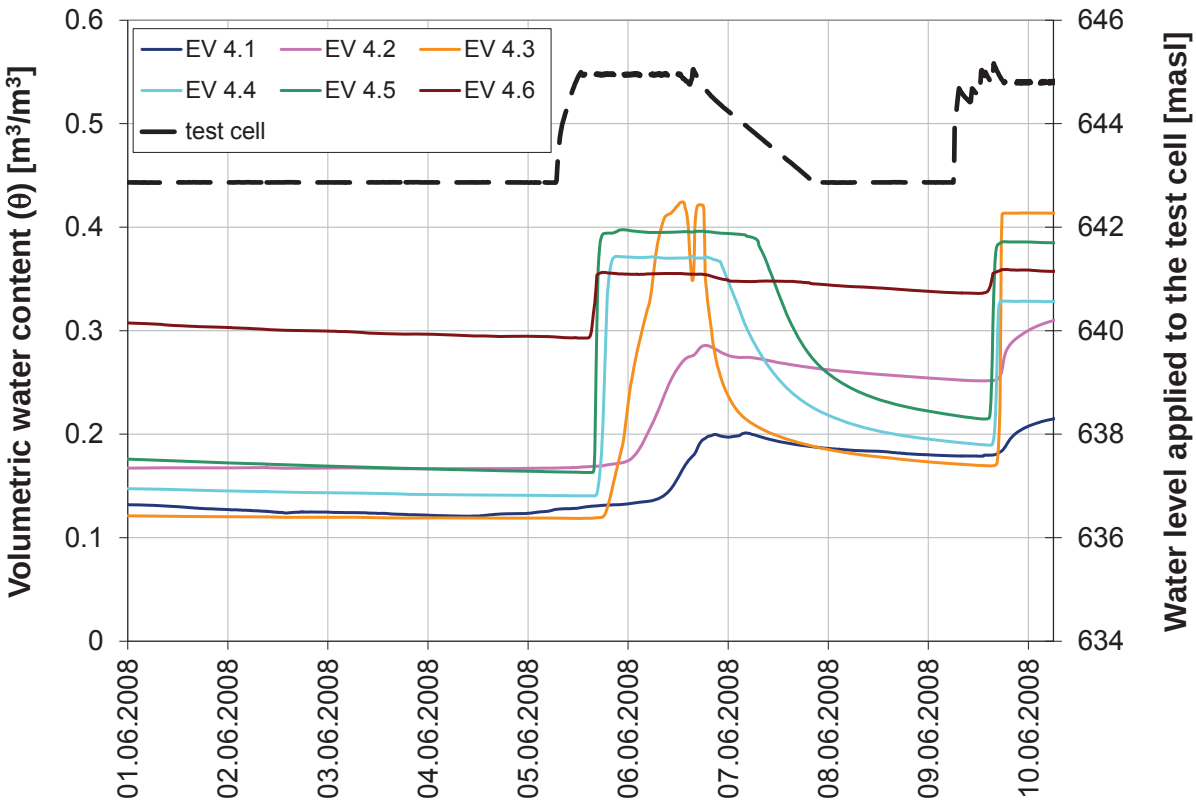

Figure 3.16: Volumetric water content measured by EnviroSmart 4 (X=27.68 m ; Y=4.65 m) over 9 days before the breaching experiment on 10.06.2008.

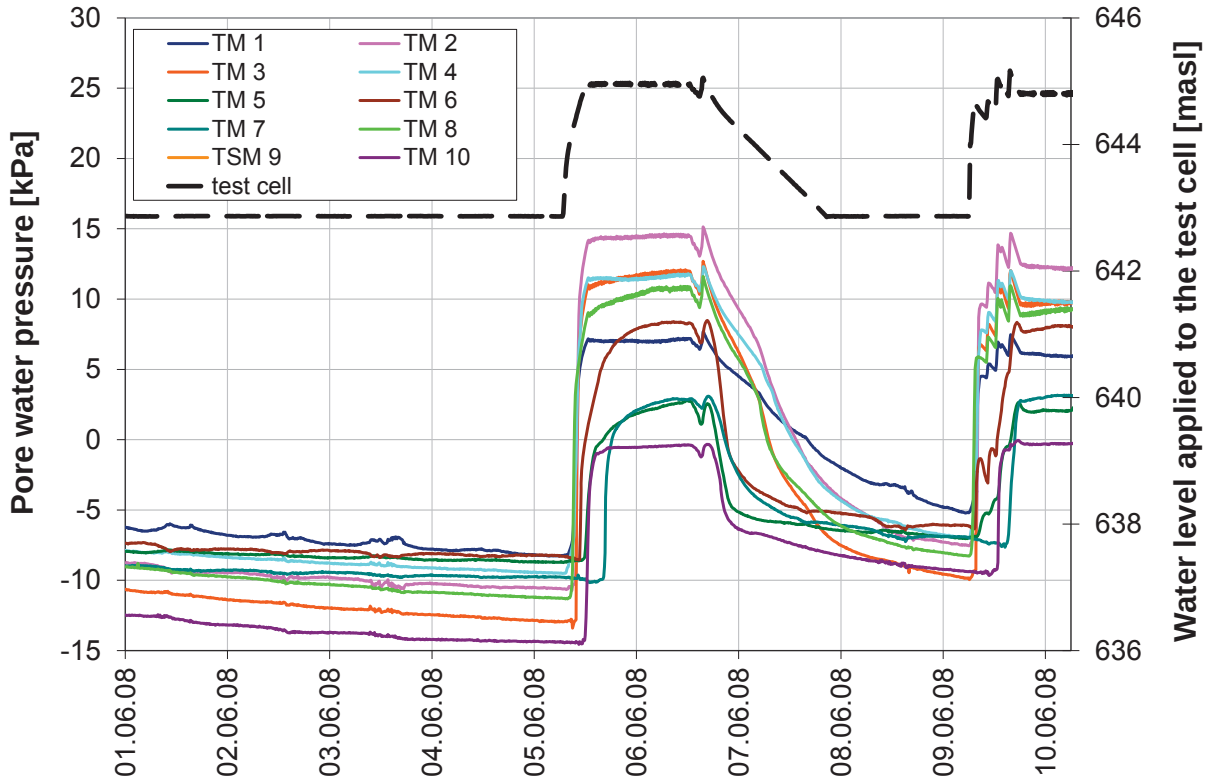

Figure 3.17: Pore water pressures measured by tensiometer devices over 9 days before the breaching experiment on 10.06.2008.

3.2.2.2 Preparation of the dyke for the overflow test

Some activities were carried out on the day before the overflow test, i.e. on 09.06.2008, with the aim of preparing the test cell for the overflow experiment. Firstly, a square notch, of dimensions 0.35 × 0.35 m, was dug in the center of the crest to concentrate the flow onto a specific path. Some sandbags were placed along the crest so that water would not flow along the whole dyke crown when raising the level but through the notch, as previously done by other research projects such Höeg et al. (2004). Finally, a grid of 0.5 × 0.5 m was painted over the slope so that the development of the breach could be followed visually (Figure 3.18).

Additionally, a hole of diameter 0.25 m was drilled at one side of the cell to drain the water that had overflowed (Figure 3.19) to prevent excessive accumulation of water in the trench on the air-side, once the overflow phase had begun. Unfortunately, the diameter was not big enough to allow all the water overflowing to be drained and the test had to be stopped until the pounded water had drained away (c.f. Section 3.2.2.6).

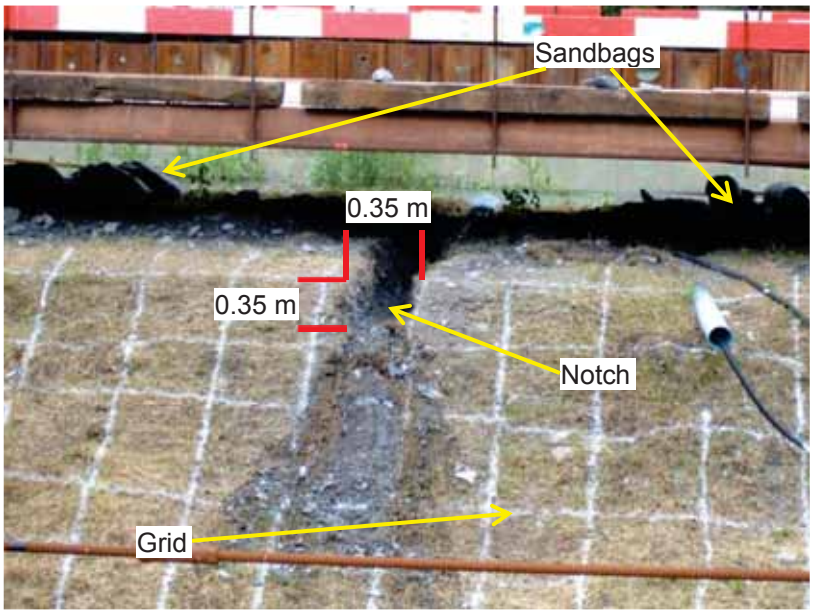

Figure 3.18: Activities for preparing the dyke for the breaching test: A notch of 0.35 x 0.35 m was excavated and sandbags were placed over the crest to the right and left of the notch. Finally, a grid of 0.5 x 0.5 m was painted over the slope's surface (Photograph by VAW on 9.06.2008).

a) View from inside the cell.

b) Pipe connected to direct the water flow into the trench at the toe of the air-side slope and the pipe system.

Figure 3.19: Hole drilled to drain the water that had overflowed (Photograph by VAW on 10.06.2008).

3.2.2.3 Increase of water level on the water-side

Figure 3.20 shows the water level change immediately prior to and during the test. A water level of 642.8 masl was the initial condition at mid-morning on the day before the test (9.06.2008), so that the base condition was that of a steady state flow towards the drainage trench on the air-side. The level was raised in several steps with a pump on the day before the test until it reached 645.10 masl at 10:30 (Figure 3.21).

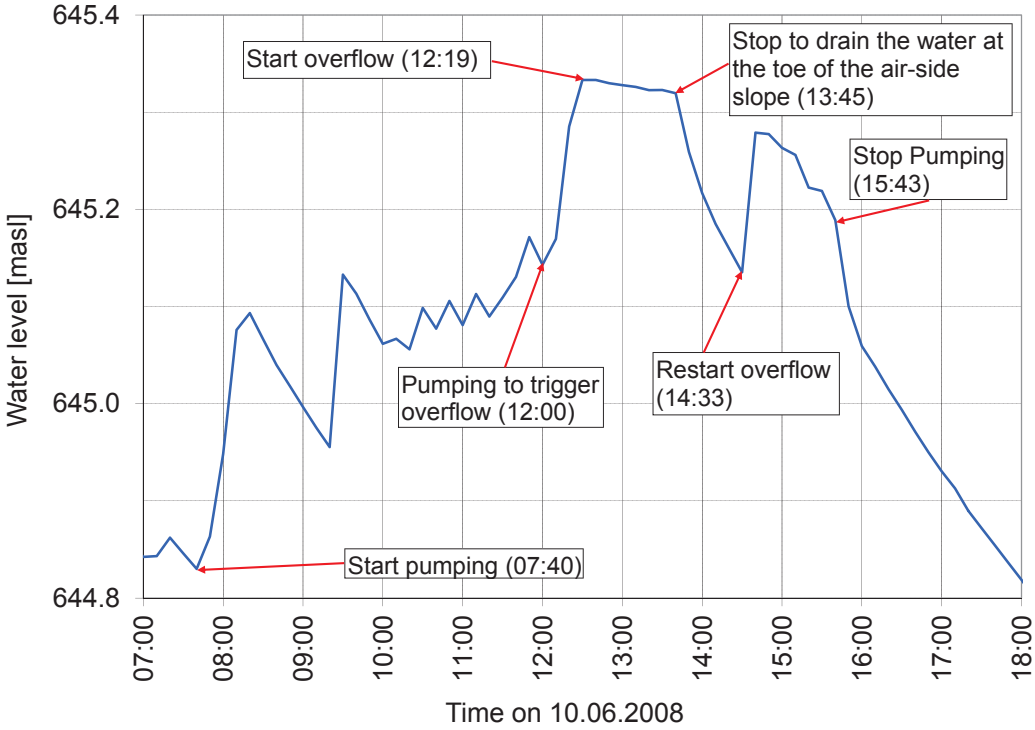

Figure 3.20: Water level on the water-side of the dyke during the day of the experiment (10.06.2008).

Figure 3.21: Water pumped to reach the overflow level (Photograph by VAW on 10.06.2008).

3.2.2.4 Artificial raining on the air-side

Artificial rain was initiated through a sprinkler located in the middle of the air-side slope at 11:42 to saturate the slope surface (Figure 3.22). The rain lasted for 25 minutes with an intensity of 40 mm/hr (measured with a rain gauge), implying that 16 mm of rainfall fell in this period.

Figure 3.22: Artificial raining before the overflow test (photograph by VAW on 10.06.2008 at 11:53).

3.2.2.5 Initial symmetrical overflow

Pumping was started at 12:00 to raise the water level in the cell to 645.28 masl. The flow over the dyke started at 12:19. The flow was mainly focused through the initial notch, which eroded with time (Figure 3.23). However, some water also flowed in gaps between the sandbags over the shoulders of the dyke. The flow on the right side was greater than on the left side (view from the direction of the flow). The flow discharge over the shoulders of the dyke started to decrease (but did not disappear completely) at 12:25. This was a consequence of placing more sandbags on the sides to try to seal them of the flow.

The flow over the slope between 12:15 and 13:53 exhibited a shape that was more or less symmetrical and triangular. The term symmetrical refers to a shape that was almost mirrored along the mid-line of the slope (Figure 3.24), with two branches at the bottom of the flow surface. A marked preference was noted for flow to the left side branch. This might be a consequence of the initial irregularities on the surface on the air-side slope of the dyke, which lead to dimples on the surface (Figure 3.8).

Figure 3.23: Initial flow focused mainly onto the excavated notch (photograph by P.A. Mayor on 10.06.2008 at 13:00).

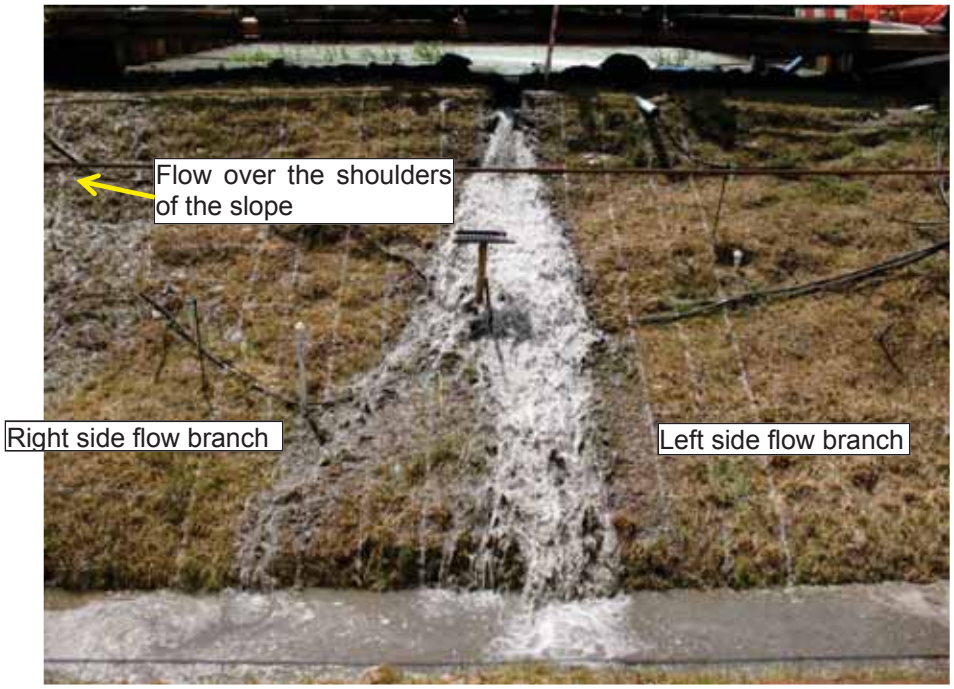

Figure 3.24: Initial symmetric overflow, showing where there was also some unintended flow over the dyke shoulders (photograph by VAW on 10.06.2008 at 12:21).

Flow caused the sand below the notch to erode in the first phase, until it reached a stone blocks layer. Water flowed over the grass cover during this process, with minor erosion or deformation. A second phase was defined by the development of tension cracks along the crest of the dyke, followed by a local slump failure, on the air-side, which did not lead to complete collapse. The last phase was constituted by internal erosion of the dyke material on the air-side, leading to significant surface settlement in a channel along and close to the centerline of the dyke, but without causing total failure of the structure.

It had been expected that erosion of the notch would advance through the dyke with basal and lateral erosion as observed in previous field tests (cf. Section 2.4); however, the coarse interlocking nature of the very coarse gravel layer, which guaranteed that the erodability was much lower than expected, combined with the grass cover, prevented this, although significant internal erosion, of finer soil layers developed, as the overflow test progressed.

The air-side slope experienced a failure event due to a complex mechanism, which started with a deformation of the upper slope of the dyke at its centerline that later was evidenced with the development of tension cracks along the crown of the slope. Some cracks of approximately 20 mm width, were detected on the right side of the dyke crown at 13:03. These started to widen as consequence of the movement of the whole mass, Figure 3.25 presents the evolution of the cracks, while Figure 3.26 shows the complementary perspective taken from the left side of the cell.

Figure 3.27 illustrates how, at the end of the experiment, these cracks were of the order of magnitude of 0.3 m. It was seen that some of the water was flowing over the dyke shoulders could flow directly inside the dyke body due to the significantly larger macro-permeability given by the cracks. This has two main effects; firstly, the pore pressures have risen in the crack causing a hydrostatic pressure to develop that adds a lateral component of water pressure acting on the crack, and secondly, that water could flow directly inside the dyke body, increasing the saturation degree. Both processes led to a drop in the overall stability.

Water flowing into the dyke, through the cracks, led to a major susceptibility of the soil at the failure surface to be eroded by internal processes.

The mass stopped moving significantly at 13:18. From that point on, a new process was noticed thereafter. Some material was being ejected in the form of a soil 'volcano' by an internal erosion process on the left side of the drainage trench (Figure 3.28). At the same time as fine material was being washed out, surface settlements became increasingly evident on the slope, creating a pattern of channels, which confirmed the ongoing internal erosion. The channel created on the left side coincides almost perfectly with one of the large deformation zones described above, which is shown in Figure 3.31.

Deformations close to the centerline are greater than at the sides, most probably because the sheet piles provided some additional resistance to lateral deformation due to interface friction, and the material on the sides deformed with more constraints than along the centerline. This led to the central zone of material to ‘detach’ from the rest of the sliding material, creating a triangular zone of material with larger deformations. This zone is delineated in Figure 3.31.

10.06.2008 at 13:03 (from right).

10.06.2008 at 13:04 (from left).

10.06.2008 at 13:06 (from right).

10.06.2008 at 13:07 (from left).

10.06.2008 at 13:10 (from right).

10.06.2008 at 13:12 (from below).

10.06.2008 at 13:18 (on right side).

Figure 3.25: Evolution of the tension cracking process on air-side of the dyke, from various perspectives (Photographs by P.A. Mayor).

10.06.2008 at 13:02.

10.06.2008 at 13:10.

10.06.2008 at 13:12.

10.06.2008 at 13:14.

10.06.2008 at 13:15.

10.06.2008 at 13:16.

10.06.2008 at 13:17.

10.06.2008 at 13:18.

Figure 3.26: Slope failure process as viewed from cell coordinates X= 27.5 m, Y= 12.5 m (photographs by VAW).

Figure 3.27: Crack width on the crest of the dyke the day after the experiment (Photograph by P.A. Mayor on 11.06.2008).

a) (From toe). *b) (From crest).*

c) (From crest). *d) (From above).*

Figure 3.28: Ejected material at the toe of the air-side slope due to internal erosion (photographs by VAW and P.A. Mayor on 10.06.2008 at 13:33).

3.2.2.6 Temporary lowering of water level

The discharge capacity of the hole drilled in the sheet pile wall was insufficiently large to allow the water pounded on the air-side to drain. Therefore, water started to accumulate, firstly in the drainage trench (Figure 3.4b) and subsequently at the bottom of the slope, until it reached 642.5 masl, which was 0.5 m above ground level. The decision of stop pumping water was taken to allow the water level in the cell to drop naturally so that water could be pumped out of the trench. This phase took place between 13:45 and 14:33, when it was possible to observe and take samples from the ejected material.

Figure 3.29: Accumulated water in the drainage trench (photograph by VAW on 10.06.2008 at 13:46).

3.2.2.7 Asymmetrical overflow

Once the accumulated water was pumped out of the drainage trench, the experiment was continued by raising the water level again on the water-side of the dyke. Continual material ejection accompanied by subsidence along the centerline of the air-side slope were clear indication of internal erosion at the same time as the water level increased.

Flow was more or less symmetrical as before, when water started to flow over the dyke once more. Whereupon, preferential internal erosion advanced on the left side of the dyke, leading to water to flow on that side mainly. This caused asymmetrical flow to develop, as shown in Figure 3.30. This was also partially owing to constriction of the flow breadth at the notch due to local collapse of a block of soil, which fell onto the flow (Figure 3.30). This block slid into the notch due to instability caused by saturation at the base of the vertical walls of the notch.

The debris was removed manually in an attempt to increase the flow breadth, but without success. The experiment was concluded at 15:52, as no major deformations or changes in the state of the dyke were observed.

Figures 3.31 and 3.32 show the final configuration of the dyke the day after the overflow experiment. Accumulations of superficial and internally eroded material are appreciable, mainly at the left side of the flow.

Figure 3.30: Flow breadth restricted by a block of soil.

Figure 3.31: State of the air-side slope of the dyke one day after the overflow experiment. The rectangle indicates the place were a pit was dug for post- analysis (cf. Section 3.2.4). The black lines delineate the zone which presented larger deformations were observed in the lower slope (photographs by P.A. Mayor on 11.06.2008).

Figure 3.32: Lateral view of the dyke one day after the experiment (from X=27.5 m, Y=0 m). The rectangle indicates the place were a pit was dug for post-analysis (cf. Section 3.2.4). (photograph by P.A. Mayor on 11.06.2008).

3.2.3 Measurements during the overflow experiment

Readings of the piezometric heads (Figure 3.33) show that changes in the water level in the test cell, again, had a minimal effect on the phreatic water surface below the main body. Nevertheless, slight increments of 0.15 m on the piezometric heads were observed for P2, P4 and P5. Once again, behavior of devices 4 and 5, 3 and SB03 were quite similar. Piezometer 2 continued showing lower piezometric heads than those for piezometer 1, which was located below in the same borehole.

Figures 3.34 to 3.39 show some relevant results from the measurements made during the breaching test. Volumetric water content and suction measurements from sensors (Figure 3.4 and Table 3.2) on both water and air-sides of the dyke indicate that most of the dyke was in a saturated condition in these locations at the beginning of the overflow phase.

Particular exceptions include TDR 2 (Figure 3.34), EV 3 (Figure 3.37) and to a greater extend EV 4 (Figure 3.38). An increase of the volumetric water content was observed by these sensors at 12:30 approximately. The increase in the water content continued until 13:15, where the values stabilized. This coincides with the failure of the air-side slope (13:02-13:18). The increase in the volumetric water content indicates a change in the volume of the soil, presumably due to the proximity of the sensor to the failure surface.

The pore water pressure (PWP) measurements (Figure 3.39) confirm this assumption. The PWP of TM 5, 6 and 9 had a drop at around 13:20. This drop might be caused by the volumetric change due to failure of the slope. These results help to identify the location of the failure surface, as it should cross in the vicinity of the sensor registering those changes.

Additionally, a sudden drop in volumetric water content to values close to 8% was detected by gauges EV 3.1 and EV 3.2. As they are the devices closest to surface of the air-side slope, and were coincidentally located at the place at which larger deformations due to internal erosion occurred, these measurements could be explained as a consequence of the loss of surrounding material due to internal erosion, and therefore gauges were in contact with loose desaturated soil.

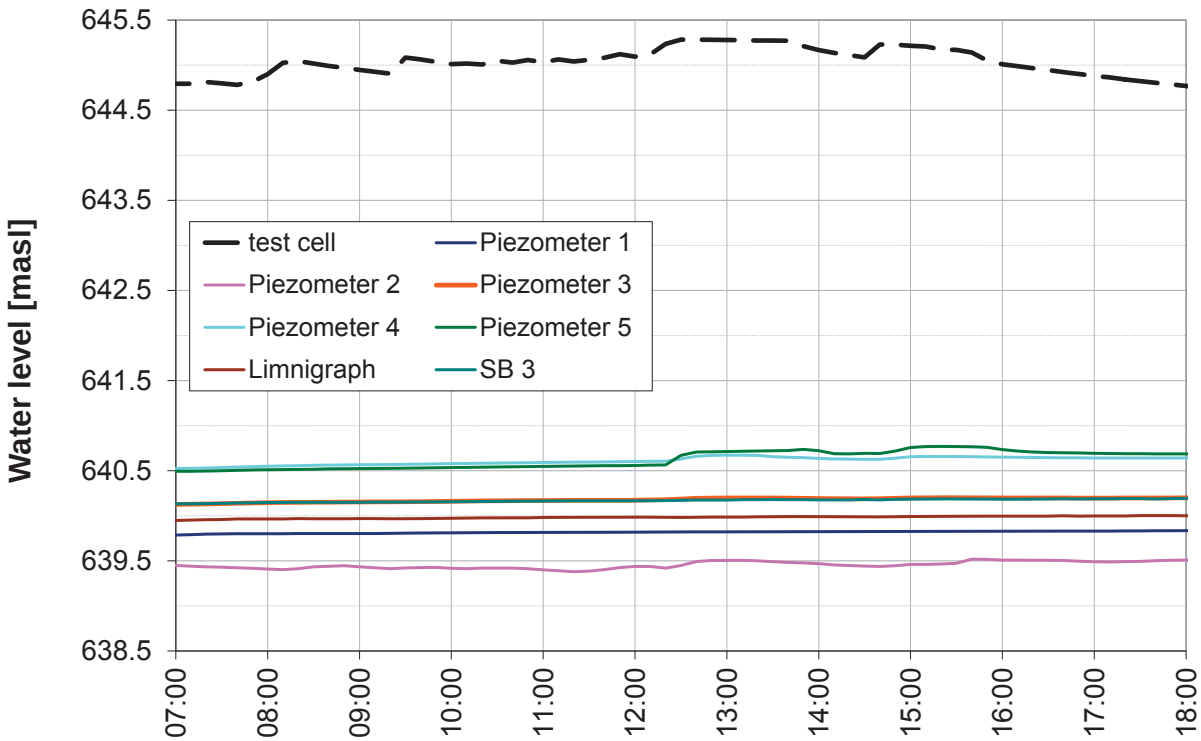

Figure 3.33: Piezometric water heads during the breaching experiment.

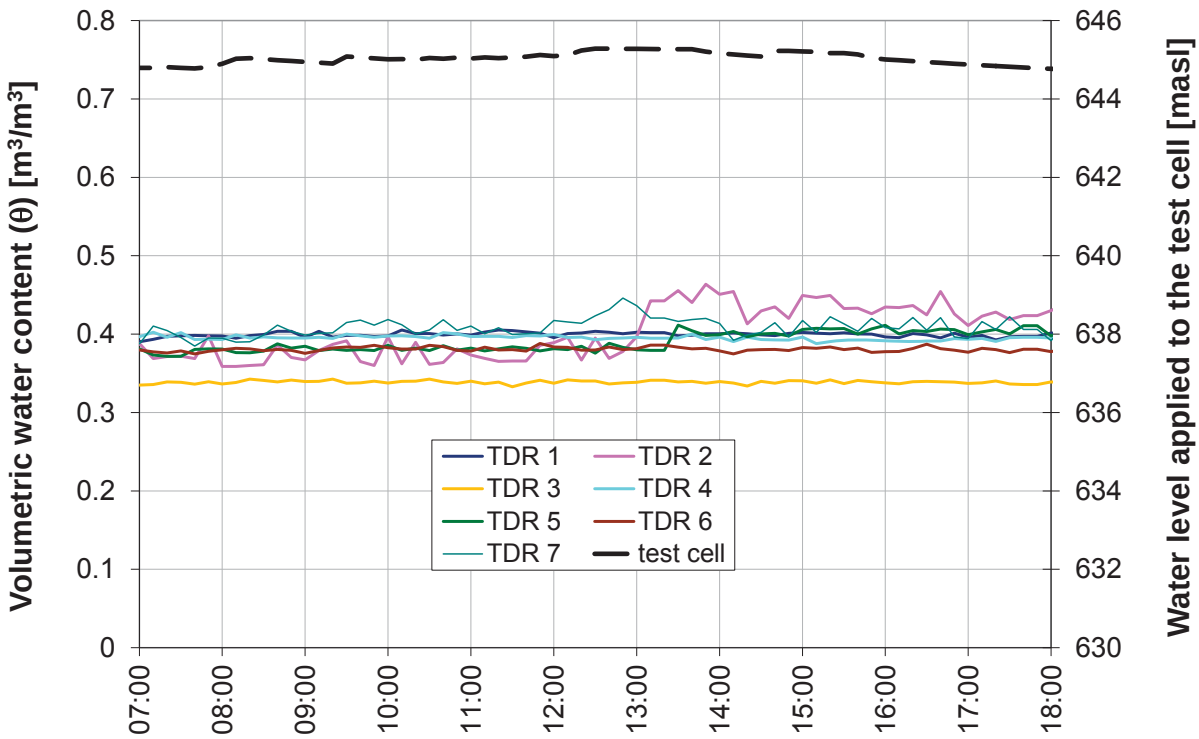

Figure 3.34: Volumetric water content measured by TDR devices during the breaching experiment.

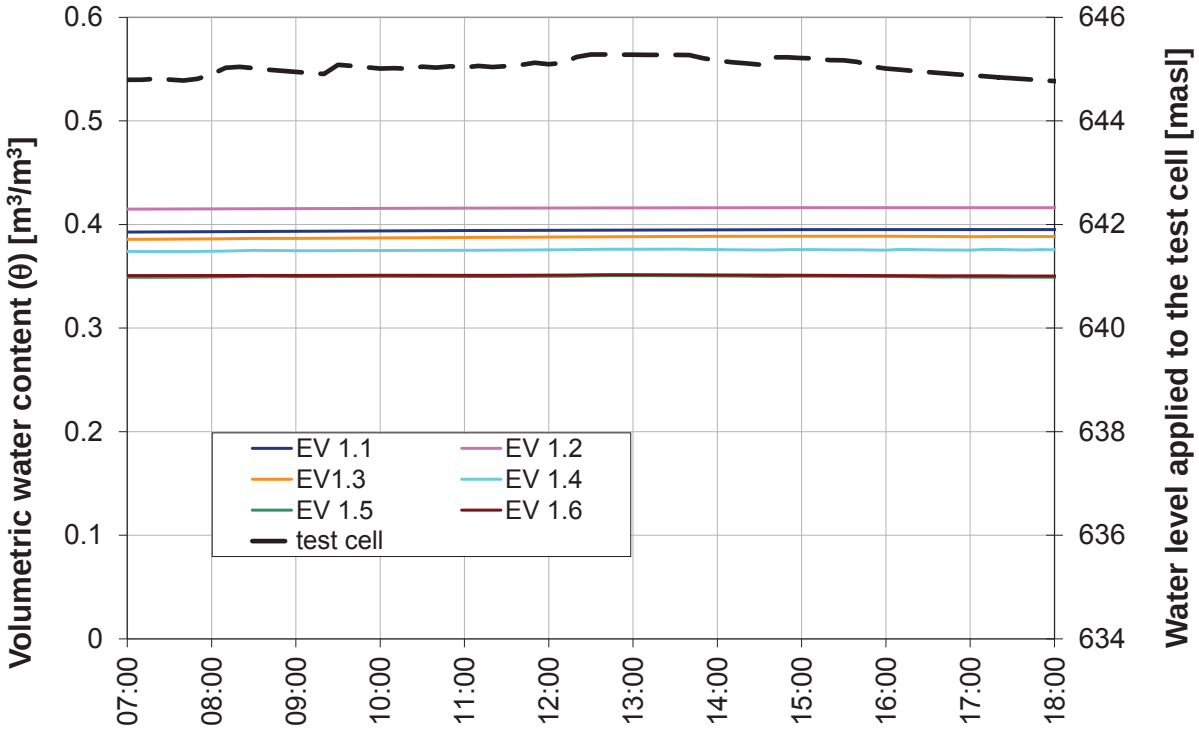

Figure 3.35: Volumetric water content measured by EnviroSmart 1 (X=13.42 m ; Y=3.63 m) during the breaching experiment.

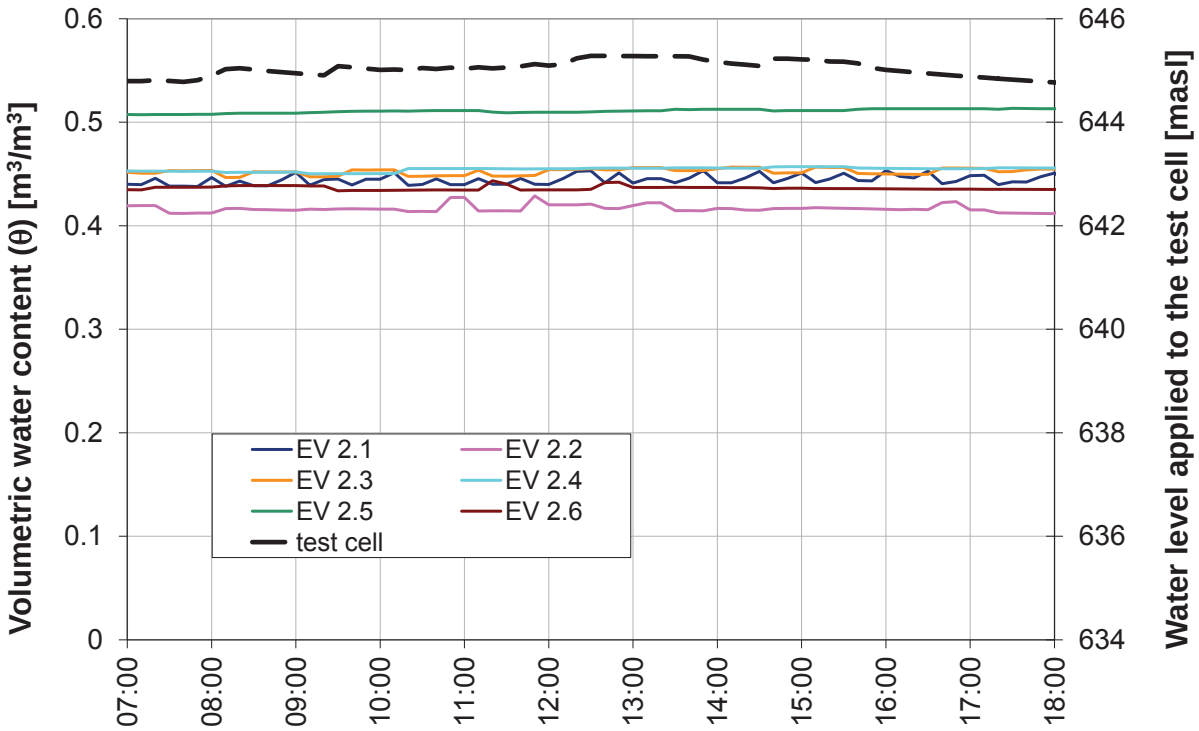

Figure 3.36: Volumetric water content measured by EnviroSmart 2 (X=15.71 m ; Y=6.61 m) during the breaching experiment.

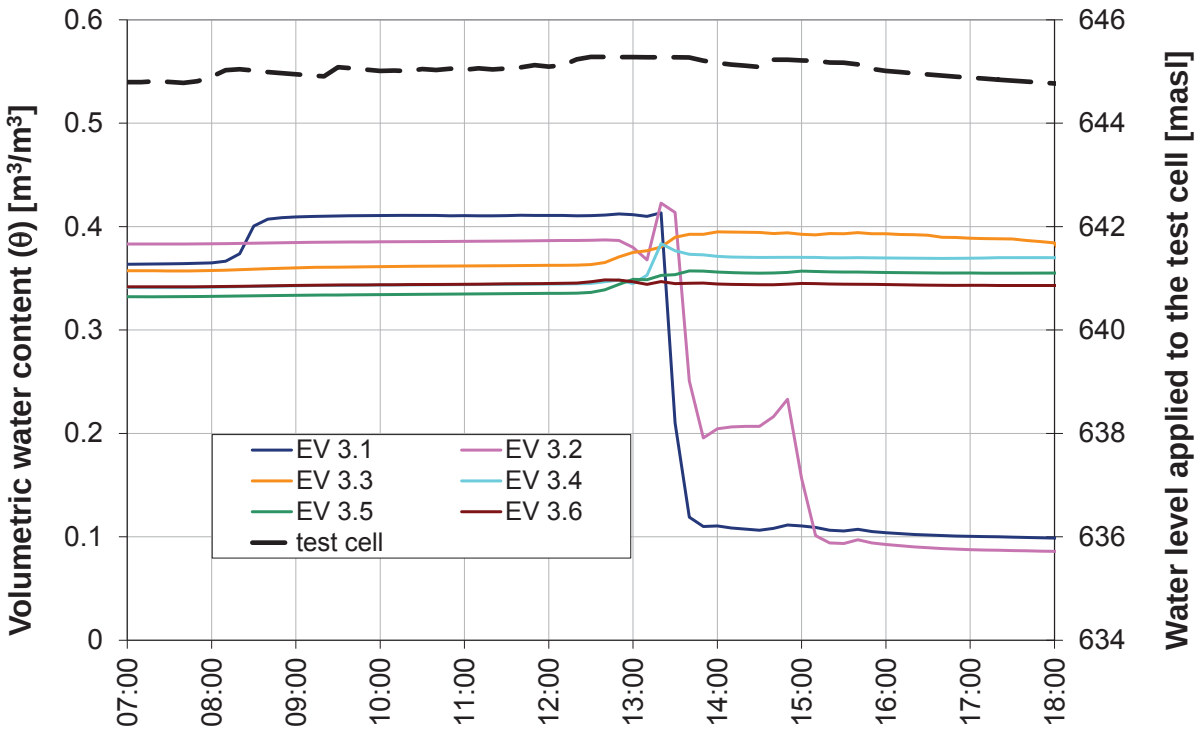

Figure 3.37: Volumetric water content measured by EnviroSmart 3 (X=25.80 m ; Y=9.05 m) during the breaching experiment.

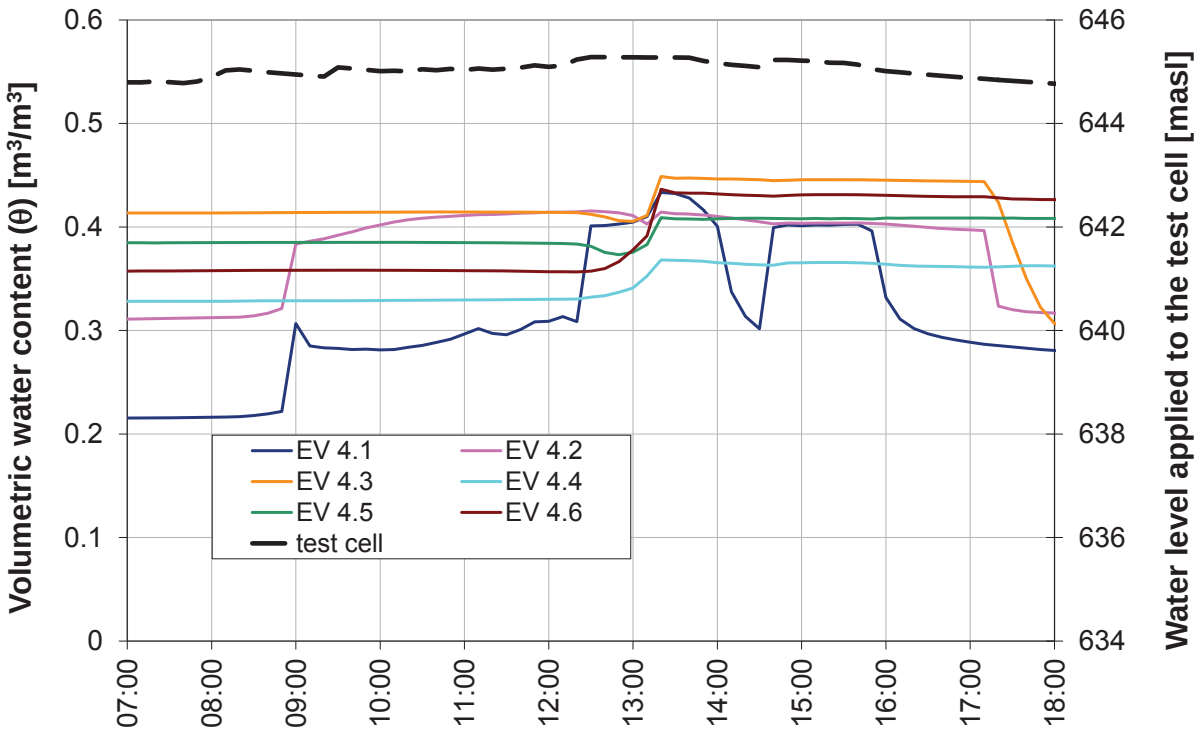

Figure 3.38: Volumetric water content measured by EnviroSmart 4 (X=27.68 m ; Y=4.65 m) during the breaching experiment.

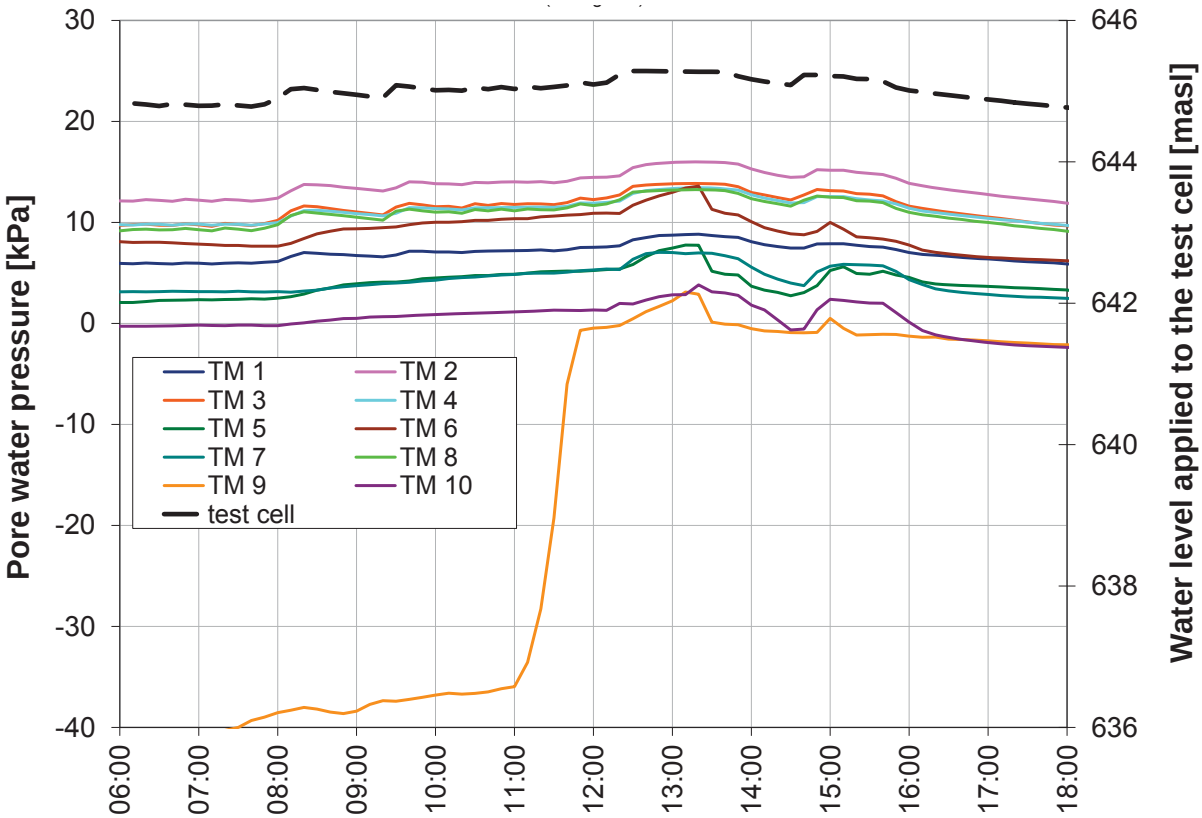

Figure 3.39: Water pressure measured by tensiometer devices during the breaching experiment.

3.2.4 Investigation after the experiment

The state of the dyke was investigated on 11.06.2008, i.e. one day after the overflow experiment. Some soil samples from key points within the test cell were taken.

The depth of the slip surface could be defined by exposing the depths at which the measurement devices had bent. For example, TM 5 (X=25.8 m, Y=8.44 m) has been bent at approximately 1.00 m depth (Figure 3.40).

The magnitude of the vertical settlement due to the internal erosion close to the centerline was measured to be approximately 0.5 m (Figure 3.41). This deformation is consistent along the centerline (with a trend to the left side of the flow).

Figure 3.42 shows the gravel constituting the upper part of the dyke. The thicknesses of the materials composing the upper part of the dyke were determined as the top 0.35 m for the upper soil layer, underlain by 0.25 m thickness of larger stone fragments that exhibit marked anisotropy.

A pit was dug on each side of the dyke to collect some soil samples. This was located at the place of maximum deformation on the air-side slope, whereas it was dug on the centerline on the water-side slope (see Figure 3.43). The pit on the air-side had dimensions 1.0 × 0.6 m and 0.6 m depth, and it was dug at X=25.80 m, Y=8.44 m. The inspection of the pit revealed

that the soil surrounding the roots of the vegetation (grass) had been transported by internal erosion bellow the grass cover (Figure 3.44). This caused internal pipes, which explain the diverse deformations of the air-side of the dyke. This coincides with the guidelines from FEMA (2005), which state that roots can create preferential seepage paths leading to internal erosion problems. This can produce a potentially dangerous increase in hydraulic seepage gradient and internal erosion or piping problems in dykes.

Mériaux et al. (2006) explain how the development of a deep, fine root system may weaken the structure through localized loss of fill density. Furthermore, they comment on aging of vegetation in that rotten roots may leave a 'pipe' (rotting occurs throughout the life of a tree and of course massively on its death), promoting internal erosion. The authors analyzed some dykes on the Rhone River in France. Although the material of the dyke was different (mainly gravel), it is interesting that the authors claim that roots avoid pure gravel material and concentrate on growing extensively in sand-silt horizons and the layers of topsoil buried by the periodic dyke heightening operations.

Figure 3.40: Bend in the tube for TM 5 indicating a probable slip surface at a depth of 1.0 m at X=25.8 m, Y=8.44 m (photograph by A. Askarinejad on 11.06.2008).

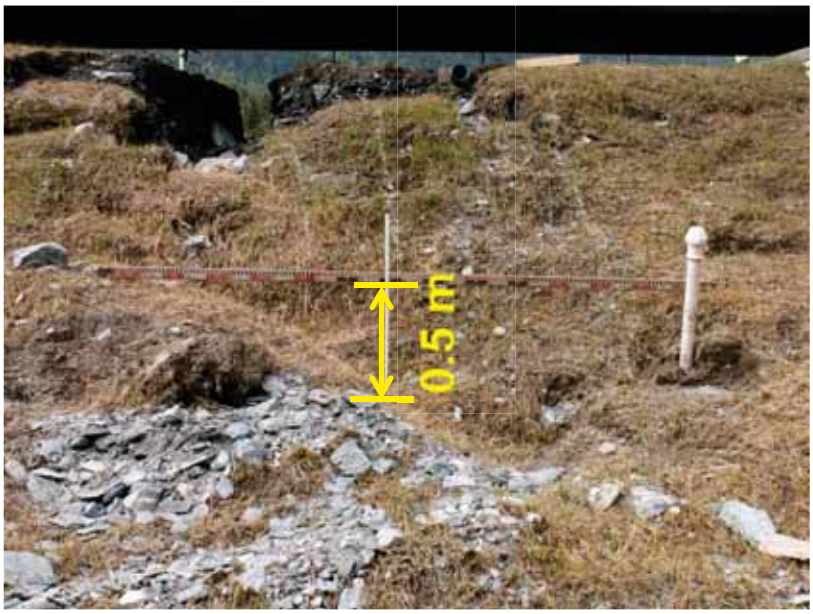

Figure 3.41: Final deformed state of the air-side slope.

Figure 3.42: Gravel layer in the upper part of the dyke, showing the notch (photographs by P.A. Mayor on 11.06.2008).

Pit on the air-side of the dyke (Figure 3.31).

Samples from sandy material on the air-side.

Figure 3.43: Soil sampling on both sides of the dyke, after the experiment (photographs by A. Askarinejad on 11.06.2008).

Figure 3.44: Marked erosion in the area of the roots. Left corresponds to point A *in Figure 3.31. Right corresponds to point* B *in Figure 3.31 (photographs by P.A. Mayor on 11.06.2008).*

3.3 Experiment evaluation and modeling

3.3.1 Initial simulation

A numerical simulation was carried out by VAW (Fäh & Volz, 2008) prior to the overflow test to predict the dyke behavior. A solution was obtained using BASEMENT (Laboratory of Hydraulics, 2008). A homogenous, highly erodible, saturated material was assumed for this

simulation, which coincided with the software options available at the time. Continuous erosion was expected, from the initial state of the body of the dyke, based on this simulation (Figure 3.45a), as erosion would advance down through the dyke accompanied by lateral slumping. However, the coarse interlocking nature of the blocky stone layer, the low erodibility of a very coarse gravel layer on top of the dyke, combined with the grass cover, prevented this, as shown above. This explains the difference between the predicted and measured profiles presented in Figure 3.45b.

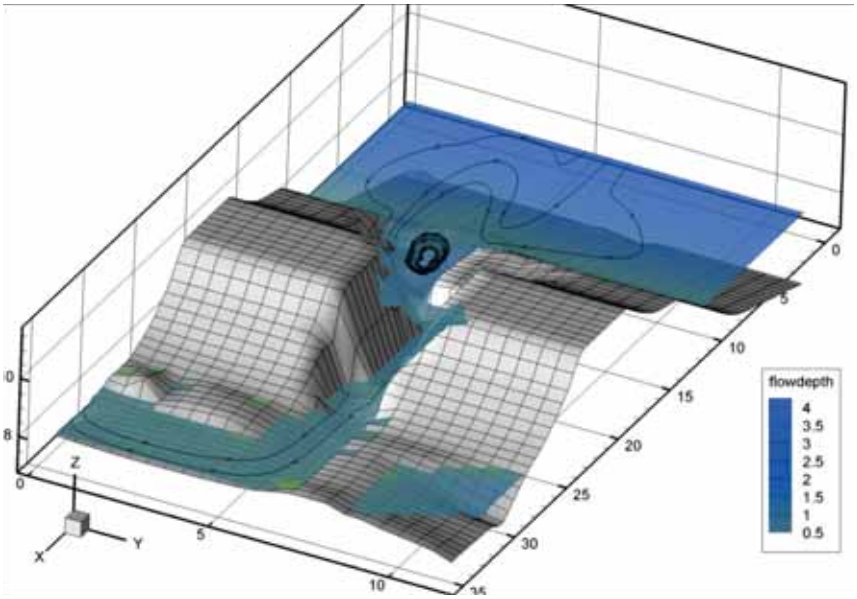

a) Breach development in three-dimensional view.

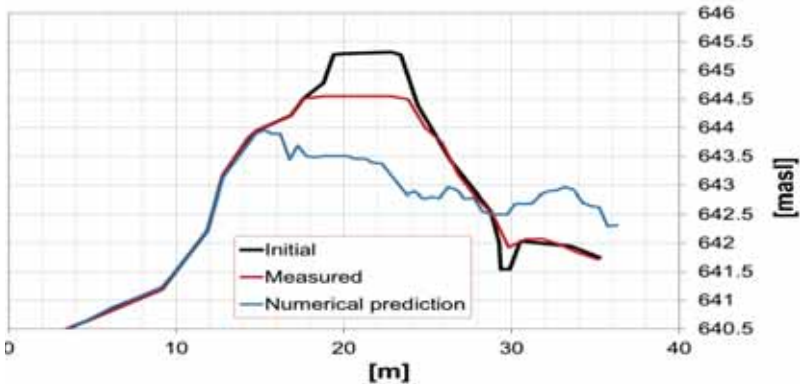

b) Cross section with predicted and measured profiles due to the overflow and breaching action.

Figure 3.45: Predicted behavior of the breach experiment by Fäh & Volz (2008).

3.3.2 Image processing analyses

A photographic record of the experiment was made with three different cameras. Two of them observed the dyke from the front (X=35.26 m, Y=6 m) and one from the side (X= 27.5 m, Y= 12.5 m) (Figure 3.26). Further image analyses were carried out on the series of these photographs to analyze the behavior of the deformations with time.

Analyses were carried out using Particle Image Velocimetry (PIV) (cf. Section 2.3.5.1) to determine the deformation process of the slope surface. The picture area is divided into small patches. A characteristic texture is assigned to the patch and identified in the next photograph. Thus, net deformations can then be quantified so that the displacement vectors can then be plotted.

The analyses were performed on pictures that were taken every minute from both the front and side of the air-side of the dyke. Figure 3.46 presents both grids of patches used. Each patch corresponds to approximately 0.125 $\times$ 0.125 m. A gap in the meshes was left intentionally on the left side of the slope. This corresponds to a cable placed on the terrain and it was found to cause significant noise when the analyses were performed.

The displacement vectors 1 hour after the beginning of the experiment are shown in Figure 3.47 as example of the results obtained. The displacement vectors are plotted in the plane of the camera, which is not completely parallel to the camera. This explains why some of the plotted vectors point to the sides instead of indicating completely downslope movements, which are greater on the right hand side of the slope (left side of the figure) because of the formation of tension cracks and slumping, as the slope failed partially. Nonetheless, the mechanisms are interesting because they show that a unit in the upper part of the slope translated more or less in the same direction, with larger deformations near the dyke's crown, whereas the left hand side of the slope (right side of the figure) shows a zone of large deformations. This corresponds to the superficial settlement observed due to internal erosion. This causes some vectors to be aligned away from the downslope direction.

Figures 3.48 and 3.49 present the results of the PIV analysis for the air-side slope, based on the grids presented in Figure 3.46. These represent the deformation path followed by each element of the grid from the beginning of the test (12:00) until the end (15:52). In both cases, the large deformations on the lower part of the left side of the flow are detected. These illustrate the deformation caused by the loss of material from internal erosion.

The analysis from the front of the air-side slope view illustrates how the shoulder of the slope on the right side of the slope (left side of the figure) deforms more than the left side. The analysis from the lateral view illustrates clearly the slump in the bottom half of the left side of the slope.

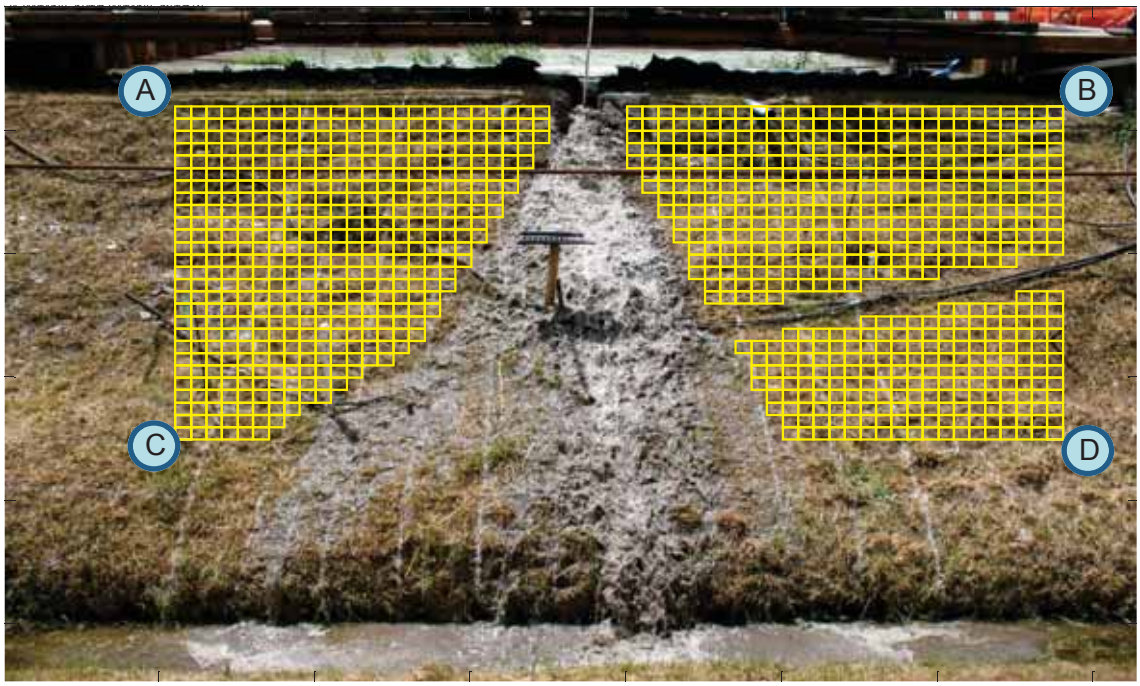

a) Grid for the pictures taken from the front.

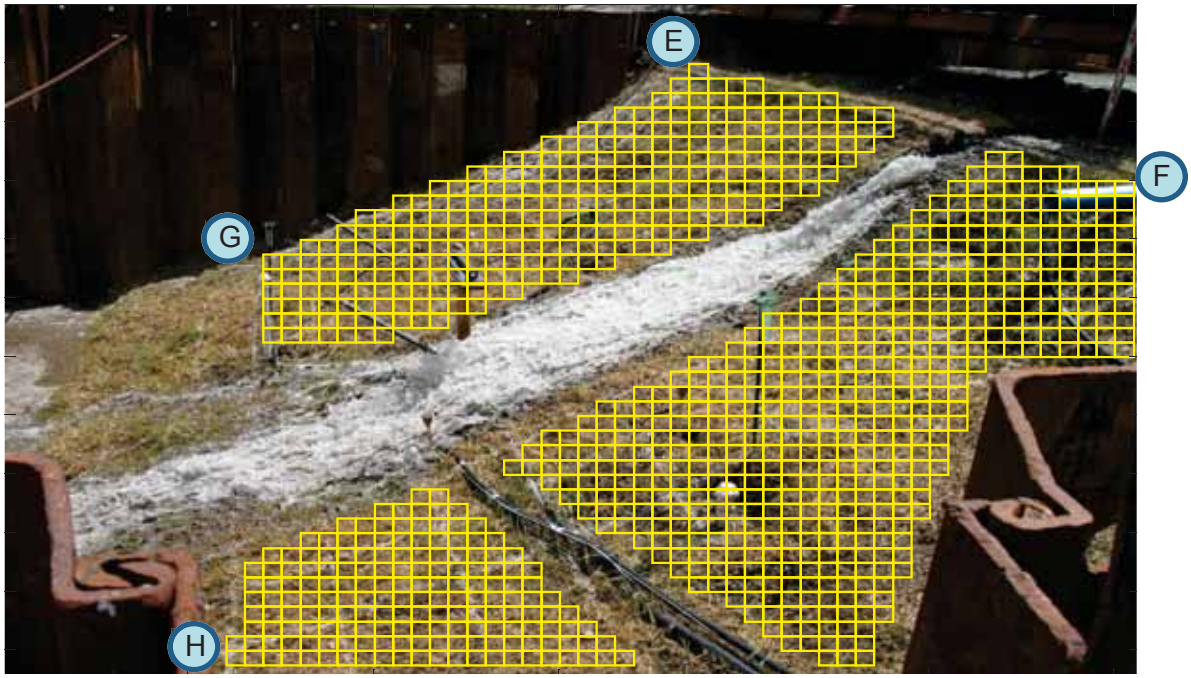

b) Grid for the pictures taken from the side.

Figure 3.46: Grids of patches for the PIV analyses of the air-side slope.

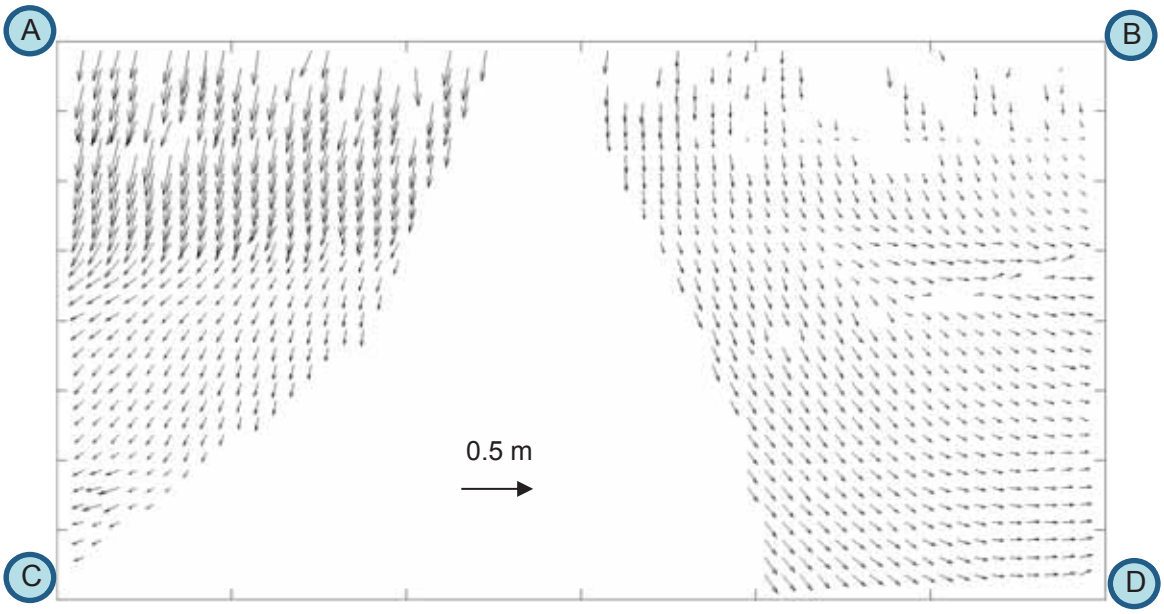

Figure 3.47: Particle Image Velocimetry (PIV) analysis of the air-side of the dyke in the field test showing net displacement vector in the plane of the camera at 13:00, 1 hour after the experiment begun.

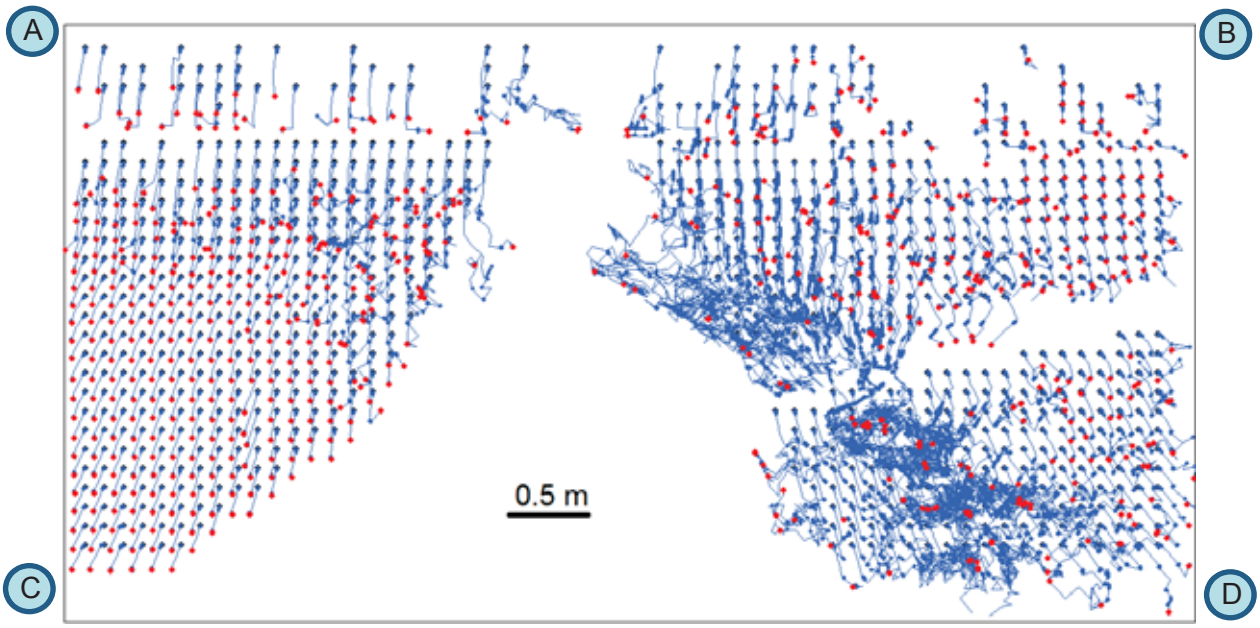

Figure 3.48: Displacement pattern of the air-side slope analyzed with Particle Image Velocimetry from the pictures taken from the front side of the slope from 12:00 to 15:52.The initial positions are marked with the blue dots. The final positions are illustrated with the red points.

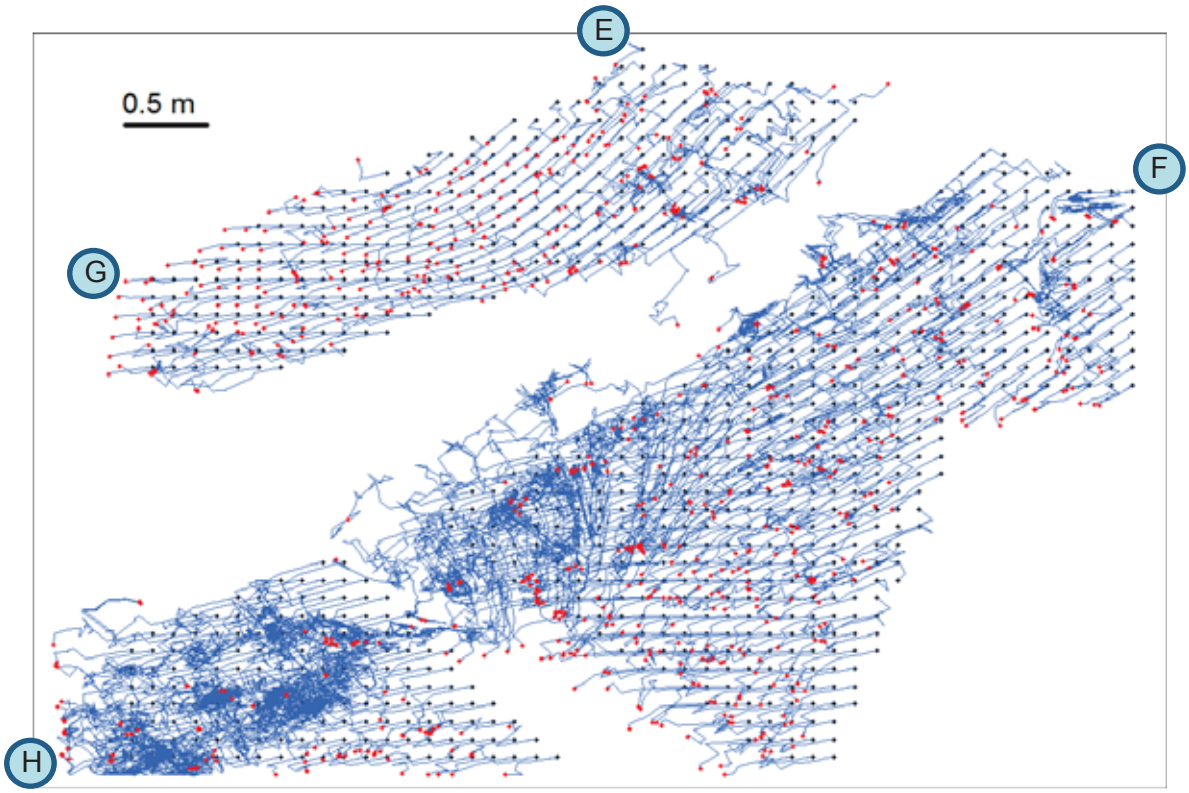

Figure 3.49: Displacement pattern of the air-side slope analyzed with Particle Image Velocimetry from the pictures taken from the front side.

An additional analysis was performed using photogrammetry techniques (cf. Section 2.3.5.2) with the software PhotoScan (AgiSoft LLC, 2013). Figure 3.50 is a 3D view of the air-side slope at the end of the test. This view is the result of the photogrammetric restitution from five different pictures taken by P. Mayor and VAW.

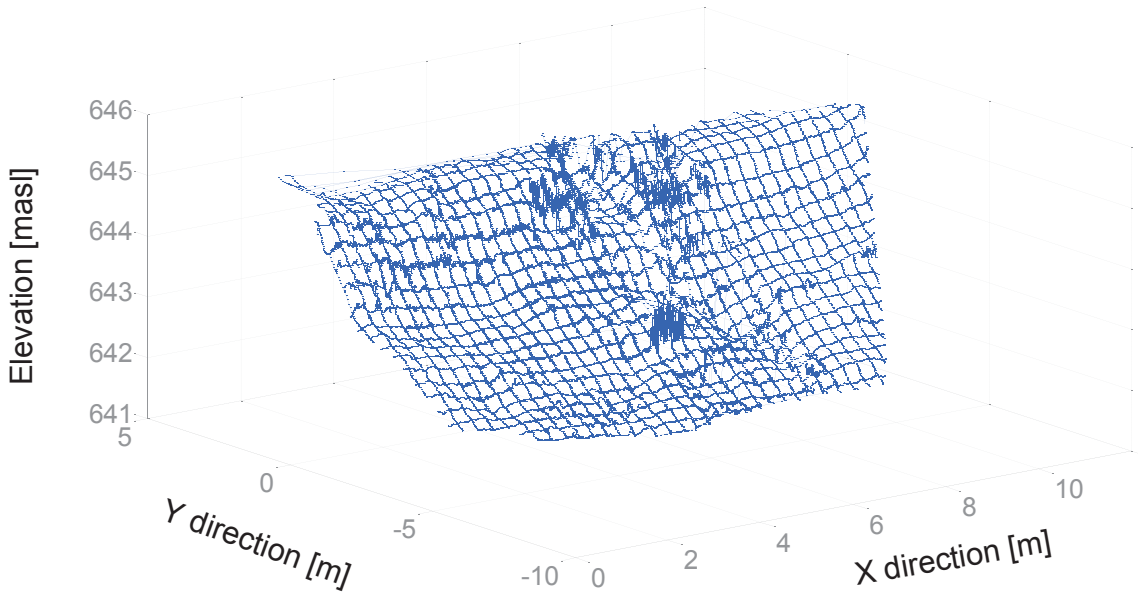

Figure 3.50: Three-dimensional view of the air-side slope at the end of the test after photogrammetric restitution.

Figure 3.51 presents of 4 cross sections made from the photogrammetric restitution compared to the initial cross section of the slope (bold black line). The distance between sections is 3 m, and the first section is located at Y=0.2 m. The initial is drawn for comparison. The erosion process is evident in the middle section (Y=6.2 m), whereas a change in the shape is clear in the other sections. For instance, the movement from the slide crown and tension crack is clear in the other 3 sections, in which the profiles protrude from the initial section in the upper part.

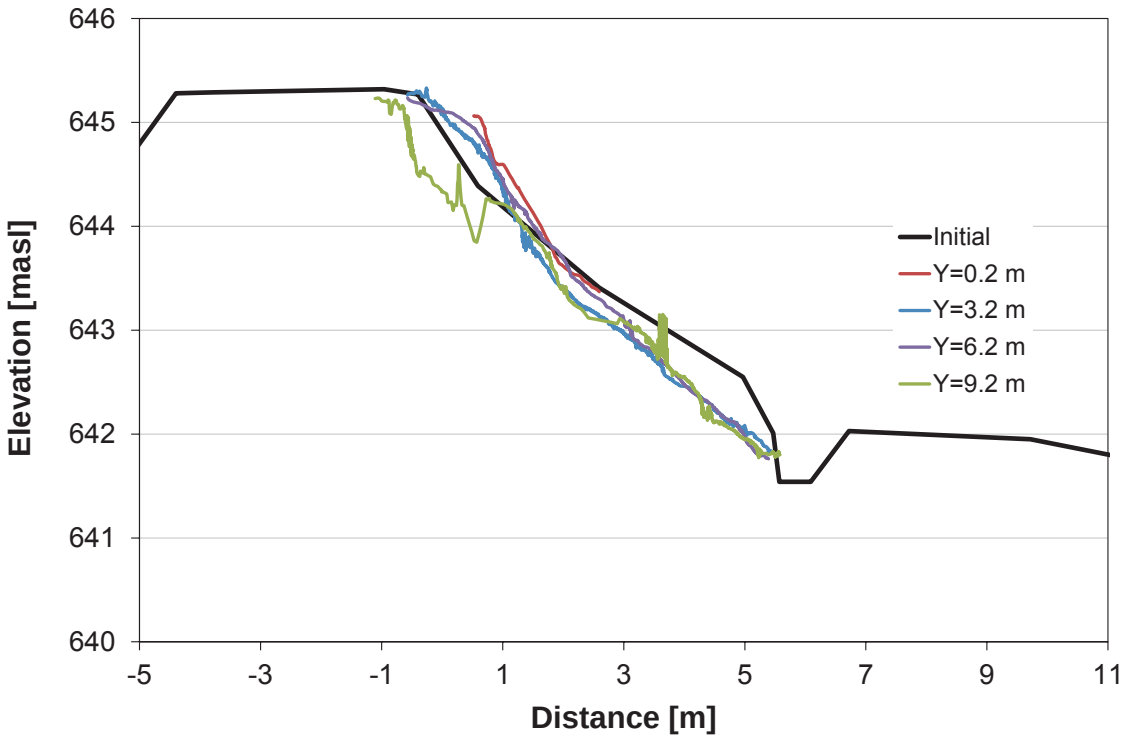

Figure 3.51: Comparison of the cross sections from the photogrammetric restitution with the initial shape of the slope.

3.3.3 Soils

Three types of soils were sampled during and after the overflow experiment, and these were classified in the laboratory. The first sample corresponds to the soil, which forms the main body of the dyke. The second sample was the material ejected from the internal erosion process during the overflow experiment. The third sample corresponds to the stony layer on top of the dyke.

Figure 3.52 summarizes the particle size distribution of these soils. The main component of the dyke is a silty sand (SM), whereas the top layer is classified as silty gravel (GM). The piped material is also a silty sand (SM), whose characteristics are quite similar to the main body's material albeit slightly coarser (d_{50}=0.22 mm), indicating that the erosion process included a coarser fraction than the body of the dyke.

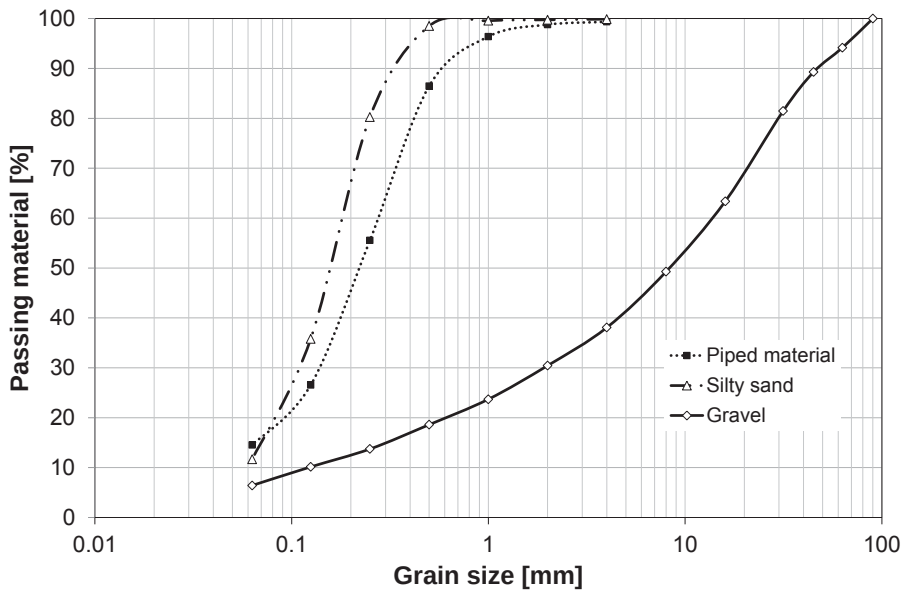

Figure 3.52: Grain size distribution of materials sampled after the overtopping experiment. The piped material was sampled from the soil volcano at the toe of the dyke. The silty sand was sampled from the body of the dyke. The sample of the gravel comes from the blocky stone layer on the upper part of the dyke.

The soil water retention curves (SWRC) were determined for reconstituted samples of the silty sand forming the main body of the dyke. In Section 2.2.2.4 is expounded that density modifies the SWRC. Therefore, four tests were performed representing the soil two at different depths (2 and 5 m). This results in applying different overburden pressure (σ_v) to the specimens. Two different densities were tested for each depth. These correspond to the maximal and minimal densities of the material determined with the vibratory table test (ASTM International, 2002a). However, it was difficult to control density when preparing the loose samples, leading to the conditions given in Table 3.4.

Tests were conducted through both the drying and wetting paths. This is relevant as the SWRC is known to show hysteretic behavior (cf. Section 2.2.2.4), which might influence the stability of soil structures subjected to varying water levels in the river.

Figures 3.53 and 3.54 show the SWRC obtained when the material is subjected to an overburden pressure of 40 kPa and 80 kPa respectively. Table 3.4 summarizes the main characteristics obtained for the SWRC in the laboratory. The parameters *AEV*, θ_{sat} and θ_{res} presented in the table were explained in Section 2.2.2.4.

Density affects the SRWCs obtained, as expected. The AEV ranges between 7 and 9.5 kPa, with the lower value representing looser states (Test 1 and 3 with e > 0.95), irrespective of the overburden pressure. There is also no obvious influence of the overburden pressure on the results at denser states (Tests 2 and 4 with e between 0.72 and 0.75). A slight difference in θ_{res} was also found by comparing tests 2 and 4 in Table 3.4.

Morales et al. (2011) compared the SWRCs obtained in the laboratory to those obtained in the field, back-calculated from data of pair-wise devices Tensiometer-TDR and Tensiometer-Envirosmart. A good correlation between the parameters was found providing that, at least for the soil tested, the described laboratory tests represented reasonably the interaction between water and soil on the full-scale engineering structure.

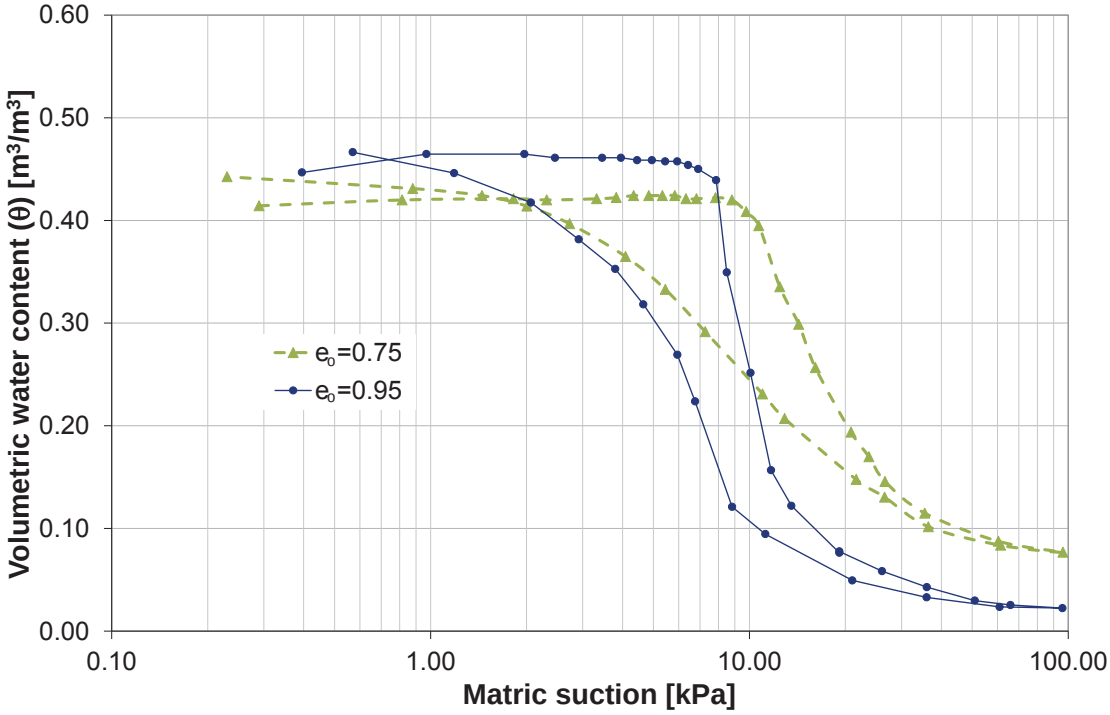

Figure 3.53: SWRC obtained in the laboratory at σ_v = 40 kPa for the silty sand .

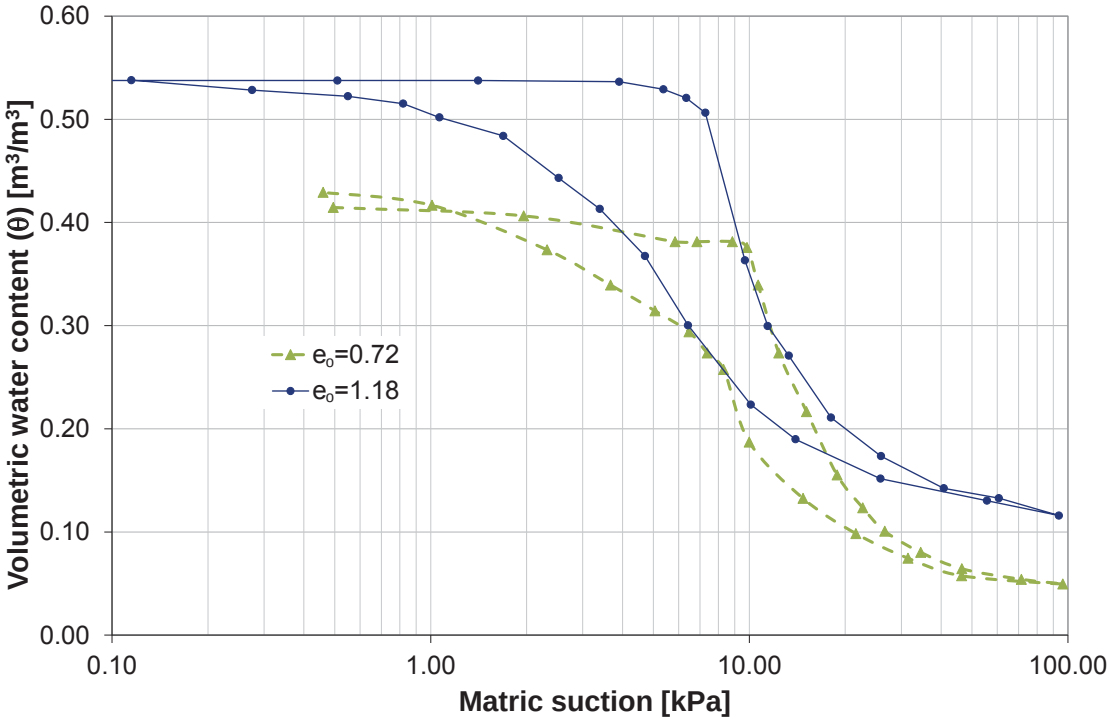

Figure 3.54: SWRC obtained in the laboratory at σ_v = 80 kPa for the silty sand.

Table 3.4: Conditions for the determination of the SWRC in the laboratory.

Test	σ_v [kPa]	Representative depth [m]	e [-]	Unit weight [kN/m^3]	AEV [kPa]	θ_{sat} [-]	θ_{res} [-]
1	40	2.5	0.95	13.95	8.5	0.46	0.02
2	40	2.5	0.75	15.54	9.5	0.43	0.08
3	80	5.0	1.18	12.48	7.0	0.54	0.12
4	80	5.0	0.72	15.81	9.5	0.43	0.05

Additional laboratory tests were performed by Springman & Mayor (2009) and Springman et al. (2009) on a similar silty sand, and the results are shown in Table 3.5.

Table 3.5: Additional material parameters for the silty sand.

k_{sat} at e_o [m/s]	e_0 [-]	C_c [-]	C_s [-]		$\gamma_{d\ max}$ [kN/m^3]	ϕ' [°]
1.3×10^{-6}	0.72	0.088	0.014	0.021	15.9	35.8

3.3.4 Ground model

It is essential to build a reliable ground model, which can reflect the behavior observed effectively. However, it is a challenging task to achieve for such structure, which has been subjected to variable and unknown geological and hydraulic conditions. Therefore, some assumptions had to be made when constructing the model.

The complexity in conditions for these system of dykes on the Rhone River was pointed out by Mueller (2007); Springman et al. (2008) and Mayor et al. (2008). The first two works analyzed dyke sections along the Rhone River at approximately 4 km upstream the field test close to the city of Visp, whereas the latter describes a first approach to the ground model of the section dyke analyzed here. As the dykes at Baltschieder and Visp were constructed under similar conditions and over similar soils, the use of information from the former is considered suitable for contributing to the analysis of the latter.

Figure 3.56 shows the ground model adopted. The model is the outcome of the exhaustive evaluation of previous publications, logs from three boreholes drilled inside the cell (Figure 3.56), grain size distributions from samples, and the analysis of the field measurements to identify trends on the overall behavior.

Six different zones of soil were defined for the ground model. Firstly, several intercalations of gravel and silty sand were found, in similar way to those found by Springman et al. (2008) and Mayor et al. (2008). The main body of the dyke is composed of the silty sand from the fluvial sediments and the hydraulic response was studied in detail by Mayor et al. (2008) and Morales et al. (2013).

A fourth soil is the coarse gravel found on the crest of the dyke, which had a dual purpose to raise the retention height and to provide a stiff material to act as subbase for the road on top of the dyke. The thickness of this layer was estimated as 0.6 m (Figure 3.55a).

The fifth soil is a fill that covers the air-side slope (Figure 3.55b). It was identified from the pit dug one day after the experiment (Figure 3.32). This material had been used to increase the breadth of the dyke section to enable its height to be raised without facing instability problems due to steeper slopes. The considerable amount of vegetation and associated root development in this soil layer will probably reduce the permeability, as noted by Gabr et al. (1995).

The field measurements showed that water reached the air-side relatively fast (Mayor, 2013). However, if the dyke was composed of completely homogenous silty sand as initially deduced, the modeling could not represent this behavior. Therefore, it was thought that a higher permeability material could have been placed inside the body of the dyke. This is not completely unrealistic, as the original dyke section, corresponding to the first correction of the Rhone River, most probably had a gravel layer on top, as had been used for the second correction. A material is found in boreholes SB01 and SB02 at a depth of 4.0 m and is described as poorly graded gravel (GP), confirming the assumption.

On the other hand, for water to reach rapidly the air-side, not only a high permeable material was required but also some 'ponding' of water in the middle section of the dyke. This led to the assumption of a low-permeability material isolating the gravel layer at 641.3 masl. As a consequence, a silty clay was defined to be a continuation of the silt found above at 1.0 m depth the gravel layer in borehole SB03.

Figure 3.55: Photographs indicating the change in materials. Left: gravel layer on the dyke's crest. Right: Cover material on the air-side of the slope.

Table 3.6 presents the soil parameters defined for the materials. k_{sat} refers to the hydraulic conductivity under saturated conditions estimated with the Kozeny–Carman approach (Kozeny, 1927) as described by Carrier (2003) (cf. Section 2.2.2.6). This equation has been proven to be effective for several types of soils, including those with a fine-grained particle

size distribution (Chapuis & Aubertin, 2003). A value of k_{sat} was assumed for the soils for which the grain size distribution was not known (fill, silt and silty-clay). The variation of the hydraulic conductivity with suction was determined using the approach by Fredlund & Xing (1994), which makes use of the SWRC for its estimation.

d_{10} and d_{60} correspond to the grain sizes for which 10 % and 60 % of the soil sample passing the given sieve size respectively. These are the average value obtained from the sieve curves.

α, n, m, θ_{sat} *and* θ_{res} are the parameters of the SWRC for the Van Genuchten model (van Genuchten, 1980) (cf. Section 2.2.2.5). These parameters were fitted using the software SWRC fit (Seki, 2007). The silty sand was defined for the drying and wetting paths. The hysteretic behavior is an important element, and as shown in the next section, is quite important for the model calibration.

The values of the SWRC for the silty sand are derived from an average from the curves determined in the laboratory and field. an estimation was made with the modified Kovacs approach (Aubertin et al., 2003) for the 'Rhone gravel' and 'crest gravel'. This method only requires the values d_{10}, d_{60}, θ_{sat} and θ_{res} to determine the SWRC. The comparison revealed that the approach predicts reasonably well the SWRC. Mayor (2013) presents similar results and shows that the parameters obtained from this relationship represents the values obtained in the laboratory and the field accurately enough to be used in engineering design calculations.

The SWRC for the cover material was assumed to be the same as for the silty sand, and curves in the database from GeoStudio ® were used for the silt and silty clay.

γ, c' and ϕ' are the bulk unit weight, effective cohesion and the critical friction angle. The values for the silty sand, Rhone gravel and crest gravel were taken from the analyses performed by Mueller (2007) and Springman et al. (2008), excepting the γ of the crest gravel which was assumed to be 20 kN/m^3.

3.3.4.1 Model calibration

The model was calibrated by simulating the fourth phase of the original experiment (Mayor, 2013). It took place between 25.04.2008 and 05.06.2008 (just before the overflow experiment). Figure 3.57 illustrates the development of the phase in seconds (0 seconds corresponds to 00:00 on 25.04.2008) following the time at which water was pumped out of the cell. After this, there were three cycles of raising-lowering the water table. The first two cycles lasted 2 days and the maximum water level was 644.5 masl, whereas the third cycle lasted 4 days and the maximum water level was 644.7 masl. The phase ended with 6 days, when there was no water inside the cell and the soil was in a drying cycle.

Figure 3.56: Ground model for the test cell at Baltschieder, as assumed for further numerical modeling.

Table 3.6: Material parameters of the ground model.

Name	k_{sat} [m/s]	d_{10} [mm]	d_{60} [mm]	α [1/kPa]	n [-]	m [-]	θ_{sat} [m^3/m^3]	θ_{res} [m^3/m^3]	γ [kN/m^3]	c' [kPa]	ϕ' [°]
Rhone gravel	1.66×10^{-3}	0.091	3.675	1.469	3.324	0.699	0.402	0.021	17.4	0	40
crest gravel	2.68×10^{-3}	0.125	12.70	3.687	3.196	0.687	0.403	0.017	20.0	0	40
silty sand	6.24×10^{-5}	0.040	0.244	0.159 / 0.721	6.382 / 2.5	0.843/ 0.6	0.396 / 0.396	0.100 / 0.100	15.5	0	35.8
fill	5.00×10^{-5}	-	-	0.159	6.382	0.843	0.396	0.1	15.5	3	25
silt	1.00×10^{-5}	-	-	0.068	1.783	0.439	0.400	0.015	-	-	-
silty clay	1.00×10^{-7}	-	-	0.034	1.676	0.403	0.400	0.006	-	-	-

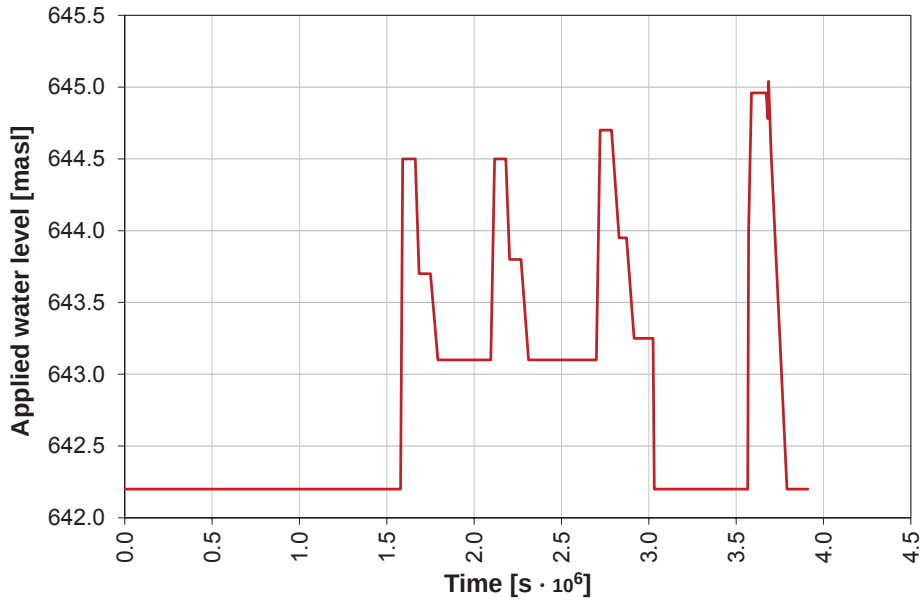

Figure 3.57: Water level applied during the 4th phase, and used to calibrate the model.

The numerical model should reflect the following main features:

1) Although the water table is increased 2.5 m on the water side, the maximum water pressure registered is around 14 kPa at TMs 1 and 2. The minimum water pressure during the cycles stage is -12 kPa at TM 3.
2) The water pressure in TM 1 is lower than in TM 2. This is only possible if there is a pounding of water under TM 2 and drainage under TM 1.
3) The maximum and minimum water pressures are -8 and -15 kPa respectively at the end of the 4th phase at TMs 1 and 10.
4) There should be no or minimum response of TDRs 2, 5 and 7 for the first two flood cycles and then a complete saturation for the third cycle. Complete drying is expected at the end of phase 4.
5) TDRs 3, 4 and 6 should remain saturated after 1.5 $\times 10^6$ seconds (Figure 3.57). TDRs 3 and 6 should reduce to $\theta \approx 0.2$ m^3/m^3 during the drying stage.
6) All of the Envirosmart (EV) 1 gauges should saturate fast at the beginning of the first flood cycle, after which, gauges 1.1 and 1.2 should dry up to $\theta \approx 0.2$ m^3/m^3. All gauges should exhibit values ranging between $\theta \approx 0.12$ m^3/m^3 and $\theta \approx 0.25$ m^3/m^3 at the end of the phase.
7) All of the EV gauges 2 should saturate fast at the beginning of the each flood cycle, then gauges should dry with values between $\theta \approx 0.15$ m^3/m^3 and $\theta \approx 0.35$ m^3/m^3.
8) During the first flood cycle, none of the EV 3 gauges should be affected. Whereas gauge EV 3.6 almost reaches full saturation for the second cycle. Gauges 3.1 and 3.2 show a maximum $\theta \approx 0.18$ m^3/m^3 for the third cycle.
9) Gauge EV 4.4 starts the phase from a high value of volumetric water content ($\theta \approx$ 0.25 m^3/m^3) and responds to both initial flood cycles, whereas these cycles are just detected for the rest of gauges. Not all gauges are saturated for the third cycle.

The simulation was carried out with the SEEP module of the GeoStudio suite (Krahn, 2012a), which is used to analyze steady-state and transient flow problems. It was found during the simulation that peak values of the volumetric water content were observed when a transition between wetting and drying cycles was taking place. This was found to be a numerical issue of the software, which does not incorporate an algorithm to handle the hysteresis of the SWRC. This is an important point for materials such the silty sand, which exhibit very steep SWRCs. For instance, the value of θ ranges between 0.35 to 0.14 m^3/m^3 in the drying and wetting curves respectively for a common value of suction of 5 kPa.

A simple horizontal scanning curve was programmed on a Matlab routine to take the hysteresis into account. Figure 3.58 illustrates the resulting curve for the TDR 2, involving 3 cycles of sudden change between wetting to drying paths and vice versa.

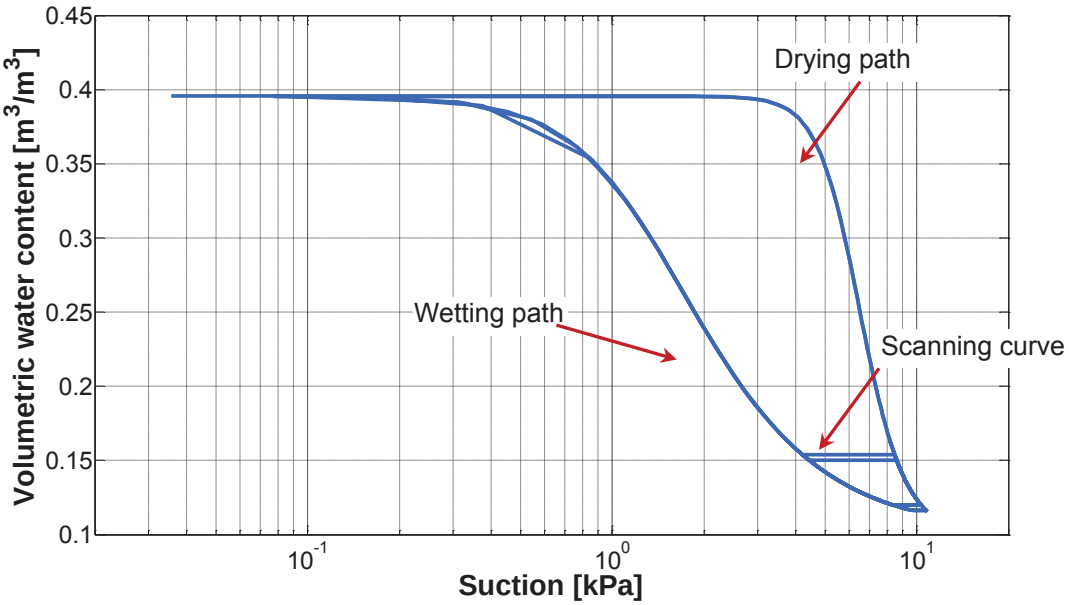

Figure 3.58: Soil water retention curve for TDR 2 after the simulation including a horizontal scanning curve.

Charts comparing both field measurements and the simulation are presented in Appendix 2. Most of the features mentioned above are represented successfully by the model. It is suggested that the model represents the response satisfactorily despite the differences found. Notwithstanding, this is just a two-dimensional model of a three-dimensional problem. This leads to uncertainties deriving from diverse assumptions made in terms of the representative geology and material properties.

3.3.5 Modeling of the overflow experiment

3.3.5.1 Groundwater flow

The overflow experiment was modeled by applying the water levels shown in Figure 3.59. Seven stages are defined for the overflow process: I) Increase of the water level to the maximum water level applied to the cell so far (644.96 masl), II) the water level is keep at that height for 1.14 days, III) the water level is lowered until 2 days before the experiment takes place, IV) the cell is prepared for the overflow test by increasing the water level up to 645.16 masl, V) the water is lowered to 644.8 masl the night before the experiment, VI) the water level is increased in the morning of the experiment until the water level reaches the excavated notch, and VII) the overflow process takes place.

The silty sand was defined with the appropriate material parameters for each stage of the cycle, i.e. to suit either a wetting or a drying cycle.

A total of 600 time steps were defined for analyzing the experiment. the minimum factor of safety was determined for each time step using the limit equilibrium method from the SLOPE module in GeoStudio (Krahn, 2012c).

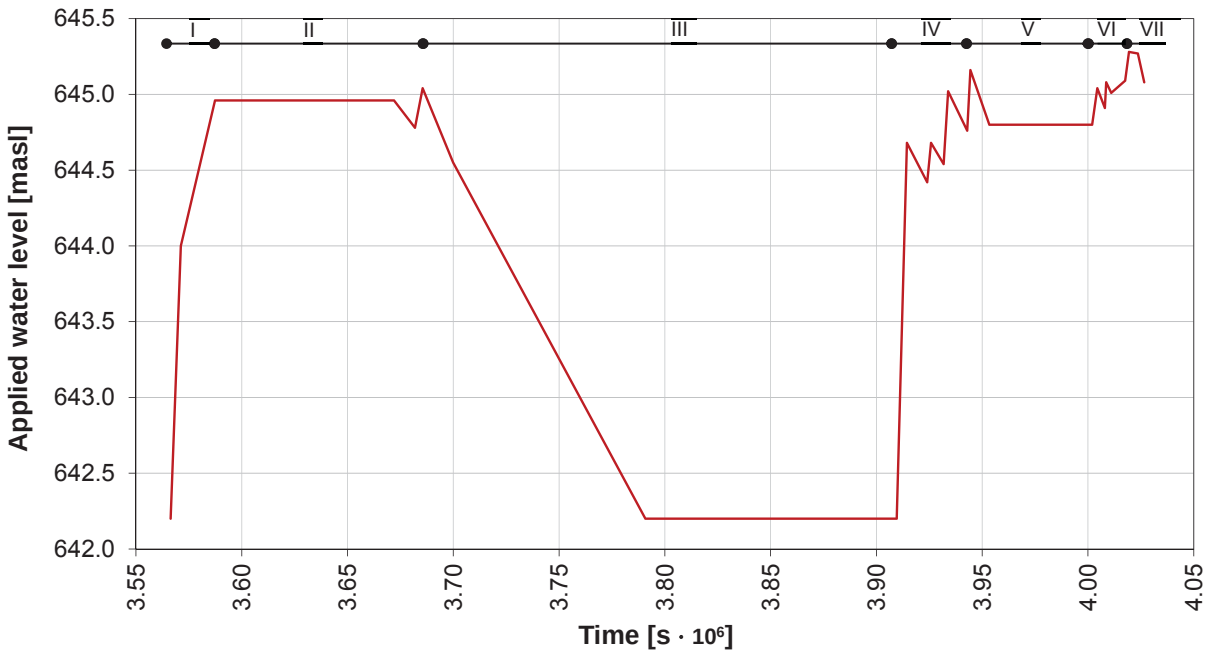

Figure 3.59: Water level for the modeling of the overflow experiment.

The pore water pressures (Figure 3.60) for the sensors on the water-side (TM 1, 2, 3, 4, and 8) show a fast reaction to the change in water level, whereas the reaction of the sensors on the air-side (TM 5, 6, 7, 9 and 10) present some lag. This is an indication of the time required for water to reach the air-side. TM 9 shows implausible results in the field measurement. This is most probably due to cavitation of the device. The lags in time shown by the devices on the air-side in the numerical model are similar to that measured in the field. The best fit is given for TM 7. Pore water pressures in the field test vary between -10 and 15 kPa, and be-

tween -18 and 19 kPa in the numerical model. However, the response of these devices is quicker in the field than in the numerical model.

The comparison between the field measurements and the numerical simulation of the volumetric water content for the TDRs is shown in Figure 3.61. The reaction times of the TDRs sensors are also good reflected by the model, excepting TDR 2, which exhibits a larger reaction time in the numerical model than in reality. However, it, together with TDRs 5 and 7, presents larger lags in time, as observed in the field measurements (Figure 3.12). TDRs 3 and 6 remain almost fully saturated during the experiment. This, together with the small drop in θ after the water level was lowered are well reproduced by the model, although the response of TDR 4 is not fully represented, while in the field it remains saturated, in the numerical model θ drops its value close to the residual volumetric water content. This reflects a greater ponding of water, which is fully reproduced by the model. This also explains the slower desaturation of TDR 1 in the field than in the simulation.

Results for EV 1 (Figure 3.62) show a large agreement for the field measurements and the numerical simulation, except for the gauge EV 1.5. The field measurements show a desaturation of this gauge despite the gauge EV 1.6, which lies below, remains saturated. Another difference reflecting a ponding process at X=16 m is detected by examining the results of EV 2 (Figure 3.63), for which the desaturation process in the field is not as fast as for the simulation. The field measurements also indicate that the lower gauges remain almost fully saturated. Nevertheless, field and simulated values show a complete saturation of the material during the last cycle.

EV 3 and 4 (Figures 3.64 and 3.65) were found to be the most challenging to model. Both are located on the air-side, and the lower gauges are located in the silty sand, whereas the upper gauges are placed in the fill layer. In addition, the lack of knowledge of the hydraulic behavior of the fill layer material has a large influence on the results. Therefore, the results for the gauges, which are assumed to be located in the silty sand (EV 3.4, 3.5, 3.6, 4.5 and 4.6), exhibit similar results for the field and the numerical calculation.

Notwithstanding, pore water pressures for both water and air-side are, as discussed above, quite similar; therefore, reliable for the stability calculation performed afterwards.

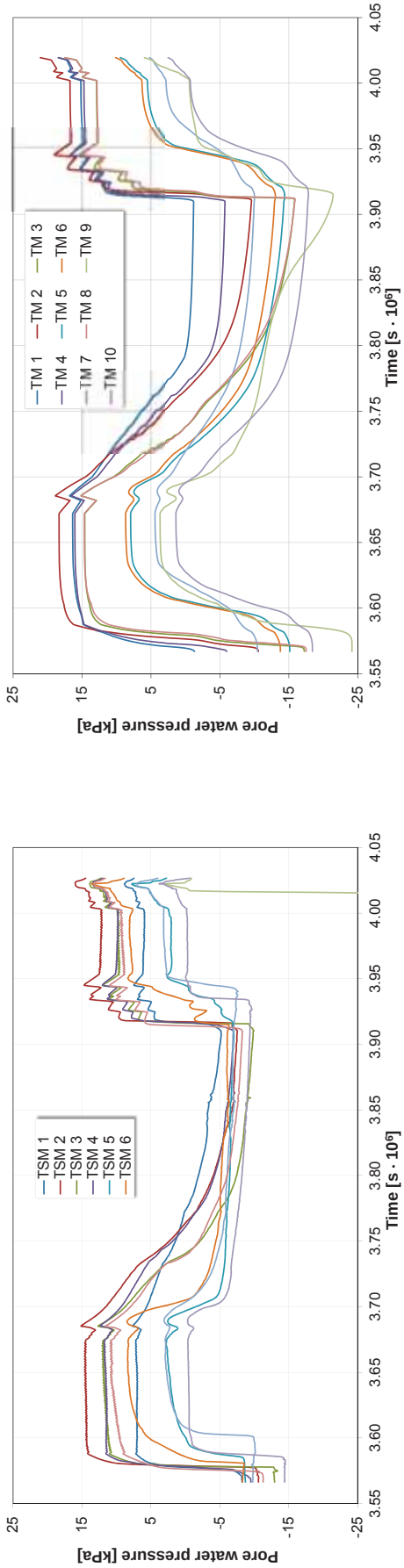

Figure 3.60: Comparison of the pore water pressures between the field measurements (left) and the numerical simulation (right).

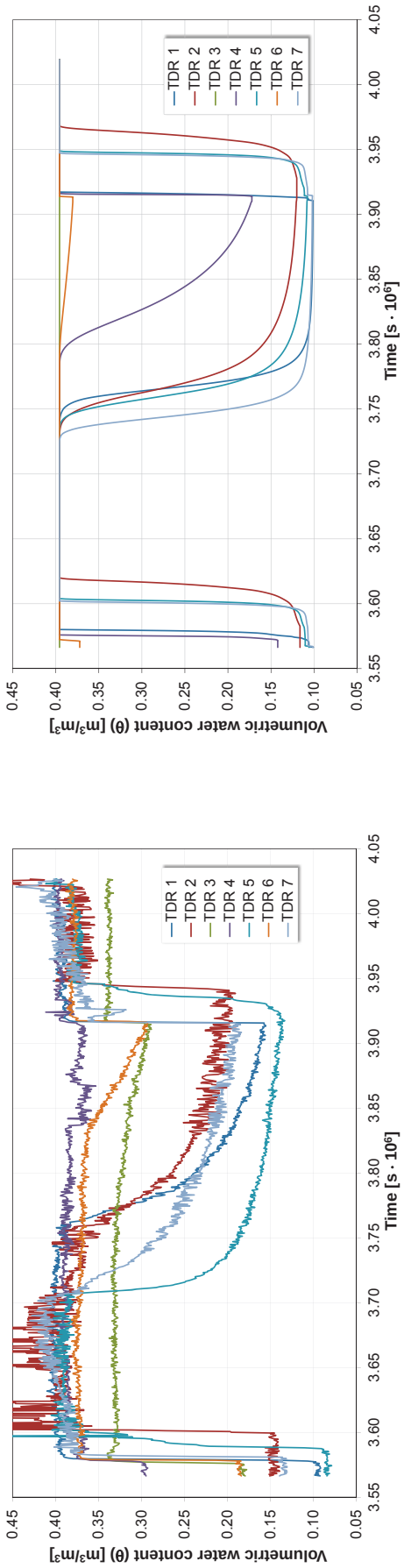

Figure 3.61: Comparison of the TDR devices between the field measurements (left) and the numerical simulation (right).

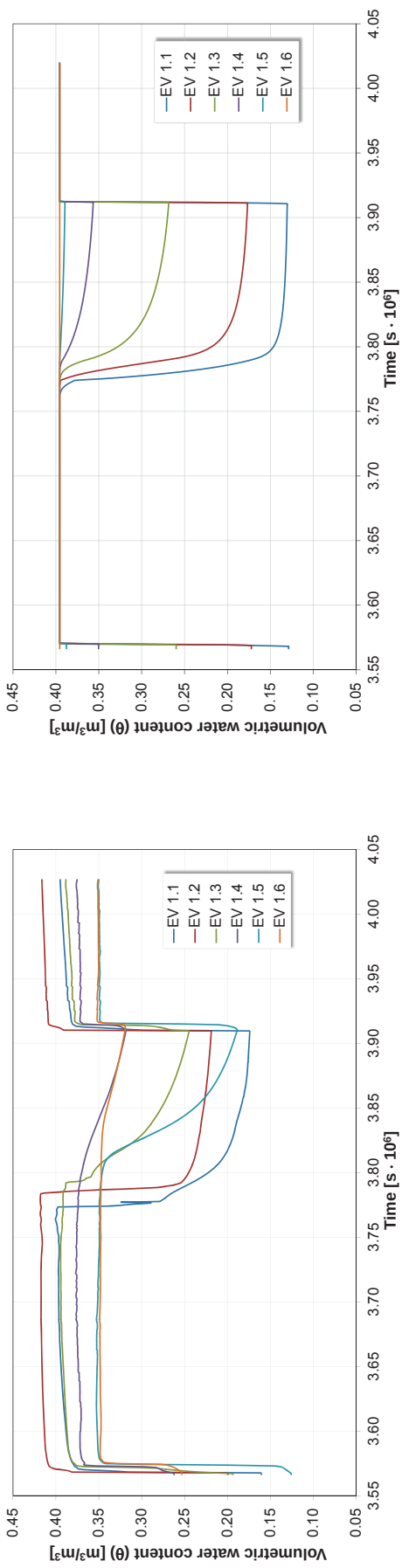

Figure 3.62: Comparison of the Envirosmart 1 (EV 1) between the field measurements (left) and the numerical simulation (right).

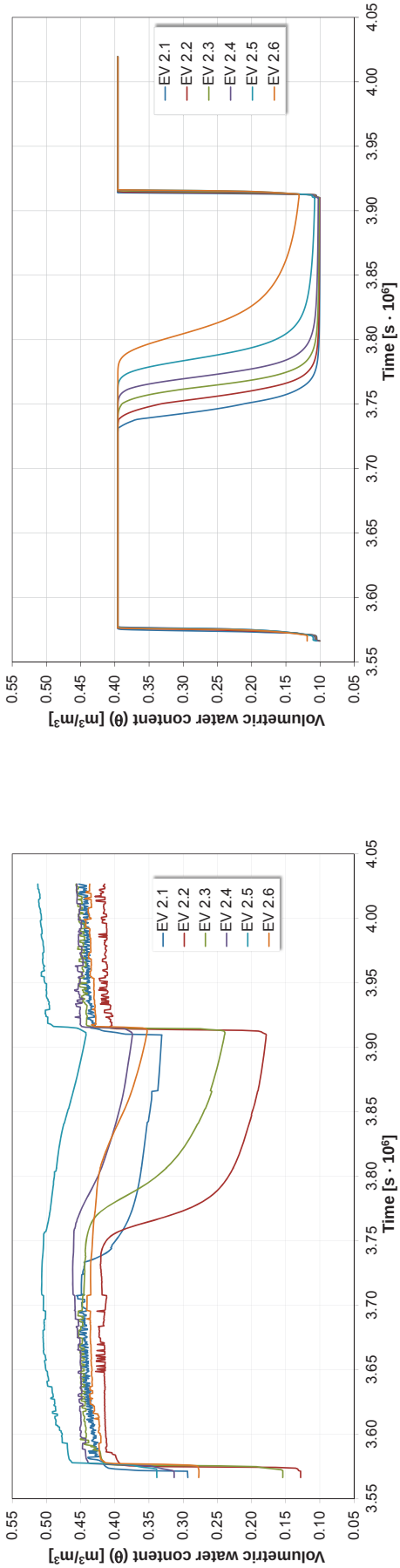

Figure 3.63: Comparison of the Envirosmart 2 (EV 2) between the field measurements (left) and the numerical simulation (right).

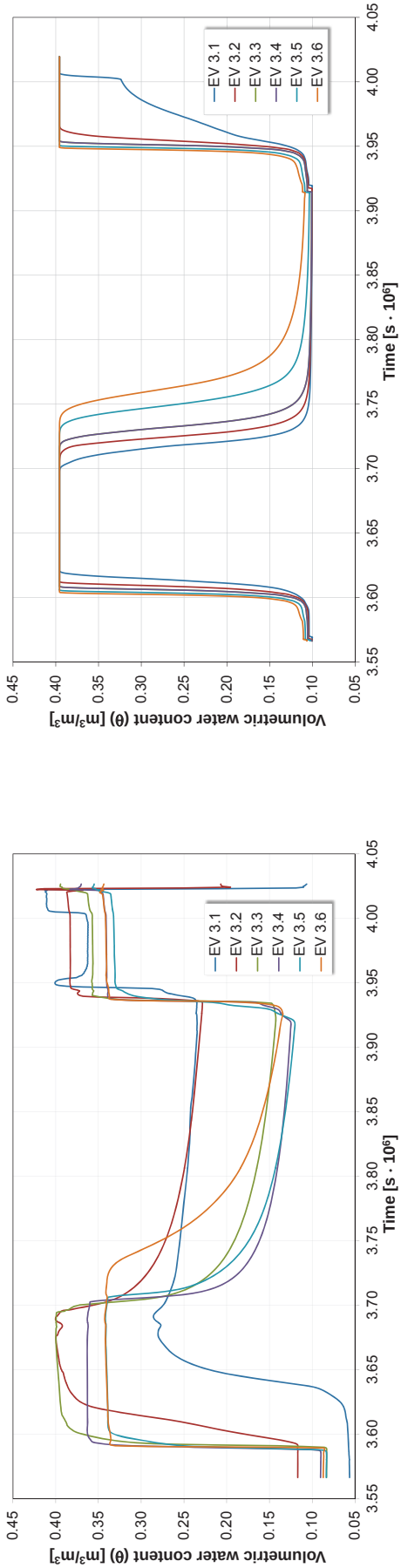

Figure 3.64: Comparison of the Envirosmart 3 (EV 3) between the field measurements (left) and the numerical simulation (right).

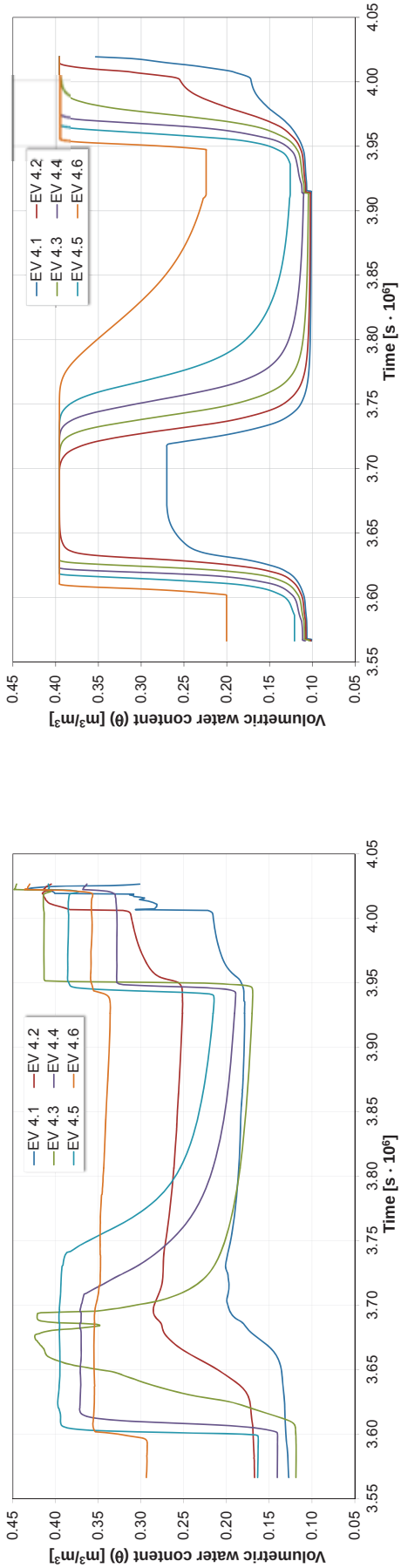

Figure 3.65: Comparison of the Envirosmart 4 (EV 4) between the field measurements (left) and the numerical simulation (right).

3.3.5.2 Slope stability

The evolution of the global factor of safety (FoS) with time (Figure 3.66) shows how it decreases significantly when the water level is raised. The factor of safety drops to 1.046 when in the first flood cycle water reaches the level 644.6 masl, i.e. this is a metastable condition, which requires just a small variation in the loading conditions for failure to occur, which happened subsequently during the stage VII, when the water level was raised to 645.28 masl to achieve the overflow.

The air-side slope became increasedly unstable under these conditions until the slope failed (Figure 3.66) at time 4016655 seconds of the analysis, which corresponds to 11:45 a.m. on 10.06.2008. This time is 1.25 hours before the first deformation at 13:02 were noticeable (cf. Table 3.3). Nonetheless, it is considered that the numerical model developed is able to reproduce the response observed in the field experiment in a plausible and accurate way.

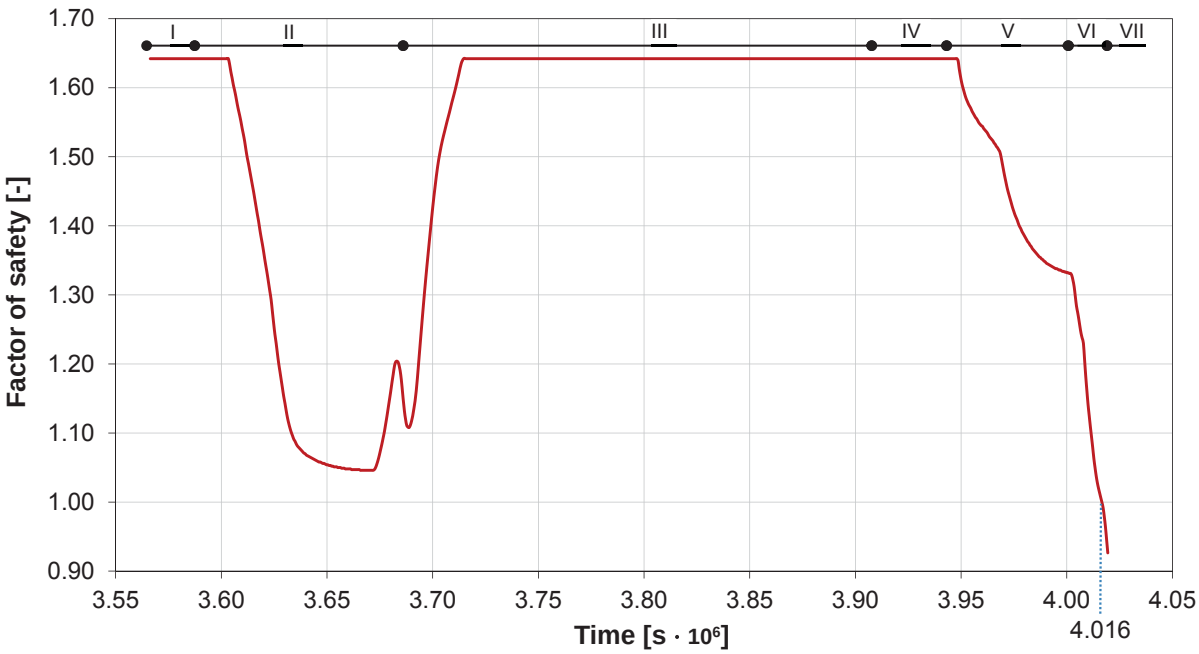

Figure 3.66: Evolution of the factor of safety with time for the overflow experiment.

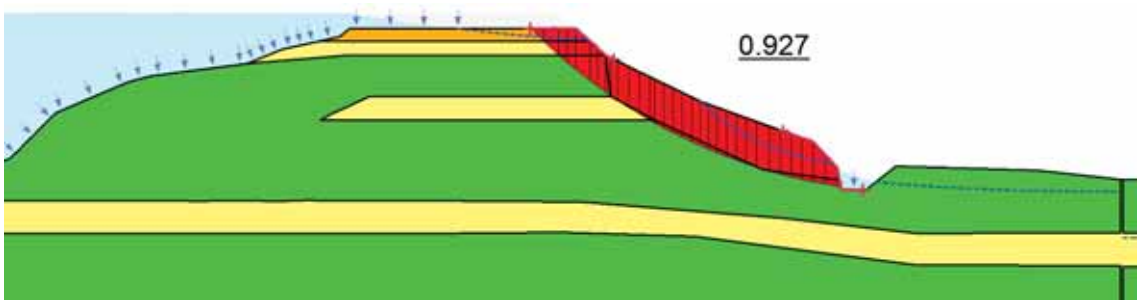

Figure 3.67: Critical failure surface in the air-side slope at 12:00 on 10.06.2008.

Another interesting feature of the slope stability analysis is the shape of the critical surface (Figure 3.67). Figure 3.40 illustrates how tensiometer 5 was bent, marking the depth of the

slip surface at approximately 1.0 m below ground surface. The critical slip surface lies, in the same location at a depth of 0.942 m for the numerical evaluation. Once again, the numerical model reproduces the observed behavior quite accurately.

Figure 3.68 shows the assumed slip surface respect to the measurement sensors. The failure surface crossed through TM 7, TDR 2, EV 4.3, EV 3.3, and TM 9. This explains the response observed by the sensors, for which an increase of the water content and a decrease of the pore water pressure were observed. The location of the failure surface, as indicated by the figure, confirms this as discussed in Section 3.2.3.

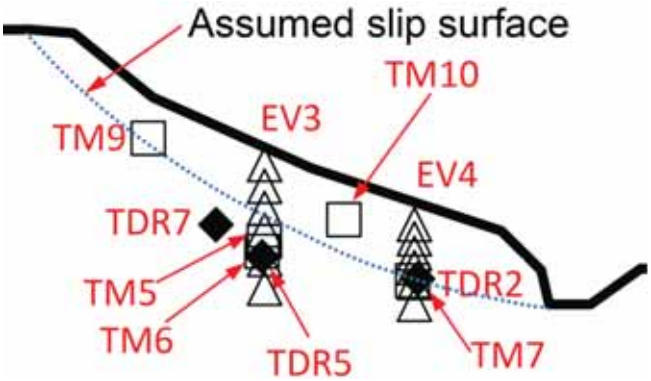

Figure 3.68: Location of critical failure surface in the air-side slope with respect to the measurement sensors.

The slip surface is located near the contact between the silty sand and the fill material on the air-side slope (Figure 3.67). This explains the complete failure process: Firstly, the water table is raised in the cell, causing the FoS for the air-side slope to drop until slope to becomes unstable condition. The soil slides along the critical surface, which coincides with the contact between the silty sand and a material, which has lower permeability partially due to the presence of roots.

The movement of the slid soil is not homogenous in plane strain across the section, due to the shear stress mobilized along the sheet pile walls. As a consequence, the soil in the middle section of the dyke (Y≈6 m) has larger deformations that the soil close to the walls (Y=0 m and Y=12.5 m). This produces a second failure, in which a triangular-shaped mass of soil detach in the center of the slope. The triangular zone corresponds to the zone in which larger settlements were observed and marked in Figure 3.31.

Water starts to flow more rapidly along the failure surface. However, a larger water flow occurs along the borders of the triangular-shaped zone. This, together with the lower permeability material on top (fill layer), lead to the suffusion of the silty sand material. This was confirmed by comparing the sieve curve of the ejected material with the silty sand forming the main body of the dyke, in which both were highly similar (Figure 3.52).

At the same time as the silty sand is ejected as a form of internal erosion, the lower permeability material on top settles, creating the channels visible on the surface of the slope, which provide any overflowing water with a preferential path.

4 Physical modeling

4.1 Scaling factors for hydraulic problems

Some basic scaling factors are given in Section 2.3.2. However, scaling of hydraulic problems strongly depends on the actual problem to be solved. This refers to the inherent difference arising from analyzing a pure seepage flow, a superficial flow, a mixed flow (seepage with a subsequent superficial flow), an erosion or a piping problem. Different approaches that may be adapted to solve these problems have been defined. Each one of these makes certain assumptions to develop a set of scaling factors.

4.1.1 Approaches to the formulation of scaling factors

It has been confirmed theoretically and experimentally that the seepage velocity may be scaled as $v_m=v_p \cdot n$, where n is the acceleration scaling factor, and m and p denote the model and prototype respectively (Goodings, 1979, 1982; Cargill & Ko, 1983; Goodings, 1984; Khalifa et al., 2000; Singh & Gupta, 2000; Thusyanthan & Madabhushi, 2003)

Darcy's law $v=k \cdot i$ requires that either the hydraulic gradient (i) or the permeability coefficient (k) has to be directly proportional to n for appropriate scaling to be achieved. The controversy created by the existence of this duality of options has often been overlooked, as final seepage velocity is considered to be important in many cases (Thusyanthan & Madabhushi, 2003). This is not the case when analyzing superficial erosion and piping.

The analysis of these problems involves, among others, consideration of the critical shear stress of soil, which is, at the same time, dependent on the hydraulic gradient (Goodings, 1982; Foster et al., 2000; Wan & Fell, 2004b; Bonelli et al., 2007). A review of the way in which the scaling factors are established is essential in order to decide which set of scaling factors is to be adopted.

Defining the energy gradient ∇e as the loss of potential energy of the fluid per unit of length, i.e. $\nabla e = \frac{\Delta U}{l}$ where U is the potential energy, determined as: $U = m \cdot g \cdot h$ and ΔU is the potential energy difference between two points is helpful. Two methodologies have been followed for determining scaling factors of hydraulic problems in centrifuge modeling (Goforth et al., 1991; Khalifa et al., 2000):

1) Expressing the potential energy per unit weight (not specific unit weight).

$$\frac{U}{W} = \frac{m \cdot g \cdot h}{m \cdot g} = \boxed{h} \qquad 4.1$$

Here, energy is defined by the hydraulic potential (head), with units of length.

2) Expressing the potential energy per unit volume.

$$\frac{U}{V} = \frac{m \cdot g \cdot h}{V} = \frac{\rho \cdot V \cdot g \cdot h}{V} = \boxed{\rho \cdot g \cdot h} \qquad 4.2$$

Here, energy is defined by a pressure potential, with units of pressure. The difference between them might be explained by the following example:

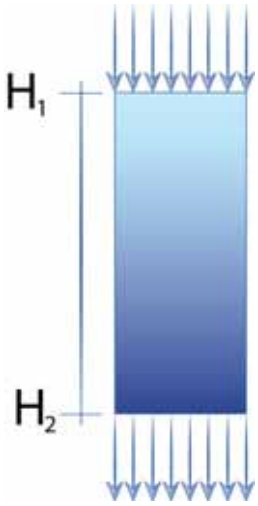

Formulation 1:

$$\Delta e_m = \Delta H_m = H_{1_m} - H_{2_m}$$
$$\Delta e_p = \Delta H_p = H_{1_p} - H_{2_p} = \left(H_{1_m} - H_{2_m}\right) \cdot n$$
$$l_m = H_{1_m} - H_{2_m}$$
$$l_p = \left(H_{1_m} - H_{2_m}\right) \cdot n$$
$$i_m = \frac{\Delta U_m}{l_m} = 1$$
$$i_p = \frac{\Delta U_p}{l_p} = 1$$
$$\boxed{\frac{i_m}{i_p} = 1}$$

Formulation 2:

$$\Delta e_m = \rho \cdot n \cdot g \cdot \left(H_{1_m} - H_{2_m}\right)$$
$$\Delta e_p = \rho \cdot g \cdot \left(H_{1_m} - H_{2_m}\right) \cdot n$$
$$l_m = H_{1_m} - H_{2_m}$$
$$l_p = \left(H_{1_m} - H_{2_m}\right) \cdot n$$
$$i_m = \frac{\Delta U_m}{l_m} = \rho \cdot n \cdot g$$
$$i_p = \frac{\Delta U_p}{l_p} = \rho \cdot g$$
$$\boxed{\frac{i_m}{i_p} = n} \qquad 4.3$$

The energy gradient is dimensionless within formulation 1, whereas it has dimensions of pressure per length [$ML^{-2}T^{-2}$] in formulation 2. In the first case, the energy gradient is the same in the model and prototype, whereas a scale factor *n* is obtained for the second case. This can be explained by the way in which the permeability parameter *k* in Darcy's equation is defined.

Formulation 1: $$v = k_1 \cdot \frac{\Delta H}{l} = \frac{K \cdot \rho \cdot g}{\mu} \frac{\Delta H}{l} \qquad 4.4$$

Formulation 2: $$v = k_2 \cdot \frac{\Delta P}{l} = \frac{K}{\mu} \frac{\Delta P}{l} \qquad 4.5$$

Here P [$ML^{-1}T^{-2}$] is the water pressure, K [L^2] is the intrinsic permeability, ρ [ML^{-3}] is the soil density, g [LT^{-2}] is the gravity acceleration, and μ [$ML^{-1}T^{-1}$] is the dynamic viscosity. The parameter k_1 [LT^{-1}] is often referred to as hydraulic conductivity, whereas k_2 [$M^{-1}L^3T$] is known as mobility. Al-Doury (2010) presents a comprehensive analysis, along with historical milestones, of the confusion derived from the use of different units and nomenclature for the proportionality constant in Darcy's law.

According to Goodings (1982) and Khalifa et al. (2000), the time for seepage between two points is $1/n^2$ less in the model than in the prototype. This can be easily demonstrated:

$$v_m = \frac{l_m}{t_m} \quad \rightarrow \quad t_m = \frac{l_m}{v_m} = \frac{l_p}{n} \cdot \frac{1}{v_p \cdot n}$$
$$t_m = \frac{l_p}{v_p} \cdot \frac{1}{n^2} = \frac{t_p}{n^2} \qquad 4.6$$

Superficial erosion and piping problems have not been analyzed extensively following both kinds of approaches. Hence, there is no unique set of scaling factors that is accepted by the whole physical modeling community, which leaves the door open for further sets to be proposed.

4.1.2 Laminar flow

Table 4.1 summarizes the scaling factors following both formulations, based on the assumption of a laminar flow condition. The limit for this condition is often determined with the Reynolds number (Equation 4.7), where ρ [ML^{-3}] is the fluid density, v [LT^{-1}] is the velocity of flow, d [L] is the pipe diameter for confined flow or the depth for surface flow, and μ [$ML^{-1}T^{-1}$] is the dynamic viscosity.

$$\mathrm{Re} = \frac{\rho \cdot v \cdot d}{\mu} \qquad 4.7$$

The Reynolds number is limited to around 1.0 for water flow through porous media (Bear, 1972; Singh & Gupta, 2000). However, this limit might vary between $1.0 \leq \mathrm{Re} \leq 10$ depending upon the soil type (Goodings, 1984; Khalifa et al., 2000). The validity of Darcy's regime can be verified by relating the Reynolds number to a friction factor F_f (Equation 4.8).

$$F_f = \frac{i \cdot g \cdot d_{ch} \cdot \eta^2}{v^2} \qquad 4.8$$

Here i [-] is the hydraulic gradient (formulation 1), g [LT^{-2}] is the gravity acceleration, η [-] is the soil porosity, v [LT^{-1}] is the macro (Darcy's) velocity and d_{ch} [L] is a characteristic dimension of the soil particles. Goodings (1994) used $d_{ch}=d_{50}$, while Khalifa et al. (2000) determined it with a relationship that takes the tortuosity into account. The straight part of the graph F_f vs Re determines the range of validity for Darcy's flow (laminar condition), as shown in Figure 4.1.

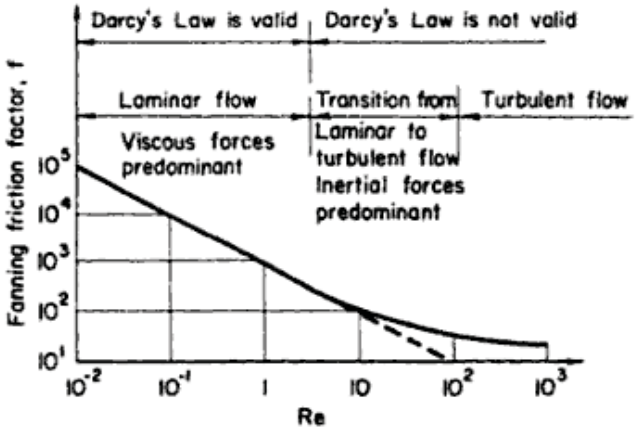

Figure 4.1: Validity of Darcy's flow regime (after Bear, 1972).

Table 4.1: Scaling factors for hydraulic problems under laminar flow in water (adapted from Cargill & Ko, 1983; Khalifa et al., 2000).

	Water head	Water pressure	Energy gradient	Hydraulic conductivity	Mobility	Time	Velocity
	[L]	[$ML^{-1}T^{-2}$]	[-] / [$ML^{-2}T^{-2}$]	[LT^{-1}]	[$L^3M^{-1}T^1$]	[T]	[LT^{-1}]
Formulation 1	n	-	1	n	-	n^2	n
Formulation 2	-	1	n	-	n	n^2	n

4.1.3 Turbulent flow

Forchheimer (1901) observed that the deviation from linearity in Darcy's law increased with flow rate, and attributed the non-linear increase in pressure gradient to inertial losses in the porous medium, which are proportional to v^2. He proposed a second proportionality constant β to describe the increasing contribution to pressure drop caused by inertial losses (Barree & Conway, 2004). Therefore, after the laminar flow range is exceeded, the relationship between the hydraulic gradient and velocity is no longer linear and must be adjusted by the Forchheimer non-linear factor (Khalifa et al., 2000; Sidiropoulou et al., 2007; Bezuijen & Steedman, 2010).

The factor β is generally deduced experimentally from the slope of the Forchheimer graph (Figure 4.2) (i.e., the plot of the inverse of the apparent permeability $1/k_{app}$ vs. a dimensional pseudo Reynolds number $\rho v/\mu$), as shown by Equation 4.9 (after Huang & Ayoub, 2008), where k_{app} [LT^{-1}] is the apparent permeability and k_1 [LT^{-1}] is the hydraulic conductivity (Equation 4.4). In this case β has units of time [T].

$$\frac{1}{k_{app}} = \frac{\Delta P}{\mu \cdot v} = \frac{1}{k_1} + \beta \frac{\rho \cdot v}{\mu} \qquad 4.9$$

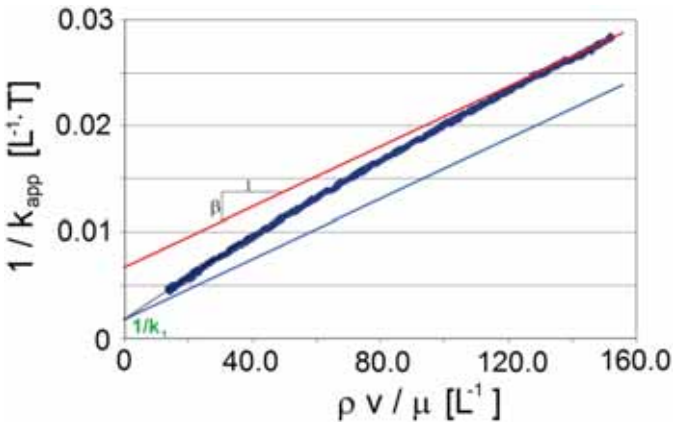

Figure 4.2: Forchheimer plot (modified from Barree & Conway, 2004).

The hydraulic gradient is determined with Equation 4.10. Parameters *a* and *b* are evaluated with expressions deduced either theoretically or empirically. These equations have varying degrees of accuracy in their application, depending on the assumptions made and simplifications of the geometry of the pore space and grains, and on the number and quality of data used to derive them (Sidiropoulou et al., 2007). These authors also conducted a comprehensive analysis of the most commonly used expressions, including some derived from the Kozeny-Carman formulation. The authors also found, based on a comparison with experimental data, Equations 4.11 and 4.12 to be the most representative.

$$i = a \cdot v + b \cdot v^2 \qquad 4.10$$

$$a = \frac{150 \cdot \rho_w \cdot (1-\eta)^2}{g \cdot \eta^3 \cdot d_{eq}{}^2 \cdot \mu} \qquad 4.11$$

$$b = \frac{2 \cdot (1-\eta)}{g \cdot \eta^3 \cdot \mathrm{d}_{eq}} \qquad 4.12$$

Several authors recently discussed the validity of the Forchheimer equation in the turbulent flow range, and whether the factor β is constant over the range of flow rates of practical interest. Barree & Conway (2004) and Lai et al. (2009) claim that this parameter is non-linear of for large Reynolds numbers (Figure 4.2). Huang & Ayoub (2008) explained this, based on an analytical derivation of the Forchheimer equation from the Navier-Stokes equation, and revealed that the nature of the Forchheimer flow regime is laminar with additional inertia effects. The inertia resistance factor β can then be used to characterize this flow regime, and therefore becomes an intrinsic property of the porous media.

Turbulent flow scaling is not common within geotechnical centrifuge publications. To the knowledge of the author, only Goodings (1994) and Bezuijen & Steedman (2010) have approached this problem. The former concluded that the phreatic surface of turbulent flow is a function not only of the problem geometry, but also of the velocity, which, in turn, is a function of particle size. The authors defined also the need to scale the particle size by *n*. This implies

that velocities in the model and prototype will be equal, while the seepage time in the model will be *n* times smaller than in the prototype.

Bezuijen & Steedman (2010) did an analytical study substituting Darcy's velocity in the Forchheimer equation. Solving for the hydraulic conductivity k_1, hydraulic conductivity becomes proportional to $\sqrt{d_{15}}$ for turbulent flow instead of d_{15}^2 as in the case of laminar flow. However, there is no experimental evidence to confirm these relationships as yet.

4.1.4 Superficial flow, dyke breaching and erosion

Overflow and erosion are important processes that must be considered when designing dykes, dams and embankments, or evaluating their response to flooding. Scaled models offer a safe and relatively inexpensive way to study these processes. Therefore, they might offer a well-suited approach to investigating the problem further.

Gilbert & Miller (1991) describe the processes acting when a dam is overtopped, and ultimately breached, as an interaction of several processes such as: open channel flow, seepage, erosion and sediment transport. The authors also explain that it would not be difficult to achieve similitude between the model and prototype with respect to any one of these processes acting singularly. However, as these processes begin to occur simultaneously, it becomes difficult to the point of impossibility to satisfy similitude completely, because these events occur at different time scales. Different flow regimes might be acting simultaneously as well. For instance, according to Goodings (1984), the flow resulting from overflowing of the embankment and seepage emerging from the downstream face is turbulent. However, the former is steady non-uniform while the latter is steady and uniform.

Centrifuge modeling of the overflow processes of a dyke has been considered in several research publications such as Kusakabe et al. (1988a), Ko et al. (1989a, 1989b, 1989c), Okumura et al. (1998), Bezuijen & den Adel (2006) and Seo et al. (2006). However, relatively little attention has been given to scaling issues. The principal academic information regarding the scaling of superficial erosion is derived from the theoretical analyses of Goodings (1979, 1982, 1984), Bezuijen & den Adel (2006) and Bezuijen & Steedman (2010).

Goodings extended the approach of using a Shields diagram, as explained in Henderson (1966) (cf. Figure 2.2). This diagram relates a dimensionless shear stress τ^* [-] with the boundary Reynolds number Re^* [-], and defines a threshold for the movement of particles at the bed of the flow. The particles remain stable at the bottom of the flow, below the Shields curve (shaded zone in Figure 2.2). A state above the curve implies that particles will be dragged by the flow. A parameter *T* might also be calculated in order to obtain the value of the critical dimensionless shear stress for a specified grain size.

The boundary Reynolds is obtained by replacing the velocity term in Equation 4.7 by the shear velocity u^* [LT^{-1}], which is a way of rewriting the shear stress in terms of velocity. In Equations 4.13 to 4.15, τ_0 [$ML^{-1}T^{-2}$] is the shear stress at the bottom of the flow, d_w [L] the depth of the water, S_f [-] is the slope of the total energy line (assumed equal to the channel

slope for very low inclinations), G_s [-] is the specific gravity of the soil grains, and ρ_w, γ_w are the density and unit weight of water. The equations imply also that τ^* is independent of the gravity level or fluid density, but dependent on the energy line and the flow depth.

$$u^* = \sqrt{\frac{\tau_o}{\rho_w}} \qquad 4.13$$

$$\tau^* = \frac{\tau_0}{\gamma_w \cdot (G_s - 1) \cdot d_{50}} = \frac{\rho_w \cdot g \cdot d_w \cdot S_f}{\rho_w \cdot g \cdot (G_s - 1) \cdot d_{50}} \qquad 4.14$$

$$\mathbf{Re^*} = \frac{\rho_w \cdot u^* \cdot d}{\mu} = \sqrt{\frac{\tau_o}{\rho_w}} \frac{\rho_w \cdot d}{\mu} \qquad 4.15$$

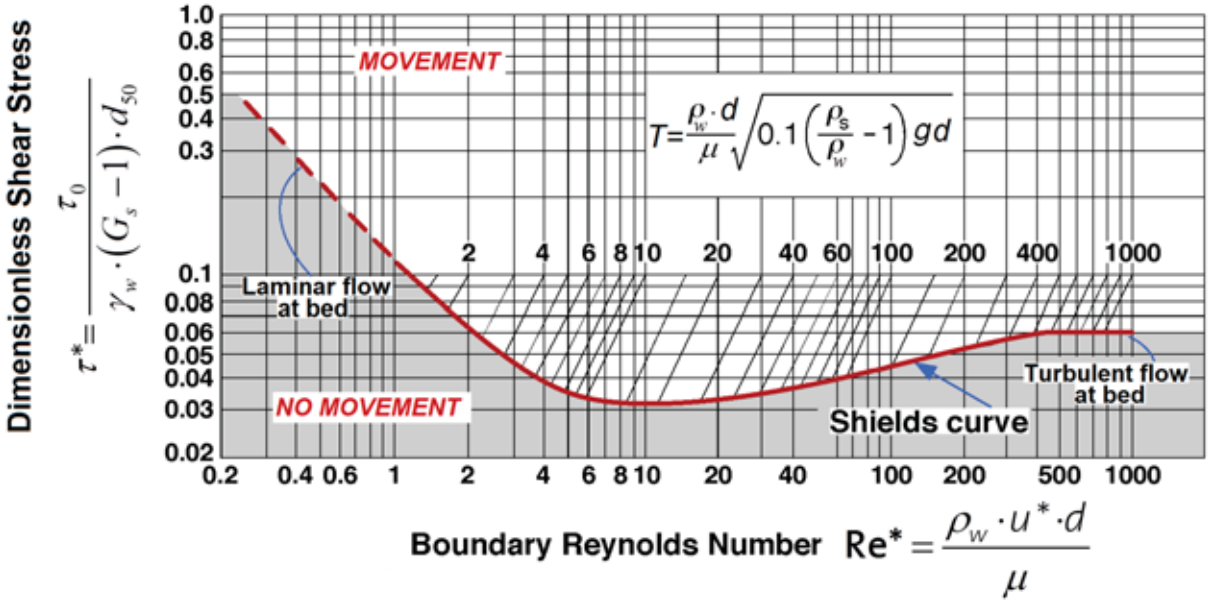

Figure 4.3: Shields diagram for dimensionless critical shear stress (modified from Henderson, 1966; U.S.A.C.o.E., 1994).

The Shields diagram is valid for a slope with a very flat bed, for which $\sin(\theta) \approx \theta \approx S \approx S_f$. As this is not correct for steep slopes, such as those in an embankment, some correction factors C_f (Equations 4.16 to 4.19) have been proposed by Goodings (1979, 1982, 1984) and Macchione & Sirangelo (1988).

$$\tau^*_\beta = \tau^* \cdot C_f \qquad 4.16$$

$$C_f = \cos\theta \cdot \sqrt{\left(1 - \frac{\tan^2\theta}{\tan^2\phi'}\right)} \qquad \text{Goodings (1979)} \qquad 4.17$$

$$C_f = \frac{1}{\cos\theta \cdot (\tan\phi' - \tan\theta)} \qquad \text{Goodings (1982, 1984)} \qquad 4.18$$

$$C_f = 1 - \frac{\tan\theta}{\tan\phi'} \qquad \text{Macchione \& Sirangelo (1988)} \qquad 4.19$$

Here, ϕ' is the angle of internal friction and θ is the slope of the embankment. The difference between these is evident, as seen in Figure 4.4 for ϕ' =30°. The behavior indicated by Goodings' 1979 equation is quite similar to that of Macchione & Sirangelo's, decreasing from 1.0 when θ = 0.0 to 0.0 when $\theta = \phi'$. Meanwhile, the correction factor by Goodings (1982, 1984) increases with the slope inclination becoming undetermined at $\theta = \phi'$. This correction factor is also inconsistent, as $\tau^*_\beta(\theta = 0) \neq \tau^*$.

None of the authors explain the basis from which these expressions were derived, which might become a major issue when analyzing or modifying them. Furthermore, more than 20 years have passed since they were proposed, and no experimental evidence has been presented to confirm or refute them.

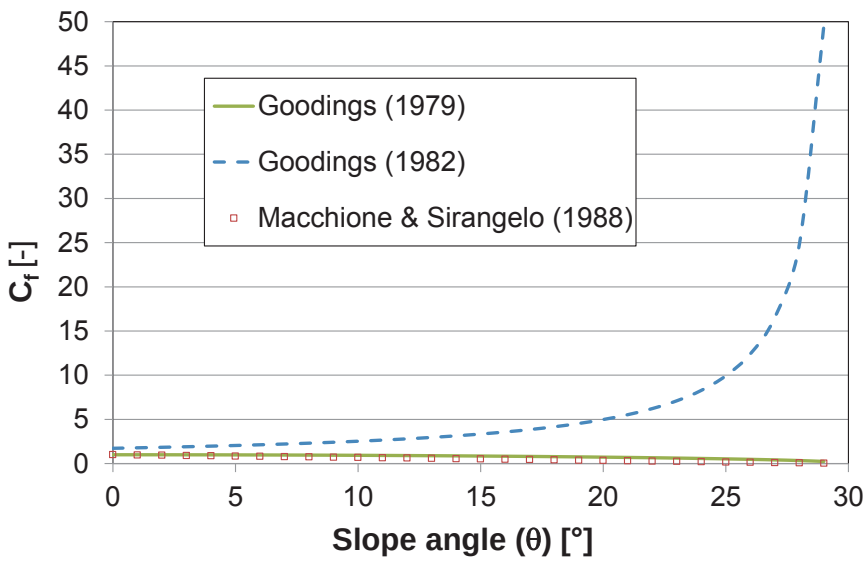

Figure 4.4: Slope correction factor for ϕ' = 30°.

Scaling of the Shields entrainment function when gravity is increased is not clear either. Bezuijen & Steedman (2010) state that the gravity influence in the equations defining the parameters of the Shields function cancel each other, so $\tau^*_p = \tau^*_m$. Goodings (1979) deduced that the flow depth should be scaled as $y_p = n^{0.3} \cdot y_m$ based on analysis of the Manning equation for open channel flow, implying that $\tau^*_p = n^{0.3} \cdot \tau^*_m$. However, that work also defines the shear stress to be scaled as $\tau_p = \tau_m \cdot n$, leading to an upper gravity level above which no erosion would be feasible in a centrifuge (cf. Figure 4.5).

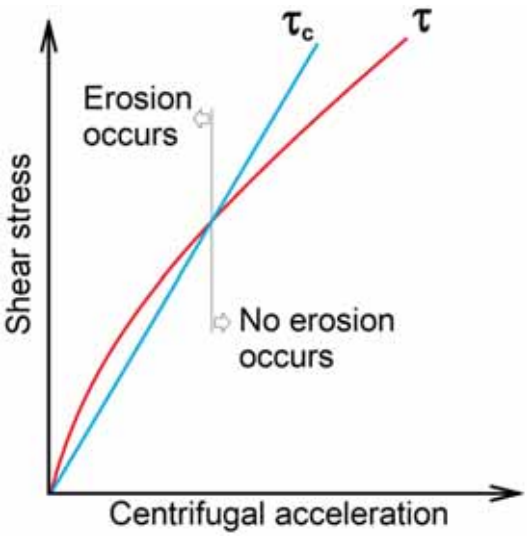

Figure 4.5: Effect on erosion characteristics with change in centrifugal loading at constant discharge (adapted from Goodings, 1979). τ is the exerted shear stress, whereas τ_c is the critical shear stress determined with the Shields diagram.

4.1.5 Unsaturated flow

Although many centrifuge applications require consideration of unsaturated soil mechanics to explain the response, relatively few data are available on scaling laws for unsaturated soils (Garnier et al., 2007; Caicedo et al., 2010). Work has been mostly focused on: flow and water-retention characteristics (Goforth et al., 1991; Burkhart et al., 2000; Crancon et al., 2000; Thorel et al., 2000), capillary rise (Rezzoug et al., 2000a; Grattoni et al., 2001; Bagge et al., 2002; Dell'avanzi et al., 2004; Rezzoug et al., 2004) and contaminant transport (Cooke & Mitchell, 1991; Culligan et al., 1996; Kumar, 2007). The common scaling factors obtained from these centrifuge tests are summarized in Table 4.2.

Table 4.2: Scaling factors for replicating unsaturated soil behavior on centrifuge tests.

Capillarity height (Hc_m/Hc_p)	1/n
Drainage velocity (v_m/v_p)	n
Drainage time (t_m/t_p)	$1/n^2$
$SWRC_m$ / $SWRC_p$	1/n

Most of them have used the same soil for the model and prototype, which agrees with the suggestion from Caicedo et al. (2010), who assert that it is better to use the same soil in the model as in the prototype, due to the complexities of unsaturated soils. Then the suction curve is identical and the profile of water content at equilibrium in a soil column is scaled in the same ratio as the length.

Soga et al. (2000) remarked that, in order to achieve these scaling factors (Table 4.2) for drainage velocity and time, three conditions need to be satisfied:

1. The capillarity pressure-saturation and the relative permeability-saturation relationships need to be independent of the fluid velocities (i.e. no dynamic effects).

2. The model geometry needs to be scaled by 1/n.
3. The pressures at the boundaries have to be the same as in the prototype.

A theoretical analysis of the movement of water in capillary tubes, representing soil, was carried out by Rezzoug et al. (2000b). An amplification factor *n* for the capillarity height and time was found, when the radius of the tube is decreased by *n*. Unfortunately, the authors did not mention any practical consequence of scaling the grain size, as it might change the characteristics of flow through unsaturated media.

4.1.6 Effects of scaling the grain size on the scaling of flow

Scaling the grain size influences the scaling of other properties. The effect of grain scaling of the 15 percentile of the particle diameter (d_{15}) on hydraulic conductivity, time and flow velocity is presented in Table 4.3 as derived by Bezuijen & Steedman (2010). The effect of grain scaling on the scaling of time is shown in Table 4.4.

Table 4.3: Influence of grain scaling on hydraulic properties (after Bezuijen & Steedman, 2010).

Scaling of grain size (d_{15}):	**[-]**	**1/√n**	**1/n**
Laminar flow/water			
k_m / k_p	1	1/n	$1/n^2$
$t_{s,m}$ / $t_{s,p}$	$1/n^2$	1/n	1
$v_{s,m}$ / $v_{s,p}$	n	1	1/n
Laminar flow/viscous liquid			
k_m / k_p	1/n	$1/n^2$	$1/n^3$
$t_{s,m}$ / $t_{s,p}$	1/n	1	n
$v_{s,m}$ / $v_{s,p}$	1	1/n	$1/n^2$
Turbulent flow/water			
k_m / k_p	1/√n	$1/n^{0.75}$	1/n
$t_{s,m}$ / $t_{s,p}$	1/(n√n)	$1/n^{1.25}$	1/n
$v_{s,m}$ / $v_{s,p}$	√n	$n^{0.25}$	1

Table 4.4: Influence of grain scaling on time scaling of hydraulic processes (after Goodings, 1984).

	$\frac{t_m}{t_p}$	$\frac{D_m}{D_p}$	$\frac{t_m}{t_p}$ when $\frac{D_m}{D_p} = \frac{1}{N^{1/2}}$
laminar flow			
a) steady state seepage	$\frac{1}{N^2}$	1	$\frac{1}{N}$
b) pore water pressure dissipation	$\frac{1}{N^2}$	1	$\frac{1}{N}$
c) groundwater surges	$\frac{1}{N^2}$	1	$\frac{1}{N}$
turbulent flow			
a) steady state seepage	$\frac{1}{N}$	$\frac{1}{N}$	-
b) groundwater surges	$\frac{1}{N}$	$\frac{1}{N}$	-
c) surface flow	$\frac{1}{N}$	N/A	-
d) sediment transport	$\frac{1}{N^2}$	$\frac{1}{N}$	-
mass soil movement	$\frac{1}{N}$	N/A	-

Normally a characteristic size is mentioned for hydraulic properties as a measure for the pore dimension of the soil (Rezzoug et al., 2004). For some researchers it is d_{10}, while others assume d_{15} or d_{50}. To the knowledge of the author, there is no scaling factor that includes the full particle size distribution, which might be more representative. For instance, Carrier (2003) presented a formulation for the hydraulic conductivity based on the assumptions embodied in the Kozeny-Carman equation (cf. Section 2.2.2.6). An 'effective diameter' is used by considering the whole grain distribution (Equation 4.20), whereby f_i is the fraction of particles between two sieve sizes d_1 and d_2.

$$d_{effective} = \frac{100\%}{\sum\left(\frac{f_i}{\sqrt{d_1}\cdot\sqrt{d_2}}\right)} \qquad 4.20$$

Hamilton (1997) presented an equivalent particle size diameter (Equation 4.21) based on the analysis of the moments (Equation 4.22) of the sieve curve, where M_j is the j-th moment of the curve and n is the number of particles with diameter d.

$$d_{eq}^{\ 2} = \sum_i \frac{x_i}{d_i} \Big/ \sum_i \frac{x_i}{d_i^3} \qquad 4.21$$

$$M_j = \sum_i d_i^{\ j} \cdot n_j \qquad 4.22$$

4.2 Instrumentation

4.2.1 New semi-circular strongbox

One of the greatest problems for modeling a dyke in a geotechnical centrifuge facility is related to its size. If the response of the dyke under a process of transient water level control is to be modeled correctly, then both the air and the water-side of the structure have to be represented. Achieving this goal attains more relevance as the height of the model increases and the slopes are flatter, which becomes restrictive in some cases given the limited space available in centrifuge strongboxes.

Model construction for centrifuge testing always represents a challenge, not only in geometric terms, but also to replicate the soil and the stress history of the planned prototype. Beam centrifuges have the advantage that the model can be built at 1-g and then tilted in-flight as the radial acceleration increases. However, the plan area available might be too small for modeling both slopes of a dyke in correct relation to the model height. Drum centrifuges, on the other hand, offer a larger area on which the model can be built. Nevertheless, the disadvantage is that the model surfaces must stand in a vertical position for a prolonged time once mounted in the drum during dyke construction and preparation before testing under n-g.

Using strongboxes that can be placed in the drum prior to testing is one option to overcome part of this challenge, even though the model still has to be stable when it is rotated to be installed in the channel of the drum. The drum centrifuge facility at ETH Zurich uses two types of strongboxes: a cylindrical box of 0.40 m in diameter and 0.20 m depth (Springman et al., 2001), and a cubic box of dimensions 0.40 × 0.40 m in plan view and 0.20 m depth (Chikatamarla, 2005; Weber, 2007).

Preliminary dyke modeling was planned in the rectangular box, as shown in Figure 4.6. A representative model height was defined to be 100 mm at a gravity level of 50-g. Slopes had a 1:2.0 gradient. These geometrical characteristics required the water side slope to be foreshortened. Therefore, low water levels could not be simulated properly.

The above limitations led to the design of a new strongbox that overcomes these difficulties. A semi-circular strongbox was found to be the most appropriate design. The new box allows larger dyke models to be created with the possibility of varying the slope gradient. A full description of the new box is presented below.

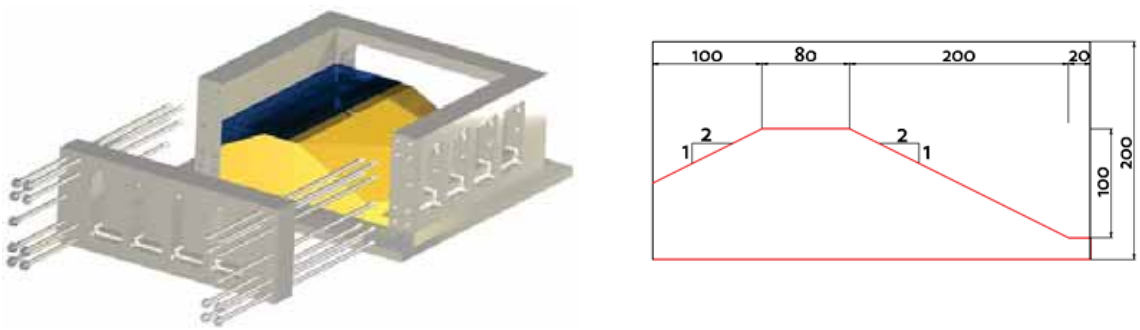

Figure 4.6: Preliminary concept for dyke modeling inside the 0.40 m cubic strongbox at 50-g (units in mm).

4.2.1.1 Description of the new strongbox

The new strongbox (Figure 4.7) is composed of two plates (bottom and top), two lateral walls, a curved modular base (Section 4 and Figure 4.8) and seven connecting struts. The box is fixed to the channel of the drum centrifuge by eight M12 screws. The form of the box is an annular sector of internal dimensions 1000 × 500 × 300 mm, as illustrated in Figure 4.7. The length (1000 mm) is determined by the top and bottom plates (cf. Sections 4.2.1.4, 4.2.1.5 and Figure 4.9a). The height of the box (500 mm) is given by the length of the connection struts (the box is designed to stand without the need for both lateral walls, cf. Sections 4.2.1.6, 4.2.1.7 and Figure 4.7). The width (300 mm) is given by the length of the shortest dimension of the side walls (cf. Section 4.2.1.6 and Figure 4.10b).

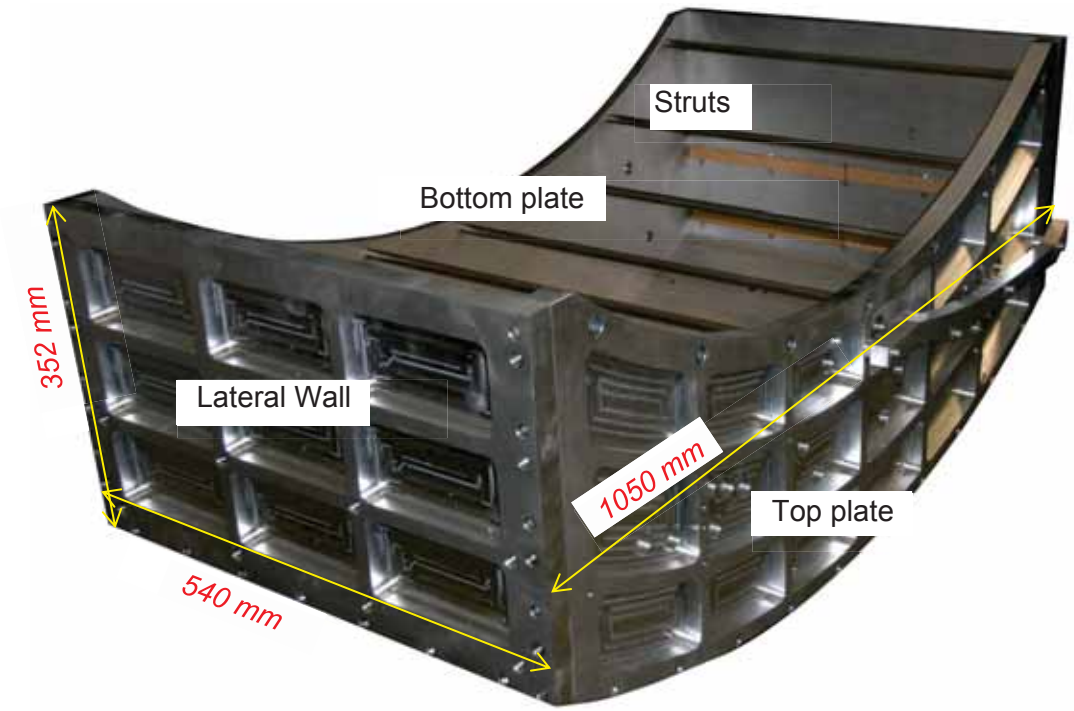

Figure 4.7: New semi-circular strongbox at ETH Zurich. The dimensions correspond to the external measurements.

Table 4.5 presents a comparison of the features of the three types of strongboxes. Although the new strongbox has a similar weight, it can hold about 6.3 and 4.9 times the volume of the cylindrical and rectangular boxes, respectively. This allows larger models to be created, which may be more representative of the physical problems to be analyzed. The new box was also designed to allow measuring sensors up to 25 mm in diameter to be inserted, as described in Section 4.2.1.4.

Table 4.5: Features of the strongboxes at ETH Zurich.

Strongbox type	Available soil volume [m^3]	Surface area [m^2]	Box weight [N]	Max. weight with soil* [N]	Design g-level
Semi-circular	0.156	0.500	680	3800	100
Cylindrical	0.025	0.125	750	1250	250
Cubic	0.032	0.160	670	1310	200

** assuming γ=20 kN/m^3*

4.2.1.2 Materials

The structure, except for the connection struts, is made of anticorodal-110, which is an aluminum alloy of Swiss origin. The struts are made of standard steel *St37-2,* and the bolts are manufactured from high strength steel. Material properties are listed in Table 4.6.

Table 4.6: Material properties of the strongbox components.

	Anticorodal-110	Steel (St37-2)	Steel for bolts
Composition	Magnesium (0.6%) Silicon (1.0%) Aluminum (98.4%)	Carbon (0.17%) Magnesium (1.4%) Sulphur (0.045%) Iron (98.4%)	Carbon (0.25-0.5%) Magnesium (1.5%) Sulphur (0.05%) Iron (98.2-97.25%)
Unit weight [kN/m^3]	27	78.5	78.5
Yield strength [MPa]	240	235	640
Ultimate strength [MPa]	295	360	800
Young's modulus [GPa]	69	210	210
Poisson's ratio [-]	0.325	0.28	0.28

4.2.1.3 Modular base

The design of the modular base was driven by the challenges of constructing a massive curved plate of 15 mm in thickness and 1.04 m in length (Figure 4.8). Therefore, the whole arc was divided into five sections. Each section is connected to the top and bottom plate by four M6 screws. The joints between sections are sealed with silicon in order to ensure that they are watertight.

Each piece has a curved surface on the exterior face, to fit the drum shape with a radius of 1.1 m, and a flat surface inside the drum (Figure 4.8b). This means that the internal surface of the strongbox will be a five-sided polygon instead of a curved shape (Figure 4.8c). This is a minor detail that does not hinder correct modeling of the dyke.

Additionally, two circular drainage filters were located in the central piece. These are used to saturate and drain the water out when the model is built (cf. Section 4.3.2).

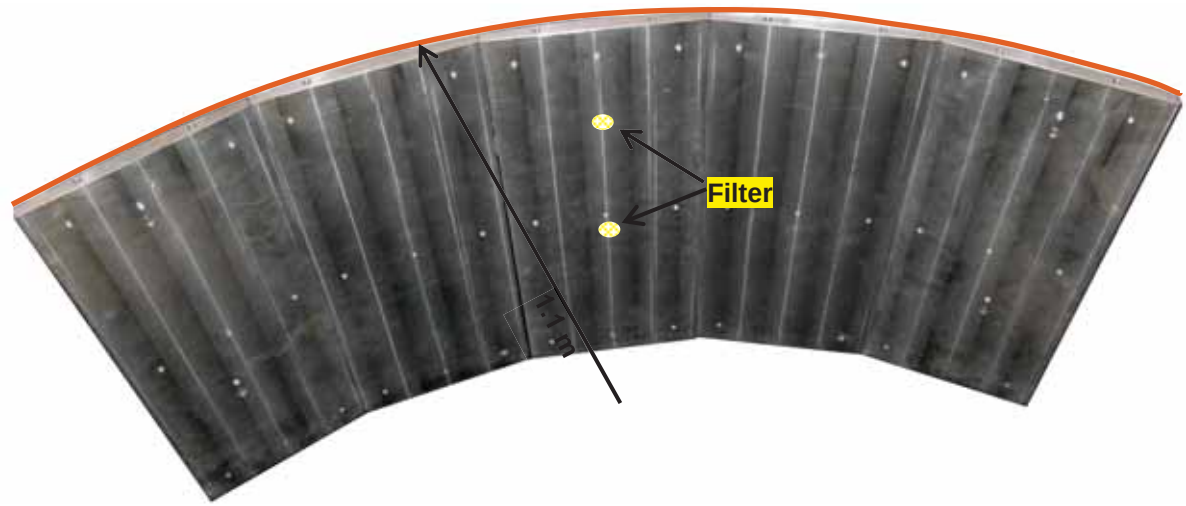

a) Complete view.

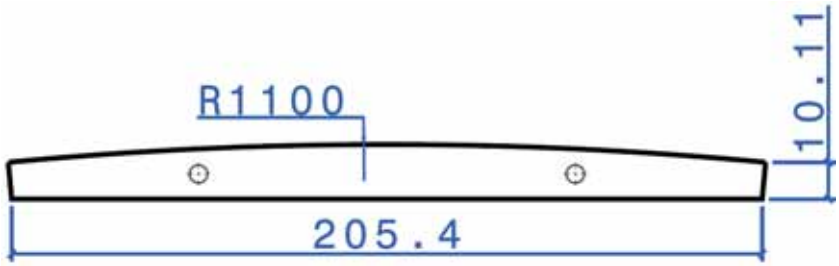

b) Detail of each section (dimensions in mm).

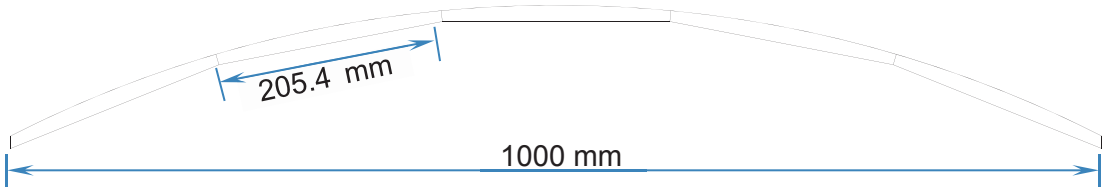

c) Plan view of the base after assembly.

Figure 4.8: Modular base.

4.2.1.4 Top plate

The shape of the top plate, in plan view, is an annular sector. The straight sides are parallel to the line joining the center of the annulus in the middle of the curved section. The distance between the straight sides is 1000 mm (Figure 4.9a). The external radius is 1100 mm to fit the radius of the drum centrifuge (as described in Springman et al., 2001). The distance between the two radii is 300 mm.

The plate has variable thickness to reduce weight while assuring a stiff response to loading and structural stability. It was designed to work as a waffle slab with thickness of 25 mm and 12.5 mm on its thicker and thinner sectors respectively, as shown in Figure 4.9b.

The plate has 18 holes with M25 × 1.5 thread. These allow several measuring sensors that are larger (>15 mm) than those usually installed in a centrifuge model to be inserted within the soil mass to suit the different slope gradients to be analyzed (cf. Section 4.3.3). Up to four coaxial cables (with their connectors) can be passed through each hole as well. Thus, up to 72 sensors can be inserted within the soil mass. This is an improvement over the other strongboxes, as only sensors up to a diameter of 8 mm can be embedded in the centrifuge model.

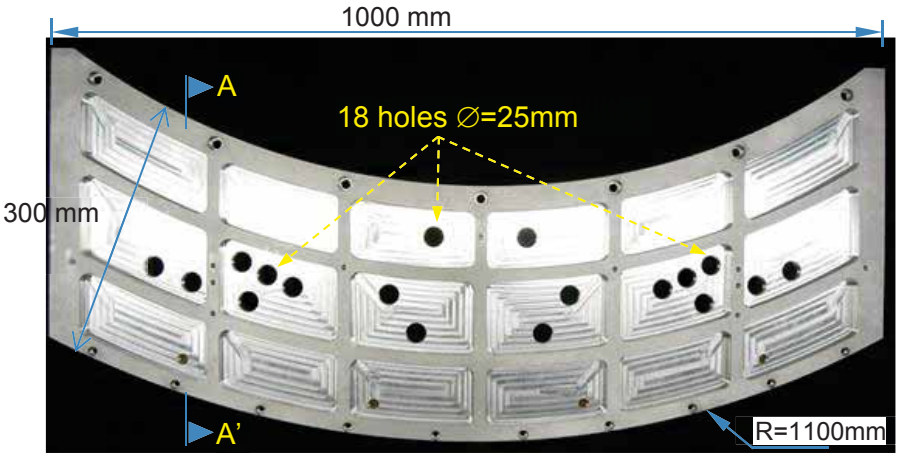

a) Plan view with ∅ = 25 mm holes.

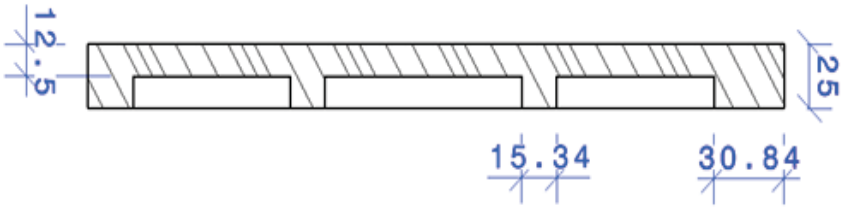

b) Cross section A-A' (dimensions in mm).

Figure 4.9: Top plate.

4.2.1.5 Bottom plate

The bottom plate has the same shape as the top plate, but the difference lies in the performance under load in the centrifuge. This plate is fixed to the wall at the bottom of the channel of the centrifuge, and large deformations are not expected. Therefore, the whole plate is 15 mm thick across and does not include any milled sections.

4.2.1.6 Lateral walls

The lateral walls are rectangular, and of internal dimensions 540 × 300 mm. Each wall is clamped to the top, bottom plates and modular base by five M10, four M8 and seven M6 screws, respectively. The walls are also designed to be removed prior to testing if needed. This design feature was introduced with future research projects in mind, which might require

the use of an external strongbox for building the model, and at the same time, access to the entire channel of the drum centrifuge for testing.

Each wall has two ports for drainage, as seen in Figure 4.10b. Each drainage port is 500 mm long, 20 mm wide and made of a metallic filter plate. The separation between them is 120 mm. The lower drainage port is used for saturating the material during the model construction (cf. Section 4.3.2), whereas the upper drainage port is used for supplying the water on the water-side of the dyke.

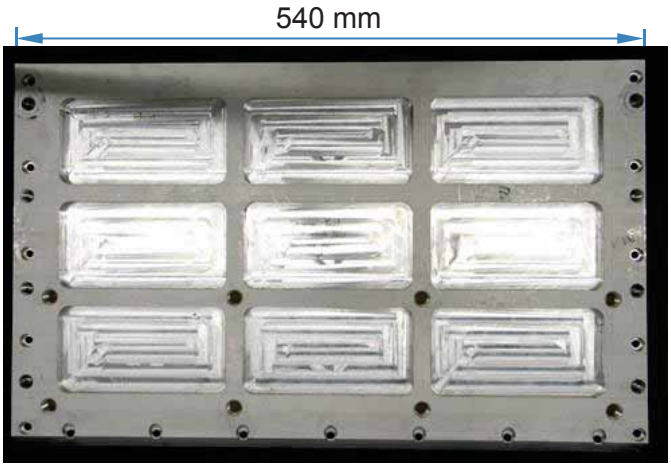

a) External view.

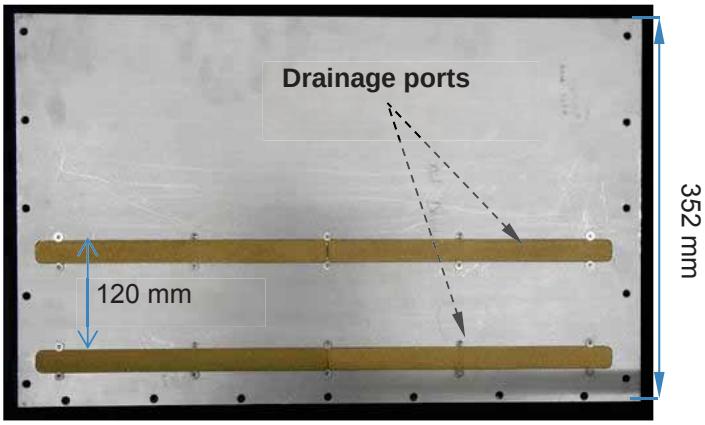

b) Internal view.

Figure 4.10: Lateral walls.

4.2.1.7 Connection struts

Seven struts are needed to prop between the top and bottom plates along their internal radius. Their main function is to reduce displacements of the top plate. In this case, they are the main structural elements preventing the top plate from excessive bending.

4.2.1.8 Stress analysis

Every new element to be used in a centrifuge facility has to be designed with a sufficient factor of safety, and verified with an initial proof-test according to the design principles given by Schofield (1980). Morales et al. (2012a) and Morales et al. (2012b) present a deeper view of the analyses performed, and the main results for an acceleration field equivalent to 100-g are summarized in Table 5. The stresses acting under these conditions are evaluated as a von Mises stress σ_{vm} (Equation 4.23) and compared to the ultimate stress of the material in service in the strongbox to ensure that this is smaller and that the item can be considered safe (Beer et al., 2002).

$$\sigma_{vm} = \sqrt{\frac{(\sigma_1 - \sigma_2)^2 + (\sigma_2 - \sigma_3)^2 + (\sigma_1 - \sigma_3)^2}{2}} \qquad 4.23$$

Table 4.7: Results from the analysis for the new strongbox for an acceleration field equivalent to 100-g.

Item	Units	With lateral walls	Without lateral walls
Maximum von Mises stress on struts	MPa	54.7	52.1
Factor of safety in rods	-	*6.6*	*6.9*
Maximum von Mises stress on top plate	MPa	61.5	66.1
Factor of safety in top plate	-	*4.8*	*4.8*
Maximum von Mises stress on lateral wall	MPa	51.8	N/A
Factor of safety in lateral wall	-	*5.7*	*N/A*
Maximum von Mises stress on strut bolts	MPa	105.4	108.7
Factor of safety in strut bolts	-	*7.6*	*7.4*
Maximum von Mises stress on connection bolts	MPa	253.2	361.2
Factor of safety in bolts	-	*3.2*	*2.2*
Maximum total displacement top plate	mm	0.179	0.212
Maximum total displacement lateral wall	mm	0.293	N/A
Maximum total displacement struts	mm	0.362	0.366

4.2.2 Water level control system

A system is designed to set the water levels and the transient cycles of raising and decreasing the water level, which can be followed by holding a constant water level during an overflow phase. A two-chamber box has been developed to provide a controlled water level to the system. A thin wall separates the two chambers of this device, as shown in Figure 4.11. The device is connected to the arm of an actuator placed on the tool plate of the drum centrifuge (Figure 4.11a). The location of the box can be varied along a radius from the center of the drum, as shown in Figure 4.12, so that different positions, and hence water levels, can be set in-flight.

The water control device is made of anticorodal-110, i.e. the same material used for the strongbox (Figure 4.11b). The external dimensions of the device are 200 × 100 × 85 mm with 10 mm thick walls, enclosing a volume of 1.22 liters. The device has a maximum discharge rate of 500 ml/s.

Water flows continuously through a pipe connected to an external water supply into the bigger chamber of the device. The outlet of this chamber is connected to the upper drainage line of the strongbox by a plastic hose of 10 mm in diameter. When the water reaches the height of the dividing wall, it overflows into the second chamber, which lets the water flow out of the system, maintaining a fixed height given by the height of the dividing wall, as shown in Figure 4.11b.

The water surface is curved due to the acceleration field. Therefore, the water height in both the water-level device and the strongbox is the same, due to Archimedes' principle (Figure 4.12). The water level is measured on the water side of the dyke by a pore pressure transducer (PPT) sensor.

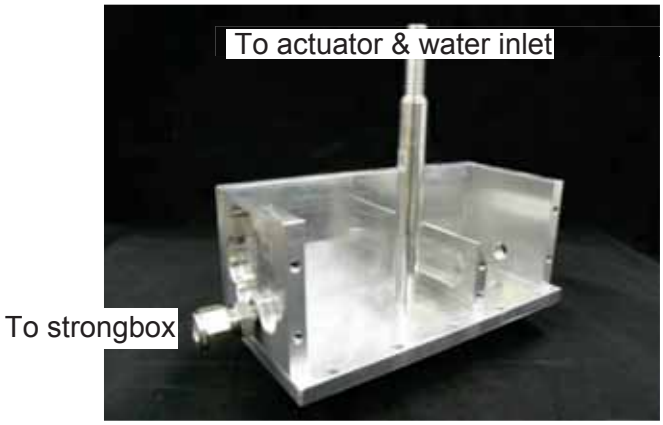

a) Photograph.

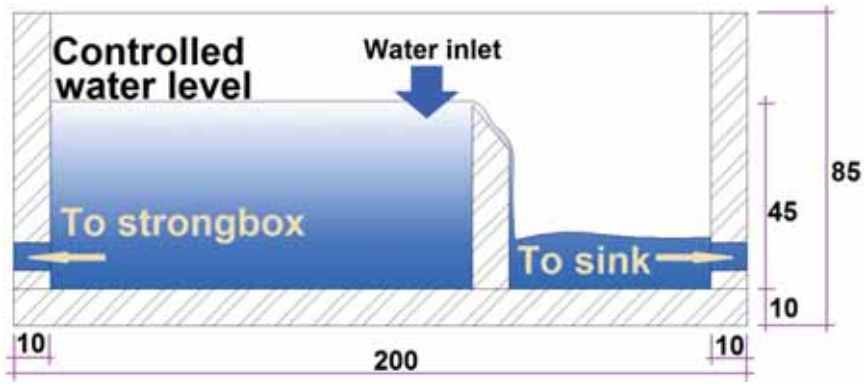

b) Cross section (dimensions in mm).

Figure 4.11: Water control device.

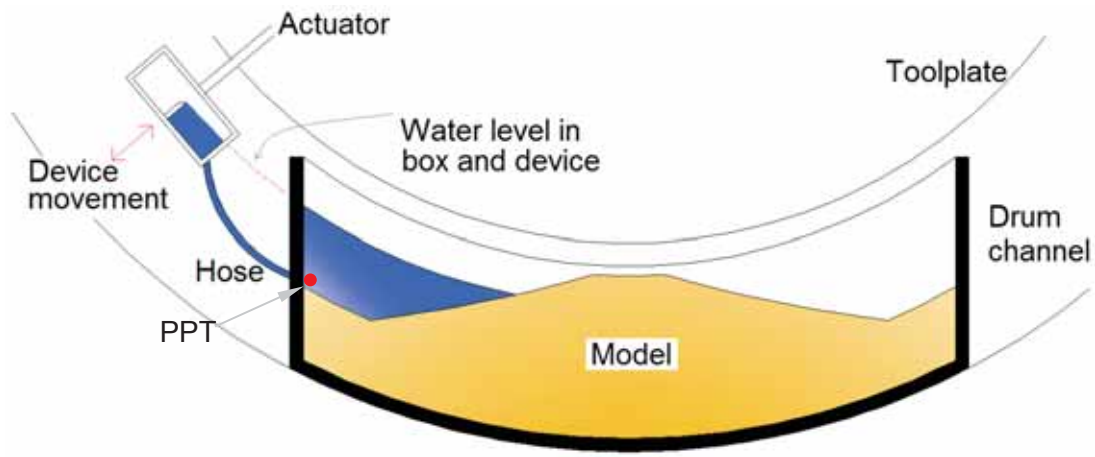

Figure 4.12: Water level control in the strongbox.

4.2.3 Water pressure and suction measurement

Measurement of water pressures (positives and negatives) is of high interest when analyzing the behavior of water flow through dykes. In physical modeling, and especially in centrifuge modeling, this task is challenging to achieve as the sensors have to be small enough to have a small area of influence of measurement but at the same time to measure in a specific location with sufficient accuracy.

The pore pressure transducer (PPT) Druck PDCR-81 is the sensor that has been most commonly used to measure pore water pressure in centrifuge models. The device has been demonstrated to be a robust and accurate sensor. A schematic view of the sensor is presented in Figure 4.13a. The device consists of an instrumented silicon diaphragm supported on an internal glass cylinder, which is connected to a porous filter by a steel outer casing (Take, 2003). The porous filter has a high air entry value. The space between the porous filter and the diaphragm serves as water reservoir.

Changes of water pressure in the soil are transmitted to the water inside the water reservoir, which tries to equalize the pressure of the soil. This causes the diaphragm to deform, and the deformation is interpreted as a change in voltage and then, with an appropriate calibration factor, as change in water pressure.

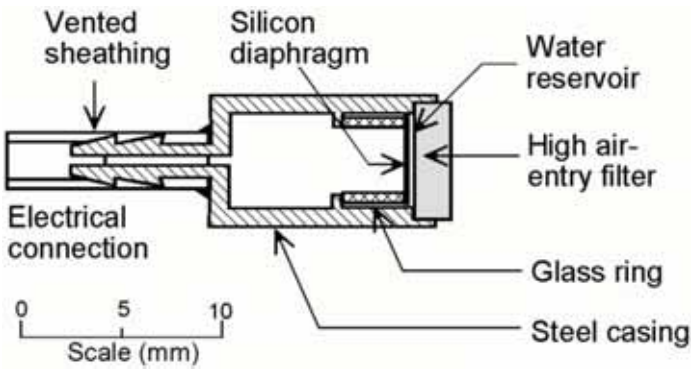

a) Schematic view (after König et al., 1994).

b) Photograph.

Figure 4.13: Pore pressure measurement transducer Druck PDCR-81.

Table 4.8: Suction measurement techniques (after Pan et al., 2010).

		Technique (Method)	Suction Range [kPa]	Equilibrium Time
Direct suction measurement	Matric suction	Axis-transition technique	0-1500	hours
		Tensiometer		hours
		Suction sensor		minutes
Indirect suction measurement	Matric suction	Time domain reflectometry	0-1500	hours
		Electrical conductivity sensor	50-1500	6-50 hours
		Thermal conductivity sensor	0-1500	hours-days
		In-contact filter paper	all	7-14 days
	Osmotic suction	Squeezing technique	0-1500	days
	Total suction	Psychrometer technique	100-10000	1 h
		Relative humidity sensor	100-8000	hours-days
		Chilled-mirror hygrometer	150-30000	10 minutes
		Non-contact filter paper	all	7-14 days

Guan (1996) and Pan et al. (2010) present a summary of the current techniques adopted to measure suctions (negative water pressures) in the laboratory and in the field. Although the device was initially designed to measure positive water pressures, the use of the PPT Druck

PDCR-81 in centrifuge modeling as a tensiometer has been successfully reported by Ridley (1993); König et al. (1994); Take & Bolton (2002); Take (2003) and Zhou et al. (2006).

Ridley (1993) reported some failures of the devices to measure high suctions due to a leak between the diaphragm and the casing caused by the outward deflection of the former. However, and based on the values measured in the field test (Chapter 3), the values of suction in this series of model tests are not expected to be high enough to cause problems due to leaks.

Tests were performed to verify the applicability of the devices in the range of pore water pressures expected in this research. Positive and negative pressures were applied stepwise to a sensor and then compared to the measured value. Figure 4.14 and Table 4.9 present the results of one of the tests. Positive pressure up to 114.4 kPa and suctions up to 42.8 kPa were applied. The relative error of the measured values, calculated with Equation 4.24 is shown in the third column of Table 4.9. The measured water pressures with the device were higher than the applied pressure within an accuracy of 7.9%.

$$\text{Relative error} = \frac{\text{Measured pressure - Applied pressure}}{\text{Applied pressure}} \times 100\% \qquad 4.24$$

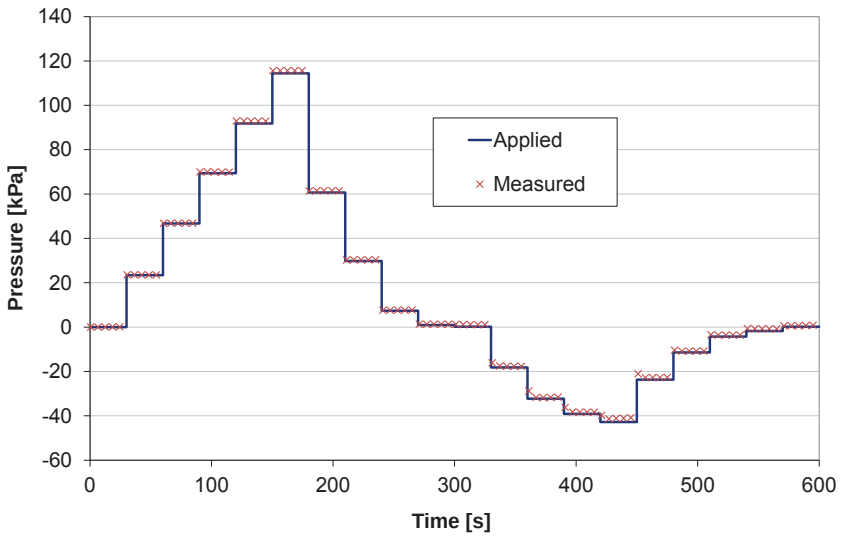

Figure 4.14: Test for suction measurements with Druck PDCR-81 devices at ETH Zurich.

The PPT Druck PDCR-81 has a fixed glued porous filter. This might be a large disadvantage if the filter cracks, as its replacement could be complicated. Furthermore, the manufacture of this device has been discontinued. Therefore, new options have to be found by geotechnical centrifuge laboratories.

At ETH Zurich, a new generation of PPTs has been acquired for testing and analysis of their performance. The devices are transducers produced by a Swiss company (www.keller-druck.com). The schematic view of the sensor (series 7) is shown in Figure 4.15. The porous stone can be removed and replaced, because a threaded casing has been used. As the po-

rous filter is thicker, the sustainable duration of suction measurement is increased, as reported by Ridley (1993).

Table 4.9: Results of test for pore pressure suction measurements with Druck PDCR-81 devices at ETH Zurich.

Time [s]	Applied pressure [kPa]	Measured pressure [kPa]	Relative error [%]		Time [s]	Applied pressure [kPa]	Measured pressure [kPa]	Relative error [%]
0	0.00	0.00	0.00		300	1.10	1.19	7.90
30	23.40	23.55	0.66		330	-18.20	-17.17	-5.65
60	46.70	46.81	0.24		360	-32.30	-31.75	-1.70
90	69.40	69.96	0.80		390	-39.10	-38.35	-1.91
120	91.80	92.88	1.17		420	-42.80	-41.36	-3.37
150	114.40	115.58	1.03		450	-23.70	-22.77	-3.91
180	60.70	61.35	1.07		480	-11.40	-10.87	-4.67
210	29.80	30.23	1.44		510	-3.90	-3.64	-6.79
240	7.40	7.53	1.75		540	-0.86	-0.82	-5.11
270	1.20	1.26	5.09		570	0.53	0.56	4.98

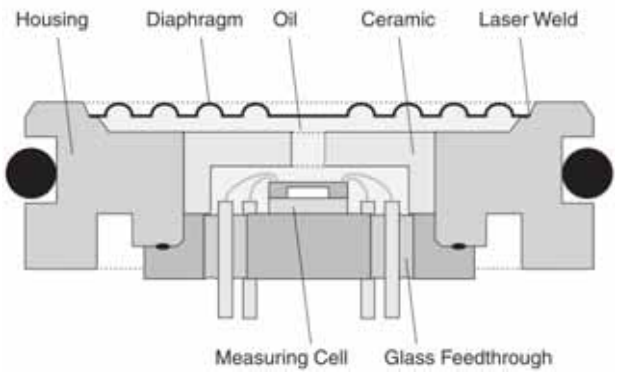

a) Schematic view (modified from www.keller-druck-com).

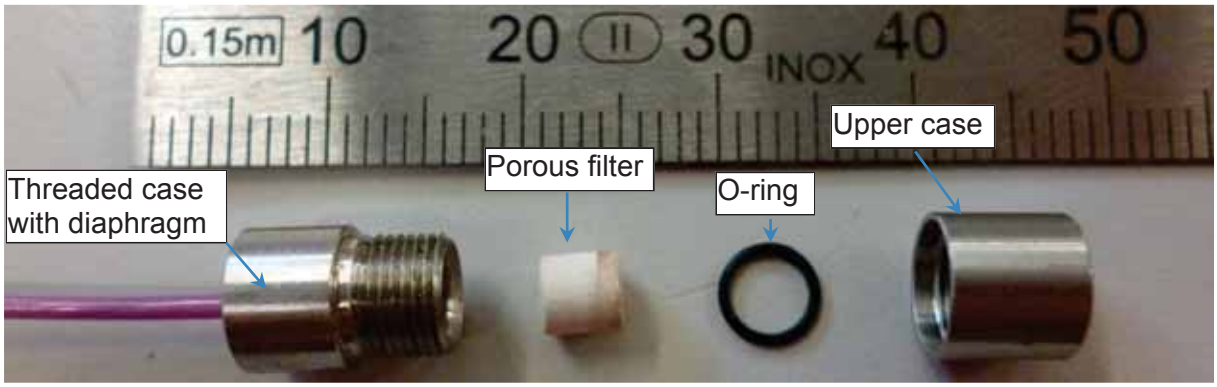

b) Photograph.

Figure 4.15: Pore pressure transducer Keller series 7.

4.2.3.1 Saturation

Take (2003) and Take & Bolton (2003) have shown the importance of initial saturation of small tensiometers in the accuracy of the measurements achieved. Take (2003) mentions that each research group has developed its own saturation procedure based on their experience with the devices and the air entry value of the porous filters. Guan & Fredlund (1997) state that the sustainable tension in the suction sensor appeared to be related to the characteristics of the porous filter. In the following section paragraphs, the main saturation procedures are described alongside the procedure used at ETH Zurich and the description of the procedure followed to saturate the sensors in this research project.

Guan & Fredlund (1997) found that six cycles of pressurization produced the maximum sustainable tension in the suction sensor. Each cycle included the application of a positive pressure of 12000 kPa for 1 hour, followed by a negative pressure of –85 kPa for 1 hour.

Ridley & Burland (1999) assembled the suction sensor with a dry porous filter and placed it in an evacuated chamber with a small amount of de-aired water. However, the water and the filter did not make contact until the chamber was completely evacuated. After about 10 min, the chamber was upended to submerge the suction sensor in the now de-aired water. The evacuation continued for a further 1 hour. Finally, the air was allowed back into the chamber very slowly using a fine valve, keeping the suction sensor submerged at atmospheric pressure.

Take (2003) and Take & Bolton (2003) adopted a similar procedure to Ridley & Burland (1999). The difference was the inclusion of a second stage of tensiometer saturation involving the application of high positive pressures to force any remnants of the air phase into solution that might be entrained within the tensiometer.

The usual procedure followed at ETH Zurich is based on the proposal of Ridley (1993), in which it is suggested that the time required for saturation can be reduced by cycling from high positive pressures to low negative pressures. Therefore, ten cycles of positive and negative pressure are applied with an approximate duration of 10 seconds each.

Muraleetharan & Granger (1999) studied the effect of the saturation fluid on the performance of the PPT Druck PDCR-81 to measure suctions. They defined the hydraulic conductivity and the air entry value (AEV) of the porous filter as the most influential parameters. They concluded that it is desirable to have a porous element with a high air entry value (to measure a large range of matric suction) and a high hydraulic conductivity (for faster response) and to be saturated with a high viscosity fluid (to reduce air diffusion).

The AEV of the filter is measured in pressure units (kPa), and is related to the surface tension of the fluid-air interface T (kN/m) and the equivalent radius of the pore space R (m), as indicated in Equation 4.25. To increase the AEV for the same filter, the surface tension has to be increased.

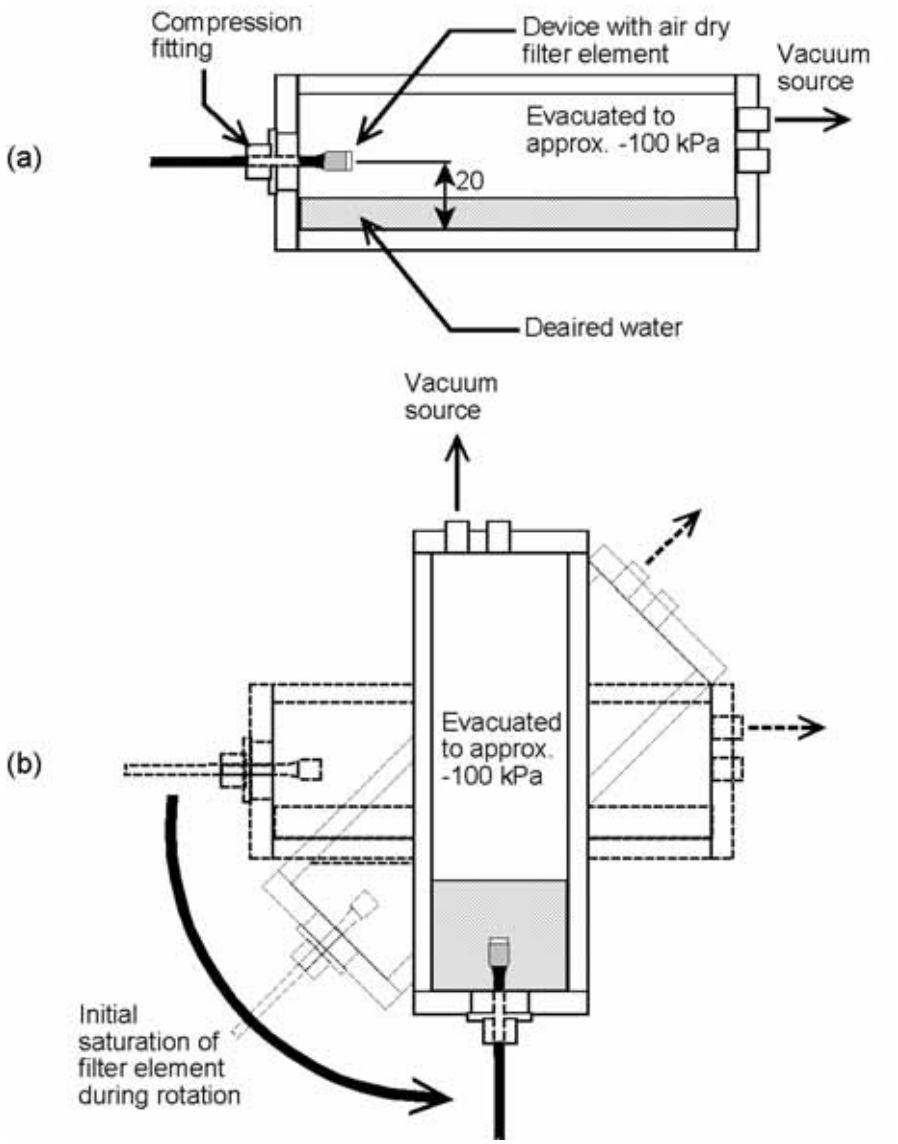

Figure 4.16: Initial saturation process based on Ridley & Burland (1999) (taken from Take, 2003).

$$AEV = \frac{2 \cdot T}{R} \qquad 4.25$$

A mixture of 50% de-aired water and 50% glycerin increases the viscosity 5.5 times and the density 1.13 times (Lambe, 1981). The increased viscosity increases the drag force on the diffusing air molecules. Therefore, the porous filter can remain saturated for a longer time (Askarinejad et al., 2012c). However, the AEV of the filter for the fluid mixture decreases as the surface tensions for water and glycerin are 72.8 and 63.4 mN/m at 20° respectively. Nevertheless, the decrease is about 7% only, and, as concluded by Muraleetharan & Granger (1999), it has no impact on the measurement of low suction values.

Subsequently, a saturation procedure based on the methods described above was adopted in this research project. First, a new saturation chamber was built (Figure 4.17), allowing four

sensors to be saturated simultaneously. A mixture of 50% de-aired water and 50% glycerin was used.

1. The chamber is partially filled with the fluid mixture.
2. The sensors are inserted in the new saturation chamber.
3. The chamber is subjected to -30 kPa vacuum. At this stage, the fluid is not in contact with the sensors.
4. The saturation chamber is rotated slowly through 90 degrees, so the sensors are now in contact with the fluid. The vacuum is kept for 1.5 hours. Then the vacuum is released.
5. Ten cycles of positive pressure (90 kPa) and negative pressure (-30 kPa) are applied. Each cycle has a duration of one minute, 30 seconds under positive pressure and 30 seconds under negative pressure.
6. The sensors finish the saturation under atmospheric pressure for 30 minutes.

Figure 4.17: New PPT saturation chamber at ETH Zurich.

The porous filters of the new PPTs manufactured by Keller AG are extracted and submerged into the fluid mixture, applying an -80 kPa vacuum for one week to warranty their initial saturation (Figure 4.18b). Then the reservoir is filled with the fluid mixture (Figure 4.18c), the casing is closed (Figure 4.18d) and the transducer is ready to be saturated with the procedure described above.

a) The porous filter is extracted from the casing.

b) The filter is subjected to a vacuum of -80 kPa for one week.

c) The reservoir is filled with the water-glycerin mixture.

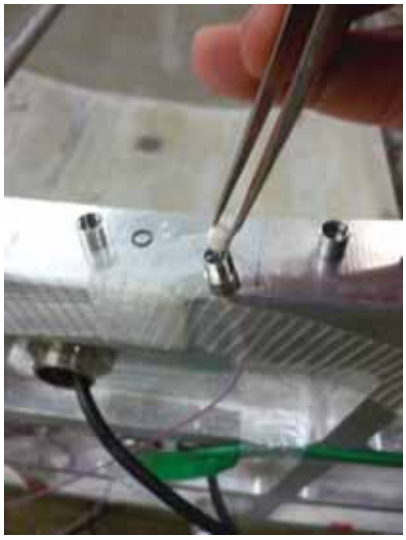

d) The filter is replaced, together with the O-ring and the casing is screwed into place.

Figure 4.18: Preparation process for saturation of the new Keller PPTs.

4.2.4 Volumetric water content measurement

As mentioned in Chapter 2, there are two main techniques for estimating the volumetric water content: capacitance and Time Domain Reflectometry (TDR). The advantage of capacitance gauges is their reduced size, whereas their main disadvantage is the large influence volume of the measurement. This is an inconvenience when it is scaled up to prototype dimensions. Figure 4.19 shows the influence volume for a commonly used device, which is an elliptic cylinder with major and minor axes of 60 and 40 mm. When scaled up, for instance with a factor of n=35, it represents a measurement within a width of 2.1 m and a height of 1.4 m.

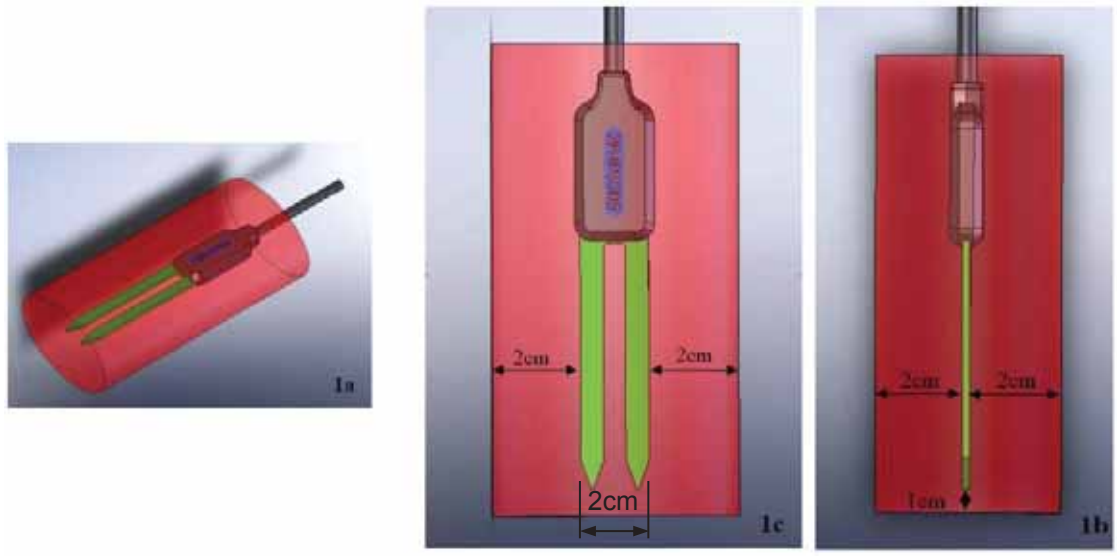

Figure 4.19: Influence volume for a typical capacitance gauge (taken from www.decagon.com).

Although TDRs can be used in a centrifugal field without any significant perturbation of measurement quality (Crancon et al., 2000), TDR sensors are generally too large since the length of the measurement rods is usually of the order of 0.2 m. However, smaller TDR devices have been developed and tested recently with good results (Persson & Haridy, 2003), such that shown in Figure 4.20. It is 95 mm long, with measuring rods that are only 20 mm long, with a 5 mm separation between them. However, the body of this device is too big for insertion in the centrifuge.

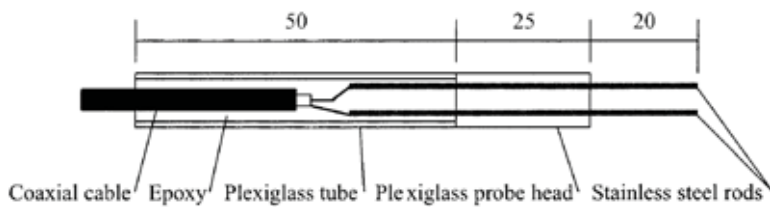

Figure 4.20: Miniature TDR device with dimensions in mm (after Persson & Haridy, 2003).

Walker (2000) and Hanumantha-Rao & Singh (2011) opined that the measurement volume is restricted to the separation between the external rods, and cited this to be a disadvantage of the TDR sensors. However, if this is the case, this is in fact an advantage for centrifuge modeling as the influence volume at prototype scale is smaller, making it more representative. For instance, the measurement diameter for the TDR sensor in Figure 4.20 will be 0.175 m at prototype scale (n=35).

Eight small commercial TDR sensors (model T3F) manufactured by East 30 Sensors in the USA were used (Figure 4.21). The sensor has three rods with an external distance of 13 mm and 60 mm length attached to a head of dimensions 25 × 13 × 13 mm. This means a measurement diameter of 0.45 m in prototype scale at 35-g. The offset calibration and the soil specific calibration are described in the following section.

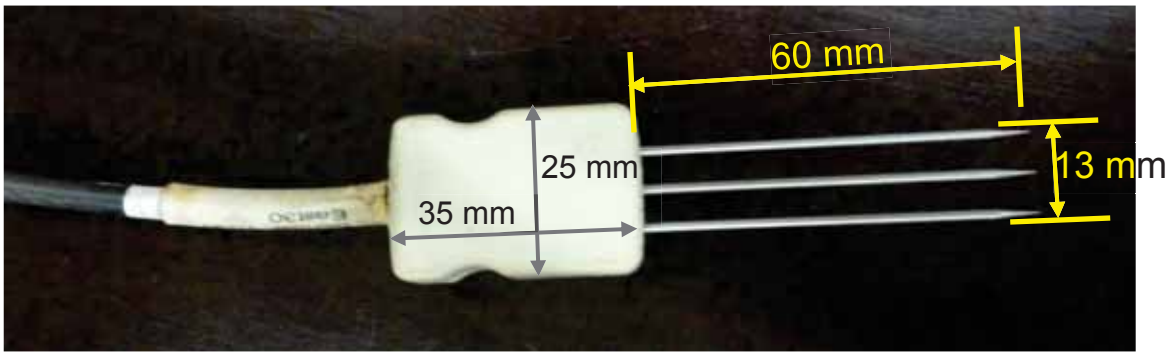

Figure 4.21: The model T3F TDR sensor used for the centrifuge modeling.

4.2.4.1 Offset estimation

The sensor offset was defined in Section 2.2.2.3 as the distance (or time) required for the signal wave to cross the sensor head. This value can be estimated through a double reflection analysis procedure (Heimovaara, 1993) by finding the points at which the wave form of the TDR signal changes the slope direction, and back calculating the offset of the sensor from this data.

Heimovaara (1993) noted that the resulting impedances a sensor installed in a soil in order to measure water content fall between the impedances of the sensor in water and in air when. However, an estimation of the offset can be complicated, as the wave form for the sensor in the air does not exhibit the first reflection, as shown in Figure 4.22.

To deal with this problem, Skierucha et al. (2008) proposed that the choice of calibration media should include one material of low (air, benzene or ertacetal) and another of high dielectric permittivity (acetone, ethanol, methanol or water). At the same time, the authors recommended that air should not be used as the calibration medium for the TDR sensor rods of length less than 0.10 m due to some convolution effects.

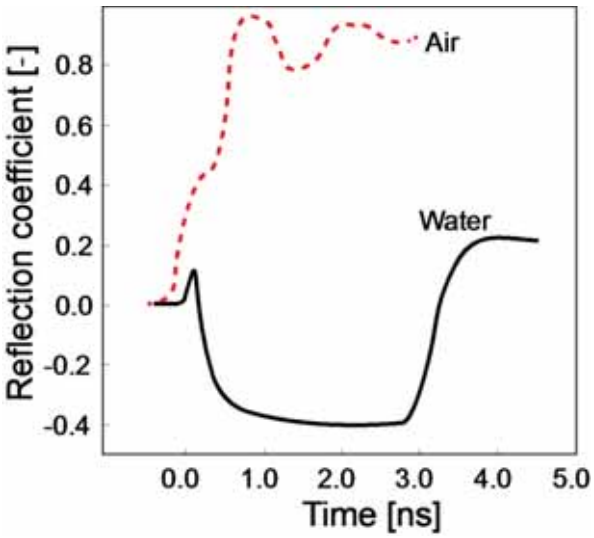

Figure 4.22: Wave forms for a TDR sensor submerged in water and air (adapted from Heimovaara, 1993).

The offset can be determined from Equation 4.26, where L_o is the offset in meters, L_1 and L_2 are the total length of the wave form for fluid 1 and 2 respectively, and ε_1 and ε_2 are the dielectric permittivity of the fluids.

$$L_o = \frac{L_1 \cdot \sqrt{\varepsilon_2} - L_2 \cdot \sqrt{\varepsilon_1}}{\sqrt{\varepsilon_2} - \sqrt{\varepsilon_1}} \qquad 4.26$$

The offset was calibrated with two pairs of fluids in this research program (Figure 4.23): de-aired water & air, and de-aired water and benzene. The use of benzene gives a clearer first reflection, as shown in Figure 4.24. The total length L was calculated with the procedure described in Campbell Scientific (2009). The dielectric permittivity of water and benzene are calculated from Equations 4.27 (Campbell Scientific, 2009) and Equation 4.28 (Skierucha et al., 2008) respectively, where the temperature T is given in degrees Celsius.

Figure 4.23 presents the set-up used to estimate the offset of all eight TDR sensors. It consists of a TDR100 cable tester, a CR1000 data logger and an SDMX50 multiplex. All of them were manufactured by Campbell Scientific. Table 4.10 summarizes the results of the offset estimation. The average offset is 0.0925 with a standard deviation of 0.00302, which indicate that all sensors have comparable offset, and therefore, provide reliable measurements.

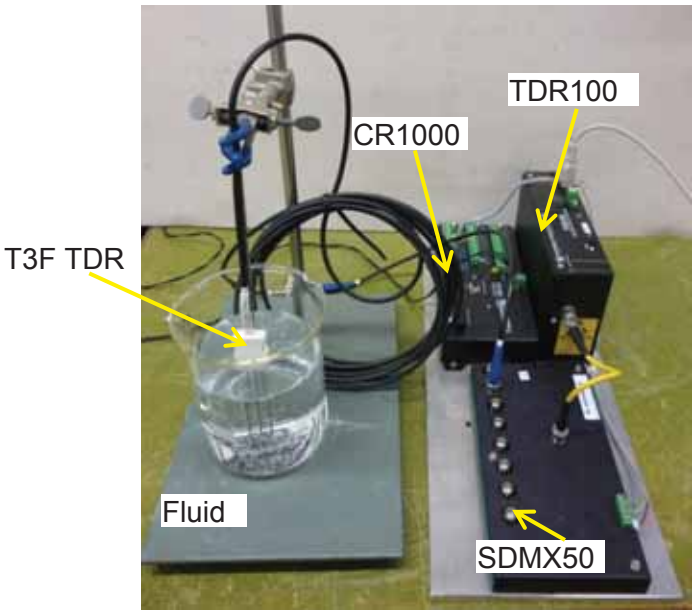

Figure 4.23: Experimental set-up for offset estimation of the T3F TDRs.

$$\varepsilon(T)_{water} = 78.54 \cdot \left[1 - 4.5791\times10^{-3} \cdot (T-25) + 1.19\times10^{-5} \cdot (T-25)^2 - 2.8\times10^{-8} \cdot (T-25)^3\right] \qquad 4.27$$

$$\varepsilon(T)_{benzene} = 2.67 - 0.916\times10^{-3} \cdot (T+273) - 0.143\times10^{-5} \cdot (T+273) \qquad 4.28$$

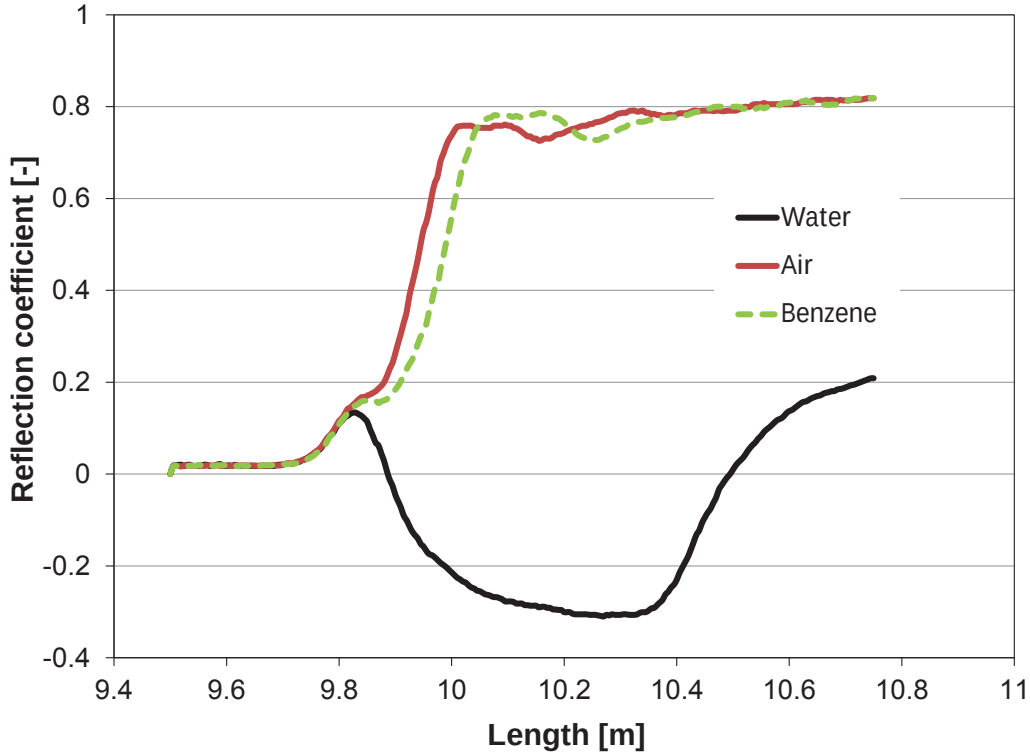

Figure 4.24: Wave forms for a model T3F TDR sensor, as used for the centrifuge modeling and submerged in water, air and benzene.

Table 4.10: Results for the offset estimation of the eight TDR sensors model T3F used for the centrifuge modeling.

	L_{water} [m]	L_{air} [m]	L_o water-air [m]	$L_{benzene}$ [m]	L_o water-benzene [m]	L_o average [m]
TDR 1	0.626	0.154	0.095	0.188	0.100	0.097
TDR 2	0.632	0.144	0.083	0.185	0.095	0.089
TDR 3	0.620	0.144	0.085	0.186	0.099	0.092
TDR 4	0.617	0.143	0.083	0.185	0.097	0.090
TDR 5	0.622	0.150	0.090	0.190	0.103	0.097
TDR 6	0.627	0.142	0.081	0.184	0.094	0.088
TDR 7	0.621	0.146	0.086	0.188	0.100	0.093
TDR 8	0.622	0.147	0.087	0.188	0.100	0.094

4.2.4.2 Soil specific calibration

Topp et al. (1980) present a calibration relationship between the volumetric water content θ, and the apparent length read from the TDR sensor. This has been commonly used in engineering practice, as it shows reliable results. However, Take et al. (2007), among others, show the importance of performing a calibration of the relationship for the specific soil to be measured. The approach presented by Take et al. (2007) for this calibration was followed in this research project.

a) Moisture condition value equipment.

b) 1000 gr of soil (Perth sand) are introduced in the mold.

c) A metallic plate is placed over the soil.

d) The soil is compacted with ten blows.

e) The final height of the sample is measured.

f) The plate is removed.

Figure 4.25: Specimen preparation process for soil specific calibration of the TDR sensors.

The procedure adopted to prepare a soil specimen for calibrating the TDR sensors is shown in Figure 4.25. Soil was prepared at six different gravimetric water contents (0, 4, 8, 12, 16, and 20%), a sample was prepared as follows. 1000 gr of Perth sand are placed inside a mold of 0.10 m in diameter and leveled to a uniform depth. A metallic plate is positioned to ensure

a flat surface during the compaction. Then, ten blows with the hammer of a Moisture Condition Value (MCV) (BSI, 2002) equipment are imposed on the material. This machine is designed always to provide the same falling height (Parsons & Boden, 1979).

a) Four sensors are inserted on one side.

b) Another four sensors are inserted on the other side.

c) The sensors are arranged to form a square shape.

d) All the sensors are connected to TDR system (cable tester, multiplex and data logger.

e) View of the specimen after extraction from the mold.

f) Comparison between the lengths of the sensor and specimen.

Figure 4.26: Procedure for soil specific calibration of the model T3F TDRs.

The plate is removed and a second layer of Perth sand, weighting 1000 gr is compacted in the same way. The final height is measured and the total volume calculated. The volumetric water content θ of the sample can be estimated from the volume and the gravimetric water content *w*.

All of the TDR sensors are inserted once the specimen is prepared, four at each face (Figure 4.26a-b). 50 measurements are taken for each TDR sensor and each volumetric water content for a total of 2400 measurements. The average values of $\sqrt{K_a}$ are presented in Table 4.11.

The values are plotted in Figure 4.27. The best fit curve, given by Equation 4.29, is compared with the 'universal' curve from Topp et al. (1980). It is clear that both relations are closely fitted in the middle range. However, they differ for the extreme values. This illustrates the importance of generating a calibration curve (Equation 4.29) for the specific soil in which the TDR sensors would be used.

The calibration curve was determined using the method of the least squares of the average values of each gravimetric water content (last row in Table 4.11). The correlation has a coefficient of determination (R^2) of 0.9999.

Table 4.11: Average values of $\sqrt{K_a}$ from all eight TDR sensors for different gravimetric water contents.

	Gravimetric water content [%]					
	0	**4**	**8**	**12**	**16**	**20**
θ [m^3/m^3]	0.000	0.066	0.112	0.161	0.234	0.292
Porosity [-]	0.156	0.262	0.382	0.562	0.736	0.156
TDR 1	1.636	2.085	2.507	2.975	3.516	4.139
TDR 2	1.780	2.260	2.655	3.014	3.625	4.193
TDR 3	1.578	2.083	2.408	2.752	3.493	4.097
TDR 4	1.603	2.073	2.472	2.945	3.649	4.161
TDR 5	1.630	2.146	2.495	2.811	3.637	4.122
TDR 6	1.649	2.207	2.509	2.939	3.372	4.063
TDR 7	1.694	2.136	2.555	2.864	3.593	4.212
TDR 8	1.638	2.149	2.493	2.932	3.790	4.077
Average	**1.651**	**2.142**	**2.512**	**2.904**	**3.585**	**4.133**

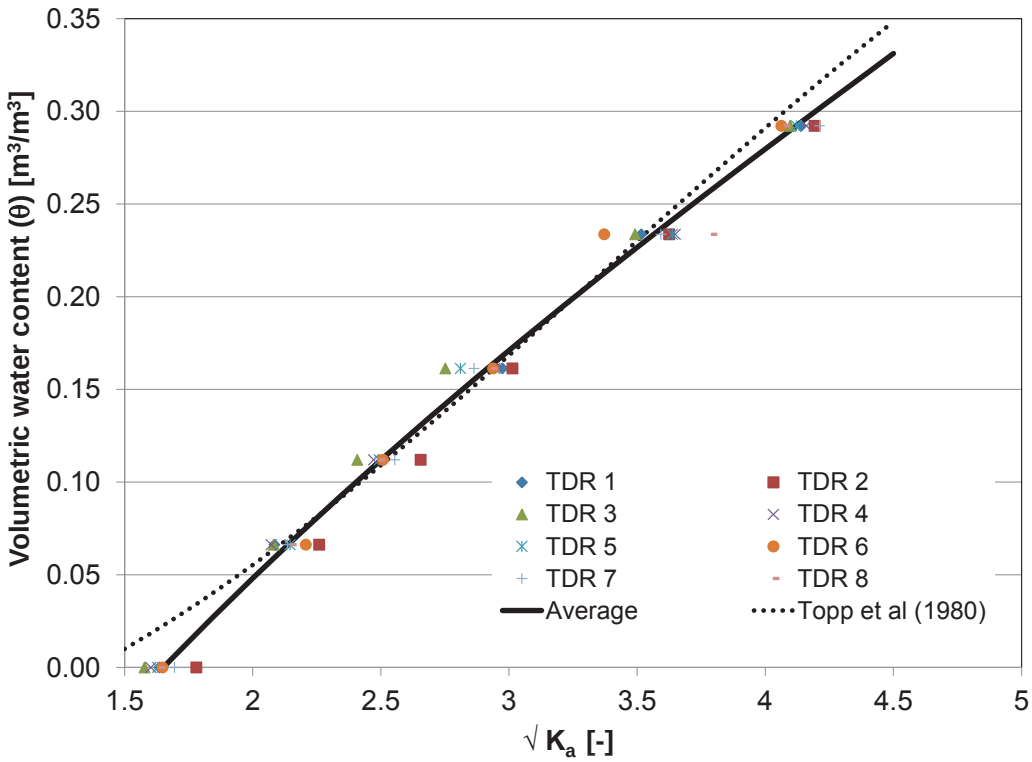

Figure 4.27: Results for PPTs soil specific calibration compared with the 'universal' curve by Topp et al. (1980).

$$\theta = 0.0015 \cdot K_a^{\frac{3}{2}} - 0.0208 \cdot K_a + 0.1986 \cdot K_a^{\frac{1}{2}} - 0.278 \qquad 4.29$$

4.2.5 Photographic monitoring

Three photogrammetry cameras uEye Gigabit Ethernet UI-6240 C were installed to monitor the general dyke behavior and deformation during the test. Figure 4.28 presents the camera and its dimensions, while Table 4.12 presents its main features. The same cameras have already been used under an enhanced gravity field by Askarinejad et al. (2012c) and Askarinejad (2013) performing well.

a) Photograph.

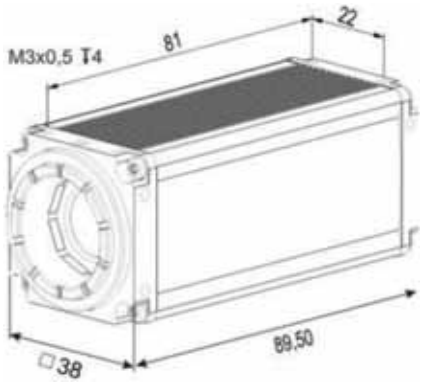

b) Schematic view (dimensions in mm).

Figure 4.28: Photogrammetry camera uEye GigE UI-6240 C.

Table 4.12: Specifications for photogrammetry cameras uEye GigE UI-6240 C (adapted from www.ids-imaging.com)

Interface	GigE
Lens Mount	C-Mount
Sensor Technology	CCD (Sony)
Model Description (color)	UI-6240RE-C
Model Description (mono)	UI-6240RE-M
Resolution (h x v)	1280 x 1024
Resolution Depth	12bit (12bit ADC)
Resolution Category / Pixel Class	1.3 Megapixel
Sensor Size	1/2"
Shutter	Global
Maximum frame-rate	15 Hz
Exposure Time in Freerun Mode	66 µs – 1360 ms
Exposure Time in Trigger Mode	66 µs – 10 min
AOI Modes	horizontal + vertical
Binning Modes	Vertical
Subsampling Modes	Vertical
Sensor Model (m/c)	ICX205AL / ICX205AK
Pixelpitch in µm	4.65
Optical Size	5.952 x 4.762 mm
Protection Classes	IP65/67
Dimensions	H: 89.50 mm, W: 38.00 mm, L: 38.00 mm
Mass	195.00 g
Power Supply	12 V

Due to physical limitation in the data acquisition system, the image frequency was set to 2 Hz although the camera allows up to 15 Hz (Table 4.12). Nevertheless, thanks to the resolution of the camera, it was possible to create a high definition video with a code in Matlab (Appendix 5).

4.2.6 Tool plate

One of the main features of a drum centrifuge is the amount of space on a versatile tool plate, in which most of the instrumentation can be mounted. The tool plate was adapted for this series of experiments to accommodate all three photogrammetry cameras, the acquisition boxes for the TDRs and PPTs, the computer controlling the data logging and the actuator, to adjust the radial extension of the water control system. The tool plate was also equipped with a wireless data transmission for real time monitoring. Figures 4.29 to 4.31 illustrate the distribution of the devices across the tool plate.

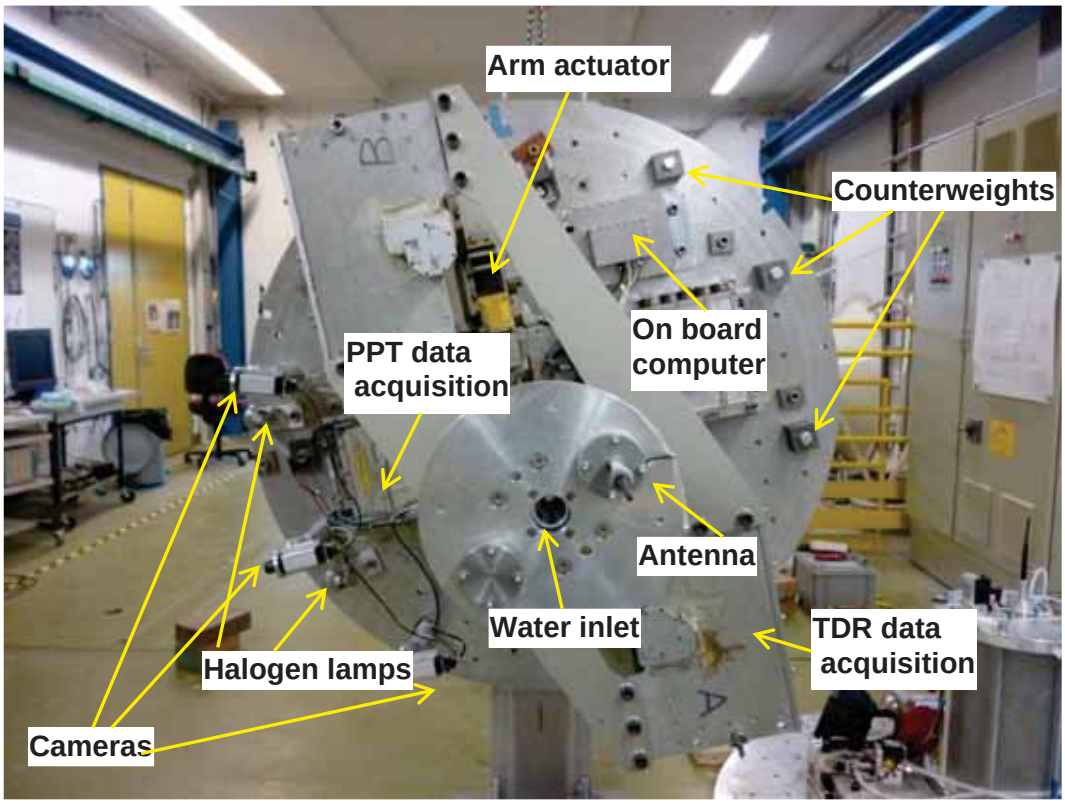

Figure 4.29: Plan view of the tool plate.

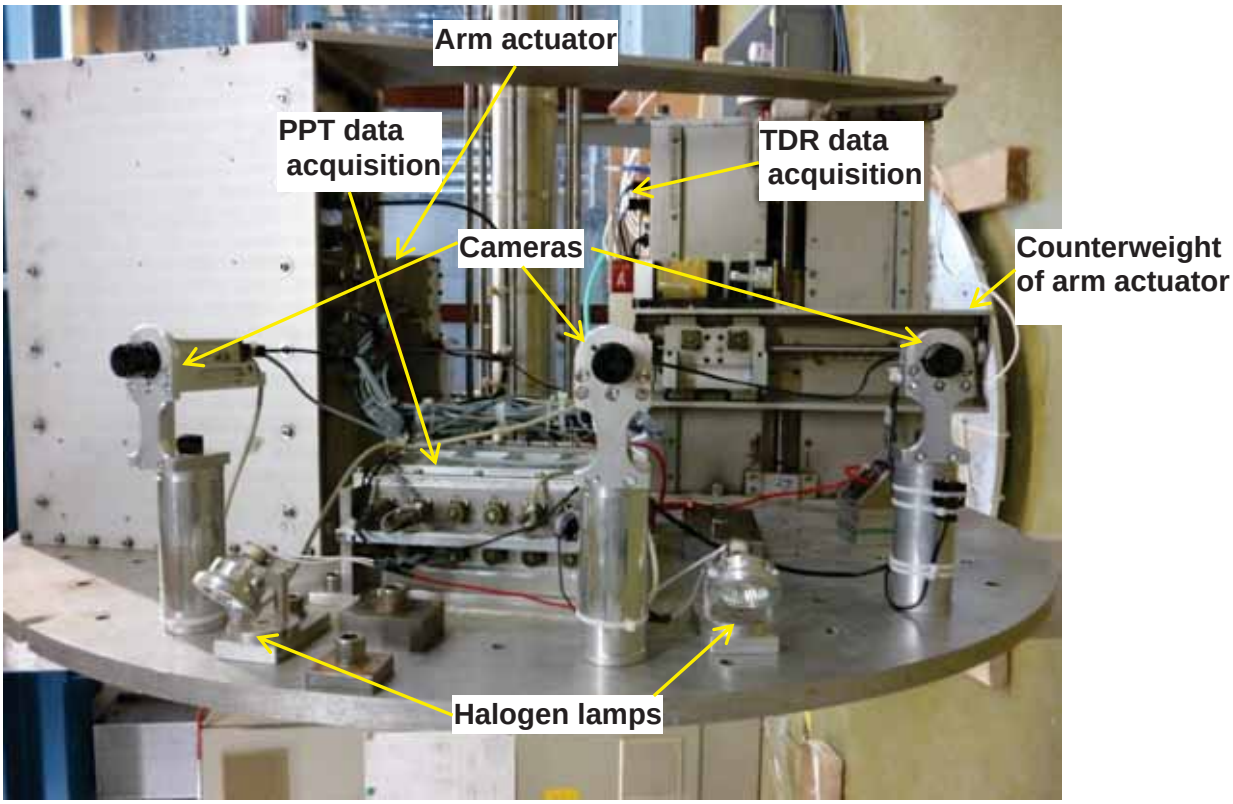

Figure 4.30: Front view of the tool plate.

New casings were designed for many of the devices. These casings, as for the strongbox, must be able to carry loads imposed the increased gravity field without problems. Furthermore, it has to be proven that the mounted devices are in equilibrium before the tool plate can be used during a test (Figure 4.32). A slight imbalance in the tool plate could cause a big moment when spinning the plate.

The equilibrium verification is done in the preparation laboratory. The tool plate is tilted through 90 degrees and then rotated several times, verifying that it never stops at the same position. If the tool plate tends to stop at the same point, this indicates that some of the devices at the lower part are heavier. Then some small counterweights have to be added to counteract this.

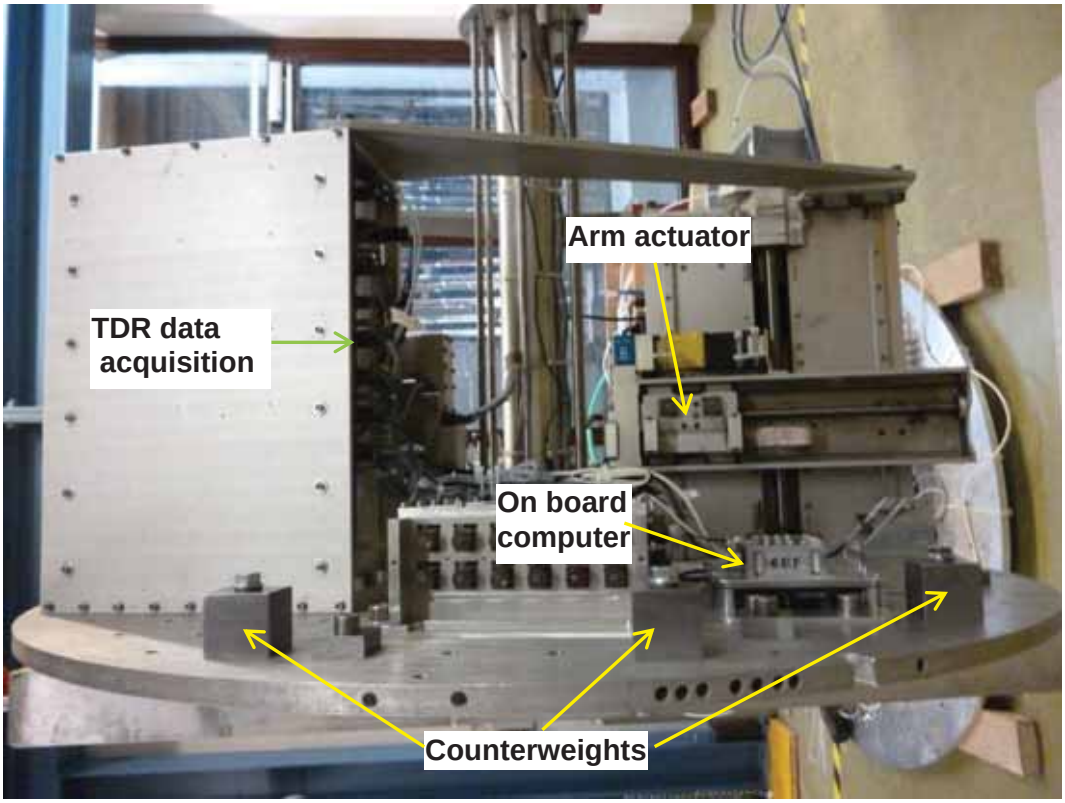

Figure 4.31: Rear view of the tool plate.

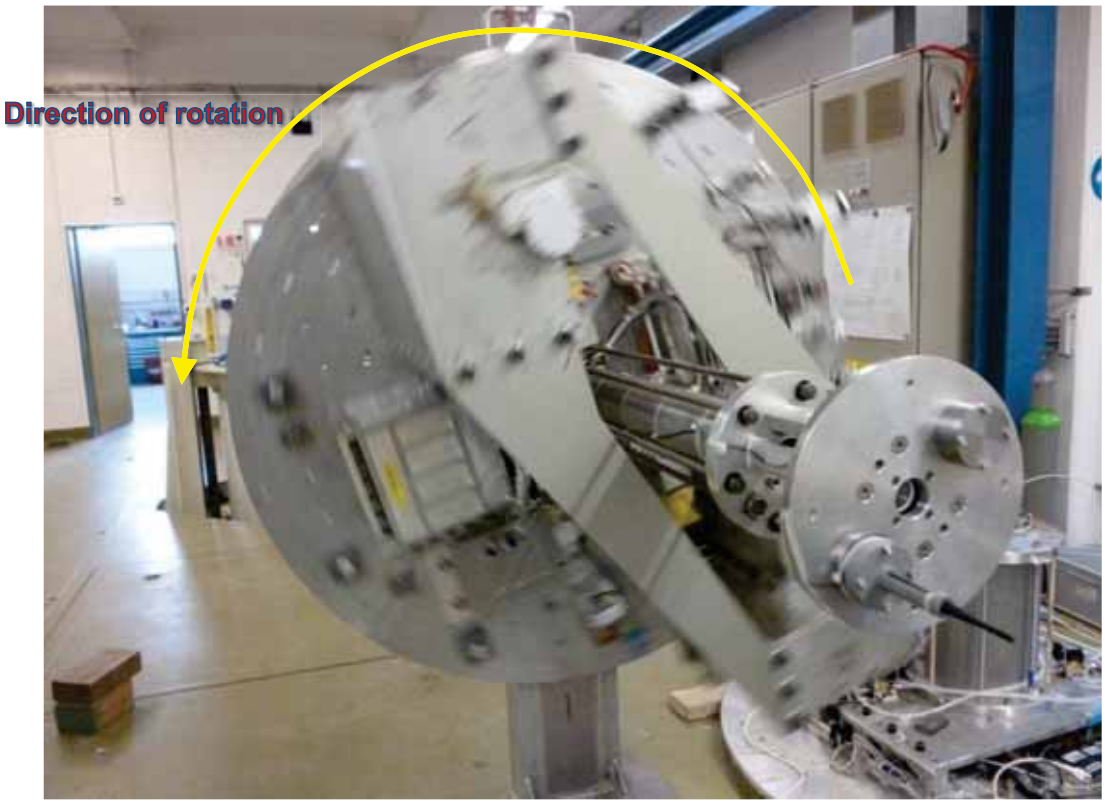

Figure 4.32: Equilibrium test of the tool plate.

4.3 Model preparation

4.3.1 Perth sand

4.3.1.1 Physical properties

A uniform poorly graded sand from 15 km from the coast near Perth, Australia, is used to model the dyke in the centrifuge. The form of the grains is rounded (Figure 4.33) as a consequence of aeolian transportation (Buchheister, 2009). Figure 4.34 presents the grain size distribution of the material obtained by three different methods and compared with the curve given by the manufacturer (Buchheister, 2009). The three methods are: a sieve analysis at ETH Zurich, laser diffractometer analysis and automatic evaluation with software based on pictures zoomed forty times.

The curve obtained with the laser diffractometry presents the largest deviation from the size distribution given by the manufacturer. The maximum grain size has a difference of 196%, from 0.3 mm (manufacturer) to 0.89 mm (laser diffractometry).

This might be explained as a normal consequence of the technique. Experiments have demonstrated that differences in the particle size of silty and sandy materials generated by laser diffraction analysis and dry sieving deviations are significant (Beuselinck et al., 1998; Eshel et al., 2004; Blott & Pye, 2006).

The small differences between the curves obtained were not analyzed by Buchheister (2009) in great depth because it was not relevant for tests conducted at 1-g. Nevertheless, these differences might play an important role when they are scaled up to prototype scale, e.g. for a model scaled at 35-g, the maximal grain size would be 10.50 mm (manufacturer) and 31.15 mm (laser diffractometry).

Table 4.13: Parameters from the grain size distribution (adapted from Buchheister, 2009).

	Maximum grain size [mm]	**Minimum grain size [mm]**	**d_{10} [mm]**	**d_{30} [mm]**	**d_{50} [mm]**	**d_{60} [mm]**	**C_u [-]**	**C_c [-]**
Manufacturer	0.30	0.05	0.17	0.23	0.23	0.25	1.52	0.97
Sieve analysis (ETHZ)	0.50	0.08	0.14	0.21	0.23	0.25	1.79	1.26
Laser diffractometry	0.89	0.09	0.18	0.23	0.27	0.30	1.67	0.98
Software	0.70	0.09	0.12	0.18	0.24	0.26	2.17	1.04

Table 4.13 summarizes the parameters obtained from all grain size distributions. d_{10}, d_{30}, d_{50}, d_{60} are the particle sizes for which 10, 30, 50, and 60% of the material has a smaller grain size. C_u and C_c are the uniformity and curvature coefficients respectively. The material is classified as poorly graded sand (SP), according to the Unified Soil Classification System (USCS).

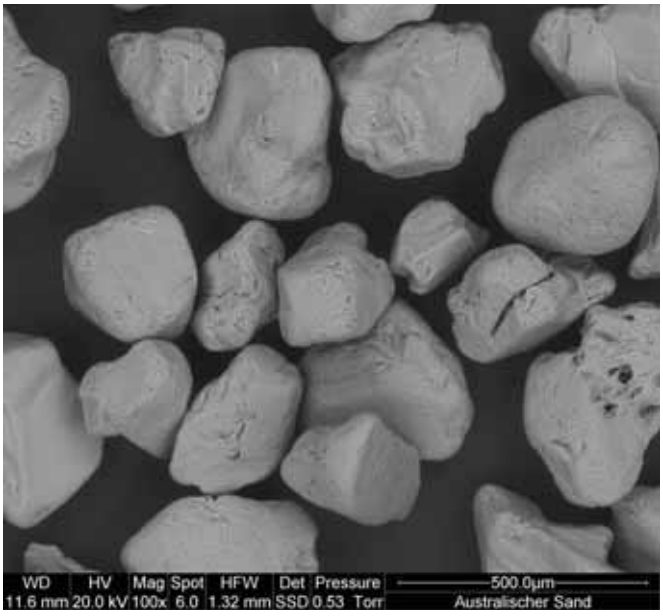

Figure 4.33: Image of grains of Perth sand taken with an Environmental Scanning Electron Microscope (ESEM) (after Buchheister, 2009).

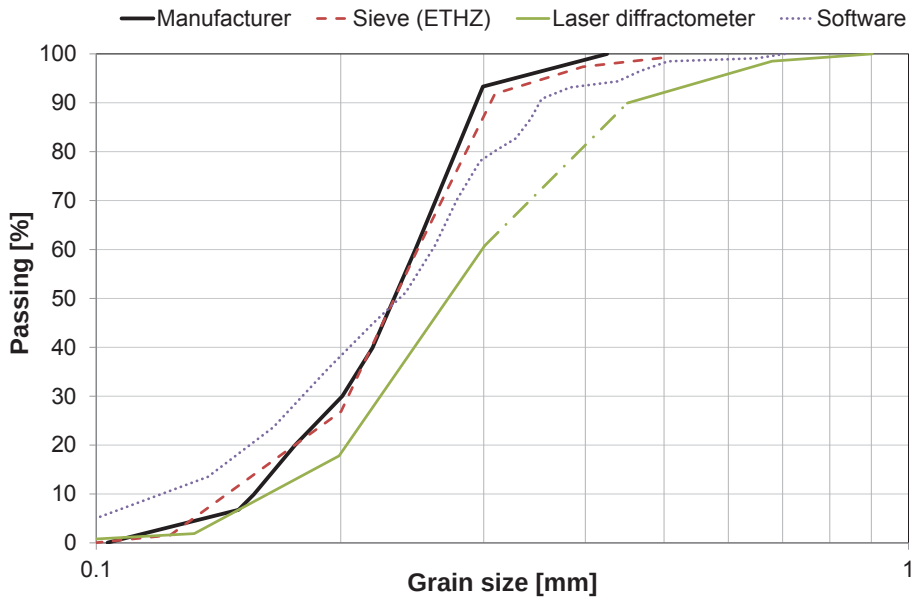

Figure 4.34: Grain size distribution of the Perth sand (adapted from Buchheister, 2009).

Table 4.14: Density properties of Perth sand.

Parameter	Symbol	Units	Buchheister, 2009	Nater, 2005	Average
Specific density	(ρ_s)	[kg/m^3]	2650	2650	2650
Minimum dry density	($\rho_{d\ max}$)	[kg/m^3]	1510	1515	1513
Maximum dry density	($\rho_{d\ min}$)	[kg/m^3]	1729	1801	1765
Minimum void ratio	(e_{min})	[-]	0.533	0.471	0.502
Maximum void ratio	(e_{max})	[-]	0.755	0.749	0.752

The density properties, as presented by Buchheister (2009) and Nater (2005) and their averages, are listed in Table 4.14. These were obtained following the international standards given by ASTM International (2002a, 2002b). The maximum dry density is 1765 kg/m^3, which corresponds to a void ratio of 0.502.

The maximum density of the material was also studied by using the pluviation technique. Pluviation consists in a rain of granular soil particles in a mold. It is obtained by gravity and using appropriate diffusers (Lo Presti et al., 1992). This method was used by Nater (2005) and Arnold (2011). Whereby, a cylindrical canister of 1.0 m height × 0.45 m diameter with a hopper shape at one end was used.

The influence of flow rate and falling height was investigated by modifying the hopper of the canister to obtain constant flow rates. A disc with a hole of defined diameter was placed at the hopper aperture (Figures 4.35a and 4.35b). The depositional intensity, defined as the weight of soil falling per unit area per unit time (Lo Presti et al., 1992), is presented in Table 4.15 for each hole diameter. The depositional intensity varies by the same amount as the area of the drilled hole. The sand flows through a tube with an attached mesh (Figures 4.35c and 4.35d). This mesh ensures the uniformity of the sand rain in a similar fashion to that pre-

sented by Cresswell et al. (1999). A sieve was also used to pluviate the material (in Figure 4.35e).

Nine pots of known volume were located in a geometrical array as shown in Figure 4.35f. Diverse sizes of pots were used to decrease the influence of pot dimensions (open area and height). Figure 4.36 illustrates the dry density, as an average of all nine pots, obtained for all four depositional intensities and with the sieve for falling heights between 0.1 m and 0.7 m.

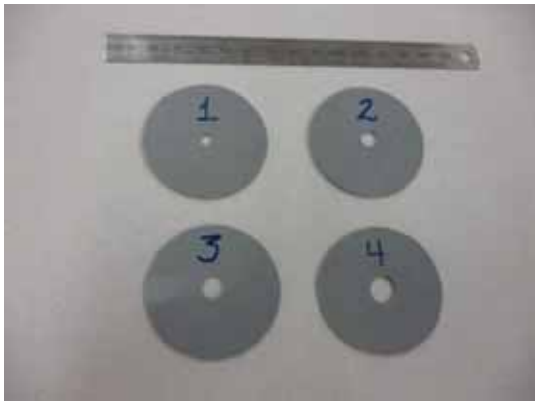

a) Discs with different hole diameter were prepared.

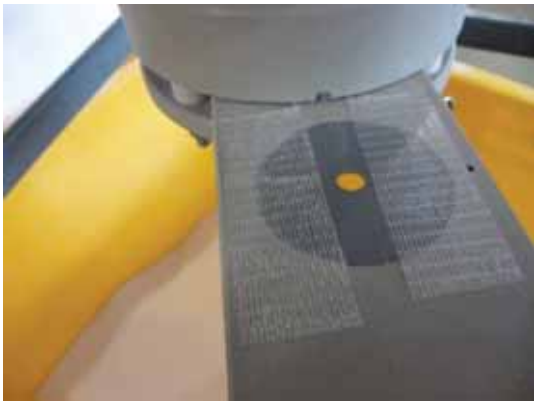

b) Each disc is placed in the aperture of the canister.

c) The sand flows inside a tube to a mesh.

d) The sand is uniformly pluviated.

e) A sieve is also used to pluviate the sand.

f) Geometrical array of pots.

g) Dry pluviation with the canister.

Figure 4.35: Procedure used to analyze the dry densities obtained with dry pluviation.

In general, larger densities are obtained with a higher falling height and smaller depositional intensity, although the trends are not fully uniform. These might be explained as a consequence of one or more of the aspects affecting the accommodation of the grains during pluviation and listed by Vaid & Negussey (1984): the actual void ratio for a given height drop depends on some average grain size, gradation, and characteristics of the mold (geometry and smoothness). Nevertheless, the results are generally in concordance with the previous findings from Vaid & Negussey (1984), Lo Presti et al. (1992) and Cresswell et al. (1999).

The use of the sieve for dry pluviation allows for a large flow rate (approx. 6000 gr/min) but keeping a low depositional intensity, hence a larger dry density.

Table 4.15: Flow rates and depositional intensities obtained for different hole diameters on the disc and the sieve for dry pluviation.

Disc ID	Hole diameter [mm]	Flow rate [gr/min]	Depositional intensity [gr/min/cm^2]
1	5	225	16.24
2	7.1	637	45.98
3	8.7	1093	78.89
4	10	1638	118.19
Sieve	450	6000	12.22

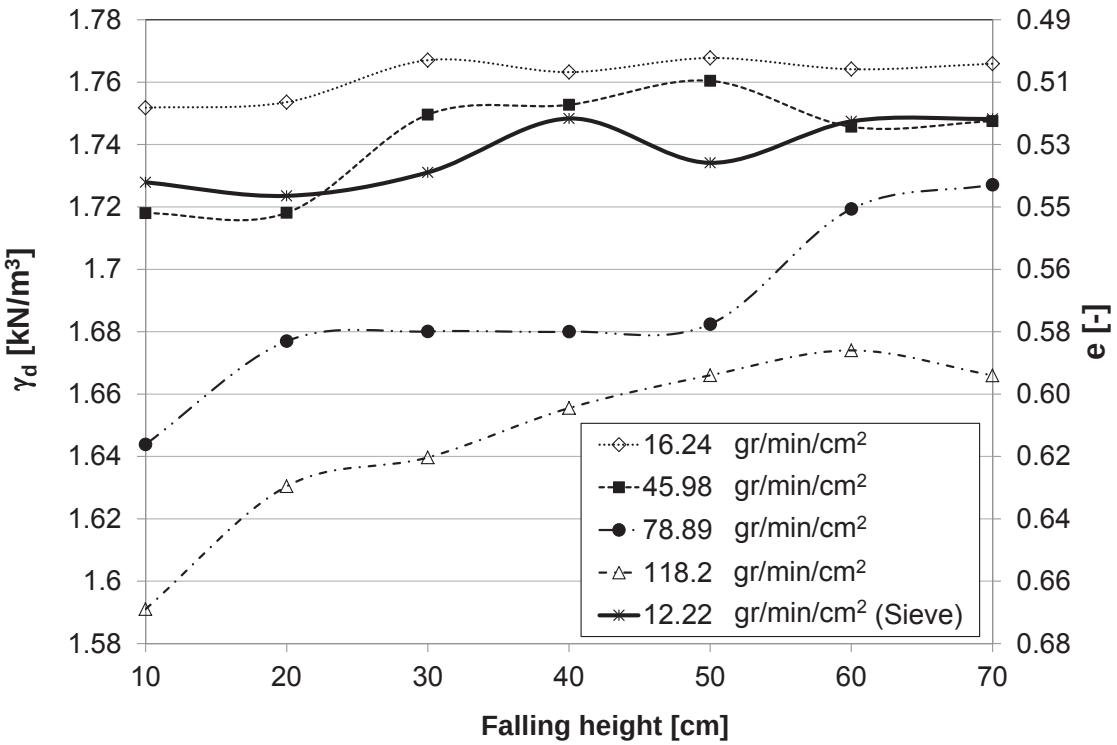

Figure 4.36: Dry unit weights and void ratios obtained by dry pluviation.

Figure 1.2 presents the results of a Proctor modified test following the standard by ASTM International (2009). The dry unit weight obtained varies between 15.78 and 16.30 kN/m^3, with an optimal gravimetric water content of 13.5%, which is close to the value at which the dyke model is stable to be tilted through 90° to be placed in the drum centrifuge (Morales et al., 2013).

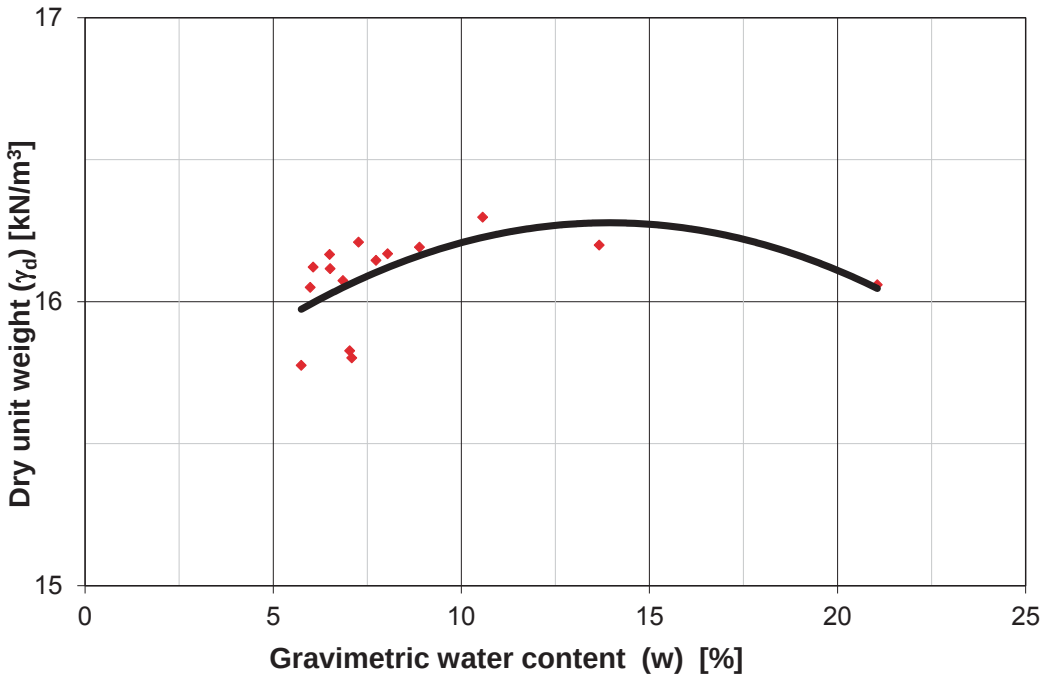

Figure 4.37: Dry density obtained with the Proctor modified test.

4.3.1.2 Mechanical properties

Compressibility characteristics

Nater (2005) and Arnold (2011) report the compressibility of dry Perth sand in an oedometer. Figure 4.38 shows the variation of the confined deformation modulus *(M_E)* obtained from the tests (after Arnold, 2011), when increasing the normal stress.

The confined deformation modulus *(M_E)* is commonly used in Germany and Switzerland (Lang et al., 2011) and is defined in Equation 4.30, where $\Delta\sigma'$ is the vertical effective stress increment and $\Delta\varepsilon$ is the vertical strain. It is the inverse of the coefficient of volume change *(m_v)* (Lambe & Whitman, 1969).

$$M_E = \frac{\Delta\sigma'}{\Delta\varepsilon} = \frac{1}{m_v} \qquad 4.30$$

The influence of the density on the stiffness is shown in Figure 4.39 (after Nater, 2005). The figure corresponds to a reference normal stress of 50 kPa. It is notable that the stiffness increases more than four times between the minimum and maximum values of dry density.

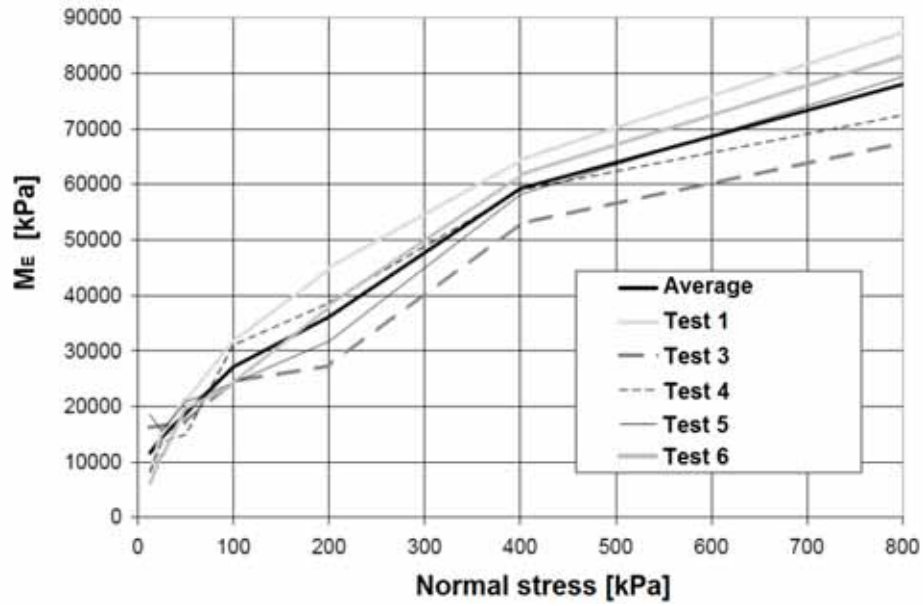

Figure 4.38: Oedometric confined deformation modulus M_E at different normal stresses applied to Perth sand (adapted from Arnold, 2011).

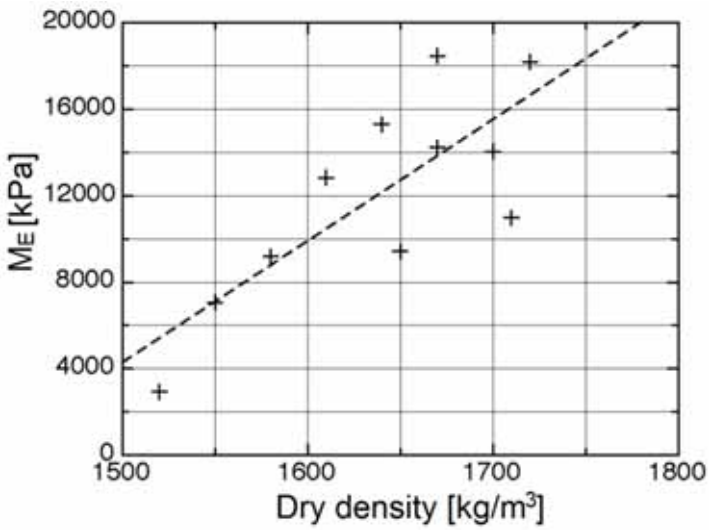

Figure 4.39: Oedometric confined deformation modulus M_E as function of the dry density of Perth sand (adapted from Nater, 2005).

A series of tests was carried out under oedometric conditions to analyze the influence of the unsaturated state of the soil specimen. The tests were performed at different values of controlled suction. The specimens were prepared in the Fredlund apparatus, described in Section 2.2.2.5. The values of suction were selected to cover the range of suctions of the sand (cf. Section 4.3.1.3).

Dry sand was pluviated from a height of 0.30 m with the help of a funnel, which has adapted the disc number 1 of Figure 4.35a (Figure 4.40a). It has an aperture of 5 mm and generates a depositional intensity of 16.24 gr/min/cm^2 (Table 4.15). This guarantees a constant density in all the prepared specimens. The specimen is then saturated from the bottom, as is done

for the built model (cf. Section 4.3.2). Finally, a PVC plate (5 mm thick) is placed over the saturated material, for a uniform load, and the Fredlund cell is closed. Pressurized air is applied to increase the matric suction. Once the water is drained from the specimen and the desired suction value is reached, the vertical stress of the specimen is increased with the sequence given in Table 4.16.

a) Dry pluviation.

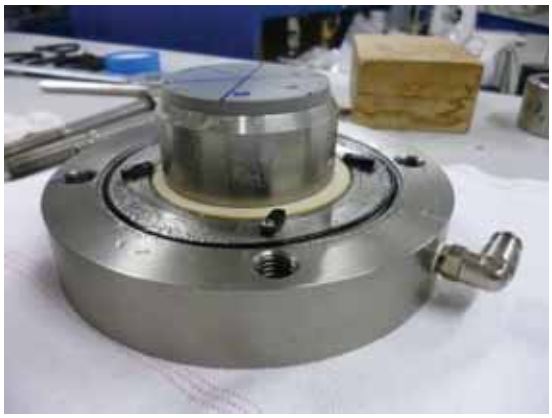

b) Specimen prepared with the PVC loading plate.

Figure 4.40: Specimen for unsaturated oedometric test on Perth sand.

Table 4.16: Normal stresses for tests carried out on unsaturated specimens of Perth sand under oedometric conditions in unsaturated state.

Step	Normal stress [kPa]	Step	Normal stress [kPa]
1	34	11	171
2	41	12	86
3	82	13	171
4	171	14	342
5	257	15	513
6	342	16	684
7	513	17	1027
8	684	18	1369
9	513	19	2
10	342		

The results of all tests are plotted in the *ln(1+e)* vs *ln(p)* space, and presented in Appendix 3. The axes were selected to be consistent with the proposal by Mašín (2005) and Mašín & Khalili (2008). The values parameters λ^*, κ^* and N are presented as a function of suction in Table 4.17 and Figures 4.41, 4.42 and 4.43. These parameters are used in the hypoplasticity formulation by Mašín (2005). Their change with suction is required for the unsaturated formulation by Mašín & Khalili (2008).

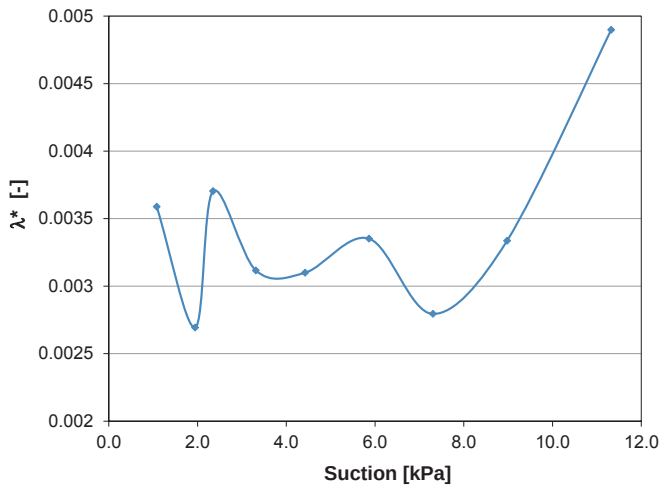

Figure 4.41: Variation of parameter λ with suction for Perth Sand at an average void ratio of 0.52.*

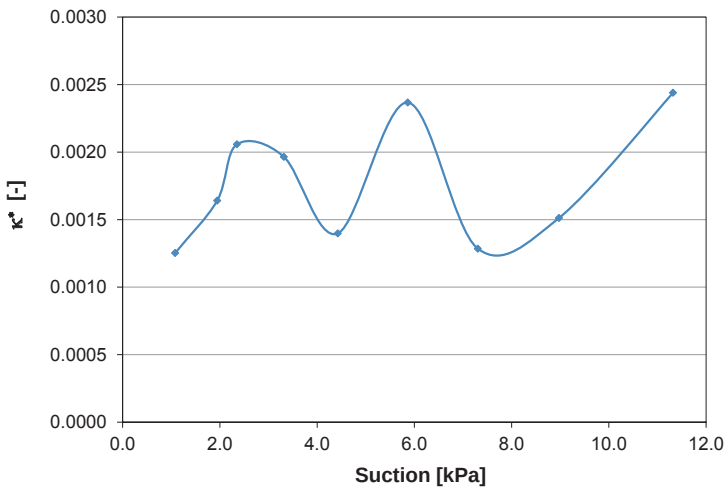

Figure 4.42: Variation of parameter κ with suction for Perth Sand at an average void ratio of 0.52.*

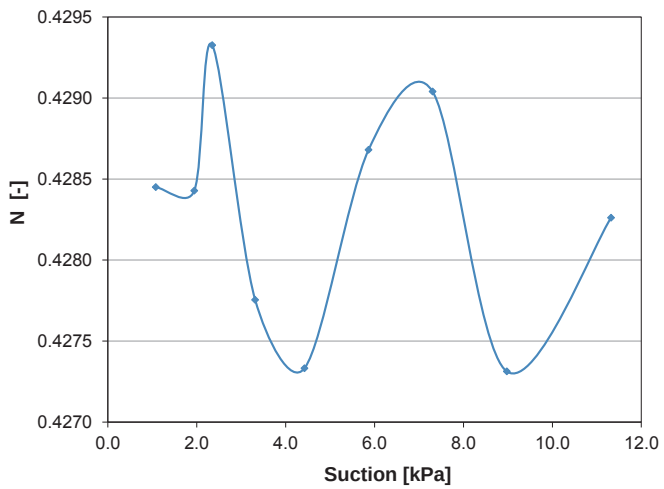

Figure 4.43: Variation of parameter N with suction for Perth Sand at an average void ratio of 0.52.

Table 4.17: One-dimensional normal stress-volume change parameters of Perth sand for different values of suction.

Test	e [-]	Suction [kPa]	λ* [-]	κ* [-]	N [-]
1	0.521	1.080	0.0036	0.0013	0.4285
2	0.523	1.945	0.0027	0.0016	0.4284
3	0.527	2.350	0.0037	0.0021	0.4293
4	0.520	3.315	0.0031	0.0020	0.4278
5	0.516	4.425	0.0031	0.0014	0.4273
6	0.520	5.865	0.0034	0.0024	0.4287
7	0.520	7.305	0.0028	0.0013	0.4290
8	0.514	8.975	0.0033	0.0015	0.4273
9	0.514	11.320	0.0049	0.0024	0.4283

Shear strength characteristics

The shear strength characteristics of dry Perth sand have been investigated by Nater (2005), Buchheister (2009) and Arnold (2011), through a range of CIDC (consolidated isotropically drained compression) triaxial tests. Nater (2005) performed 10 tests at different values of relative density (D_R) and cell pressures (Figure 4.44). The critical friction angle ϕ'_{crit} varies between 29° and 34° and the maximum friction angle ϕ'_{max} between 31° and 38°. The relative density has only a small influence on ϕ'_{crit}, whereas a clear difference in the values obtained for ϕ'_{max} is found for values of D_R < 50%. The cell pressure did not appear to exert any influence on the results within the range tested.

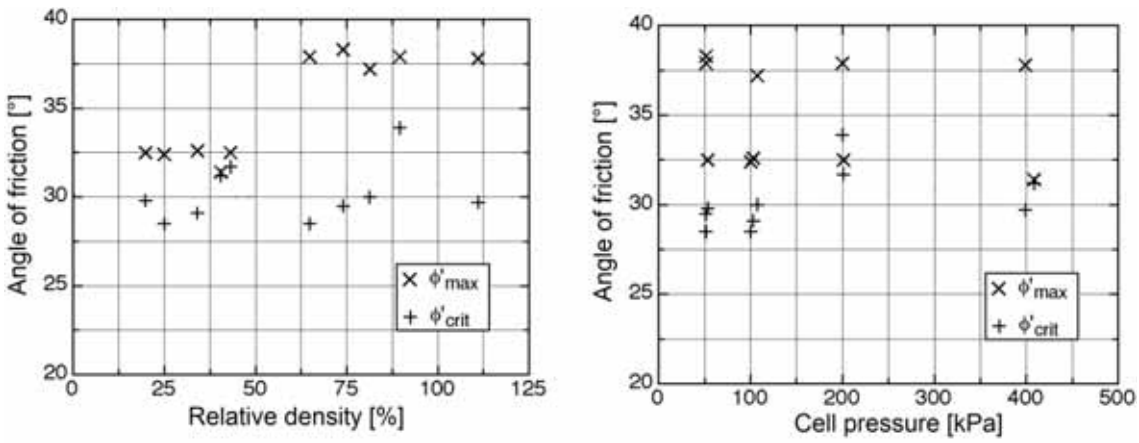

Figure 4.44: Influence of the relative density and cell pressure on the maximum and critical friction angles (modified from Nater, 2005).

Buchheister (2009) reports the results of eight CIDC triaxial tests in dry sand, with relative densities between 27 and 70%. These values correspond to a loose to medium dense compacted sand (Lambe & Whitman, 1969) and only the critical state angle of friction is reported for each test. The maximum friction angle is reported to be 32°, which is consistent with the results shown in Figure 4.44.

Arnold (2011) presents results for CIDC triaxial tests on dense sand. The average value of ϕ'_{crit} is 29.7°, whereas ϕ'_{max} ranges between 39-42° for cell pressures of 40-10 kPa, respectively. Again, the values are consistent with those obtained by Nater (2005) and presented in Figure 4.44. The results are summarized in Table 4.18.

Table 4.18: Results of triaxial tests on dry sand (adapted from Buchheister, 2009; Arnold, 2011).

Test	e [-]	D_R [%]	σ'_3 [kPa]	ϕ'_{max} [°]	p'_{crit} [kPa]	q'_{crit} [kPa]	ϕ'_{crit} [°]	ψ [°]	c' [kPa]
ARN_1	0.540	65.2	10	41.9			29.5	12.4	0
ARN_2	0.530	68.5	15	39.3			29.8	9.5	0
ARN_3	0.530	68.5	20	39.3			29.7	9.6	0
ARN_4	0.510	74.4	40	39.0			29.6	9.4	0
BUCH_1	0.696	26.8	53.1	*32.0* *	88.9	107.5	30.21		
BUCH_2	0.699	25.3	52.4	*32.0* *	78.9	79.3	25.50		
BUCH_3	0.658	43.5	100.3	*32.0* *	167.6	201.9	30.11		
BUCH_4	0.683	32.5	98.7	*32.0* *	159.5	182.5	28.72		
BUCH_5	0.653	46.0	205.2	*32.0* *	328.1	368.7	28.24		
BUCH_6	0.630	56.1	205.4	*32.0* *	365.4	480.1	32.61		
BUCH_7	0.638	52.8	406.5	*32.0* *	727.6	963.5	32.85		
BUCH_8	0.598	70.7	401.3	*32.0* *	629.5	684.7	27.41		

* Indicated as an average value

Two series of triaxial tests were carried out on unsaturated sand for this research project. One series was performed at constant gravimetric water content (undrained condition), whereas the second series was conducted under drained conditions, i.e. the water was allowed to drain out of the sample.

The specimens were prepared in a similar fashion to the oedometer tests in the previous section, as shown in Figure 4.45. The dry sand was pluviated from a height of 0.30 m. The specimen was then saturated from the bottom, and the excess water was pumped out later until an average gravimetric water content of 13% was obtained.

The specimen is then placed inside the cell and connected to two taps and to the loading frame. A water pressure transducer (Keller PR11) was mounted on the line for one of the taps to measure pore pressure and suction. The second tap was connected to a volume change device. This tap was left open during shearing for the drained condition and left closed for the tests carried out under undrained conditions.

The results in the *p'-q* space (Equations 4.31 and 4.32) are shown in Figures 4.46 and 4.47. The other tests results are shown in Appendix 4. The effective stresses were calculated from the Bishop effective stress (cf. Section 2.2.1.2). Table 4.19 presents the values obtained from the tests. The values of critical and maximum friction are quite similar angles do not present too much difference with the values obtained for the dry sand. However, an apparent cohesion is deduced for the peak strength mobilized when a straight line is fitted to the data.

This apparent cohesion is 10.5 kPa for the drained condition and 17.6 kPa for the undrained. This apparent cohesion is a direct consequence of the matric suction causing the grains to adhere together and implying a shear resistance at p'=0 kPa. This apparent cohesion is lost as the material reaches the critical state.

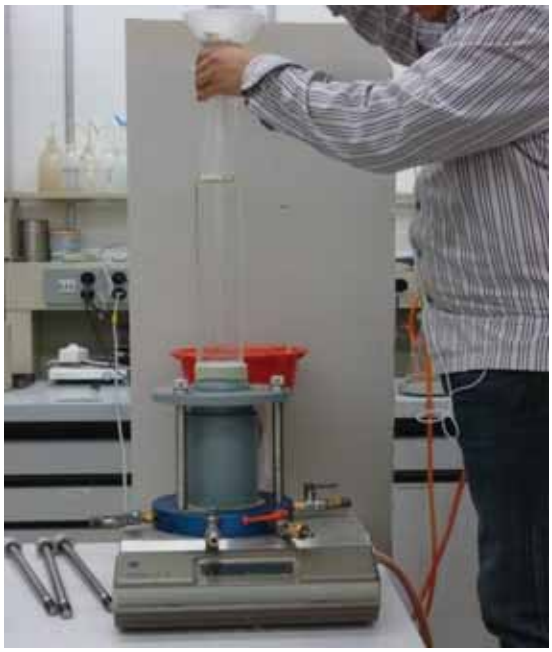

a) Dry pluviation of sand from 0.30 m height.

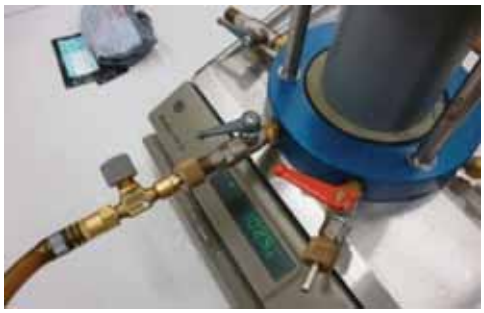

b) Water is added from the bottom until the specimen is saturated.

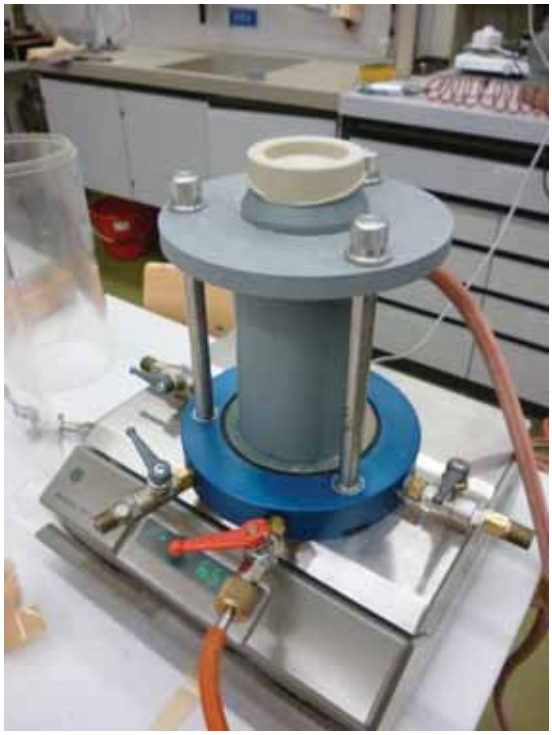

c) Water is pumped out until a gravimetric water content of 13% is reached.

d) The sample is placed in the cell, consolidated and sheared.

Figure 4.45: Procedure followed for the unsaturated triaxial tests.

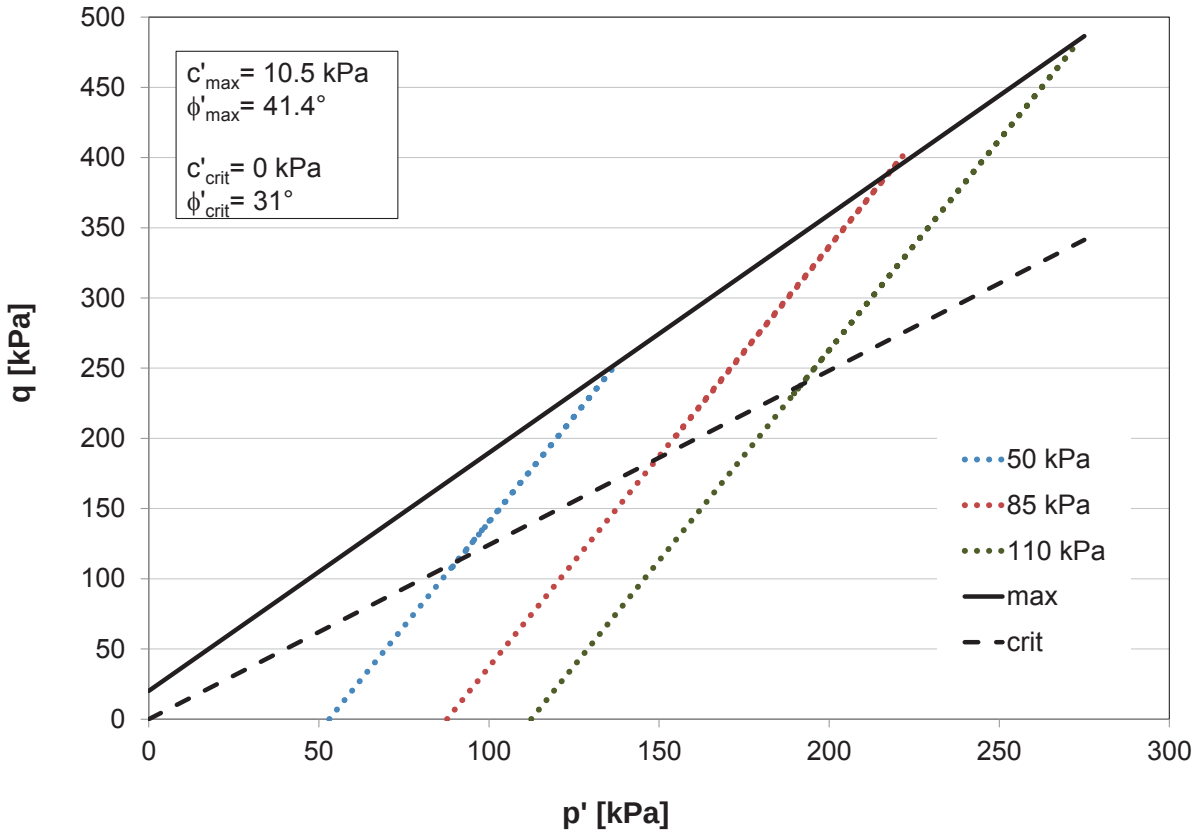

Figure 4.46: Results in p'-q space for the tests under drained conditions (CIDC).

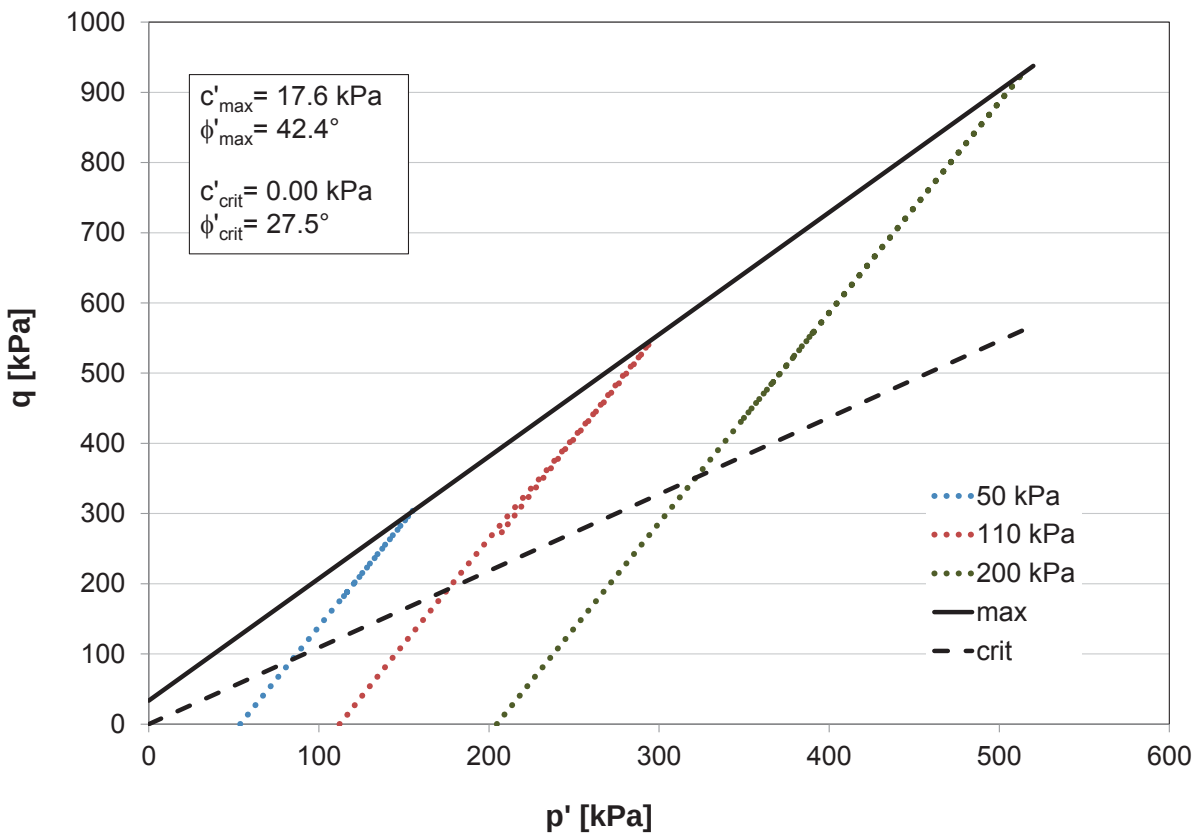

Figure 4.47: Results in p'-q space for the tests under undrained conditions (CIUC).

$$p' = \frac{\sigma_1 + 2 \cdot \sigma_3}{3} + \left[\left(\frac{AEV}{u_a - u_w} \right)^{0.55} \cdot (u_a - u_w) \right] \quad 4.31$$

$$q = \sigma_1 - \sigma_3 \quad 4.32$$

$$M = q / p' \quad 4.33$$

Table 4.19: Results obtained from 12 triaxial tests on unsaturated Perth sand.

		σ_3 [kPa]	e [-]	p' [kPa]	q [kPa]	M [-]	ϕ' [°]	c'_{app} [kPa]
Drained (CIDC)	Maximum	50	0.52	136.09	248.94	1.80	41.4	10.5
		85	0.54	221.73	401.57			
		110	0.46	271.54	477.22			
	Critical	50	0.52	88.38	105.72	1.25	31.0	0.0
		85	0.54	153.68	197.77			
		110	0.46	189.52	231.47			
Undrained (CIUC)	Maximum	50	0.53	156.01	306.44	1.77	42.4	17.6
		100	0.54	295.15	544.02			
		200	0.54	514.13	928.50			
	Critical	50	0.53	130.94	175.93	1.16	27.5	0.0
		100	0.54	241.16	269.64			
		200	0.54	410.47	433.88			

4.3.1.3 Hydraulic properties

The hydraulic conductivity of Perth sand in the saturated state was determined from a constant head test (Bardet, 1997). The specimen was prepared in a cylindrical container of 0.10 m diameter and 0.11 m height, at a void ratio of 0.56.

The specimen was saturated allowing de-aired water to flow through for one hour with a hydraulic gradient of 4.62. After that, 25 measurements were taken until the value of the estimated hydraulic conductivity was stable (Figure 4.50). The saturated hydraulic conductivity was determined as 0.0165 m/s for e = 0.56.

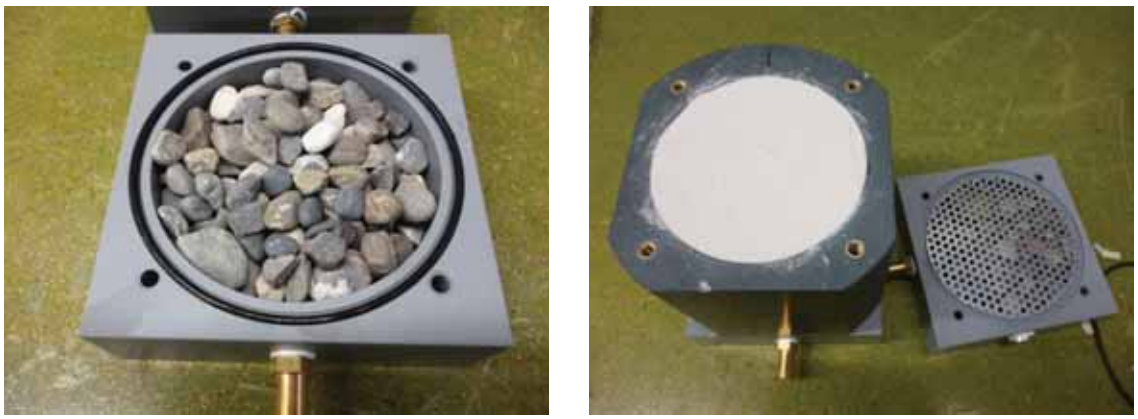

Figure 4.48: Specimen to estimate the hydraulic conductivity in saturated Perth sand.

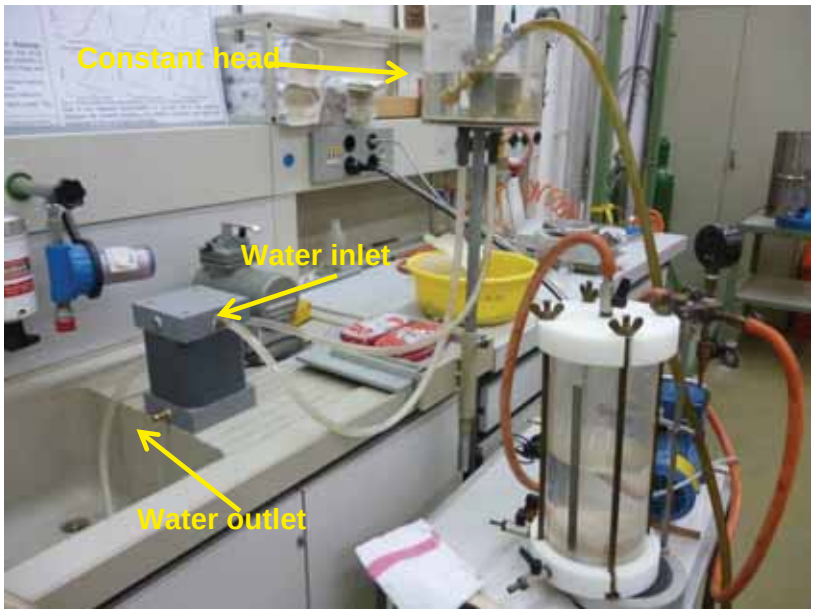

Figure 4.49: Set up for constant head test.

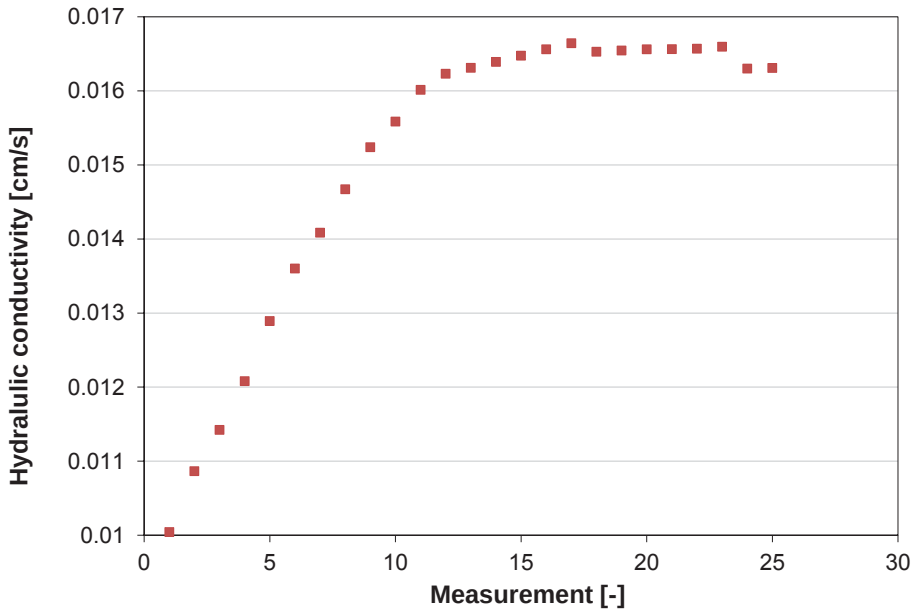

Figure 4.50: Results for the determination of hydraulic conductivity of saturated Perth sand (e=0.56).

A comparison between the value of hydraulic conductivity determined in the constant head test and the values estimated with the formulation by Kozeny-Carman (Kozeny, 1927; Carrier, 2003) (Equation 2.44) is presented in Table 4.20. The latter is an analytical formulation, which uses the grain-size distribution to estimate the saturated hydraulic conductivity. All four grain-size distributions from Section 4.3.1.1 were used for the comparison.

Three estimations give a value above that determined and one gives a smaller value. The estimations fall in the range of half and two times the measurement. However, Chapuis &

Aubertin (2003) comment that this range of accuracy of the Kozeny-Carman formula is typical.

Table 4.20: Hydraulic conductivities estimated with the Kozeny-Carman equation compared with the value determined in the laboratory (k_{sat} = 0.165 cm/s at e = 0.56).

	Estimated hydraulic conductivity [m/s]	**Estimated / determined**
Vendor	0.0087	0.53
Sieve ETHZ	0.0286	1.74
J-image	0.0219	1.32
laser	0.0316	1.92

In addition, knowledge of the hydraulic parameters under unsaturated conditions is needed in order to model the behavior of the soil properly. This includes the relationship between volumetric water content θ and the hydraulic conductivity, as a function of the water suction. The former is often referred to as the Soil Water Retention Curve (SWRC) (cf. Section 2.2.2.4).

Figure 4.51 shows the SWRC based on the axis-translation technique (Fredlund & Rahardjo, 1993), as obtained from a specimen of Perth sand that was reconstituted to a predefined void ratio of 0.55 in a Fredlund apparatus, and subjected to both drying and wetting paths. The void ratio of 0.55 is similar to that in the centrifuge models, after finishing sample preparation. It is a key point, as the SWRC is non-unique and is highly dependent on density, as demonstrated e.g. by Askarinejad et al. (2010) and Morales et al. (2011).

The main parameters deduced from the SWRC are the Air Entry Value (AEV), defined as the value of matric suction at which the air enters into the voids and begins to desaturate the soil matrix; and the Water Entry Value (WEV), which is the value of matric suction at which the water starts to displace air in the porous medium soil during a wetting process (Wang et al., 2000). θ_{sat} is defined as the volumetric water content when the material is saturated, whereas θ_{res} is the residual volumetric water content, i.e. the amount of water that remains trapped in the soil even at high matric suctions. A summary of the values obtained is given in Table 4.21.

Table 4.21: Hydraulic properties of Perth sand under unsaturated conditions, e = 0.55.

AEV [kPa]	**WEV [kPa]**	**θ_{sat} [m^3/m^3]**	**θ_{res} [m^3/m^3]**
2.40	*9.50*	*0.36*	*0.03*

The SWRC presented in Figure 4.51 shows a hysteretic response when the specimen is subjected to a drying path followed by a wetting process. The drying path is horizontal until the Air Entry Value (AEV) of 2.4 kPa is reached. From that point on, the path follows a relatively steep curve until it reaches the θ_{res}, whereupon the wetting process begins. The material begins to saturate once the Water Entry Value (WEV) of 9.5 kPa is reached and follows a flatter gradient in (θ-s) space, without overlapping with the curve obtained for the drying path.

The hydraulic conductivity function (Figure 4.52) was deduced from the SWRC, as indicated by Fredlund & Xing (1994).

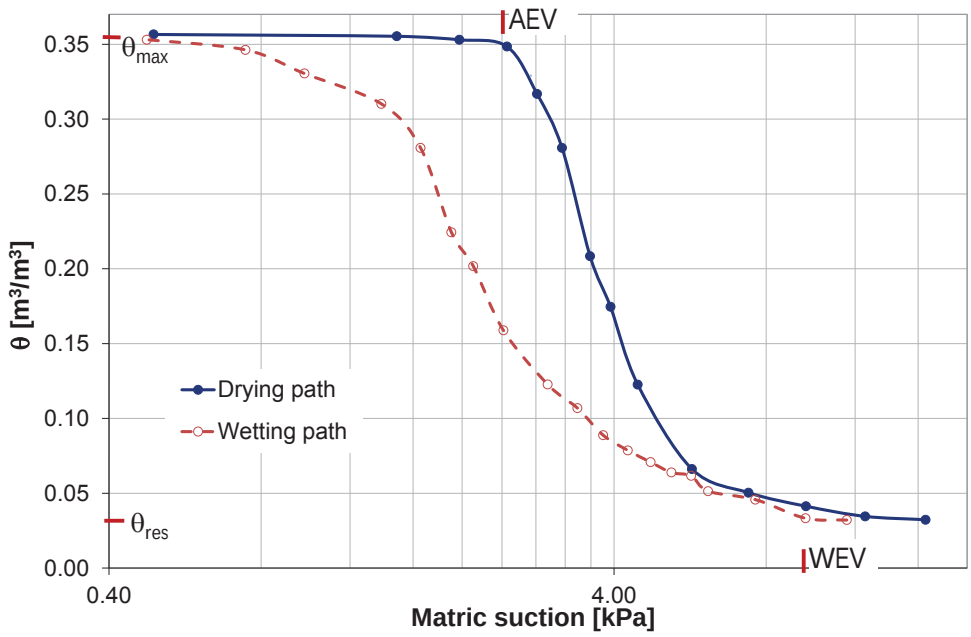

Figure 4.51: Soil Water Retention Curve (SWRC) obtained with the axis-translation technique for Perth sand, e=0.55.

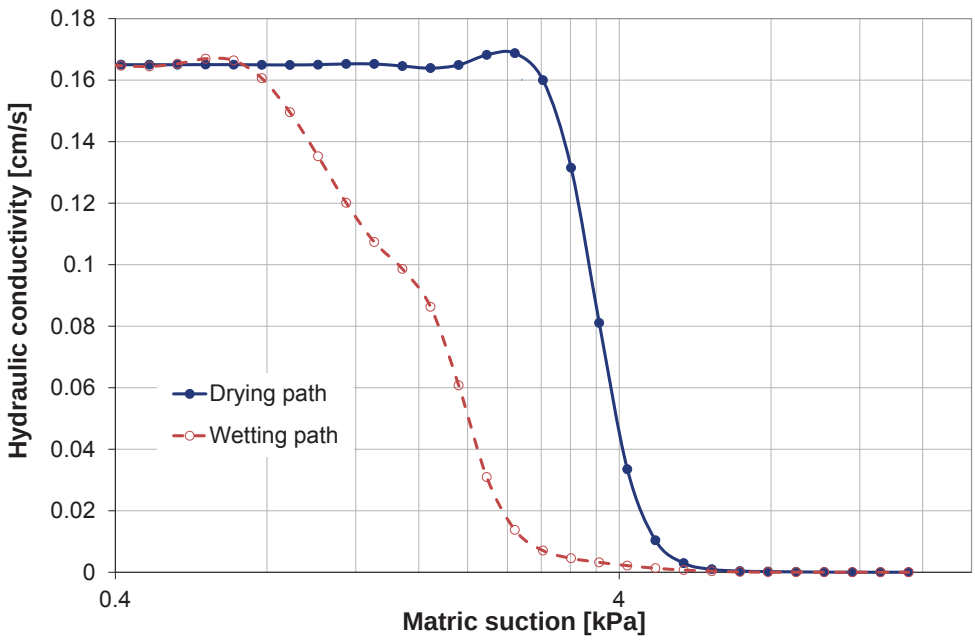

Figure 4.52: Hydraulic conductivity function for Perth sand, e=0.55.

4.3.2 Procedure for model preparation

The procedure followed to prepare the centrifuge model is based on the procedure given in Nater (2005). Firstly, the box is filled completely with sand by dry pluviation (Figures 4.54a and 4.54b), with particles falling freely with a small depositional intensity from a constant

height of 0.90 m from the bottom of the box. According to Cresswell et al. (1999), dry pluviation is a well-known and widely used method for the preparation of sand samples for laboratory testing, and it has the advantage over tamping and vibratory methods of compaction of achieving a uniform density without grain crushing. It also prevents localized shearing zones and segregation of any layer that might appear if the dry soil is poured into the container (Figure 4.53).

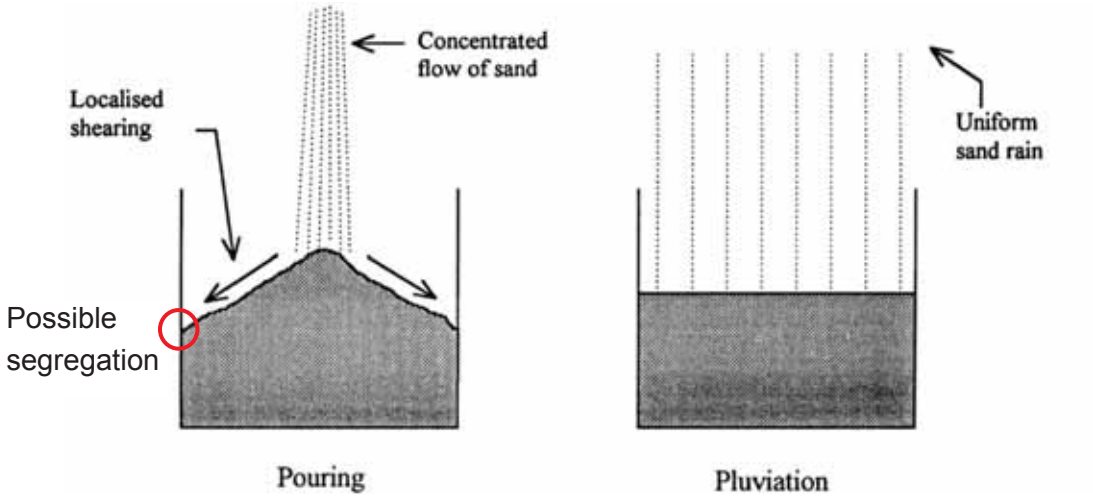

Figure 4.53: Differences between pouring and pluviation of sand in air at the same rate (after Cresswell et al., 1999).

Secondly, the sand is saturated by adding water from the bottom of the model through the lower drainage ports in the lateral walls and in the central piece of the modular base (Figure 4.54c). The water height is set slightly above the soil surface. Once the water table reaches the surface of the soil model, water is then drained out of the sample until a gravimetric water content of 13% is achieved (Figure 4.54d). Vacuum is applied to suck the water out to the required degree through the bottom of the box by using a pump, and pipes which are connected to the filters on the modular base. The water content is not uniformly distributed in the soil mass after pumping. So, an equalization period of 6 hours is required.

The slopes are shaped next. This is done with a specially designed template and a cutting blade (cf. Section 4.3.3 and Figure 4.54e). Finally, the model is tilted through 90° to be placed in the drum channel (Figure 4.54f). The increase of stiffness, as a result of the suction in the soil, allows the surface to remain stable in the vertical plane for a short period of time, which is long enough to place and fix the model into the channel of the drum and to start the centrifuge test.

The measured densities before testing in the centrifuge are shown in Table 4.22 for different points on the bottom of the model. These were measured with standard cylindrical sampling tubes of 50.8 mm (2 inches) in diameter and 25.4 mm (1 inch) in height. It is seen that consistent densities can be achieved with the method described above.

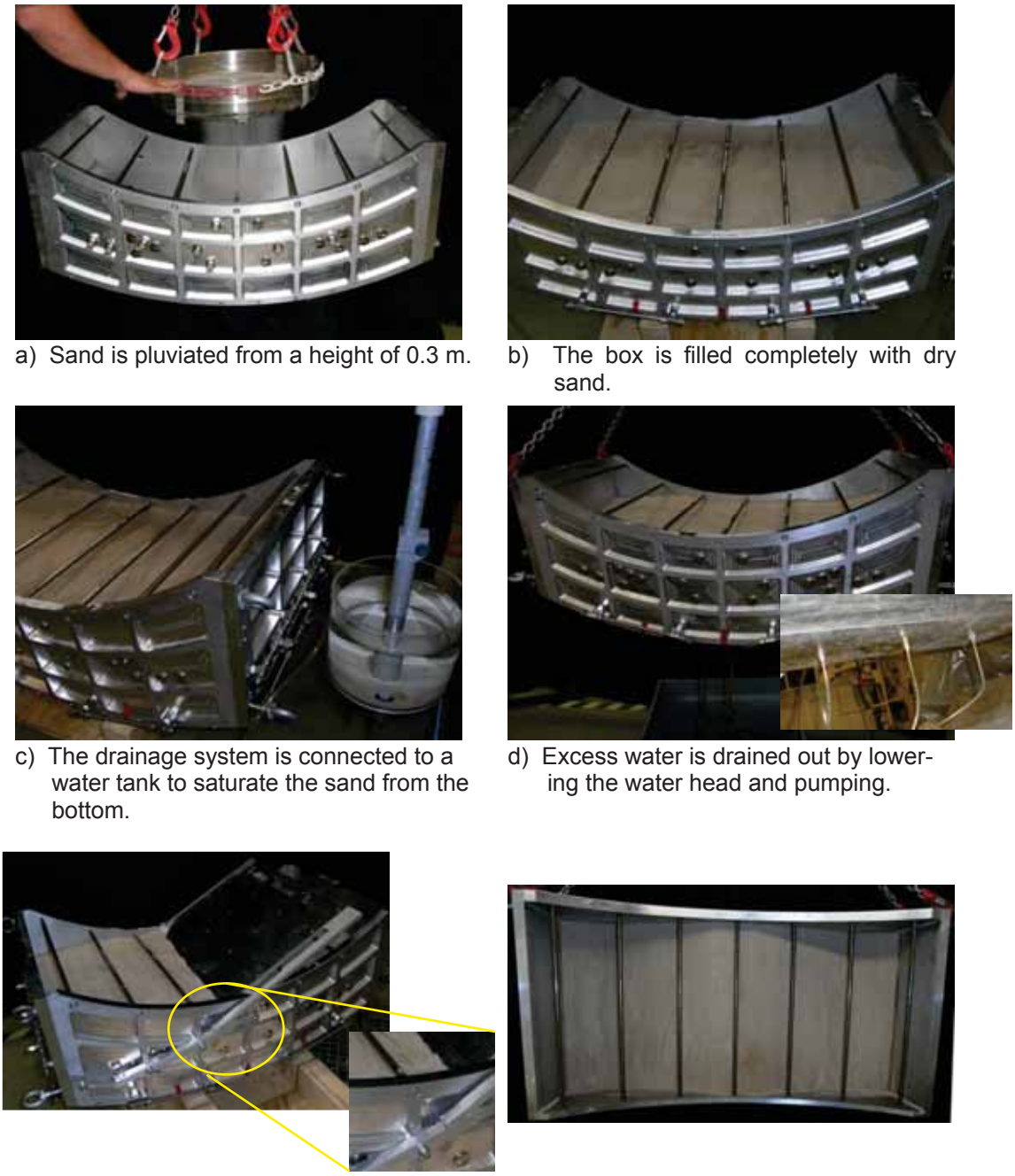

a) Sand is pluviated from a height of 0.3 m.

b) The box is filled completely with dry sand.

c) The drainage system is connected to a water tank to saturate the sand from the bottom.

d) Excess water is drained out by lowering the water head and pumping.

e) The slopes are shaped with the cutting devices.

f) Once the model is finished, it is tilted through 90°.

Figure 4.54: Procedure for building the dyke model.

Table 4.22: Densities achieved with the proposed construction method.

Sample	Volume [mm^3]	Soil weight [N]	w [%]	γ [kN/m^3]	γ_d [kN/m^3]	e [-]
1	51.48	0.867	17.47	16.86	14.35	0.57
2	51.48	0.872	16.89	16.95	14.50	0.58
3	51.48	0.877	18.14	17.05	14.43	0.57

4.3.3 Slopes shaping system

According to the US Army Corps of Engineers (2000) guidelines on levee construction, a 1V on 2H slope is generally accepted as the steepest slope that can be constructed easily and ensure stability, whereas a 1V on 3H slope is the steepest slope that can be traversed conveniently with conventional mowing equipment . It can be accessed during inspections without difficulty. Following these guidelines, a new system was developed to cut slopes with gradients 1:2.0, 1:2.5 and 1:3.0.

The system has a rigid cutter blade (Figure 4.55) and two guiding pieces with the desired slope angles (Figure 4.56). All of the components of the system are made of aluminum. The cutter consists of a plate with a sharp edge and two lateral limbs, whose edges are aligned with the plate edge (Figure 4.55b). The guiding pieces define the shape of the slopes in the model, which is not completely straight, as the increase of the gravity level with model depth is taken into account. The guides constructed for the three different slope gradients are shown in Figure 4.56 for an increased gravity of 33.3-g at the centroid of the dyke.

Once the container is filled with unsaturated soil (Figure 4.54d), the guiding pieces are attached to the bottom and top plates. Firstly, excess material is removed manually with a trowel just above the expected slope surface. The cutter is then used to remove the remaining excess material and to create the final shape of the dyke model, as shown in Figure 4.54e. As the guides and the sharp edge of the cutter are aligned, the soil inside the box has the same shape as the slope guides. Any combination of slope gradients is possible for water and air-sides, as the slope guides are interchangeable. Guides of different geometries might also be manufactured for future projects.

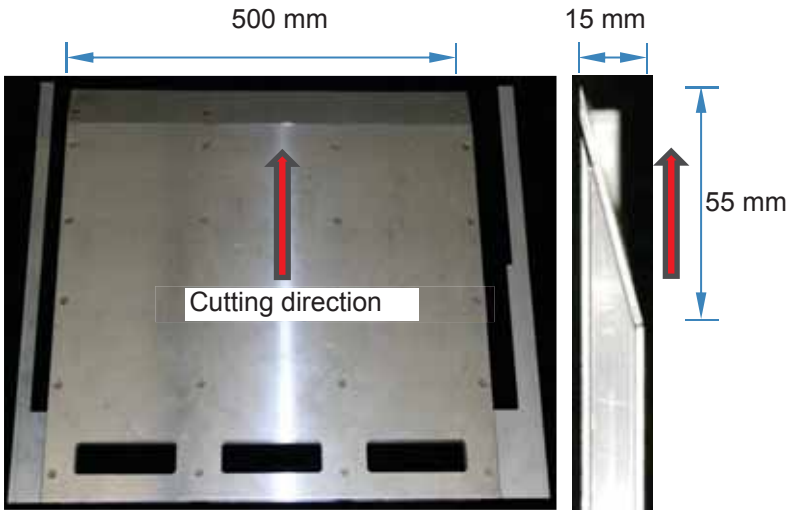

a) Plan view. *b) Side view.*

Figure 4.55: Soil cutter blade used to remove excess soil and to shape the model.

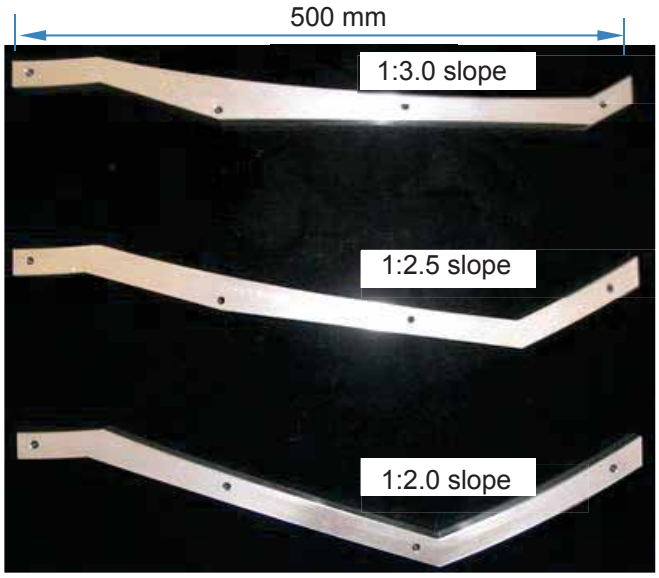

Figure 4.56: Slope guides. These are located to the side of the box and the cutter blade is pushed along them to shape the dyke model.

4.3.4 Construction & installation challenges

Morales et al. (2013) present an analysis of the stability of the model preparation. Notwithstanding the expected response of the model, a series of challenges occurred.

The first requirement was to find the optimal water content. Although it seems a simple task, it required several trials to find a range of water contents within which the model remains stable after rotation and installation in the drum centrifuge. When the soils contains too much water, the suction is reduced and the model slumps as a single block (Figure 4.57a). When the model has too little water, it usually remains stable after tilting. However, it becomes quite unstable with small vibrations due to the inhomogeneous distribution of the water. In that case, the model breaks into small blocks, as shown in Figure 4.57b. Finally, it was found that the gravimetric water content of the model should be between 12 and 14%, a value which is coincidentally close to the optimal water content found from the modified Proctor test (cf. Section 4.3.1.1).

a) Model slumping with high water content. b) Model failing in blocks with low water content.

Figure 4.57: Models that became unstable due to incorrect water content.

Another challenge was a gap of approximately 0.5 mm, which typically developed while installing the model inside the drum centrifuge (Figure 4.58). This deformation is generally caused by vibrations when sliding the box containing the model into the drum channel.

The soil deforms and an active shear wedge is developed when the test is running and the acceleration in the model is increased (Figure 4.58). This does not affect the stability of the model, but it leaves a loose zone behind it. When flows through this zone during the flooding phase, the supply flow rate is insufficient for the water table to rise to the top of the dyke, foiling the plans for overflow.

Two measures were adopted to prevent this. Firstly, a PTFE (generic term for Teflon®) film is stuck to the top face of the bottom annular ring of the drum channel, as well as to the external lower face of the bottom of the strongbox. A Teflon-Teflon contact has an approximate coefficient of friction of 0.04, reducing the force required to push the strongbox into the drum.

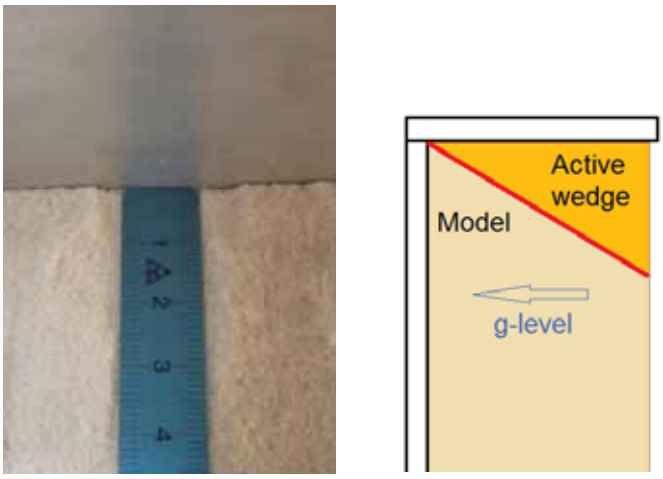

Figure 4.58: (left) Gap on top of the tilted sand model after installation inside the drum centrifuge; (right) active wedge that develops after increasing the g-level.

A thin layer of a soil composed of a mixture of the Perth sand with an expansive material (bentonite MX-80) is placed in the upper part of the model separated from the model by a 1 mm thick PVC plate (cf. Figure 4.59). This material does not prevent the gap from forming, but once it makes contact with water, the volumetric expansion of the material closes the gap. Further details about the swelling potential of this bentonite can be found in Montes-H et al. (2003).

A swelling test was conducted to determine the expansion potential of different mixes of sand and bentonite. A cylindrical sample (100 mm diameter × 85 mm height) was connected to a water supply at the base in order to saturate the specimen from the bottom. A cap was placed on top of the specimen. The deformations of the sample were measured from the displacement of the cap (Figure 4.60).

Figure 4.59: Model with a thin PVC wall separating the sand in the model and the mixture of sand-bentonite.

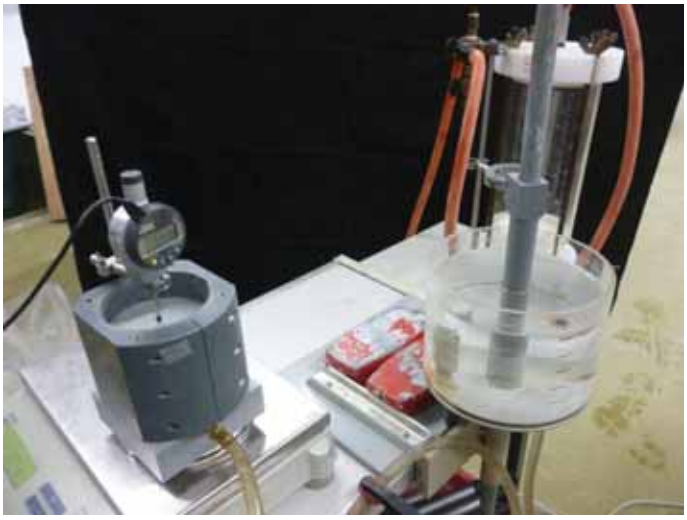

Figure 4.60: Setup for swelling test on a 100 mm diameter specimen of 85 mm height.

Figure 4.61 shows the results from the swelling test. The content of bentonite changes the permeability of the material, as well as the time required for saturation of the sample, which is given beside each curve. The mixture of 97% sand and 3% bentonite was chosen over the other mixtures, because it gives a volumetric expansion potential of 10% within 1 hour after the mixture is in contact with water.

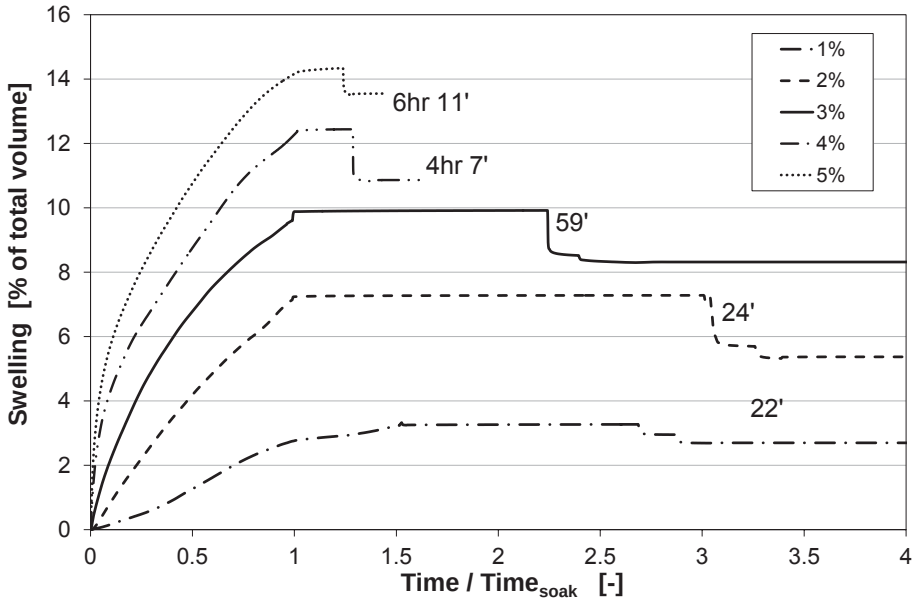

Figure 4.61: Swelling potential for different mixtures of sand and bentonite.

4.3.5 Additional activities

The general procedures followed to build a model for centrifuge modeling have been described in Section 4.3.2. However, some of the tests required special components, for instance, the installation of a toe filter and a cut-off wall (cf. Section 4.4).

4.3.5.1 Box preparation

Some activities needed to be done before the small-scale model building could begin, or during its construction. The pore pressure transducers (PPT) must be saturated following the procedure described in Section 4.2.3.1, and the TDR sensors must be cleaned of soil.

Once the measurement devices were ready to be used, they were inserted inside the box, depending on the corresponding slope gradient of the model, through the holes drilled on the top plate of the strongbox (cf. Section 4.2.1.4) and on the PVC plate that separated the model from the mixture with bentonite.

Each pair of TDR-PPT devices was knotted together with tape. A thin aluminum rod was attached along the bundled cable to provide stability and ease of handling. Some rods were duct taped at the exact position at which the pair of sensors should be located (Figure 4.62a). A thread from which the devices hang was attached to the rod. The length of the thread was such that, when extended, it reached the exact depth at which the devices must be placed (Figure 4.62b). The location of the devices for each slope gradient is given in Section 4.4.

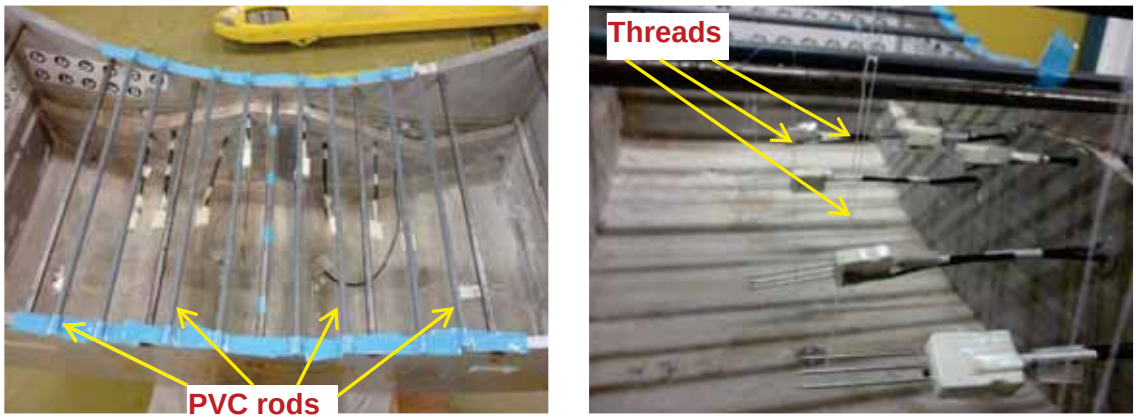

a) Rods taped to help locate the devices. *b) The pair of sensors hangs from the rods at the defined height.*

Figure 4.62: Preparation of the measuring devices inside the box.

4.3.5.2 Cut-off wall

A cut-off wall is one of the protection measures that can be constructed in an existing dyke, and hence was important to study whether it proved to be effective (cf. Section 4.4). The wall was modeled by a PVC plate of 1 mm thickness. The height of the wall was such that it corresponds to 6.5 m at prototype scale.

The wall was placed before the sand was pluviated. The wall was fixed to the lower plate of the strongbox and the PVC wall that separates the model from the mixture with bentonite. The joints were sealed with plasticine to guarantee watertightness (Figure 4.63).

a) *b)*

Figure 4.63: a) The cut-off wall is placed before the material is pluviated. b) The joints between the cut-off wall and the strongbox are sealed with plasticine.

4.3.5.3 Toe filter

Secondly, the influence of a toe filter on the water flow and slope stability was investigated (cf. Section 4.4). A detailed description of its design, construction and installation is presented in the following section.

Design

The design of the filter followed the guidelines proposed by Cedergren (1977):

$$5 \cdot d_{15_{soil}} > d_{15_{filter}} < 4 \cdot d_{85_{soil}} \rightarrow 5 \cdot 0.15 > d_{15_{filter}} < 4 \cdot 0.3 \rightarrow \boxed{0.75\ \text{mm} > d_{15_{filter}} < 1.5\ \text{mm}}$$

$$d_{50_{filter}} \leq 25 \cdot d_{50_{soil}} \rightarrow d_{50_{filter}} \leq 25 \cdot 0.23\ \text{mm} \rightarrow \boxed{d_{50_{filter}} \leq 5.75\ \text{mm}}$$

Figure 4.1 shows sieve curves for both the Perth sand (sieved at ETH Zurich) and the toe filter. The filter gradings were d_{15} = 1.1 mm and d_{50} = 1.8 mm. These values satisfy the recommendation for filters given above. It is classified as SP (poorly graded sand) according to the Unified Soil Classification System (USCS) the

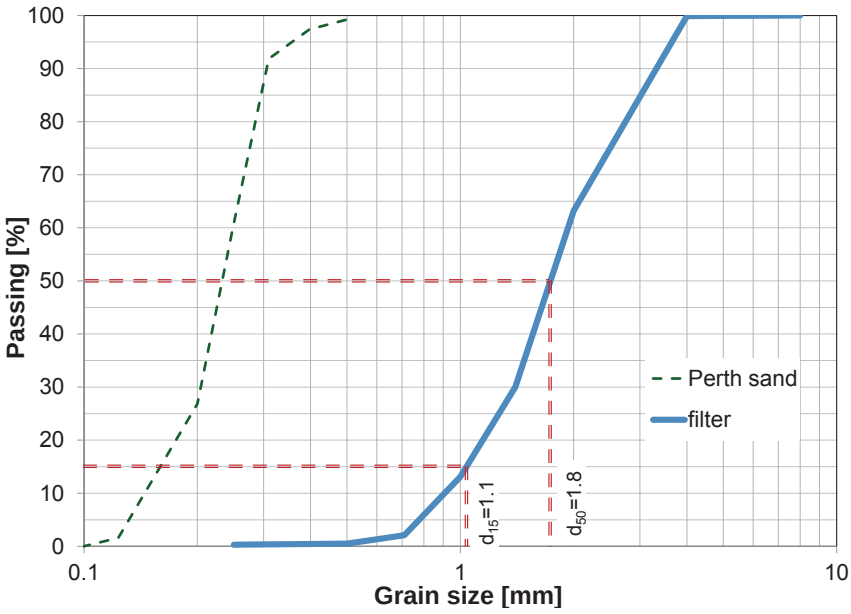

Figure 4.64: Sieve curves of Perth sand and the toe filter.

Construction

It was considered admissible to design a toe filter that could be used for several model tests. A geotextile sack consisting of a square grid of fibers with 0.05 × 0.05 mm spacing was prepared. This spacing allows the water to flow through while retaining the filter. Further information about this geotextile can be found in Kapogianni et al. (2010).

The procedure adopted to build the toe filter is illustrated in Figure 4.65. First, a wooden frame is built (Figure 4.65a). The dimensions of the internal space correspond to the size of the filter, i.e. 100 × 470 × 25 mm. The geotextile is then attached to the frame (Figure 4.65b-c) and the material is poured to fill the space (Figure 4.65d). A final cover of geotextile is welded at 261°C and the frame is removed (Figure 4.65e).

a) Wooden frame with dimensions 100 × 470 mm.

b) Geotextile is welded to the borders of the frame.

c) Geotextile is welded to create the bottom of the space.

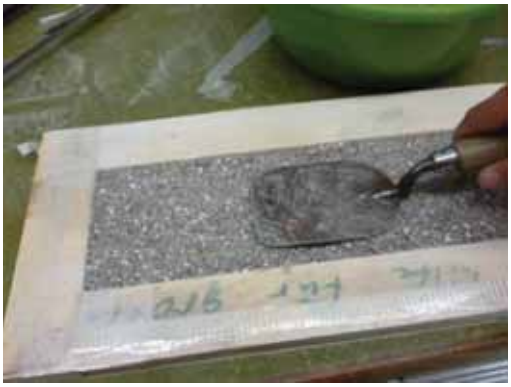

d) The soil is poured into the filter bag.

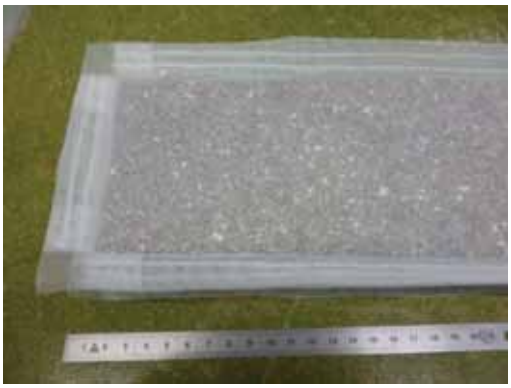

e) The wooden frame is removed.

f) The filter is ready, but it is too flexible.

g) Steel frame to hold the filter.

h) Filter ready for installation in model.

Figure 4.65: Construction of the toe filter (100 × 470 × 25 mm).

The filter prepared following this procedure turned out to be too flexible (Figure 4.65f), and therefore it became complicated to install one inside the soil model. For that reason, a steel case was manufactured to retain and stiffen the filter inside (Figure 4.65g). Once the filter was finished, it was inserted inside the steel case to be ready for use in the model (Figure 4.65h).

Installation

The filter was placed in the model during the sand pluviation stage (Figure 4.66) with an inclination (Figure 4.67), which corresponds to a horizontal position in the prototype.

Figure 4.66: Installation of the toe filter during the dry pluviation.

Figure 4.67: Location of the filter.

4.3.5.4 Insertion of the sand-bentonite mixture

After several unsuccessful trials to build a model that allowed an overflow to take place. The construction of the centrifuge model required the inclusion of a mixture of sand with bentonite. The model was built complete with pure Perth sand, as indicated in Section 4.3.2. The zone to be filled with the mixture was then removed (Figure 4.68a), using an industrial vacuum cleaner. The gap remained stable, as the rest of the material is in an unsaturated state,

and the mixture of sand and bentonite was poured inside in a loose state with the help of a funnel (Figure 4.68b). Since this might lead to undesired settlement of the sand-bentonite mixture when the model was spun in the centrifuge, it was compacted with a rod densify the mixture.

a) The zone to be filled with the mixture was removed.

b) The space was filled with the mixture first with a funnel and then compacted.

Figure 4.68: Insertion of the sand-bentonite mixture in the centrifuge model.

4.3.5.5 Density verification

The density following air pluviation and the increase and decrease in centrifugal acceleration was verified for each test. Four small pots were placed during the pluviation phase at different locations inside the body of the dyke (Figure 4.69a). These pots have a cylindrical shape, with a small filter at the bottom, so water can flow freely through the material inside and have the same saturation as the sand surrounding the pot (Arnold, 2011).

a) The pots were placed inside the model during the dry pluviation.

b) The water content is determined at the end of the test.

Figure 4.69: Small pots placed inside the strongbox to verify the final density of the centrifuge models.

The pots are carefully extracted at the end of the test, and the gravimetric water content of the material is estimated. With this value and the volume of the pot, it is possible to determine the bulk and dry density of the model.

4.3.5.6 Deformation markers

Some visual marks were located over the slope of the air-side of the dyke to follow the deformations and erosion patterns during the test (Figure 4.70). These markers were also useful to reference the pictures for photogrammetry analyses. The models featuring the toe filter have 20 markers (grid of 5 × 4), with 24 markers otherwise (grid of 6 × 4). At prototype scale, the distance is 3.5 m between the four markers in each row. The distance of each row of markers is defined to correspond to 0.80 m in height (Figure 4.70a).

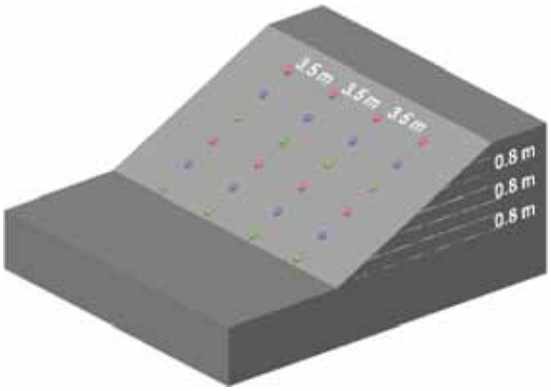

a) Grid used to place the markers (6 × 4).

b) Locating the markers over the slope.

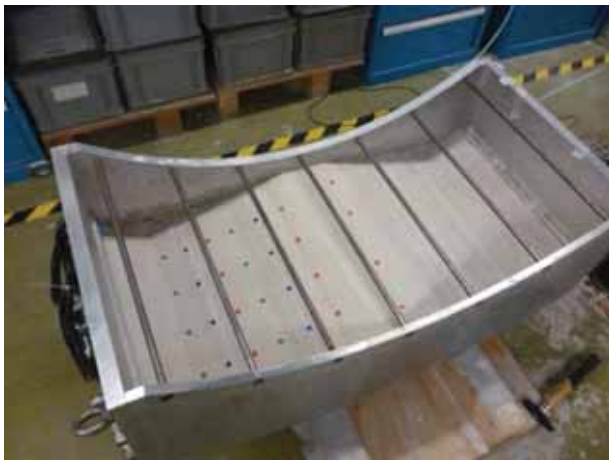

c) View of the completed model with all markers in place.

Figure 4.70: Visual markers for tracking displacements and development of erosion.

4.4 Cross sections and testing program

Three slope gradients (1:2.0, 1:2.5, 1:3.0) were analyzed, as they form the most common dyke geometries (US Army Corps of Engineers, 2000). Figures 4.71 to 4.76 present the cross sections for both the model and prototype scale used for this research project.

The green points with crosses represent the place at which a TDR sensor and a PPT were placed pair-wise. Measurements of volumetric water contents and pore water pressures were made at eight different positions within the dyke model for each centrifuge test. Monitoring both variables, volumetric water content and water pressure, in real time at almost the same place, is then possible for each test, as was achieved in the Baltschider field test (Mayor et al., 2008). These variables determine the unsaturated state of the soil, which has an effect on the mechanical response of the dyke (Fredlund & Rahardjo, 1993; Mayne et al., 2009; Casini et al., 2010; Brönnimann, 2011; Sheng et al., 2011).

The blue points in the figures represent additional PPTs that were placed in the model. These additional sensors were installed after some tests had already been performed to give a better insight into the flow behavior, hence not all the models have data at those points.

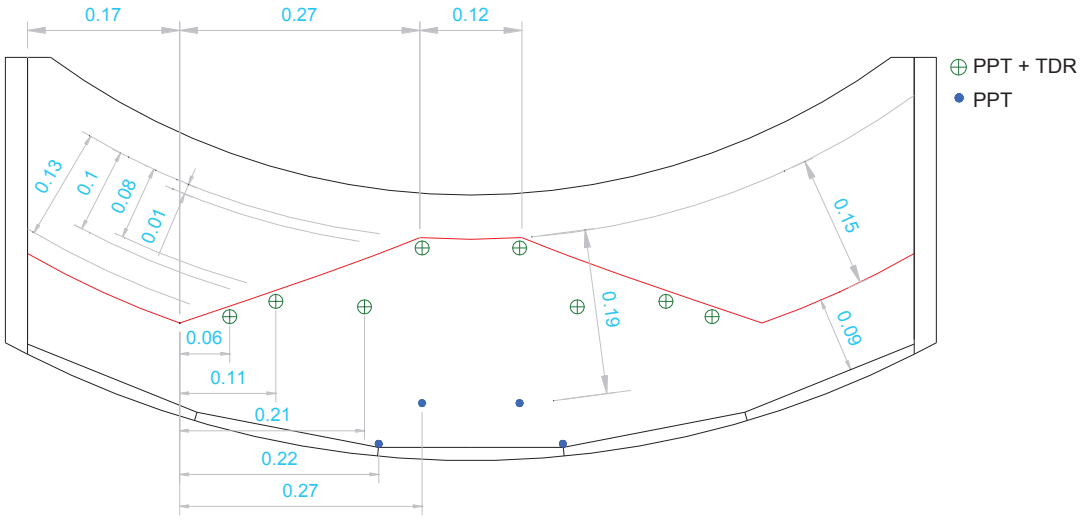

Figure 4.71: Cross section of the centrifuge model of the dyke with slopes 1:2.0 (dimensions in m).

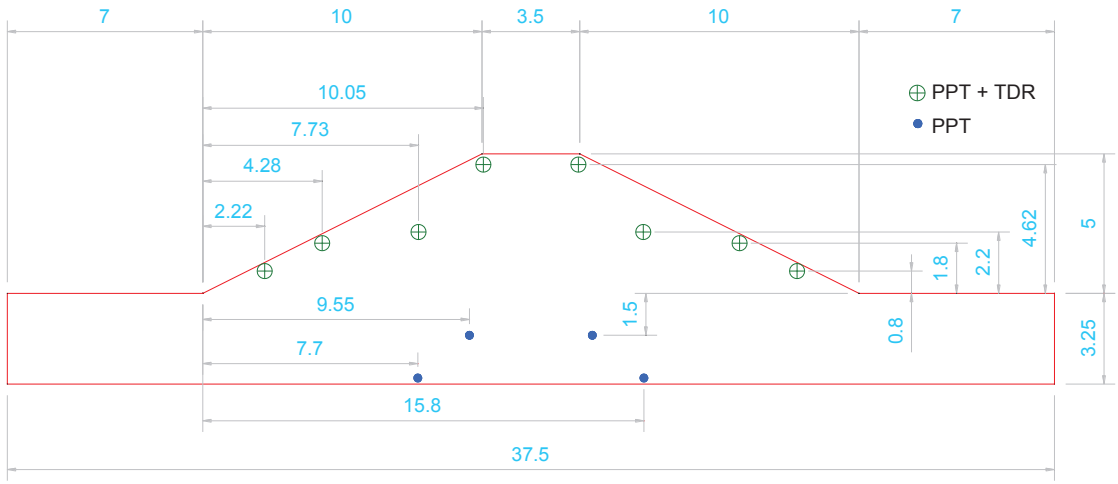

Figure 4.72: Cross section of the prototype of the dyke with slopes 1:2.0 (dimensions in m).

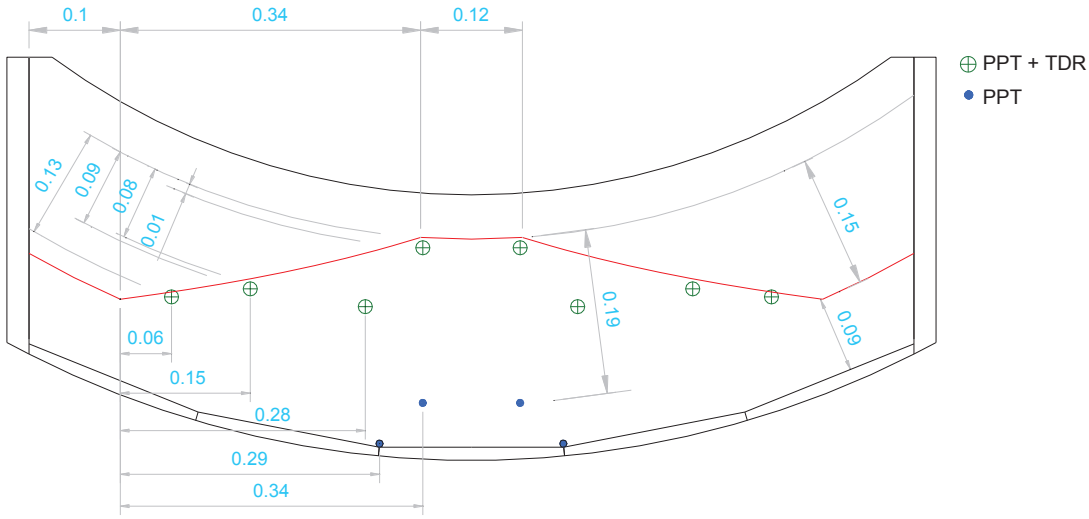

Figure 4.73: Cross section of the centrifuge model of the dyke with slopes 1:2.5 (dimensions in m).

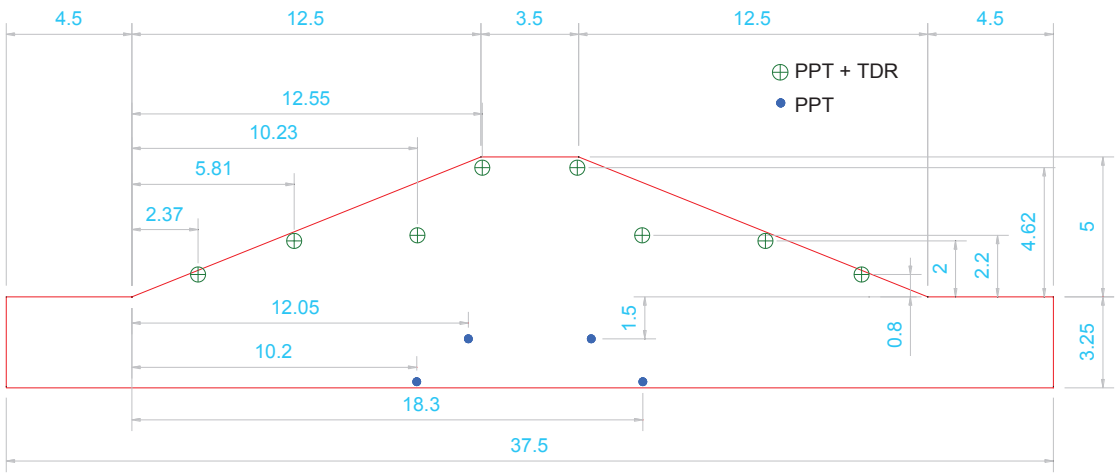

Figure 4.74: Cross section of the prototype of the dyke with slopes 1:2.5 (dimensions in m).

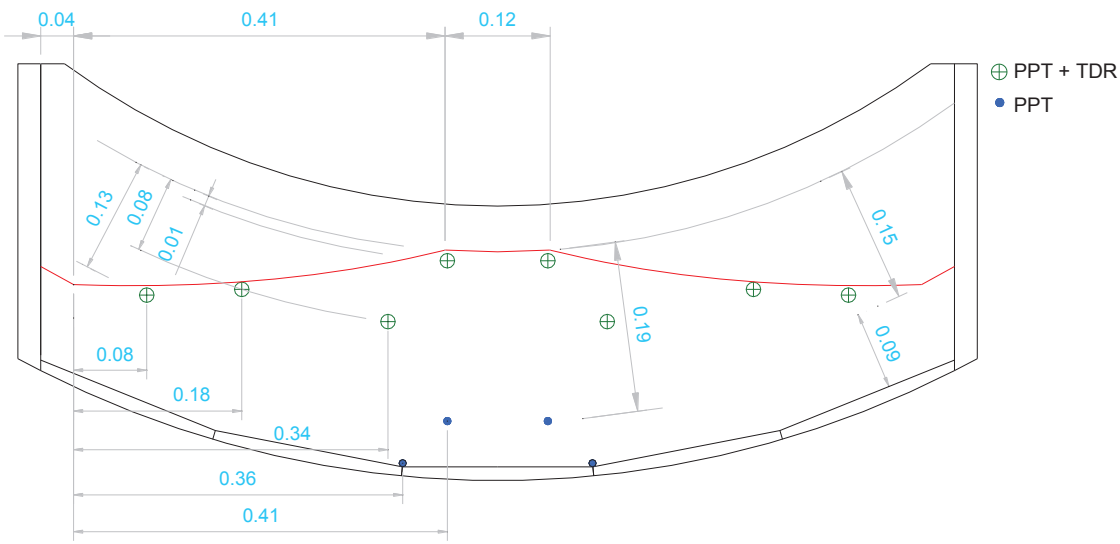

Figure 4.75: Cross section of the centrifuge model of the dyke with slopes 1:3.0 (dimensions in m).

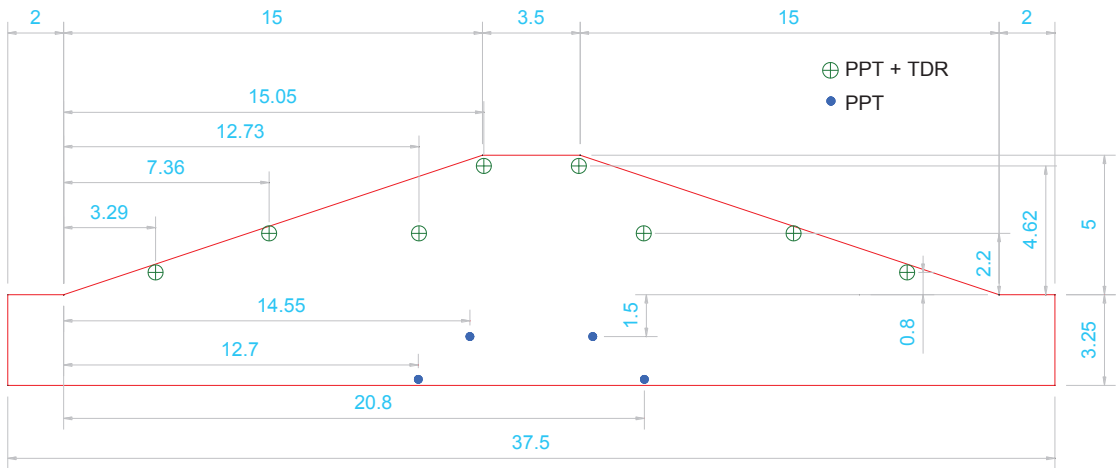

Figure 4.76: Cross section of the prototype of the dyke with slopes 1:3.0 (dimensions in m).

Although maintenance and river management should be considered first, construction measures may be adopted if the first options are insufficient to maintain the safety of the structure (Mayor, 2009). A common approach to limiting flow through a dyke is to install a cut-off wall. These can be constructed in different ways including sheet piling, diaphragm walls (DW) or mixed-in-place walls (MIPW) (Girsch, 2003). The wall acts a safety measure to change the seepage water pattern so that the degree of saturation within the soil mass is modified and the air-side slope remains stable, even during high water levels expected in a critical flood. DW were employed for the River Engelberger Aa (Springman & Teysseire, 2004) and MIPW for the 3rd Rhone Correction. A DW is included in the modeling phase for each slope gradient. The effects of the DW during overflow and breaching have not yet been assessed. This indicates both the importance and the benefit of analyzing the effect of the wall on the dyke behavior via centrifuge testing, whereby failure of a model can be generated without damage to infrastructure and danger of loss of life.

Another feature investigated in the range of centrifuge modeling tests was the inclusion of a filter at the toe of the air-side slope to draw down the phreatic surface in the air-side slope, which would enable it to be constructed more steeply. The cut-off wall modifies the seepage pattern, and therefore the response of the structure by preventing flow from emerging mid-way up the air-side slope.

Figure 4.77 presents the series of tests that was carried out. Four tests were performed for each slope gradient: one with the dyke in a homogeneous condition, one with the toe filter, another with the cut-off wall, and a fourth with both the toe filter and the cut-off wall.

Figure 4.78 indicates the water level, at prototype scale, imposed on the model for each test. Three floods are simulated. The first two floods are simulated, following a sinusoidal shape and with a duration of 20 days each before the final overflow phase is applied.

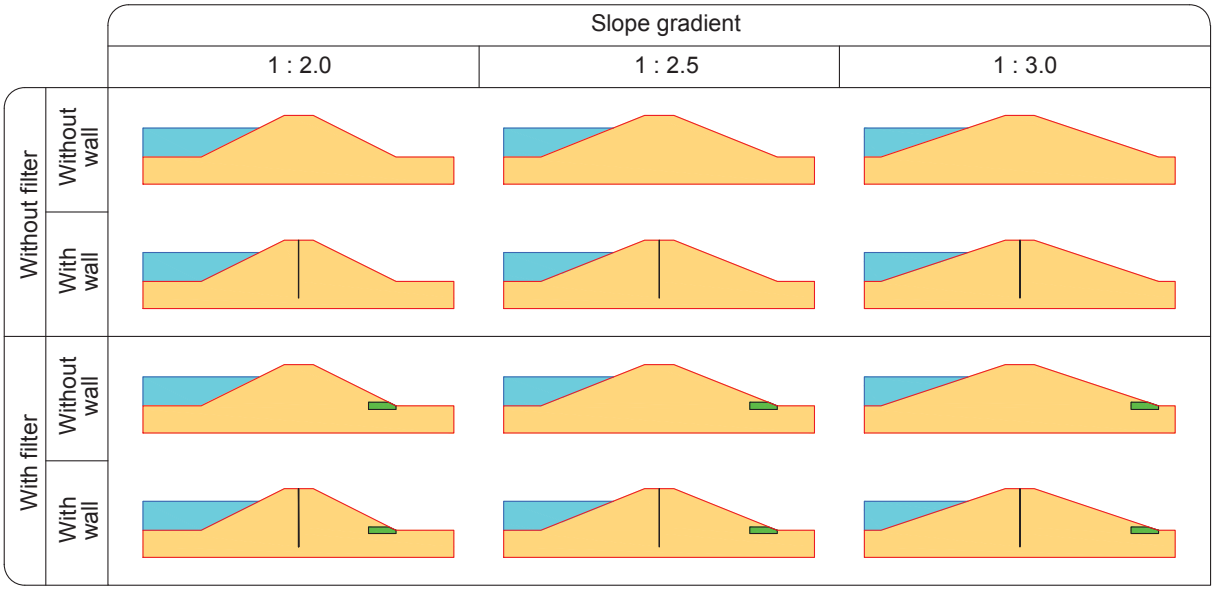

Figure 4.77: Centrifuge modeling series configuration with height of dyke 150 mm (5 m prototype scale), different side slopes from 1:2 to 1:3, with a central cut-off wall and with a filter at the toe of the air-side slope.

For the third and final flood, the simulation followed more realistic conditions by applying an actual flood hydrograph. Figure 4.79 is the discharge hydrograph on the Hagneck canal on the River Aare during the summer flood in 2005. An initial steady-state condition was assumed with the water level at 1.4 m. The maximum discharge (1500 m^3/s) is assumed to correspond to the flood level at the maximum height of the dyke (5.0 m). Then the discharge hydrograph was scaled to a corresponding water level for the dyke.

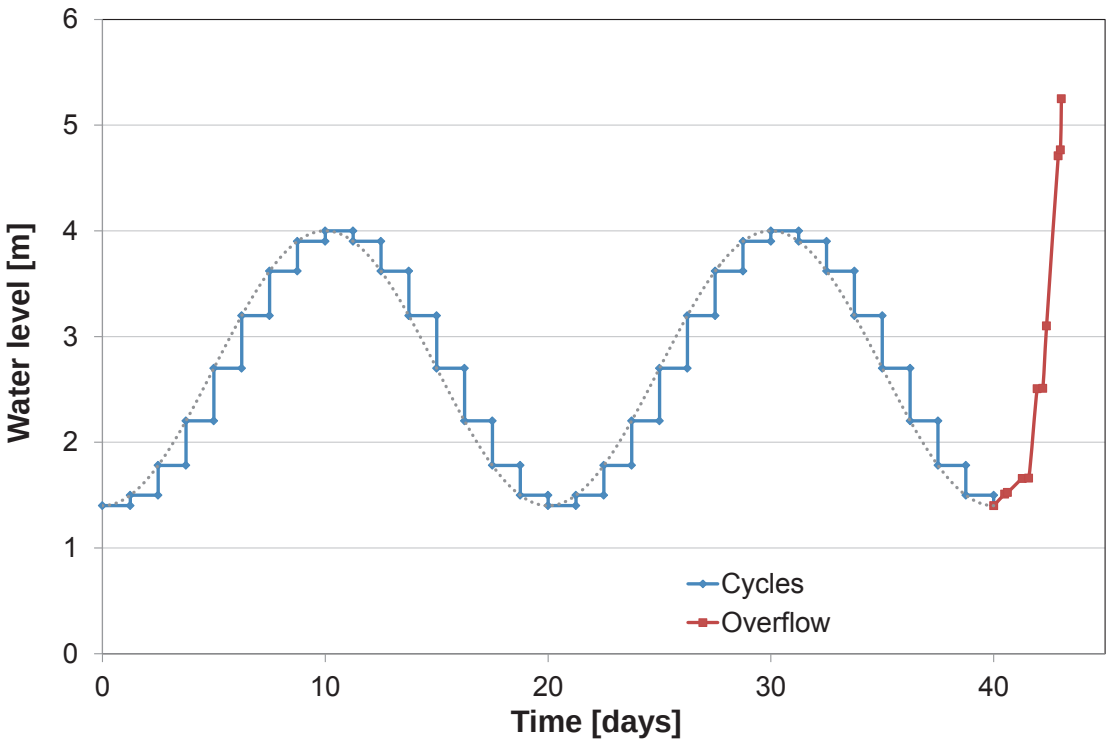

Figure 4.78: Water level imposed on each centrifuge model for all tests (at prototype scale).

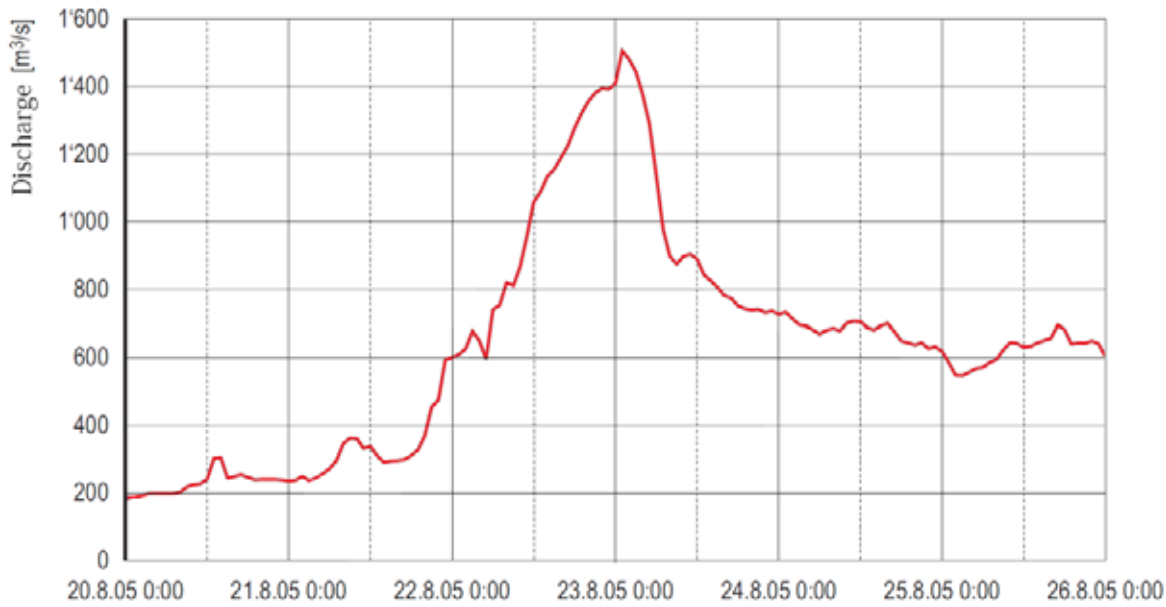

Figure 4.79: Discharge hydrograph at the Hagneck canal during the 2005 flood (adapted from Bezzola & Hegg, 2007).

4.5 Analysis of the results

The results are analyzed for each one of the four types of dyke: homogeneous dyke; dyke with a toe filter; dyke with a cut-off wall; and dyke with both a cut-off wall and a toe filter. Each group of results is presented from three tests, corresponding to each different slope gradient used for each type of dyke. A general assessment of the behavior of all the models is given at the end of the section.

The performance of the dyke is evaluated, based on the pore pressures and volumetric water contents measured during each test. Failure mechanisms occurring during the flooding cycles, and during the overflow phase, are also analyzed. All times reported correspond to prototype scale (n = 33.3).

Pore water pressure was measured every second (at model scale), whereas the volumetric water content was measured every 30 seconds. These represent a logging frequency of 1109 seconds (0.31 hours) and 33267 seconds (9.24 hours) at prototype scale. The TDR100 cable tester requires a minimum sampling time of 3 seconds per sensor (Campbell Scientific, 2010). This implies a minimum sampling rate of 24 seconds for 8 sensors, which means that it is not possible to achieving higher frequencies than 0.3 Hz logging the volumetric water content.

Time equal to 0 days in the results charts corresponds to the moment at which the flood cycles begin.

4.5.1 Homogeneous dyke

The locations for the measuring points in the dyke are shown in Figure 4.80. The figure corresponds to the dyke with slope gradient 1:2.0. However, the location of the sensors for the other two slope gradients is similar. The exact location of the sensors for all the slope gradients is given in Section 4.4. The green circles with a cross represent the points at which both water pressure and water content was measured. The blue circles are points where only pore water pressure was measured. The red point corresponds to the place, where the applied water level was measured.

Information about the volumetric water content is available from eight sensors (1–8) for all three tests except for the models with 1:2.0 and 1:2.5 slope gradients, for which TDRs 4 and 1 respectively, failed.

Pore water pressure measurement was not possible at all points, owing to faulty sensors. The model with slope gradient 1:2.0 had 12 points of pore water pressure measurement. The model with slope gradient 1:2.5 had 7 points (1, 3, 4, 5, 6, 7, 8), and the test with slope gradient 1:3.0 only had 8 sensors (1–8).

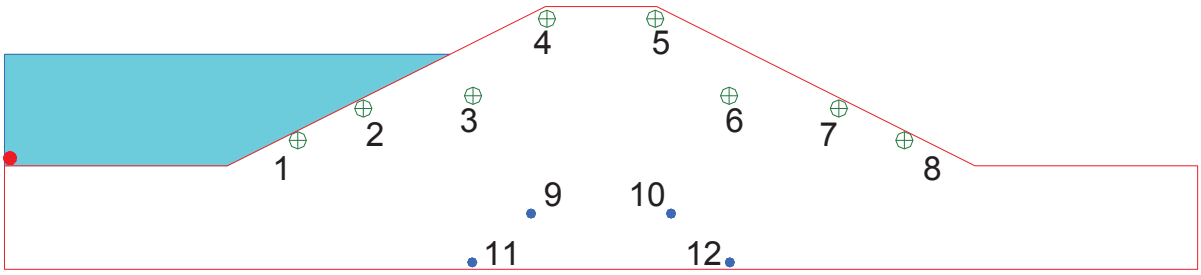

Figure 4.80: Location of the sensors for the homogeneous dyke.

The water level imposed was the same, except for the model with slope gradient 1:2.5. A failure in the software controlling the arm of the actuator forced the arm to be driven manually, which led to a different imposed water level. Notwithstanding this challenge, a similar pattern was followed, i.e. two flood cycles up to 40 kPa, and a subsequent overflow process.

The density of the models was verified from measurements of weights and volume for four small pots filled with sand (cf. Section 4.3.5.5). The values determined for all three tests are presented in Table 4.2, whereby γ_{bulk} refers to the bulk unit weight of the material, γ_{dry} is the dry unit weight, e is the void ratio, D_R is the relative density, and θ_{sat} is the volumetric water content at saturation (equal to the porosity of the model). *Aver* means the average value for the four specimens taken. It is concluded that models could be prepared with similar density characteristics.

The pore water pressure results are presented for the three related tests in Figures 4.81 to 4.83. An immediate reaction of water pressure to the change in water level was seen at point 1. However, the measured values are almost identical to those externally imposed on the model with slope gradient 1:2.0. This might be a result of the sensor being located few millimeters below the planned position, leading to greater pressures being measured. A differ-

ence of approximately 6.5 kPa between the applied level and the measured values was found for the other two models in this group of tests. This is close to the expected difference of 8 kPa.

Table 4.23: Density parameters for all three tests on a homogeneous dyke.

Slope gradient	Specimen	γ_{bulk} [kN/m^3]	γ_{bulk_aver} [kN/m^3]	γ_{dry} [kN/m^3]	γ_{dry_aver} [kN/m^3]	e [-]	e_{aver} [-]	D_R [%]	D_{R_aver} [%]	θ_{sat} [%]
1:2.0	1	20.02	19.99	16.76	16.69	0.58	0.59	69.54	67.06	0.37
	2	19.88		16.56		0.60		62.06		
	3	20.20		17.00		0.56		78.10		
	4	19.87		16.46		0.61		58.54		
1:2.5	1	20.18	19.97	16.93	16.84	0.56	0.57	75.83	72.32	0.36
	2	20.00		16.95		0.56		76.24		
	3	20.08		16.95		0.56		76.24		
	4	19.62		16.53		0.60		60.98		
1:3.0	1	20.19	18.83	16.94	16.99	0.56	0.56	75.98	77.86	0.36
	2	18.81		17.22		0.54		85.64		
	3	18.82		17.12		0.55		82.26		
	4	17.48		16.71		0.59		67.56		

Water pressures at point 2 showed a delay in the reaction to the change in the water table. The water pressure followed the same pattern as the water level applied. In the model with 1:2.0 slope gradient, the pressures were always positive, with a maximum value of 30.4 kPa when the water level was high, and a minimum value of 3.9 kPa at the end of both flood cycles. This is different from the model with 1:3.0 slope gradient, where the maximum pressure was 22.5 kPa, and the pressure dropped to -3.2 kPa after each flood cycle. Pressure increased to 42 and 33.2 kPa during the overflow phase.

The response at point 3 was similar for all three tests. A larger lag was seen in the response to water level change than for previous points. The maximum water pressure was about 16 kPa for the two flood cycles and 25 kPa for the overflow phase. Suctions were measured after the water level was lowered, with earlier initiation of suctions, longer duration and higher magnitude, for the steeper slope, with a range from -2.8 to 6.3 kPa. The value of suction suddenly jumped from 2.9 to 0 kPa at 15.4 and 33.6 days for the model with slope gradient 1:3.0. This is owing to cavitation of the sensor, which could not stand more suction pressure at that moment.

Measurements for point 4 showed a small influence of the water level change in the data. Positive water pressure values were measured only during the overflow process, otherwise suctions were recorded. Measurements at point 5 showed implausible values for the slope gradient 1:2.0, and are considered to be caused by either a fault in the sensor or in the data logger, otherwise there appears to be no influence on the measurements.

Water pressures at point 6 only indicate a slight influence of the change in water table. Time lag for the reaction was 5.0, 4.5 and 6.75 days for slope gradients 1:2.0, 1:2.5 and 1:3.0, respectively. The maximum pressure achieved varies with the slopes: i.e. 6.5, 0.9 and

3.1 kPa for slope gradients 1:2.0, 1:2.5 and 1:3.0, respectively. The maximum pressure during the overflow stage was approximately 20 kPa.

At point 7, the water pressure was again different for each slope gradient. The values for the slope with gradient 1:2.0 showed a cyclic behavior, with values varying between -4.3 and 5.8 kPa during the cycles, and a maximum pressure of 25.3 kPa during the overflow process. No influence of the changing water level was seen for the test with slope gradient 1:2.5, until initiation of the overflow, when a maximum positive pressure of 2.9 kPa was measured. A similar response was seen for the 1:3.0 gradient, for which a pressure of 16 kPa was measured during the overflow process.

Point 8 showed a response, which reflects the change in the water level but smothered. This means that it is not possible to recognize the water steps applied in the response of the sensors, in contrast to points 1, 2 and 3, where the loading steps can be clearly identified. The maximum pressures were 20.3, 5.3 and 7.0 kPa for the slope gradients 1:2.0, 1:2.5 and 1:3.0, respectively. The corresponding minimum water pressures were 8.74, 2.19 and -0.87 kPa. Pore water pressure increased to a value of approximately 35 kPa for all three models during the overflow phase.

Measurement points 9 and 10 were located at the same depth, with a distance of 4.4 m between them. The former showed water pressures greater than the applied, whereas the latter showed smaller pressures when the water level was high, and greater pressures than that measured at applied location when the water level was lowered. As a consequence, the difference of pressure between these points decreased when the water was lowered. This means that water drains faster at point 9 than at point 10, which is expected, as the water at point 9 tends to drain to both the air and water sides of the dyke, whereas point 10 tends to drain towards the air-side only.

Similar behavior was found for points 11 and 12 during the first two flood cycles, for which the pressure difference, when the water level was high, was 12.1 kPa reducing to 5.5 kPa when the water level was lowered.

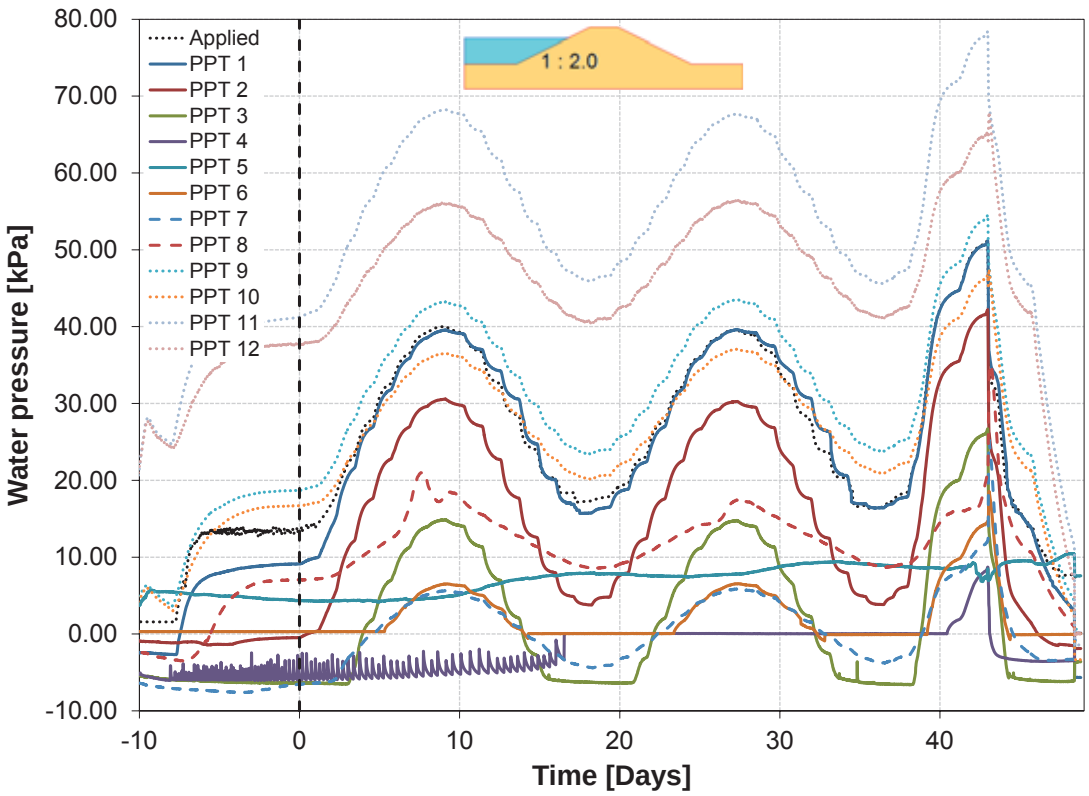

Figure 4.81: Water pressures for the homogeneous dyke with slopes 1:2.0, for two flood cycles an overflow phase as shown in Figure 4.78.

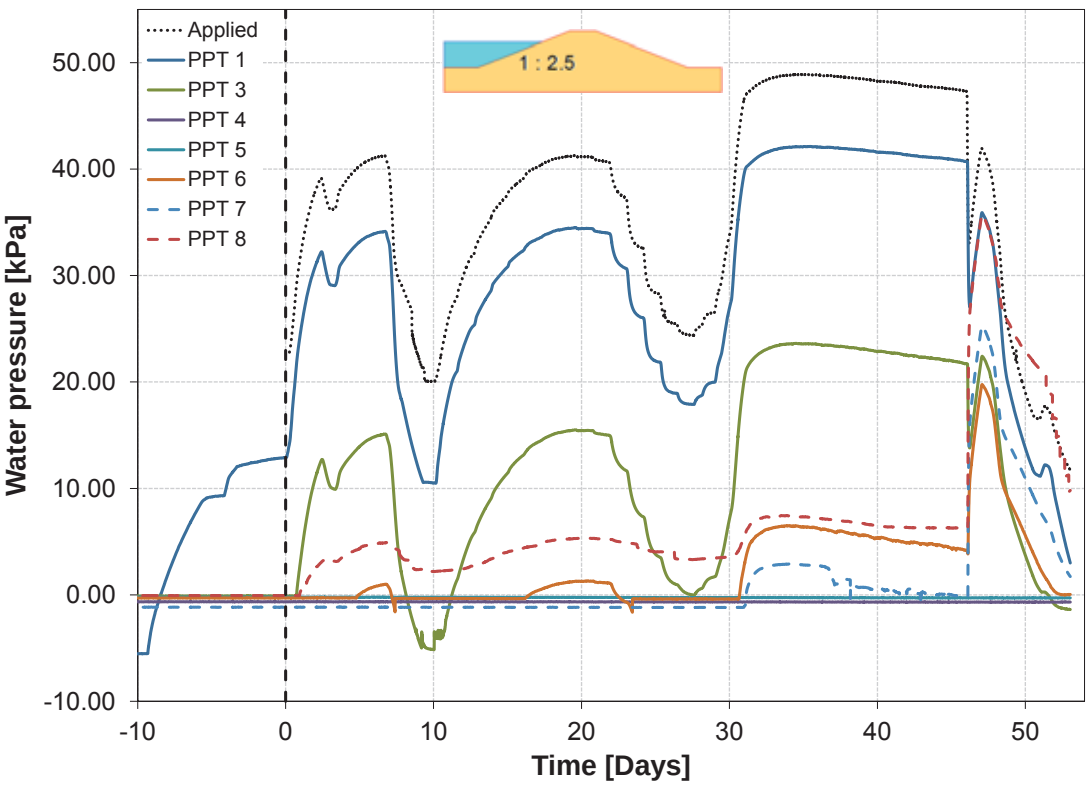

Figure 4.82: Water pressures for the homogeneous dyke with slopes 1:2.5, for two flood cycles an overflow phase as shown in Figure 4.78.

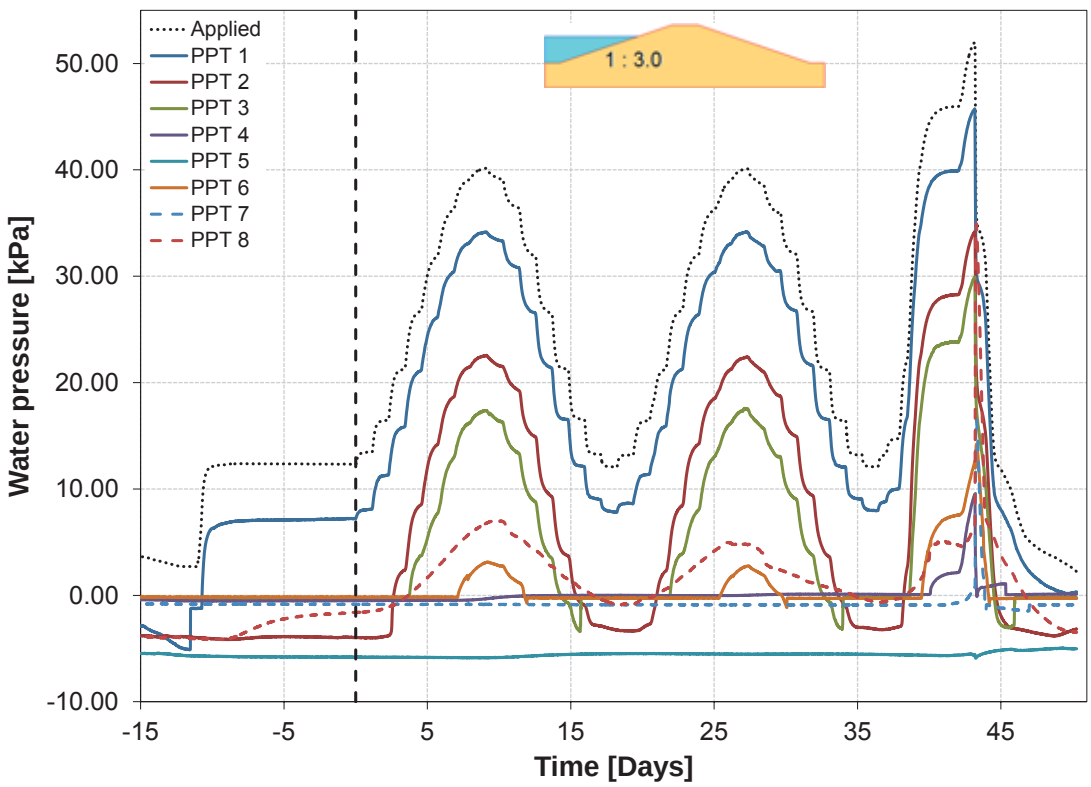

Figure 4.83: Water pressures for the homogeneous dyke with slopes 1:3.0, for two flood cycles an overflow phase as shown in Figure 4.78.

The results of volumetric water content for the three related tests are presented in Figures 4.84 to 4.86. The volumetric water content at point 1 showed complete saturation during the entire test, for two of the three cases, since the measurements for the slope with a gradient of 1:2.5 were faulty.

Volumetric water content at point 2 showed a delay in the reaction to the change in the water table. The soil became saturated rapidly after about 3 days when the water level was raised to a depth of about 2 m. However, the response was different when the water level was lowered in that drainage, and hence desaturation, was much more effective in the flatter slopes. The volumetric water content reduced until it is 0.27, 0.12 and 0.07 m^3/m^3 for the slope gradients 1:2.0, 1:2.5 and 1:3.0, respectively during the intermediate cycles.

The volumetric water content at point 3 increased rapidly after about 4 days, with a lag corresponding to the water pressures applied, after the water table had been raised. The values decreased to a residual value after the water level was lowered. An exception was seen for the slope gradient 1:2.5, in which the water content lowered to 0.23 m^3/m^3, and the initial rise preceded that of TDR 2.

The measurements of volumetric water content at points 4 and 5 showed that the soil at these points was at the residual water content (in an unsaturated state) during the flood cycles, and once the overflow process was performed, θ increased to saturation values (approximately 0.35 m^3/m^3) for the flattest slope at point 4 only.

The water content response for point 6 was similar for the slope gradients 1:2.0 and 3.0, for which the volumetric water content reached a value close to the saturated condition ($\theta \approx$ 0.36 m^3/m^3) after about 6 days; a condition that was maintained until the water level was lowered. The water content for the 1:2.5 slope gradient increased later and more gradually to 0.33 m^3/m^3 for the first flood cycle and 0.27 m^3/m^3 for the second cycle. This point reached full saturation during the overflow process.

The water content at point 7 depended also on the slope gradient. For the 1:2.0 gradient, full saturation was reached for each flood cycle, and reduced to the residual water content when the water level was lowered. This was similar to data obtained from TDR 6 and was consistent with that observed for the pore pressures. The water content increased subsequently for each flood cycle for the 1:2.5 gradient. During the first cycle, it reached 0.12 m^3/m^3 and 0.15 m^3/m^3 during the second cycle. It saturated during the overflow process. No influence of the changing water level was observed by TDR 7 during the water cycles for the test with a slope gradient of 1:3.0, which only became saturated during the overflow phase. Once again, this corresponds to the water pressure measurements.

The effect of the slope gradient on the water content at point 8 was clear. The soil remained almost saturated during the whole test (after the first 3 days of the initial water conditions applied before time=0 days) for the steepest model, decreasing from 0.33 to 0.29 m^3/m^3. The soil saturated when the water level was raised for the medium steep model starting on day 7, and decreased to 0.12 and 0.29 m^3/m^3 when the water level was lowered. Infiltration began above TDR 8 at day 2, for the model with 1:3.0 gradient, and saturation was reached during the first flood cycle after 6 days. Subsequently, the value reduced gradually until the overflow. This might be a consequence of the detachment of soil, owing to local failure processes as explained below.

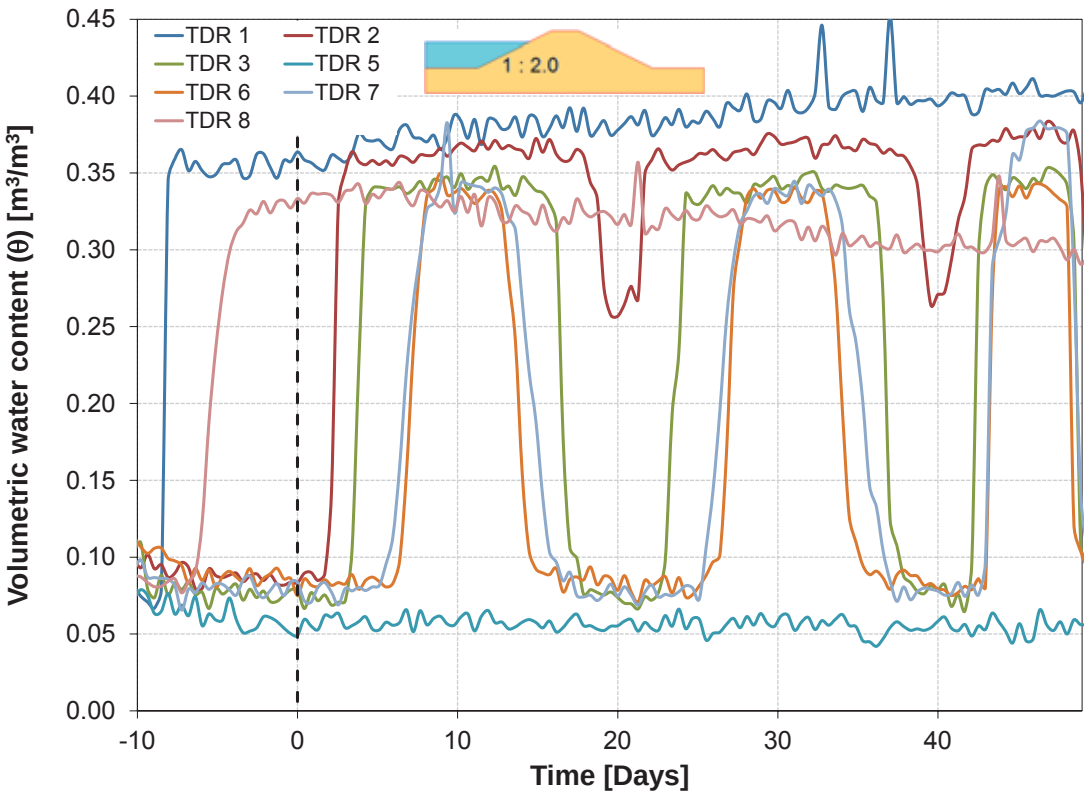

Figure 4.84: Volumetric water contents for the homogeneous dyke with slopes 1:2.0, for two flood cycles an overflow phase as shown in Figure 4.78.

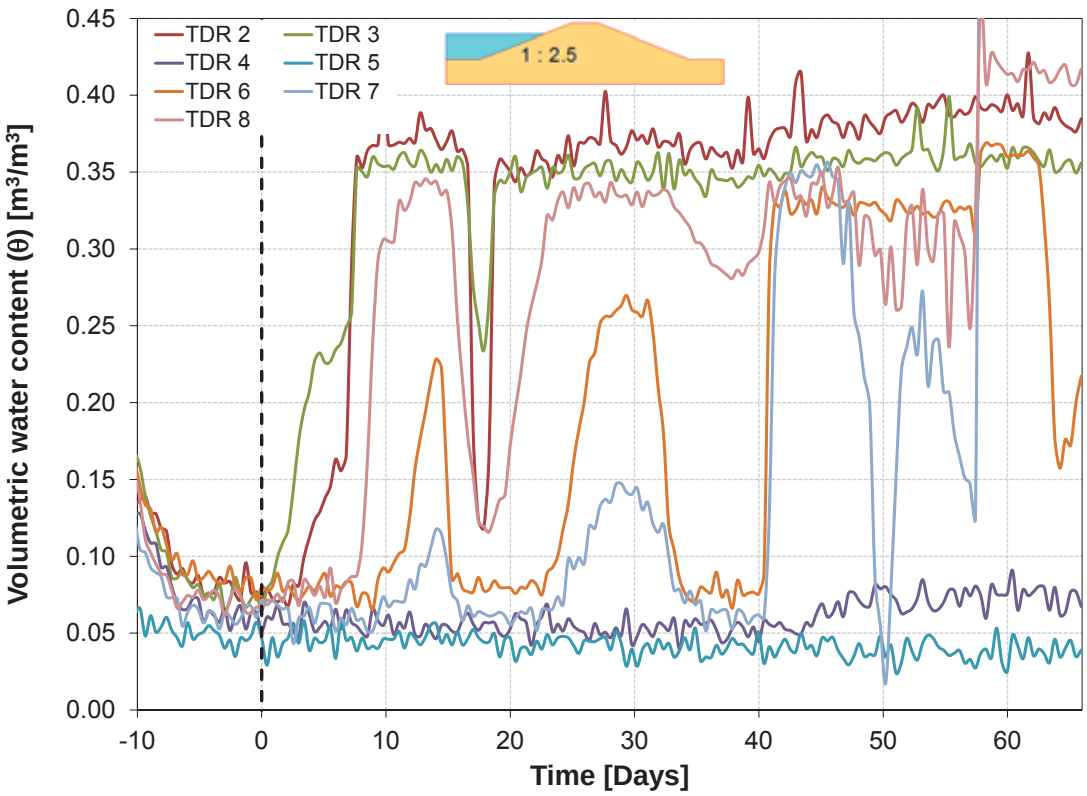

Figure 4.85: Volumetric water contents for the homogeneous dyke with slopes 1:2.5, for two flood cycles an overflow phase as shown in Figure 4.78.

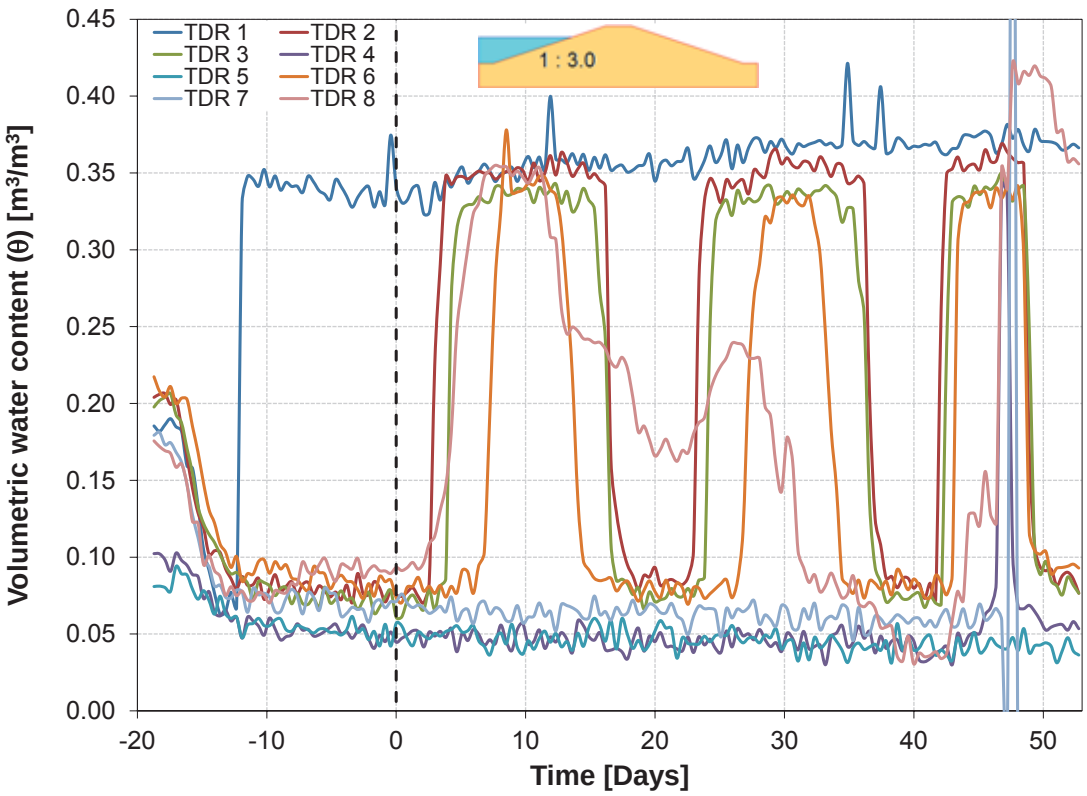

Figure 4.86: Volumetric water contents for the homogeneous dyke with slopes 1:3.0, for two flood cycles an overflow phase as shown in Figure 4.78.

4.5.1.1 Failure and breaching mechanism

Before the overflow process

This type of dyke, without a toe drain or a cut-off wall (homogenous), experienced instabilities on the air-side, during the flood cycles for all three slope gradients. The failure mechanism was a planar failure. A block of soil became unstable and was then detached from the slope and flushed out by the water, which emerged as a spring from beneath (Figure 4.87). This created a vertical ridge of approximately 0.6 m in height (Figure 4.88), which developed across the width of the dyke.

The process led to a retrogressive failure, as shown in Figure 4.89. The advance of the crown of the planar slip took place in two stages. Firstly, the retrogressive failure advanced progressively, until the time at which the first flood cycle reached its maximum water level. From that moment on, and during the second flood cycle, the crown of the slid mass remained almost unchanged. The second stage of failure took place during the overflow phase, and after the water level had exceeded the previous maximum water level.

More soil slid from the lower part of the model, owing to the influence of the 1-g level that is always present in the test, and which was caused by the earth's gravitational field. No influence of the slope gradient was observed in this process.

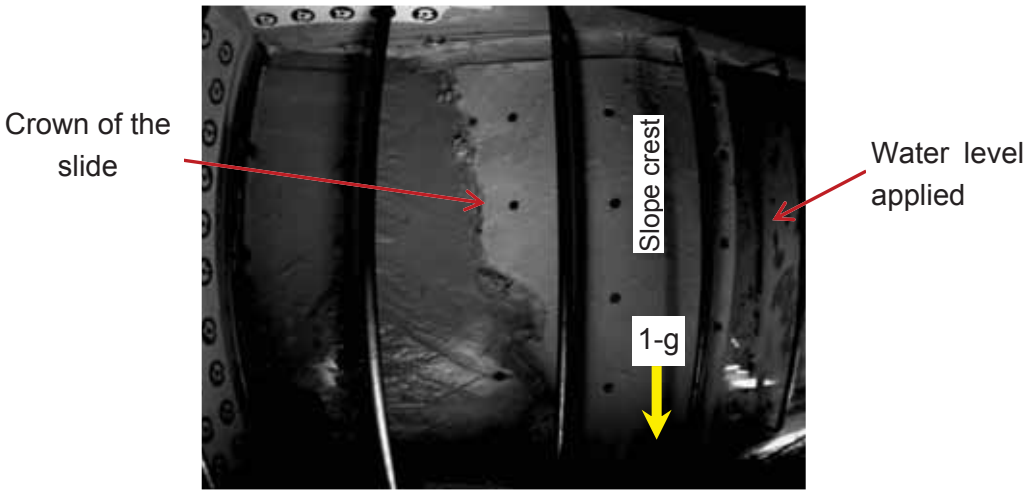

Figure 4.87: Example of planar failure on the air-side of the model. Model with slope gradient 1:2.0, 48.3 days after of the start of the flood cycle.

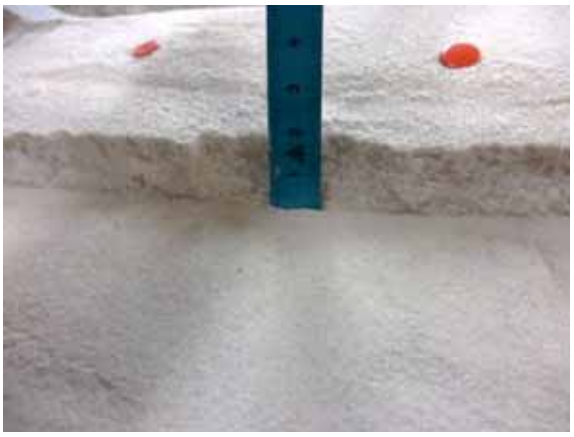

Figure 4.88: Vertical ridge on the air-side slope due to instability during the flood cycles. Model with slope gradient 1:2.0, after the end of the test.

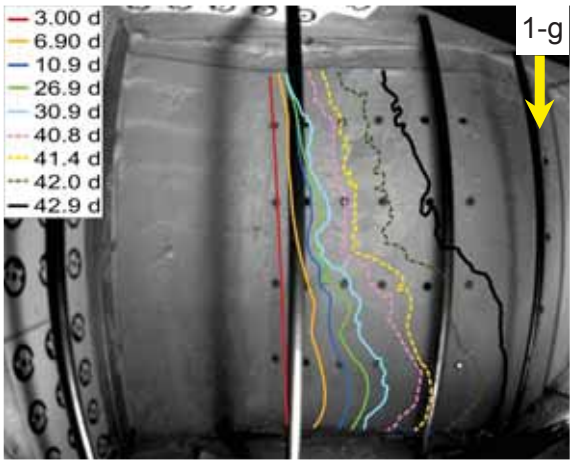

a) Slope gradient 1:2.0.

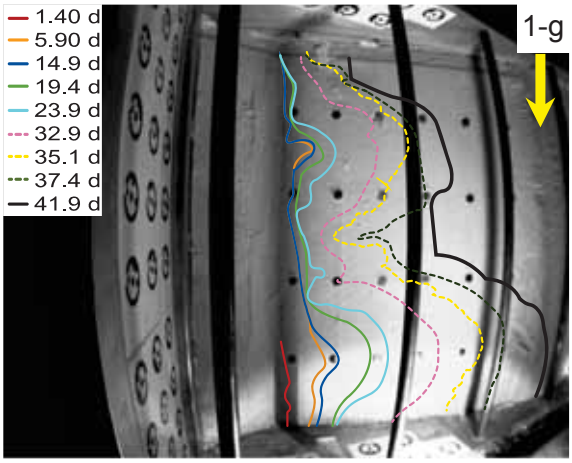

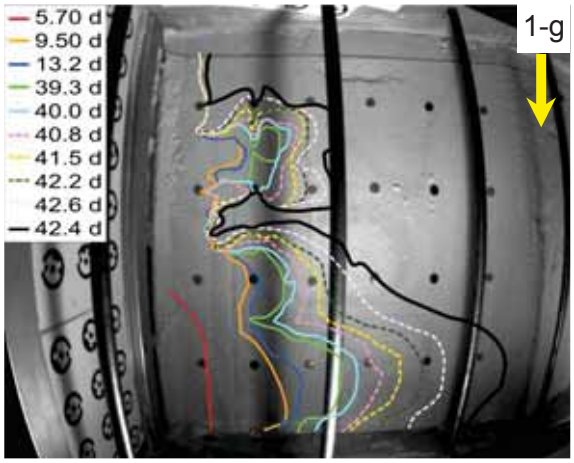

b) Slope gradient 1:2.5. *c) Slope gradient 1:3.0.*

Figure 4.89: Development of the retrogressive failure mechanism on the air-side of the homogenous dyke (in days in prototype scale). Time zero corresponds to the beginning of the flood cycles.

During the overflow process

The breaching mechanism was similar for all three slope gradients. As an example, the breaching process for the model with slope gradient of 1:2.5 is shown in Figure 4.90. The soil surface began to erode, creating a breach throat, through which water flowed rapidly. The breach throat broadened as a consequence of two simultaneous processes: the erosive action of the water over the soil, and local slope failures.

Figure 4.91 illustrates the process of slope instability on the ridge of the breach throat. The erosion process caused a vertical ridge to form, which was sustained by the apparent cohesion from the unsaturated condition of the soil. As long as the water flowed on the base of the ridge, the soil above saturated, decreasing the suction and hence the apparent cohesion, thus decreasing the effective stress. The instability of the material was first evidenced by the formation of tension cracks along the crest of the ridge or laterally along the breach. The soil slid along an almost vertical surface, which created a new ridge.

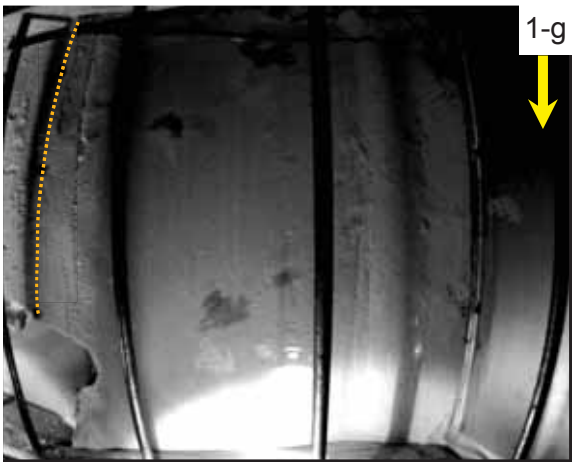

a) At 0 min.

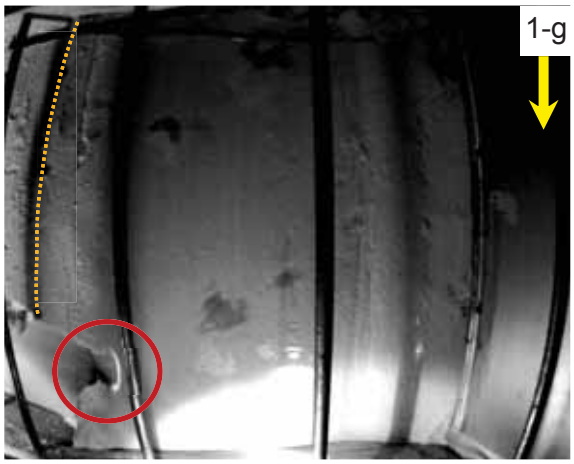

b) After 9.25 min.

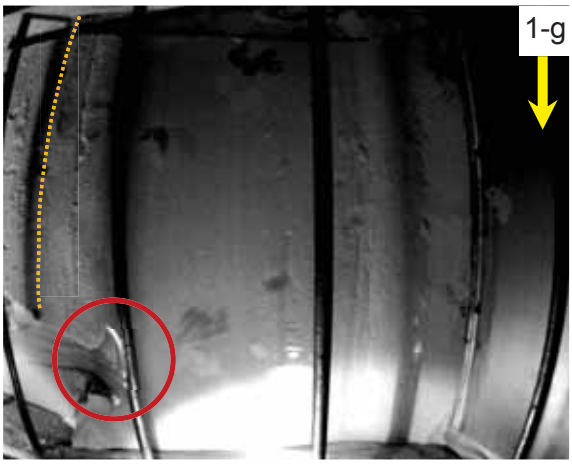

c) After 18.51 min.

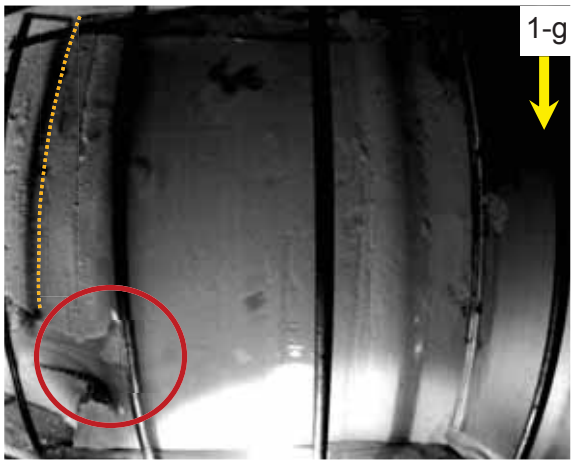

d) After 27.77 min.

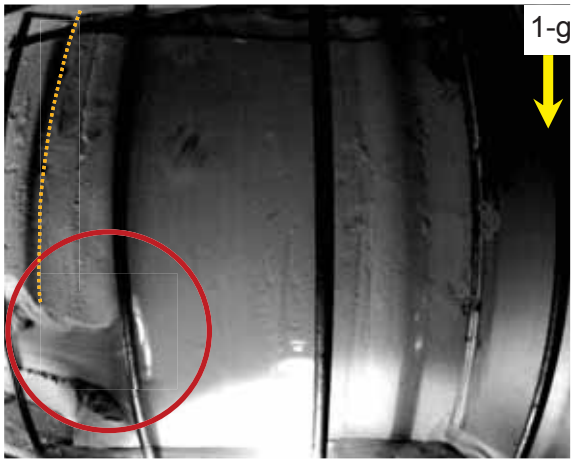

e) After 46.28 min.

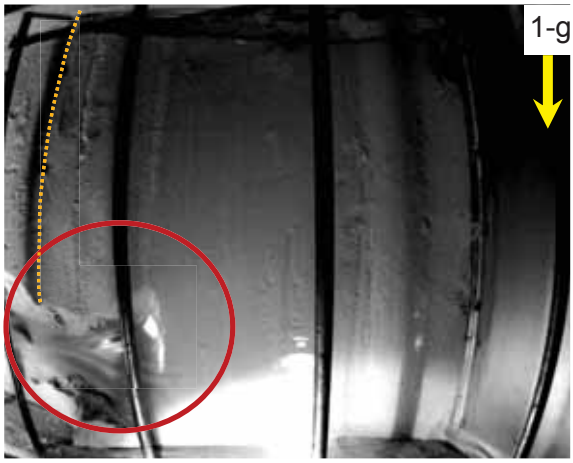

d) After 64.08 min.

Figure 4.90: Breach development of the homogeneous dyke with slope gradient 1:2.5. Time zero corresponds to the moment at which breaching began (46.09 days after the beginning of the flood cycles). The yellow dotted line indicates the crest of the dyke.

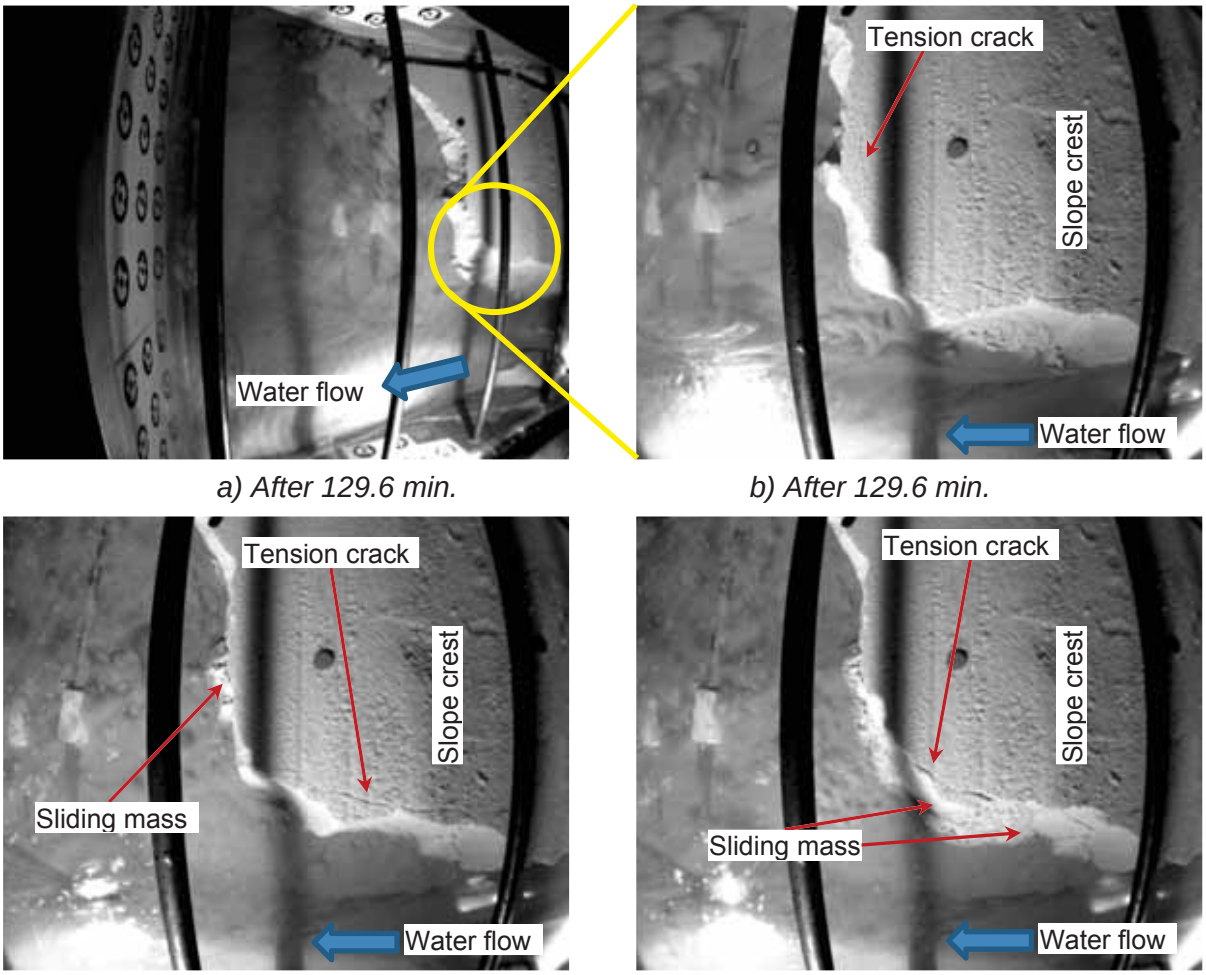

a) After 129.6 min. *b) After 129.6 min.*

c) After 180.52 min. *d) After 185.15 min.*

Figure 4.91: Slope instability of the breach wall for the homogeneous dyke with slope gradient 1:2.5. Time zero corresponds to the moment at which the flood cycles began.

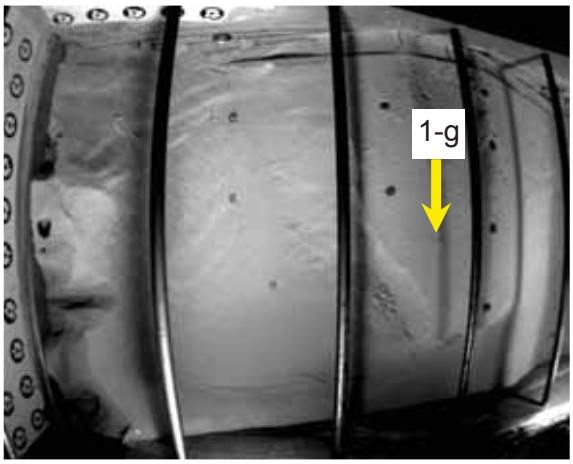

a) Slope gradient 1:2.0.

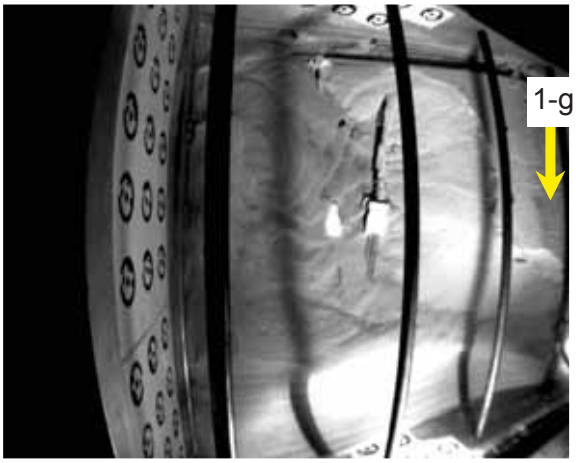

b) Slope gradient 1:2.5.

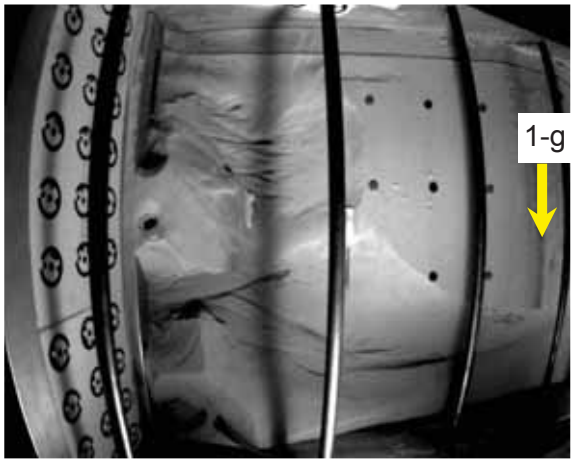

c) Slope gradient 1:3.0.

Figure 4.92: Final condition of the homogeneous dyke after overflow.

The final configuration of the air-side slopes for all three tests is shown in Figure 4.92, and an enlarged view of the breach zone in Figure 4.93. A similar breaching mechanism, as described above, was observed for all three tests. The wall of the breach throat was not completely vertical, but rather trapezoidal.

a) 1:2.0.

b) 1:2.5.

c) 1:3.0.

Figure 4.93: Breaching zone of the homogeneous dyke after overflow for all three slope gradients.

Table 4.24 summarizes the time required for the breach to develop completely, the width of the breach at the slope surface, and the depth of the breach zone at the crest of the slope for each of the slope gradients modeled. No clear trend becomes evident for the time required for breaching to develop. The model with the intermediate slope gradient (1:2.5) required the least time to erode the largest area, whereas the model with slope gradient 1:2.0 required most time to erode the smallest area of all three.

Table 4.24: Summary of the breaching characteristics for the homogenous dyke.

Slope gradient	Breaching time [min]	Width [m]	Depth [m]	Area [m^2]*
1:2.0	101.83	4.17	2.33	9.72
1:2.5	64.80	6.66	2.66	17.72
1:3.0	92.57	5.00	2.23	11.15

** Calculated as width × depth.*

Figure 4.94 shows the photogrammetric restitution of the model with slope gradient 1:3.0. Two pictures taken in-flight simultaneously were used to build the three-dimensional image. Some errors are visible at a length of 5.66 m. These are a result of an interpretation error caused by the struts of the semi-circular box in that position. The figure shows clearly the breach throat where the water overflows, as well as the accumulation zone at the toe of the slope and the ridge, owing to the planar failure that occurred during the flood cycles. Figures 4.95 and 4.96 show the longitudinal and transversal sections obtained from the restitution. The breach throat has a trapezoidal shape of 5 m breadth on top and 2.5 m on the bottom, with a depth of 1.85 m (at length 1 m). This value is different from the measured value of 2.23 m (Table 4.24). This might be a result of low precision achieved from the two pictures used for the restitution.

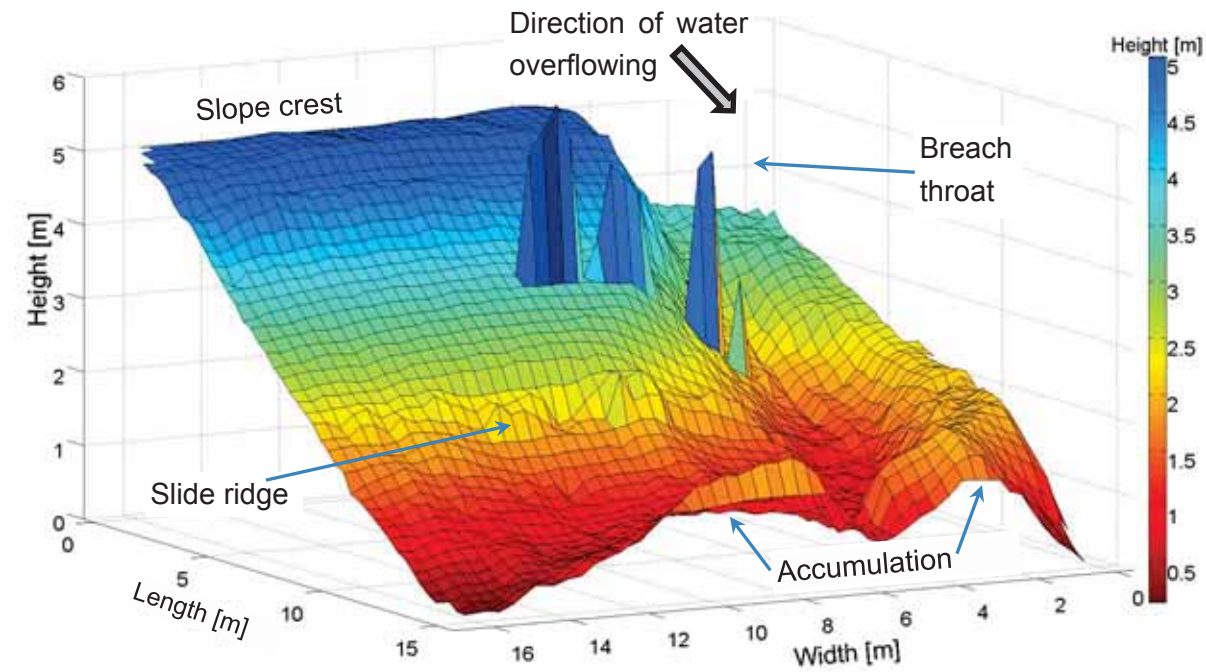

Figure 4.94: Three dimensional restitution of the air-side slope of the homogeneous dyke with slope gradient 1:3.0, by photogrammetric techniques.

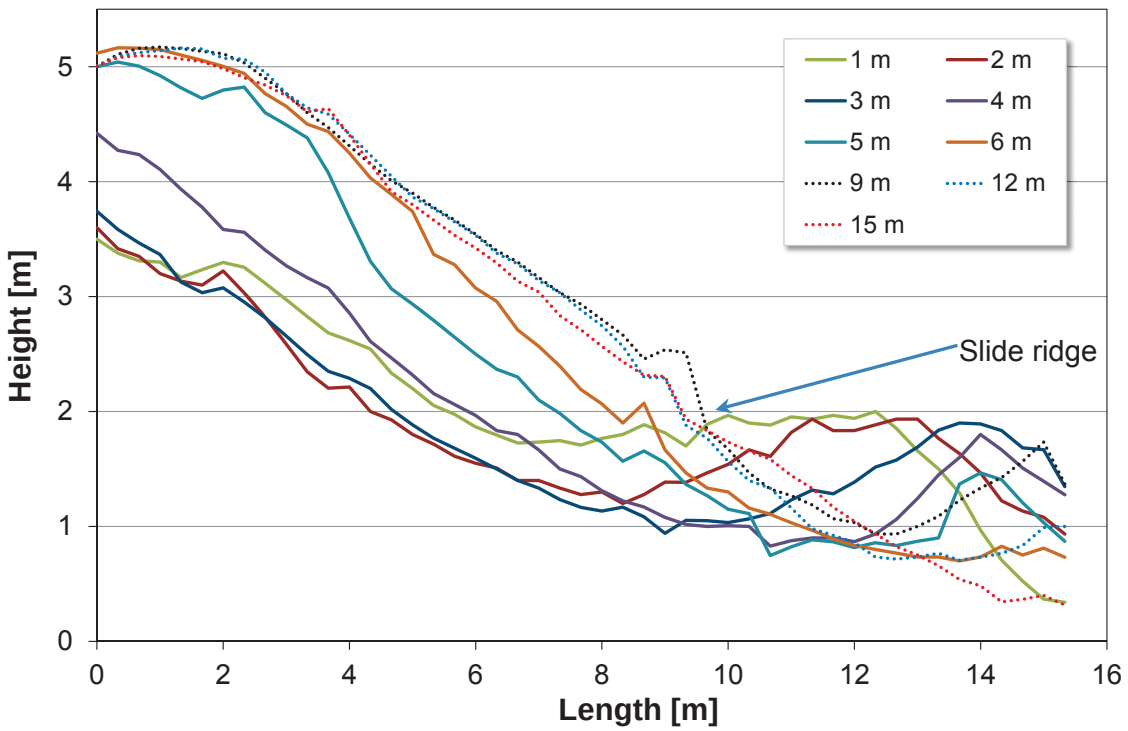

Figure 4.95: Longitudinal sections of the slope at specific values of the width of the homogenous dyke with a slope gradient of 1:3.0, based on the photogrammetric restitution (Figure 4.94).

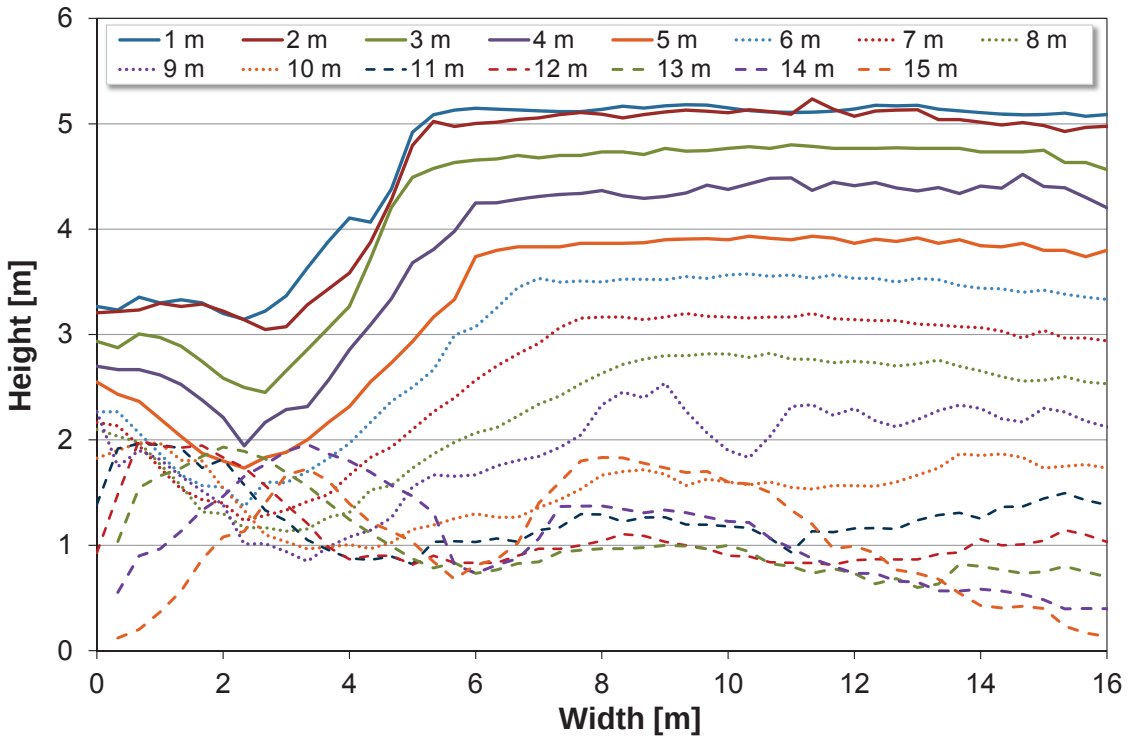

Figure 4.96: Transversal sections of the slope at specific values of the length of the homogenous dyke with a slope gradient of 1:3.0, based on the photogrammetric restitution (Figure 4.94).

4.5.2 Dyke with toe filter

Figure 4.97 shows the location of the sensors for this type of dyke. The main difference with the homogeneous dyke is that the PPT 8 lay above the toe filter. The results for the density parameters are presented in Table 4.25. Unfortunately, only data for the slope gradients of 1:2.0 and 1:3.0 are available. The construction method leaded to models of similar density, which allows the results from different tests to be compared.

Continual pore water pressure measurement was not possible at all points due to some faulty sensors. Twelve points of pore water pressure measurement were achieved for the model with slope gradient 1:2.0, whereas the model with a slope gradient of 1:2.5 had 6 points (3, 4, 5, 6, 7, 8), and the test with a slope gradient of 1:3.0 had 8 sensors (1–8). The green symbols represent the points at which both water pressure and water content was measured. The blue symbols are points where only water pressure was measured. The red point corresponds to the place, where the applied water level was measured.

All three tests have information on the volumetric water content from eight sensors (1–8), except for the model with slope gradients of 1:2.0, for which TDR 4 failed.

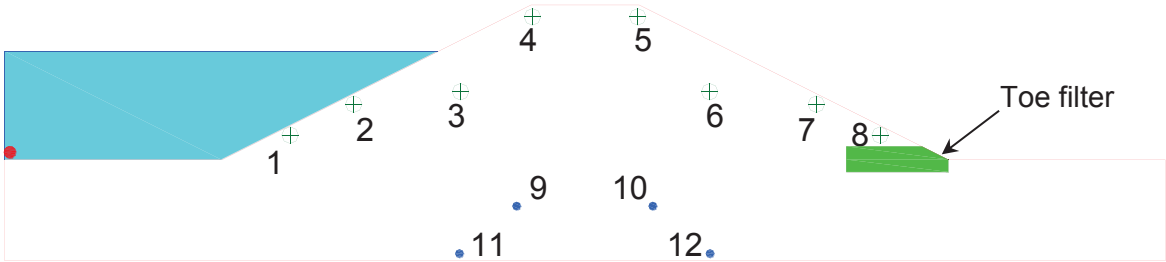

Figure 4.97: Location of the sensors for the dyke with toe filter.

Table 4.25: Density parameters for two tests on a dyke with toe filter.

Slope gradient	Specimen	γ_{bulk} [kN/m^3]	γ_{bulk_aver} [kN/m^3]	γ_{dry} [kN/m^3]	γ_{dry_aver} [kN/m^3]	e [-]	e_{aver} [-]	D_R [%]	D_{R_aver} [%]	θ_{sat} [%]
1:2.0	1	19.75	19.85	16.62	16.61	0.59	0.60	64.28	63.89	0.37
	2	19.74		16.57		0.60		62.76		
	3	19.94		16.67		0.59		66.21		
	4	19.96		16.56		0.60		62.34		
1:3.0	1	20.15	20.10	16.89	16.85	0.57	0.57	74.16	72.69	0.36
	2	20.25		16.90		0.57		74.62		
	3	20.07		16.76		0.58		69.68		
	4	19.92		16.84		0.57		72.32		

The pore water pressures at prototype scale are presented in Figures 4.98 to 4.100, as measured for the three slope gradients. The pore water pressure at point 1 was comparable with that obtained for the homogeneous dyke. It reflected immediately the change in the water level for the slope gradient of 1:2.0. The high pressure values indicate that the sensor was dislocated some millimeters lower than planned, as happened with the previous dyke. A difference of 10 kPa, which was expected, was found for the model with slope gradient 1:3.0,

when the water level was high. This difference increased to 12.8 kPa when the water level was lowered.

The maximum water pressure at point 2 was 27.3 and 20.4 kPa for the 1:2.0 and 1:3.0 slope gradients, respectively. This was approximately 3 kPa below the values measured for the homogenous dyke, whereas the minimum pressures were 2.17 and -2.93 kPa, which are similar to those measured before. The filter only starts to drawdown the water table when the water is raised.

The water pressures registered at point 3 were also similar to the values measured for the homogeneous dyke. The maximum pressures were 13.4, 12.2 and 13.4 kPa during the flood cycles, and 26.9, 25.3 and 24.6 kPa during the overflow process. This means that no influence of the toe filter was observed in the response of pore water pressures for this point.

Like the homogeneous dyke, points 4 and 5 showed no response to the flood cycles. Whereas the values increased to between 5.91 and 9.1 kPa for PPT 4, and between -0.4 and 1.4 kPa for PPT 5 during the overflow phase.

An important difference may be observed from data obtained at point 6 with respect to the homogenous dyke: there was no effect of changing the water level for the slope gradients 1:2.0 and 1:2.5, for which the pressure increased during the overflow to 16.1 and 13.0 kPa, respectively. However, an influence was observed for the slope gradient 1:3.0, for which the pore pressure increased to 4.1 kPa at each flood cycle and to 15.9 kPa during the overflow event.

A maximum pressure of 1.28 kPa was measured at point 7 during the flood cycles, for the model with a slope gradient of 1:2.0. No reaction was observed for the other two slope gradients, and the measurements were -1.08 and -0.94 kPa, respectively, through the first part of the test. The maximum pressures during the overflow were 23.2, 13.2 and 18.2 kPa.

As expected, data obtained for the pore pressures at point 8 confirmed a greater influence of the filter on the response. The pore water pressure fluctuated during the flood cycles, between 3.4 and 4.0 kPa for the slope gradient 1:2.0, with a maximum pressure of 31.4 kPa during the overflow phase. Values between -0.78 and 2.3 kPa were measured for the dyke with 1:3.0 gradients during the cycles, with 26.4 kPa during overflow. An increment in the water pressure was only noticed during the overflow phase for the gradient 1:2.5, for which a maximum value 27.9 kPa was observed.

Similar behavior was observed at Points 9 and 10 in the dyke with a toe filter and a slope gradient of 1:2.0 as for the homogeneous dyke, i.e. pressures at point 9 were greater than the applied pressure, and pressures at point 10 were smaller than those applied when the water level was high, and greater when the water level was lowered. However, the maximum pressure at point 9 (41.4 kPa) was smaller than that of the homogeneous dyke by 1.7 kPa, and the difference of pressure at the lower water level was reduced significantly, indicating more effective drainage at point 9 with the toe filter. The pore pressure increased to 54.7 kPa during the overflow.

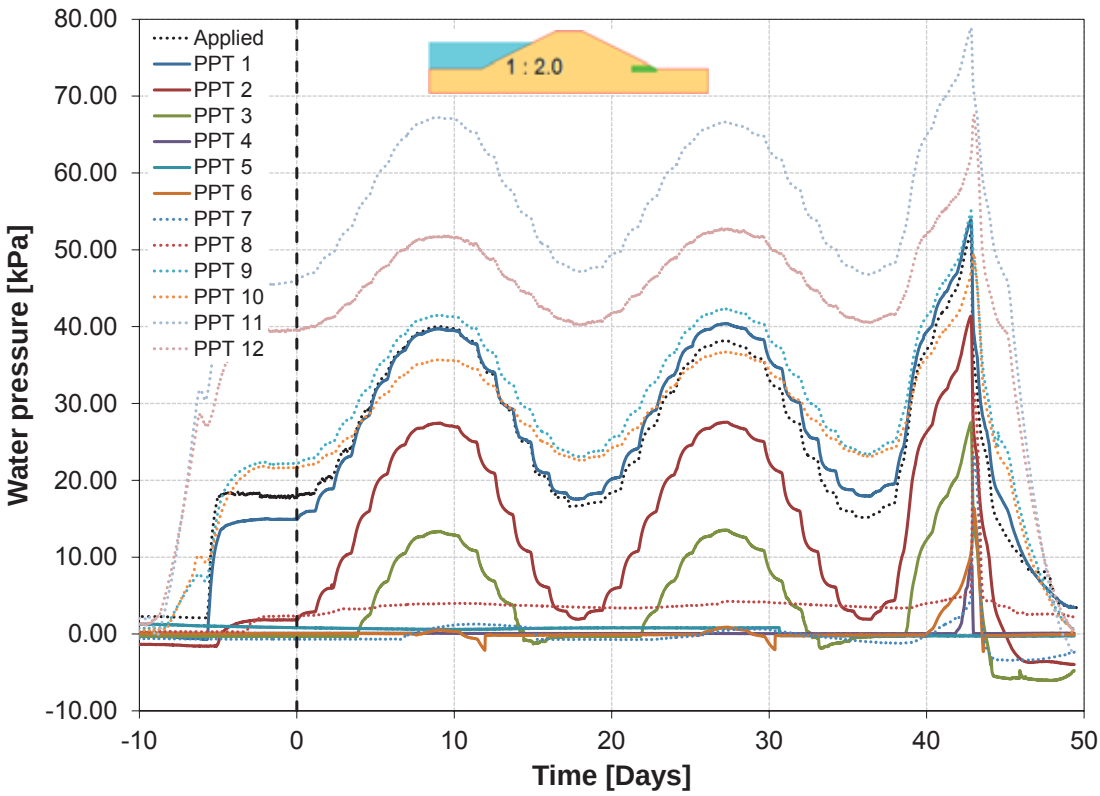

Figure 4.98: Water pressures for the dyke with toe filter and slopes 1:2.0, for two flood cycles an overflow phase as shown in Figure 4.78.

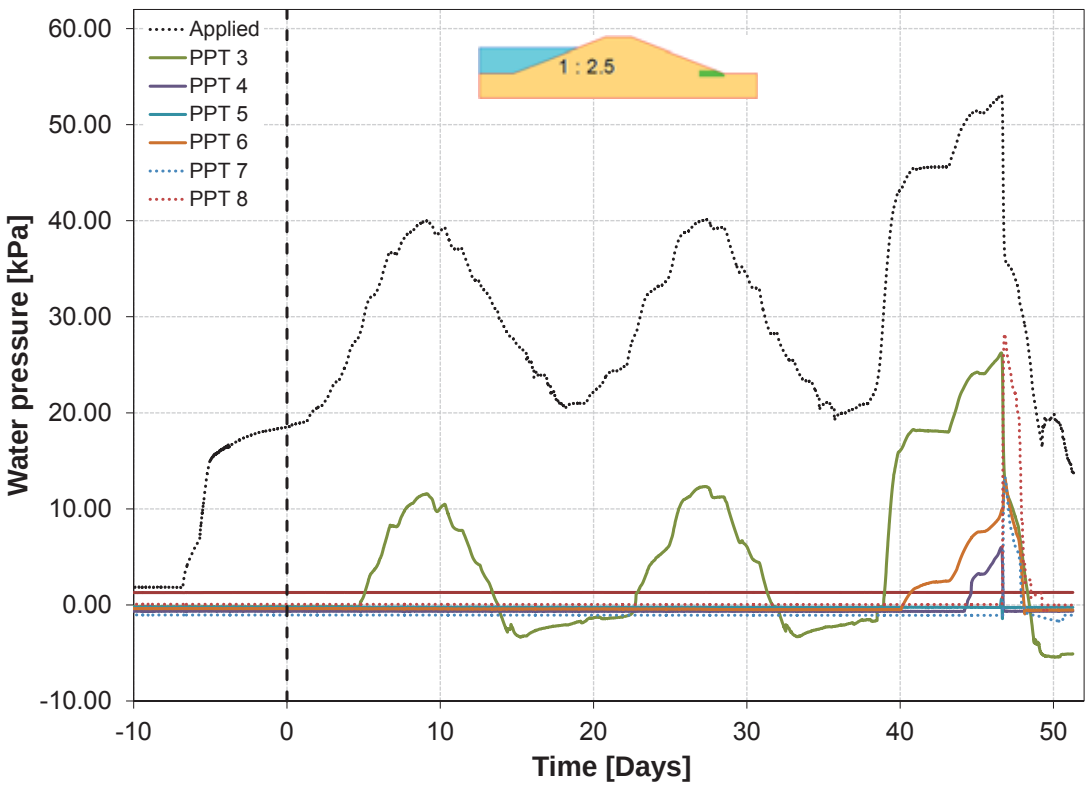

Figure 4.99: Water pressures for the dyke with toe filter and slopes 1:2.5, for two flood cycles an overflow phase as shown in Figure 4.78.

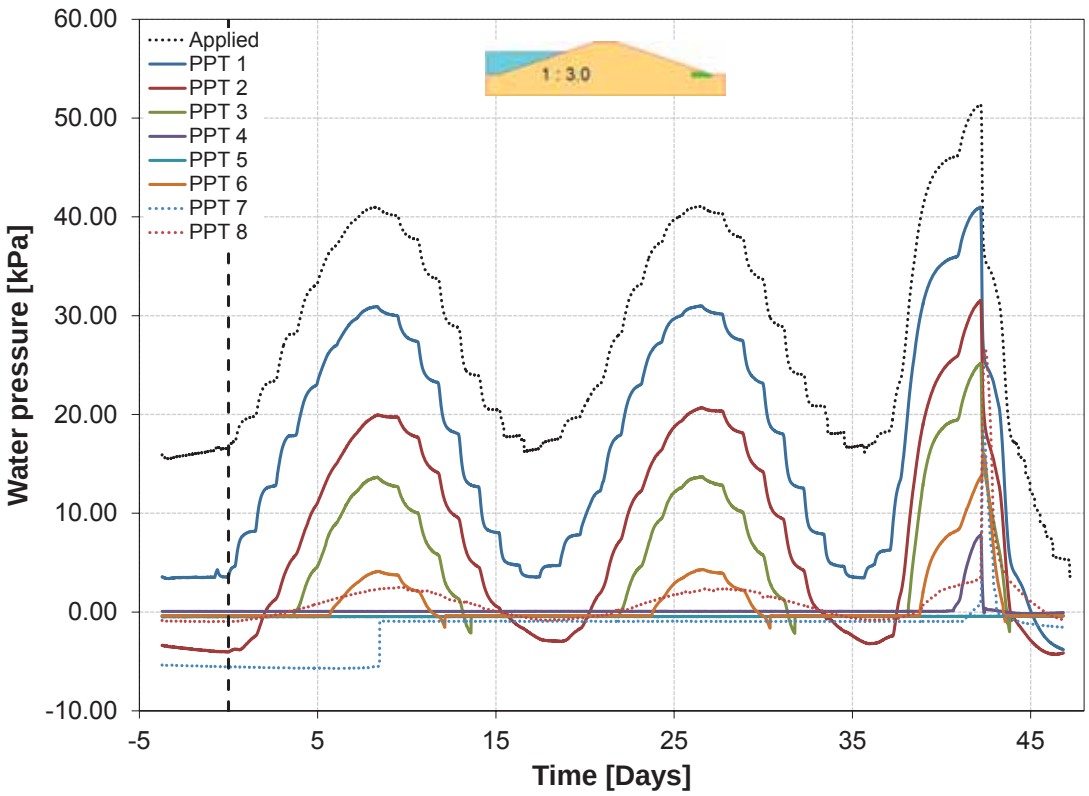

Figure 4.100: Water pressures for the dyke with toe filter and slopes 1:3.0, for two flood cycles an overflow phase as shown in Figure 4.78.

Behavior and values for points 11 and 12 for the dyke with a toe filter were almost identical to those of the homogeneous dyke. No influence of the toe filter was then seen on those points.

The evolution of volumetric water content is shown in Figures 4.101 to 4.103. As for the homogeneous dyke, the water content at point 1 showed that the soil was fully saturated during the flood cycles and the overflow process.

The water content at point 2 was similar for all three slope gradients. The soil saturated between 1 to 3 days after the water level was raised, and returned to the residual value when the water was lowered, except for the slope gradient 1:2.0, for which the minimum water content was 0.11 m^3/m^3; slightly above the residual value (0.08 m^3/m^3).

The same reaction was observed at point 3, with the exception that the maximum value of water content was below that observed for points 1 and 2 but it could be still considered as fully saturated. The values for TDR 3 were lower as the slopes become flatter (1:2.0 slope: 0.38 m^3/m^3, 1:2.5 slope: 0.33 m^3/m^3 and 1:3.0 slope: 0.32 m^3/m^3).

A failure of the TDR 4 led to corrupted results for the slope gradient 1:2.0, hence they were omitted. No reaction was observed at this point for the 1:2.5 slope, and a saturated condition was reached during the overflow phase for the slope with a gradient of 1:3.0.

Reaction of the water content at position 5 was observed for the slope gradients of 1:2.0 and 1:3.0, for which the soil only saturated during overflow.

Raising the water level had no influence on the water content at position 6 for the model with a slope gradient of 1:2.0. The soil increased the water content up to 0.28 m^3/m^3 for the slope gradient of 1:2.5, without becoming fully saturated, whereas, the response for the flattest slope gradient shows that the soil saturated during each flood cycle, and reached the residual water content after the water level was lowered.

A small effect of the changing water level was observed at position 7. The TDR sensors only showed an increment in the water content during the overflow phase for the slope gradient of 1:2.0, whereas no influence was measured during the whole test for the gradients 1:2.5 and 1:3.0. A problem with the TDR cable led to a measuring error during the overflow phase of the test with a slope gradient of 1:3.0.

At position 8, the measurements showed that the soil did become saturated when the water level was at its maximum. However, complete desaturation was also not achieved. The maximum and minimum water contents were 0.33 and 0.27 m^3/m^3 for the slope with a gradient of 1:2.0, whereas they were 0.23 and 0.15 m^3/m^3 for the slope with a gradient of 1:3.0 for the first flood cycle and 0.27 and 0.14 m^3/m^3 for the second cycle. Subsequently, the soil became fully saturated during the overflow phase. A similar problem with the TDR cable led to a measurement error during the overflow phase of the test with a slope gradient of 1:3.0.

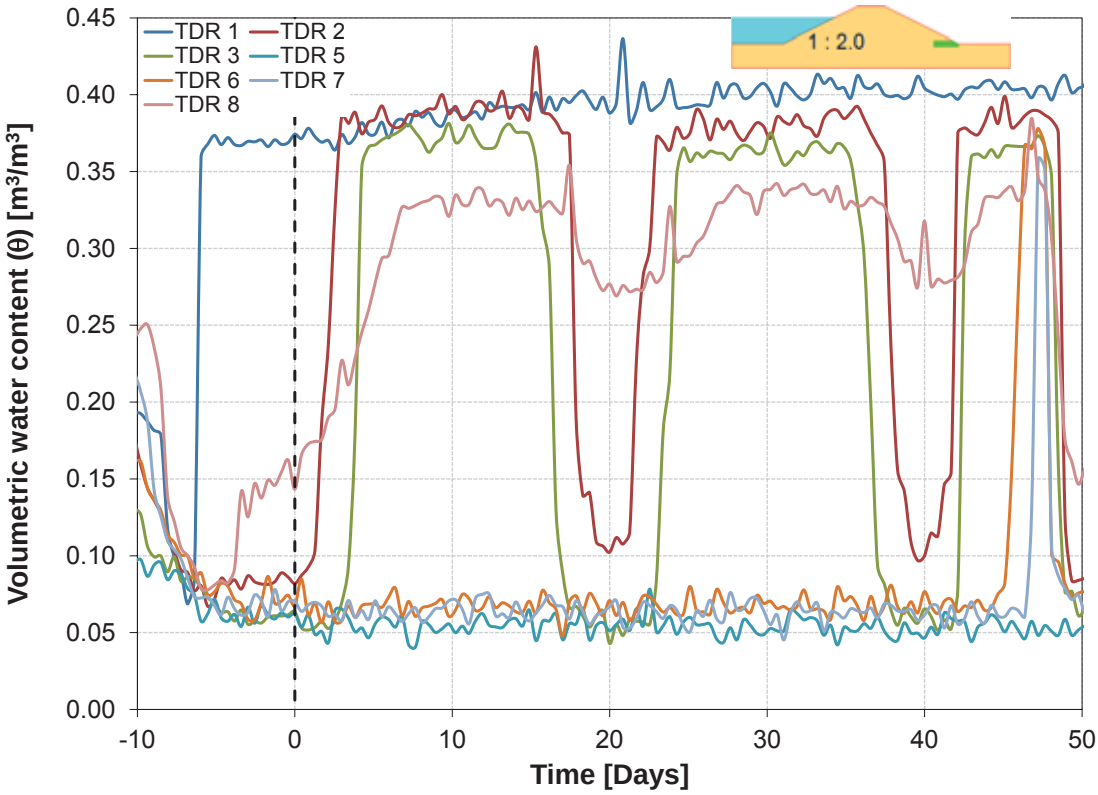

Figure 4.101: Volumetric water contents for the dyke with toe filter and slopes 1:2.0, for two flood cycles an overflow phase as shown in Figure 4.78.

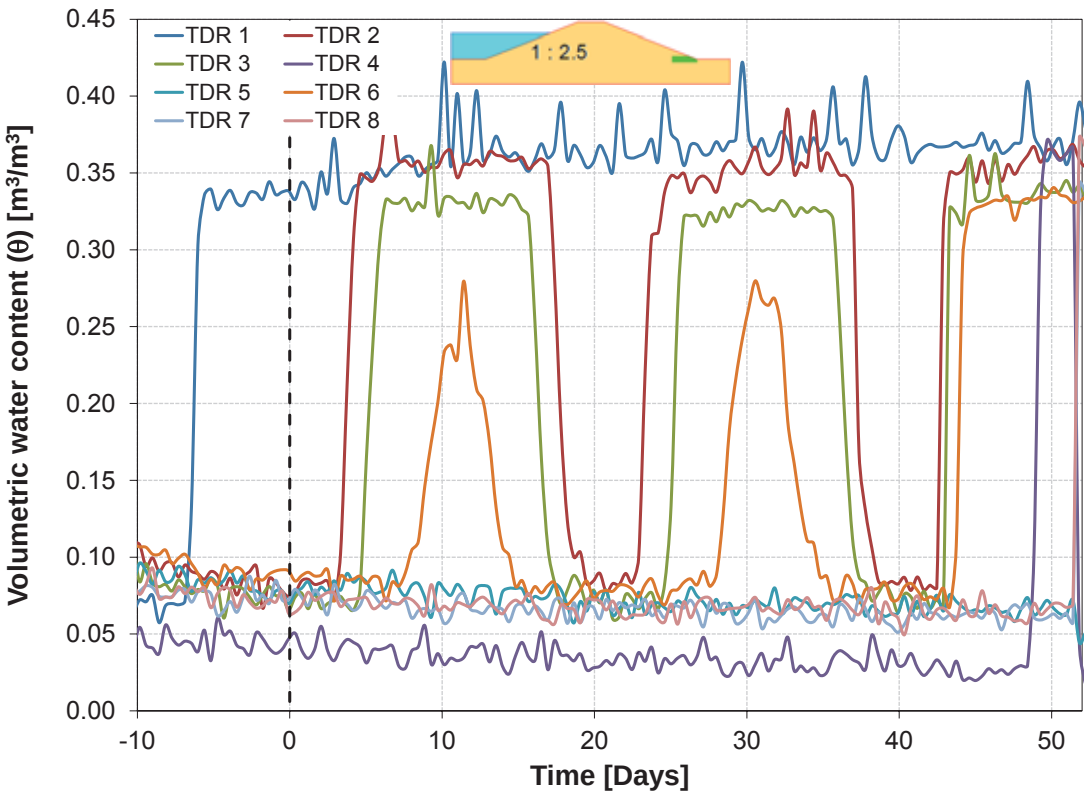

Figure 4.102: Volumetric water contents for the dyke with toe filter and slopes 1:2.5, for two flood cycles an overflow phase as shown in Figure 4.78.

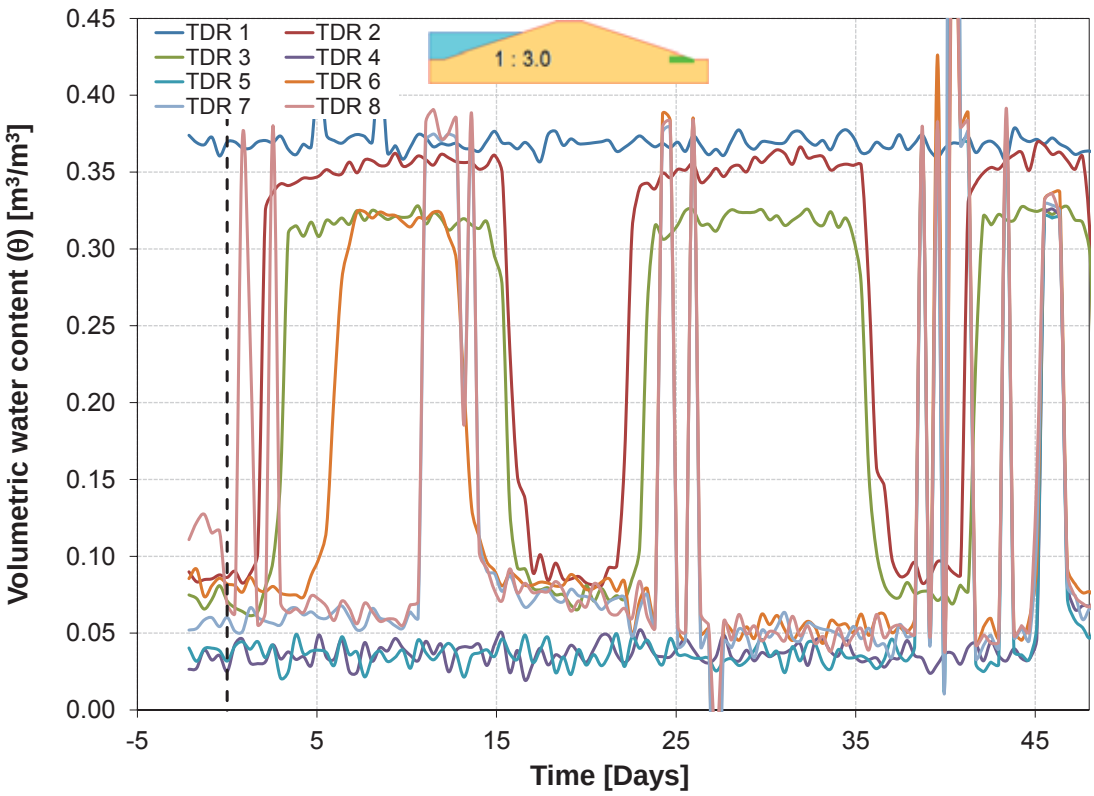

Figure 4.103: Volumetric water contents for the dyke with toe filter and slopes 1:3.0, for two flood cycles an overflow phase as shown in Figure 4.78.

4.5.2.1 Failure and breaching mechanism

No slope instability was observed during the flood cycles for this type of dyke, confirming the effect of the filter in preventing erosion and instabilities events on the air-side. Figure 4.104 illustrates the breaching mechanism developed for the model with a slope gradient of 1:3.0. This was, nonetheless, similar for the other slope gradients.

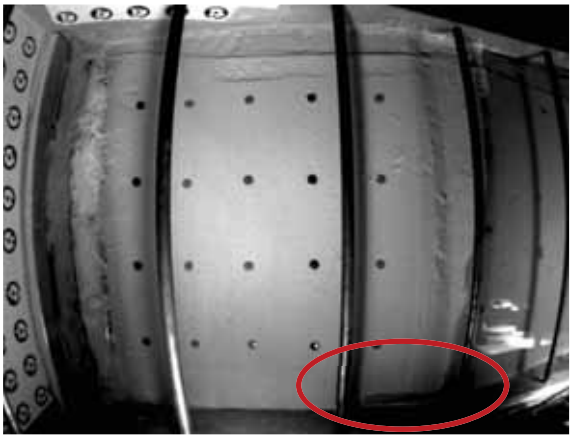

a) After 9.26 min.

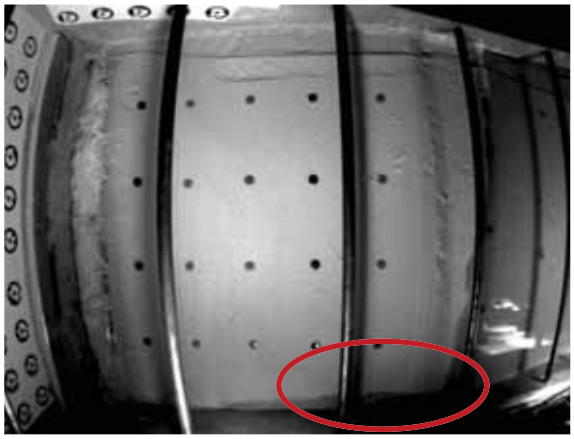

b) After 18.5 min.

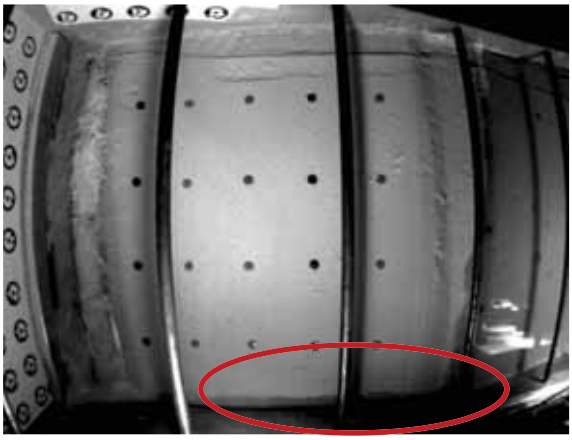

c) After 37.03 min.

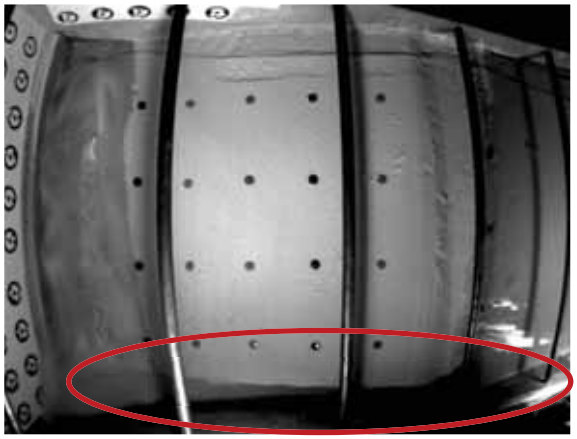

d) After 74.06 min.

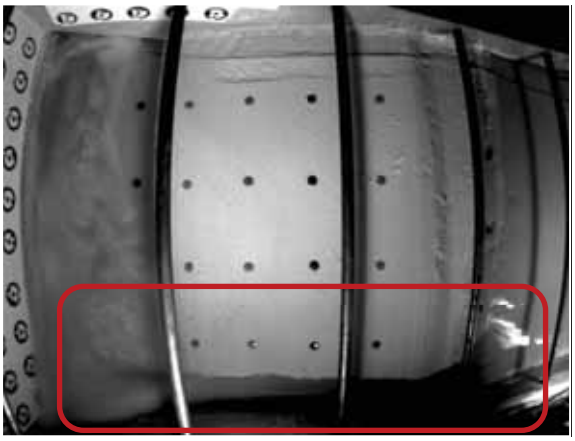

e) After 92.57 min.

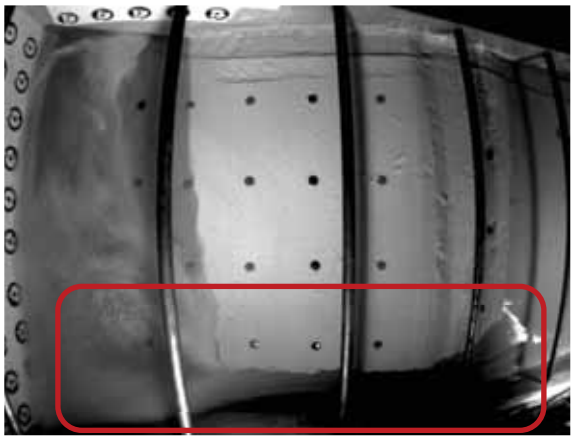

d) After 111.09 min.

Figure 4.104: Breach development of the dyke with toe filter with a slope gradient of 1:3.0. Time zero corresponds to the moment at which breaching began (41.8 days).

Water started eroding the superficial material, creating a notch, which deepened with time. The breach zone was a narrow channel, whose crest was almost a straight line along the cross section of the dyke. It widened owing to the effect of the same two actions: soil erosion and slope instability, which generated vertical ridges in the unsaturated sand. This was a similar behavior to that observed for the homogenous dyke.

The main difference between the failures observed is that the breach for the model with slope gradient 1:3.0 developed in the lower part of the model, whereas, the breach was located in the upper part for the other two models, where the wall that separates the mixture of sand-bentonite was located.

Figure 4.105 shows the final configuration of the air-side slopes for all three tests, and an enlarged view of the breach zone is revealed in Figure 4.106. A similar breaching mechanism, as described above, was observed for all three tests.

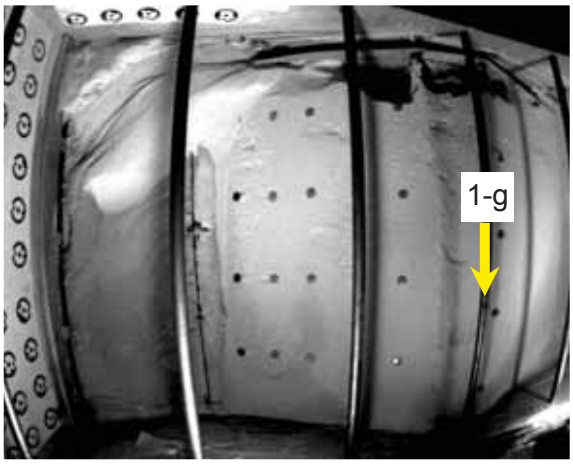

a) Slope gradient 1:2.0.

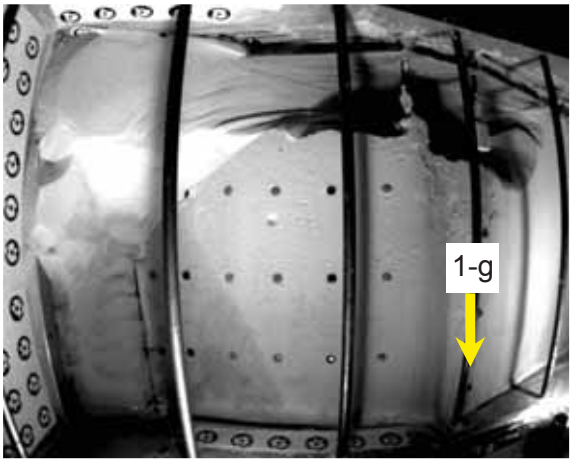

b) Slope gradient 1:2.5.

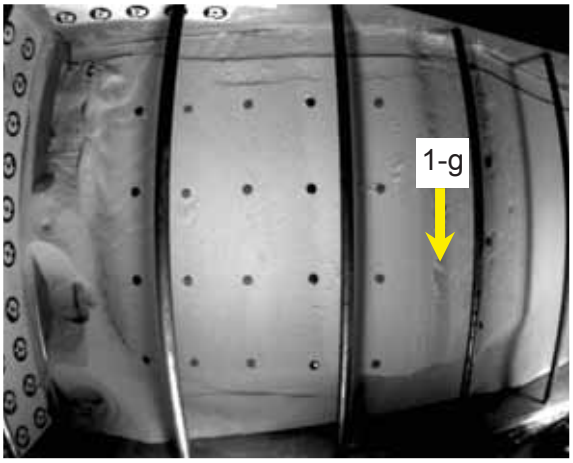

c) Slope gradient 1:3.0.

Figure 4.105: Final condition of the dyke with a toe filter, after overflow.

a) 1:2.0. b) 1:2.5. c) 1:3.0.

Figure 4.106: Breaching zone of the dyke with toe filter after overflow for all three slope gradients.

The time required for the breach to develop completely is summarized in Table 4.26, including the width of the breach at the slope surface, and the depth of the breach zone at the crest of the slope, for each of the slope gradients modeled. The required time for the breach to be developed completely was, on average, 3.24 times longer than for the homogeneous dyke. This is a key point when assessing hazard and risk.

Similar to what happens with the homogenous dyke, the steepest slope required more time the breach to develop fully despite the smaller area (at about 50 - 60% of the area of the breach in the homogenous dyke).

Table 4.26: Summary of the breaching characteristics for the dyke with toe filter.

Slope gradient	Breaching time [min]	Width [m]	Depth [m]	Area [m^2]*
1:2.0	370.30	2.33	2.33	5.43
1:2.5	305.49	3.63	2.60	9.44
1:3.0	163.64	3.33	1.90	6.33

** Calculated as width × depth.*

4.5.3 Dyke with a cut-off wall

Figure 4.107 shows the location of the sensors for this type of dyke. The results for the density parameters are presented in Table 4.27. Unfortunately, data are only available for the slope gradients 1:2.0 and 1:2.5. The construction method led to models of similar density, which allows the results from different tests to be compared.

The models with a slope gradient of 1:2.0 and 1:3.0 had 11 points at which pore water pressure was measured (1–10 and 12), whereas the model with slope gradient 1:2.5 had 8 sensors (1–8). All three tests have information from the volumetric water content from 8 sensors (1–8), except for the models with 1:2.0 and 1:3.0 slope gradients, for which TDRs 4 and 5, failed, respectively.

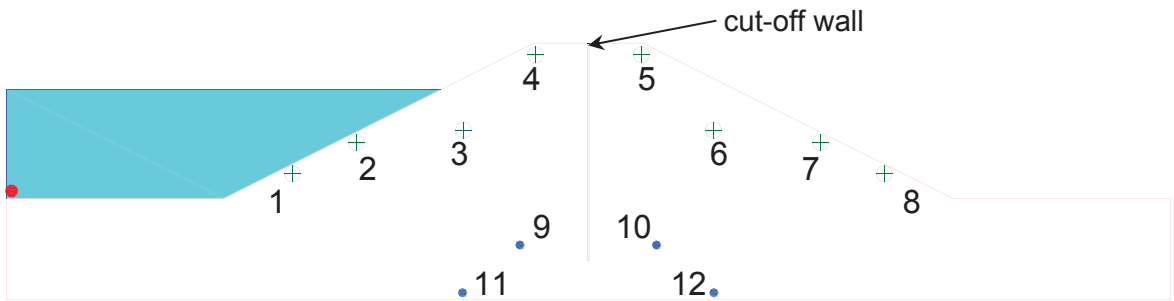

Figure 4.107: Location of the sensors for the dyke with a cut-off wall.

Table 4.27: Density parameters for two tests on a dyke with a cut-off wall.

Slope gradient	Specimen	γ_{bulk} [kN/m^3]	γ_{bulk_aver} [kN/m^3]	γ_{dry} [kN/m^3]	γ_{dry_aver} [kN/m^3]	e [-]	e_{aver} [-]	D_R [%]	D_{R_aver} [%]	θ_{sat} [%]
1:2.0	1	18.18	18.60	16.71	16.85	0.59	0.57	67.66	72.69	0.36
	2	18.71		16.72		0.59		67.98		
	3	19.03		16.96		0.56		76.59		
	4	18.50		17.01		0.56		78.52		
1:2.5	1	20.10	19.56	16.92	16.86	0.57	0.57	75.22	73.31	0.36
	2	19.68		16.78		0.58		70.34		
	3	18.34		16.77		0.58		70.07		
	4	20.13		16.98		0.56		77.60		

Figures 4.108 to 4.110 illustrate the pore water pressures during the tests. A trend in the response of water pressures at point 2 was confirmed for this type of dyke. The water pressures increased near to 30 kPa for the steepest slope (1:2.0), which is a similar value to that measured at point 1. Additionally, the pressures were always positives, being above 0 kPa even when the water level was lowered. Maximum and minimum pore pressures for the other two slope gradients were around 20 and -3 kPa, at the maximum and minimum water levels, respectively.

Furthermore, a time lag occurred in the drainage when lowering the water level, during the flooding cycles of the model with a slope gradient of 1:2.0. This means that the minimum pressure was reached 2.7 days after the water level was lowered. This might be a consequence of water being retained on the water-side of the dyke by the cut-off wall, thus leaving only one drainage path through the lower sand layer, around the cut-off wall.

The response of the water pressure at point 3 was similar to that observed in the other two types of dykes. The main difference is that the water pressure reaches a maximum of 20.9 kPa for the test with a slope gradient of 1:2.5. This confirms the conjecture that water was retained on the water-side, increasing the height of the water table, hence the high pressures registered, although suctions up to 6.8 kPa were only measured partially during the recovery cycles.

PPTs 4 and 5 showed no reaction, neither presented cavitation during the flood cycles. An increase in the water content during the overflow phase was noticed.

The influence of the slope inclination was clear at point 6. The flatter the slope, the greater the water pressures. In this way the maximum pressures measured during the flood cycles were 0.94, 1.88 and 3.44 kPa, while during overflow they rose to 8.5, 14 and 12.7 kPa.

The reaction at point 7 during the flood cycles varied only for the slope gradient 1:2.0. The water pressure reached a maximum of 2.3 kPa for both cycles for this case. The maximum pressures were 7.0, 4.4 and 10.9 kPa during the overflow process, for the slope gradients 1:2.0, 1:2.5 and 1:3.0, respectively.

The water pressures at point 8 were positive for all types of slope gradient. The maximum values during the cycles were 14.4, 9.4, 8.9 kPa, whereas the minimum pressures were 6.4, 3.7, 2.0 kPa, for the slope gradients 1:2.0, 1:2.5 and 1:3.0, respectively. The maximum pressures measured were 17.1, 13.3 and 27.8 kPa during the overflow process.

Pressures were measured at point 9 for two tests, corresponding only to the slope gradients of 1:2.0 and 1:3.0. These showed a significant increase in the pressure compared to the values measured at the same point for the homogenous dyke, and with the toe filter due to the ponding of the groundwater on the upstream side of the cut-off wall. The maximum and minimum pressures registered were: 48.2, 44.1 kPa and 26.6, 22.5 kPa. This shows that the values are greater, compared to the other types of dyke, for both raising and lowering of the water level.

The pore water pressures were measured at point 10, for the same models as for point 9. However, the pressures at this point did not show a significant increase when compared to the other types of dyke. This confirms that the wall, as expected, confines the water on the water side, increasing the water pressures. A value of almost 24 kPa in the pore pressure was observed at point 10 after each flood cycle for the model with a slope gradient of 1:3.0. However, the shift in the time to reach the peak value, as well as the initial value, might indicate an error in the measurements for this specific point.

The water pressures at point 12 showed a noteworthy difference between both models in which they were recorded. While the behavior was almost identical to the one observed for the other two types of dyke for a slope gradient of 1:2.0, whereas for a slope gradient of 1:3.0, it showed a delay in reaching the peak value (46.5 kPa), which is smaller than for the other types of dyke.

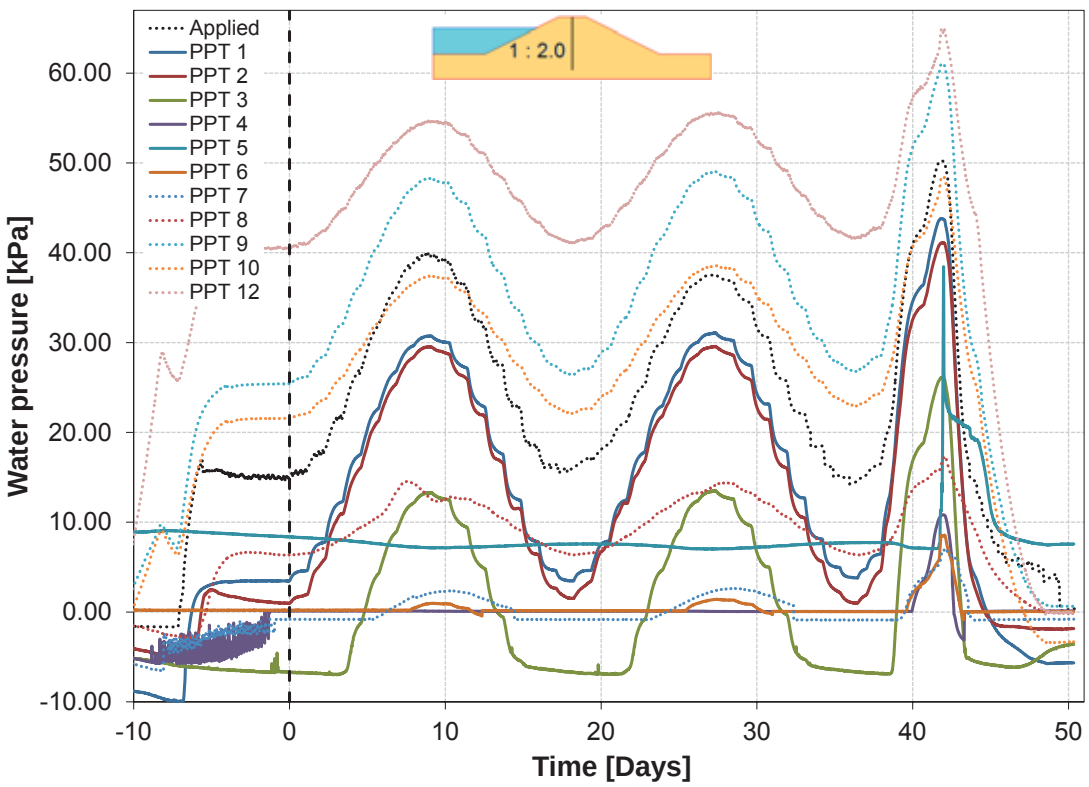

Figure 4.108: Water pressures for the dyke with a cut-off wall and slopes 1:2.0, for two flood cycles an overflow phase as shown in Figure 4.78.

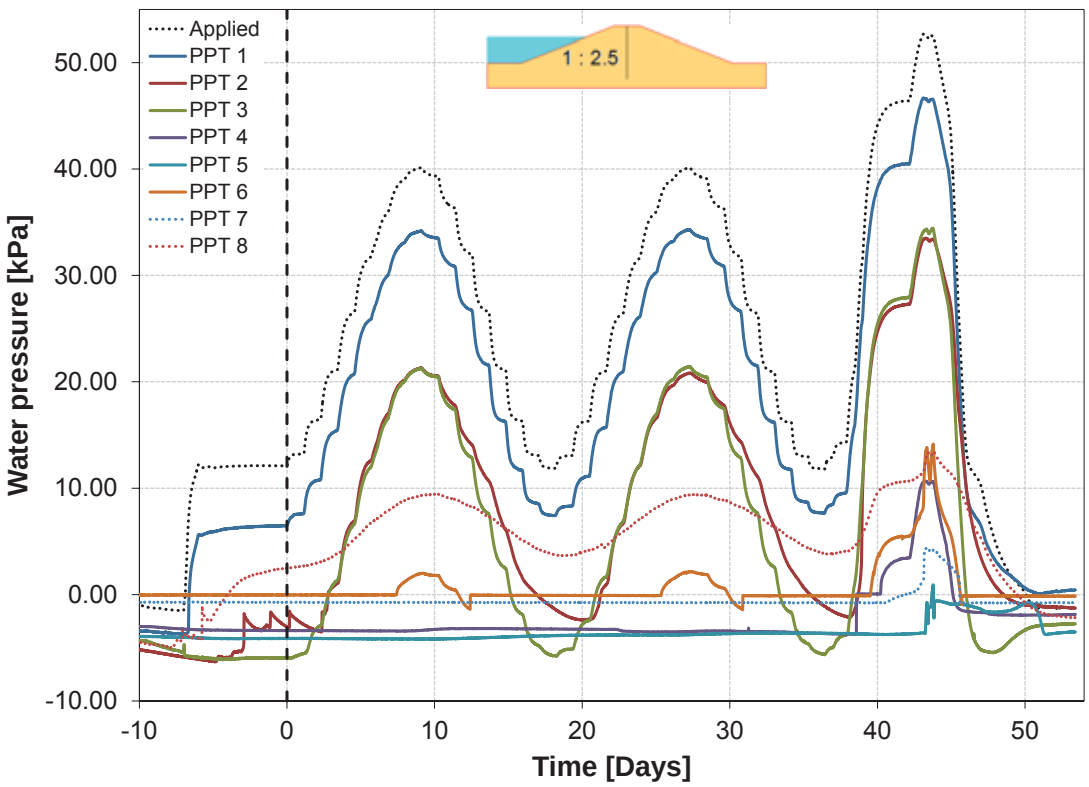

Figure 4.109: Water pressures for the dyke with a cut-off wall and slopes 1:2.5, for two flood cycles an overflow phase as shown in Figure 4.78.

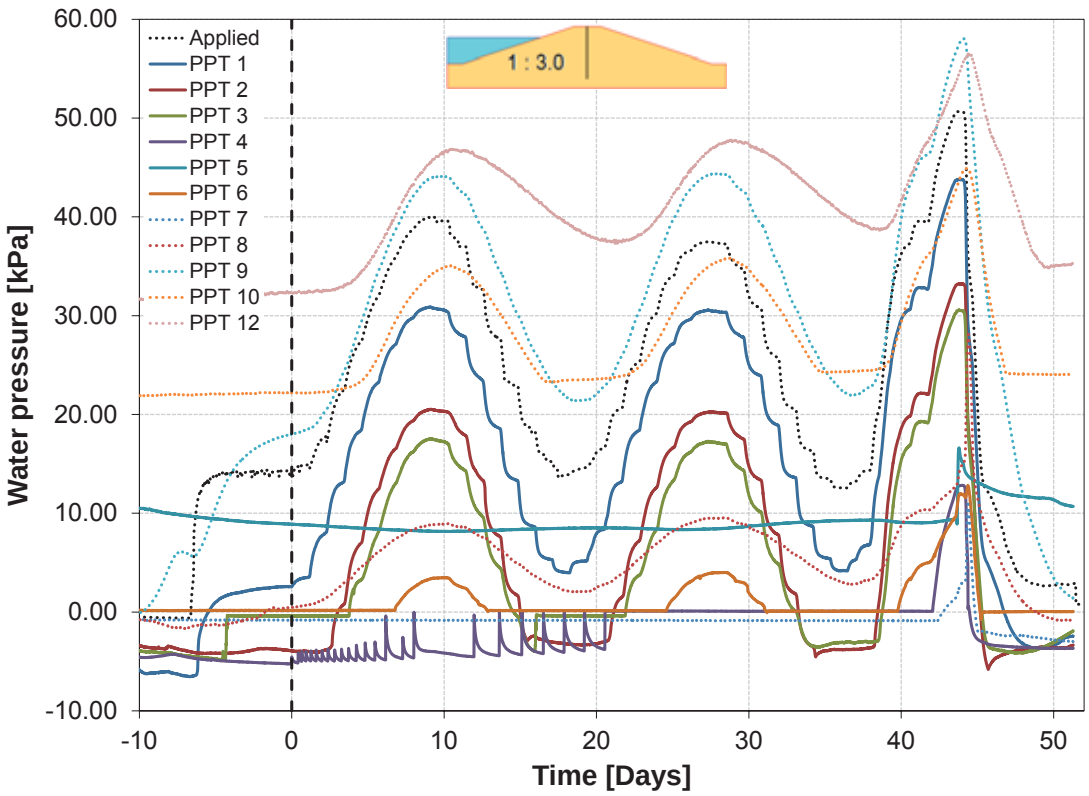

Figure 4.110: Water pressures for the dyke with a cut-off wall and slopes 1:3.0, for two flood cycles an overflow phase as shown in Figure 4.78.

The response of the TDR sensors to determine volumetric water content for the three tests carried out is presented in Figures 4.111 to 4.113. Like the other types of dyke, the soil at point 1 was in a saturated state during the whole test, for all three slope gradients.

The reaction of the sensor used to measure water content at point 2, for all three tests, was similar to that of the dyke with a toe filter, i.e. the soil saturated after the water level was raised for all three slope gradients, returning to the residual value when the water was lowered, except for the slope gradient 1:2.0, for which the minimum water content was 0.22 m^3/m^3. This is twice the value measured for the other types of dyke.

The response was similar for all three models at point 3. The soil saturated after the water level was raised, and the water content reached the residual value when it was lowered.

The volumetric water content at points 4 and 5 remained at the residual value during both flood cycles, and increased to values close to saturation during the overflow event.

The response at point 6, was different for each slope gradient. Only a slight effect of the flood cycles was observed in the model with a slope gradient of 1:2.0. The water content increased to 0.10 m^3/m^3 during the first cycle and to 0.12 m^3/m^3 during the second cycle. The water content in the soil increased close to saturation for the slope gradient of 1:2.5, and decreased to the residual value afterwards. In contrast, the water content only increases to 0.27 m^3/m^3 for the slope at 1:3.0. Again, the residual value was measured after the water level was lowered. All the models were completely saturated during the overflow process.

The model with a slope gradient of 1:2.0 was the only one that exhibited a change in the water content for point 7 during the flood cycles. The values were close to these measured at point 6, i.e. 0.09 and 0.11 m^3/m^3 for each of the flood cycles. During the overflow phase, all the models showed an increase until a saturation condition was reached.

The response of the water content at point 8 was also dependent on the slope gradient. While the values showed almost saturated conditions from the beginning for the model with 1:2.0 slopes, with a small gradual decrease with time, the other two models showed a decrease in the water content after the water level was lowered. The minimum values were 0.25 and 0.23 m^3/m^3, for the slopes with a gradient of 1:2.5 and 1:3.0, respectively.

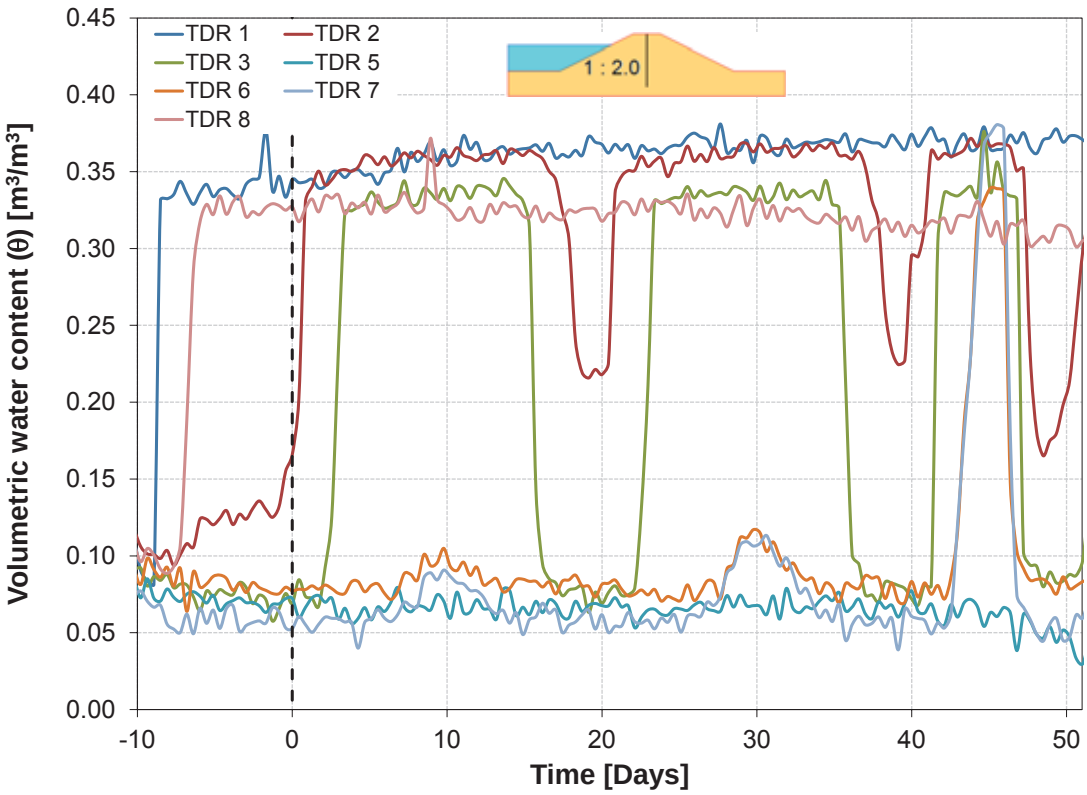

Figure 4.111: Volumetric water contents for the dyke with a cut-off wall and slopes 1:2.0, for two flood cycles an overflow phase as shown in Figure 4.78.

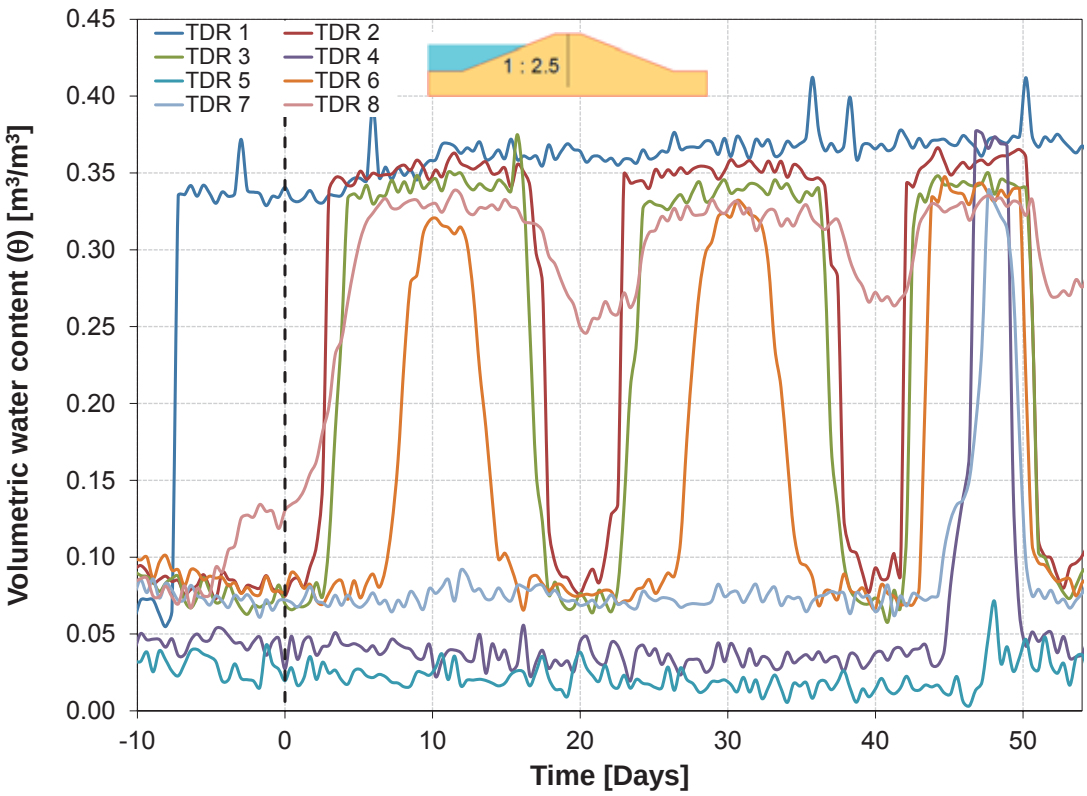

Figure 4.112: Volumetric water contents for the dyke with a cut-off wall and slopes 1:2.5, for two flood cycles an overflow phase as shown in Figure 4.78.

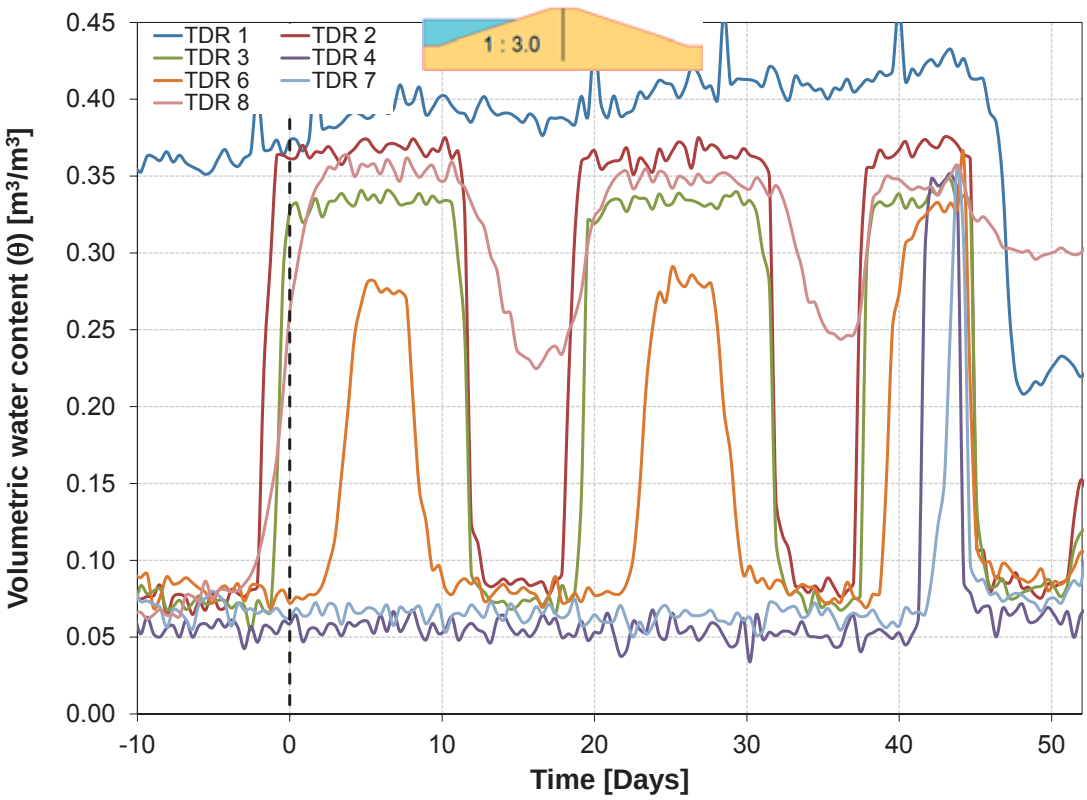

Figure 4.113: Volumetric water contents for the dyke with a cut-off wall and slopes 1:3.0, for two flood cycles an overflow phase as shown in Figure 4.78.

4.5.3.1 Failure and breaching mechanism

Before the overflow process

Instability events developed on the air-side slope for this type of dyke, which were similar to those observed for the homogeneous dyke. However, the zone affected was significantly smaller than of the homogenous dyke. The affected area did not reach the mid-height of the slope, as seen in Figure 4.114. The influence of the permanent 1-g acceleration vector is again clear on the lower parts of the model, for which the instability was greater than in the upper part of the model.

The instability process, as for the homogeneous dyke, had two stages. The first took place during the first flood cycle. The unstable zone increased progressively until the water reached its maximum level on the water-side of the dyke. It remained almost unchanged when the water level was lowered, and during the second flood cycle.

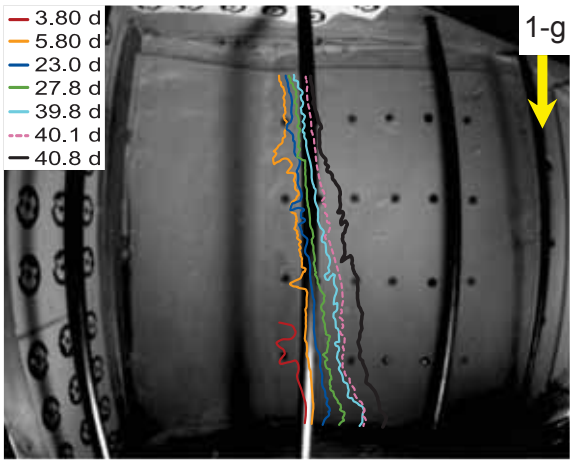

a) Slope gradient 1:2.0.

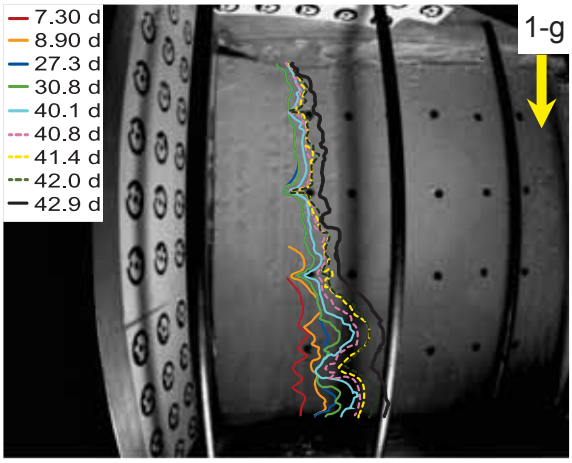

b) Slope gradient 1:2.5.

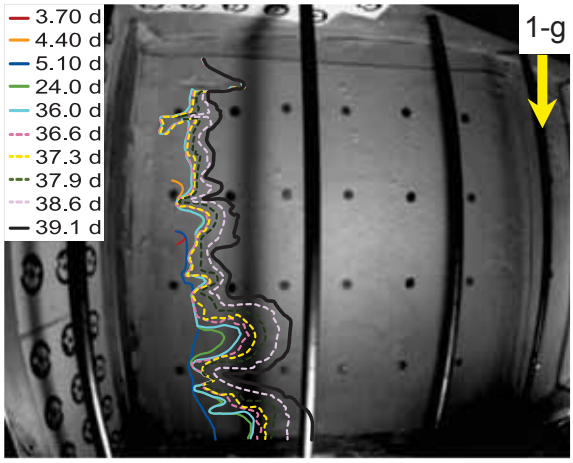

c) Slope gradient 1:3.0.

Figure 4.114: Development of the retrogressive failure mechanism on the air-side of the dyke with a cut-off wall (in days at prototype scale).

The second stage of the instability process occurred during the overflow phase, and only when the water level had reached the previous maximum level, i.e. the maximum level during the flood cycles. Material continues sliding down the slope, enlarging the unstable zone from that moment on, until the time at which the overflow had been completed.

Figure 4.115 illustrates the instability process with a sequence of pictures of the slope gradient of 1:2.0. Although these were actually taken during the overflow event, they portray the process taking place.

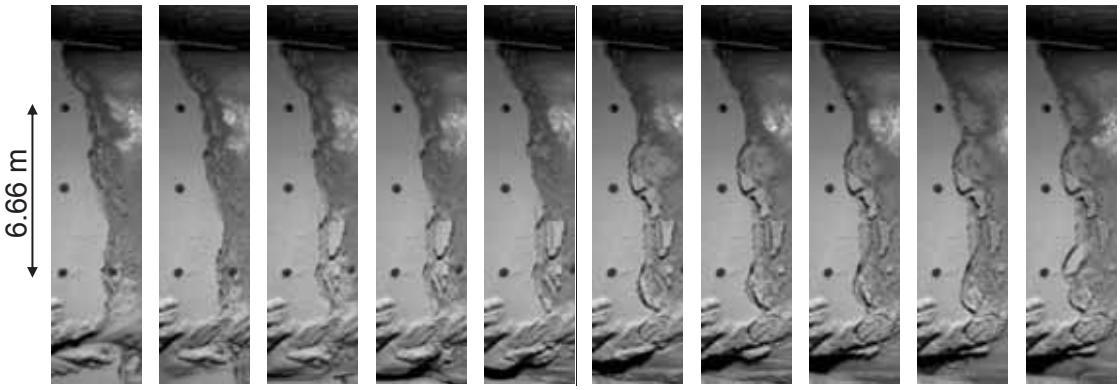

Figure 4.115: Sequence of pictures illustrating the slope instability process on the air-side slope (gradient 1:2.0) from left to right during the flood cycles. Each frame was taken every 9.26 minutes at prototype scale (83.32 minutes in total).

During the overflow process

The breaching mechanism observed for the dyke with a cut-off wall is illustrated in Figure 4.116. A breach throat started to develop in the zone of the crest of the dyke, closer to the air-side (red circle in Figure 4.116a). This is a similar process to that observed for the homogeneous and toe-filter dykes. When the throat reached the cut-off wall (Figure 4.116b), it could not continue increasing towards the water side. The soil in front of the wall, i.e. on the air-side, started to be eroded, creating a narrow and shallow breach zone in the vicinity of the wall. Water flowing out of the breach zone eroded the soil downslope. However, the material was not transported and deposited at the foot of the slope, but in the middle of the slope instead. Water that had overflowed the dyke surrounded the previously deposited material. As a consequence, a deposition fan was generated in the middle of the slope.

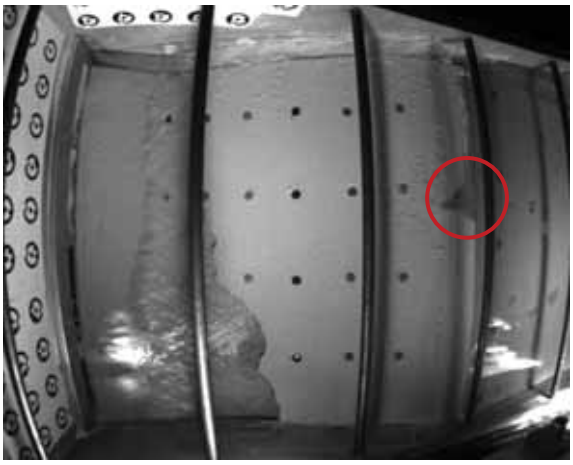

a) At 0 min.

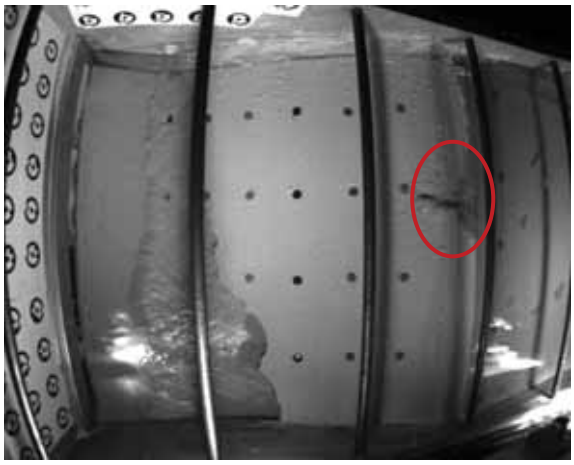

b) After 18.51 min.

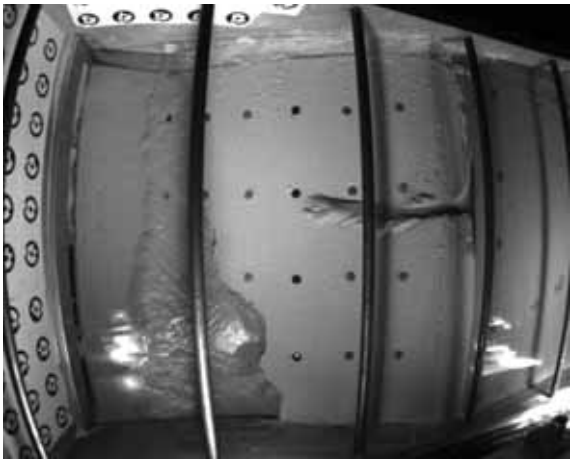

c) After 83.32 min.

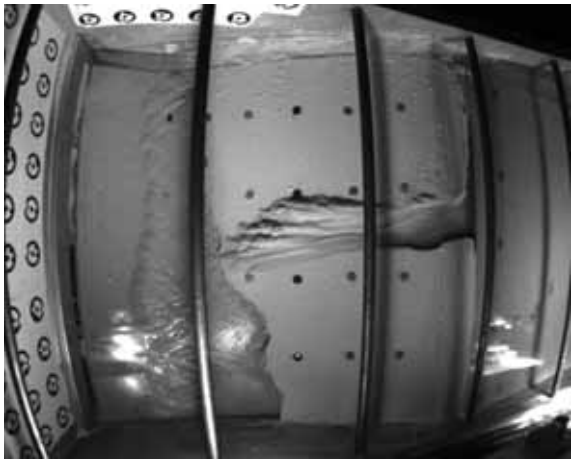

d) After 148.12 min.

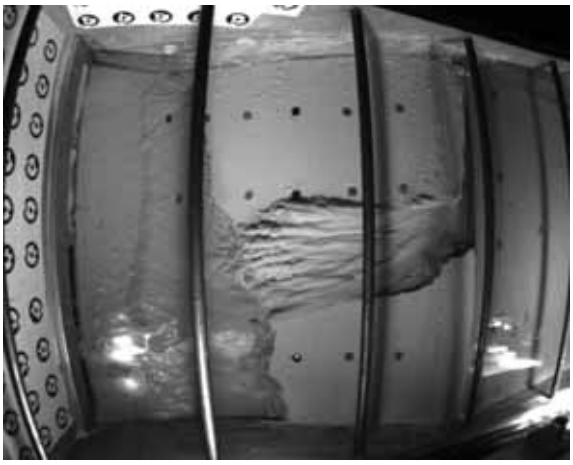

c) After 212.92 min.

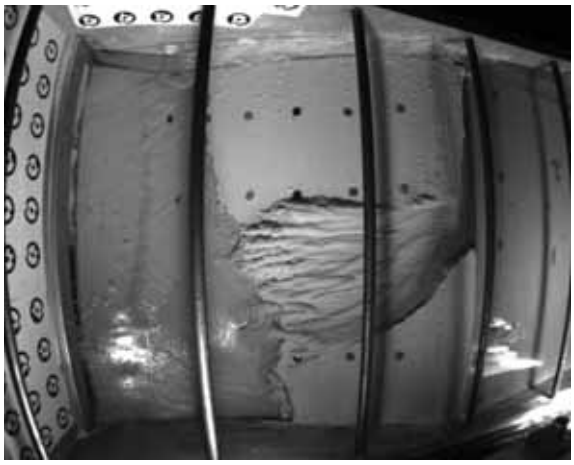

d) After 277.72 min.

Figure 4.116: Breach development of the dyke with a cut-off wall with a slope gradient of 1:2.5. Time zero corresponds to the moment at which breaching began (50.1 days).

Figure 4.117 shows the final configuration of the air-side slopes for all three tests, and Figure 4.118 shows an enlarged view of the breach zone. A similar breaching mechanism to that described above (Figure 4.116) was observed for all three tests.

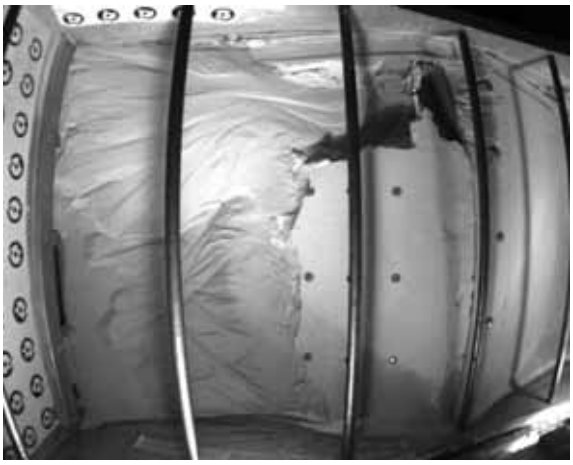

a) Slope gradient 1:2.0.

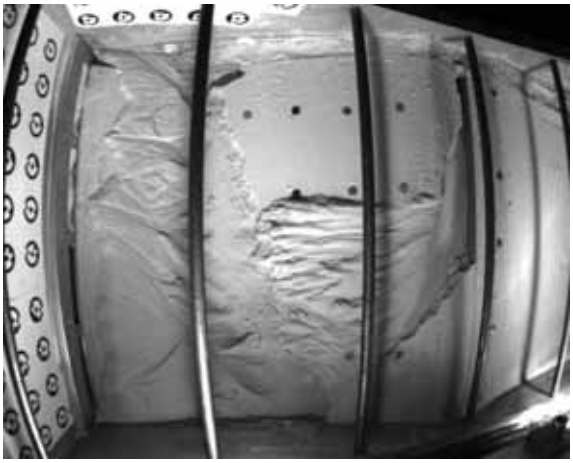

b) Slope gradient 1:2.5.

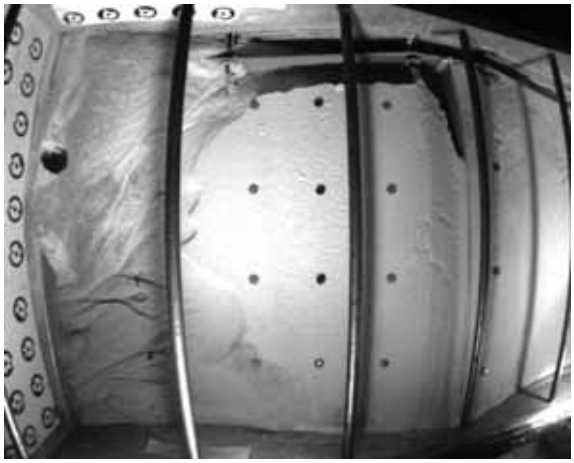

c) Slope gradient 1:3.0.

Figure 4.117: Final condition of the dyke with a cut-off wall, after overflow.

a) 1:2.0.

b) 1:2.5.

c) 1:3.0.

Figure 4.118: Breaching zone of the dyke with a cut-off wall, after overflow, for all three slope gradients.

The failure process was described in Section 4.5.1.1 as a coupled process of erosion and slope instability, and an example of the slope stability of the ridge of the breach was shown. Figure 4.119 illustrates the erosive process. Water overflowing downslope erodes the foot of the ridge of the breach. As a consequence, the foot of the ridge losses its support, leading to the slope instability.

Figure 4.119: Breach zone developed eroding along the cut-off wall.

The time required for the breach to develop completely is summarized in Table 4.28, together with the width of the breach at the slope surface, and the depth of the breach zone at the crest of the slope for each of the slope gradients modeled. Once again, the time taken for the breach to develop did not show any clear trend. The model with the intermediate slope gradient (1:2.5) required less time to erode the smallest area, whereas the model with the slope gradient of 1:2.0 required more time to erode the largest area, of all three. However, the average time to erode the material was 5.75 and 1.78 times greater than the time required for the homogeneous dyke and the dyke with a toe filter, respectively.

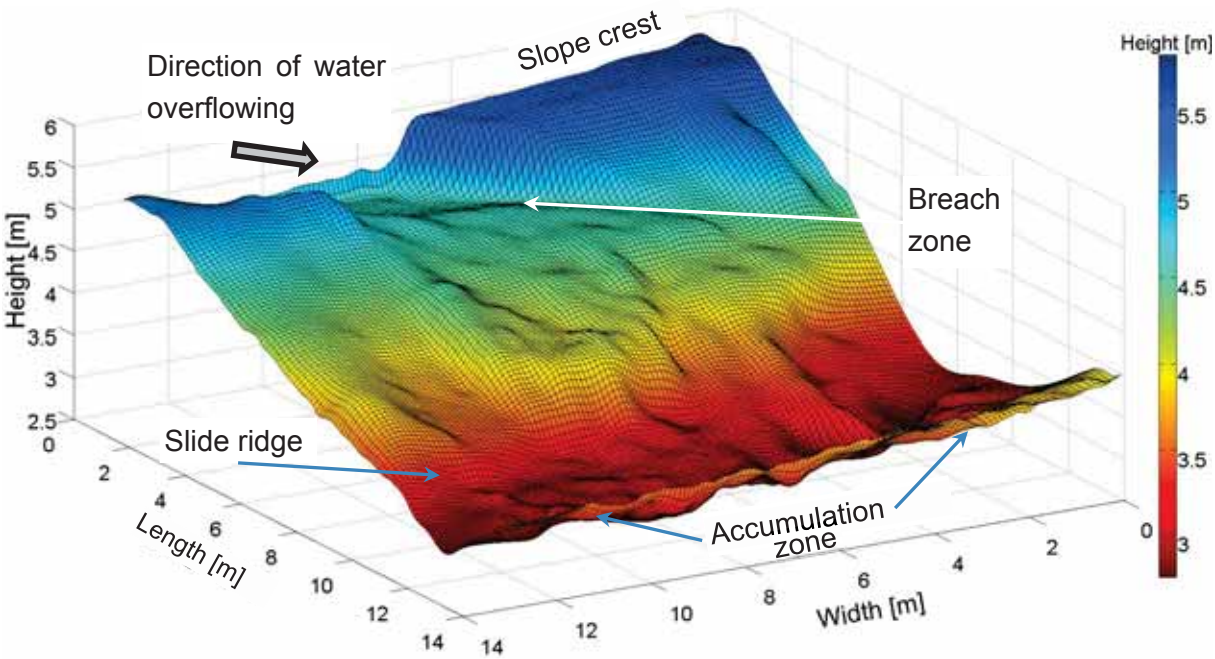

Figure 4.120: Three dimensional restitution of the air-side slope, by photogrammetric techniques of the dyke with a cut-off wall and a slope gradient of 1:2.5.

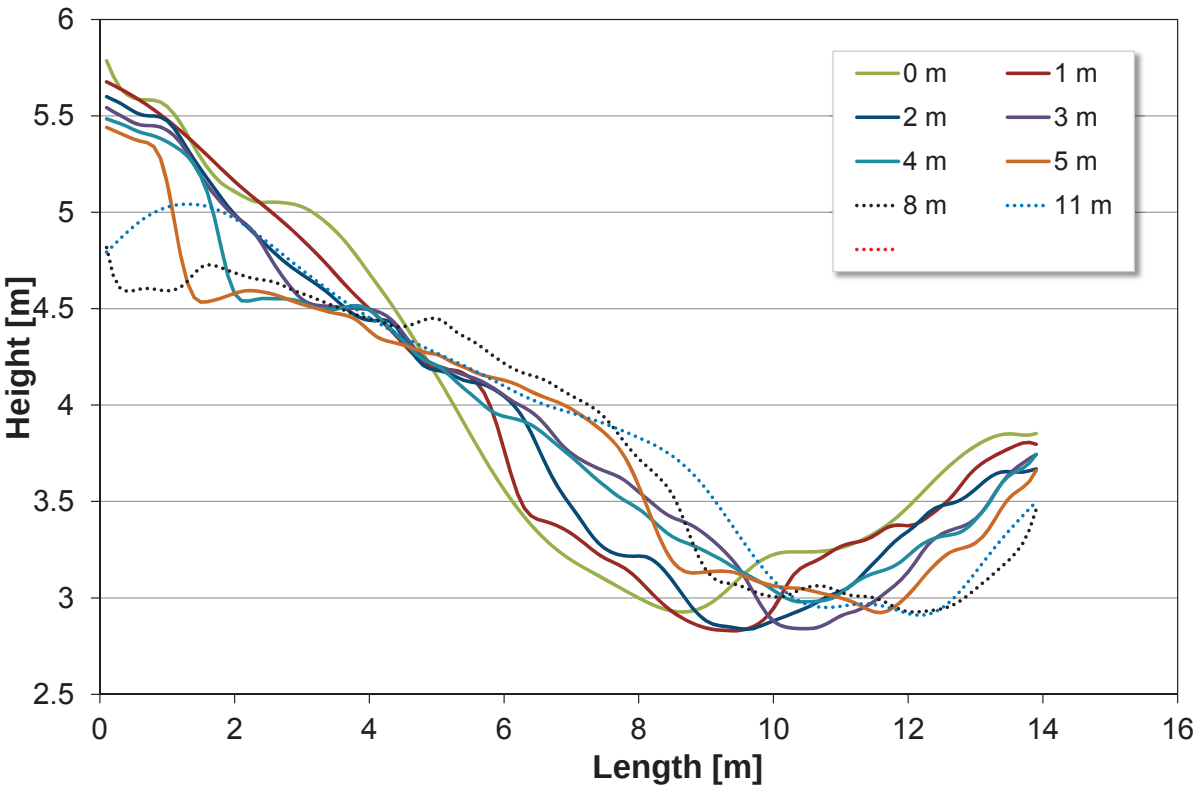

Figure 4.121: Longitudinal sections of the slope at specific values of the width of the dyke, based on the photogrammetric restitution.

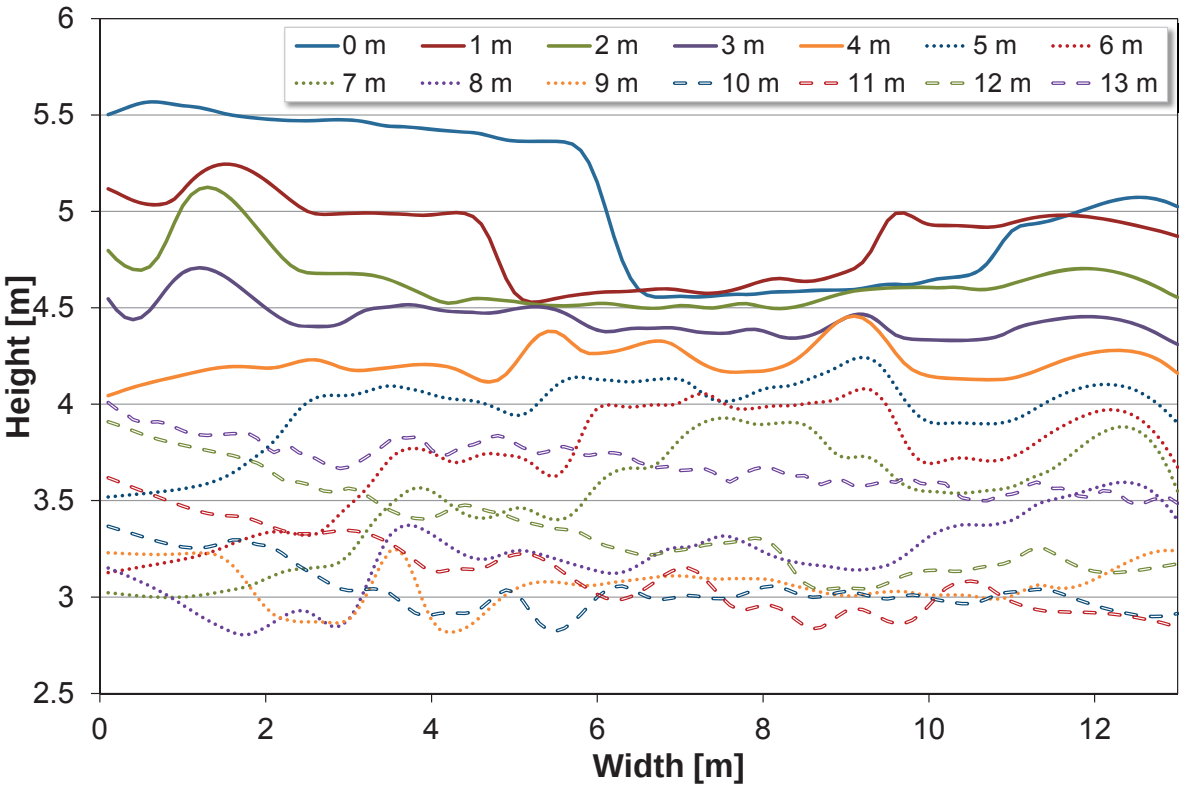

Figure 4.122: Transversal sections of the slope at specific values of the length of the dyke, based on the photogrammetric restitution.

Table 4.28: Summary of the breaching characteristics for the dyke with a cut-off wall.

Slope gradient	Breaching time [min]	Width [m]*	Depth [m]	Area [m^2]**
1:2.0	620.24	4.16 / 3.83	1.66	6.36
1:2.5	277.72	9.15 / 3.95	0.50	1.98
1:3.0	592.47	4.53 / 1.43	1.80	2.57

** First value correspond is in the middle of the breach throat, the second value is near the wall*
***Calculated as width × depth.*

4.5.4 Dyke with a cut-off wall and a toe filter

Figure 4.123 shows the location for the measuring points in the dyke. The density characteristics of all three tests are given in Table 4.29. The actuator did not work for the test with a slope gradient of 1:3.0, and the water supplier could not be moved. Therefore, the water-side of the dyke could be filled without fully controlling the water level. Only one flood cycle was carried out for this model, as well as the subsequent overflow phase.

Pore water pressure measurement was not possible at all points owing to some faulty sensors. The model with a slope gradient of 1:2.0 had 11 points of pore water pressure measurement (1–10, and 12). The other two models had 8 points (1–8). All three tests had information from the volumetric water content from 8 sensors (1–8), except for the model with a slope gradient of 1:3.0, for which the TDRs 1 and 3 failed.

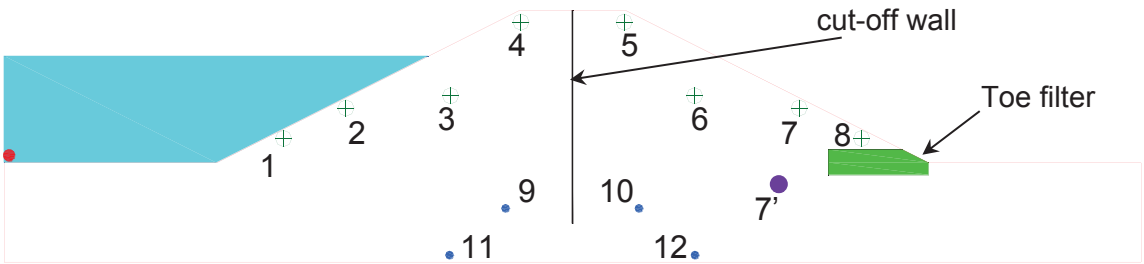

Figure 4.123: Location of the sensors for the dyke with a cut-off wall and a toe filter.

Table 4.29: Density parameters for all three tests on a dyke with cut-off wall and toe filter.

Slope gradient	Specimen	γ_{bulk} [kN/m^3]	γ_{bulk_aver} [kN/m^3]	γ_{dry} [kN/m^3]	γ_{dry_aver} [kN/m^3]	e [-]	e_{aver} [-]	D_R [%]	D_{R_aver} [%]	θ_{sat} [%]
1:2.0	1	20.10	20.23	16.88	16.93	0.57	0.57	74.05	75.64	0.36
	2	20.26		16.89		0.57		74.30		
	3	20.32		17.04		0.56		79.60		
	4	20.24		16.90		0.57		74.62		
1:2.5	1	20.15	19.21	17.08	17.01	0.55	0.56	80.87	78.60	0.36
	2	18.20		17.13		0.55		82.85		
	3	19.94		17.09		0.55		81.26		
	4	18.53		16.76		0.58		69.41		
1:3.0	1	19.81	19.09	16.72	16.70	0.59	0.59	67.98	67.27	0.37
	2	18.86		16.81		0.58		71.24		
	3	18.12		16.78		0.58		70.39		
	4	19.57		16.49		0.61		59.46		

The reaction of the pore water pressure to the flood cycles and overflow is shown in Figures 4.124 to 4.126. The pore pressure at point 1 responded in a similar fashion to the other three types of dyke, i.e. it reacted quickly and mirrored the change in water level. Pore pressure reached circa 36 kPa at peak during the flood cycles and 10 kPa for the two steeper dykes. Pressures were lower at about 6 kPa for the dyke with the flattest slopes.

The maximum and minimum water pressures at point 2 during the flood cycles were close to 20 and -3.5 kPa, except for the model with slope gradient 1:2.0, for which the maximum pressure was 24.4 kPa. This indicates that the phreatic level of water retained for that slope gradient is higher on the water-side of the dyke by the wall.

The reaction of the water pressure at point 3 was almost identical as for point 2, but approximately 4.5, 1.7 and 0.3 kPa below that, for the slope gradients of 1:2.0, 1:2.5 and 1:3.0, respectively. The response during the overflow process was consistent for PPTs 1-3, with pore pressures approximately 12 kPa higher than for the peaks during the flood cycles. This was also consistent with the pressure applied.

As for most of the other dyke types, no reaction to the water level change was measured at points 4 and 5 during the flood cycles. Positive values of pressure developed at point 4 during the overflow process, with maximum values of 10.3, 9.09 and 8.07 kPa, whereas there was no reaction during the overflow stage at point 5, for any of the tested slope gradients.

The most noticeable feature was observed at point 6, when compared to the other types of dyke. There was no influence of the flood cycles on the water pressures, at this point for the dyke with cut-off wall and toe filter. The pressure increased during the overflow process to 4.0, 8.3 and 10.0 kPa, for the slope gradients of 1:2.0, 1:2.5 and 1:3.0, respectively.

No influence of the flood cycles was observed at point 7 for the flatter slopes 1:2.5 and 1:3.0. The pressure increased to 14.1 kPa for the model with a 1:3.0 slope gradient during the overflow process. The pressure did not change for the other slope gradient (1:2.5). The pore water pressures measured for the model with slope gradient 1:2.0 were wrong, as they do not correspond to point 7 as shown in Figure 4.123. Unfortunately, PPT 7 moved from this position during the construction of that model to a lower position, as shown in Figure 4.127 (and marked as 7’ in Figure 4.123). Nonetheless, PPT 7 showed a clear response to the cycling pore pressures, but this was more damped than for the water-side with a difference between peak and trough of 6.1 kPa. It reached 31 kPa during overflow.

The water pressure measured at point 8 was different for each slope gradient. Pressures were always positive for the slope gradient of 1:2.0, with values between 2.6 and 4.8 kPa during the flood cycles, and a maximum of 5.72 kPa during the overflow. On the other hand, pressure was always negative for the model with a 1:2.5 slope gradient. Suction varied between 2.3 and 3.6 kPa during the cycles, and increased to 0.5 kPa during the overflow stage. However, pore water pressures were also positive for the model with a slope gradient of 1:3.0 after 4 days. The maximum value was 7.4 kPa during the single flood cycle, and increased to 26.8 kPa during the overflow.

The response and values of the pore pressure at point 9 were similar to those observed in the models of the dyke with the cut-off wall, confirming the increase of the water table in the soil on the water-side, as a result of the wall. Pore pressure transducers at point 10 were only installed in the steepest dyke, and allow comparison with pore pressures measured on the downstream side of the cut-off wall.

Pore pressure values between 21.6 and 34.6 kPa were measured during the flood cycles. The difference in pore pressure between points 9 and 10 was 13.6 kPa at the peaks and 3.6 kPa in the troughs of the flood cycles. The difference was 15.5 kPa during the overflow. These values were smaller than for the dyke with the cut-off wall only, indicating the draining effect of the toe filter at this point. The values were, in fact, smaller than those measured for the dyke with the toe filter only. This might be a consequence of both the rise in the water table on the water-side owing to the wall, and the increase in drainage as a result of the filter.

Pore water pressure values at point 12 during the flood cycles were between 42.8 and 53.5 kPa. The maximum value lies between that measured for the dyke with a cut-off wall only (54.37 kPa), and the dyke with a toe filter only (51.59 kPa). The differences confirm the influence of the filter at this point. The minimum value was closer to that measured for the model with the cut-off wall only, which indicates that despite the draining influence of the filter, the water retained by the wall on the water-side of the dyke creates a greater effect on the hydraulic gradient. Hence, greater water pressures were measured at this point for the dyke with a cut-off wall only.

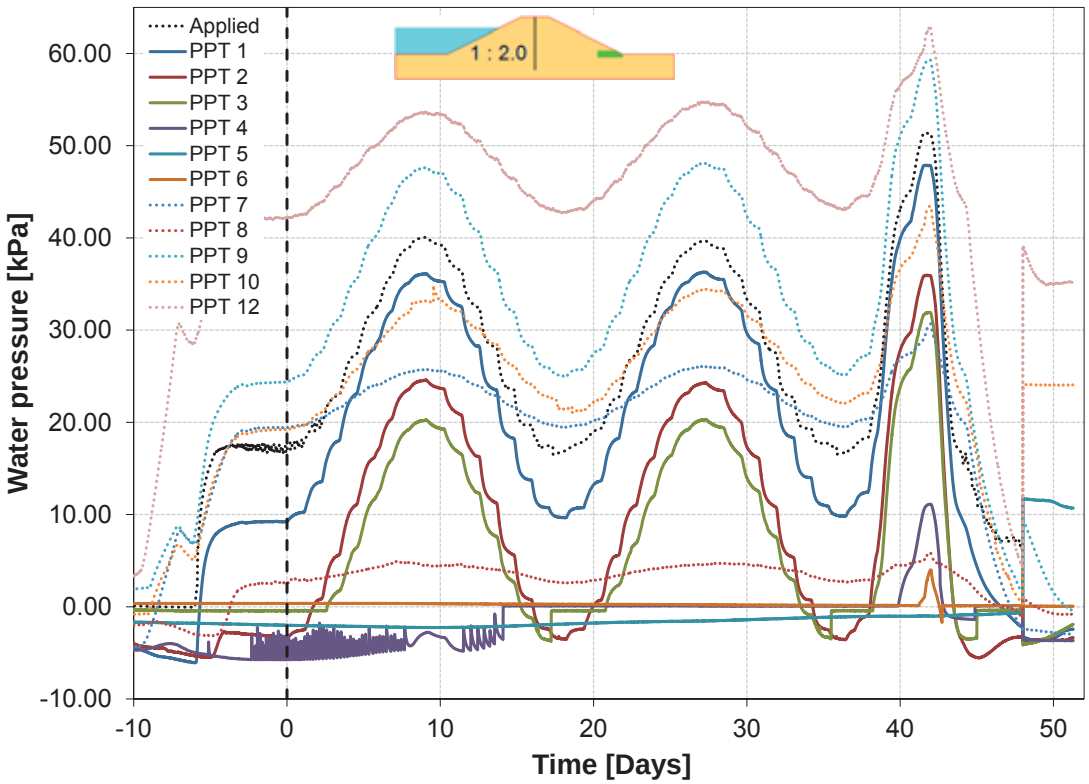

Figure 4.124: Water pressures for the dyke with a cut-off wall and a toe filter with slopes 1:2.0, for two flood cycles an overflow phase as shown in Figure 4.78.

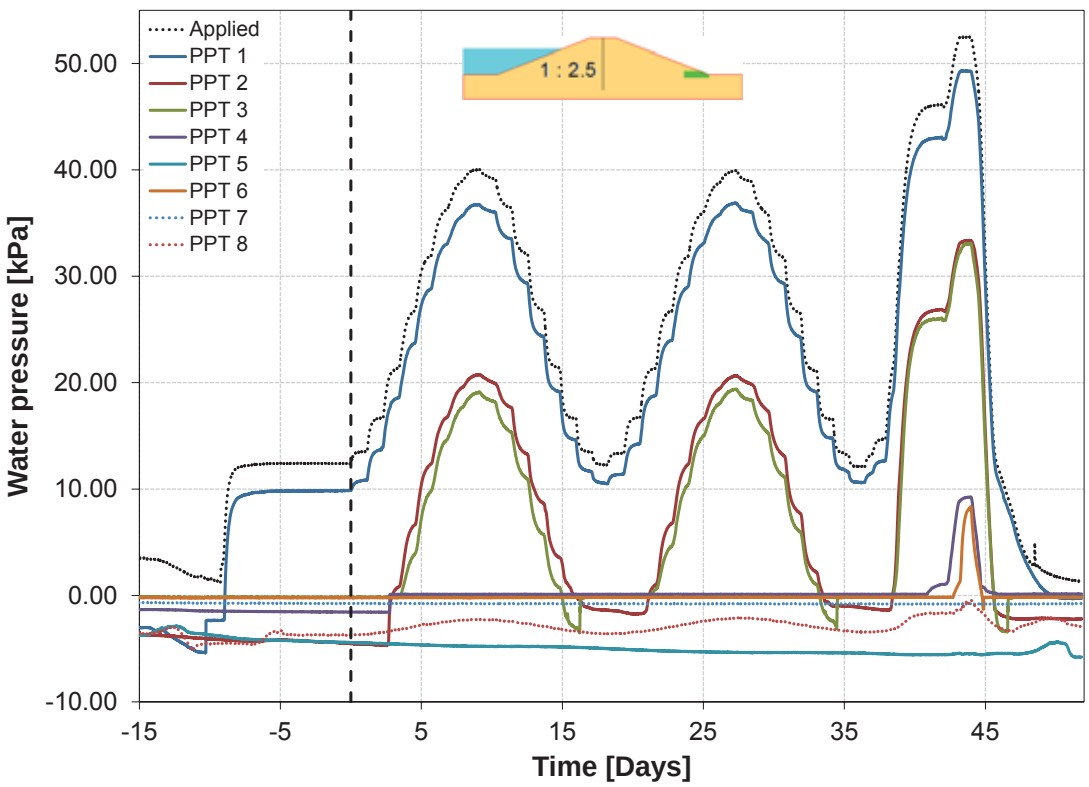

Figure 4.125: Water pressures for the dyke with a cut-off wall and a toe filter with slopes 1:2.5, for two flood cycles an overflow phase as shown in Figure 4.78.

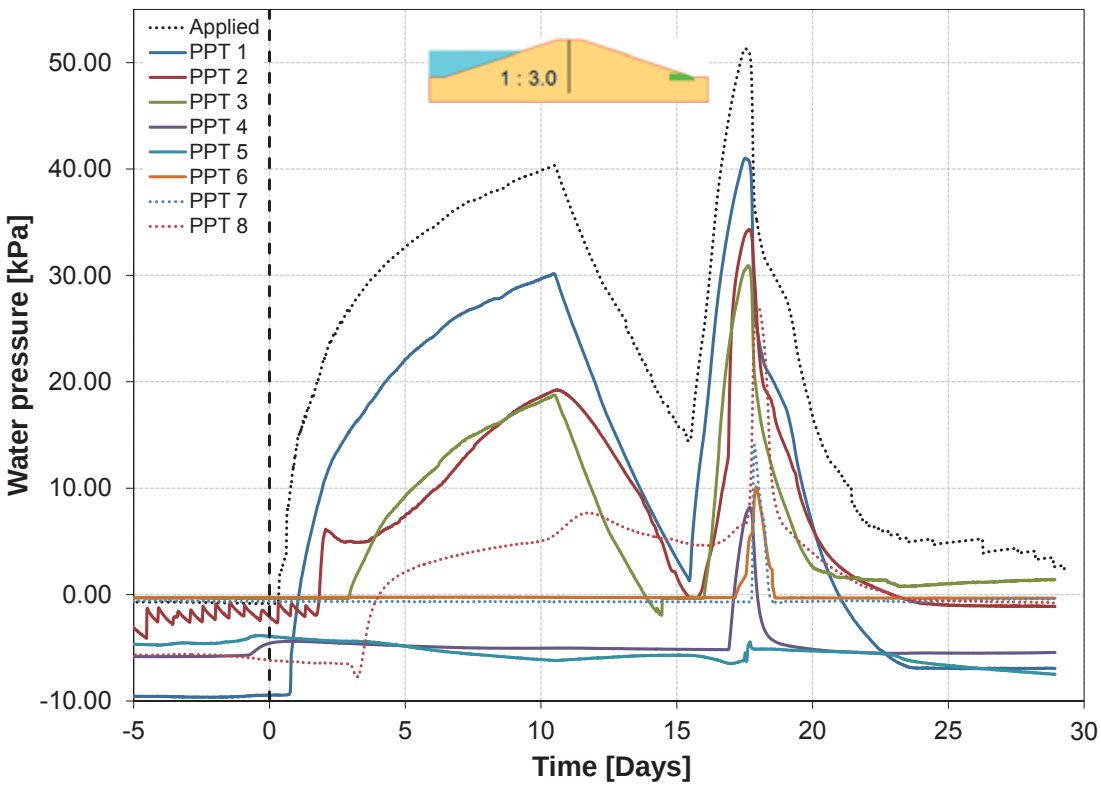

Figure 4.126: Water pressures for the dyke with a cut-off wall and a toe filter with slopes 1:3.0, for two flood cycles an overflow phase as shown in Figure 4.78.

Figure 4.127: Wrong positioning of PPT 7 for test with slope gradient 1:2.0, as shown in Figure 4.123.

Figures 4.128 to 4.130 show the response of the volumetric water content for the dyke with both a cut-off wall and a toe filter. Results are shown for all 8 TDRs, except for the model with slope gradient 1:3.0, for which the measurements from TDR 1 and TDR 3 were faulty, due to loose connections of the coaxial cable.

The soil at point 2 saturated after the water level was raised. The water content decreased to 0.20 m^3/m^3 for the model with a slope gradient of 1:2.0, and to the residual value for the other two models with flatter slopes. This behavior resembles that observed for the dyke with the cut-off wall only. Both types of dykes reveal that the effect of the water retained on the waterside is greater for the slope gradient of 1:2.0.

At point 3, the water content for both models (1:2.0 and 1:2.5 slope gradients) behaved in a similar fashion. The soil saturated and drained to the residual values after the water level was raised and lowered. Saturation was achieved again at this point during the overflow process.

Points 4 and 5 remained on the residual value of the water content during the flood cycles. Saturation was reached at point 4 during the overflow process for all three tests, whereas the soil at point 5 remained at the residual water content, excepting the model with the flattest slope gradient of 1:3.0, for which the volumetric water content reached 0.31 m^3/m^3.

Point 6 showed a similar response to that at point 4, i.e. the water content remained at the residual value until the overflow phase, during which it saturated fully. Nonetheless, a small increase was detected for the model with a slope gradient of 1:3.0 during the flood cycle. The results match the measurements of pore water pressure for this point, which indicate no influence, to a small influence of the flood cycles on the flow parameters at this specific point.

The water content at point 7 was not influenced by the change in the water table during the flood cycles, whereas the water content increased to 0.21 and 0.39 m^3/m^3, during the overflow process, for the models with 1:2.0 and 1:3.0 slope gradients. No influence of the overflow phase on the model with a slope gradient of 1:2.5 was observed.

Reaction of the water content at point 8 was different for each slope gradient analyzed. Water content increased gradually until the soil became almost saturated (θ = 0.34 m^3/m^3) during the first flood cycle for the model with the 1:2.0 slope gradient. From that point on, it remained at this level of saturation until the end of the test. No observable influence was found as the water level was lowered. No reaction was seen during the flood cycles or during the overflow phase for the model with a slope gradient of 1:2.5. A slower saturation process took place during the single flood cycle for the model with the slope gradient of 1:3.0. The volumetric water content at point 8 reached a maximum value of 0.3 m^3/m^3 during the flood cycles, which increased to 0.34 m^3/m^3 during the overflow process.

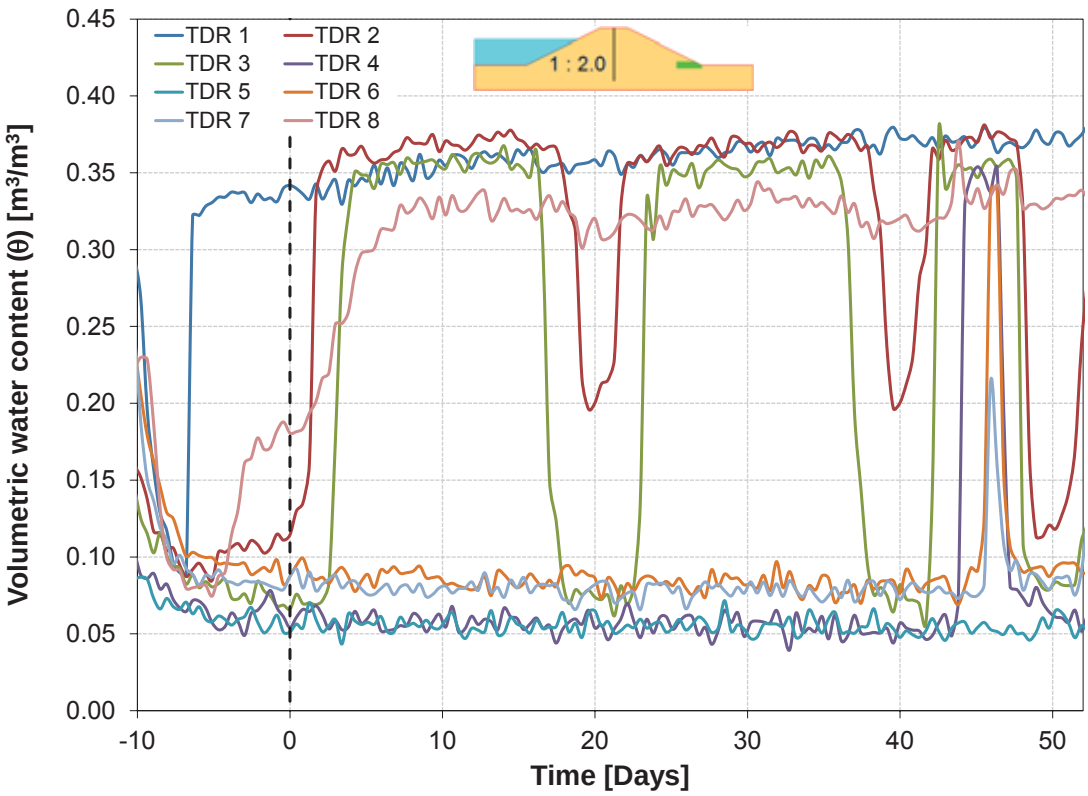

Figure 4.128: Volumetric water contents for the dyke with a cut-off wall and a toe filter and slopes 1:2.0, for two flood cycles an overflow phase as shown in Figure 4.78.

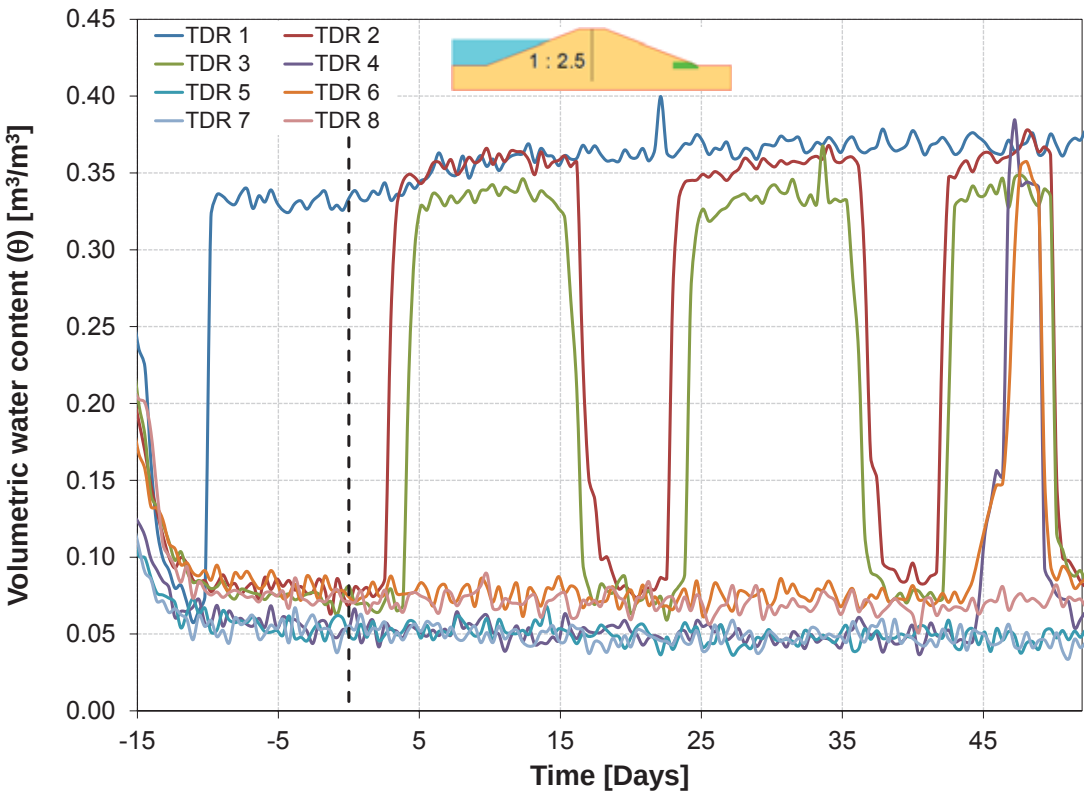

Figure 4.129: Volumetric water contents for the dyke with a cut-off wall and a toe filter and slopes 1:2.5, for two flood cycles an overflow phase as shown in Figure 4.78.

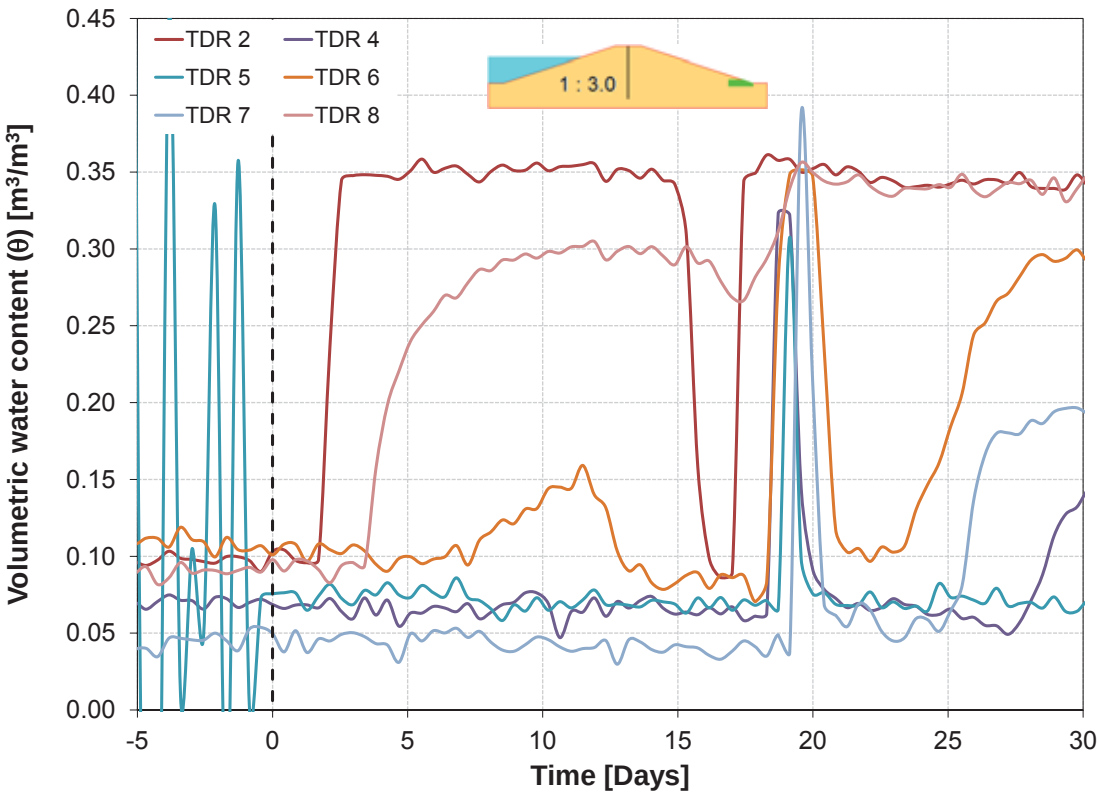

Figure 4.130: Volumetric water contents for the dyke with a cut-off wall and a toe filter and slopes 1:3.0, for two flood cycles an overflow phase as shown in Figure 4.78.

4.5.4.1 Failure and breaching mechanism

The breach developed almost identically to that of the dyke with the cut-off wall only. When the water started overflowing, a breach throat started to develop in the zone of the crest of the dyke closer to the air-side (Figure 4.131a-b). This is a similar process to that observed for the homogeneous and toe filter dykes. However, the throat could not continue increasing towards the water-side when it reached the cut-off wall. As in this case, the wall acted as a barrier for the breach (Figure 4.131c).

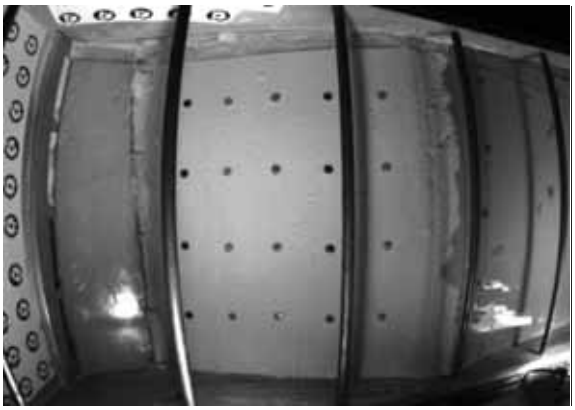

a) At 0 min.

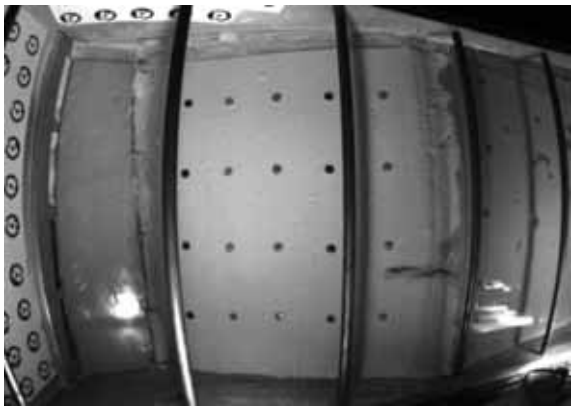

b) After 46.29 min.

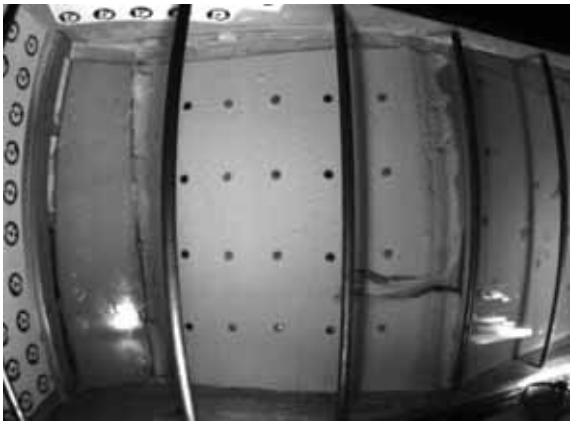

c) After 157.37 min.

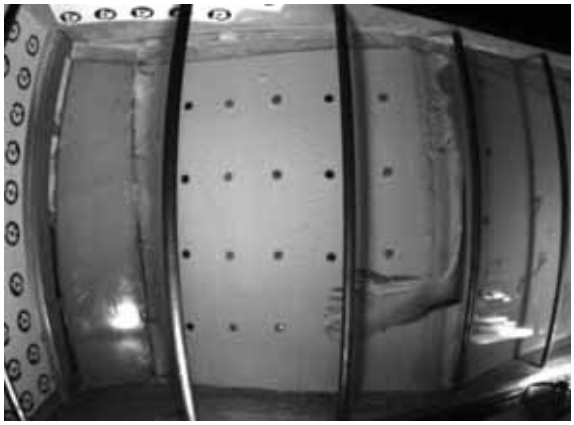

d) After 259.21 min.

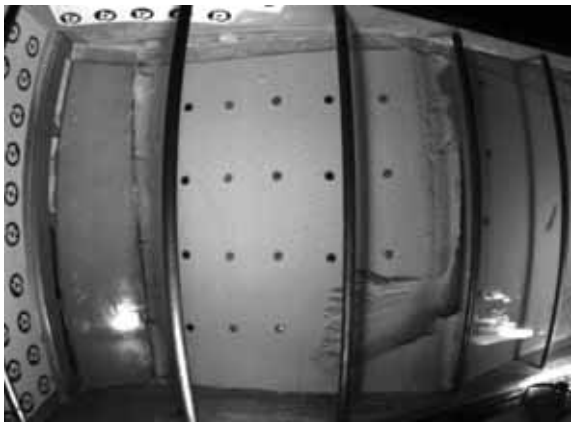

e) After 361.04 min.

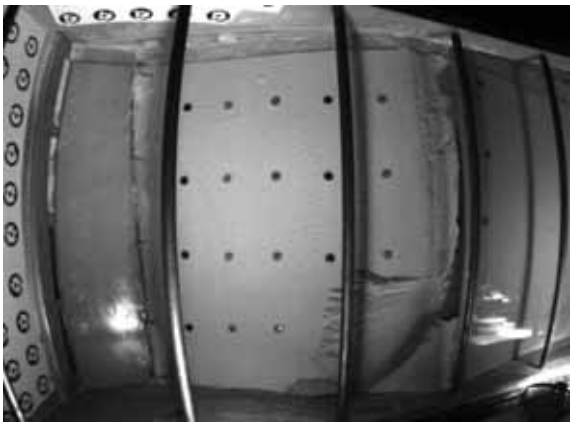

f) After 462.87 min.

Figure 4.131: Breach development of the dyke with cut-off wall and toe filter with slope gradient 1:2.5. Time zero corresponds to 50.42 days (beginning of the breaching).

The breach in the crest of the air-side slope continued widens, but it does not reach the water-side slope. This creates a narrow and shallow breach zone in the vicinity of the cut-off wall (Figure 4.131d-f). Water flowing out of the breach zone eroded the material downslope. However, the material was not transported and deposited on the foot of the slope, but in the middle of the slope instead. Water ponded on the air-side slope surrounding the previously deposited material. As consequence, a deposition fan was generated in the middle of the slope (Figure 4.131f).

The final configuration of the air-side slopes is depicted in Figure 4.132 for all three tests on dykes with a cut-off wall and a toe filter after the overflow event, and Figure 4.133 shows an enlarged view of the breach zone. A similar breaching mechanism to that described above was observed for all three tests. However, the model with slope gradient 1:3.0 had a slightly different final breaching configuration, because shortly after the water started overflowing and eroding the vicinity of the wall (ad for the other tests) the water overflowing started eroding the zone of the mixture sand-bentonite instead of the main body of the dyke. Therefore, most of the water flowed through this zone after some minutes, hindering a larger growth of the breach zone.

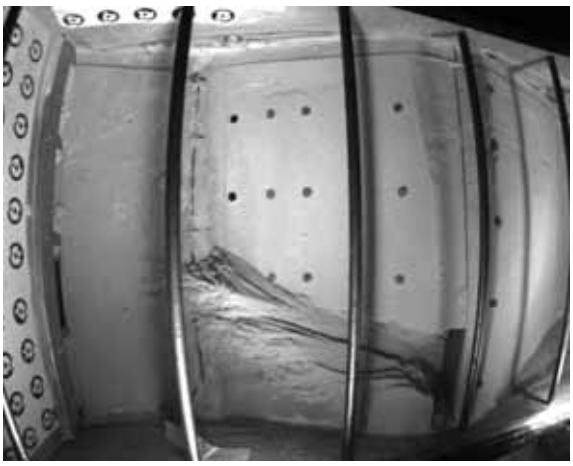

a) Slope gradient 1:2.0.

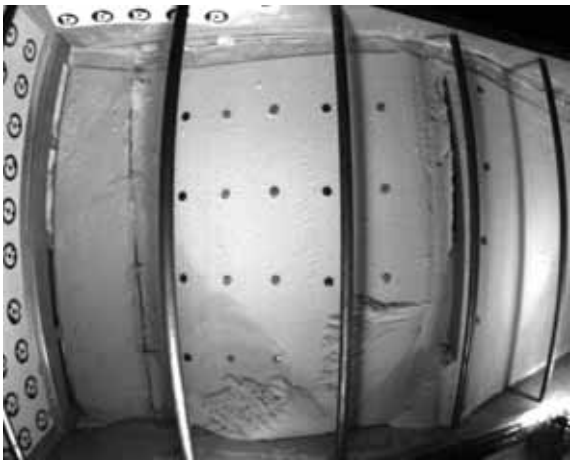

b) Slope gradient 1:2.5.

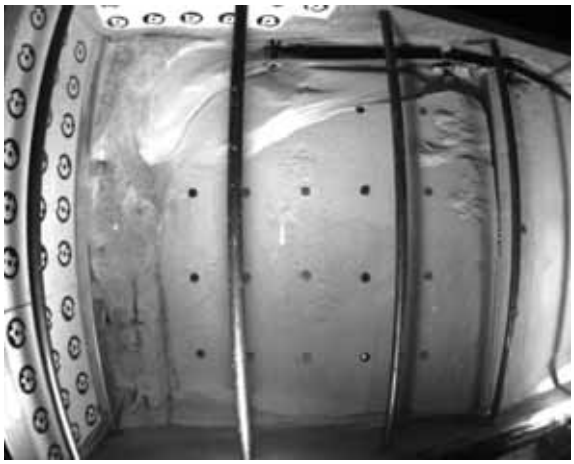

c) Slope gradient 1:3.0.

Figure 4.132: Final condition of the dykes with a cut-off wall and a toe filter, after overflow.

Figure 4.133: Deposited material at the foot of the slope of the air-side of the model with slope gradient 1:2.0.

a) 1:2.0. *b) 1:2.5.* *c) 1:3.0.*

Figure 4.134: Breaching zone of the dyke with cut-off wall and toe filter after overflow for all three slope gradients.

Table 4.30 summarizes the time required for the breach to develop completely, the width of the breach at the slope surface, and the depth of the breach zone at the crest of the slope for each of the slope gradients modeled. As for the other three types of dyke, the model, which required more time to breach completely, is the steepest dyke.

The model with the flattest slope gradient (1:3.0) requires less time to erode the smallest area. However, this is a consequence of a shorter period subjected to overflow, owing to the erosion of the zone with the mixture sand-bentonite, as described above. The average time to erode the material was 6.8, 2.1 and 1.18 times greater than the time required for the homogeneous dyke, the dyke with a toe filter and the dyke with a cut-off wall, respectively. The average time was calculated only for the models with slope gradients 1:2.0 and 1:2.5, because the other model had a slightly different breaching mechanism.

Table 4.30: Summary of the breaching values for the dyke with cut-off wall and toe filter.

Slope gradient	Breaching time [min]	Width [m]*	Depth [m]	Area [m^2]**
1:2.0	749.85	5.47 / 4.05	1.53	6.20
1:2.5	425.84	11.33 / 3.33	0.83	2.76
1:3.0	314.75	6.66 / 1.66	0.60	1.00

** First value correspond is in the middle of the breach throat, the second value is near the wall*

***Calculated as width × depth.*

4.5.5 General assessment

The performance of two different dyke protection measures and a combination of both of them was investigated for three different slope gradients. The performance of a homogenous dyke was also analyzed and presented as a reference. Each type of dyke exhibited similar characteristics in the behavior of the seepage flow through the dyke, which can be analyzed though the pore water pressure and volumetric water content. The breaching mechanisms were also comparable and consistent for all three slope gradients modeled.

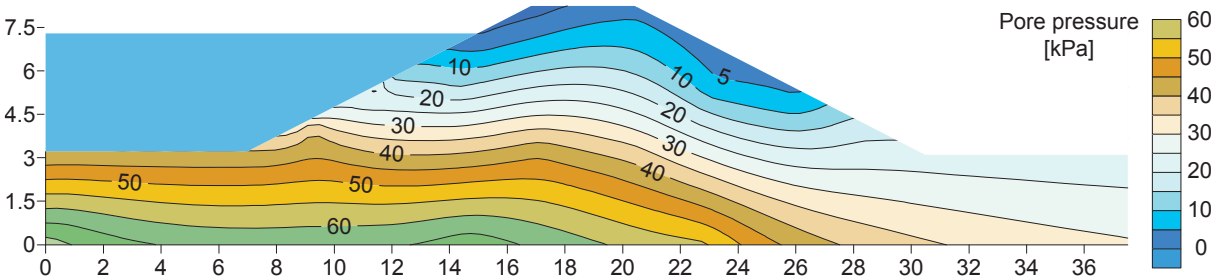

a) Homogeneous dyke.

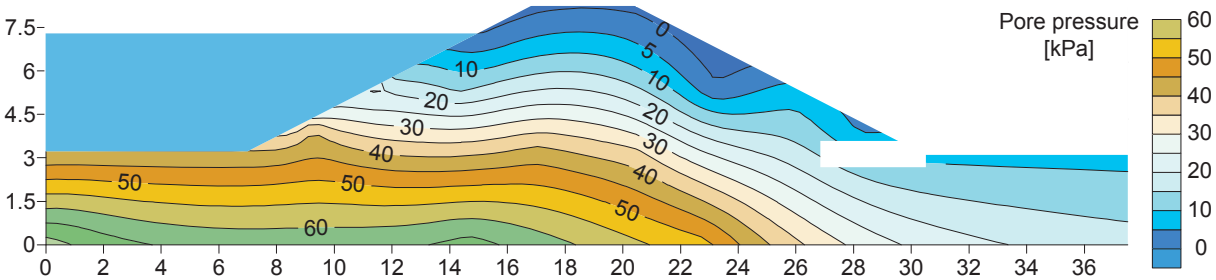

b) Dyke with toe filter.

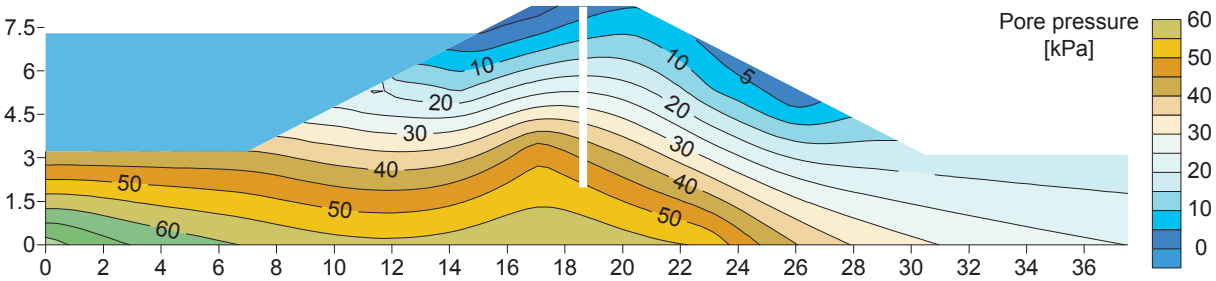

c) Dyke with cut-off wall.

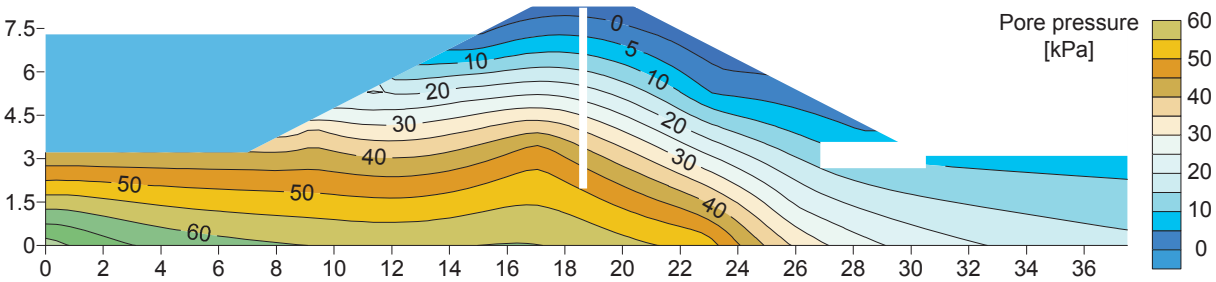

d) Dyke with cut-off wall and toe filter.

Figure 4.135: Pore water pressure for the four types of dyke modeled (slope gradient 1:2.0) at the maximum water level during the flood cycles.

Figure 4.135 shows the isobar contours for the different types of dykes for the maximum flood level. These were derived by Kriging, a popular method for interpolating spatial data (Stein, 1999). The models with slope gradients 1:2.0 were chosen, as they were the models which had more points at which the pore water pressure was measured. Water emerged on the air-side slope for the dykes without a toe filter, which decreases the effective stresses leading to local failures. However, the cut-off wall lowers the water pressures on the air-side and showing a small area in unsaturated condition. This explains why the local failure for this type of dyke did not advance further up the slope, as it did for the homogeneous dyke.

The cut-off wall also induced ponding of the water on the water-side, with a larger influence at the bottom of the wall. It was expected that the wall would decrease the pore water pressures more on the air-side. However, the high hydraulic conductivity of the Perth sand might have had an influence on the rapid flow of the water to the air-side after dodging the wall. This effect might be analyzed with further research on this topic.

The dykes without a toe filter exhibited local planar failure events on the air-side during flooding and overtopping. Initially, it was thought to be due exclusively to an internal erosion process exclusively. However, the failure was planar instead of increasing upstream, thus creating large eroded areas as was observed in the tests from Kusakabe et al. (1988a); Ko et al. (1989b) and Okumura et al. (1998).

This planar failure was similar to that observed by Bezuijen & den Adel (2006) (Figure 2.68). Some blocks of partially saturated soil detached from the slope and were flushed downslope by the water springing on the air-side. The failure was about 0.6 m deep at prototype scale, and develops across the whole width of the dyke. The increase in the pore water pressure, and the subsequent decrease in the effective stress, in the proximity of the zone where water springs emerge on the air-side slope, led to an unstable condition. This was confirmed from the numerical simulations presented in the next chapter.

The failure zone extended up to the slope on every occasion that the water level reaches a new maximum high. If the water was lowered, the springing point also lowered, and the soil once again became unsaturated and more stable. This is deduced by observing that the unstable zone increases in dimension until the first flood cycle reached its maximum water level, and then starts to increase again during the overflow phase only. The area affected by instability is greater for the homogenous dyke, for which the instability zone could reach the crest of the dyke, whereas, this zone did not reach the mid-height of the dyke for the dyke with the cut-off wall.

On the one hand, the phreatic level is lowered for the dyke with a toe filter, impeding it from springing on the air-side slope, thus preventing the instability process from occurring on this slope. However, Figure 4.135b-c show pore pressure greater than zero on the air-side slope. This was due to water ponding at the foot of the dyke after ejected from the toe filter. On the other hand, the use of a cut-off wall decreased the zone affected by planar instability, while it delayed the development of the breach zone. The breach area and volume were also smaller

than observed for dykes without the wall, because water could not erode sand on the water-side slope.

As a consequence, the breach zone was contained on the air-side only. This also means that even when the dyke is subjected to high water levels, the water-side of the dyke maintains its cross section. As the water-side cannot be eroded during the overflowing event, the amount of water flowing towards the area protected by the dyke is smaller than for the cases in which the water can create a complete breach throat (dykes: homogeneous and with toe filter). This would provide more time for the affected areas to be evacuated.

The cut-off wall to be leveled with the crown of the dyke avoids the problems observed during the flood due to hurricane Katrina in New Orleans, in which the protruding wall was displaced towards the air-side by the water inducing another failure mechanism as preferential seepage occurred and extended the tension crack between the wall and the soil (Sasanakul et al., 2008; Ubilla et al., 2008; Sasanakul et al., 2010; Steedman & Sharp, 2011) (cf. Section 2.3.6.3).

The use of both protective measures (cut-off wall and toe filter) sums up their advantages such lowering of the water table and pore pressures, which in turn creates larger unsaturated zones. These increase the overall stability of the air-side slope. Additionally, there is a delay on the development of the breach, which do not erode the whole cross section of the dyke, but is only restricted to the downstream side of the cut-off wall. Therefore, this combination offers a viable option where dykes must be stable under all design flood conditions for their entire life span, which often exceeds 100 years.

5 Numerical modeling

Numerical modeling was carried out for all of the 12 dyke prototypes that had been tested by small-scale models under enhanced gravity in the centrifuge (Chapter 4). The objective was to corroborate the flow behavior and instability events observed with the centrifuge modeling.

The modeling was performed with the software GeoStudio 2012 (Krahn, 2012a). This is composed of several calculation modules, each one on a specific geotechnical topic. The SEEP-W module was used to model the unsaturated groundwater flow. The software solves Richards equation (Equation 2.32) two-dimensionally with a Finite Element Method (FEM) approach (cf. Section 2.5.1.1).

A two-dimensional slope stability analysis of the central section was carried out with the SLOPE-W module for each time step. This analysis is based on a limit equilibrium analysis, using the method from Morgenstern & Price (1965), as this method satisfies both momentum and force equilibrium, as described in Section 2.5.1.2 and in Figure 2.85. This type of analysis is generally regarded as being conservative (Askarinejad et al., 2012b), and is preferred over the c'-ϕ reduction method (Brinkgreve & Bakker, 1991), which assumes a linear and simultaneous decrease of cohesion and friction, which is not the case in natural, unsaturated soils.

The definition of the boundary conditions and soil properties are presented first, followed by the results of the pore water pressures (PWP) at key points. An initial qualitative comparison is given between the behavior of PWP from the centrifuge and numerical modeling, followed by a quantitative comparison in which the maximum and minimum values are presented, together with the difference between them, which was found to be more representative. A subsequent section is dedicated to the analysis of the stability of both the air and water-side slopes. At the end, an assessment of the differences in the flow pattern induced by the different protective measures is presented.

5.1 Boundary conditions

The solution via the FEM requires the problem to be discretized into small elements interconnected to each other, thus creating a mesh. Quadrilateral and triangular elements are usually used to solve a two-dimensional solution. The use of one or both types of elements depends on the criteria of the user, or on the limitations of the solving software. Further information regarding mesh discretization and elements can be found in Zienkiewicz et al. (2005).

Both types of elements were used in the analysis. The quadrilateral elements had 8 nodes and 9 integration points, whereas the triangular elements had 3 nodes and 3 integration nodes. These are the highest order elements offered by the software. The cut-off wall was modeled with impermeable interface elements. Table 2.2 presents a summary of the nodes and elements used for each simulation. As an example, the mesh used for analyzing the

dyke with a slope gradient of 1:2.5 with a cut-off wall and toe filter is shown in Figure 5.1. The meshes were similar for the other simulations.

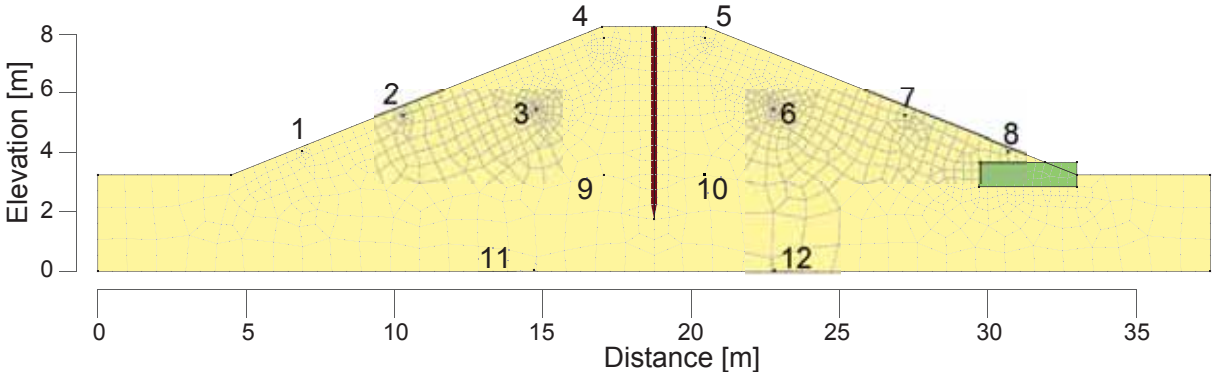

Figure 5.1: FEM mesh for the dyke with a slope gradient of 1:2.5 with a central cut-off wall (red) and a toe filter (green). The numbers indicate the points were the pore water pressure is analyzed.

Table 5.1: Mesh properties for the boundary value problems.

Slope gradient	Description	Nodes	Elements
1:2.0	Homogeneous	2637	863
	Toe filter	2645	866
	Cut-off wall	2715	889
	Cut-off wall and toe filter	2723	892
1:2.5	Homogeneous	2778	908
	Toe filter	2789	912
	Cut-off wall	2856	934
	Cut-off wall and toe filter	2867	938
1:3.0	Homogeneous	3095	1011
	Toe filter	3106	1015
	Cut-off wall	3173	1037
	Cut-off wall and toe filter	3184	1041

Each analysis was performed in seven phases (Table 5.2). The analysis starts with a period of 8.5 days, in which the water level is set at 1.4 m for the flow to reach a steady-state condition. From that moment, two flooding cycles were applied with a final sudden flood, which reaches the crest of the dyke. A subsequent rapid drawdown was applied. This pattern of water level variation (Figure 5.2) corresponds to that applied in most of the centrifuge tests. Time zero corresponds to the moment at which the flood cycles begin.

An initial suction of 4 kPa was defined in the soil at the beginning of the simulation to correspond to the suction applied during the construction of the small-scale models in order to allow the surface of the model to remain vertical prior to its installation in the channel of the geotechnical centrifuge, as described by Morales et al. (2013).

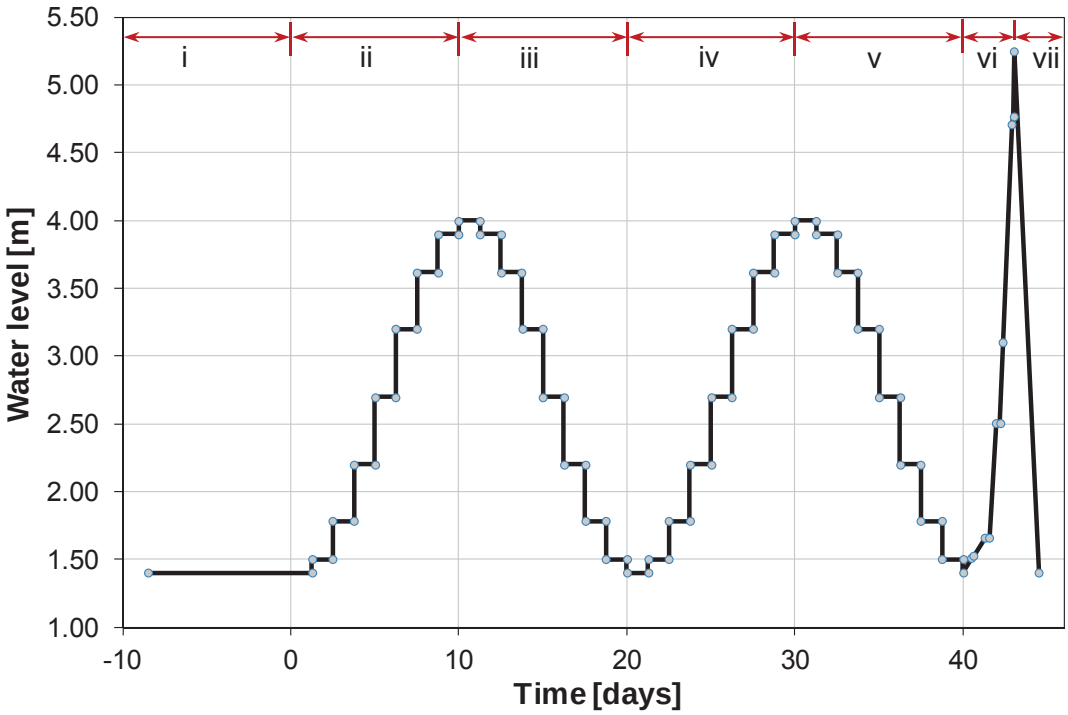

Figure 5.2: Water level imposed for all dyke models. The height is measured from the toe of the dyke.

Table 5.2: Analysis phases imposed for all dyke models.

Phase	Description	Duration [days]	Time steps
i	Water flow until steady state	8.5	204
ii	Increase of the water level of the first flood cycle	10	240
iii	Decrease of the water level of the first flood cycle	10	240
iv	Increase of the water level of the second flood cycle	10	240
v	Decrease of the water level of the second flood cycle	10	240
vi	Increase of the water level until overflow	3.04	73
vii	Rapid drawdown	2.6	63

5.2 Soil properties

Two types of soils are modeled in the boundary value problems: Perth sand and a filter of granular soil. The flow properties of the Perth sand include the SWRC, and the hydraulic conductivity function, as described in Section 4.3.1.3 and shown in Figure 4.51 and Figure 4.52, respectively.

The water saturates the soil progressively during the phases in which the water level is raised (i, ii, iv, vi). Therefore, the unsaturated parameters from the wetting path of the SWRC were used. On the other hand, the parameters from the drying path were used for those phases in which the water level is lowered (iii, v, vii).

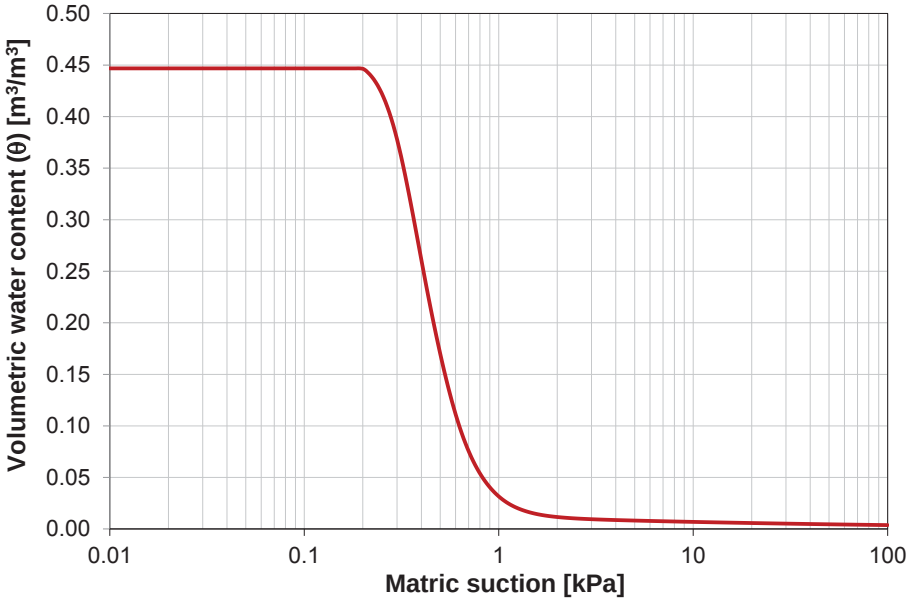

Figure 5.3: Soil water retention curve for the toe filter.

The grain-size distribution of the toe filter (Figure 4.64) was used to estimate the SWRC (Figure 2.1), and the relationship between hydraulic conductivity and matric suction (Figure 5.4). The former was estimated with the Modified-Kovacs approach presented by Aubertin et al. (2003) (cf. Section 2.2.2.5), whereas the latter was estimated from the SWRC following the approach by Fredlund & Xing (1994). The saturated hydraulic conductivity was estimated with the formulation of Kozeny-Carman, as described by Carrier (2003). The void ratio of the filter was assumed to be 0.8.

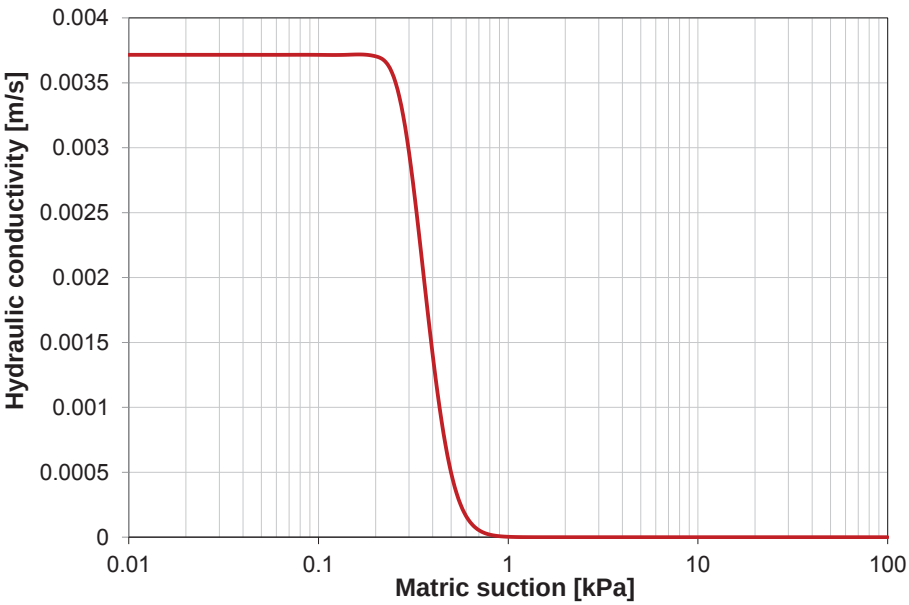

Figure 5.4: Hydraulic conductivity function for the toe filter.

The soil parameters used for the slope stability analysis are given in Table 5.3. The friction angle of Perth sand corresponds to that estimated from triaxial tests (cf. Section 4.3.1.2), whereas the bulk unit weight is an average of the values achieved during the construction of

the small-scale models that were reported in Section 4.5. The friction angle and unit weight for the toe filter were taken from typical values obtained for gravel.

The shear strength is based on a linear elastic perfect plastic model (Mohr-Coulomb). The increase in the shear strength due to suction was taken into account for Perth sand with the in-built function of GeoStudio, which follows the proposal by Vanapalli et al. (1996) (Equation 5.1). In this equation, τ and σ are the shear and normal stresses, θ, θ_{res}, and θ_{sat} are the current, residual and saturated volumetric water contents, respectively, u_a is the air pressure, u_w is the pore pressure, c' is the cohesion and ϕ' is the friction angle of the soil.

Table 5.3: Soil parameters used for the slope stability analysis.

Soil	ϕ' [°]	c' [kPa]	γ [kN/m³]
Perth sand	31	0	17.4
Filter	35	0	18.0

$$\tau = c' + (\sigma - u_a)\tan\phi' + (u_a - u_w)\left[\frac{\theta - \theta_{res}}{\theta_{sat} - \theta_{res}}\tan\phi'\right] \quad 5.1$$

5.3 Results

The results are presented in a similar manner to how they were shown for the centrifuge modeling, i.e. for each type of dyke. The pore water pressure (PWP) is plotted for 12 points (Figure 5.1), corresponding to the 12 measurement points in the small-scale models tested in the geotechnical centrifuge (cf. Section 4.4).

5.3.1 Homogeneous dyke

Figures 5.5 to 5.7 show the PWPs obtained for the homogeneous dyke for all three slope gradients. The behavior observed is quite similar to that observed in the centrifuge tests, with points 1 and 2 reacting almost immediately to the water level change. The difference in PWP between points 11 and 12 is greater at the maximum water level than at the minimum level. Similar behavior is exhibited by the PWP between points 9 and 10.

The slope steepness does not have much influence on the development of the PWPs. The greatest influence is observed at points 2, 6, 7, 9, 10 and 12, for which the PWPs vary from 21.42, -0.56, -2.34, 32.71, 27.09, 51.99 kPa (slope gradient 1:2.0) to 17.82, 2.82, -5.00, 33.87, 28.18, 55.22 kPa (slope gradient 1:3.0), at the maximum water level.

A comparison of the PWP values obtained from centrifuge and numerical modeling for all three slope gradients is given in Table 5.4. The comparison shows that the PWP differences between the maximum and minimum water levels (numbers in blue) are similar for both centrifuge and numerical modeling. However, some of the PWP values are greater in the centrifuge modeling. For instance, the PWPs at point 1 were 39.38 and 15.68 kPa (difference 23.7 kPa) in the centrifuge model, whereas in the numerical model they were 31.43 and 5.92

kPa (difference 25.52 kPa). Similar behavior is observed for other measurement points. This confirms the explanation given in the analysis of the results from the centrifuge modeling (cf. Section 4.5), in the sense that some of the sensors were located slightly below the point that they were planned to be, causing the measurements to be some kPa greater than expected. Values in red in Table 5.4 represent measurements with problems due to faulty sensors or cavitation of water in the ceramic stone or cavity behind it.

Table 5.4: Comparison of the results from the physical models (phys) and the numerical simulations (num) of the pore water pressures (PWP) at the maximum and minimum water level, and their difference calculated as $PWP_{max} - PWP_{min}$ for the homogeneous dyke (all pressures in kPa). Faulty data is shown in red.

Point		Slope gradient					
		1: 2.0 phys	1: 2.0 num	1: 2.5 phys	1: 2.5 num	1: 3.0 phys	1: 3.0 num
1	Max	39.38	31.43	34.06	31.63	34.14	31.54
	Min	15.68	5.92	10.62	7.08	7.99	6.00
	Diff	*23.70*	*25.52*	*23.44*	*24.55*	*26.16*	*25.54*
2	Max	30.46	21.42	n.s.	19.51	22.53	17.82
	Min	3.87	-4.49	n.s.	-6.27	-3.02	-6.91
	Diff	*26.59*	*25.91*	n.s.	*25.78*	*25.55*	*24.73*
3	Max	14.78	15.38	15.00	14.39	17.33	14.02
	Min	-6.29	-6.67	-4.51	-6.68	-0.23	-6.66
	Diff	*21.07*	*22.06*	*19.51*	*21.07*	*17.56*	*20.68*
4	Max	-3.92	-6.55	-0.65	-6.35	-0.32	-6.36
	Min	0.06	-8.22	-0.65	-8.21	0.01	-8.20
	Diff	*-3.98*	*1.67*	*0.01*	*1.85*	*-0.33*	*1.84*
5	Max	4.78	-6.50	-0.23	-6.37	-5.84	-6.40
	Min	7.87	-8.23	-0.23	-8.23	-5.49	-8.22
	Diff	*-3.09*	*1.72*	*0.01*	*1.86*	*-0.35*	*1.82*
6	Max	6.35	-0.56	0.89	1.63	3.11	2.82
	Min	0.07	-7.12	-0.34	-6.99	-0.27	-6.92
	Diff	*6.28*	*6.56*	*1.22*	*8.62*	*3.37*	*9.74*
7	Max	5.51	-2.34	-1.16	-3.86	-0.84	-5.00
	Min	-4.21	-7.66	-1.17	-7.91	-0.88	-8.06
	Diff	*9.72*	*5.32*	*0.01*	*4.06*	*0.05*	*3.05*
8	Max	17.22	1.93	4.85	0.69	6.78	1.77
	Min	8.76	-4.91	2.37	-5.57	-0.56	-4.85
	Diff	*8.46*	*6.84*	*2.49*	*6.26*	*7.34*	*6.63*
9	Max	43.09	32.71	n.s.	32.87	n.s.	33.87
	Min	23.55	10.88	n.s.	11.12	n.s.	11.42
	Diff	*19.54*	*21.84*	n.s.	*21.76*	n.s.	*22.44*
10	Max	36.39	27.09	n.s.	27.98	n.s.	28.18
	Min	20.32	9.05	n.s.	9.42	n.s.	9.46
	Diff	*16.07*	*18.03*	n.s.	*18.56*	n.s.	*18.71*
11	Max	68.08	65.59	n.s.	65.59	n.s.	65.61
	Min	46.08	42.15	n.s.	42.42	n.s.	41.97
	Diff	*22.00*	*23.44*	n.s.	*23.17*	n.s.	*23.64*
12	Max	55.98	51.99	n.s.	53.81	n.s.	55.22
	Min	40.77	37.51	n.s.	38.15	n.s.	38.65
	Diff	*15.20*	*14.47*	n.s.	*15.65*	n.s.	*16.56*

n.s. No sensor placed in model.

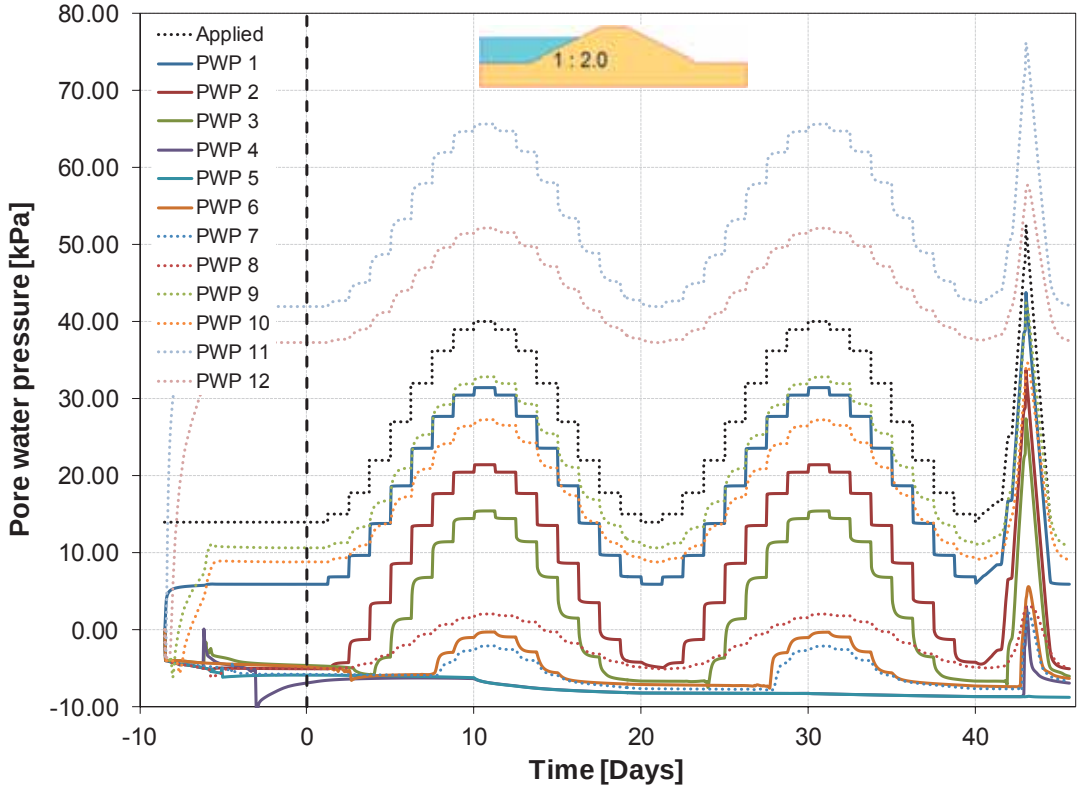

Figure 5.5: Pore water pressures for the homogeneous dyke with slopes 1:2.0 for two flood cycles and the overflow phase, as shown in Figure 5.2.

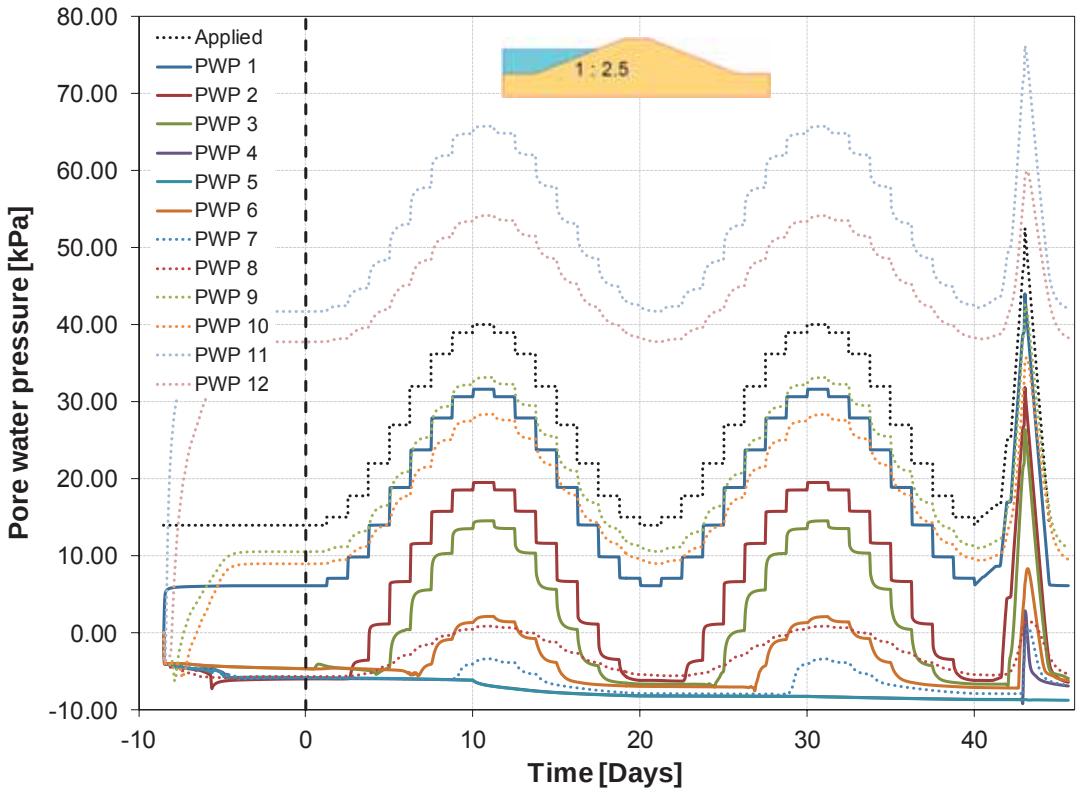

Figure 5.6: Pore water pressures for the homogeneous dyke with slopes 1:2.5 for two flood cycles and the overflow phase, as shown in Figure 5.2.

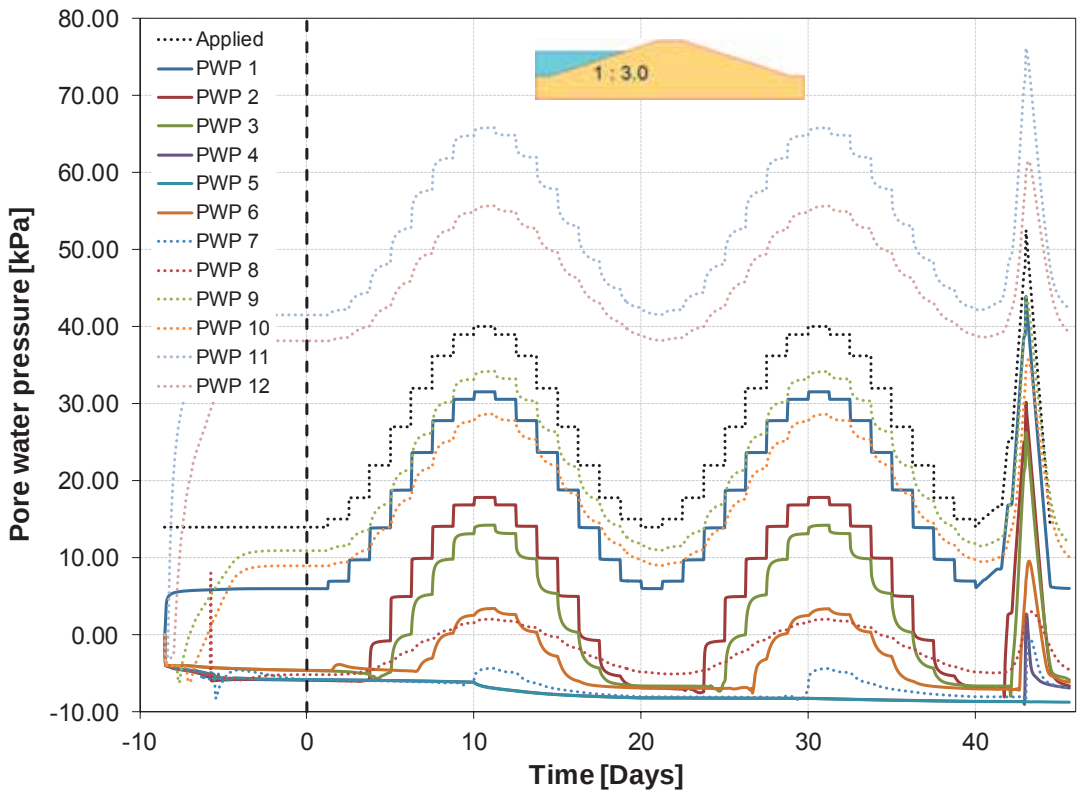

Figure 5.7: Pore water pressures for the homogeneous dyke with slopes 1:3.0 for two flood cycles and the overflow phase, as shown in Figure 5.2.

5.3.2 Dyke with toe filter

The PWP for the dykes with a toe filter is shown in Figures 5.8 to 5.10 for all three slope gradients, and the quantitative comparison with the values from the centrifuge modeling is given in Table 5.5. Similar characteristics are found for both types of modeling, such as the difference in PWP at the maximum water levels is larger than at the minimum water level between points 9 and 10, and between points 11 and 12.

The PWP at points 6, 9, 10, 11, and 12, most of them located on the air-side, increases for flatter slope gradients for both maximum and minimum water level, except for point 11, at which the PWP decreases when the water level is at its minimum. On the other hand, PWP at points 2, 3, and 5, all of them located on the water-side, is greater for those dykes with steeper slopes. Constant values of PWP (change < 0.6 kPa) are estimated for points 1, 4, 5, and 7. The constant response at point 7, which is located at mid-height of the air-side slope, indicates that the toe filter was effective in lowering the water table.

The PWP at point 8 (close to the filter) is always negative (suction) and shows a small variation due to the change in the water table, except for the slope gradient of 1:3.0, for which the variation in PWP is 3.6 kPa. Similar behavior was observed in the centrifuge modeling. This also demonstrates the effect of the toe filter on lowering the phreatic level.

The differences in PWP at the maximum and minimum water levels are similar for both types of model except for point 3, at which a difference of approximately 7 kPa between both types of modeling is found for all three slope gradients. Again, some PWP are greater in the centrifuge modeling, for the same reasons as for the homogeneous dyke, and described above.

Table 5.5: Comparison of the results from the physical models (phys) and the numerical simulations (num) of the pore water pressures (PWP) at the maximum and minimum water level, and their difference calculated as $PWP_{max} – PWP_{min}$ for the dyke with a toe filter (all pressures in kPa). Faulty data is shown in red.

Point		Slope gradient					
		1: 2.0 phys	1: 2.0 num	1: 2.5 phys	1: 2.5 num	1: 3.0 phys	1: 3.0 num
1	Max	39.54	31.40	n.s.	31.62	30.72	31.53
	Min	17.61	5.88	n.s.	6.11	3.61	5.98
	Diff	*21.94*	*25.52*	n.s.	*25.51*	*27.11*	*25.55*
2	Max	27.30	21.37	n.s.	19.48	19.38	17.81
	Min	2.05	-4.64	n.s.	-6.33	-2.00	-6.94
	Diff	*25.25*	*26.01*	n.s.	*25.81*	*21.38*	*24.75*
3	Max	13.23	14.95	11.26	13.91	13.38	13.65
	Min	-0.27	-6.69	-3.02	-6.68	-0.41	-6.68
	Diff	*13.50*	*21.64*	*14.28*	*20.58*	*13.79*	*20.33*
4	Max	0.09	-6.41	-0.66	-6.82	0.06	-6.34
	Min	0.07	-8.23	-0.66	-8.25	0.07	-8.20
	Diff	*0.03*	*1.82*	*0.01*	*1.43*	*-0.01*	*1.85*
5	Max	0.62	-6.35	-0.22	-6.34	-0.45	-6.47
	Min	0.78	-8.22	-0.23	-8.21	-0.46	-8.23
	Diff	*-0.16*	*1.87*	*0.01*	*1.87*	*0.01*	*1.76*
6	Max	0.37	-4.02	-0.40	-0.89	3.78	1.21
	Min	-0.10	-7.14	-0.42	-6.98	-0.36	-6.94
	Diff	*0.46*	*3.12*	*0.03*	*6.09*	*4.14*	*8.15*
7	Max	0.67	-6.15	-1.06	-6.53	-5.64	-6.67
	Min	-0.72	-8.01	-1.06	-8.24	-0.93	-8.32
	Diff	*1.40*	*1.87*	*0.00*	*1.71*	*-4.71*	*1.65*
8	Max	3.91	-4.60	0.06	-6.18	2.17	-3.07
	Min	3.51	-6.03	0.05	-6.73	-0.60	-6.67
	Diff	*0.39*	*1.43*	*0.01*	*0.55*	*2.77*	*3.60*
9	Max	41.31	31.18	n.s.	31.67	n.s.	33.13
	Min	23.28	10.09	n.s.	10.19	n.s.	10.81
	Diff	*18.03*	*21.09*	n.s.	*21.48*	n.s.	*22.32*
10	Max	35.53	24.40	n.s.	25.94	n.s.	26.82
	Min	22.82	7.91	n.s.	8.37	n.s.	8.58
	Diff	*12.71*	*16.49*	n.s.	*17.57*	n.s.	*18.24*
11	Max	67.02	64.59	n.s.	64.79	n.s.	65.07
	Min	47.37	41.59	n.s.	41.49	n.s.	41.46
	Diff	*19.65*	*23.00*	n.s.	*23.29*	n.s.	*23.61*
12	Max	51.59	48.07	n.s.	50.89	n.s.	53.47
	Min	40.58	36.07	n.s.	36.95	n.s.	37.61
	Diff	*11.02*	*12.00*	n.s.	*13.94*	n.s.	*15.85*

n.s. No sensor placed in model.

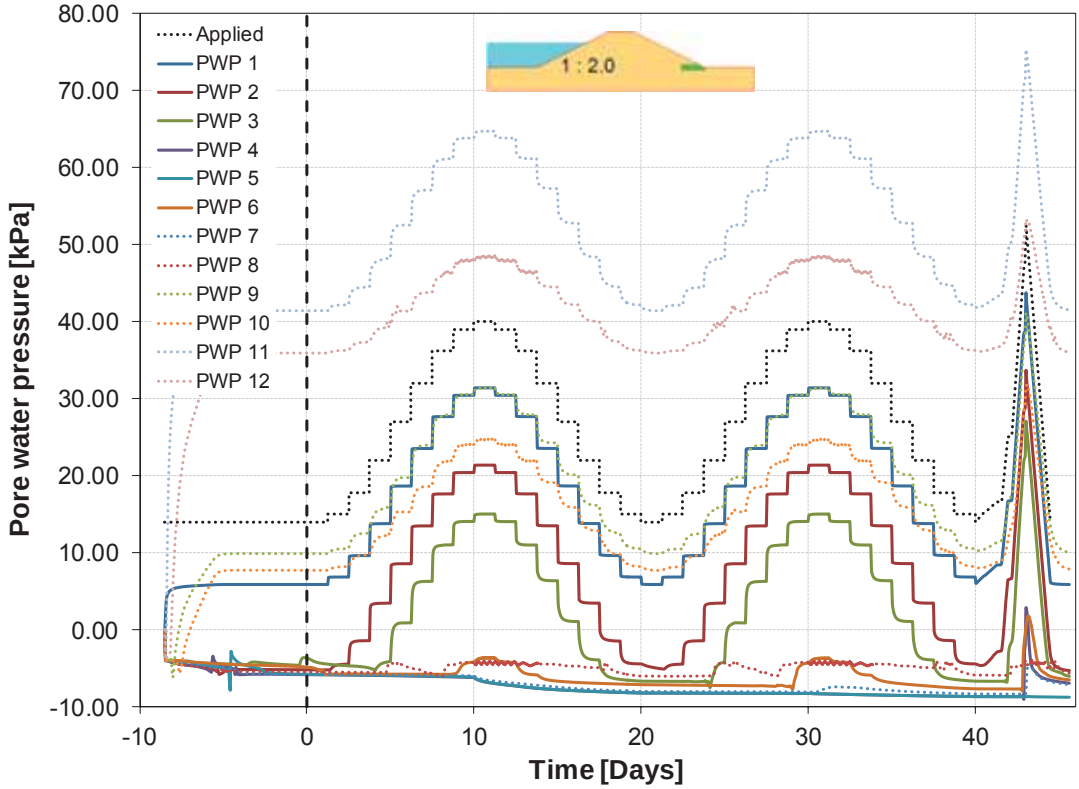

Figure 5.8: Pore water pressures for the dyke with a toe filter and slopes 1:2.0 for two flood cycles and the overflow phase, as shown in Figure 5.2.

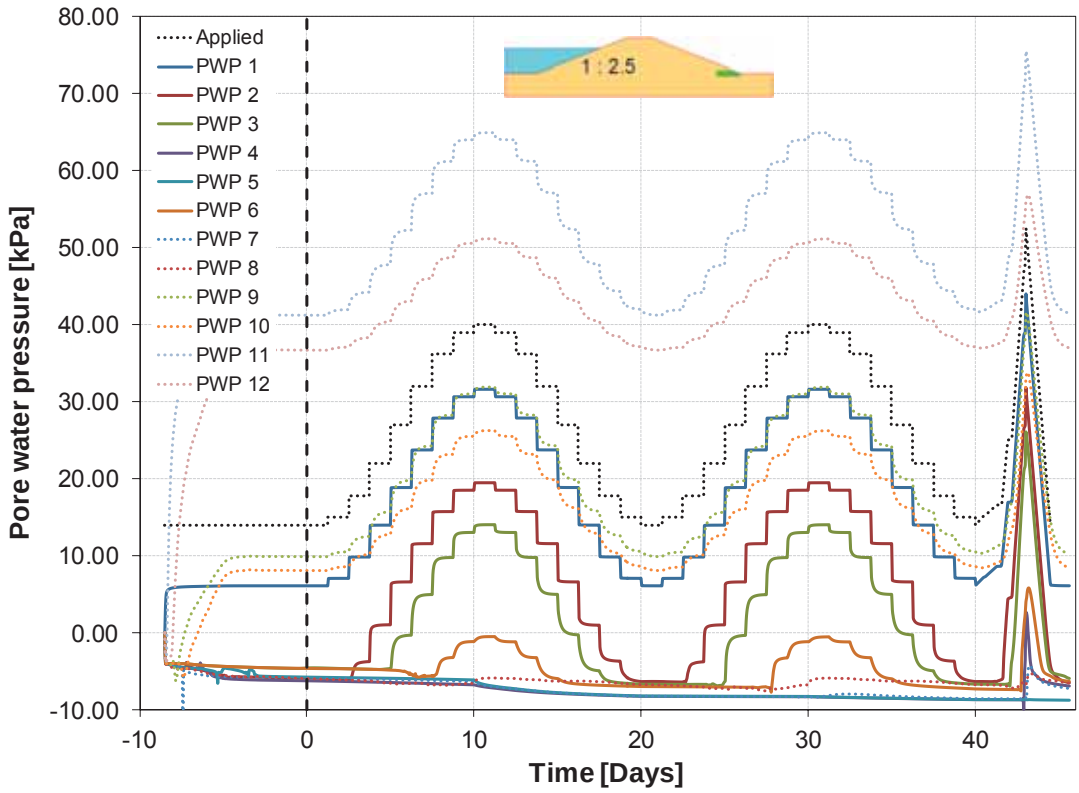

Figure 5.9: Pore water pressures for the dyke with a toe filter and slopes 1:2.5 for two flood cycles and the overflow phase, as shown in Figure 5.2.

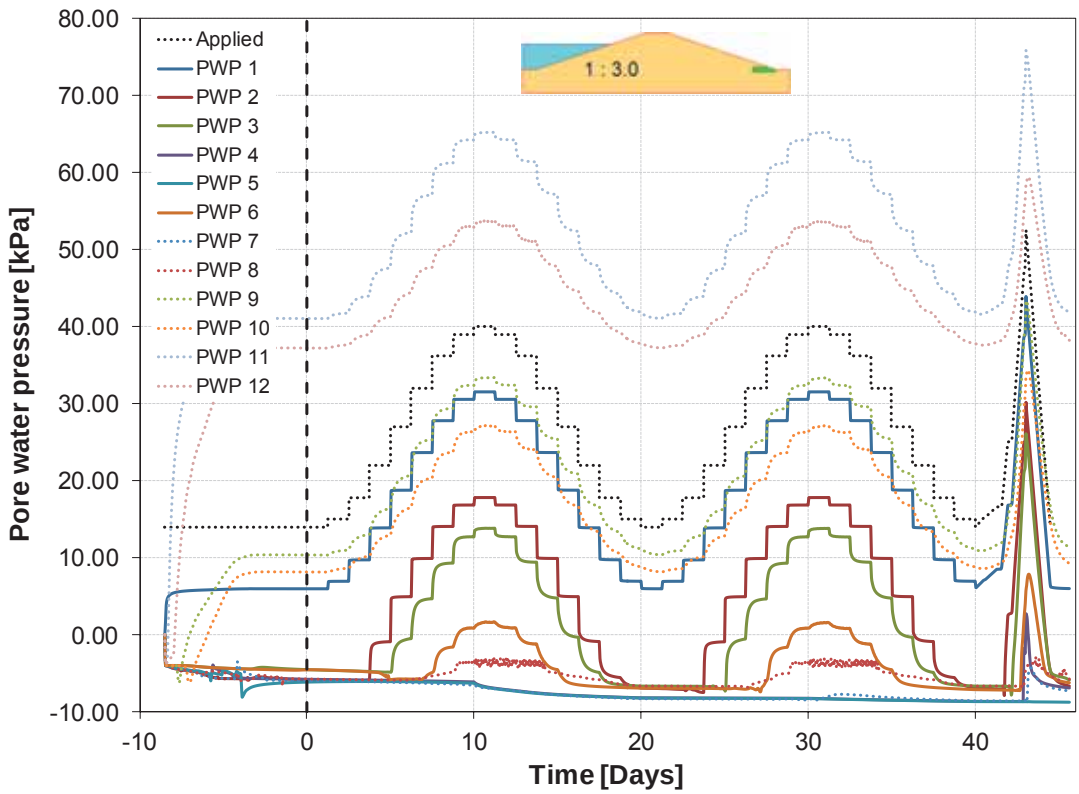

Figure 5.10: Pore water pressures for the dyke with a toe filter and slopes 1:3.0 for two flood cycles and the overflow phase, as shown in Figure 5.2.

5.3.3 Dyke with a cut-off wall

Figures 5.11 to 5.13 present the development of PWP with time for the dyke with a cut-off wall. The comparison between the values calculated and those measured values during the centrifuge modeling is presented in Table 5.6, with good agreement in the differences of PWP between high and low water levels.

There is no significant variation in PWP at points 1, 3, 4, 5, 8, and 11 if the slope gradient is modified. The average values are, respectively, 31.61, 15.65, -6.37, -6.17, -0.23, 66.18 kPa at the maximum water level, and 6.08, -6.64, -8.20, -8.23, -5.26, 42.34 kPa at the minimum water level. Furthermore, the PWP at point 8 is similar to that observed for the homogeneous dyke, i.e. greater than for the dyke with the toe filter. This is influenced by water springs developing on the air-side slope.

An increase in PWP at points 9 and 10 is observed with the decrease of the slope gradient for both maximum and minimum water levels. 34.64 and 21.07 kPa are the PWP at the maximum water level for the slope gradient of 1:2.0, and these increase to 36.68 and 25.00 kPa for the slope gradient of 1:3.0. The pressures are 11.53 and 8.15 kPa for the steeper slopes at the minimum water level, and they increase to 13.31 and 10.07 kPa for the shallower.

Points 6 and 12, which are located on the air-side slope, do not exhibit significant change in the PWP at the minimum water level for all three slope gradients. On the other hand, their

values of PWP increase when the water level is at its maximum. PWP varies from -5.56 and 47.89 kPa for the slope gradient of 1:2.0 to -0.59, and 51.66 kPa for the slope gradient of 1:3.0, respectively.

Table 5.6: Comparison of the results from the physical models (phys) and the numerical simulations (num) of the pore water pressures (PWP) at the maximum and minimum water level, and their difference calculated as $PWP_{max} - PWP_{min}$ for the dyke with a cut-off wall (all pressures in kPa). Faulty data is shown in red.

Point		Slope gradient					
		1: 2.0 phys	1: 2.0 num	1: 2.5 phys	1: 2.5 num	1: 3.0 phys	1: 3.0 num
1	Max	30.60	31.46	33.96	31.63	30.85	31.73
	Min	3.63	5.94	7.50	6.12	4.06	6.19
	Diff	*26.96*	*25.53*	*26.46*	*25.51*	*26.79*	*25.55*
2	Max	29.38	21.48	21.00	19.55	20.52	17.64
	Min	1.87	-4.39	-0.85	-6.06	-3.15	-6.93
	Diff	*27.51*	*25.87*	*21.85*	*25.62*	*23.66*	*24.57*
3	Max	13.15	16.13	20.93	15.47	17.54	15.36
	Min	-6.56	-6.65	-5.54	-6.63	-0.35	-6.64
	Diff	*19.71*	*22.77*	*26.47*	*22.10*	*17.89*	*22.00*
4	Max	0.10	-6.50	-3.41	-6.31	-3.98	-6.31
	Min	0.09	-8.24	-3.24	-8.19	-4.03	-8.18
	Diff	*0.02*	*1.74*	*-0.17*	*1.88*	*0.05*	*1.86*
5	Max	7.19	-6.39	-4.16	-6.45	8.19	-5.67
	Min	7.57	-8.22	-3.88	-8.23	8.47	-8.24
	Diff	*-0.38*	*1.84*	*-0.28*	*1.77*	*-0.27*	*2.57*
6	Max	0.80	-5.56	1.69	-3.41	3.35	-1.59
	Min	0.13	-7.14	-0.05	-6.99	0.14	-6.94
	Diff	*0.67*	*1.58*	*1.74*	*3.59*	*3.21*	*5.35*
7	Max	1.91	-5.85	-0.73	-6.62	-0.85	-6.56
	Min	-0.84	-7.96	-0.72	-8.17	-0.86	-8.26
	Diff	*2.75*	*2.12*	*-0.01*	*1.55*	*0.01*	*1.71*
8	Max	13.40	-0.18	9.11	-0.91	8.80	0.40
	Min	6.62	-5.18	3.98	-5.66	2.29	-4.95
	Diff	*6.78*	*5.01*	*5.13*	*4.75*	*6.50*	*5.35*
9	Max	48.08	34.64	n.s.	34.70	43.87	36.68
	Min	26.74	11.53	n.s.	11.48	22.17	13.31
	Diff	*21.34*	*23.11*	n.s.	*23.22*	*21.70*	*23.36*
10	Max	37.20	21.07	n.s.	22.50	34.02	25.00
	Min	22.43	8.15	n.s.	8.53	23.44	10.07
	Diff	*14.77*	*12.92*	n.s.	*13.96*	*10.58*	*14.92*
11	Max	n.s.	66.14	n.s.	66.16	n.s.	66.23
	Min	n.s.	42.46	n.s.	42.32	n.s.	42.25
	Diff	n.s.	*23.68*	n.s.	*23.84*	n.s.	*23.98*
12	Max	54.37	47.89	n.s.	49.86	45.47	51.66
	Min	41.42	36.97	n.s.	37.61	39.68	38.17
	Diff	*12.95*	*10.92*	n.s.	*12.25*	*5.80*	*13.50*

n.s. No sensor placed in model.

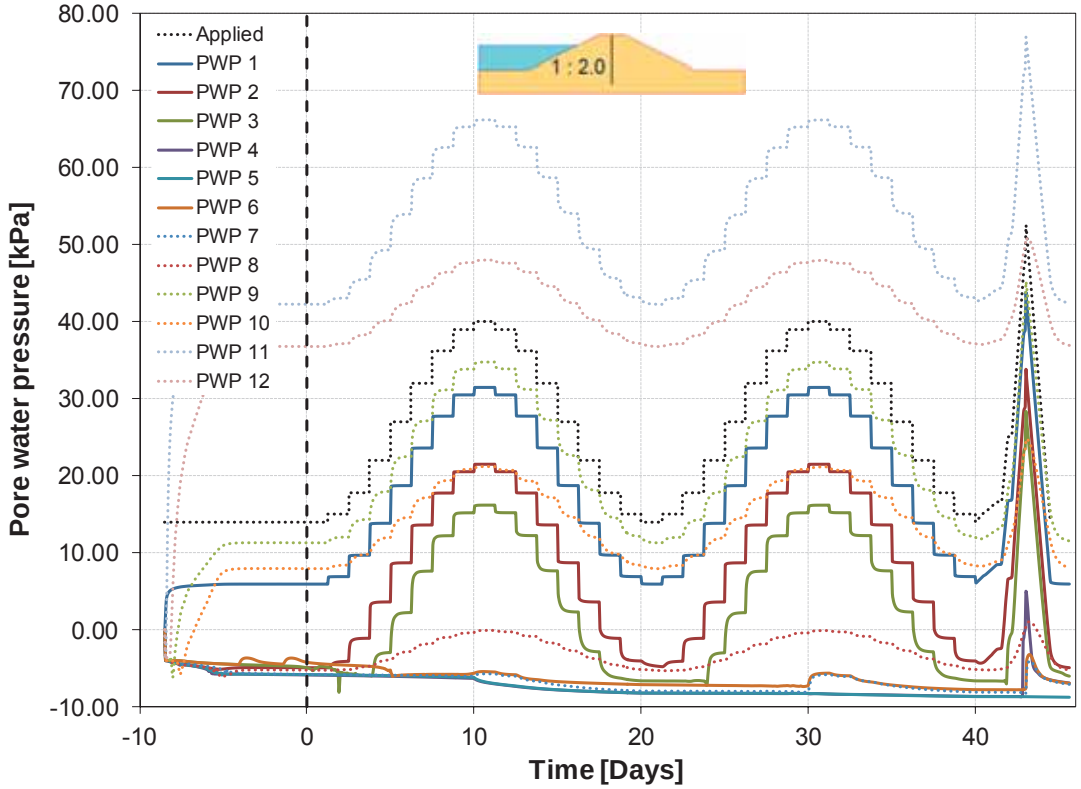

Figure 5.11: Pore water pressures for the dyke with a cut-off wall and slopes 1:2.0 for two flood cycles and overflow phase, as shown in Figure 5.2.

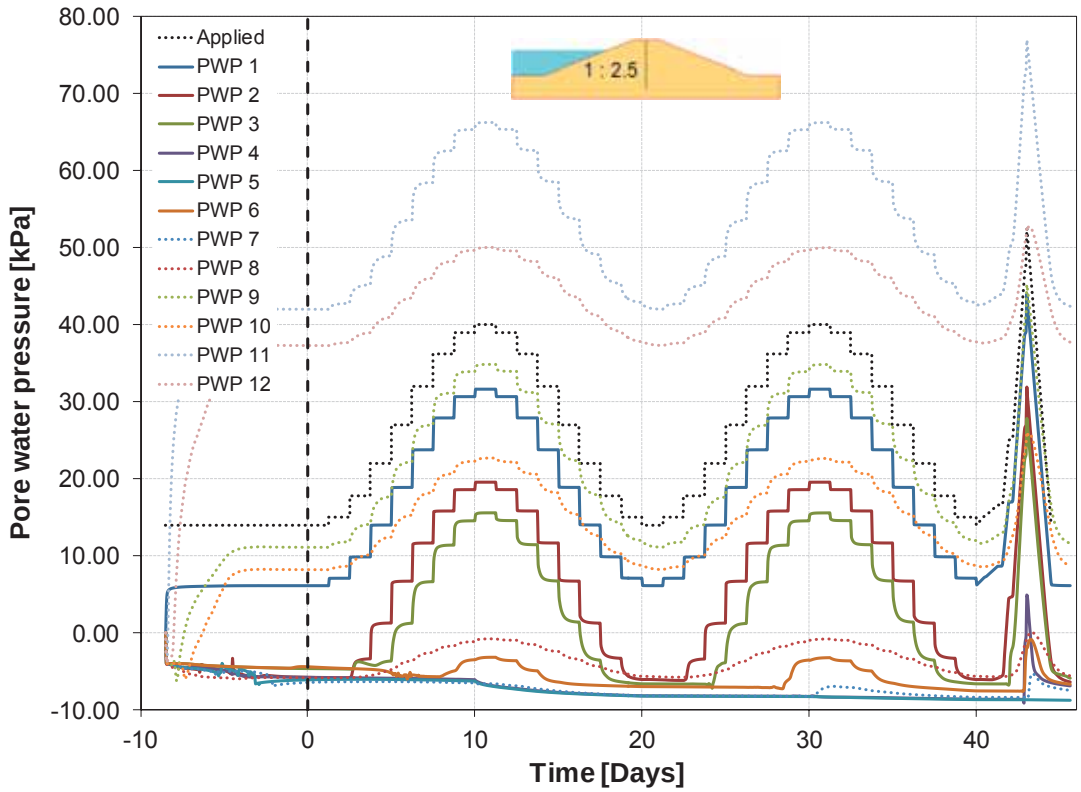

Figure 5.12: Pore water pressures for the dyke with a cut-off wall and slopes 1:2.5 for two flood cycles and overflow phase, as shown in Figure 5.2.

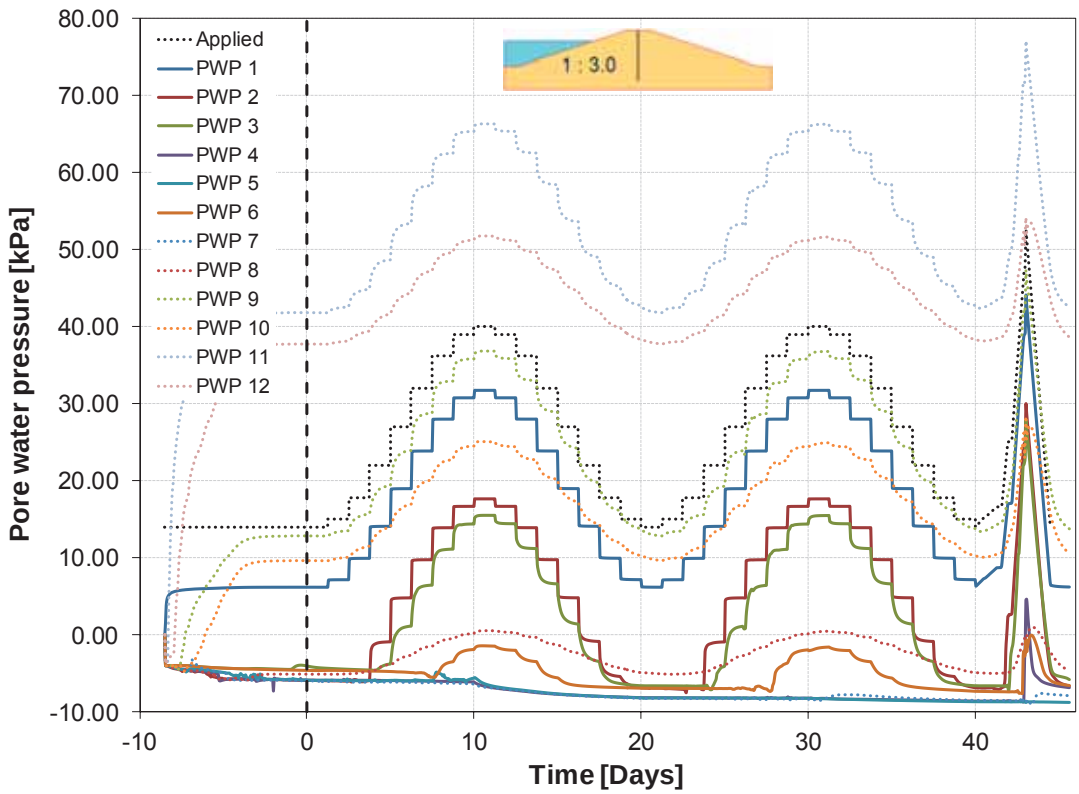

Figure 5.13: Pore water pressures for the dyke with a cut-off wall and slopes 1:3.0 for two flood cycles and overflow phase, as shown in Figure 5.2.

5.3.4 Dyke with a cut-off wall and toe filter

The PWP evolution for the dyke with both protective measures, a cut-off wall and a toe filter, is illustrated in Figures 5.14 to 5.16. The comparison with the centrifuge modeling is presented in Table 5.7.

PWP at points 1, 3, 4, 5, 7 and 11 does not change with a change in the slope gradient, and average values of 31.54, 15.32, -6.39, -6.38, -6.47 and 65.58 kPa are obtained at the maximum flood level, and 6.01, -6.65, -8.21, -8.22, -8.21 and 41.88 kPa when the water is lowered. The response of the PWP at point 8 is similar to that observed for the dyke with the toe filter, i.e. negative pressures are predicted and there is low influence of the flood cycles. This demonstrates again the effect of the filter in lowering the water table. Furthermore, PWP for the dyke with a cut-off wall and toe filter is less than for the case with the toe filter only. For instance, the values for all three slope gradients are -4.60, -6.18, -3.07 kPa for the dyke with a toe filter only, whereas the PWP are -6.47, -6.96, -4.9 kPa for the dyke with a toe filter and a cut-off wall. This is consequence of the wall, which lowers the phreatic line in the air-side even more than when only the toe filter is used.

An increase in PWP at points 6, 9, 10 and 12 is observed with the decrease of the slope gradient for both maximum and minimum water level. The PWPs at the maximum water level are -5.58, 33.77, 18.29 and 44.35 kPa for the slope gradient of 1:2.0, and increase to -3.81, 34.76, 21.56 and 49.38 kPa for the slope gradient of 1:3.0. The pressures are -7.14, 10.93,

7.05 and 35.64 kPa at the minimum water level, and they increase to -6.94, 11.32, 7.90 and 37.15 kPa when the slope is flatter.

PWP at point 6 exhibits a different behavior for the different slope gradients, as no change during flooding is calculated for the steepest slope (1:2.0). However, for the flatter slope the cyclic flood causes the PWP to increase. A similar behavior was observed for this location in the centrifuge tests.

The comparison between the numerical and the centrifuge modeling (Table 5.7) presents good agreement for most of the differences of PWP between the high and low water levels. Exceptions are points 7, and 8 for the slope gradient of 1:2.0, and point 2 for the dyke with slope gradient of 1:2.5. The inconsistency of point 7 is due to its incorrect position during the preparation of the centrifuge model, as explained in Section 4.5.4. However, no plausible explanation for the divergence of the other points is found.

Table 5.7: Comparison of the results from the physical models (phys) and the numerical simulations (num) of the pore water pressures (PWP) at the maximum and minimum water level, and their difference calculated as $PWP_{max} – PWP_{min}$ for the dyke with a cut-off wall and a toe filter (all pressures in kPa). Faulty data is shown in red.

Point		Slope gradient					
		1: 2.0 phys	1: 2.0 num	1: 2.5 phys	1: 2.5 num	1: 3.0 phys	1: 3.0 num
1	Max	35.94	31.44	29.91	31.63	36.50	31.54
	Min	9.76	5.91	2.02	6.11	10.72	5.99
	Diff	*26.18*	*25.53*	*27.89*	*25.51*	*25.78*	*25.55*
2	Max	24.39	21.45	18.89	19.53	20.39	17.84
	Min	-3.36	-4.51	0.24	-6.20	-1.34	-6.92
	Diff	*27.75*	*25.95*	*18.64*	*25.73*	*21.72*	*24.75*
3	Max	20.03	15.89	18.46	15.18	18.63	14.87
	Min	-0.41	-6.66	-0.34	-6.65	-0.13	-6.65
	Diff	*20.44*	*22.56*	*18.80*	*21.83*	*18.77*	*21.52*
4	Max	-3.51	-6.41	-5.04	-6.39	0.10	-6.38
	Min	0.10	-8.22	-5.15	-8.20	0.11	-8.21
	Diff	*-3.61*	*1.81*	*0.11*	*1.81*	*-0.01*	*1.83*
5	Max	-2.24	-6.31	-6.14	-6.43	-4.77	-6.39
	Min	-1.90	-8.21	-5.72	-8.22	-4.94	-8.22
	Diff	*-0.34*	*1.90*	*-0.42*	*1.80*	*0.17*	*1.83*
6	Max	0.35	-5.58	-0.26	-5.58	-0.20	-3.81
	Min	0.28	-7.14	-0.30	-6.99	-0.20	-6.94
	Diff	*0.07*	*1.57*	*0.04*	*1.40*	*0.00*	*3.13*
7	Max	25.60	-6.21	-0.69	-6.40	-0.76	-6.80
	Min	19.59	-8.04	-0.70	-8.22	-0.79	-8.36
	Diff	*6.01*	*1.83*	*0.01*	*1.82*	*0.03*	*1.56*
8	Max	4.65	-6.47	5.20	-6.96	-2.33	-4.90
	Min	2.69	-6.22	4.87	-7.08	-3.57	-6.73
	Diff	*1.96*	*-0.25*	*0.33*	*0.12*	*1.24*	*1.84*
9	Max	47.38	33.77	n.s.	33.95	n.s.	34.76
	Min	25.20	10.93	n.s.	10.93	n.s.	11.32

	Diff	*22.18*	*22.83*	n.s.	*23.03*	n.s.	*23.44*
10	Max	33.03	18.29	n.s.	20.33	n.s.	21.56
	Min	22.38	7.05	n.s.	7.61	n.s.	7.90
	Diff	*10.65*	*11.25*	n.s.	*12.72*	n.s.	*13.66*
11	Max	n.s.	65.47	n.s.	65.60	n.s.	65.69
	Min	n.s.	42.00	n.s.	41.88	n.s.	41.76
	Diff	n.s.	*23.47*	n.s.	*23.72*	n.s.	*23.93*
12	Max	53.46	44.35	n.s.	47.16	n.s.	49.38
	Min	42.83	35.64	n.s.	36.52	n.s.	37.15
	Diff	*10.63*	*8.72*	n.s.	*10.64*	n.s.	*12.23*

n.s. No sensor placed in model.

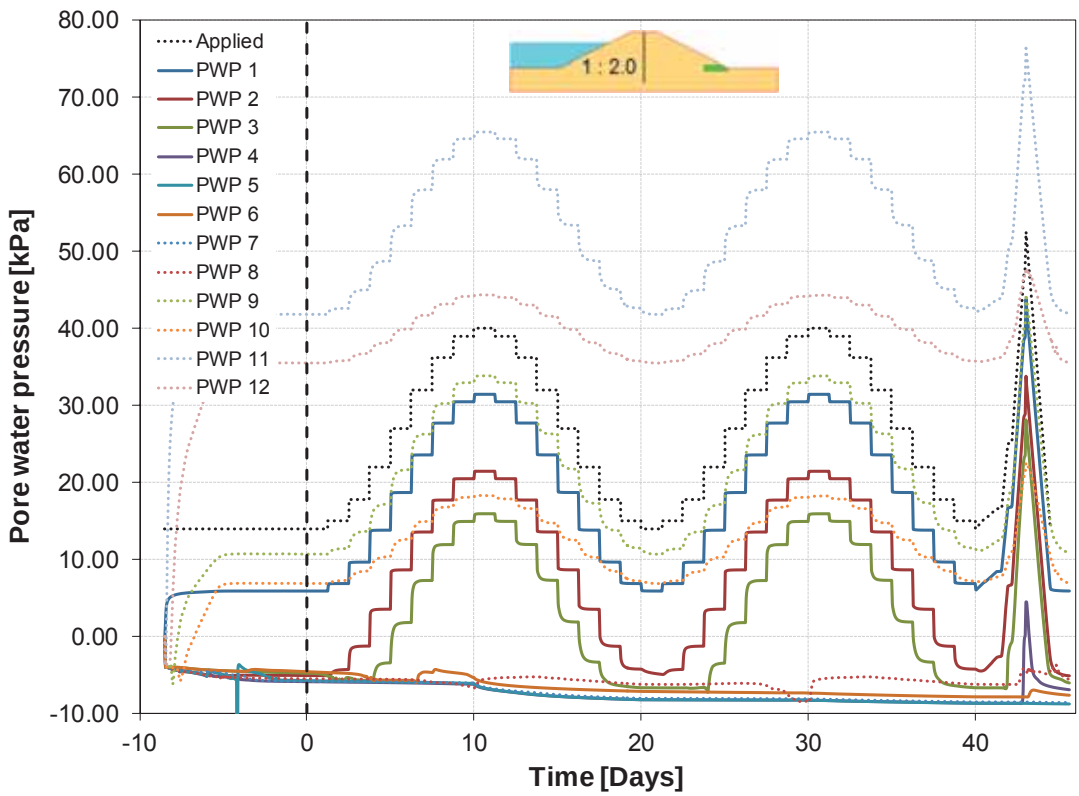

Figure 5.14: Pore water pressures for the dyke with a cut-off wall and toe filter and slopes 1:2.0 for two flood cycles and overflow phase, as shown in Figure 5.2.

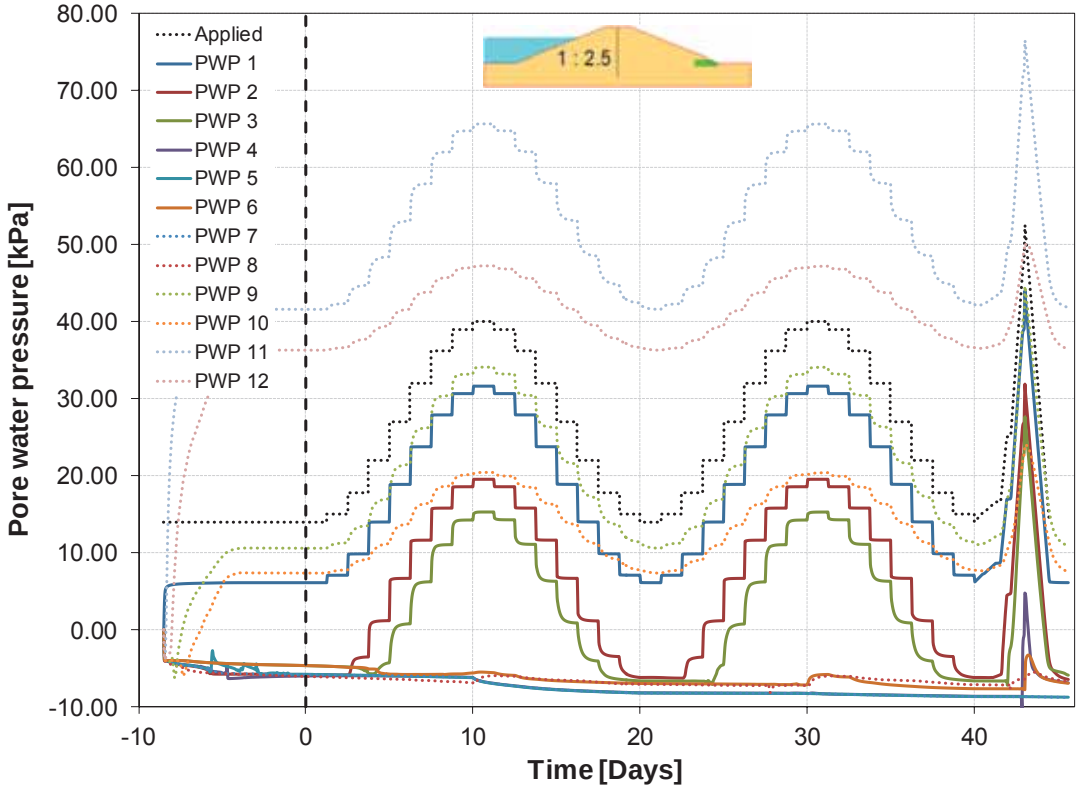

Figure 5.15: Pore water pressures for the dyke with a cut-off wall and toe filter and slopes 1:2.5 for two flood cycles and overflow phase, as shown in Figure 5.2.

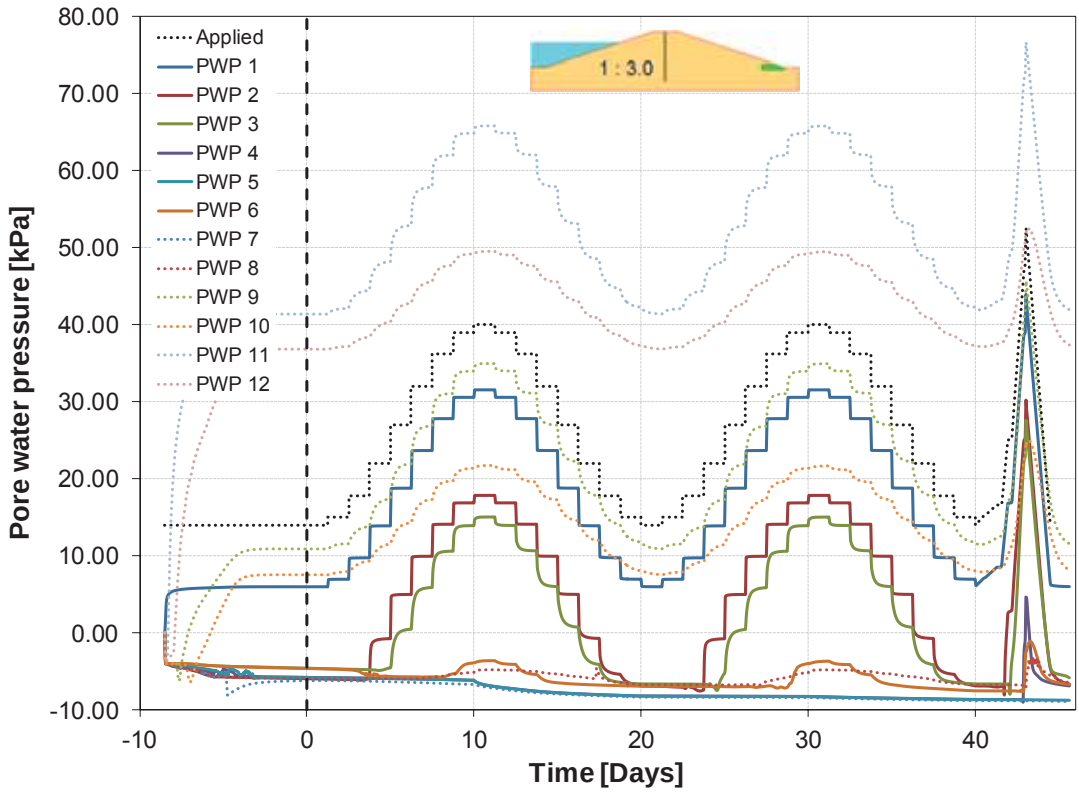

Figure 5.16: Pore water pressures for the dyke with a cut-off wall and toe filter and slopes 1:3.0 for two flood cycles and overflow phase, as shown in Figure 5.2.

5.3.5 Slope stability

The stability of both the air and water-side slopes is analyzed for each slope gradient. The influence of each protective measure on the factor of safety (FoS) (Equations 2.51 and 2.52) is compared with that from the homogeneous dyke. At the end of the section, the main values are summarized in tables.

The Euro Code EC7 recommends partial safety factors to be used for design of geotechnical structures. However, and according to Bolton (1993), the partial safety factor safeguard against predictable deformations, whereas the global factors are used to check for safety against collapse. Therefore, a global safety factor was preferred for carrying out the following analyses.

Figures 5.17 and 5.18 show the FoS for the dyke with a slope gradient of 1:2.0 for both air and water-side slopes. Again, time zero corresponds to the moment at which the flood cycles begin. The FoS decreases below 1.0 on the air-side slope of the homogeneous dyke and the dyke with a cut-off wall. This explains the slope instabilities observed for those dykes in the centrifuge model tests (cf. Sections 4.5.1 and 4.5.3). The homogeneous dyke reached an unstable condition 5.5 days after the beginning of the first flood cycle. This is 1.04 days sooner than for the dyke with a cut-off wall. This might explain the greater damage to the homogeneous dyke observed in the physical modeling, as the time at failure condition is longer, a larger volume of soil on the air-side slope experienced failure.

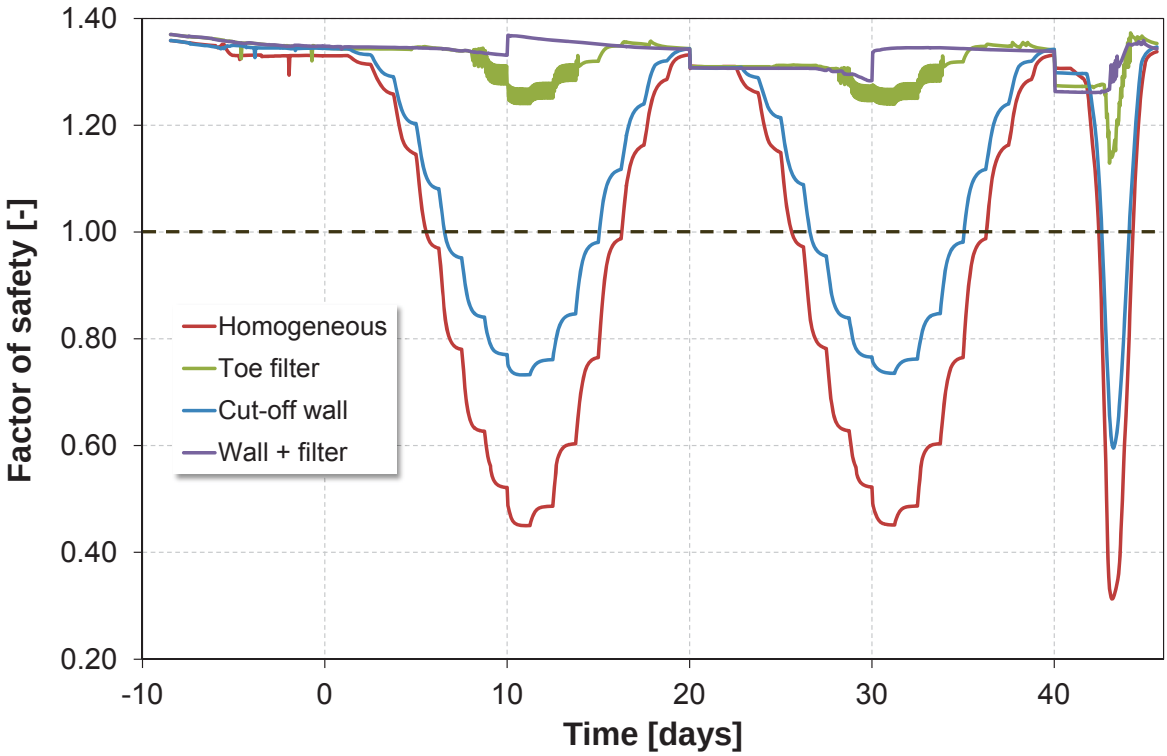

Figure 5.17: Global factor of safety to assess the slope stability of the air-side slope of the dykes with slopes 1:2.0 for two flood cycles and overflow phase, as shown in Figure 5.2.

The FoS of the dyke with a toe filter drops from 1.34 to 1.24 during the flooding cycles and to 1.13 during the overflow phase. The dyke with a cut-off wall and toe filter presents the smallest change in the FoS, varying from 1.28 to 1.37 during the flood cycles and decreasing to 1.26 during the overflow phase, it therefore, remains stable during the whole process.

A sudden jump in the FoS is also observed at the times at which a change in the water level is imposed. This is a consequence of the adaptations necessary to cope with modeling the hysteretic behavior of the SWRC with the current numerical implementation of SEEP-W. In consequence, different material properties were applied for the wetting and drying phases. The hydraulic conductivity influences the numerical solution of the pore water pressures. As a consequence, these pressures might differ slightly between the last time step of the wetting (or drying) phase and the first time step of the drying (or wetting) phase. Therefore, the critical slip surfaces are different, so their corresponding FoS.

The water-side slope remains stable during the flood cycles, overflow, and rapid drawdown phases. Furthermore, no large influence of the protection measures on the FoS is observed for this slope (difference in FoS is 0.05). The FoS decreases during the phase in which water starts flowing towards the air-side to establish a steady-state condition. This is owing to the loss of the additional shear strength given to the soil due to initial suction, because the soil starts to saturate. The FoS at the beginning of the flood cycles varies between 1.23 and 1.245, and increases during the flood cycles. This is the opposite behavior of that observed on the air-side slope, and is due to the stabilizing effect of the weight of the rising water.

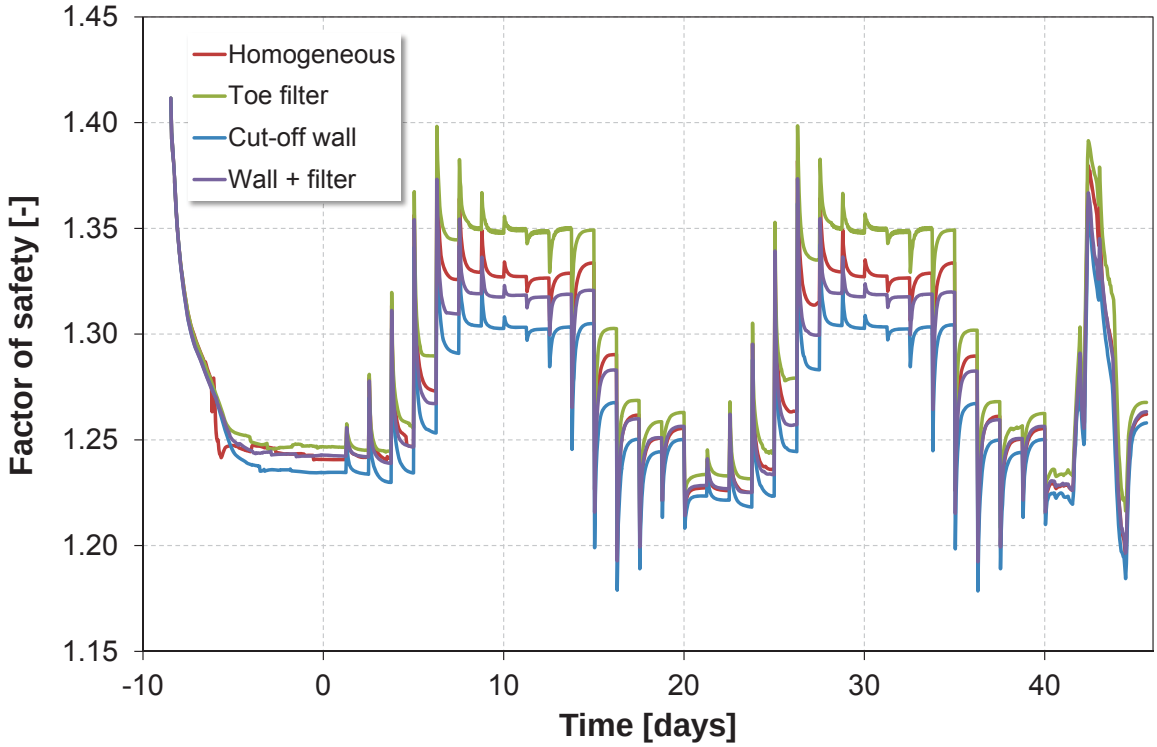

Figure 5.18: Global factor of safety to assess the slope stability of the water-side slope of the dykes with slopes 1:2.0 for two flood cycles and overflow phase, as shown in Figure 5.2.

The FoS ranges between 1.30 and 1.35 at the maximum water level. The minimum FoS (1.30) corresponds to the dyke with a cut-off wall, and the maximum (1.35) to the dyke with the toe filter. This is due to the ponding effect on the water-side due to the wall (cf. Section 4.5.3). The wall prevents water from draining fast towards the air-side; therefore, greater pore water pressures build up on the water-side slope, which leads to lower effective stresses, and hence a lower FoS. The inclusion of the toe filter, together with the wall, increases the FoS, as the toe filter increases the draining capacity of the dyke. However, the FoS remains smaller than for the homogeneous dyke.

Another feature observed in the behavior of the FoS on the water-side slope are some peak values at the beginning of each loading step (change in the external water level). When the water level is raised, the FoS increases suddenly, and decays progressively with time. Unsurprisingly, the opposite response is seen when the water is lowered, for which a sudden decrease is observed, increasing afterwards.

This is explained as follows: when the water is raised suddenly, the resisting force given by the weight of the water over the slope increases. However, the pore water pressures in the soil do not increase immediately, and the effective stresses do not decrease. This results in an increase of the resisting forces without an increase in the driving forces, leading to an increase of the FoS. The soil continues saturating upwards as the water front moves upwards due to the new water level imposed. This results in an increase of the pore water pressures and, ultimately, a gradual decrease of the FoS.

The same analysis can be done for those steps in which the external water level is lowered. The water level is suddenly lowered at the beginning of the step. Therefore, the resisting force given by the weight of the water acting on the slope is decreased, but the pore water pressures do not decrease immediately. This results in a sudden decrease of the FoS. The water front inside the dyke lowers with time, as well as the pore water pressures. This results in an increasing FoS.

Figure 5.19 presents the FoS for the air-side slope of the dykes with a slope gradient of 1:2.5. The behavior is similar to that observed for the slope gradient of 1:2.0. The FoS decreases below 1.0 for the homogeneous dyke after 6.54 days, and after 7.71 days for the dyke with a cut-off wall. This means 1.17 days after the homogeneous dyke. In general, the FoS are larger than for the slope gradient of 1:2.0, ranging between 0.54 and 1.56 at the maximum water level in comparison with 0.45 and 0.73 for the dyke with a slope gradient of 1:2.0.

The dykes with a toe filter and with a cut-off wall and toe filter exhibit a greater change in FoS than those observed for those with a slope gradient of 1:2.0. For the dyke with a toe filter it changes from 1.67 in the steady-state flow condition to 1.46 at the maximum water level, and 1.31 during the overflow phase. For the dyke with a cut-off wall and toe filter, it changes from 1.67 to 1.56 and 1.51 at steady-state, maximum water level and overflow, respectively. The jump in the FoS is observed only for the change from a drying to a wetting phase (t = 20, 40 days), and its cause was described above.

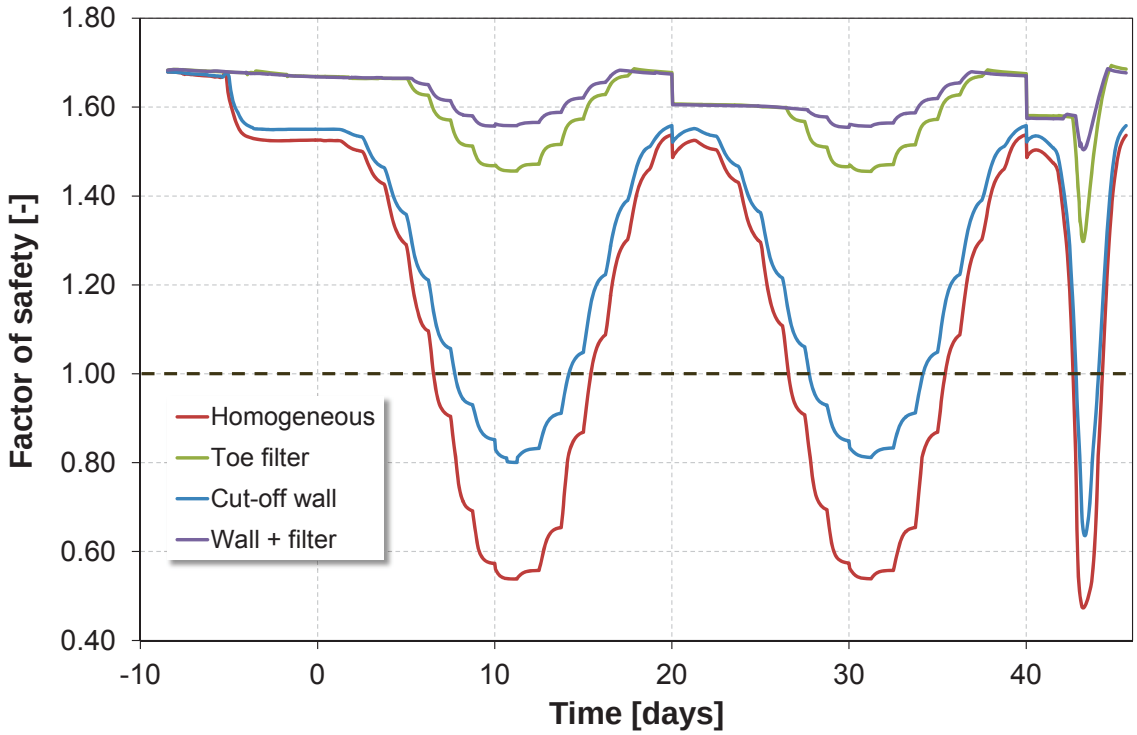

Figure 5.19: Global factor of safety to assess the slope stability of the air-side slope of the dykes with slopes 1:2.5 for two flood cycles and overflow phase, as shown in Figure 5.2.

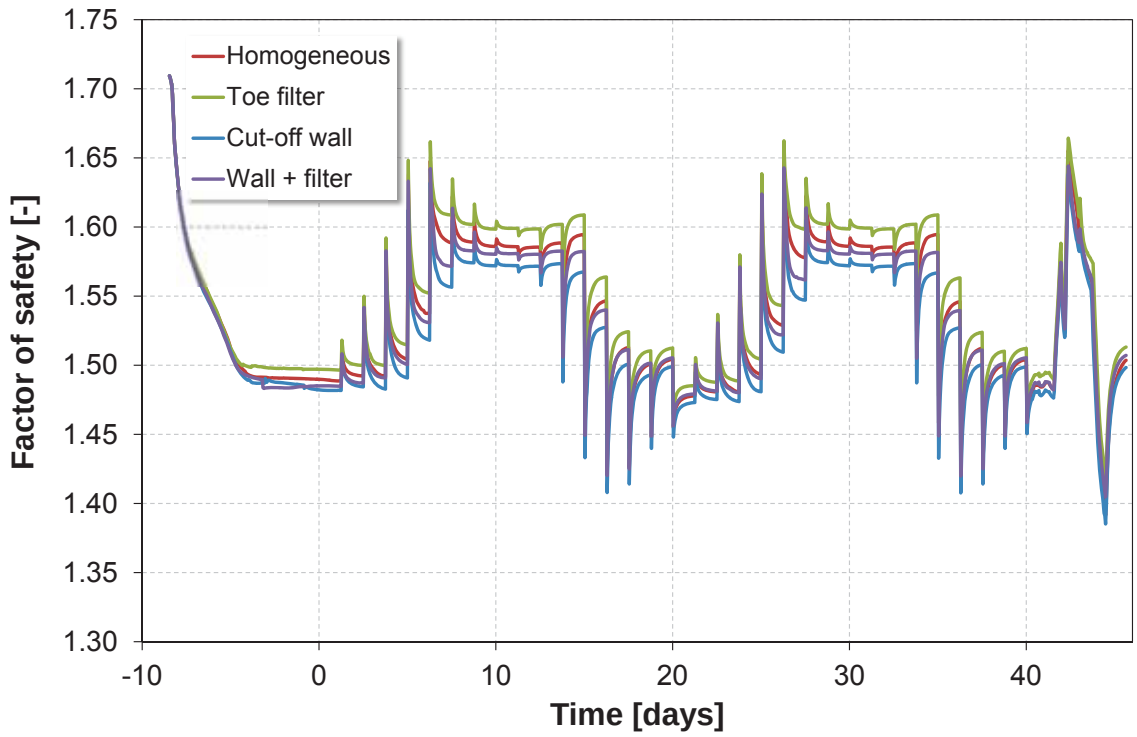

Figure 5.20: Global factor of safety to assess the slope stability of the water-side slope of the dykes with slopes 1:2.5 for two flood cycles and overflow phase, as shown in Figure 5.2.

The FoS of the water-side slope (Figure 5.20) is, in general, greater than those for the dykes with a slope gradient of 1:2.0. However, the difference in FoS between the different protective measures is smaller. It varies between 1.57 and 1.60 at the maximum water level, whereas it ranges between 1.41 and 1.44 at the minimum water level during the flood cycles.

The same process observed for the slope gradient of 1:2.0, in which a peak value in FoS is followed by its decrease in time, is observed in this case. In the same way, the difference between the peak value of FoS and its subsequent equilibrium value is greater when the water level is at the mid height of the dyke than when it is at the maximum or minimum levels. Table 5.8 compares the difference in FoS for each change step in the water level of the dyke with the toe filter.

The development of the FoS on the air-side slope is shown in Figure 5.21 for all four dykes with a slope gradient of 1:3.0. The behavior is similar to that observed for the other two gradients. The FoS are greater than those for the flatter slopes, which is expected because the angle of the slope (18.43°) is almost half of the friction angle (31°).

Table 5.8: Differences between peak and subsequent equilibrium FoS for the dyke with the toe filter.

Time [days]	Water level [m]*	FoS $_{peak}$ [-]	FoS $_{equilibrium}$ [-]	Difference [-]
1.29	1.50	1.52	1.50	0.02
2.54	1.78	1.55	1.50	0.05
3.79	2.20	1.59	1.52	0.07
5.04	2.70	1.65	1.55	0.10
6.29	3.20	1.66	1.61	0.05
7.54	3.62	1.63	1.60	0.03
8.79	3.90	1.62	1.60	0.02
10.08	4.00	1.60	1.59	0.01

**Measured from the toe of the dyke (Figure 5.2).*

Values of safety factor are still calculated for the homogeneous dyke and the dyke with a cut-off wall below 1.0 after 7.79 and 9.25 days of the beginning of the flood cycles, respectively. This is an indication of local instability, which in turn, was observed for centrifuge models representing the same prototype dykes.

The slope stability of the water-side slope of the dykes with a slope gradient of 1:3.0 is presented in Figure 5.22 in the form of global factor of safety. A similar evolution of FoS with time is observed for this slope gradient as for the other two flatter dykes. As occurred for the slope gradient of 1:2.5, the difference between the FoS for the different protective measures becomes smaller, and thus, at the maximum water level, the FoS varies between 1.87 and 1.89. This is 0.02 difference, which is the same as in the steady-state condition (1.72 < FoS < 1.74), and during rapid drawdown at the end of the test (1.57 < FoS < 1.59). A difference of 0.03 in FoS is observed when the water is at its minimum level (1.63 < FoS < 1.66), and during overflow (1.92 < FoS < 1.95). It can, therefore, be concluded that the protective measures have an insignificant impact on the FoS of the water-side slope.

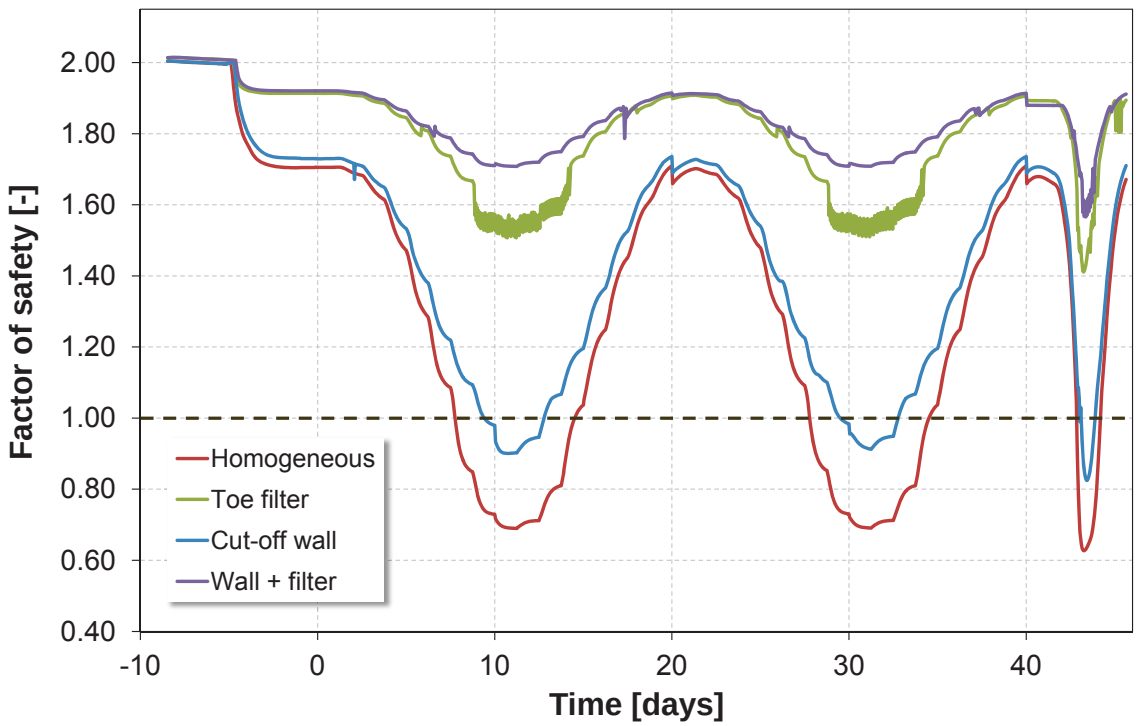

Figure 5.21: Global factor of safety to assess the slope stability of the air-side slope of the dykes with slopes 1:3.0 for two flood cycles and overflow phase, as shown in Figure 5.2.

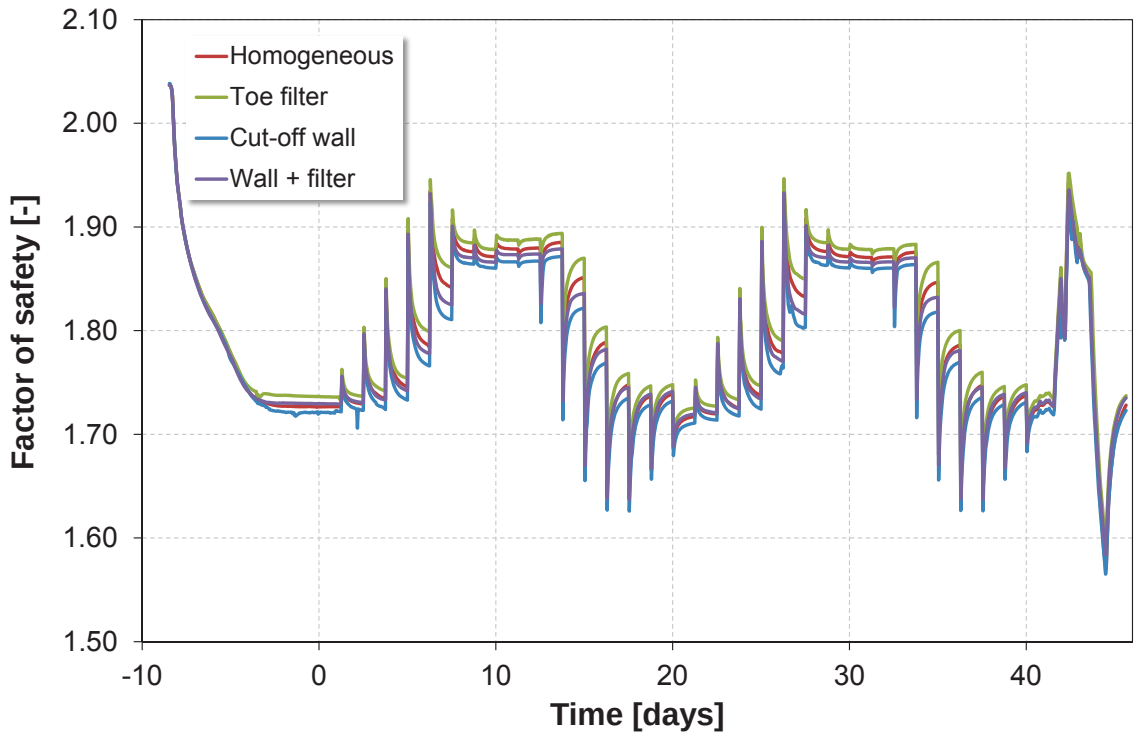

Figure 5.22: Global factor of safety to assess the slope stability of the water-side slope of the dykes with slopes 1:3.0 for two flood cycles and overflow phase, as shown in Figure 5.2.

The factors of safety obtained for the simulations are summarized in Table 5.9 for the air-side slope, and in Table 5.10 for the water-side slope. As discussed above, a cut-off wall together with a toe filter provides the largest FoS for the air-side slope; this is followed by the dyke with a toe filter and the dyke with a cut-off wall. On the other hand, the dyke with a toe filter offers the largest FoS for the water-side slope. This is owing to the accumulation of water on the water-side when a wall is installed, which causes water to pond on the water-side slope, decreasing both the effective stresses and FoS.

Table 5.9: Summary of the factors of safety (FoS) for the air-side slope.

Slope gradient	Type of dyke*	FoS steady-state	FoS $flood_{peak}$	FoS $flood_{min}$	FoS overflow	FoS rapid drawdown
1:2.0	H	1.33	0.45	1.30	0.32	1.35
	F	1.35	1.27	1.30	1.13	1.35
	W	1.35	0.73	1.30	0.60	1.35
	WF	1.35	1.37	1.30	1.26	1.35
1:2.5	H	1.52	0.54	1.52	0.49	1.54
	F	1.67	1.46	1.60	1.31	1.68
	W	1.55	0.81	1.49	0.62	1.54
	WF	1.67	1.56	1.60	1.51	1.68
1:3.0	H	1.70	0.69	1.71	0.64	1.67
	F	1.92	1.53	1.91	1.42	1.90
	W	1.72	0.90	1.72	0.89	1.69
	WF	1.92	1.71	1.91	1.58	1.90

**H=Homogeneous, F= Toe filter, W= Cut-off wall, WF= Cut-off wall and toe filter.*

Table 5.10: Summary of the factors of safety (FoS) for the water-side slope.

Slope gradient	Type of dyke*	FoS steady-state	FoS $flood_{peak}$	FoS $flood_{min}$	FoS overflow	FoS rapid drawdown
1:2.0	H	1.24	1.33	1.26	1.35	1.26
	F	1.23	1.35	1.27	1.37	1.27
	W	1.24	1.31	1.25	1.32	1.26
	WF	1.25	1.32	1.26	1.34	1.26
1:2.5	H	1.49	1.59	1.43	1.66	1.39
	F	1.50	1.60	1.44	1.66	1.42
	W	1.48	1.58	1.41	1.64	1.39
	WF	1.49	1.58	1.42	1.64	1.40
1:3.0	H	1.73	1.88	1.64	1.95	1.57
	F	1.74	1.89	1.66	1.95	1.59
	W	1.72	1.87	1.63	1.92	1.57
	WF	1.73	1.88	1.64	1.94	1.58

**H=Homogeneous, F= Toe filter, W= Cut-off wall, WF= Cut-off wall and toe filter.*

5.3.6 Effect of the protective measures on the flow pattern

The assessment of the effect of the protective measures on the flow pattern is carried out for the dyke with a slope gradient of 1:2.5 (Figures 5.6, 5.9, 5.12, and 5.15). However, a similar trend was observed for the other two slope gradients.

The PWP at points 1 and 2 is the same for all types of dyke. This is expected, as these points lie close to the surface of the water-side slope. Therefore, their reaction is controlled exclusively by the water level imposed.

At point 3, the PWP is the same for both the homogeneous dyke and the dyke with a toe filter (1.45 kPa), and has the same value (1.55 kPa) for both dykes with a cut-off wall. This implies an increase of 0.7 kPa when a cut-off wall is installed. This has already been explained, as a consequence of the restriction provided by the wall to the drainage path. A small influence of the toe filter is observed on this point during the overflow phase, in which the pressures are 2.64 and 2.61 kPa for the homogeneous dyke and with toe filter only, and 2.77 and 2.75 kPa for the dyke with a cut-off wall, and with a cut-off wall and toe filter, respectively. For all cases, the increase in PWP begins 4 days after initiating the flood and lasts for 16.5 days.

There is no observable influence of the protective measures on the PWP of points 4 and 5 during the flood cycles. The development of the PWP at point 6 is different for each type of dyke. The comparison is shown in Table 5.11, where t_{1st} and t_{2nd} are the times at which the PWP starts increasing for the first and second flood cycle, respectively. Δt_{1st} and Δt_{2nd} are the time spans, in which a change in the reaction of PWP is observed at point 6. $PWP_{max\ 1st}$ and $PWP_{max\ 2nd}$ are the maximum values of PWP observed. The reaction of the PWP to the change in water level of the flood cycle is delayed depending on the protection measure used. As a consequence, the maximum PWP and durations registered are also reduced. Thus, for the dyke with a cut-off wall and toe filter almost no influence of the flood cycle is observed on the PWP.

Table 5.11: Response of the PWP at point 6 for both flood cycles for all four types of dyke.

Dyke	t_{1st} [days]	Δt_{1st} [days]	$PWP_{max\ 1st}$ [kPa]	t_{2nd} [days]	Δt_{2nd} [days]	$PWP_{max\ 2nd}$ [kPa]
Homogeneous	6.42	8.41	2.10	26.83	7.59	2.07
Toe filter	7.42	6.41	-0.51	27.80	5.65	-0.55
Cut-off wall	7.63	6.00	-3.19	28.17	4.91	-3.26
Cut-off wall + toe filter	8.12	5.01	-5.54	30.00	4.50	-5.85

The effect of the toe filter is clear at point 7, as no influence of the flood cycles on the PWP is observed for the dykes with a toe filter. However, some influence is observed for the other two types of dykes. Thus, the homogeneous dyke exhibits a clear influence during both flood cycles, with both cycles reaching a maximum value of -3.4 kPa, whereas the dyke with a cut-off wall shows a reaction to the second flood cycle only, attaining a maximum value of -7.0 kPa.

The influence of the filter is again evident at point 8. This is a key point, as it lies just above the filter and it is close to the point where water spring will occur in dykes without a filter. The reaction for both dykes, homogeneous and with a cut-off wall, begins 2.5 days after the beginning of the flood and it lasts 16.25 days, reaching a maximum value of 0.85 kPa for the homogeneous dyke, and -0.79 kPa for the dyke with a cut-off wall. This demonstrates that the use of the wall reduces the PWP on the water-side slope, which results in larger factors of safety, as discussed in the previous section. On the other hand, the PWP at point 8 of those dykes with the filter is almost identical and shows minimal change during the flood cycles, indicating that the filter works as expected, with an influence zone that includes where point 8 is located, under a constant unsaturated condition.

The PWP evolution at point 9 for both dykes with the cut-off wall is very similar. Values are slightly greater than those for the homogeneous dyke, and with a toe filter; however, the difference of approximately 4 kPa might be considered small in engineering terms.

The largest effect of the cut-off wall is observed at point 10, which is located on the air-side of the dyke and near to the tip of the wall. The maximum PWP reduces from 27.98 kPa for the homogeneous dyke to 25.94 kPa for the dyke with a toe filter, to 22.50 kPa in the dyke with a cut-off wall, and to 20.33 kPa for the dyke with a cut-off wall and toe filter. Similarly, the minimum PWP reduces from 9.42 to 8.37, 8.53, 7.61 kPa. This reflects how the phreatic level is lowered on the air-side as an effect of the cut-off wall, as expected, and has a greater effect for the scenario of high water levels on the water-side.

The use of protective measures has no effect on the PWP calculated at point 11. This is concluded from comparing all four curves, which are almost identical. The only difference is that the PWP is 1 kPa greater for the dykes without the toe filter, i.e. homogeneous and with a cut-off wall.

The evolution of the PWP for point 12 for the dyke with a toe filter and the dyke with a cut-off wall are virtually identical, with only 1 kPa difference between them, indicating that each of these protection measures has the same effect on the PWP at this point. The maximum and minimum PWP values are 50.38 and 37.28 kPa on average. These curves lie practically in the middle of the PWP curves for the homogeneous dyke, and the dykes with a cut-off wall and toe filter, for which the maximum and minimum values are 53.81, 47.16 kPa and 38.15, 36.52 kPa, respectively.

Figures 5.23 and 5.24 show the distribution of the PWP at the maximum and minimum water levels, respectively, during the flood cycles for all four types of dyke. The critical slip surfaces are drawn for both air and water-slopes, together with their corresponding FoS.

The PWP is strongly influenced by the toe filter and the cut-off wall. It is clear how the phreatic level is lowered by the filter preventing water from forming a spring on the air-side slope. The cut-off wall lowers the phreatic level on the air-side and raises it on the water side; an effect that is more prominent in the zone near the wall. However, the effect of the wall is

lessened when the water level is at its minimum. The difference in flow pattern in this case is almost negligible.

The critical slip surface of the water-side slope, when the water level is high, is shallow, indicating a planar failure mechanism. However, in all cases it is greater than 1.0; therefore, the slope is stable, as was confirmed by the centrifuge tests. The failure mechanism changes to a circular surface when the water is lowered, but the slope remains stable.

The factor of safety of the air-side slope for the homogeneous dyke and the dyke with a cut-off wall is, as described in Section 5.3.5, below 1.0 when the water level is raised; therefore, the slope becomes unstable. The critical slip surface is small and localized at the toe of the slope, and is close to the zone where water forms a spring. This is the same behavior as was observed in the centrifuge tests, where the progressive failure began from a small planar local instability and propagated upwards. The critical slip surface for the dykes with the toe filter has a FoS greater than one, hence the slope should be stable. The surface is circular in these cases and crosses through the filter and reaches the crown of the dyke.

The critical surfaces on the air-side slope of the dykes without a toe filter evolve to a circular shape, which extend beyond the toe of the slope. On the other hand, the slip surfaces of the dykes with the filter do not cross through the filter, but above it.

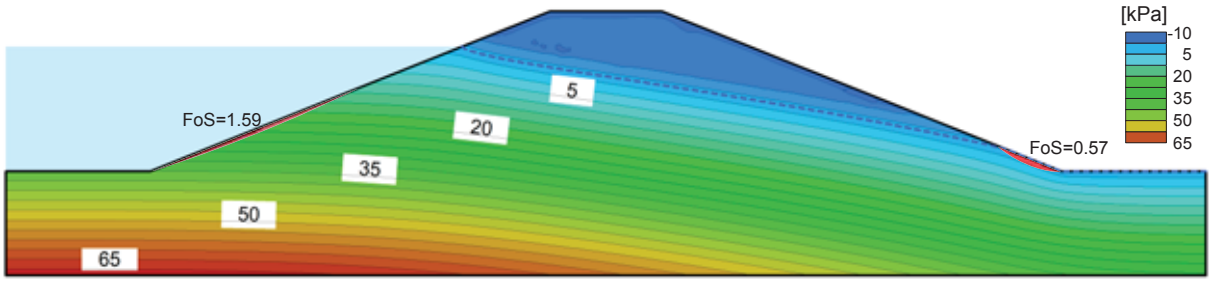

a) Homogeneous dyke.

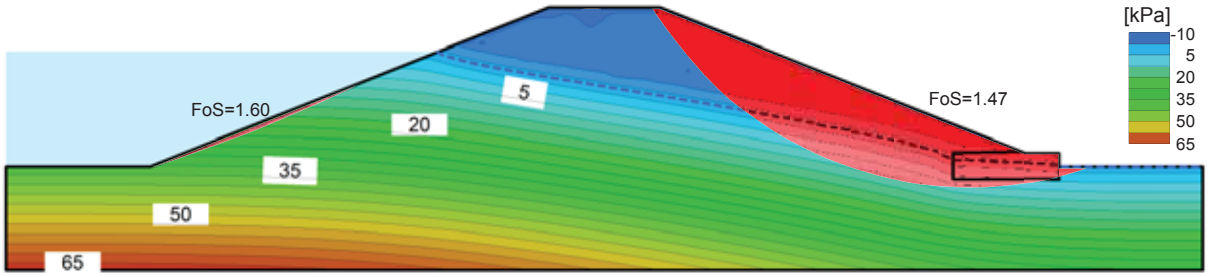

b) Dyke with a toe filter.

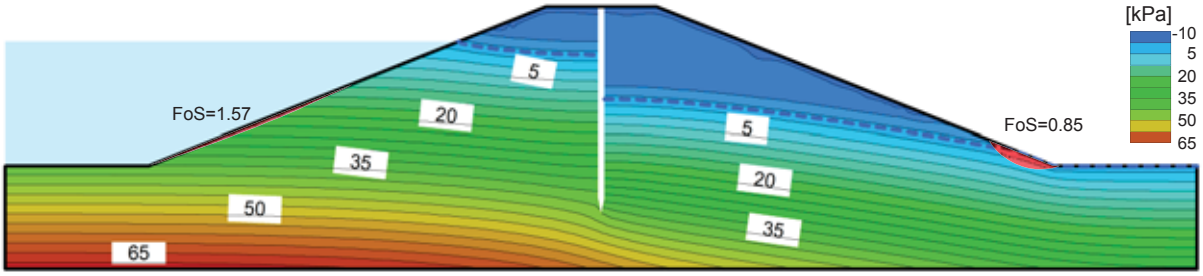

c) Dyke with a cut-off wall.

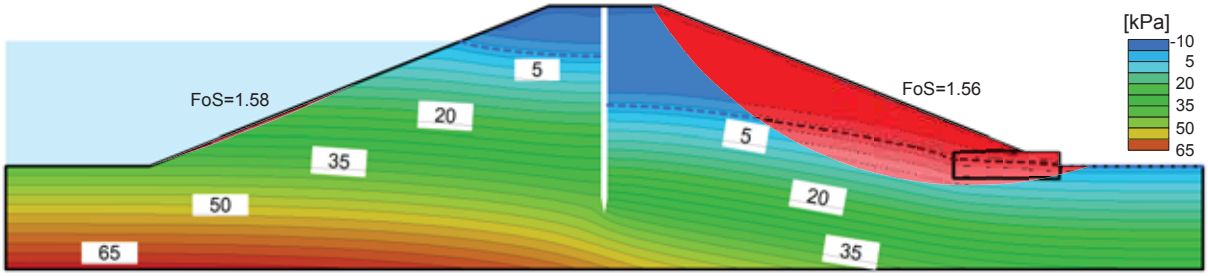

d) Dyke with a cut-off wall and toe filter.

Figure 5.23: Influence of the protection measures on the pore water pressures (PWP) for the maximum water level during the flood cycles. The pressure lines are drawn at 3 kPa intervals. The blue dashed line represents the phreatic surface. The critical slip surfaces are drawn with their corresponding factor of safety (FoS).

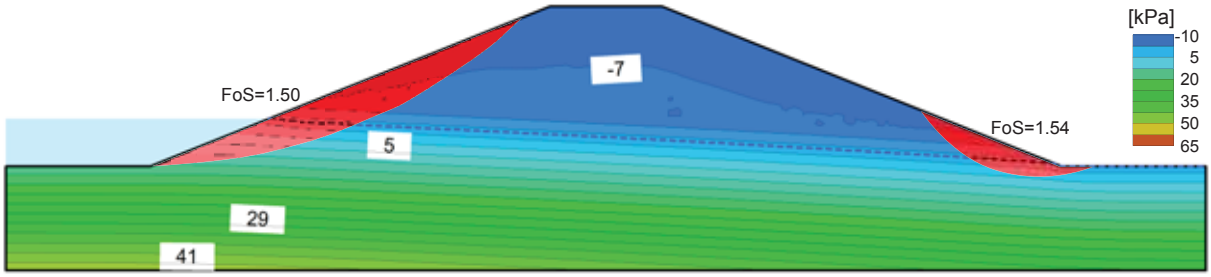

a) Homogeneous dyke.

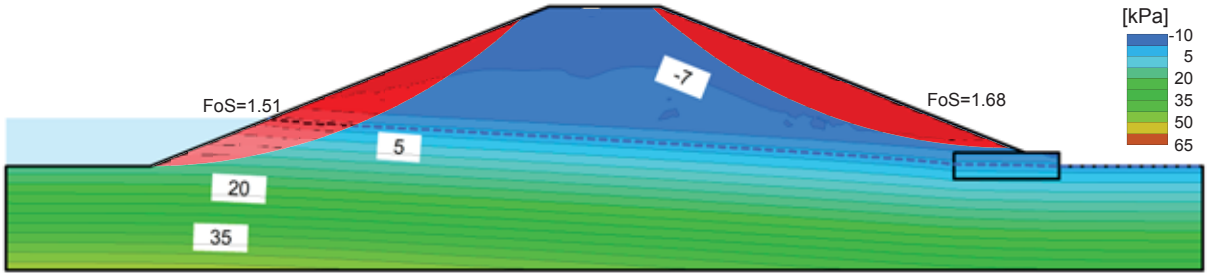

b) Dyke with a toe filter.

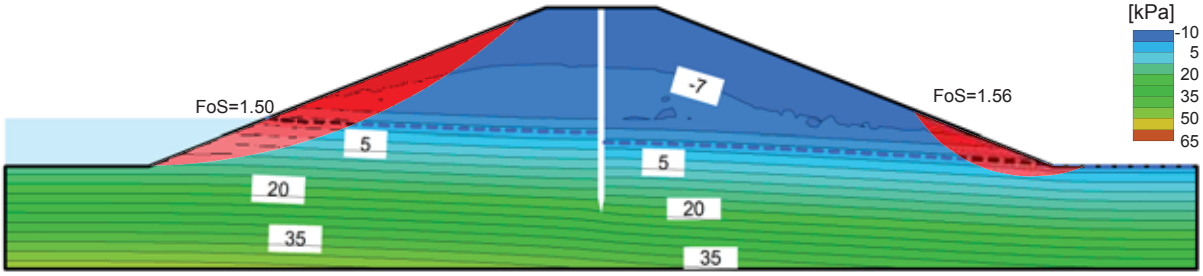

c) Dyke with a cut-off wall.

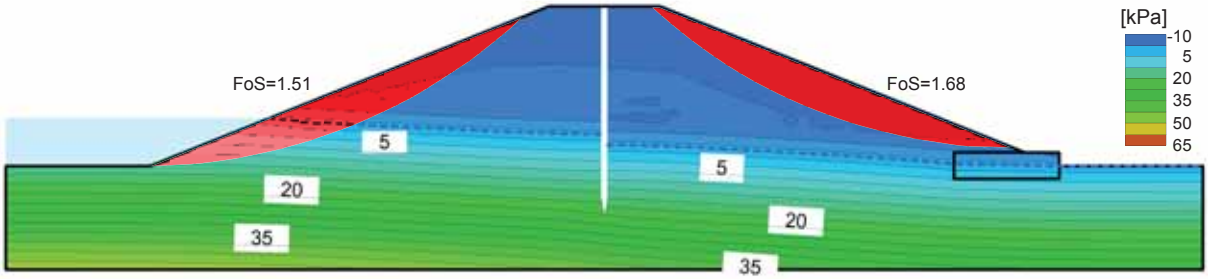

d) Dyke with a cut-off wall and toe filter.

Figure 5.24: Influence of the protection measures on the pore water pressures (PWP) for the minimum water level during the flood cycles. The pressure lines are drawn at 3 kPa intervals. The blue dashed line represents the phreatic surface. The critical slip surfaces are drawn with their corresponding factor of safety (FoS).

6 Conclusions and recommendations

This research is the result of a comprehensive analysis of the effect of transient water conditions, represented by successive flood cycling, on the seepage conditions and subsequent breaching of dykes. The study was divided into three major areas: the analysis of the results from a field test, the physical modeling of small-scaled models under an enhanced gravity field, and the numerical modeling of the flow response and the stability of the slopes.

Some specific conclusions are drawn below for each one of the three areas investigated, followed by some general conclusions, which link the results obtained to engineering practice.

6.1 Field test

The overflowing field test was performed as the concluding part of another research project (Mayor, 2013). Extensive superficial erosion of the dyke was expected, based on both a numerical simulation carried out prior to the test (Fäh & Volz, 2008), and on the experience from previous field tests (Hahn et al., 2000; Höeg et al., 2004; Vaskinn et al., 2004; Vaskinn et al., 2005). Notwithstanding that, the dyke did not erode as expected, a slide occurred on the air-side slope, followed by internal erosion.

This result showed that the combined use of grass protection on the air-side and a low erodability layer in the upper part of the dyke might help to prevent the continuous erosion of the dyke's body during an overflow event. However, the use of high permeability soils on the crown of the dyke (e.g. gravel for sub-base) might lead to rapid saturation of the air-side slope, leading to its instability. Therefore, a fine-grained soil or geotextile with low permeability should be used in order to prevent this.

The test was modeled numerically using unsaturated parameters for the soils, which were determined from specific laboratory tests. The model was found to be able to replicate the response of the dyke to the changes in water level and the slip surface that was estimated as being the most critical corresponded to that observed in the experiment. This illustrates the importance of detailed information about the ground conditions, together with a full characterization of the materials, for a complete definition of the boundary value problem. This is of special interest for old structures, for which the geological conditions and continuing general serviceability after many decades of performance are not fully known.

6.2 Physical modeling

The physical modeling was performed by testing small-scale models at an increased gravity of 33-g. This is optimal, as centrifuge testing allows the stresses in the soil mass to be replicated correctly. This is a key point, as the soil behavior is dependent on the stress level, which in turn, is one of the weaknesses of small-scale models tested at 1-g in laboratory flumes, as they neglect to scale stresses correctly.

Scaling factors for hydraulic processes were also reviewed. Up to now, two methodologies to determine scaling factors for hydraulic processes in centrifuge modeling have been proposed by previous researchers, and each methodology leads to different scaling factors. However, it has been proved that both are compatible, as each methodology is just a different way of expressing the potential energy: one expresses the potential energy per unit weight, and the other per unit volume.

The models had a height of 0.15 m that represented a 5 m height dyke at prototype scale. The modeling was planned to be a parametric study, in which 12 models were tested. The slope gradients on both the water- and air-sides were varied from 1:2.0 to 1:2.5 and 1:3.0. Four types of dykes were modeled for each one of these gradients: a homogeneous dyke was used as reference, a dyke incorporating a toe filter, another including a cut-off wall, and a fourth one in which both a toe filter and a cut-off wall were combined.

New equipment was needed to be designed and built in order to accomplish the task. Strongboxes were built to contain large models (1 m length $\times$ 0.3 m height $\times$ 0.5 m width) and to be placed, diametrically opposed, around the circumference of the drum. This allowed both sides of the dyke to be modeled with slope gradients following the current design guidelines. These features were found to be critical, as previous research projects had had to compromise on one or both of them, owing to space limitations in the centrifuge facilities used. Additionally, a water control system was built to impose an automatically controlled water level on the dyke models. This allowed the same flood pattern to be applied to all models. An exception was made in some cases when the electronic control failed, and the water level was controlled manually to follow the same cyclic pattern of flooding and recovery.

The water flowing through the dyke was monitored constantly to measure both pore water pressures and volumetric water content in at least 8 points distributed across the section of the dyke. Therefore, the response on both the water- and air-sides could be recorded. Three cameras were installed to monitor the deformations and breaching mechanisms that developed. These were also used to obtain a three-dimensional model of the breach by using photogrammetric techniques. However, the lack of enough reference points with known coordinates did not allow higher resolutions to be achieved.

Two types of breaching mechanisms were identified from the results of the physical modeling, and they were determined by the presence, or not, of a cut-off wall. If a wall is not included, water starts eroding the soil surface, creating a breach throat, through which water flows rapidly. The breach throat broadens as a consequence of two simultaneous processes: the erosive action of the water over the soil, and local slope failures of blocks of soil becoming saturated and failing as a consequence of tension cracks developing.

The second breaching mechanism was observed when a cut-off wall is placed. A breach throat starts to develop in the crest of the dyke, closer to the wall. This is a similar process to that observed for the homogeneous and toe-filter dykes. When the throat reaches the cut-off wall, it cannot continue increasing towards the water-side. Instead, the soil in front of the

wall, i.e. on the air-side, starts to be eroded, creating a narrow and shallow breach zone in the vicinity of the wall.

Some local instabilities are observed on the air-side slope when the toe filter is not included. These appear during the flooding cycles and are a consequence of the saturation in the zone where water springs form. Therefore, an increase in the pore water pressure (PWP) occurs, leading to a reduction of the effective stress. The soil is then subjected to tension forces, which cannot be withstood by the soil, due to the reduction of the apparent cohesion leading to the formation of tension cracks. These cracks delineate blocks of soil that are detached and transported by the water flowing at the spring. The failure is retrogressive and continues growing until the water level reaches a maximum; if the water is lowered, as in the case of cyclic floods, the slope remains stable and no further growth of the slide is observed.

These are important results for the design of protective measures for dykes. Dykes with a cut-off wall show a smaller breach area and volume than those observed for dykes without the wall, because water could not erode sand on the water-side slope. As a consequence, the breach zone was restricted to the air-side only. This also means that even when the dyke is subjected to high water levels, the water-side of the dyke maintains its cross section. As the water-side is not eroded during the overflowing event, the amount of water flowing towards the area protected by the dyke is smaller than for the cases in which the water can create a complete breach throat (dykes: homogeneous and with toe filter). Additionally, the dykes with a cut-off wall require more time to develop a breach, providing more time for the affected areas to be evacuated.

The physical modeling also revealed that the use of a cut-off wall helps to reduce the PWP on the air-side. However, it causes an increase in the PWP on the water-side due to ponding of the water and reduction of the drainage capacity. It also fails to prevent the occurrence of local instability for those dykes without a toe filter.

In all the cases studied, no instability events were observed on the water-side slope during the rapid drawdown. This is due to the high hydraulic conductivity of the soil, which allowed the pore water to drain and any residual pore water pressure to be dissipated rapidly.

6.3 Numerical modeling

Twelve dykes, with the same configuration as for the prototype dykes modeled physically, were simulated numerically. A further analysis of the stability of both air- and water-side slopes was performed, together with an assessment of the influence of each protective measure on the characteristics of the flow through the dyke. The analyses were performed with a decoupled method, which only took the flow in unsaturated porous media into account. A coupled analysis, i.e. flow and mechanical deformation will be desirable for those cases in which large deformations or wetting collapse are expected, which was not the case, as the models were built to achieve a high density.

The results from the numerical simulations matched, in almost every sense, the results obtained from the centrifuge modeling, including the decrease of the FoS below 1.0, indicating instability, for the dykes without a toe filter. This was possible due to the use of advanced numerical techniques, which included the analysis of flow in the unsaturated zone. However, this is only possible when the soil parameters are accurately known for both the saturated and unsaturated states. These parameters were evaluated in the laboratory, and with the help of analytical relationships, in this research project.

The most important parameters for unsaturated flow modeling are the Soil Water Retention Curve (SWRC) and the variation of hydraulic conductivity with suction. The SWRC was estimated in the laboratory and compared with the results from using the empirical approach named *Modified Kovacs* (Aubertin et al., 2003). This is a simple function, which determines the SWRC from the grain-size distribution of the soil. The results were highly comparable, indicating that the use of this method might be of practical use in general geotechnical practice, as proposed by Mayor (2013), if the long time required to determine the parameters in the laboratory tests is not available.

6.4 General

This research showed the importance of a correct definition of the Boundary Value Problem, as well as the estimation of the soil parameters for the analyses. These lead to a full and correct understanding of the problem, which will contribute to a better design of structures and protective measures.

The breaching mechanism observed for the dykes including the cut-off wall, in which the water-side maintained an intact cross-section and provided longer times for evacuation of affected areas, might be considered as key factor in risk assessment studies, as this might justify the costs of its installation.

Although the numerical simulation carried out represented the flow problem properly, the breaching mechanisms observed in the centrifuge tests were too complex to be modeled with current commercial numerical software. This, together with the current difficulty to model the complex system of tension cracks developed, enhances the importance of physical modeling as engineering design tool, as it helps in identifying the key features under the same stresses levels at which the structure will be subjected.

6.5 Recommendations for future research

Some general recommendations for upcoming research are given, based on the results obtained and observations made during the course of this research project.

A further investigation of the protective measures is encouraged. These might include the use of a cover layer over the air-side slope, simulating the presence of grass. The analysis of the erosion development of a dyke with a non-erodible layer on the crest, together with the

grass cover, is another feature that could contribute more insight into the analysis of the current body of river dykes and earth protection structures.

As the cost of the use of a cut-off wall as a protective measure depends strongly on its depth, a parametric numerical study on the influence of the wall depth on in the results is therefore recommended.

The use of an initial notch in the small-scale models will provide a more controlled breach initiation, and the breaching process will be comparable with the results found in most of the laboratory or field tests, in which notches were dug prior to overflow. This also would allow for the verification of the validity of the analytical methods for breach development, as most of them were derived from small-scale tests at 1-g, hence neglecting the stress dependency condition of the soil.

The use of photogrammetry, with at least three cameras aimed at the air-side slope would help with a better three-dimensional interpretation of the growth of the breach. Applying the process of photogrammetric restitution to several frames during breaching would be adequate for a quantitative assessment of the process of breaching, which could be used for calibration of previous or new analytical modeling approaches.

Regarding the soil characterization, the determination of the SWRC in the centrifuge at different g-levels is strongly recommended. This could lead to the proposal of a new scaling factor for this relationship. It is recommended to establish this factor based on the entire grain size distribution with an equivalent grain size, such as that estimated using the Kozeny-Carman approach.

Three-dimensional numerical analyses would be desirable, as the problem here was assumed to take place in one plane only. This is completely valid for the flooding stages prior to overflowing. The process becomes more complex once the breach starts developing, so the problem is better represented by a three-dimensional system. This is of special interest for those cases in which a cut-off wall is not included as a protective measure.

A further improvement in the numerical modeling might include the use of advanced numerical techniques, such as large deformation models or discrete elements. These might take the erosion process into account, hence providing a better understanding of the breaching process.

Finally, the use of these advanced techniques should be accompanied by the use of advanced constitutive models taking into account, in a coupled manner, both the unsaturated mechanical soil behavior and the unsaturated flow response and hysteresis processes.

7 References

Abed, A. (2008). *Numerical modeling of expansive soil behavior.* Ph.D. Dissertation, Universität Stuttgart, Stuttgart, DE.

Adrian, R.J. (1991). Particle-imaging techniques for experimental fluid mechanics. *Annual Review of Fluid Mechanics,* 23(1): 261-304.

AgiSoft LLC. (2013). *Agisoft PhotoScan User Manual Professional Edition, Version 0.9.1*. AgiSoft LLC (Pub), Calgary, CA.

Al-Doury, M.M.I. (2010). A discussion about hydraulic permeability and permeability. *Petroleum Science and Technology,* 28(17): 1740 - 1749.

Alonso, E.E., Gens, A. & Josa, A. (1990). A constitutive model for partially saturated soils. *Géotechnique,* 40(3): 405-430.

Allard, M.A., Hjortnaes-Pedersen, A.G.I. & Out, J.G. (1994). Performance of a sand hopper. In Leung, C.F., Lee, F.H. & Tan, T.S. (Editors), *Proceedings of the International Conference Centrifuge 94*, Singapore, SG., Balkema, 1: 83-88.

Allersma, H.G.B. (1996). Using centrifuge research in analysing stability of dikes. In Lafond, L.R. & Levacher, D. (Editors), *Génie civil-génie côtier : IVèmes Journées nationales*, Dinard, FR., Paralia, 1: 289-298.

Arnold, A. (2011). *Tragverhalten von nicht starren Flachfundationen unter Berücksichtigung der lokalen Steifigkeitsverhältnisse.* Ph.D. Dissertation No. 19516, ETH Zurich, Zurich, CH., doi:10.3929/ethz-a-006510865.

Arya, L.M. & Paris, J.F. (1981). A physicoempirical model to predict the soil moisture characteristic from particle-size distribution and bulk density data. *Soil Science Society of America Journal,* 45(6): 1023-1030.

Askarinejad, A. (2013). *Failure mechanisms in unsaturated silty sand slopes triggered by rainfall.* Ph.D. Dissertation No. 21423, ETH Zurich, Zurich, CH.

Askarinejad, A., Beck, A., Casini, F. & Springman, S. (2012a). Unsaturated hydraulic conductivity of a silty sand with the instantaneous profile method. In Mancuso, C., Jommi, C. & D'Onza, F. (Editors), *Unsaturated Soils: Research and Applications* (pp. 215-220), Springer Berlin Heidelberg (Pub), doi:10.1007/978-3-642-31343-1_27.

Askarinejad, A., Bischof, P., Beck, A., Casini, F. & Springman, S.M. (2012b). Rainfall induced instabilities: a field experiment on a silty sand slope in northern Switzerland. *RIG (Italian Geotechnical Journal),* LXVI(3): 50-71.

Askarinejad, A., Casini, F., Kienzler, P. & Springman, S.M. (2010). Comparison between the in situ and laboratory water retention curves for a silty sand. In Alonso, E.E. & Gens, A. (Editors), *Unsaturated soils: Proceedings oh the 5th International Conference on Unsaturated Soils*, Barcelona, ES., CRC Press, 2: 423-428.

Askarinejad, A., Laue, J., Zweidler, A., Bleiker, E., Buschor, H. & Springman, S.M. (2012c). Physical modelling of rainfall induced landslides under controlled climatic conditions. In Bezuijen, A. (Editor), *2nd Eurofuge Conference*, Delft, NL .

Askarinejad, A. & Springman, S.M. (2014). A method to eliminate "wild vectors" in PIV analysis of slope surface movements. *International Journal of Physical Modelling in Geotechnics,* In preparation.

ASTM International. (2002a). ASTM-4253 Standard test methods for maximum index density and unit weight of soils using a vibratory table: ASTM International.

ASTM International. (2002b). ASTM-4254 Standard test methods for minimum index density and unit weight of soils and calculation of relative density: ASTM International.

ASTM International. (2009). ASTM-D1557-12 Standard test methods for laboratory compaction characteristics of soil using modified effort: ASTM International.

Aubertin, M., Mbonimpa, M., Bussière, B. & Chapuis, R.P. (2003). A model to predict the water retention curve from basic geotechnical properties. *Canadian Geotechnical Journal,* 40(6): 1104-1122.

Bagge, G., König, D., Rezzoug, A., Crancon, P., Günzel, F. & Thorel, L. (2002). Centrifugal modeling of capillarity rise and drainage in sandy soils. In Phillips, R., Guo, P.J. & Popescu, R. (Editors), *Physical Modelling in Geotechnics: ICPMG '02. Proceedings of the International Conference*, Newfoundland, CA., CRC Press / Balkema, 1: 343-348.

Barbour, S.L. & Krahn, J. (2004). Numerical Modelling: Prediction or Process? *Geotechnical News,* 22(4): 44-52.

Bardet, J.P. (1997). *Experimental soil mechanics*. Prentice Hall (Pub), New Jersey, USA.

Barree, R.D. & Conway, M.W. (2004). Beyond beta factors: a complete model for Darcy, Forchheimer, and trans-Forchheimer flow in porous media. In Inc., S.o.P.E. (Editor), *SPE Annual Technical Conference and Exhibition*, Houston, USA., Society of Petroleum Engineers Inc.,, 1: 1-8.

Bear, J. (1972). *Dynamics of fluid in porous media*. American Elsevier (Pub), New York, USA.

Bear, J., Beljin, M.S. & Ross, R.R. (1992). *Fundamentals of ground-water modeling* (Technical Report), EPA: US Environmental Protection Agency, Ada, US.

Beer, F., Russell, J. & DeWolf, J. (2002). *Mechanics of Materials*. McGraw Hill (Pub).

Beuselinck, L., Govers, G., Poesen, J., Degraer, G. & Froyen, L. (1998). Grain-size analysis by laser diffractometry: comparison with the sieve-pipette method. *CATENA,* 32(3–4): 193-208, doi:10.1016/s0341-8162(98)00051-4.

Bezuijen, A. & den Adel, H. (2006). Dike failure due to surface erosion, N-g and 1-g tests. In Ng, C.W.W., Wang, Y.H. & Zhang, L.M. (Editors), *Physical Modelling in Geotechnics - 6th ICPMG '06. Proceedings of the International Conference*, Hong Kong, HK., CRC Press / Balkema, 2: 1307-1312.

Bezuijen, A. & Steedman, R.S. (2010). Scaling of hydraulic processes. In Springman, S.M., Laue, J. & Seward, L. (Editors), *Physical Modelling in Geotechnics: Proceedings of the 7th International Conference in Physical Modelling in Geotechnics (ICPMG 2010)*, Zurich, CH., CRC Press / Balkema, 1: 93-98.

Bezuijen, A., van Beek, V.M., van der Ham, G.A. & Zwanenburg, C. (2012). Overview geotechnical model tests on dike safety at Deltares. In Bezuijen, A. (Editor), *2nd Eurofuge Conference*, Delft, NL .

Bezzola, G.R. & Hegg, C. (2007). *Ereignisanalyse Hochwasser 2005 - Teil 1: Prozesse, Schäden und erste Einordnung* (Technical Report), Bundesamt für Umwelt (BAFU), Bern, CH.

Bezzola, G.R., Hegg, C., Frank, F. & Koschni, A. (2008). Vom Hochwasser lernen - Standortbestimmung. *TEC21,* 39: 24-27.

Bishop, A.W. (1955). The use of the slip circle in the stability analysis of slopes. *Géotechnique,* 5(1): 7-17.

Bishop, A.W. (1959). The principle of effective stress. *Teknisk Ukeblad,* 106(39): 859-863.

Blott, S.J. & Pye, K. (2006). Particle size distribution analysis of sand-sized particles by laser diffraction: an experimental investigation of instrument sensitivity and the effects of particle shape. *Sedimentology,* 53(3): 671-685, doi:10.1111/j.1365-3091.2006.00786.x.

Bolton, M.D. (1993). What are partial factors for? *Proceedings of the international symposium on limit state design in geotechnical engineering*, Copenhagen, DK., Danish Geotechnical Institute, 3: 565-583.

Bonelli, S., Brivios, O. & Lachouette, D. (2007). The scaling law of piping erosion. In Etay, J., Hopfinger, E.J. & Marty, P. (Editors), *Actes du 18éme Congrès Français de Mécanique*, Grenoble, FR. , Association Française de Mécanique, 1: 1-6.

Bowman, E.T., Laue, J. Imre, B. & Springman, S.M. (2010). Experimental modelling of debris flow behaviour using a geotechnical centrifuge. *Canadian Geotechnical Journal,* 47(7): 742-762, doi:10.1139/T09-141.

Bowman, E.T., Laue, J., Imre, B., Zweidler, A. & Springman, S.M. (2006). Debris flow in a geotechnical centrifuge. In Ng, C.W.W., Wang, Y.H. & Zhang, L.M. (Editors), *Physical*

Modelling in Geotechnics - 6th ICPMG '06. Proceedings of the International Conference, Hong Kong, HK., CRC Press / Balkema, 1: 311-316.

Briaud, J.L., Chen, H.C., Govindasamy, A.V. & Storesund, R. (2008). Levee erosion by overtopping in New Orleans during the Katrina Hurricane. *Journal of Geotechnical and Geoenvironmental Engineering,* 134(5): 618-632, doi:10.1061/(asce)1090-0241(2008)134:5(618).

Briaud, J.L., Ting, F.C.K., Chen, H.C., Cao, Y., Han, S.W. & Kwak, K.W. (2001). Erosion function apparatus for scour rate predictions. *Journal of Geotechnical and Geoenvironmental Engineering,* 127(2): 105-113.

Brinkgreve, R.B.J. & Bakker, H.L. (1991). Non-linear finite element analysis of safety factors. In Beer, G., Booker, J.R. & Carter, J.P. (Editors), *Computer methods and advances in geomechanics: Proceedings of the 7th International conference on computer methods and advances in geomechanics*, Cairns, AU., Balkema, 3: 1117-1122.

Brinkgreve, R.B.J., Swolfs, W.M. & Engin, E. (2011). *PLAXIS 2D 2011 Reference manual*. Plaxis bv (Pub), Delft, NL.

British Standard Instititution. (2002). BS 1377-4 : Soils for civil engineering purposes: Part 4:Compaction related tests. London, UK.: British Standard Instititution.

Brönnimann, C. (2011). *Effect of groundwater on landslide triggering.* Ph.D. Dissertation No. 5236, EPF Lausanne, Lausanne, CH., doi:10.5075/epfl-thesis-5236.

Brooks, R.H. & Corey, A.T. (1964). Hydraulic properties of porous media. *Hydrology Papers,* 3.

Buckingham, E. (1907). Studies on the Movement of Soil Moisture. *Soils bulletin of the US deparment of Agriculture* 38.

Bucky, P.B. (1931). *The use of models for the study of mining problems* (Technical Report No. 425), WL Delft Hydraulics, American Institute of Mineral & Metallurgical Engineering, New York, US.

Buchheister, J. (2009). *Verflüssigungspotenzial von reinem und siltigem Sand unter multiaxialer Belastung.* Ph.D. Dissertation No. 18312, ETH Zurich, Zurich, CH., doi:10.3929/ethz-a-006020660

Burkhart, S., Davies, M.C.R., Depountis, N., Harris, C. & Williams, K.P. (2000). Scaling laws for infiltration and drainage tests using a geotechnical centrifuge. In Garnier, J., Thorel, L. & Haza, E. (Editors), *International Symposium on Physical Modelling and Testing in Environmental Geotechnics*, La Baule, FR., Network of European Centrifuges for Environmental Geotechnic Research, 1: 191-198.

Burland, J.B. (1964). Effective stresses in partly saturated soils. *Géotechnique,* 14(2): 65-68.

Burlando, P., Christophe, A., Charbon, E., Fäh, R., Geiger, A., Germann, U., Mayor, P., Molnar, P., Rickenmann, D., Rotach, M., Scleiss, A. & Springman, S.M. (2008). *Advanced Process UNderstanding and prediction of hydrological extremes and Complex Hazards (APUNCH) workplan* (Technical Report), Swiss Federal Institute of Technology Zurich, Zurich, CH.

Caicedo, B., Tristancho, J. & Thorel, L. (2010). Potentialities and challenges of centrifuge modelling on unsaturated soils. In Springman, S.M., Laue, J. & Seward, L. (Editors), *Physical Modelling in Geotechnics: Proceedings of the 7th International Conference in Physical Modelling in Geotechnics (ICPMG 2010)*, Zurich, CH., CRC Press / Balkema, 1: 105-110.

Campbell Scientific. (2009). *TDR probes instruction manual* (Technical Report), Capmbell Scientific Canada Corporation, Alberta, CA.

Campbell Scientific. (2010). *TDR100: Time domain reflectometry system instruction manual* (Technical Report), Capmbell Scientific Canada Corporation, Alberta, CA.

Cargill, K.W. & Ko, H.Y. (1983). Centrifugal modeling of transient water flow. *Journal of Geotechnical Engineering,* 109(4): 536-555.

Carrier, W.D. (2003). Goodbye, Hazen; Hello, Kozeny-Carman. *Journal of Geotechnical and Geoenvironmental Engineering,* 129(11): 1054-1056.

Casini, F., Minder, P. & Springman, S.M. (2010). Shear strength of an unsaturated silty sand. In Alonso, E.E. & Gens, A. (Editors), *Unsaturated soils: Proceedings of the 5th International Conference on Unsaturated Soils*, Barcelona, ES., CRC Press, 1: 211-216.

Cedergren, H.R. (1977). *Seepage, drainage, and flow nets*. Wiley-Interscience (Pub).

Cleveland, L.J. & Wartman, J. (2006). Principles and applications of digital photogrammetry for geotechnical engineering. *Geotechnical Special Publication,* 149: 128-135.

Cooke, A.B. & Mitchell, R.J. (1991). Evaluation of contaminant transport in partially saturated soil. In Ko, H.Y. & McLean, F.G. (Editors), *Centrifuge 91: Proceedings of the International Conference Centrifuge 1991*, Boulder, USA., Balkema, 1: 503-508.

Craig, W.H. (1984). Centrifuge modelling for site specific prototypes. In Craig, W.H. (Editor), *The application of centrifuge modelling to geotechnical design*, Manchester, UK., University of Manchester (Pub).

Craig, W.H. (2002). The seven ages of centrifuge modelling In Springman, S.M. (Editor), *Constitutive and centrifuge modelling: Two extremes* (pp. 165-174), Lisse, NL., Balkema (Pub).

Crancon, P., Guy, C., Pili, E., Dutheil, S. & Gaudet, J.P. (2000). Modeling of capillarity rise and water retention in centrifuge test using time domain reflectometry. In Garnier, J., Thorel, L. & Haza, E. (Editors), *International Symposium on Physical Modelling and Testing in Environmental Geotechnics*, La Baule, FR., Network of European Centrifuges for Environmental Geotechnic Research, 1: 199-206.

Cresswell, A., Barton, M.E. & Brown, R. (1999). Determining the maximum density of sands by pluviation. *Geotechnical Testing Journal,* 22(4): 324-328.

Culligan, P.J., Savvidou, C. & Barry, D.A. (1996). Centrifuge modelling of contaminant transport processes. *Electronic Journal of Geotechnical Engineering,* 1.

Chanson, H. (2004). *Hydraulics of open channel flow*. Elsevier Butterworth-Heinemann (Pub), Oxford, UK.

Chapuis, R.P. & Aubertin, M. (2003). On the use of the Kozeny Carman equation to predict the hydraulic conductivity of soils. *Canadian Geotechnical Journal,* 40(3): 616-628.

Chen, H.-T., Lee, C.-J. & Chen, H.-W. (1998). The travelling pluviation apparatus for sand specimen preparation. In Kimura, T., Kusakabe, O. & Takemura, J. (Editors), *Centrifuge 98: Proceedings of the International Conference, IS-Tokyo '98*, Tokyo, JP., Balkema, 1: 143-148.

Chen, Y.H., Anderson, B.A. & Simons, L. (1987). *Development of a methodology for estimating embankment damage due to flood overtopping* (Technical Report), US Department of Transportation, Federal Highway Administration,, US Department of Transportation Federal Highway Administration.

Chikatamarla, R. (2005). *Optimisation of cushion materials for rockfall protection galleries.* Ph.D. Dissertation, ETH Zurich, Zurich, CH., doi:10.3929/ethz-a-005166443.

Chinnarasri, C., Tingsanchali, T., Weesakul, S. & Wongwises, S. (2003). Flow patterns and damage of dike overtopping. *International Journal of Sediment Research,* 18(4): 301-309.

Davies, M.C.R. & Jones, A.M. (1998). Image acquisition using an on-board camera. In Kimura, T., Kusakabe, O. & Takemura, J. (Editors), *Centrifuge 98: Proceedings of the International Conference, IS-Tokyo '98*, Tokyo, JP., Balkema, 1: 67-71.

Davis, J.L. & Annan, A.P. (1977). Electromagnetic detection of soil moisture: Progress Report I. *Canadian Journal of Remote Sensing,* 3: 76-86.

de Vries, G., Koelewijn, A.R. & Hopman, V. (2010). IJkdijk full scale underseepage erosion (piping) test: Evaluation of innovative sensor technology. In Burns, S.E., Bhatia, S.K., Avila, C.M.C. & Hunt, B.E. (Editors), *Scour and Erosion: Proceedings of the Fifth International Conference on Scour and Erosion*, San Francisco, US., ASCE, 1: 649-657, doi:10.1061/41147(392)63.

Delage, P. & Cui, Y.J. (2008). An evaluation of the osmotic method of controlling suction. *Geomechanics and Geoengineering: an International Journal,* 3(1): 1-11.

Dell'avanzi, E., Zornberg, J.G. & Cabral, A.R. (2004). Suction profiles and scale factors for unsaturated flow under increased gravitational field. *Soils and Foundations,* 44(3): 79-89.

Detert, O., König, D. & Schanz, T. (2012). Centrifuge modeling of an adaptive foundation system for embankments on soft soils. In Bezuijen, A. (Editor), *2nd Eurofuge Conference*, Delft, NL .

Disse, M. & Engel, H. (2001). Flood Events in the Rhine Basin: Genesis, Influences and Mitigation. *Natural Hazards,* 23(2): 271-290, doi:10.1023/a:1011142402374.

Drucker, D.C., Gibson, R.E. & Henkel, D.J. (1957). Soil mechanics and work hardening theories of plasticity. *Transactions of the American Society of Civil Engineers,* 122: 338-349.

Eidgenössisches Departement für Umwelt Verkehr Energie und Kommunikation (UVEK). (2008). *Hochwasser 2005 in der Schweiz - Synthesebericht zur Ereignisanalyse* (Technical Report), UVEK (Eidgenössisches Departement für Umwelt, Verkehr, Energie und Kommunikation), Bern, CH.

Ekblad, J. & Isacsson, U. (2007). Time-domain reflectometry measurements and soil-water characteristic curves of coarse granular materials used in road pavements. *Canadian Geotechnical Journal,* 44(7): 858-872.

Eshel, G., Levy, G.J., Mingelgrin, U. & Singer, M.J. (2004). Critical evaluation of the use of laser diffraction for particle-size distribution analysis. *Soil Science Society of America Journal,* 68(3): 736-743.

Fäh, R. (2007). Numerical modeling of breach erosion of river embankments. *Journal of Hydraulic Engineering,* 133(9): 1000-1009.

Fäh, R. & Volz, C. (2008). *Rhonedamm Versuchszelle Baltschieder: Simulation Dammbruch* (Technical Report), VAW-ETH Zurich, Zurich, CH.

Fell, R., Wan, C.F., Cyganiewicz, J. & Foster, M. (2003). Time for development of internal erosion and piping in embankment dams. *Journal of Geotechnical and Geoenvironmental Engineering,* 129(4): 307-314.

FEMA (Federal Emergency Management Agency). (2005). *Technical manual for dam owners - Impacts of plants on earthen dam* (Technical Report), Federal Emergency Management Agency (FEMA), security, U.S.D.o.h., Washintong, USA.

Fischer, M.P. & Keating, D.P. (2005). Photogrammetric techniques for analyzing displacement, strain, and structural geometry in physical models: Application to the growth of monoclinal basement uplifts. *Geological Society of America Bulletin,* 117(3-4): 369-382, doi:10.1130/b25484.1.

Forchheimer, P. (1901). Wasserbewegung durch boden. *Zeitschrift des Vereines Deutscher Ingenieure,* 45: 1782–1788.

Foster, M., Fell, R. & Spannagle, M. (2000). A method for assessing the relative likelihood of failure of embankment dams by piping. *Canadian Geotechnical Journal,* 37(5): 1025-1061.

Fragaszy, R.J. & Cheney, J.A. (1981). Drum centrifuge studies of overconsolidated slopes. *Journal of the Geotechnical Engineering Division,* 107(GT7): 843-858.

Fredlund, D.G. & Houston, S.L. (2013). Interpretation of soil-water characteristic curves when volume change occurs as soil suction is changed. In Caicedo, B. (Editor), *1st Pan-American Conference on Unsaturated Soils*, Cartagena, CO., CRC Press / Balkema, 1: 15-31.

Fredlund, D.G. & Krahn, J. (1977). Comparison of slope stability methods of analysis. *Canadian Geotechnical Journal,* 14(3): 429-439, doi:10.1139/t77-045.

Fredlund, D.G. & Morgenstern, N.R. (1977). Stress state variables for unsaturated soils. *Journal of the Geotechnical Engineering Division,* 102(5): 395-409.

Fredlund, D.G., Morgenstern, N.R. & Widger, R.A. (1978). The shear strength of unsaturated soils. *Canadian Geotechnical Journal,* 15(3): 313-321.

Fredlund, D.G. & Rahardjo, H. (1993). *Soil mechanics for unsaturated soils*. Wiley-Interscience (Pub), Toronto, CA.

Fredlund, D.G., Rahardjo, H. & Fredlund, M.D. (2012). *Unsaturated soil mechanics in engineering practice*. John Wiley & Sons (Pub), New Jersey, US.

Fredlund, D.G. & Xing, A.Q. (1994). Equations for the soil-water characteristic curve. *Canadian Geotechnical Journal,* 31(3): 521-532.

Fujisawa, K., Kobayashi, A. & Yamamoto, K. (2008). Erosion rates of compacted soils for embankments. *Doboku Gakkai Ronbunshuu C,* 64(2): 403-410.

Gabr, M.A., Akram, M. & Taylor, H.M. (1995). Effect of simulated roots on the permeability of silty soil. *Geotechnical Testing Journal,* 18(1): 112-115.

Gardner, W.R. (1958). Some steady-state solutions of the unsaturated moisture flow equation with applications to evaporation from a water table. *Soil Science Society of America Journal,* 85(4): 228-232.

Garnier, J. (2005). *Centrifuge modelling of unsaturated soils*. [Handout for lecture]. 1st MUSE school. Barcelona, ES.

Garnier, J. & Cottineau, L.M. (1988). La centrifugeuse du LCPC: Moyens de préparation des modelès et instrumentation. In Corté, J.F. (Editor), *Centrifuge 88: Proceedings of the International Conference on Geotechnical Centrifuge Modelling*, Paris. FR., Balkema, 1: 83-90.

Garnier, J., Gaudin, C., Springman, S.M., Culligan, P.J., Goodings, D., König, D., Kutter, B., Phillips, R., Randolph, M.F. & Thorel, L. (2007). Catalogue of scaling laws and similitude questions in centrifuge modelling. *International Journal of Physical Modelling In Geotechnics,* 7(3): 1-24.

Gaudin, C., White, D., Boylan, N., Breen, J., Brown, T. & De Catania, S. (2010). A miniature high speed wireless data acquisition system for geotechnical centrifuges. In Springman, S.M., Laue, J. & Seward, L. (Editors), *Physical Modelling in Geotechnics: Proceedings of the 7th International Conference in Physical Modelling in Geotechnics (ICPMG 2010)*, Zurich, CH., CRC Press / Balkema, 1: 229-234.

Gautam, K.P. & van der Hoek, E.E. (2003). *Literature study on environmental impact of floods* (Technical Report), TU delft, Delft, NL.

Gens, A., Sánchez, M. & Sheng, D. (2006). On constitutive modelling of unsaturated soils. *Acta Geotechnica,* 1(3): 137-147, doi:10.1007/s11440-006-0013-9.

Ghosh, S.K. (1992). History of photogrammetry - analytical methods and instruments In Fritz, L.W. & Lucas, J.R. (Editors), *XVIIth ISPRS Congress Technical Commission VI: Economic, Professional and Eductional Apsects of Photogrammetry and Remote Sensing* Washington D.C., US., The International Society for Photogrammetry and Remote Sensing, 311-327.

Gilbert, P.A. & Miller, S.P. (1991). *A Study of Embankment Performance During Overtopping* (Technical Report), US Army Engineer Waterways Experiment Station (WES), US Army Corps of Engineers, Washington D.C., USA.

Girsch, E. (2003). Mixed-in-place: A technique for the construction of subterranean walls and foundations. *Materials and Geoenvironment,* 50(1): 129-132.

Goforth, G.F., Townsend, F.C. & Bloomquist, D. (1991). Saturated and unsaturated fluid flow in a centrifuge. In Ko, H.Y. & McLean, F.G. (Editors), *Centrifuge 91: Proceedings of the International Conference Centrifuge 1991*, Boulder, USA., Balkema, 1: 497-502.

Gonzalez, R.C. & Woods, R.E. (1992). *Digital image processing*. Addison Wisley (Pub).

Goodings, D.J. (1979). *Centrifugal modelling of slope failures.* Ph.D. Dissertation, Cambridge University, Cambridge, UK.

Goodings, D.J. (1982). Relationships for centrifugal modelling of seepage and surface flow effects on embankment dams. *Géotechnique,* 32(2): 149-152.

Goodings, D.J. (1984). Relationships for modelling water effects in geotechnical centrifuge models. In Craig, W.H. (Editor), *The application of centrifuge modelling to geotechnical design*, Manchester, UK., University of Manchester (Pub).

Goodings, D.J. (1994). Implications of changes in seepage flow regimes for centrifuge models. In Leung, C.F., Lee, F.H. & Tan, T.S. (Editors), *Proceedings of the International Conference Centrifuge 94*, Singapore, SG., Balkema, 1: 393-398.

Grattoni, C.A., Jing, X.D. & Dawe, R.A. (2001). Dimensionless groups for three-phase gravity drainage flow in porous media. *Journal of Petroleum Science and Engineering,* 29(1): 53-65.

Guan, Y. (1996). *The measurement of soil suction.* Ph.D. Dissertation, University of Saskatchewan, Saskatchewan, CA.

Guan, Y. & Fredlund, D.G. (1997). Use of the tensile strength of water for the direct measurement of high soil suction. *Canadian Geotechnical Journal,* 34(4): 604-614, doi:10.1139/t97-014.

Gurung, S.B., Almeida, M.S.S. & Bicalho, K.V. (1998). Migration of zinc through sedimentary soil models. In Kimura, T., Kusakabe, O. & Takemura, J. (Editors), *Centrifuge 98: Proceedings of the International Conference, IS-Tokyo '98*, Tokyo, JP., Balkema, 1: 589-594.

Hahn, W., Hanson, G.J. & Cook, K.R. (2000). Breach morphology observations of embankment overtopping tests. In Hotchkiss, R.H. & Glade, M. (Editors), *Building Partnerships: Conference on Water Resources Engineering and Water Resources Planning and Management*, Minneapolis, US., ASCE, 1: 1-10, doi:10.1061/40517(2000)411.

Hamilton, R.T. (1997). Darcy constant for multisized spheres with no arbitrary constant. *AIChE Journal,* 43(3): 835-836, doi:10.1002/aic.690430328.

Hanumantha-Rao, B. & Singh, D.N. (2011). Moisture content determination by TDR and capacitance techniques: A comparative study. *International Journal of Earth Sciences and Engineering,* 4(6): 132-137.

Hazen, A. (1892). *Some physical properties of sands and gravels: with special reference to their use in filtration* (Technical Report), Massachusetts State Board of Health, Boston, US.

Heimovaara, T.J. (1993). Design of triple-wire time domain reflectrometry probes in practice and theory. *Soil Science Society of America Journal,* 57(6): 1410-1410.

Henderson, F.M. (1966). *Open channel flow*. MacMillan Publishing co. (Pub), New York, USA.

Heng, P.B.C., Chandler, J.H. & Armstrong, A. (2010). Applying close range digital photogrammetry in soil erosion studies. *The Photogrammetric Record,* 25(131): 240-265, doi:10.1111/j.1477-9730.2010.00584.x.

Hinnell, A.C., Ferré, T.P.A. & Warrick, A.W. (2006). The influence of time domain reflectometry rod induced flow disruption on measured water content during steady state unit gradient flow. *Water Resources Research,* 42(8): W08420.

Höeg, K., Løvoll, A. & Vaskinn, K. (2004). Stability and breaching of embankment dams: field tests on 6 m high dams. *International Journal on Hydropower & Dams,* 11(1): 88-92.

Hoekstra, P. & Delaney, A. (1974). Dielectric properties of soils at UHF and microwave frequencies. *Journal of Geophysical Research,* 79(11): 1699-1708.

Hoyois, P. & Guha-Sapir, D. (2003). *Three decades of floods in Europe: a preliminary analysis of EMDAT data* (Technical Report), WHO collaborating Centre for Research on the Epidemiology of Disasters (CRED), Catholic University of Louvain, Louvain, BE.

Huang, H. & Ayoub, J. (2008). Applicability of the Forchheimer equation for non-Darcy flow in porous media. *SPE Journal,* 13(1): 112-122.

Janbu, N. (1954). Applications of Composite Slip Surfaces for Stability Analysis. *European Conference on the Stability of Earth Slopes*, Stockholm, SE., 3: 39-43.

Jones, J.A.A. (1981). *The nature of soil piping: a review of research* (Technical Report), British Geomorphological Research Group, Geo Books, Norwich, UK.

Kapogianni, E., Laue, J. & Sakellariou, M.G. (2010). Reinforced slope modelling using optical fibre sensors and PIV analysis. In Springman, S.M., Laue, J. & Seward, L. (Editors), *Physical Modelling in Geotechnics: Proceedings of the 7th International Conference in Physical Modelling in Geotechnics (ICPMG 2010)*, Zurich, CH., CRC Press / Balkema, 2: 1125-1130.

Khalifa, A., Garnier, J., Thomas, P. & Rault, G. (2000). Scaling laws of water flow in centrifuge models. In Garnier, J., Thorel, L. & Haza, E. (Editors), *International Symposium on Physical Modelling and Testing in Environmental Geotechnics*, La Baule, FR., Network of European Centrifuges for Environmental Geotechnic Research, 1: 207-216.

Khalili, N., Geiser, F. & Blight, G.E. (2004). Effective stress in unsaturated soils: Review with new evidence. *International Journal of Geomechanics,* 4(2): 115-126.

Khalili, N. & Khabbaz, M.H. (1998). A unique relationship of chi for the determination of the shear strength of unsaturated soils. *Géotechnique,* 48(5).

Khoo, E., Okumura, T. & Lee, F.H. (1994). Side friction effects in plane strain models. In Leung, C.F., Lee, F.H. & Tan, T.S. (Editors), *Proceedings of the International Conference Centrifuge 94*, Singapore, SG., Balkema, 1: 115-120.

Ko, H.Y., Dunn, J. & Hollingsworth, T. (1989a). *Study of embankment performance during overtopping and throughflow: Report 1 - feasibility study* (Technical Report), Colorado University at Boulder, US Army Corps of Engineers, Washington D.C., USA.

Ko, H.Y., Dunn, J. & Hollingsworth, T. (1989b). *Study of embankment performance during overtopping and throughflow: Report 2 - hydraulic study and modeling of models* (Technical Report), Colorado University at Boulder, US Army Corps of Engineers, Washington D.C., USA.

Ko, H.Y., Dunn, J. & Hollingsworth, T. (1989c). *Study of embankment performance during overtopping and throughflow: Report 3 - model-prototype comparison studies* (Technical Report), Colorado University at Boulder, US Army Corps of Engineers, Washington D.C., USA.

Kondner, R. (1963). Hyperbolic stress strain response: cohesive soils. *Journal of the Soil Mechanics and Foundations Division,* 89: 115-143.

König, D., Jessberger, H., Bolton, M., Phillips, R., Bagge, G. & Renzi, R. (1994). Pore pressure measurement during centrifuge model tests: experience of five laboratories. In Leung, C.F., Lee, F.H. & Tan, T.S. (Editors), *Proceedings of the International Conference Centrifuge 94*, Singapore, SG., Balkema, 1: 101-108.

Kozeny, J. (1927). Ueber kapillare Leitung des Wassers im Boden. *Akad. Wiss. Wien,* 136(2a): 271-306.

Krahn, J. (2012a). *Geo-Studio user manuals*. GEO-SLOPE International, Ltd. (Pub), Calgary, CA.

Krahn, J. (2012b). *Seepage modeling with SEEP/W*. GEO-SLOPE International, Ltd. (Pub), Calgary, CA.

Krahn, J. (2012c). *Stability modeling with SLOPE/W*. GEO-SLOPE International, Ltd. (Pub), Calgary, CA.

Kumar, P.R. (2007). Scaling laws and experimental modelling of contaminant transport mechanism through soils in a geotechnical centrifuge. *Geotechnical and Geological Engineering,* 25(5): 581-590, doi:10.1007/s10706-007-9131-x.

Kumar, P.R. & Viswanadham, B.V.S. (2012). Use of geocomposite as an internal drain in levees: Centrifuge study. In Viswanadham, B.V.S. & Gaudin, C. (Editors), *First asian workshop on physical modelling in geotechnics - Asiafuge 2012*, Munbay, IN., Blomsburry, 1: 323-335.

Kusakabe, O., Hagiwara, T. & Kawashima, A. (1988a). Levee failures modelled in a drum centrifuge. In Corté, J.F. (Editor), *Centrifuge 88: Proceedings of the International Conference on Geotechnical Centrifuge Modelling*, Paris, FR., Balkema, 1: 147-153.

Kusakabe, O., Hagiwara, T. & Kuroiwa, H. (1988b). Design and operation of a drum centrifuge. In Corté, J.F. (Editor), *Centrifuge 88: Proceedings of the International Conference on Geotechnical Centrifuge Modelling*, Paris. FR., Balkema, 1: 77-82.

Laboratory of Hydraulics, G., Hydrology - ETH Zurich. (2008). *Reference manual of BASEMENT*. VAW-ETHZ (Pub), Zurich, CH.

Lai, B., Miskimins, J. & Wu, Y.S. (2009). Non-Darcy Porous Media Flow According to the Barree and Conway Model: Laboratory and Numerical Modeling Studies. In Inc.,

S.o.P.E. (Editor), *2009 SPE Rocky Mountain Petroleum Technology Conference*, Denver, USA., Society of Petroleum Engineers Inc., 1: 1-15.

Laloui, L. & Nuth, M. (2005). An introduction to the constitutive modelling of unsaturated soils. *Revue Européenne de Génie Civil,* 9(5-6): 651-669.

Lam, L., Fredlund, D.G. & Barbour, S.L. (1987). Transient seepage model for saturated–unsaturated soil systems: a geotechnical engineering approach. *Canadian Geotechnical Journal,* 24(4): 565-580, doi:10.1139/t87-071.

Lambe, P.C. (1981). *Dynamic centrifugal modelling of a horizontal sand stratum.* Ph.D. Dissertation, Massachusetts Institute of Technology, Cambridge, USA.

Lambe, T.W. & Whitman, R.V. (1969). *Soil mechanics*. John Wiley & Sons (Pub), New York, USA.

Lang, H.J., Huder, J., Amann, P. & Puzrin, A. (2011). *Bodenmechanik und Grundbau*. Springer-Verlag (Pub), Berlin, DE.

Laue, J. (2002). Centrifuge technology. In Springman, S.M. (Editor), *Constitutive and centrifuge modelling: Two extremes* (pp. 75-105), Lisse, NL., Balkema (Pub).

Laue, J., Gautray, J.N.F., Morales, W.F. & Askarinejad, A. (2012). Modelling in a geotechnical drum centrifuge. In Viswanadham, B.V.S. & Gaudin, C. (Editors), *First asian workshop on physical modelling in geotechnics - Asiafuge 2012*, Munbay, IN., Blomsburry, 1: 165-180.

Laue, J., Nater, P., Springman, S.M. & Grämiger, E. (2002). Preparation of soil samples in drum centrifuges. In Phillips, R., Guo, P.J. & Popescu, R. (Editors), *Physical Modelling in Geotechnics: ICPMG '02. Proceedings of the International Conference*, Newfoundland, CA., CRC Press / Balkema, 1: 143-148.

Lee, F.H. (2002). The philosophy of modelling versus testing. In Springman, S.M. (Editor), *Constitutive and centrifuge modelling: Two extremes* (pp. 113-133), Lisse, NL., Balkema (Pub).

Lee, F.H., Almeida, M.S.S. & Indraratna, B. (2010). Physical modelling of soft ground problems. In Springman, S.M., Laue, J. & Seward, L. (Editors), *Physical Modelling in Geotechnics: Proceedings of the 7th International Conference in Physical Modelling in Geotechnics (ICPMG 2010)*, Zurich, CH., CRC Press / Balkema, 1: 46-66.

Lee, Y.J. & Bassett, R.H. (2006). Application of a photogrammetric technique to a model tunnel. *Tunnelling and Underground Space Technology,* 21(1): 79-95, doi:10.1016/j.tust.2005.06.005.

Leong, E.C., Zhang, X.-H. & Rahardjo, H. (2012). Calibration of a thermal conductivity sensor for field measurement of matric suction. *Géotechnique,* 62(1): 81-85.

Lo Presti, D.C.F., Pedroni, S. & Crippa, V. (1992). Maximum dry density of cohesionless soils by pluviation and by ASTM D 4253-83: A comparative study. *Geotechnical Testing Journal,* 15(2): 180-189.

Macchione, F. & Sirangelo, B. (1988). Study of earth dam erosion due to overtopping. In Starosolszky, O. & Melder, O.M. (Editors), *Hydrology of Disasters: Proceedings of the World Meteorological Organization Technical Conference Held in Geneva*, Geneve, CH., World Meteorological Organization, 1: 212-219.

Maqsoud, A., Bussière, B., Mbonimpa, M. & Aubertin, M. (2004). Hysteresis effects on the water retention curve: a comparison between laboratory results and predictive models. *GeoQuebec 2004 : 57th Canadian Geotechnical Conference*, Quebec, CA., Canadian Geotechnical Society, 1: 8-15.

Mašín, D. (2005). A hypoplastic constitutive model for clays. *International Journal for Numerical and Analytical Methods in Geomechanics,* 29(4): 311-336.

Mašín, D. & Khalili, N. (2008). A hypoplastic model for mechanical response of unsaturated soils. *International Journal for Numerical and Analytical Methods in Geomechanics,* 32(15): 1903-1926.

Mavroulidou, M., Zhang, X., Cabarkapa, Z. & Gunn, M.J. (2009). A study of the laboratory measurement of the soil water retention curve. *CEST09: Proceedings of the 11th*

International Conference on Environmental Science and Technology, Chania, GR., University of the Aegean, 1: 907-915.

Mayne, P.W., Coop, M.R., Springman, S.M., Huang, A.B. & Zornberg, J.G. (2009). Geomaterial behavior and testing. In Hamza, M., Shahien, M. & El-Mossallamy, Y. (Editors), *17th International Conference on Soil Mechanics and Geotechnical Engineering*, Alexandria, EG., IOS Press, 4: 2777-2872, doi:10.3233/978-1-60750-031-5-2777.

Mayor, P.A. (2009). Hochwasserschutz an Wildbächen, mittleren und kleinen Gewässern in der Schweiz. In Herrmann, R.A. & Jensen, J. (Editors), *Sicherung von Dämmen, Deichen und Stauanlagen - Handbuch für Theorie und Praxis: 3. Symposium Sicherung von Dämmen, Deichen und Stauanlagen*, Siegen, DE., 1: 25-36.

Mayor, P.A. (2013). *Verhalten eines Flussdammes unter wiederholter Hochwasserbelastung.* Ph.D. Dissertation No. 19624, ETH Zurich, Zurich, CH.

Mayor, P.A. & Springman, S.M. (2012). Geotechnische Aspekte des Hochwasserschutzes am Beispiel der Rhonedämme*. Geotechnik im Hochwasserschutz* (pp. 11-20), Zurich, CH., Geotechnik Schweiz (Pub).

Mayor, P.A., Springman, S.M. & Teysseire, P. (2008). In-situ field experiment to apply variable high water levels to a river levee. In Toll, D.G., Augarde, C.E., Gallipoli, D. & Wheeler, S.J. (Editors), *Unsaturated soils. Advances in geo-engineering : 1st European conference on unsaturated soils*, Durham, UK., Taylor & Francis, 1: 947-952.

McNamara, A.M., Divall, S., Goodey, R.J., Gorasia, R.J., Halai, H., Rose, A.V., Stallebrass, S.E., Taylor, R.N. & Xu, M. (2012). The London geotechnical centrifuge centre at city University London. In Bezuijen, A. (Editor), *2nd Eurofuge Conference*, Delft, NL .

Mériaux, P., Vennetier, M., Aigouy, S., Hoonakker, M. & Zylberblat, M. (2006). Diagnosis and management of plant growth on embankment dams and dykes. *Commission Internationale des Grands Barrages, Barcelona*: 1-20.

Miao, L., Jing, F. & Houston, S. (2006). Soil-Water Characteristic Curve of Remolded Expansive Soils. In Miller, G.A., Zapata, C.E., Houston, S.L. & Fredlund, D.G. (Editors), *Unsaturated Soils 2006: Proceedings of the fourth international conference on unsaturated Soils*, Arizona, US., ASCE, 1: 997-1004, doi:doi:10.1061/40802(189)80.

Montes-H, G., Duplay, J., Martinez, L. & Mendoza, C. (2003). Swelling-shrinkage kinetics of MX80 bentonite. *Applied Clay Science,* 22(6): 279-293.

Morales, W.F., Laue, J. & Springman, S.M. (2012a). Controlled water-level system for breach analysis of levees within an enhanced acceleration field In Bezuijen, A. (Editor), *2nd Eurofuge Conference*, Delft, NL.

Morales, W.F., Laue, J. & Springman, S.M. (2013). On the use of unsaturated properties of a sandy material for centrifuge model preparation. In Caicedo, B. (Editor), *1st Pan-American Conference on Unsaturated Soils*, Cartagena, CO., CRC Press / Balkema, 1: 159-164.

Morales, W.F., Laue, J., Zweidler, A. & Springman, S.M. (2012b). Design and analysis of centrifuge devices with a Product Lifecycle Management (PLM) system. In Bezuijen, A. (Editor), *2nd Eurofuge Conference*, Delft, NL .

Morales, W.F., Mayor, P.A. & Springman, S.M. (2011). In-situ and laboratory water retention characteristics in a silty sand dyke. In Anagnostopoulos, A., Pachakis, M. & Tsatsanifos, C. (Editors), *15th European Conference on Soil Mechanics and Geotechnical Engineering*, Athens, GR., IOS Press, 1: 641-646.

Morgenstern, N.R. & Price, V.E. (1965). The analysis of the stability of general slip surfaces. *Géotechnique,* 15(1): 79-93.

Morris, M.W., Hassan, M.A.A.M. & Vaskinn, K.A. (2007). Breach formation: Field test and laboratory experiments. *Journal of Hydraulic Research,* 45(sup1): 9-17, doi:10.1080/00221686.2007.9521828.

Mudelsee, M., Börngen, M., Tetzlaff, G. & Grünewald, U. (2004). Extreme floods in central Europe over the past 500 years: Role of cyclone pathway “Zugstrasse Vb”. *Journal of Geophysical Research,* 109(D23): D23101.

Mueller, P. (2007). *Dyke stability for the third correction of the Rhone (in German).* Master thesis, ETH Zurich, Zurich, CH.

Muir Wood, D. (2002). Constitutive cladistics: the progeny of critical state soil mechanics. In Springman, S.M. (Editor), *Constitutive and centrifuge modelling: Two extremes* (pp. 35-57), Lisse, NL., Balkema (Pub).

Muir Wood, D. (2012). Prediction of soil response without constitutive models. *Lecture at ALERT Olek Zienkiewicz Course (Summerschool 2012) "Constitutive modelling of soils"*, Dresden, DE.

Muraleetharan, K.K. & Granger, K.K. (1999). The use of miniature pore pressure transducers in measuring matric suction in unsaturated soils. *Geotechnical Testing Journal,* 22(3): 226-234.

Nater, P. (2005). *Belastungs- und Verformungsverhalten von geschichteten Bodensystemen unter starren Kreisfundationen.* Ph.D. Dissertation No. 16319, ETH Zurich, Zurich, CH., doi:10.3929/ethz-a-005166336.

Noborio, K. (2001). Measurement of soil water content and electrical conductivity by time domain reflectometry: a review. *Computers and Electronics in Agriculture,* 31(3): 213-237, doi:10.1016/s0168-1699(00)00184-8.

Nuth, M. (2009). *Constitutive modelling of unsaturated soils with hydro-geomechanical couplings.* Ph.D. Dissertation, École Polytechnique Fédérale de Lausanne, Lausanne, CH., doi:10.5075/epfl-thesis-4358

Nuth, M. & Laloui, L. (2008a). Advances in modelling hysteretic water retention curve in deformable soils. *Computers and Geotechnics,* 35(6): 835-844, doi:10.1016/j.compgeo.2008.08.001.

Nuth, M. & Laloui, L. (2008b). Effective stress concept in unsaturated soils: Clarification and validation of a unified framework. *International Journal for Numerical and Analytical Methods in Geomechanics,* 32(7): 771-801, doi:10.1002/nag.645.

Okumura, T., Narita, K. & Ohne, Y. (1998). Failures of earth dam due to flooding. In Kimura, T., Kusakabe, O. & Takemura, J. (Editors), *Centrifuge 98: Proceedings of the International Conference, IS-Tokyo '98*, Tokyo, JP., Balkema, 1: 633-636.

Pan, H., Qing, Y. & Pei-Yong, L. (2010). Direct and indirect measurement of soil suction in the laboratory. *Electronic Journal of Geotechnical Engineering,* 15(A): 1-14.

Parsons, A.W. & Boden, J.B. (1979). *The moisture condition test and its potential applications in earthworks* (Technical Report), Transport and Road Research Laboratory, Laboratory, T.a.R.R.

Perez-Garcia, N., Houston, S.L., HOUSTON, W.N. & PADILLA, J.M. (2008). An oedometer-type pressure plate SWCC apparatus. *Geotechnical Testing Journal,* 31(2): 115-123, doi:10.1520/GTJ100964.

Persson, M.H. & Haridy, S. (2003). Estimating water content from electrical conductivity measurements with short time-domain reflectometry probes. *Soil Science Society of America Journal,* 67(2): 478-482.

Pham, H.Q., Fredlund, D.G. & Barbour, S.L. (2005). A study of hysteresis models for soil-water characteristic curves. *Canadian Geotechnical Journal,* 42(6): 1548–1568.

Phillips, E. (1869). Du mouvement des corps solides elastiques semblables. *Comptes Rendus des Séances de l'Académie des Sciences,* 69: 911-912.

Phillips, R. (1995). Centrifuge modelling: practical considerations. In Taylor, R.N. (Editor), *Geotechnical centrifuge technology*, Suffolk, UK., Chapman & Hall (Pub).

Pokrovsky, G.Y. & Fedorov, I.S. (1936). Studies of soil pressures and soil deformations by means of a centrifuge. In Casagrande, A., Rutledge, P.C. & Watson, J.D. (Editors), *1st International Conference on Soil Mechanics & Foundation Engineering*, Cambrigde, US. , Harvard University.

Porras Ortiz, O.F. (2004). *Small and large strain monitoring of unsaturated soil behavior by means of multiaxial testing and shear wave propagation.* Ph.D. Dissertation, Louisiana State University, Baton Rouge, US.

Potts, D.M. (2003). Numerical analysis: a virtual dream or practical reality? *Géotechnique,* 53(6): 535-573.

Potts, D.M., Axelsson, K., Grande, L., Schweiger, H. & Long, M. (2002). *Guidelines for the use of advanced numerical analysis*. Thomas Telford (Pub), London, UK.

Rezzoug, A., König, D. & Triantafyllidis, T. (2000a). Scaling rules in centrifuge modelling for capillary rise in soils. In Garnier, J., Thorel, L. & Haza, E. (Editors), *International Symposium on Physical Modelling and Testing in Environmental Geotechnics*, La Baule, FR., Network of European Centrifuges for Environmental Geotechnic Research, 1: 217-224.

Rezzoug, A., König, D. & Triantafyllidis, T. (2004). Scaling laws for centrifuge modeling of capillary rise in sandy soils. *Journal of Geotechnical and Geoenvironmental Engineering,* 130(6): 615-620.

Rezzoug, A., König, D., Triantafyllidis, T., Coumoulos, H. & Soga, K. (2000b). Numerical analysis of scaling laws for capillary rise in soils. In Garnier, J., Thorel, L. & Haza, E. (Editors), *International Symposium on Physical Modelling and Testing in Environmental Geotechnics*, La Baule, FR., Network of European Centrifuges for Environmental Geotechnic Research, 1: 225-232.

Richards, K.S. & Reddy, K.R. (2007). Critical appraisal of piping phenomena in earth dams. *Bulletin of Engineering Geology and the Environment,* 66(4): 381-402, doi:10.1007/s10064-007-0095-0.

Richards, L.A. (1931). Capillary conduction of liquids through porous mediums. *Physics,* 1(5): 318-333, doi:10.1063/1.1745010.

Ridley, A.M. (1993). *The measurement of soil moisture suction.* Ph.D. Dissertation, Imperial College, London, UK.

Ridley, A.M. & Burland, J.B. (1999). Use of the tensile strength of water for the direct measurement of high soil suction: Discussion. *Canadian Geotechnical Journal,* 36(1): 178-180, doi:10.1139/t98-080.

Rieke-Zapp, D.H. & Nearing, M.A. (2005). Digital close range photogrammetry for measurement of soil erosion. *The Photogrammetric Record,* 20(109): 69-87.

Roscoe, K.H. & Burland, J.B. (1968). On the generalized stress-strain behavior of 'wet' clay. In Heyman, J. & Leckie, F.A. (Editors), *Engineering Plasticity* (pp. 535-609), Cambridge, UK., Cambridge University Press (Pub).

Roscoe, K.H. & Schofield, A.N. (1963). Mechanical behavior of an idealised "wet clay". *2nd European Conference on Soil Mechanics*, Wiesbaden, DE., 1: 47-54.

Roscoe, K.H., Schofield, A.N. & Wroth, C.P. (1958). On the yielding of soils. *Géotechnique,* 8(1): 22-52.

Russell, A. & Khalili, N. (2005). A bounding surface plasticity model for sands in an unsaturated state. In Schanz, T. (Editor), *Unsaturated Soils: Numerical and Theoretical Approaches* (Vol. 94, pp. 99-109), Springer Berlin Heidelberg (Pub), doi:10.1007/3-540-26737-9_8.

Sanz-Ablanedo, E., Rodríguez-Pérez, J.R., Arias-Sánchez, P. & Armesto, J. (2009). Metric potential of a 3d measurement system based on digital compact cameras. *Sensors,* 9(6): 4178-4194, doi:10.3390/s90604178.

Sasanakul, I., Abdoun, T. & Sharp, M. (2010). Physical modeling studies to evaluate performance of New Orleans levees during hurricanes. In Springman, S.M., Laue, J. & Seward, L. (Editors), *Physical Modelling in Geotechnics: Proceedings of the 7th International Conference in Physical Modelling in Geotechnics (ICPMG 2010)*, Zurich, CH., CRC Press / Balkema, 2: 1195-1200.

Sasanakul, I., Vanadit-Ellis, W., Sharp, M., Abdoun, T., Ubilla, J., Steedman, S. & Scott, K. (2008). New Orleans levee system performance during hurricane Katrina: 17th Street

canal and Orleans canal North. *Journal of Geotechnical and Geoenvironmental Engineering,* 134(5): 657-667.

Schmocker, L. (2011). *Hydraulics of dike breaching.* Ph.D. Dissertation No. 19983, ETH Zurich, Zurich, CH., doi:10.3929/ethz-a-006716949

Schmocker, L., Hager , W.H. & Boes, R.M. (2010). Dike breaching due to overtopping. In Springman, S.M., Laue, J. & Seward, L. (Editors), *Physical Modelling in Geotechnics: Proceedings of the 7th International Conference in Physical Modelling in Geotechnics (ICPMG 2010)*, Zurich, CH., CRC Press / Balkema, 2: 1201-1206.

Schofield, A.N. (1980). Cambridge geotechnical centrifuge operations. *Géotechnique,* 30(3): 227-268.

Schofield, A.N. (2005). *Distributed soil properties and geotechnical design*. Thomas Telford (Pub), London, UK.

Seed, R.B., Nicholson, P.G., Dalrymple, R.A., Battjes, J.A., Bea, R.G., Boutwell, G.P., Bray, J.D., Collins, B.D., Harder, L.F., Headland, J.R., Inamine, M., Kayen, R.E., Kuhr, R., Pestana, J.M., Sanders, R., Silva-Tulla, F., Storesund, R., Tanaka, S., Wartman, J., Wolff, T.F., Wooten, L. & Zimmie, T. (2005). *Preliminary report on the performance of the new orleans levee system in hurricane Katrina on august 29, 2005*. University of California at Berkeley; American Society of Civil Engineers (Pub).

Seijffert, J.W. & Verheij, H. (1998). Grass covers and reinforcement measures. In Pilarczyk, K.W. (Editor), *Dikes and revetments: design maintenance and safety assessment* (pp. 289-302), Taylor & Francis (Pub).

Seki, K. (2007). SWRC fit - a nonlinear fitting program with a water retention curve for soils having unimodal and bimodal pore structure. *Hydrology and Earth System Sciences,* 4: 407-437.

Seo, M.W., Ha, I.S., Im, E.S., Kim, H.S., Kim, Y.S. & Kim, T.H. (2006). Centrifuge test for evaluating effects of water level change on fill dam behavior. In Ng, C.W.W., Wang, Y.H. & Zhang, L.M. (Editors), *Physical Modelling in Geotechnics - 6th ICPMG '06. Proceedings of the International Conference*, Hong Kong, HK., CRC Press / Balkema, 1: 431-434.

Shaw, B. & Baver, L.D. (1939). Heat conductivity as an index of soil moisture. *Agronomy Journal,* 31: 886-891.

Sheng, D. & Fredlund, D.G. (2008). Elasto-plastic modelling of unsaturated soils: An overview. In IACMAG (Editor), *Proceedings of the 12th International Conference of International Association for Computer Methods and Advances in Geomechanics (IACMAG)*, Goa, IN., IACMAG, 4: 2084-2105.

Sheng, D., Zhou, A. & Fredlund, D.G. (2011). Shear strength criteria for unsaturated soils. *Geotechnical and Geological Engineering,* 29(2): 145-159.

Sidiropoulou, M.G., Moutsopoulos, K.N. & Tsihrintzis, V.A. (2007). Determination of Forchheimer equation coefficients a and b. *Hydrological Processes,* 21(4): 534-554, doi:Doi 10.1002/Hyp.6264.

Singh, D.N. & Gupta, A.K. (2000). Modelling hydraulic conductivity in a small centrifuge. *Canadian Geotechnical Journal,* 37(5): 1150-1155.

Skierucha, W., Wilczek, A. & Alokhina, O. (2008). Calibration of a TDR probe for low soil water content measurements. *Sensors and Actuators A: Physical,* 147(2): 544-552, doi:10.1016/j.sna.2008.06.015.

Soga, K., Coumoulos, H., König, D. & Rezzoug, A. (2000). Some remarks on water movement in homogeneous unsaturated soils in relation to centrifuge testing. In Garnier, J., Thorel, L. & Haza, E. (Editors), *International Symposium on Physical Modelling and Testing in Environmental Geotechnics*, La Baule, FR., Network of European Centrifuges for Environmental Geotechnic Research, 1: 243-250.

Springman, S.M. (2000). Discussion on "Displacement of Structures Adjacent to Cantilever Sheet Pile Walls" by M. Georgiadis, C. Anagnostopoulos [Soils and foundations,(1999) 39(2): 99-104]. *Soils and Foundations,* 40(5): 149-152.

Springman, S.M. (2014). Lessons learnt from centrifuge modelling of sand compaction piles and implications for design. In Gaudin, C. & White, D. (Editors), *8th International Conference on Physical Modelling in Geotechnics*, Perth. AU.

Springman, S.M., Laue, J., Boyle, R., White, J. & Zweidler, A. (2001). The ETH Zurich geotechnical drum centrifuge. *International Journal of Physical Modelling in Geotechnics,* 1(1): 59-70.

Springman, S.M., Laue, J. & Seward, L. (2010). *Physical Modelling in Geotechnics: Proceedings of the 7th International Conference in Physical Modelling in Geotechnics (ICPMG 2010)*. CRC Press / Balkema (Pub), Zurich, CH.

Springman, S.M. & Mayor, P.A. (2009). *3. Rhonekorrektion - Prioritäre Massnahme Visp - Versuchszelle Baltschieder: Untersuchung des Dammverhaltens unter Berücksichtigung des ungesättigten Zustandes* (Technical Report), Institute for Geotechnical Engineering, ETH Zurich, Zurich, CH.

Springman, S.M., Mayor, P.A. & Herzog, R. (2009). *3. Rhonekorrektion: Untersuchung zur Optimierung des Materialbedarfs zum Dammbau* (Technical Report), Institute for Geotechnical Engineering, ETH Zurich, Zurich, CH.

Springman, S.M., Mayor, P.A., Müller, P. & Teysseire, P. (2008). The influence of river floods and rainfall on protection levees in the Valais. In Zhu, Liu & Qiang (Editors), *Long time effects and seepage behavior of dams: Proceedings of the 1st International Conference on long time effects and seepage behavior of dams (LTESBD08)*, Nanjing, CN., Hohai University Press, 1: 155-162.

Springman, S.M. & Teysseire, P. (2004). Geotechnik im Flussbau: Massnahmen zur Verhinderung von Damm- und Ufereinbrüchen, Sohlendurchbrüchen. *NDK Nachdiplomkurs in angewandten Erdwissenschaften*, Kloster Kappel am Albis, CH.

Stamhuis, E.J. (2006). Basics and principles of particle image velocimetry (PIV) for mapping biogenic and biologically relevant flows. *Aquatic Ecology,* 40(4): 463-479, doi:10.1007/s10452-005-6567-z.

Stanco, F., Battiato, S. & Gallo, G. (2011). *Digital imaging for cultural heritage preservation: Analysis, restoration, and reconstruction of ancient artworks* (Vol. 1). CRC Press (Pub), Boca Raton, US.

Steedman, R.S. & Sharp, M.K. (2011). Physical modelling analysis of the New Orleans levee breaches. *Proceedings of the ICE - Geotechnical Engineering,* 164(6): 353-372.

Stein, M.L. (1999). *Interpolation of spatial data: some theory for kriging*. Springer (Pub).

Stewart, D.P., Boyle, R.S. & Randolph, M.F. (1998). Experience with a new drum centrifuge. In Kimura, T., Kusakabe, O. & Takemura, J. (Editors), *Centrifuge 98: Proceedings of the International Conference, IS-Tokyo '98*, Tokyo, JP., Balkema, 1: 35-40.

Take, A.W. (2003). *The influence of seasonal moisture cycles on clay slopes.* Ph.D. Dissertation, Cambridge University, Cambridge, UK.

Take, W.A., Arnepalli, D.N., Brachman, R.W.I. & Rowe, R.K. (2007). Laboratory and field calibration of TDR probes for water content measurement. *OttawaGeo2007: The Diamond Jubilee: 60th Canadian Geotechnical Conference and 8th Joint CGS/IAH-CNC Groundwater Conference*, Ottawa, CA., Canadian Geotechnical Society, 1: 1865-1871.

Take, W.A. & Bolton, M.D. (2002). A new device for the measurement of negative pore water pressures in centrifuge models. In Phillips, R., Guo, P.J. & Popescu, R. (Editors), *Physical Modelling in Geotechnics: ICPMG '02. Proceedings of the International Conference*, Newfoundland, CA., CRC Press / Balkema, 1: 89-94.

Take, W.A. & Bolton, M.D. (2003). Tensiometer saturation and the reliable measurement of soil suction. *Géotechnique,* 53(2): 159-172.

TAW (Technical advisory committee on water defenses). (1998). *Fundamentals on water defenses* (Technical Report), Technical advisory committee on water defenses (TAW),.

Taylor, R.N. (1995). Centrifuges in modelling: principles and scale effects. In Taylor, R.N. (Editor), *Geotechnical centrifuge technology*, Suffolk, UK., Chapman & Hall (Pub).

Taylor, R.N., Grant, R.J., Robson, S. & Kuwano, J. (1998). An image analysis system for determining plane and 3-D displacements. In Kimura, T., Kusakabe, O. & Takemura, J. (Editors), *Centrifuge 98: Proceedings of the International Conference, IS-Tokyo '98*, Tokyo, JP., Balkema, 1: 73-78.

Terzaghi, K. (1925). *Erdbaumechanik auf bodenphysikalischer Grundlage*. F. Deuticke (Pub), Vienna, AT.

Terzaghi, K. (1943). *Theoretical Soil Mechanics* John Wiley & Sons, Ltd (Pub), New York, US.

Thomas, H. & Cantré, S. (2009). Applications of low-budget photogrammetry in the geotechnical laboratory. *The Photogrammetric Record,* 24(128): 332-350, doi:10.1111/j.1477-9730.2009.00551.x.

Thorel, L., Noblet, S., Garnier, J. & Bisson, A. (2000). Capillary rise and drainage flow through a centrifuged porous medium. In Garnier, J., Thorel, L. & Haza, E. (Editors), *International Symposium on Physical Modelling and Testing in Environmental Geotechnics*, La Baule, FR., Network of European Centrifuges for Environmental Geotechnic Research, 1: 251-258.

Thusyanthan, N.I. & Madabhushi, S.P.G. (2003). *Scaling of seepage flow velocity in centrifuge models* (Technical Report), Cambridge University Engineering Department, Cambridge, UK.

Topp, G.C., Davis, J.L. & Annan, A.P. (1980). Electromagnetic determination of soil water content: Measurements in coaxial transmission lines. *Water Resourses Research,* 16(3): 574-582, doi:10.1029/WR016i003p00574.

Torres, G.H. (2011). *Estimating the soil-water characteristic curve using grain-size analysis and plasticity index.* Master thesis, Arizona State University, Tempe, US.

Ubilla, J., Abdoun, T., Sasanakul, I., Sharp, M., Steedman, S., Vanadit-Ellis, W. & Zimmie, T. (2008). New Orleans levee system performance during hurricane Katrina: London Avenue and Orleans canal south. *Journal of Geotechnical and Geoenvironmental Engineering,* 134(5): 668-680.

US Army Corps of Engineers. (1994). *Engineering and design channel stability assessment for flood control projects* (Technical Report), Colorado University at Boulder, US Army Corps of Engineers, Washington D.C., USA.

US Army Corps of Engineers. (2000). *Design and construction of levees - Engineer manual* (Technical Report), Colorado University at Boulder, US Army Corps of Engineers, Washington D.C., USA.

Vaid, Y.P. & Negussey, D. (1984). Relative density of pluviated sand samples. *Soil and Foundations,* 24(2): 101-105.

van Beek, V.M., de Bruijn, H.T.J., Knoeff, J.G., Bezuijen, A. & Förster, U. (2010). Levee failure due to piping: A full-scale experiment. In Burns, S.E., Bhatia, S.K., Avila, C.M.C. & Hunt, B.E. (Editors), *Scour and Erosion: Proceedings of the Fifth International Conference on Scour and Erosion*, San Francisco, US., ASCE, 1: 283-292, doi:doi:10.1061/41147(392)63.

van der Poel, J.T. & Schenkeveld, F.M. (1998). A preparation technique for very homogeneous sand models and CPT research. In Kimura, T., Kusakabe, O. & Takemura, J. (Editors), *Centrifuge 98: Proceedings of the International Conference, IS-Tokyo '98*, Tokyo, JP., Balkema, 1: 149-154.

van Genuchten, M.T. (1980). A closed-form equation for predicting the hydraulic conductivity of unsaturated soils. *Soil Science Society of America Journal,* 44(5): 892-898.

Vanapalli, S.K., Fredlund, D.G., Pufahl, D.E. & Clifton, A.W. (1996). Model for the prediction of shear strength with respect to soil suction. *Canadian Geotechnical Journal,* 33(3): 379-392, doi:10.1139/t96-060.

Vaskinn, K.A., Løvoll, A. & Höeg, K. (2005). *IMPACT Investigation of Extreme Flood Processes and Uncertainty task WP2.1: Breach formation - large scale embankment failure* (Technical Report), HR Wallingford.

Vaskinn, K.A., Løvoll, A., Höeg, K., Morris, M., Hanson, G. & Hassan, M. (2004). Physical modeling of breach formation: Large scale field tests. *Dam Safety 2004: Proceedings of the Annual Conference of the Association of State Dam Safety Officials*, Phoenix, US., Association of State Dam Safety Officials, 1.

Vaunat, J., Romero, E. & Jommi, C. (2000). An elastoplastic hydromechanical model for unsaturated soils. In Tarantino, A. & Mancuso, C. (Editors), *Experimental evidence and theoretical approaches in unsaturated soils: Proceedings of an International workshop on unsaturated soils*, Trento, IT., Balkema, 1: 121-138.

Visser, P.J. (1998). *Breach growth in sand-dikes* Ph.D. Dissertation, Technische Universiteit Delft, Delft, NL.

Visser, P.J., Vrijling, J.K. & Verhagen, H.J. (1990). A field experiment on breach growth in sand-dikes. In Edge, B.L. (Editor), *Proceedings of 22th Conference on Coastal Engineering*, Delft, NL., ASCE, 2: 2087-2100.

Walker, J.P. (2000). *Estimating soil moisture profile dynamics from near-surface soil moisture measurements and standard meteorological data.* Ph.D. Dissertation, The University of Newcastle, New South Wales, AU.

Wan, C.F. & Fell, R. (2004a). Investigation of rate of erosion of soils in embankment dams. *Journal of Geotechnical and Geoenvironmental Engineering,* 130(4): 373-380.

Wan, C.F. & Fell, R. (2004b). Laboratory tests on the rate of piping erosion of soils in embankment dams. *Geotechnical Testing Journal,* 27(3): 295-303.

Wang, Z., Wu, L. & Wu, Q.J. (2000). Water-entry value as an alternative indicator of soil water-repellency and wettability. *Journal of Hydrology,* 231-232: 76-83, doi:10.1016/s0022-1694(00)00185-2.

Weber, T. (2007). *Modellierung der Baugrundverbesserung mit Schottersäulen.* Ph.D. Dissertation No. 17321, ETH Zurich, Zurich, CH., doi:10.3929/ethz-a-005462206

Weiler, M. & McDonnell, J. (2004). Virtual experiments: a new approach for improving process conceptualization in hillslope hydrology. *Journal of Hydrology,* 285(1): 3-18.

White, D., Randolph, M. & Thompson, B. (2005). An image-based deformation measurement system for the geotechnical centrifuge. *International Journal of Physical Modelling in Geotechnics,* 5(3): 1-12.

White, D.J. & Take, W.A. (2002). *GeoPIV: Particle Image Velocimetry (PIV) software for use in geotechnical testing* (Technical Report), University of Cambridge, Cambridge, UK.

White, D.J. & Take, W.A. (2003). *GeoPIV: 'Quick start' guide* (Technical Report), University of Cambridge, Cambridge, UK.

White, D.J., Take, W.A. & Bolton, M.D. (2001). Measuring soil deformation in geotechnical models using digital images and PIV analysis. In Contractor, D., Desai, C.S., Harpalani, S., Kemeny, J. & Kundu, T. (Editors), *The 10th International Conference on Computer Methods and Advances in Geomechanics*, Tuscon, USA., Taylor & Francis, 1: 997-1002.

White, D.J., Take, W.A. & Bolton, M.D. (2003). Soil deformation measurement using particle image velocimetry (PIV) and photogrammetry. *Géotechnique,* 53(7): 619-631.

Yakar, M. (2011). Using close range photogrammetry to measure the position of inaccessible geological features. *Experimental Techniques,* 35(1): 54-59, doi:10.1111/j.1747-1567.2009.00583.x.

Yilmazturk, F., Kulur, S. & Terzib, N. (2008). Determination of displacements in load tests with digital multimedia photogrammetry. In Jun, C. (Editor), *Proceedings of the ISPRS Congress Beijing 2008*, Beijing, CN., ISPRS, 719-722.

Zhao, Y., Gafar, K., Elshafie, M.Z.E.B., Deeks, A.D., Knappett, J.A. & Madabhushi, S.P.G. (2006). Calibration and use of a new automatic sand pourer. In Ng, C.W.W., Wang, Y.H. & Zhang, L.M. (Editors), *Physical Modelling in Geotechnics - 6th ICPMG '06. Proceedings of the International Conference*, Hong Kong, HK., CRC Press / Balkema, 1: 265-270.

Zhou, A.N., Sheng, D. & Carter, J.P. (2012). Modelling the effect of initial density on soil-water characteristic curves. *Géotechnique,* 62(8): 669-680, doi:10.1680/geot.10.P.120.

Zhou, R.Z.B., Take, W.A. & Ng, C.W.W. (2006). A case study in tensiometer interpretation: centrifuge modelling of unsaturated slope behaviour. In Miller, G.A., Zapata, C.E., Houston, S.L. & Fredlund, D.G. (Editors), *Unsaturated Soils 2006: Proceedings of the Fourth International Conference on Unsaturated Soils*, Carefree, USA., ASCE, 2: 2300-2311.

Zienkiewicz, O., Taylor, R. & Zhu, J. (2005). *The finite element method: its basis and fundamentals* (Vol. 1). Butterworth-Heinemann (Pub), Oxford, UK.

Appendix 1 Detailed results of the centrifuge tests

A1.1 Homogeneous dyke, slope gradient = 1:2.0

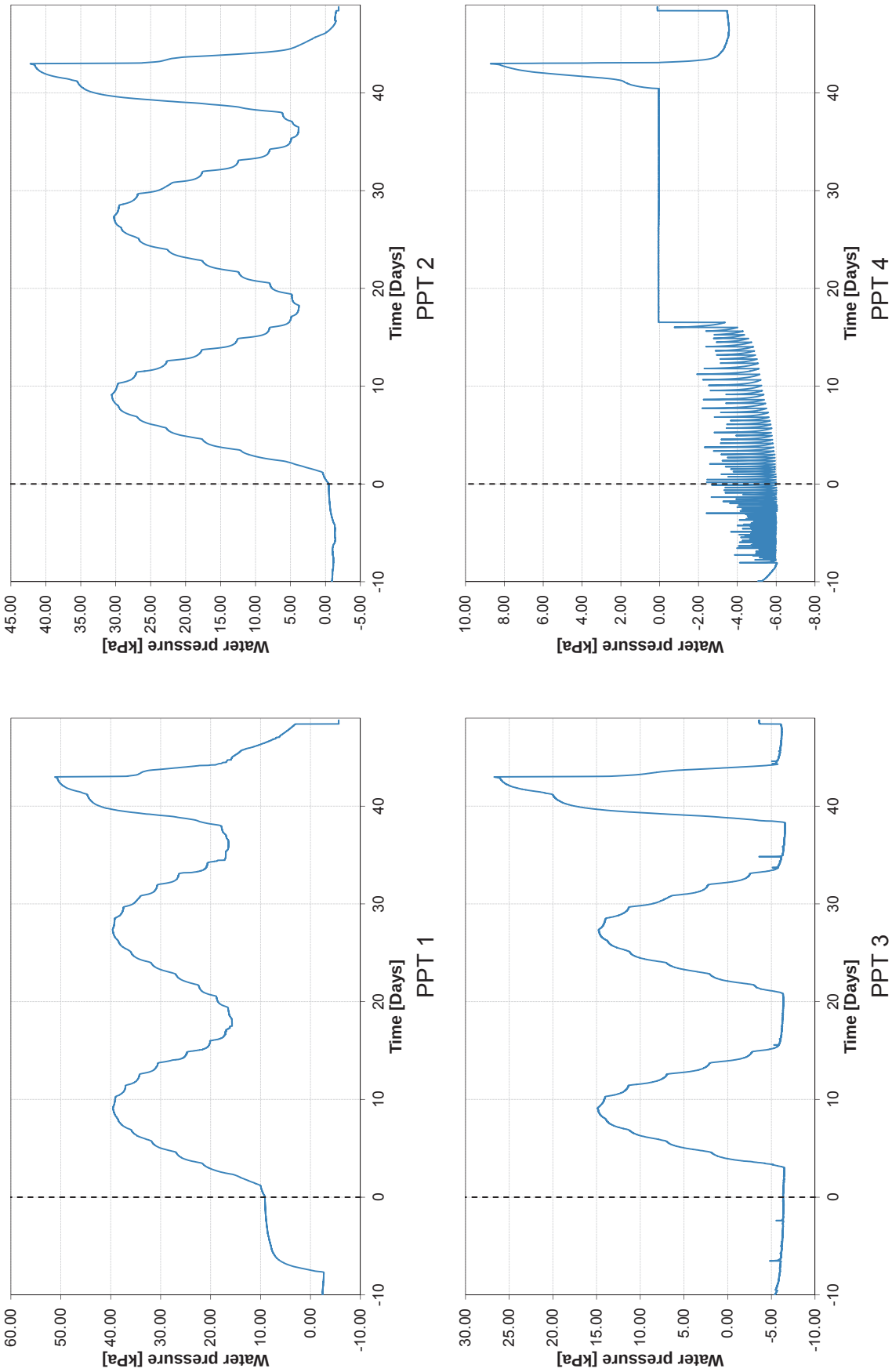

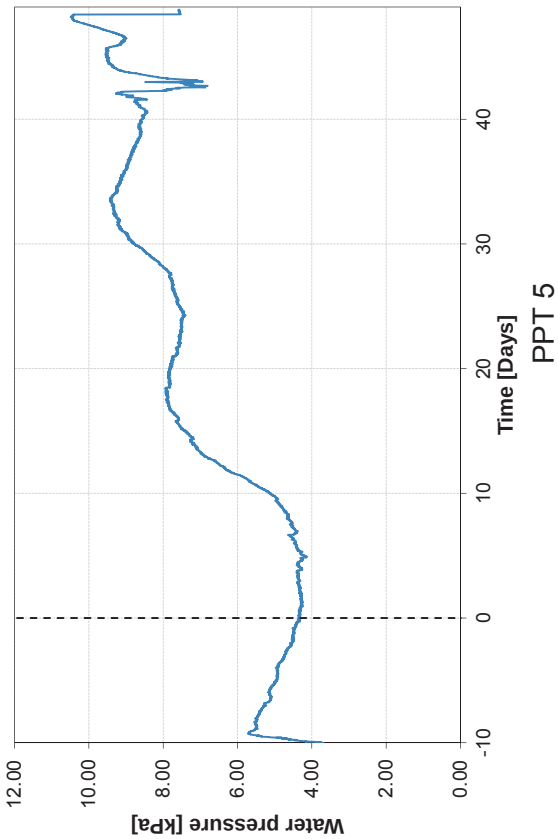

PPT 5

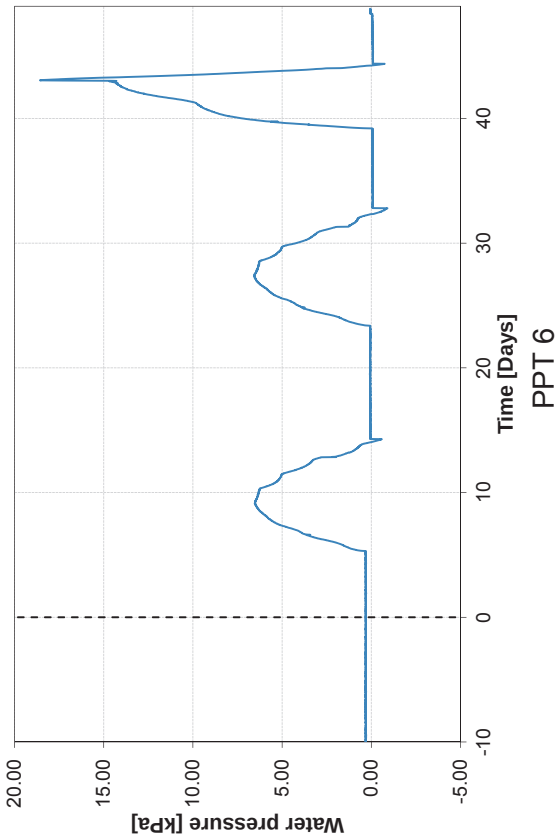

PPT 6

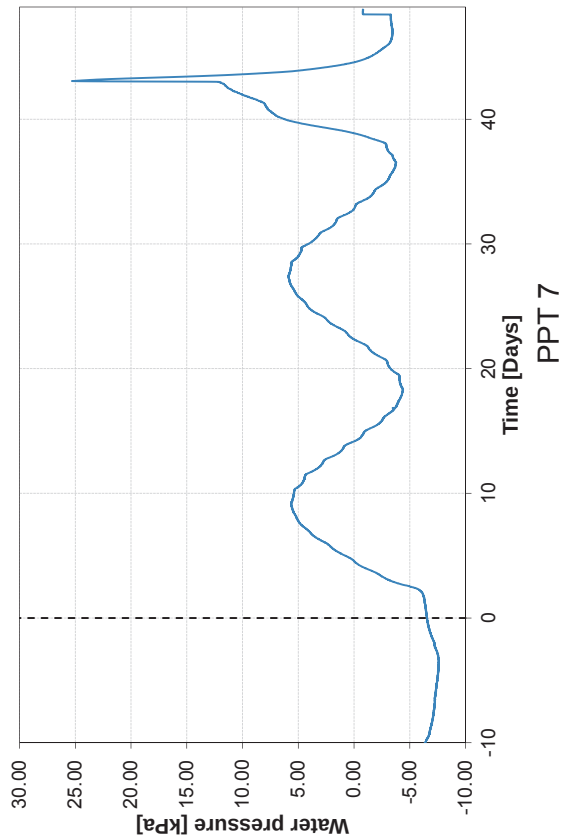

PPT 7

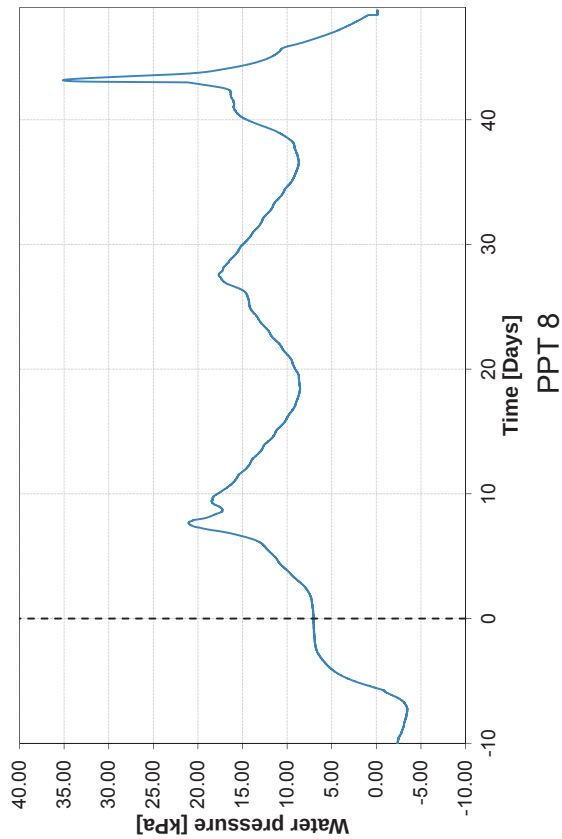

PPT 8

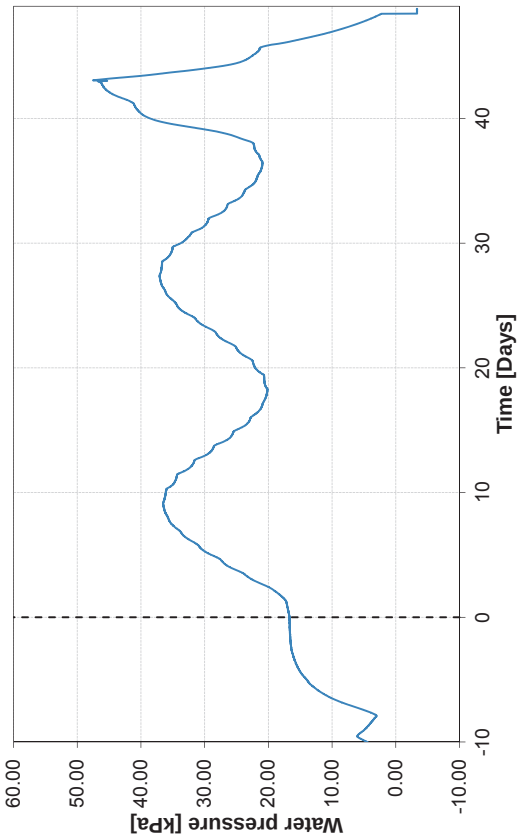

PPT 10

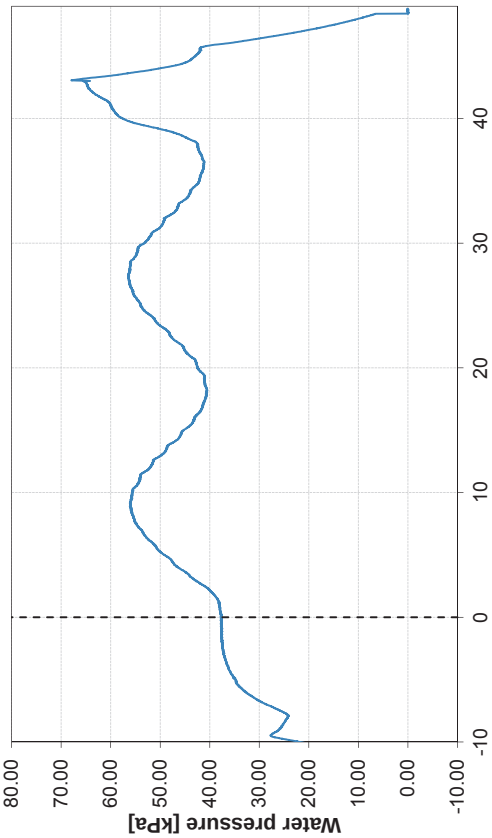

PPT 12

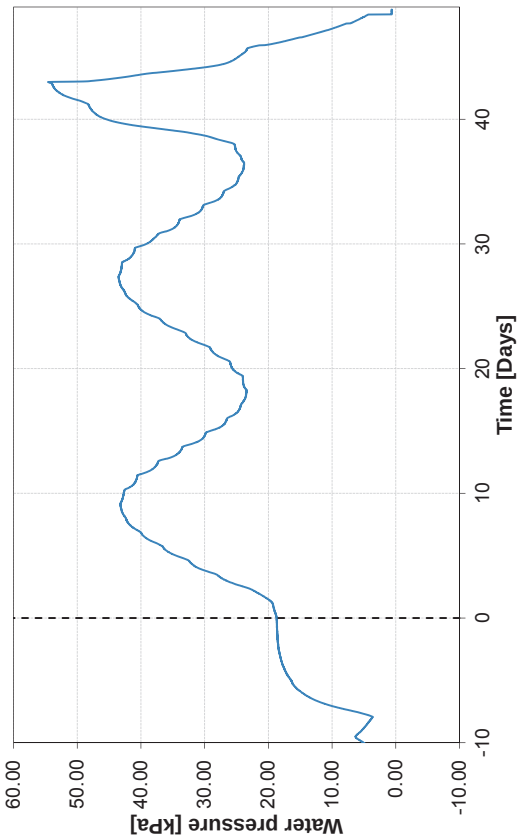

PPT 9

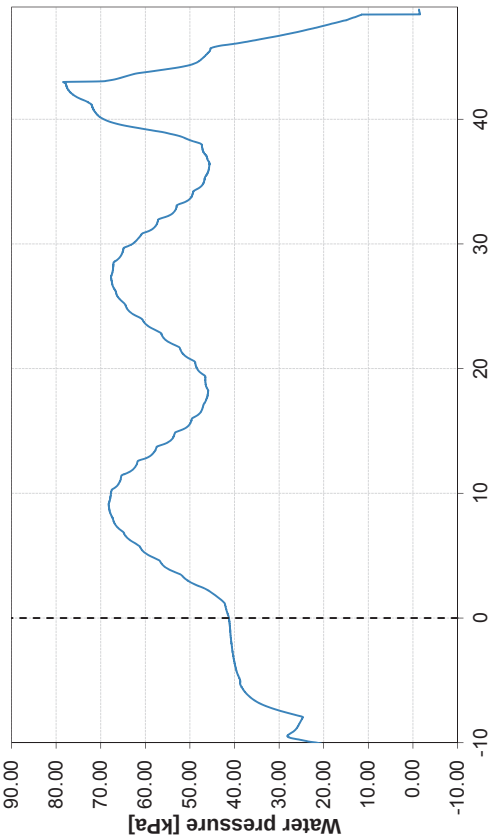

PPT 11

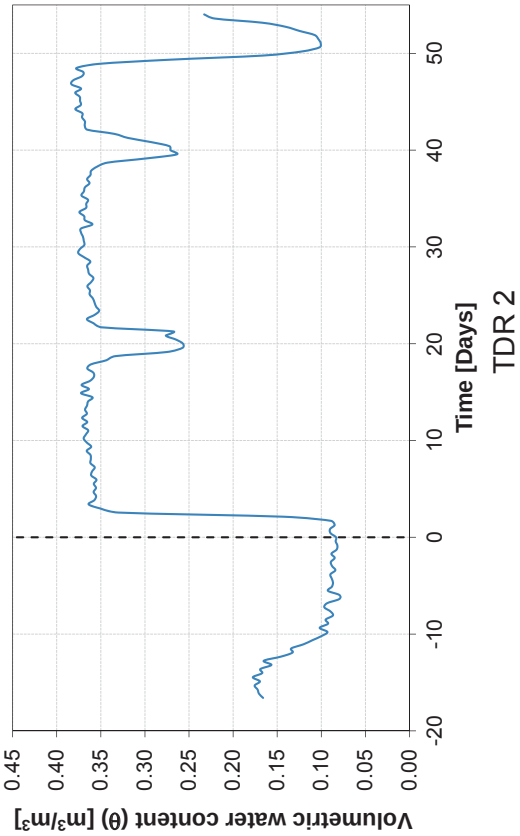
Volumetric water content (θ) [m³/m³]
0.45
0.40
0.35
0.30
0.25
0.20
0.15
0.10
0.05
0.00
-20
-10
0
10
20
30
40
50
Time [Days]
TDR 2

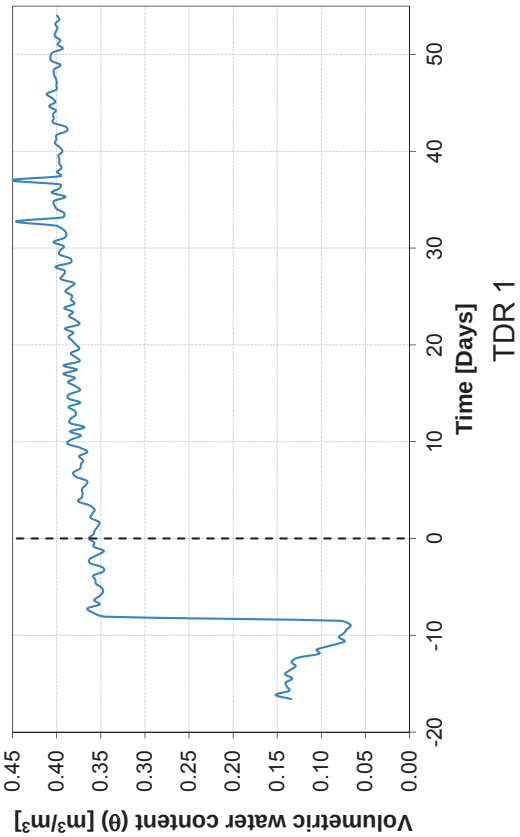
Volumetric water content (θ) [m³/m³]
0.45
0.40
0.35
0.30
0.25
0.20
0.15
0.10
0.05
0.00
-20
-10
0
10
20
30
40
50
Time [Days]
TDR 1

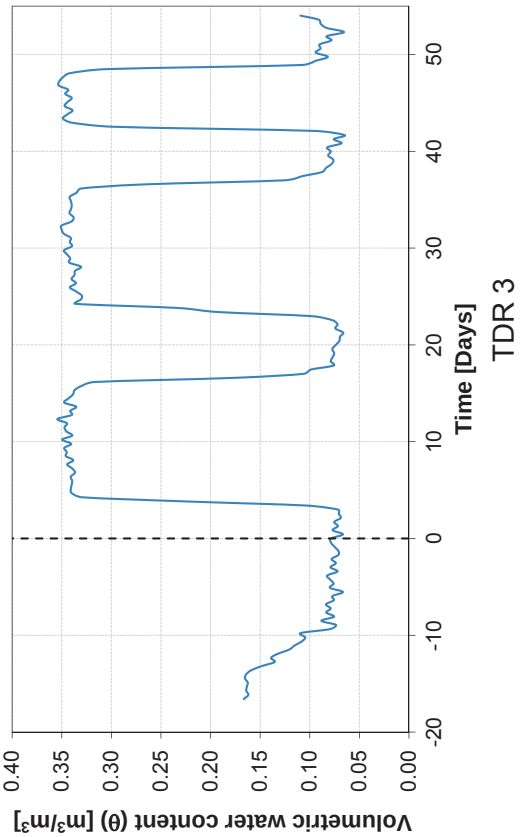
Volumetric water content (θ) [m³/m³]
0.40
0.35
0.30
0.25
0.20
0.15
0.10
0.05
0.00
-20
-10
0
10
20
30
40
50
Time [Days]
TDR 3

TDR 4

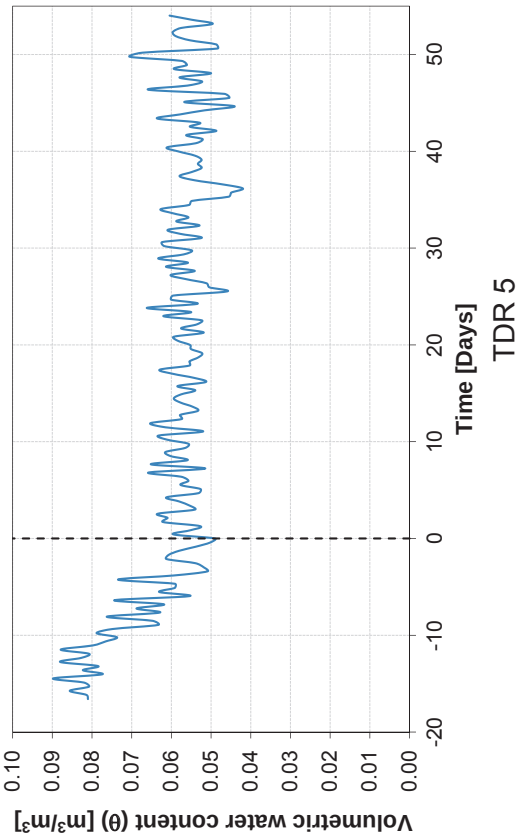

TDR 5

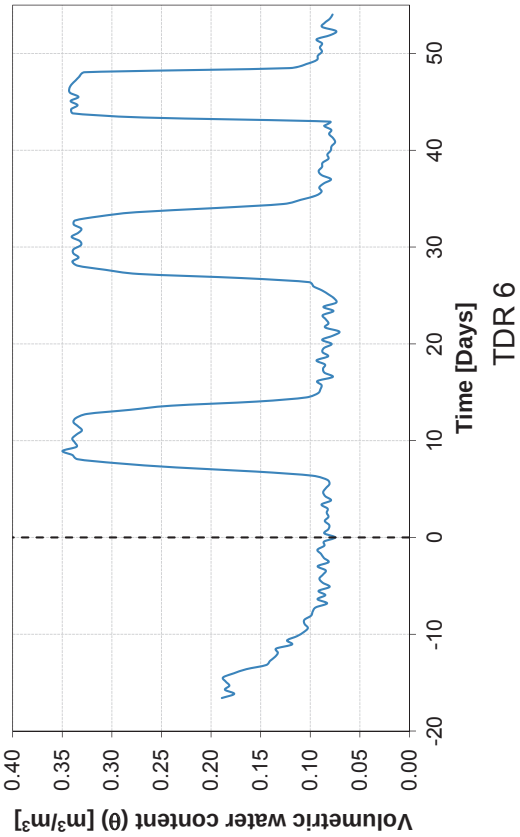

TDR 6

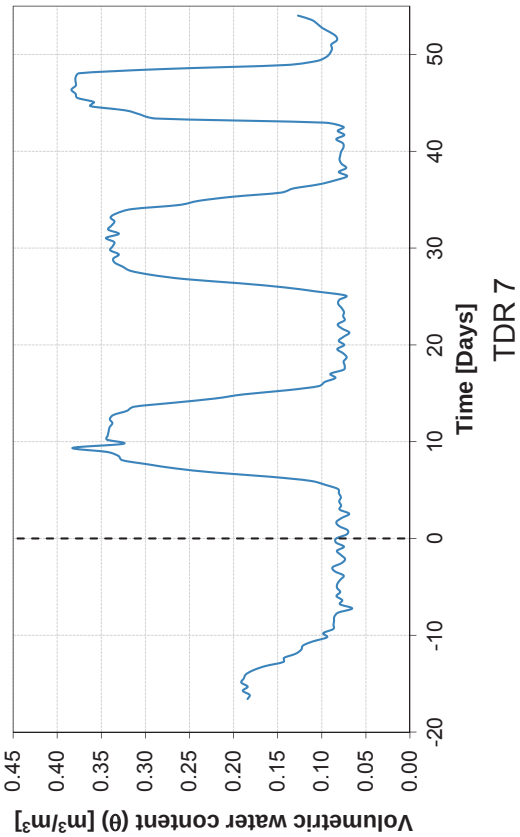

TDR 7

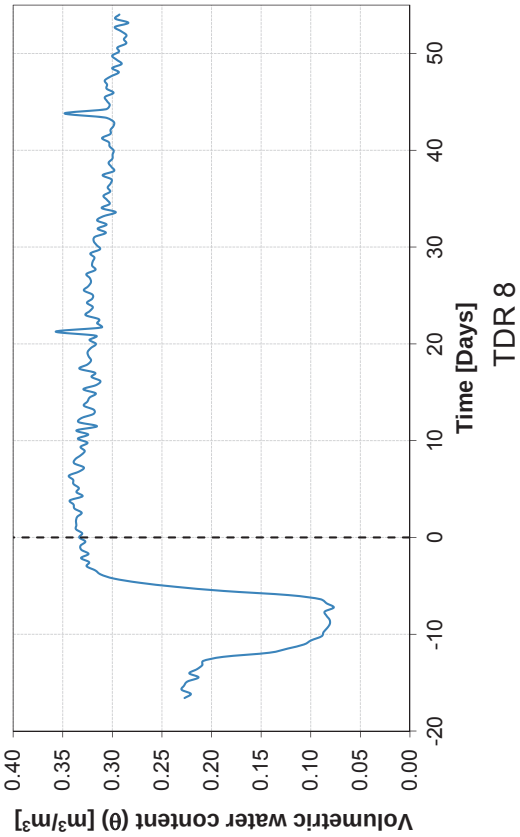

TDR 8

A1.2 Homogeneous dyke, slope gradient = 1:2.5

PPT 1	PPT 2
PPT 3	PPT 4
PPT 5	PPT 6
PPT 7	PPT 8
PPT 9	PPT 10
PPT 11	PPT 12
TDR 1	TDR 2
TDR 3	TDR 4
TDR 5	TDR 6
TDR 7	TDR 8

A1.3 Homogeneous dyke, slope gradient = 1:3.0

PPT 1	PPT 2
PPT 3	PPT 4
PPT 5	PPT 6
PPT 7	PPT 8
PPT 9	PPT 10
PPT 11	PPT 12
TDR 1	TDR 2
TDR 3	TDR 4
TDR 5	TDR 6
TDR 7	TDR 8

A1.4 Dyke with a toe filter, slope gradient = 1:2.0

PPT 1	PPT 2
PPT 3	PPT 4
PPT 5	PPT 6
PPT 7	PPT 8
PPT 9	PPT 10
PPT 11	PPT 12
TDR 1	TDR 2
TDR 3	TDR 4
TDR 5	TDR 6
TDR 7	TDR 8

A1.5 Dyke with a toe filter, slope gradient = 1:2.5

PPT 1	PPT 2
PPT 3	PPT 4
PPT 5	PPT 6
PPT 7	PPT 8
PPT 9	PPT 10
PPT 11	PPT 12
TDR 1	TDR 2
TDR 3	TDR 4
TDR 5	TDR 6
TDR 7	TDR 8

A1.6 Dyke with a toe filter, slope gradient = 1:3.0

PPT 1	PPT 2
PPT 3	PPT 4
PPT 5	PPT 6
PPT 7	PPT 8
PPT 9	PPT 10
PPT 11	PPT 12
TDR 1	TDR 2
TDR 3	TDR 4
TDR 5	TDR 6
TDR 7	TDR 8

A1.7 Dyke with a cut-off wall, slope gradient = 1:2.0

PPT 1	PPT 2
PPT 3	PPT 4
PPT 5	PPT 6
PPT 7	PPT 8
PPT 9	PPT 10
PPT 11	PPT 12
TDR 1	TDR 2
TDR 3	TDR 4
TDR 5	TDR 6
TDR 7	TDR 8

A1.8 Dyke with a cut-off wall, slope gradient = 1:2.5

PPT 1	PPT 2
PPT 3	PPT 4
PPT 5	PPT 6
PPT 7	PPT 8
PPT 9	PPT 10
PPT 11	PPT 12
TDR 1	TDR 2
TDR 3	TDR 4
TDR 5	TDR 6
TDR 7	TDR 8

A1.9 Dyke with a cut-off wall, slope gradient = 1:3.0

PPT 1	PPT 2
PPT 3	PPT 4
PPT 5	PPT 6
PPT 7	PPT 8
PPT 9	PPT 10
PPT 11	PPT 12
TDR 1	TDR 2
TDR 3	TDR 4
TDR 5	TDR 6
TDR 7	TDR 8

A1.10 Dyke with a cut-off wall and a toe filter, slope gradient = 1:2.0

PPT 1	PPT 2
PPT 3	PPT 4
PPT 5	PPT 6
PPT 7	PPT 8
PPT 9	PPT 10
PPT 11	PPT 12
TDR 1	TDR 2
TDR 3	TDR 4
TDR 5	TDR 6
TDR 7	TDR 8

A1.11 Dyke with a cut-off wall and a toe filter, slope gradient = 1:2.5

PPT 1	PPT 2
PPT 3	PPT 4
PPT 5	PPT 6
PPT 7	PPT 8
PPT 9	PPT 10
PPT 11	PPT 12
TDR 1	TDR 2
TDR 3	TDR 4
TDR 5	TDR 6
TDR 7	TDR 8

A1.12 Dyke with a cut-off wall and a toe filter, slope gradient = 1:3.0

PPT 1	PPT 2
PPT 3	PPT 4
PPT 5	PPT 6
PPT 7	PPT 8
PPT 9	PPT 10
PPT 11	PPT 12
TDR 1	TDR 2
TDR 3	TDR 4
TDR 5	TDR 6
TDR 7	TDR 8

Appendix 2 Comparison between field test and numerical modeling for model calibration

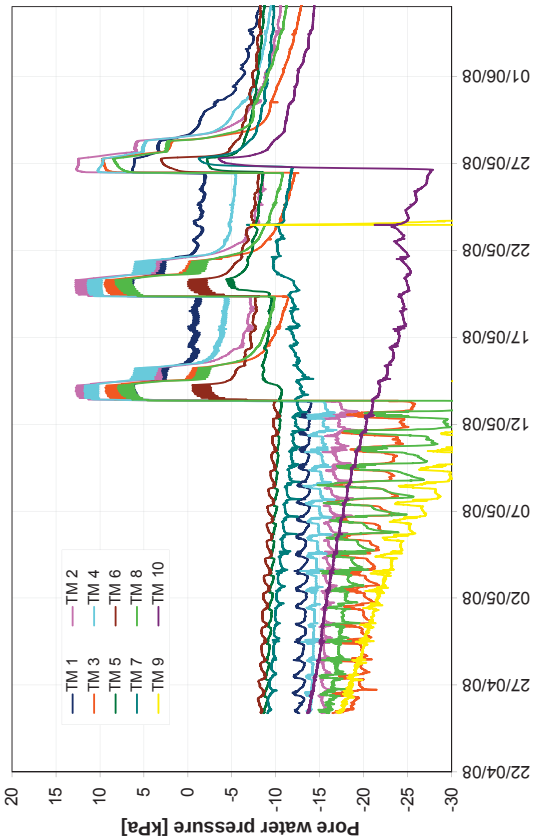
Pore water pressure [kPa]
20
15
10
5
0
-5
-10
-15
-20
-25
-30
22/04/08
27/04/08
02/05/08
07/05/08
12/05/08
17/05/08
22/05/08
27/05/08
01/06/08
TM 1
TM 2
TM 3
TM 4
TM 5
TM 6
TM 7
TM 8
TM 9
TM 10

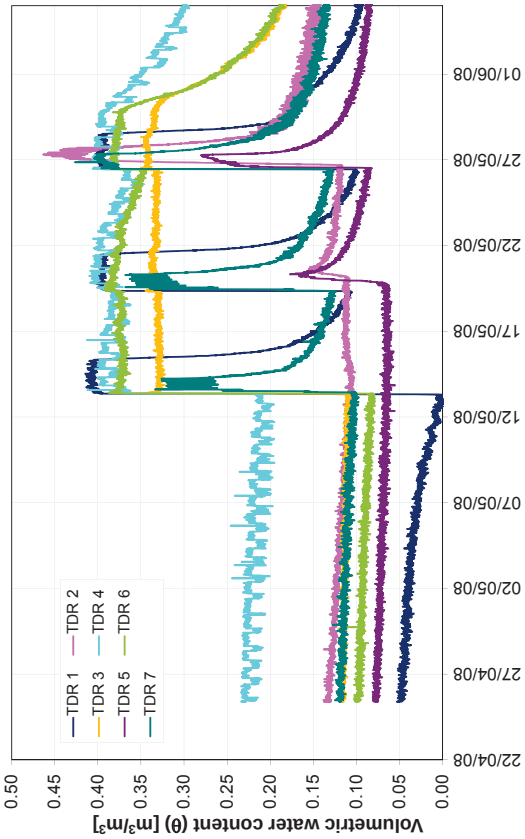
Volumetric water content (θ) [m3/m3]
0.50
0.45
0.40
0.35
0.30
0.25
0.20
0.15
0.10
0.05
0.00
22/04/08
27/04/08
02/05/08
07/05/08
12/05/08
17/05/08
22/05/08
27/05/08
01/06/08
TDR 1
TDR 2
TDR 3
TDR 4
TDR 5
TDR 6
TDR 7

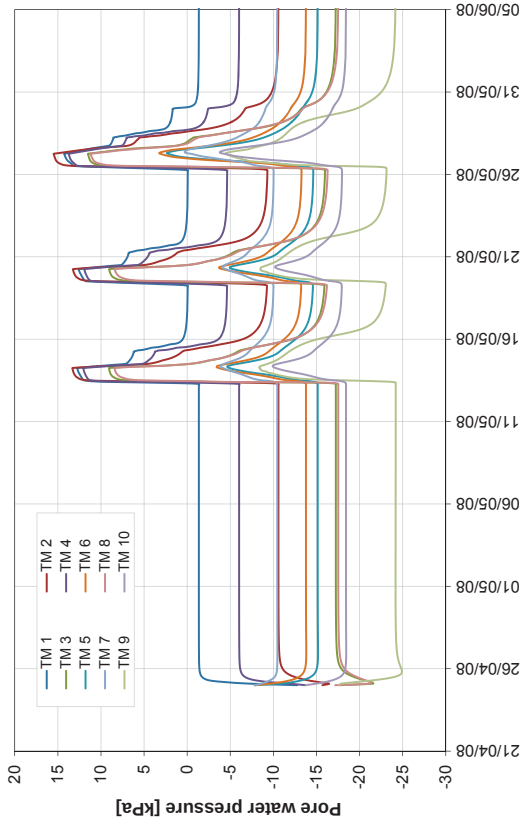
Pore water pressure [kPa]
20
15
10
5
0
-5
-10
-15
-20
-25
-30
21/04/08
26/04/08
01/05/08
06/05/08
11/05/08
16/05/08
21/05/08
26/05/08
31/05/08
05/06/08
TM 1
TM 2
TM 3
TM 4
TM 5
TM 6
TM 7
TM 8
TM 9
TM 10

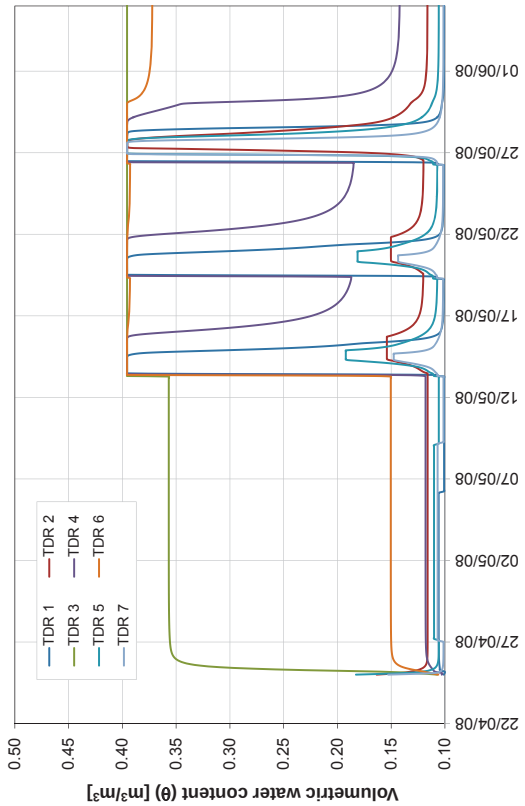
Volumetric water content (θ) [m3/m3]
0.50
0.45
0.40
0.35
0.30
0.25
0.20
0.15
0.10
22/04/08
27/04/08
02/05/08
07/05/08
12/05/08
17/05/08
22/05/08
27/05/08
01/06/08
TDR 1
TDR 2
TDR 3
TDR 4
TDR 5
TDR 6
TDR 7

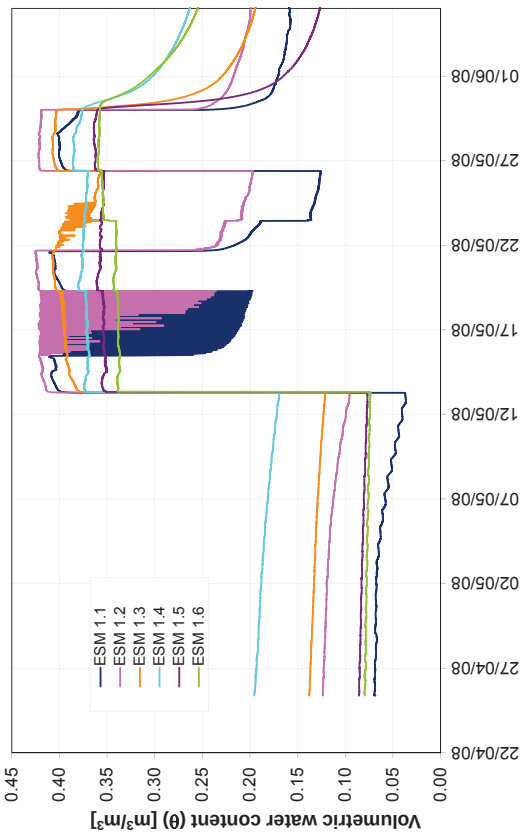
Volumetric water content (θ) [m3/m3]
0.45
0.40
0.35
0.30
0.25
0.20
0.15
0.10
0.05
0.00
22/04/08
27/04/08
02/05/08
07/05/08
12/05/08
17/05/08
22/05/08
27/05/08
01/06/08
ESM 1.1
ESM 1.2
ESM 1.3
ESM 1.4
ESM 1.5
ESM 1.6

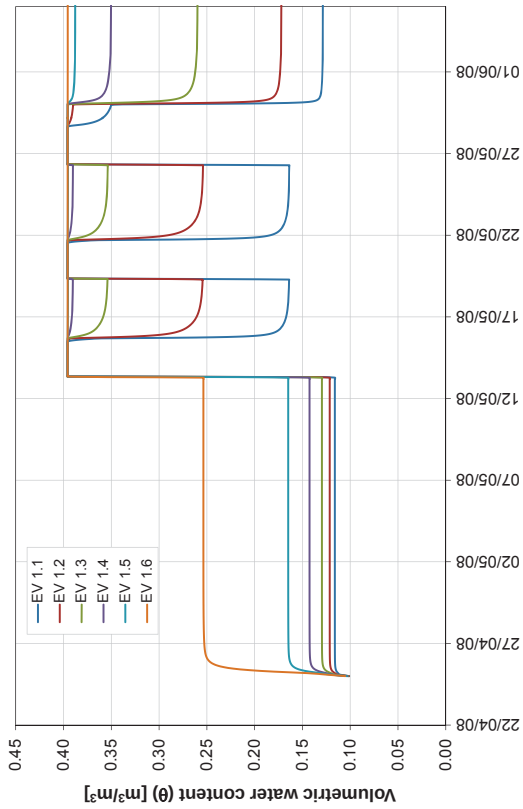
Volumetric water content (θ) [m3/m3]
0.45
0.40
0.35
0.30
0.25
0.20
0.15
0.10
0.05
0.00
22/04/08
27/04/08
02/05/08
07/05/08
12/05/08
17/05/08
22/05/08
27/05/08
01/06/08
EV 1.1
EV 1.2
EV 1.3
EV 1.4
EV 1.5
EV 1.6

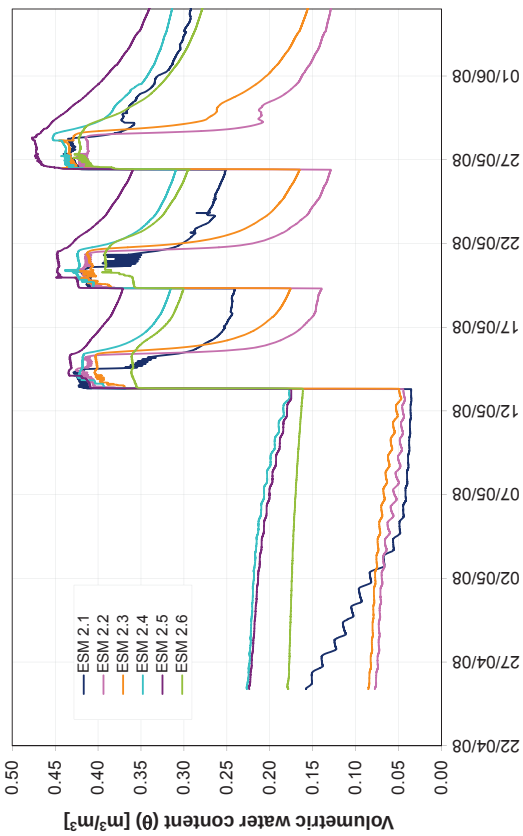
Volumetric water content (θ) [m3/m3]
0.50
0.45
0.40
0.35
0.30
0.25
0.20
0.15
0.10
0.05
0.00
22/04/08
27/04/08
02/05/08
07/05/08
12/05/08
17/05/08
22/05/08
27/05/08
01/06/08
ESM 2.1
ESM 2.2
ESM 2.3
ESM 2.4
ESM 2.5
ESM 2.6

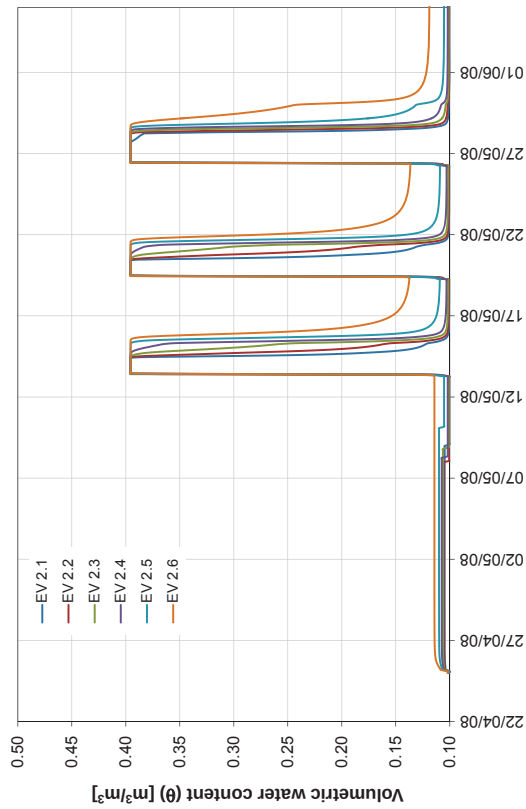
Volumetric water content (θ) [m3/m3]
0.50
0.45
0.40
0.35
0.30
0.25
0.20
0.15
0.10
22/04/08
27/04/08
02/05/08
07/05/08
12/05/08
17/05/08
22/05/08
27/05/08
01/06/08
EV 2.1
EV 2.2
EV 2.3
EV 2.4
EV 2.5
EV 2.6

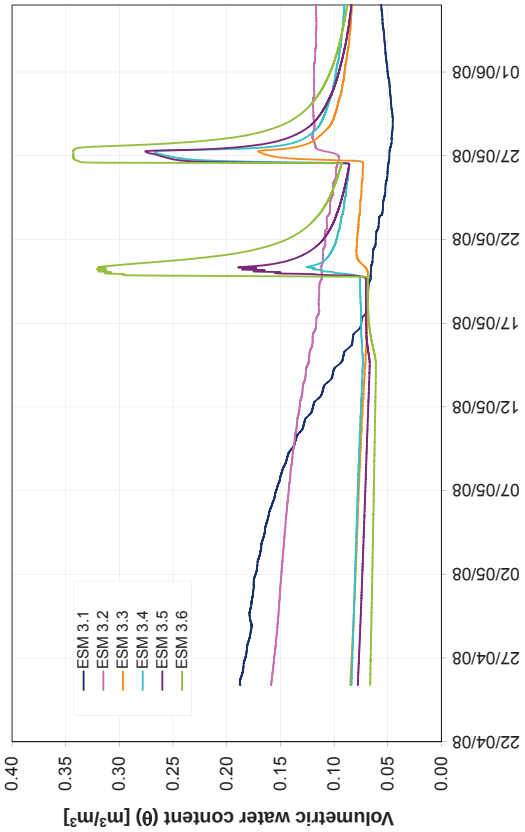
ESM 3.1
ESM 3.2
ESM 3.3
ESM 3.4
ESM 3.5
ESM 3.6
Volumetric water content (θ) [m3/m3]
0.40
0.35
0.30
0.25
0.20
0.15
0.10
0.05
0.00
22/04/08
27/04/08
02/05/08
07/05/08
12/05/08
17/05/08
22/05/08
27/05/08
01/06/08

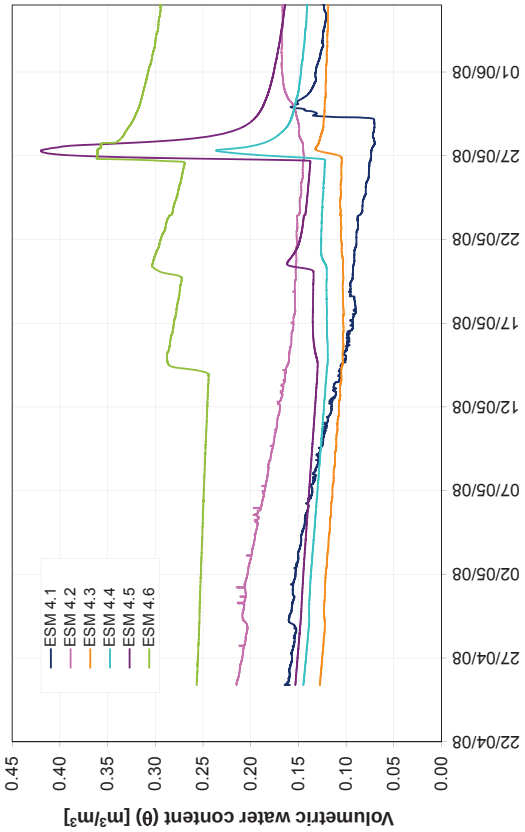
ESM 4.1
ESM 4.2
ESM 4.3
ESM 4.4
ESM 4.5
ESM 4.6
Volumetric water content (θ) [m3/m3]
0.45
0.40
0.35
0.30
0.25
0.20
0.15
0.10
0.05
0.00
22/04/08
27/04/08
02/05/08
07/05/08
12/05/08
17/05/08
22/05/08
27/05/08
01/06/08

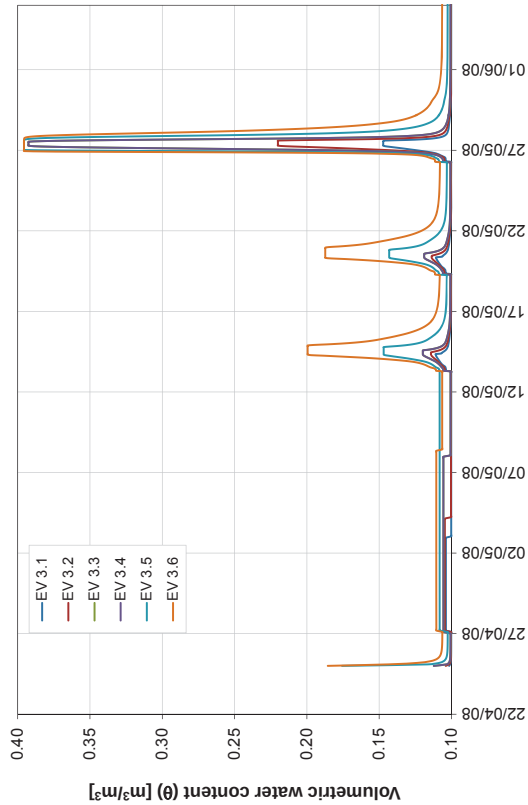
EV 3.1
EV 3.2
EV 3.3
EV 3.4
EV 3.5
EV 3.6
Volumetric water content (θ) [m3/m3]
0.40
0.35
0.30
0.25
0.20
0.15
0.10
22/04/08
27/04/08
02/05/08
07/05/08
12/05/08
17/05/08
22/05/08
27/05/08
01/06/08

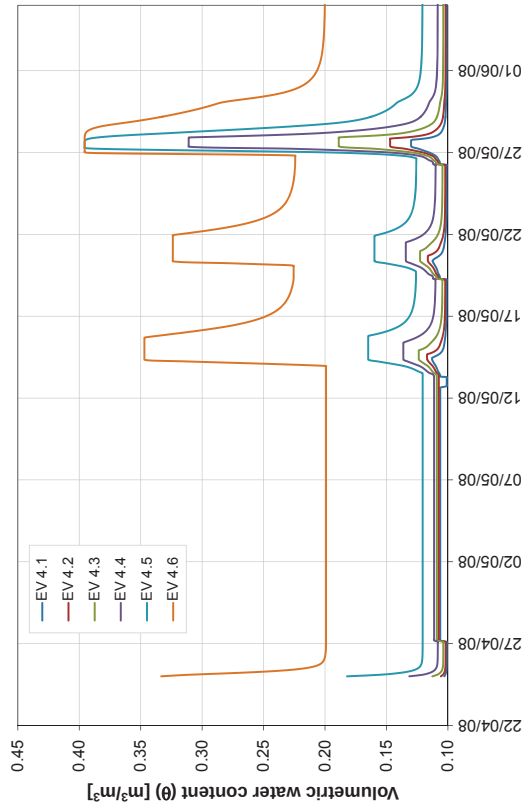
EV 4.1
EV 4.2
EV 4.3
EV 4.4
EV 4.5
EV 4.6
Volumetric water content (θ) [m3/m3]
0.45
0.40
0.35
0.30
0.25
0.20
0.15
0.10
22/04/08
27/04/08
02/05/08
07/05/08
12/05/08
17/05/08
22/05/08
27/05/08
01/06/08

Appendix 3 Oedometer tests on unsaturated Perth sand

A3.1 Matric suction = 0.96 kPa, e= 0.516

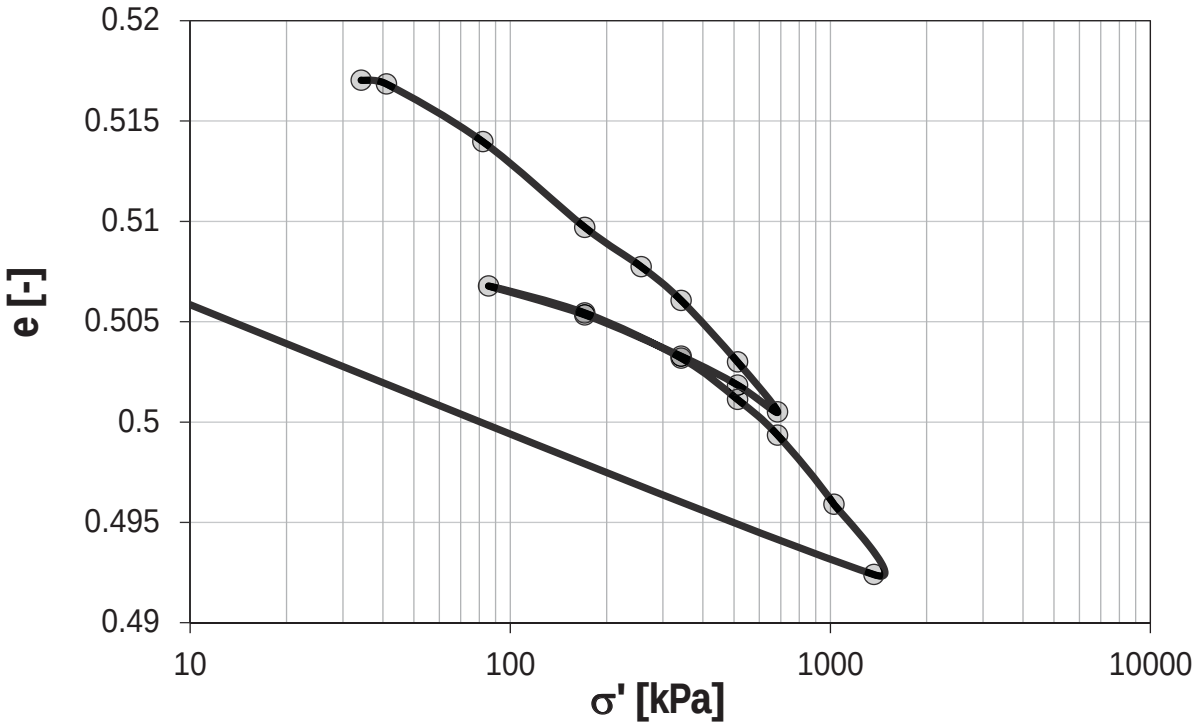

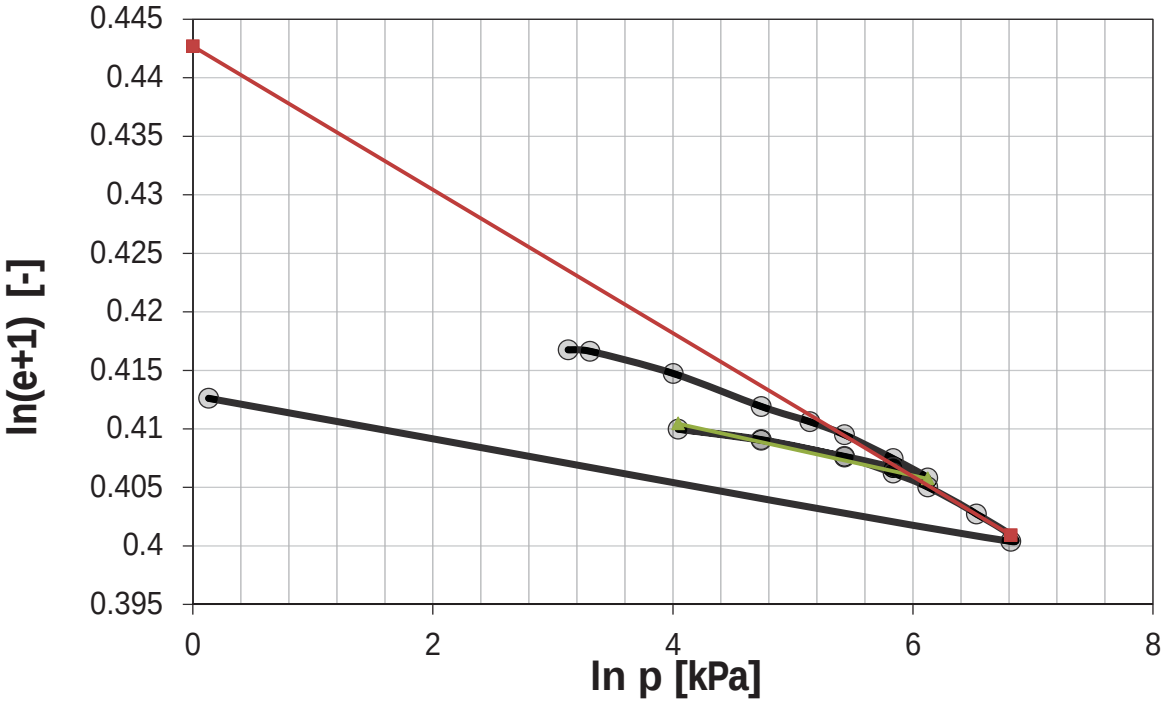

A3.2 Matric suction = 1.95 kPa, e= 0.523

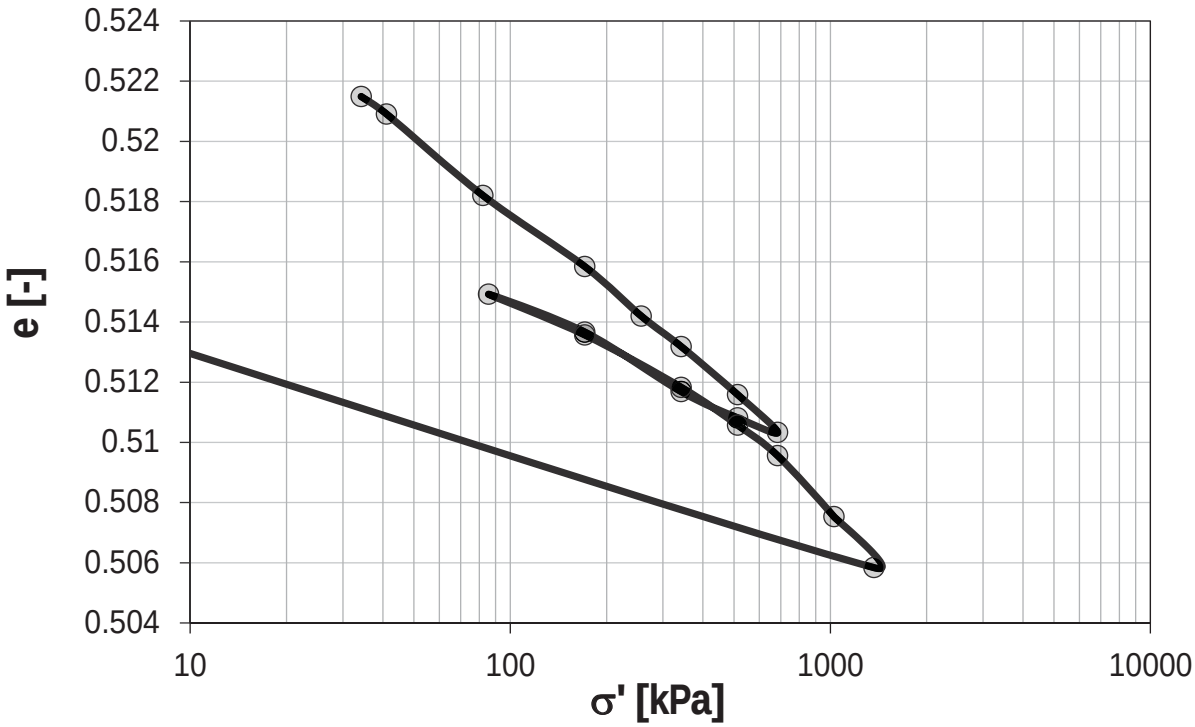

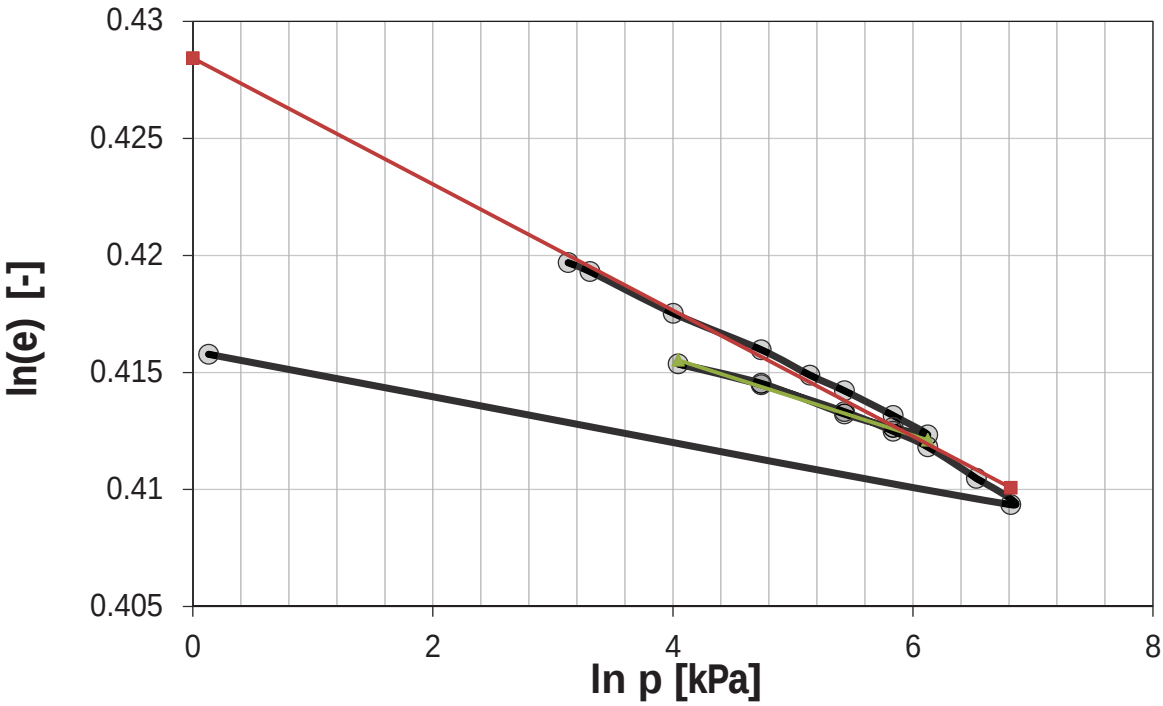

A3.3 Matric suction = 3.30 kPa, e= 0.520

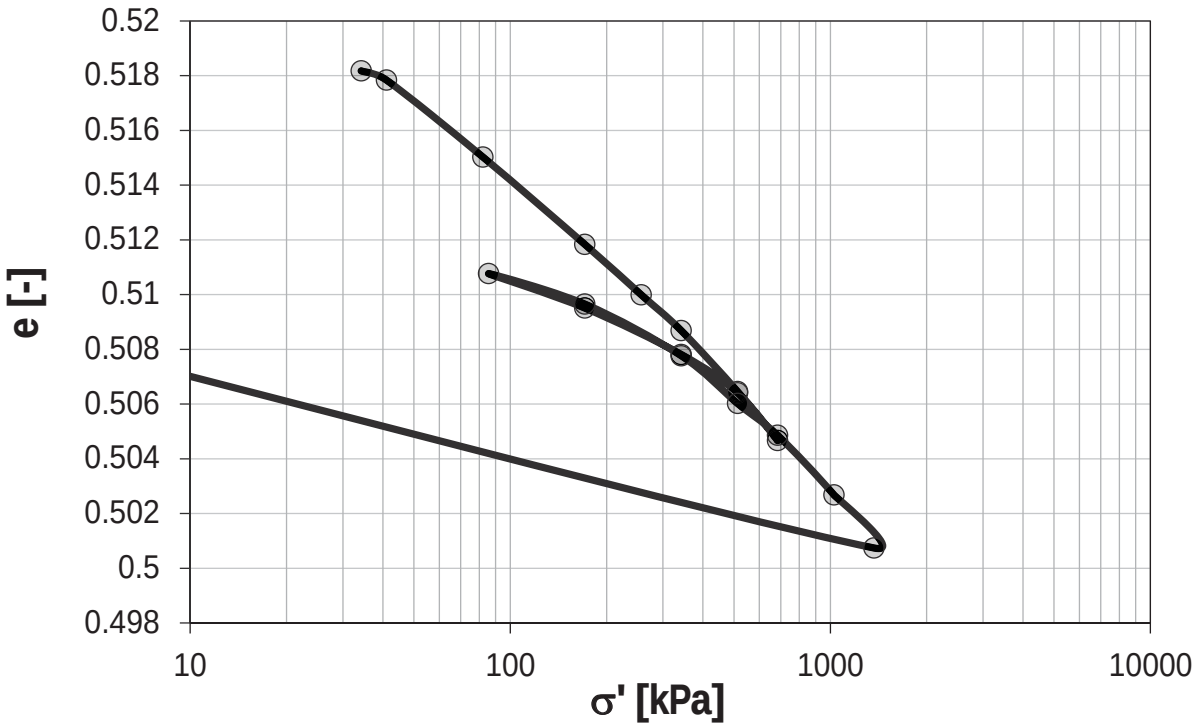

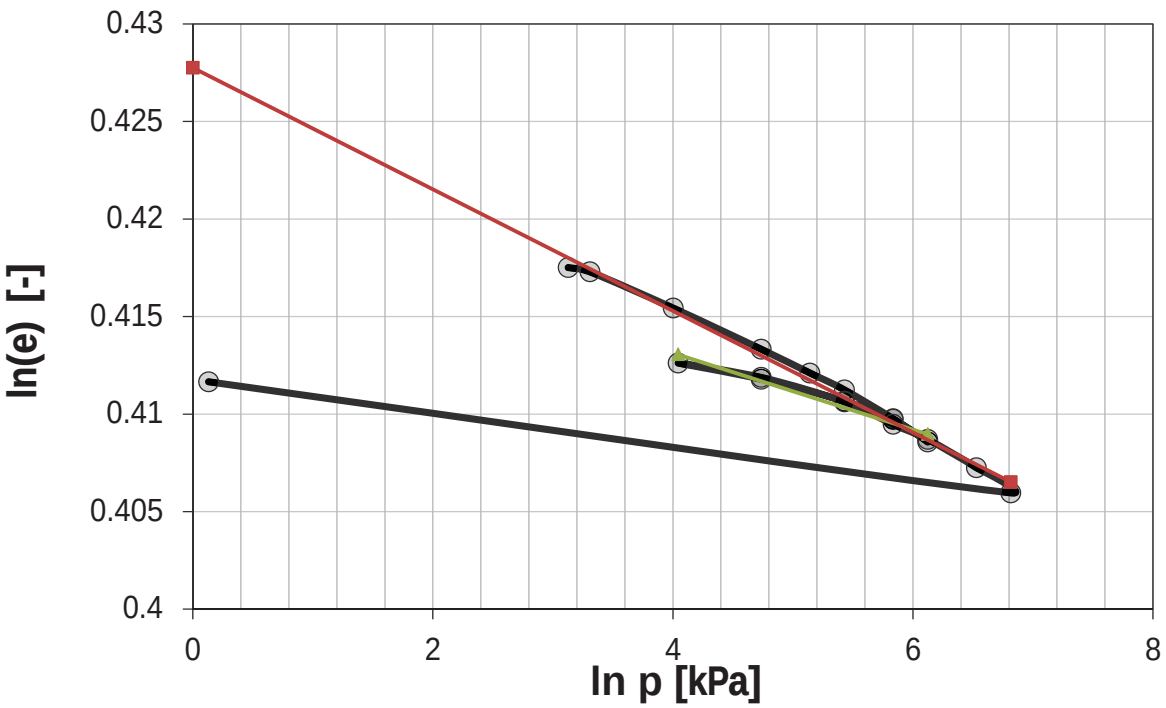

A3.4 Matric suction = 4.39 kPa, e= 0.516

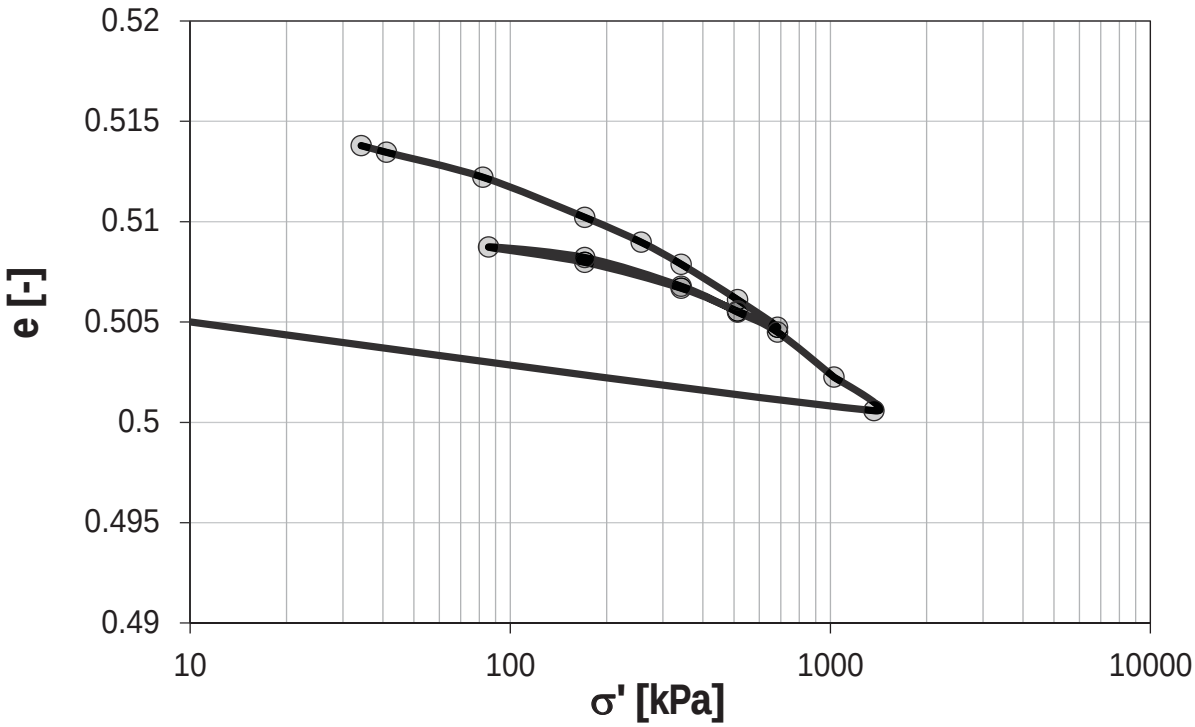

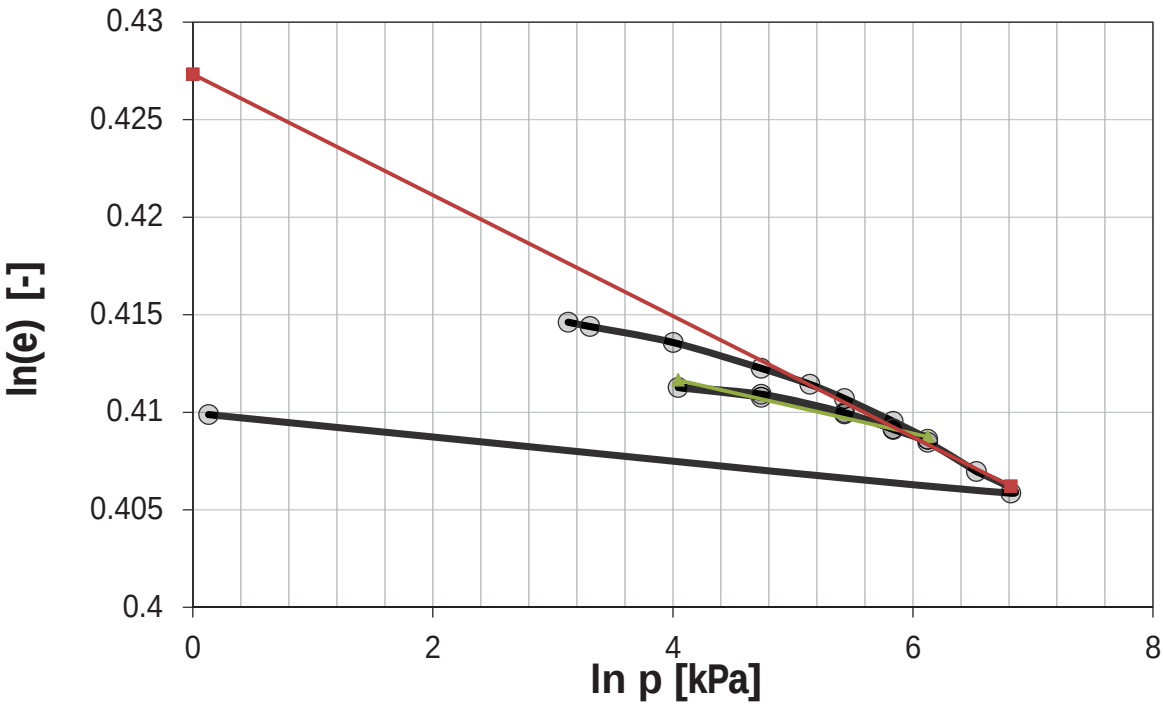

A3.5 Matric suction = 5.67 kPa, e= 0.520

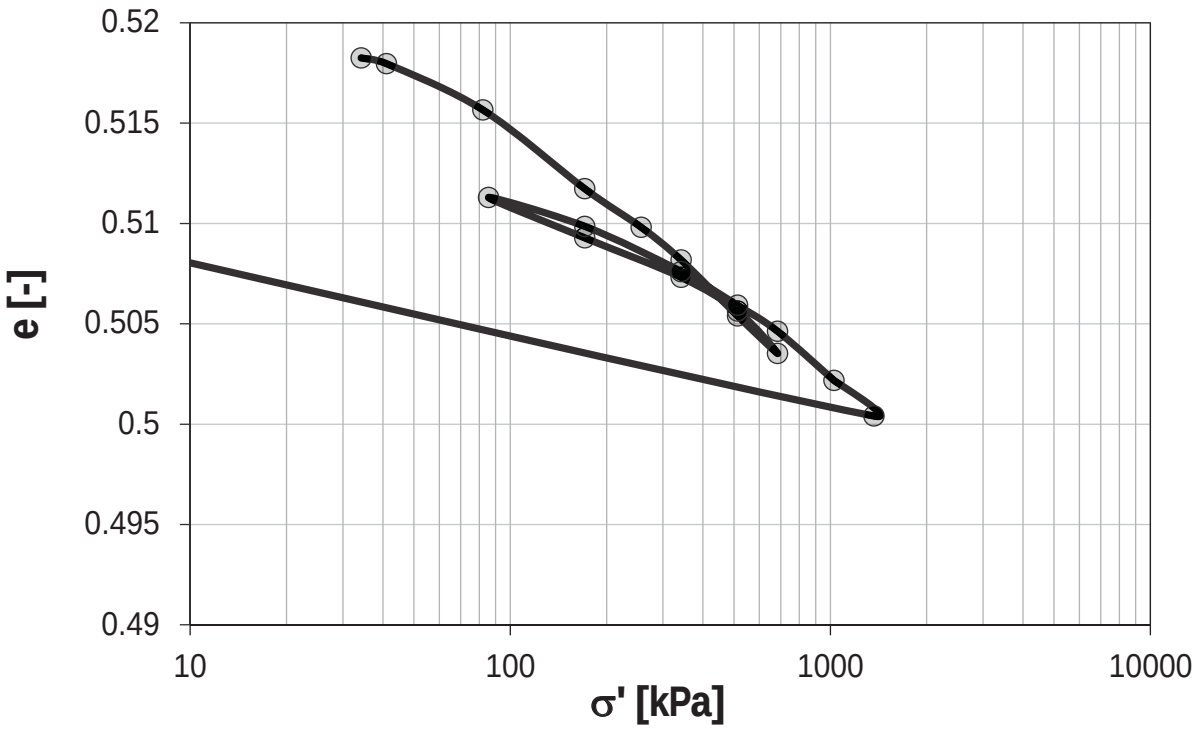

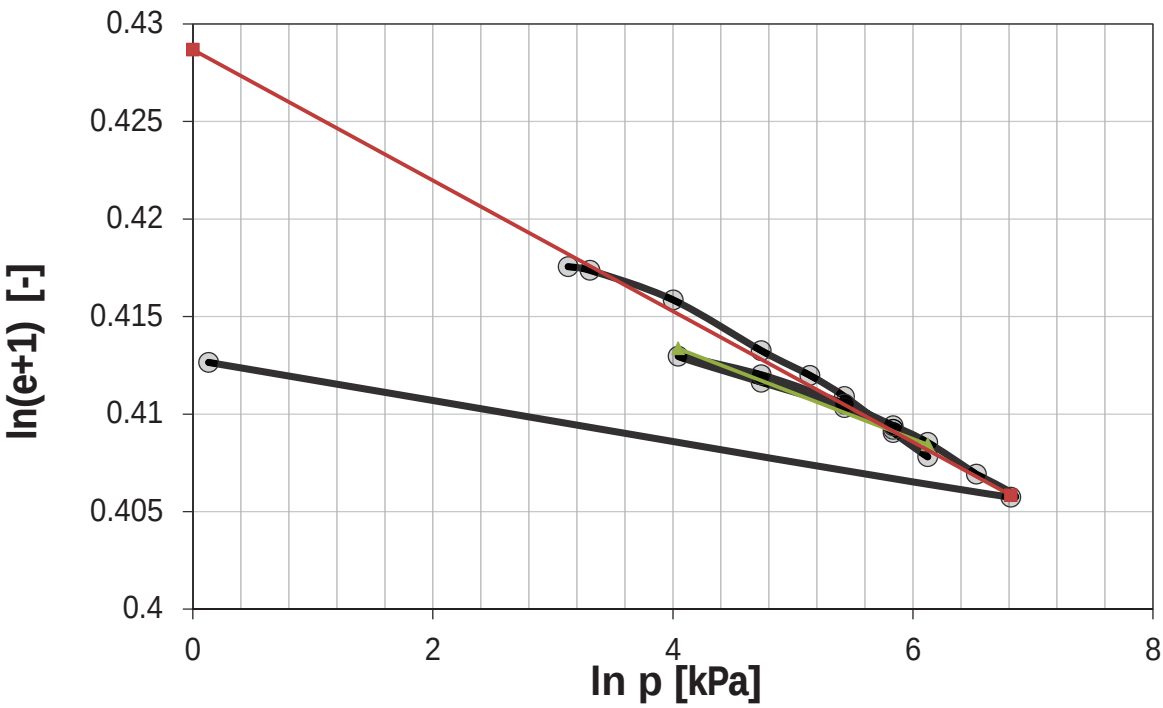

A3.6 Matric suction = 7.01 kPa, e= 0.520

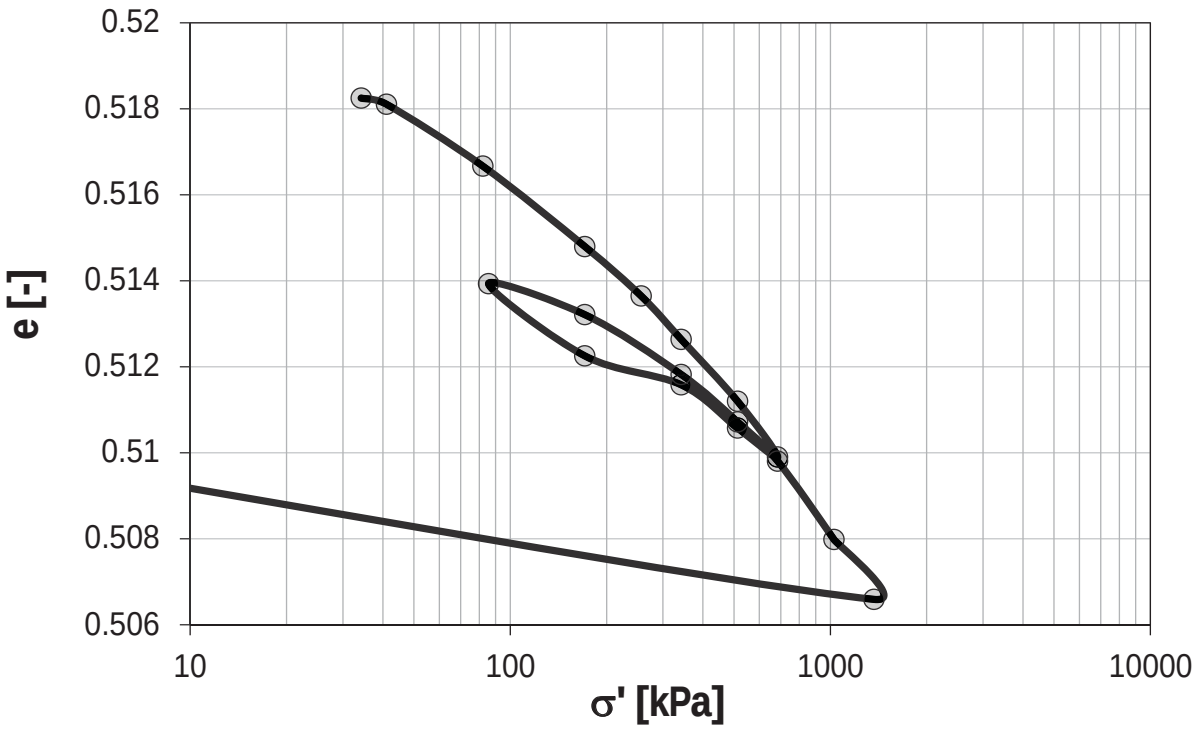

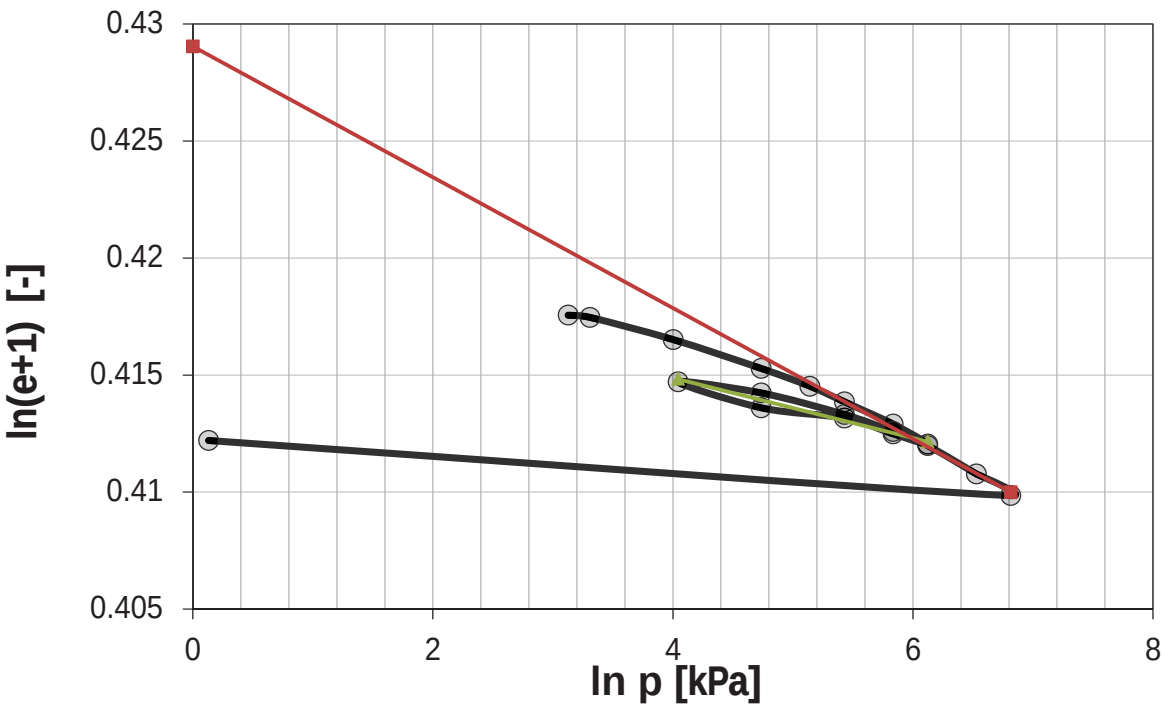

A3.7 Matric suction = 8.98 kPa, e= 0.514

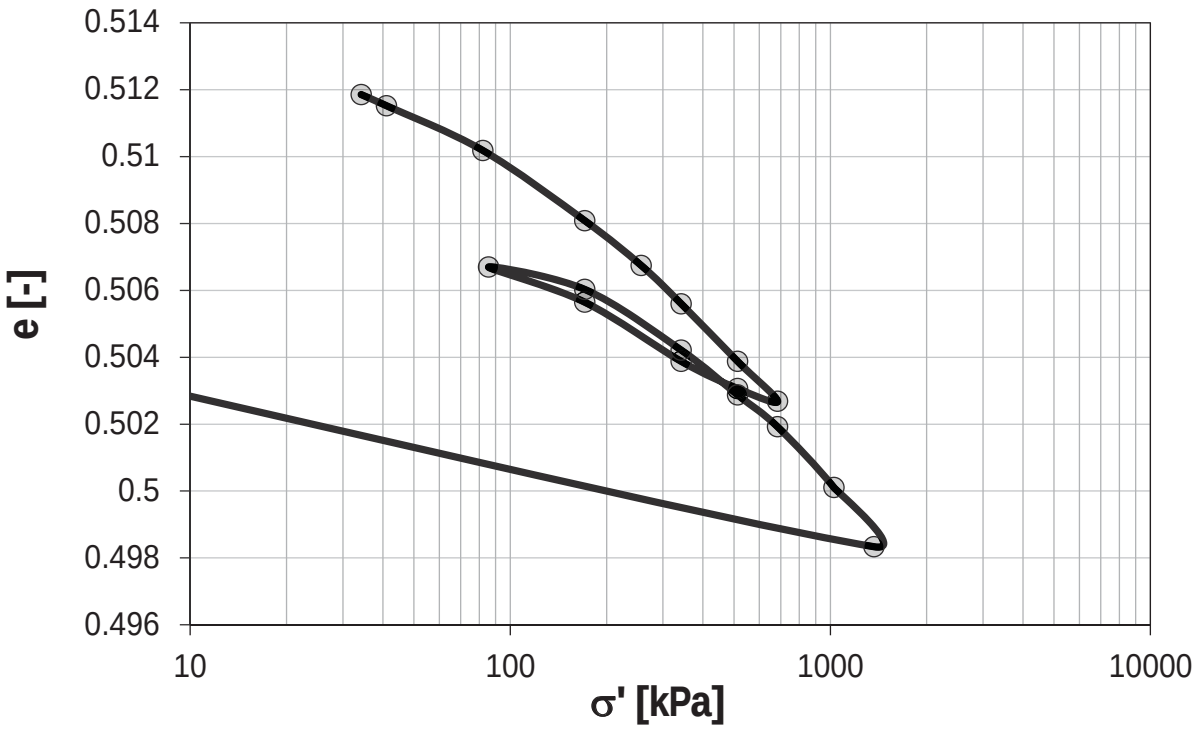

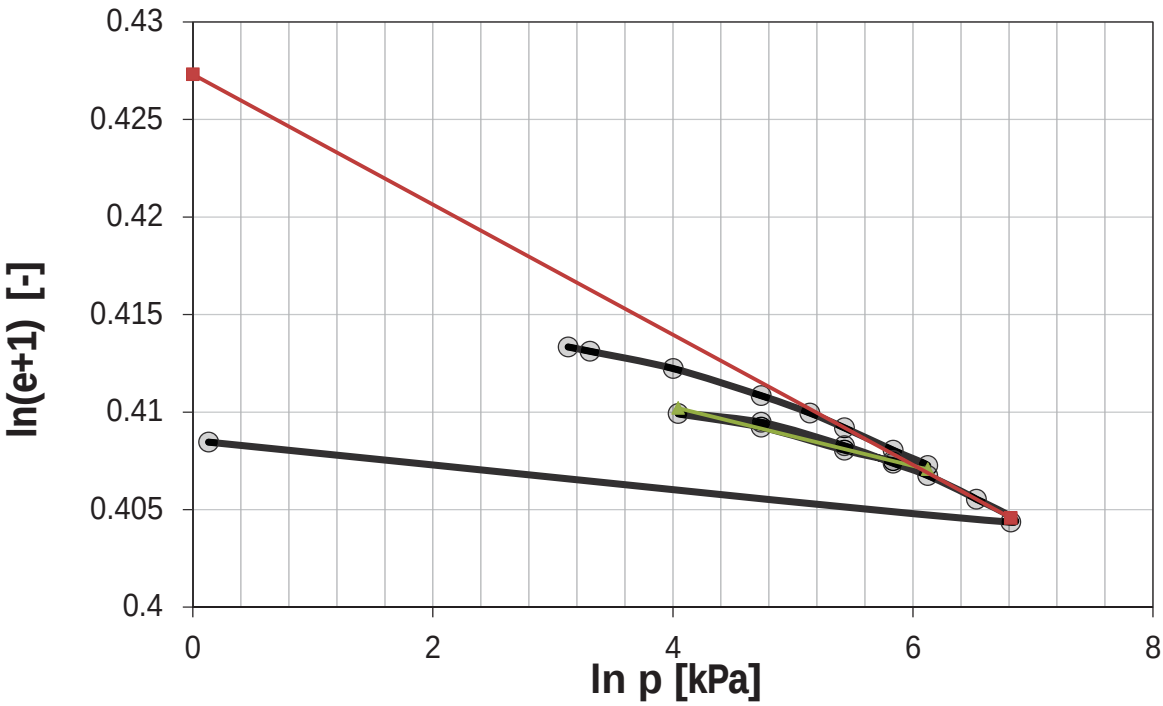

A3.8 Matric suction = 11.32 kPa, e= 0.504

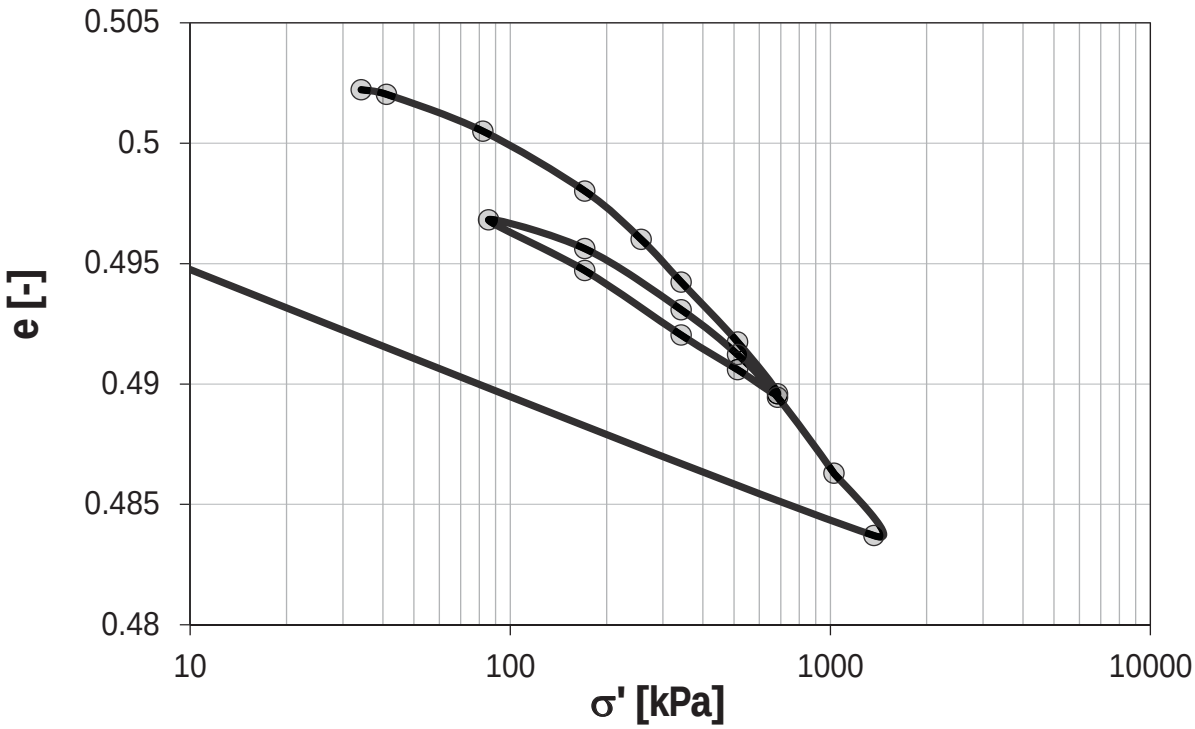

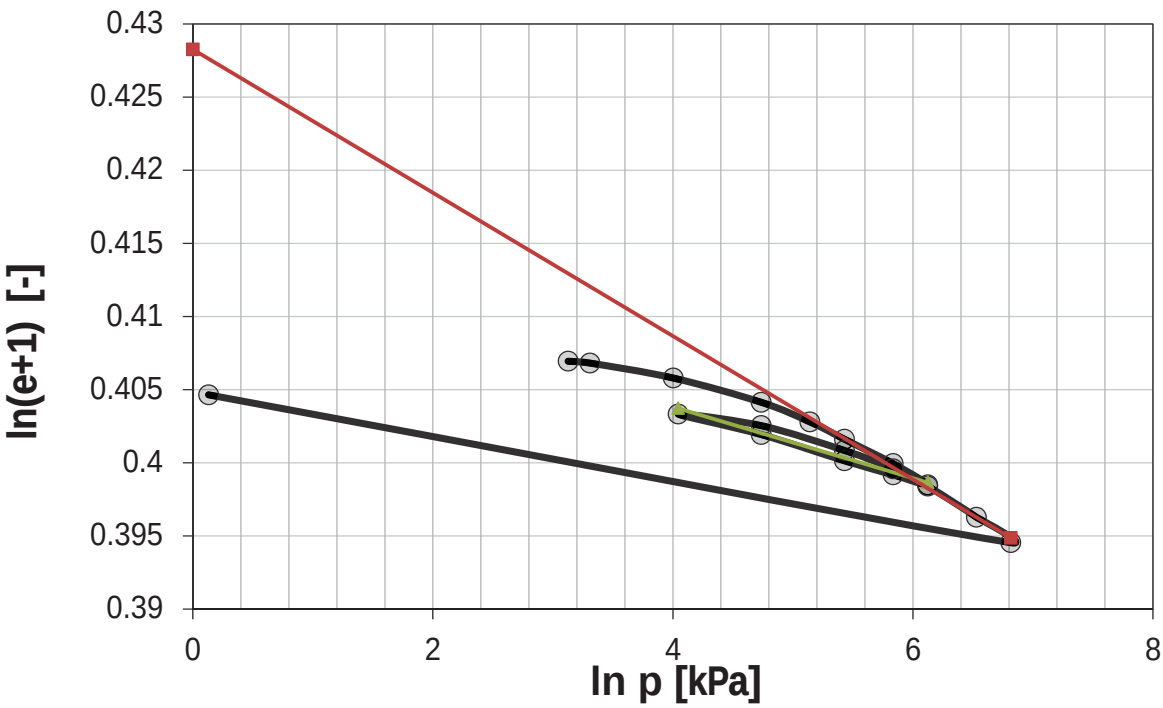

A3.9 Matric suction = 5.65 kPa, e= 0.522

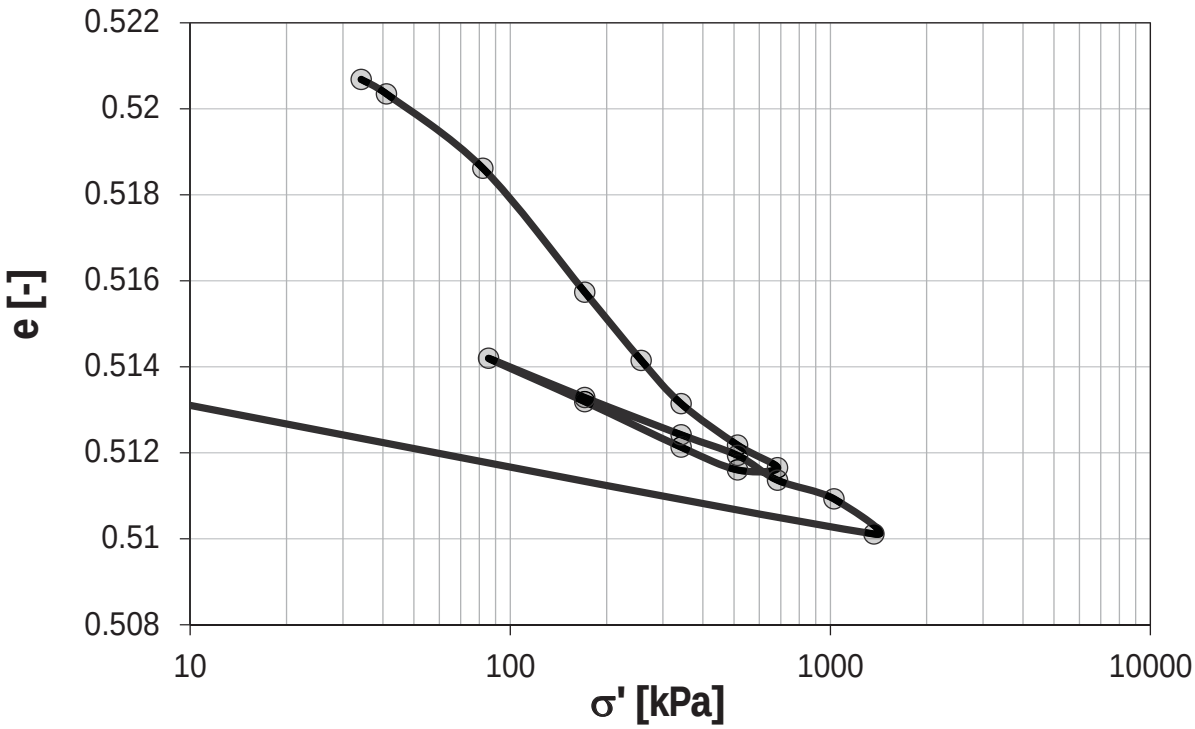

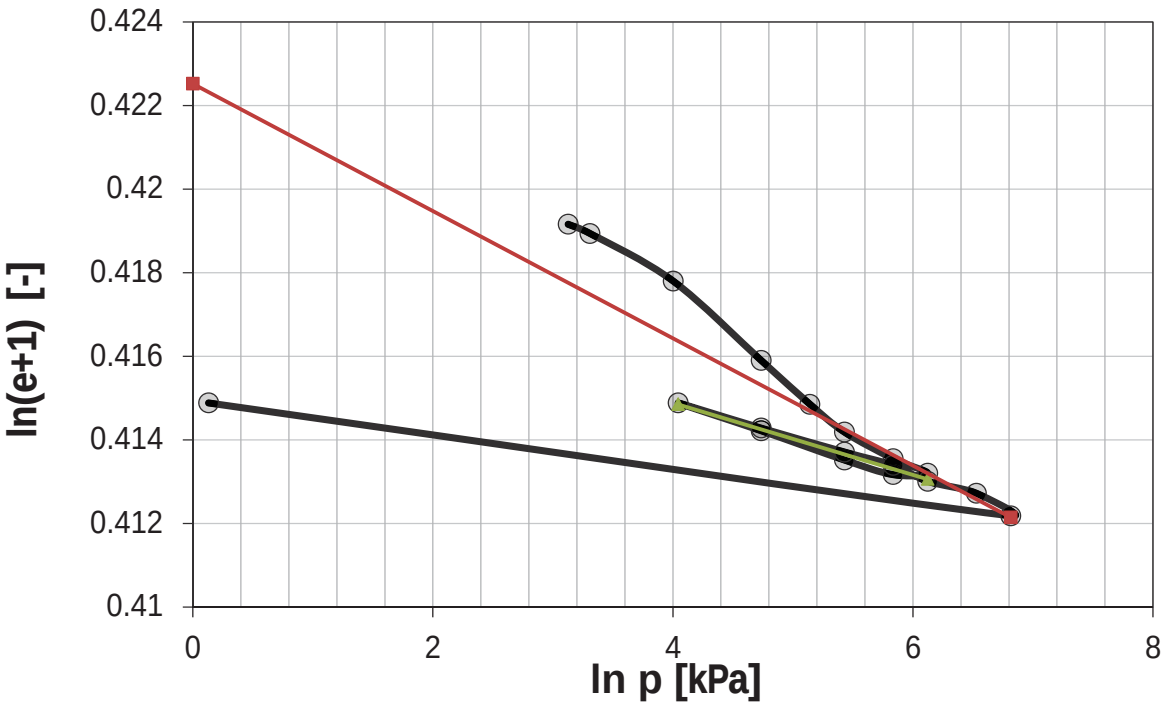

A3.10 Matric suction = 1.08 kPa, e= 0.521

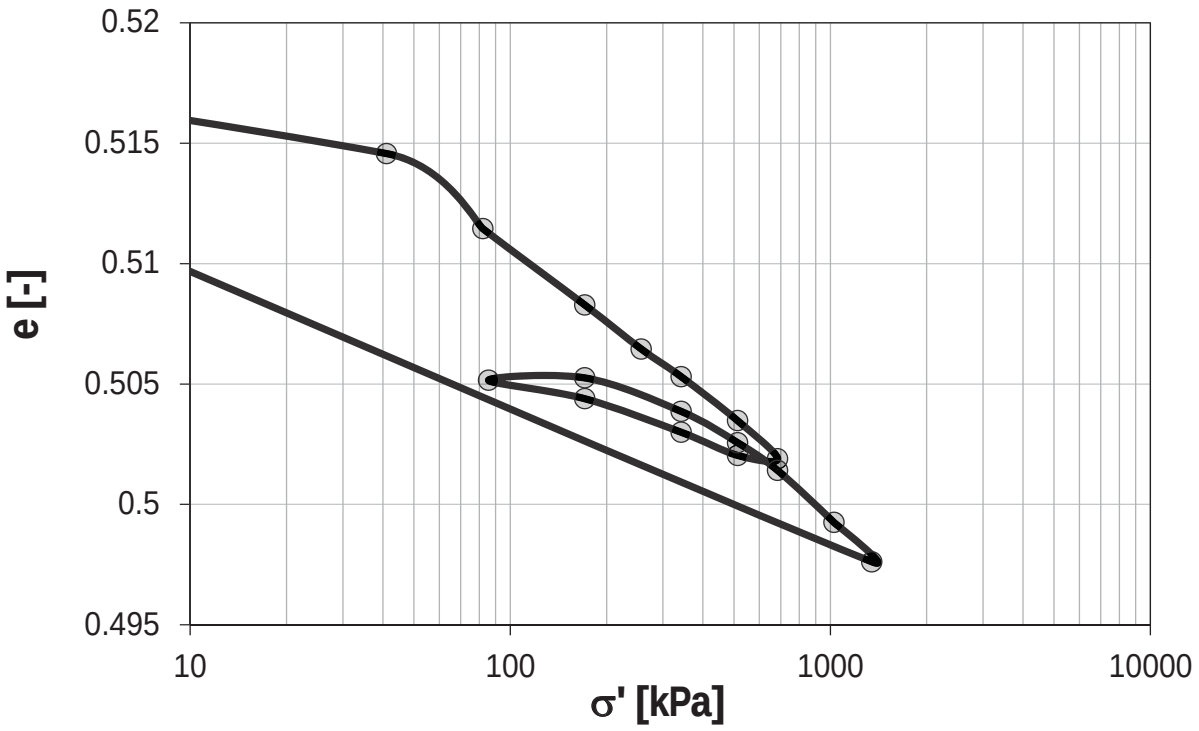

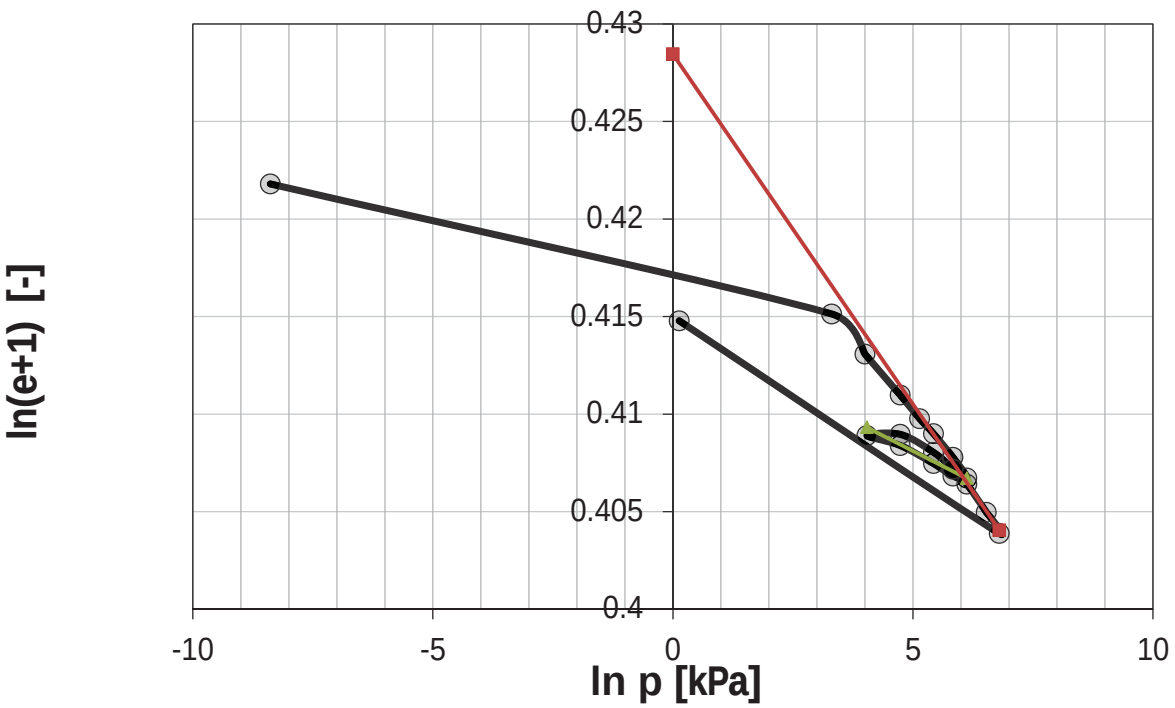

A3.11 Matric suction = 2.35 kPa, e= 0.527

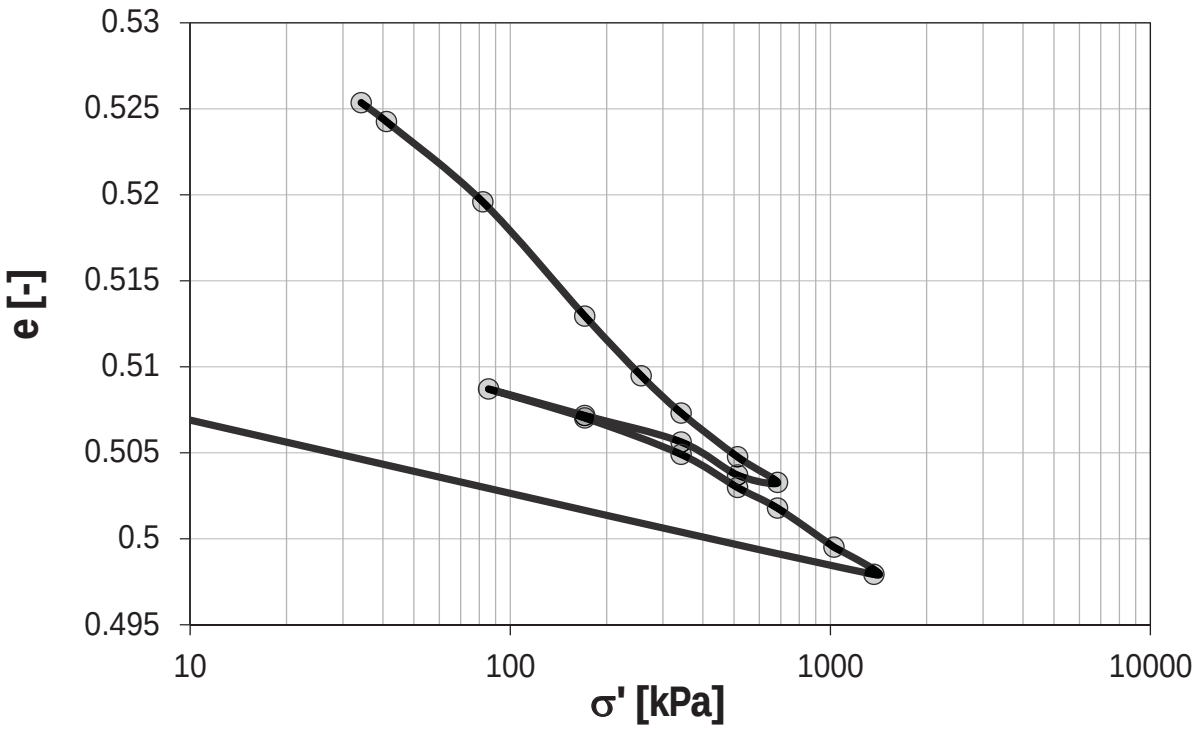

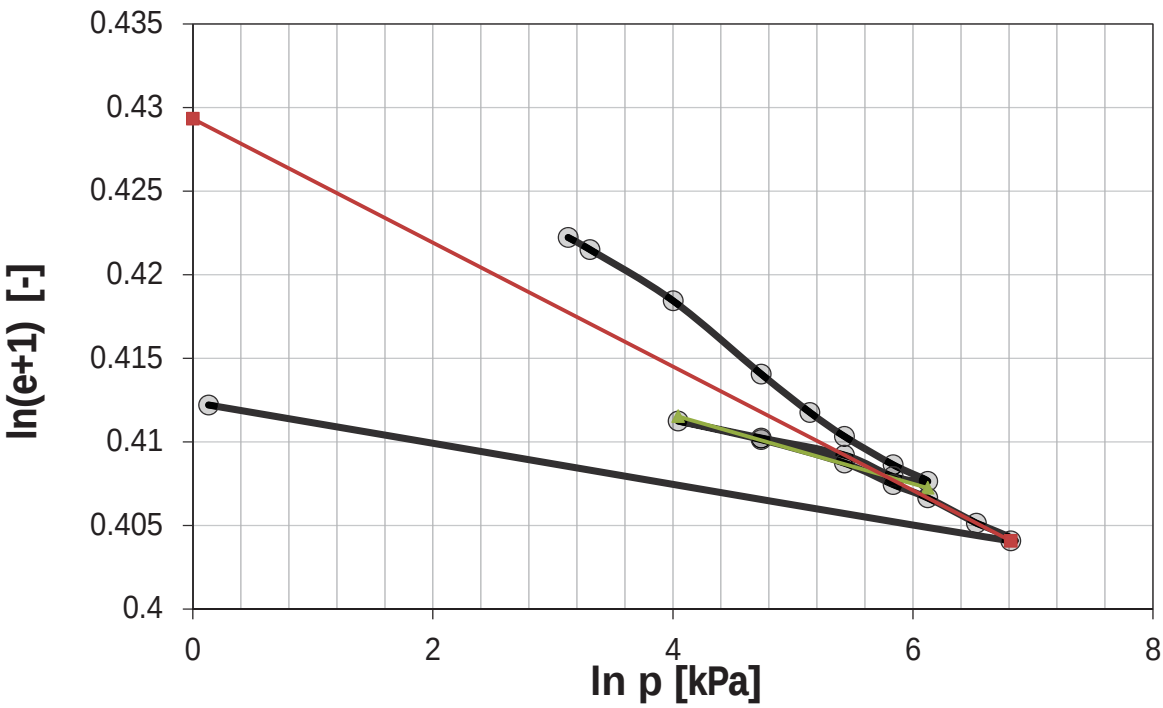

Appendix 4 Triaxial tests on unsaturated Perth sand

$$p'(classic) = \frac{\sigma_1 + 2 \cdot \sigma_3}{3} - u_w \qquad \text{A7.1}$$

$$p'(Bishop) = \frac{\sigma_1 + 2 \cdot \sigma_3}{3} + \left[\left(\frac{AEV}{U_a - U_w} \right)^{0.55} \cdot (U_a - U_w) \right] \qquad \text{A7.2}$$

$$s'(classic) = \frac{\sigma_1 + \sigma_3}{2} - u_w \qquad \text{A7.3}$$

$$s'(Bishop) = \frac{\sigma_1 + \sigma_3}{2} + \left[\left(\frac{AEV}{U_a - U_w} \right)^{0.55} \cdot (U_a - U_w) \right] \qquad \text{A7.4}$$

$$q = \sigma_1 - \sigma_3 \qquad \text{A7.5}$$

$$t = \frac{\sigma_1 - \sigma_3}{2} \qquad \text{A7.6}$$

A4.1 Drained test

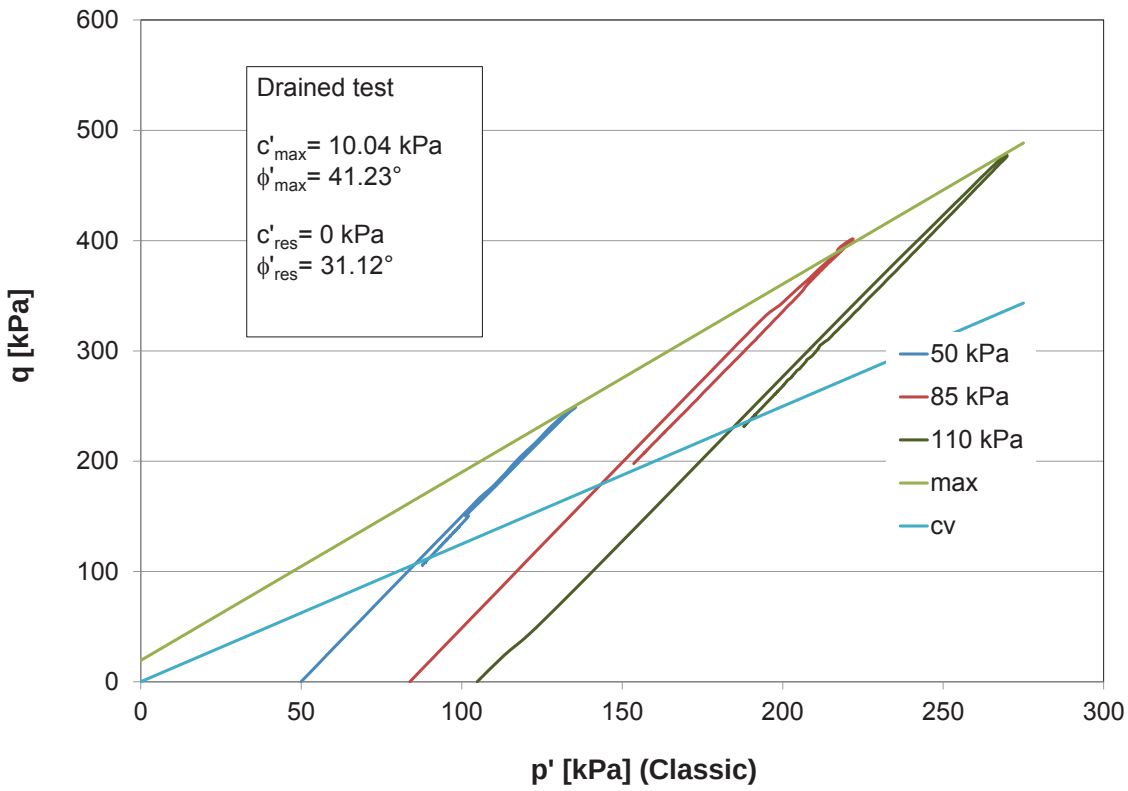

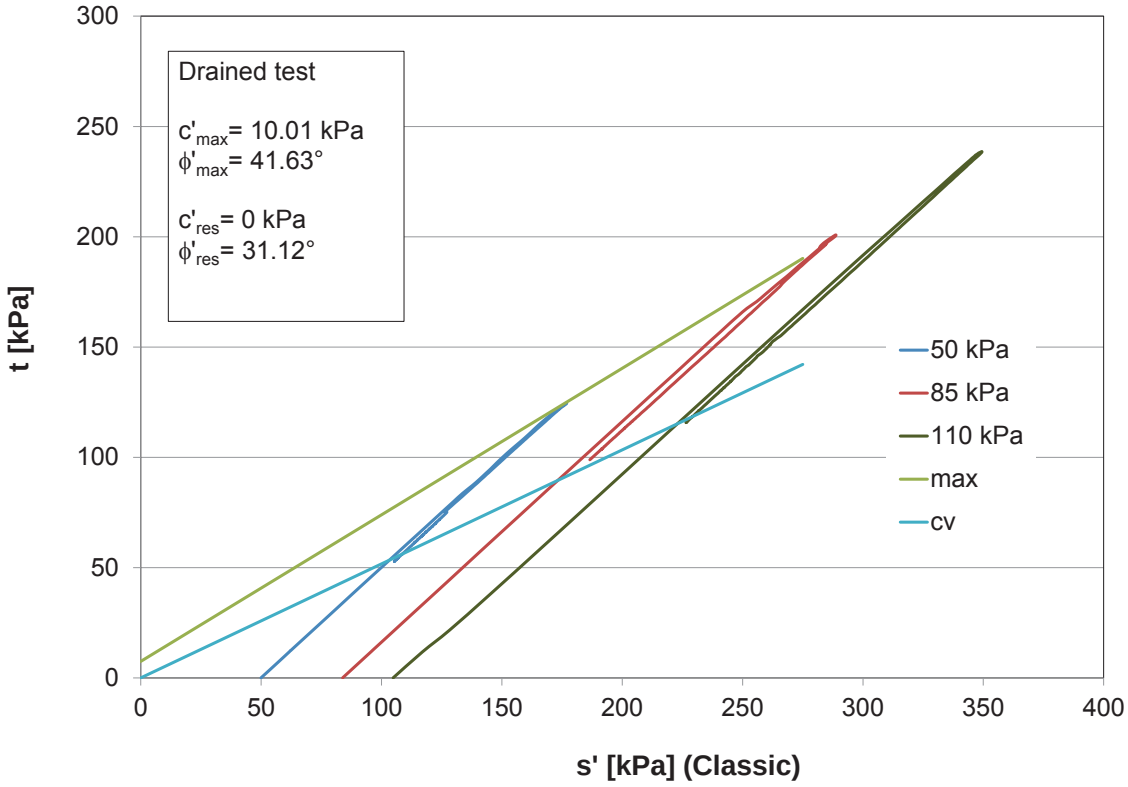
Drained test
c'max= 10.01 kPa
ϕ'max= 41.63°
c'res= 0 kPa
ϕ'res= 31.12°
50 kPa
85 kPa
110 kPa
max
cv
t [kPa]
s' [kPa] (Classic)
0
50
100
150
200
250
300
350
400

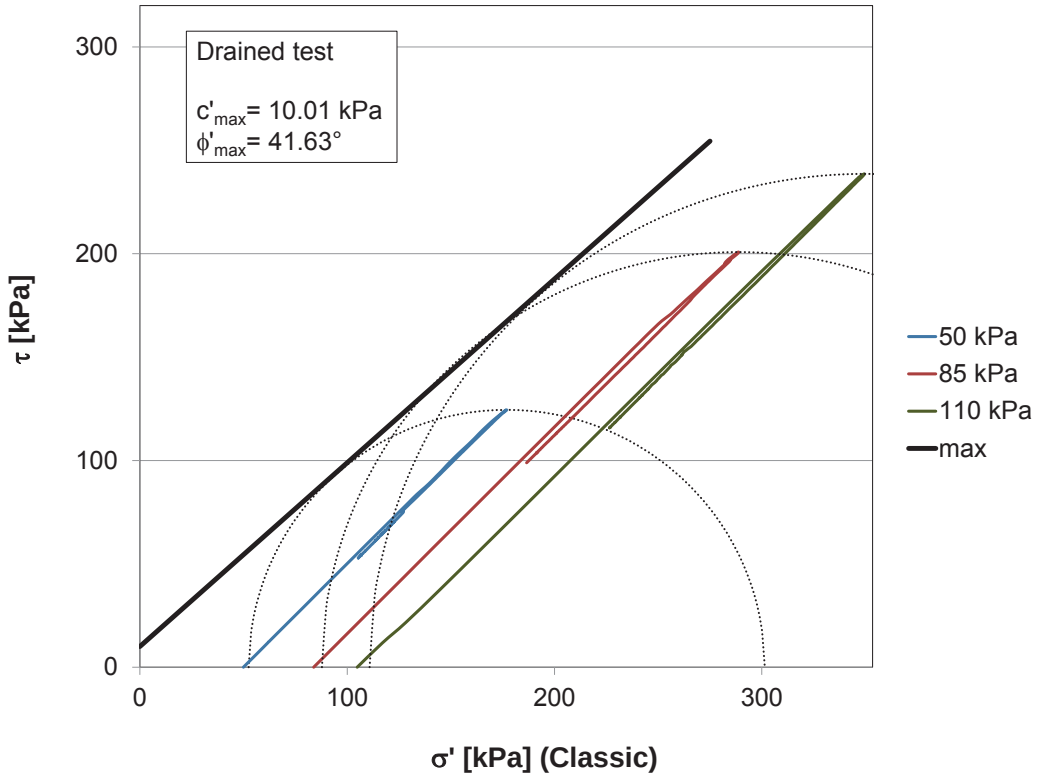
Drained test
c'max= 10.01 kPa
ϕ'max= 41.63°
50 kPa
85 kPa
110 kPa
max
τ [kPa]
σ' [kPa] (Classic)
0
100
200
300

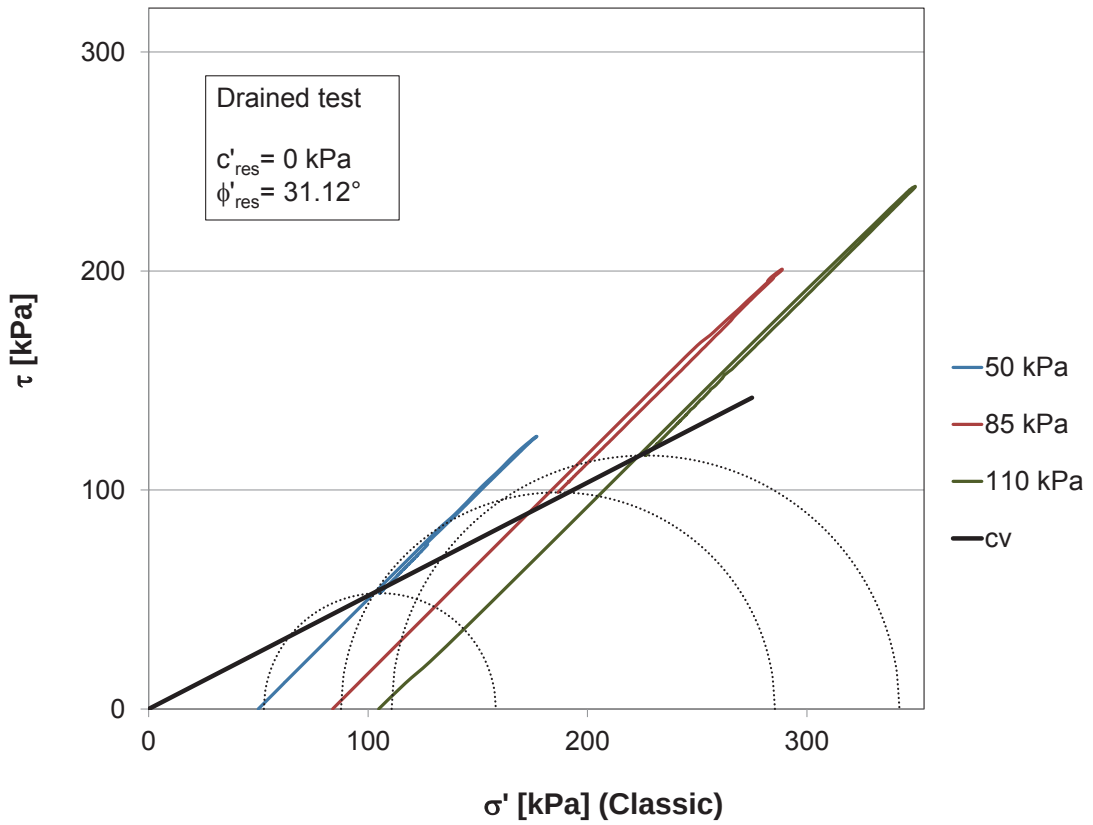
Drained test
c'res= 0 kPa
ϕ'res= 31.12°
τ [kPa]
σ' [kPa] (Classic)
0
100
200
300
50 kPa
85 kPa
110 kPa
cv

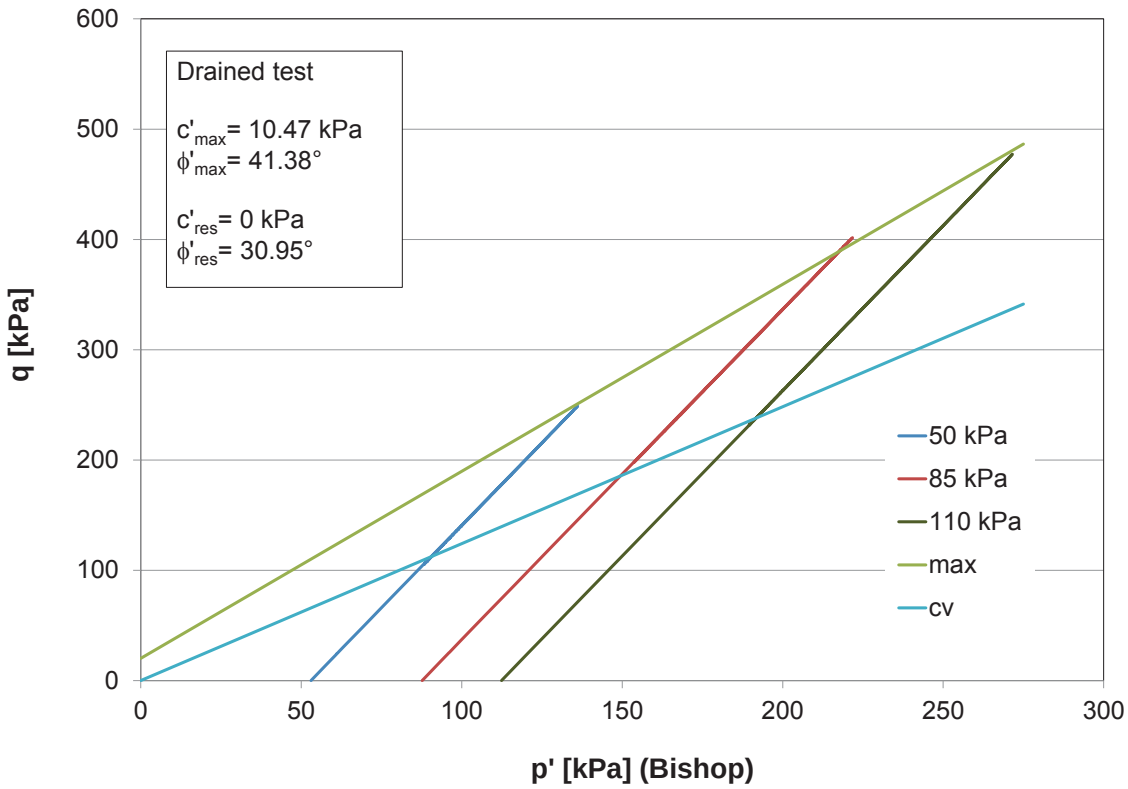
Drained test
c'max= 10.47 kPa
ϕ'max= 41.38°
c'res= 0 kPa
ϕ'res= 30.95°
q [kPa]
p' [kPa] (Bishop)
0
50
100
150
200
250
300
400
500
600
50 kPa
85 kPa
110 kPa
max
cv

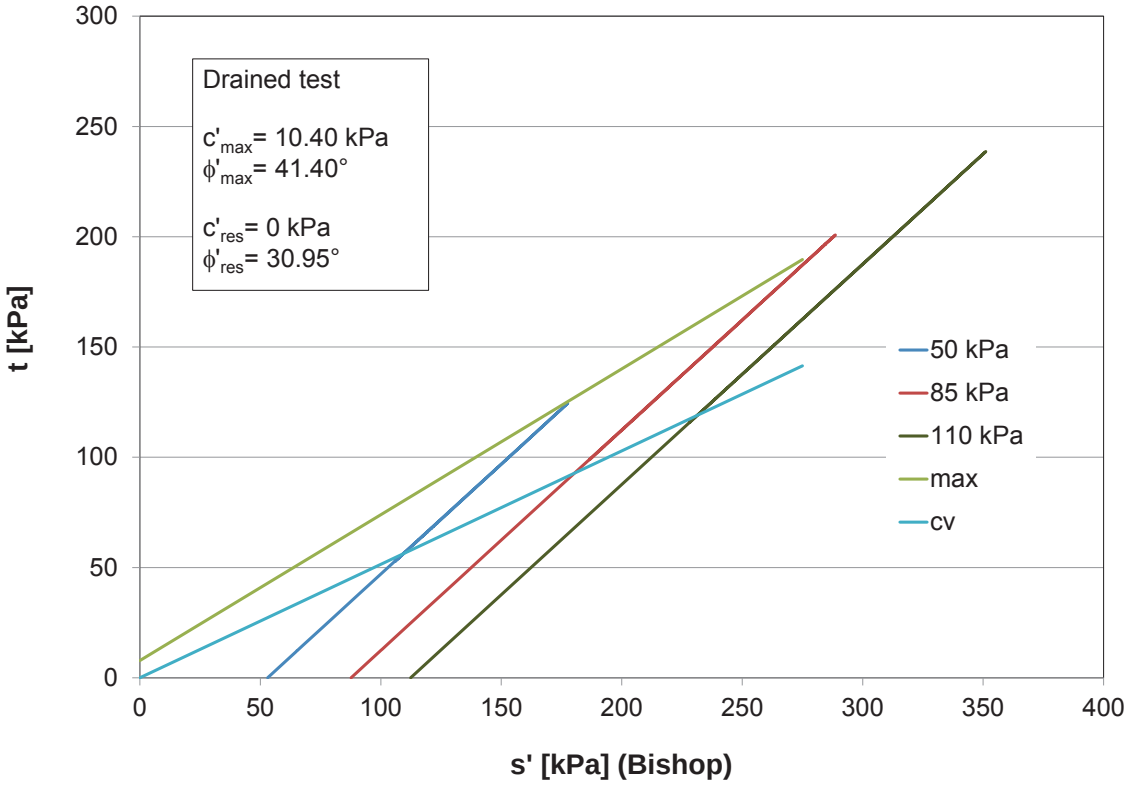
Drained test
c'max= 10.40 kPa
ϕ'max= 41.40°
c'res= 0 kPa
ϕ'res= 30.95°
50 kPa
85 kPa
110 kPa
max
cv
t [kPa]
s' [kPa] (Bishop)
0
50
100
150
200
250
300
350
400

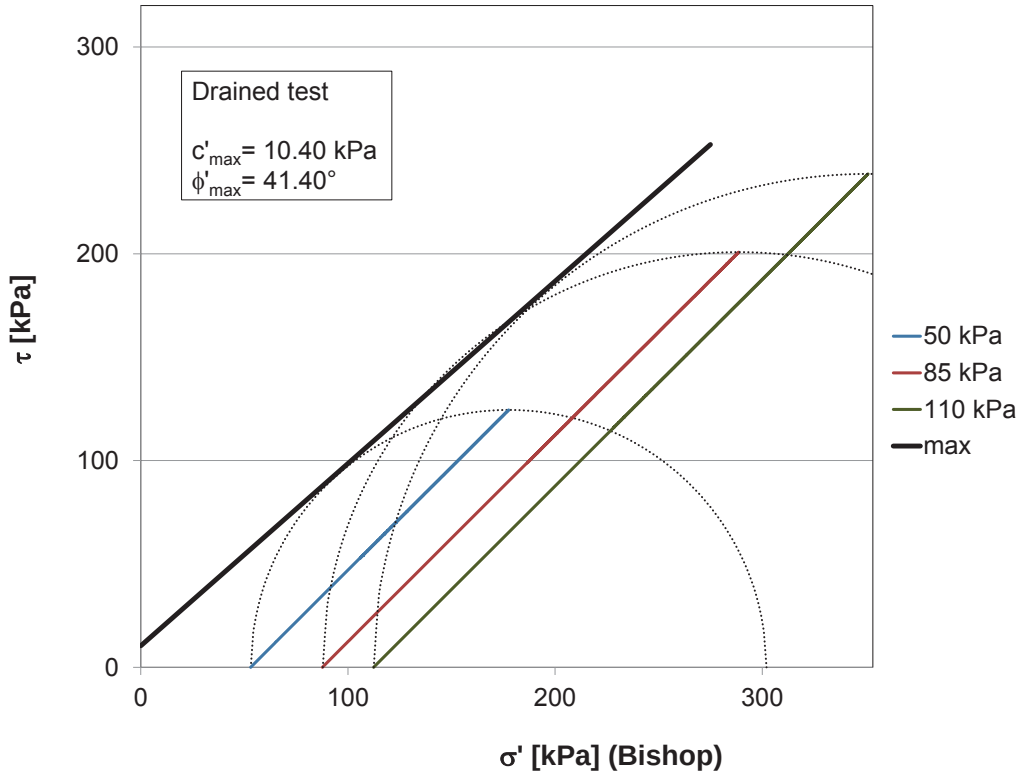
Drained test
c'max= 10.40 kPa
ϕ'max= 41.40°
50 kPa
85 kPa
110 kPa
max
τ [kPa]
σ' [kPa] (Bishop)
0
100
200
300

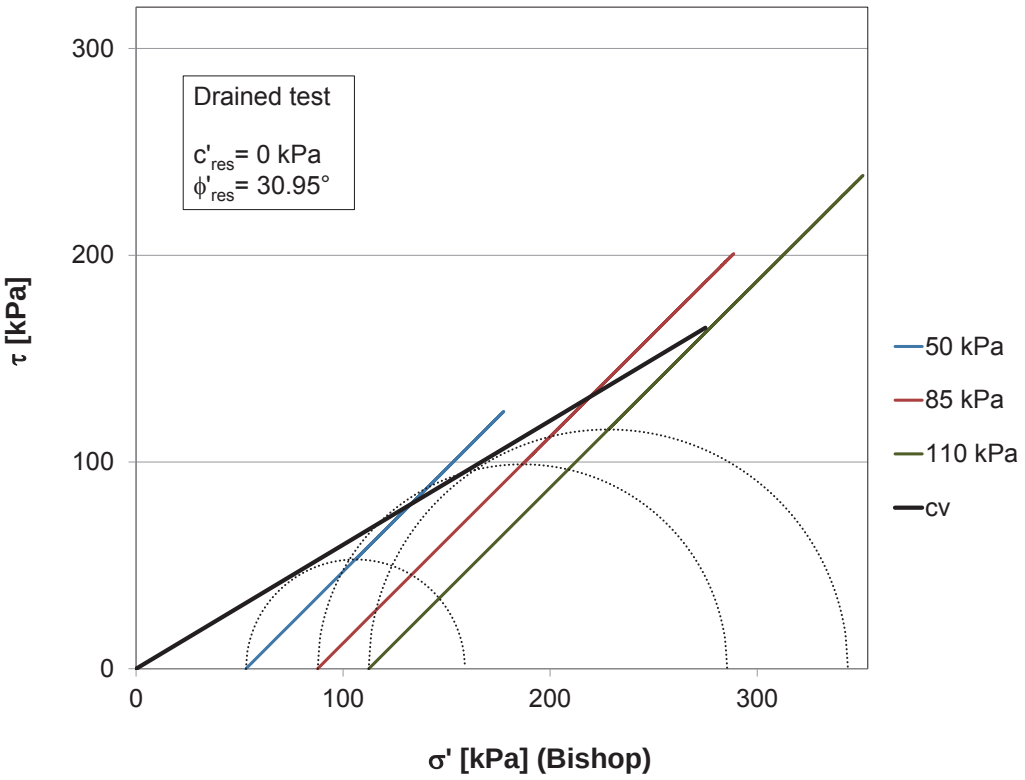

A4.2 Undrained test

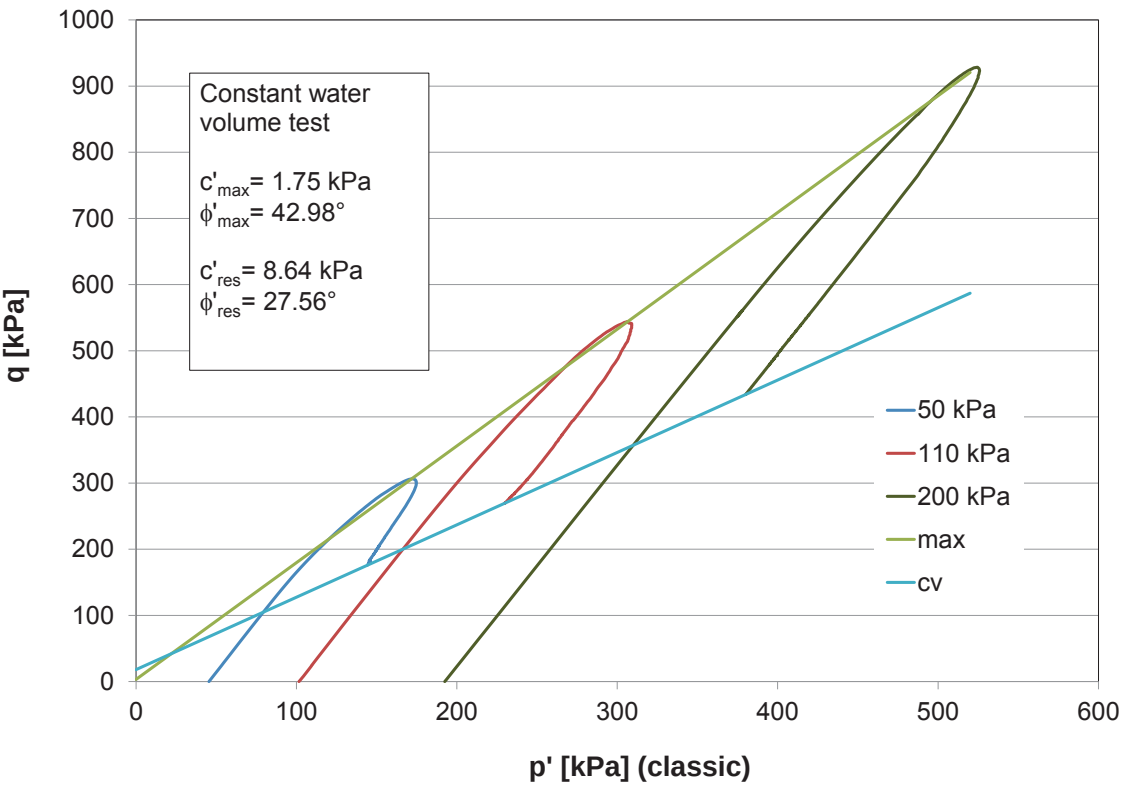

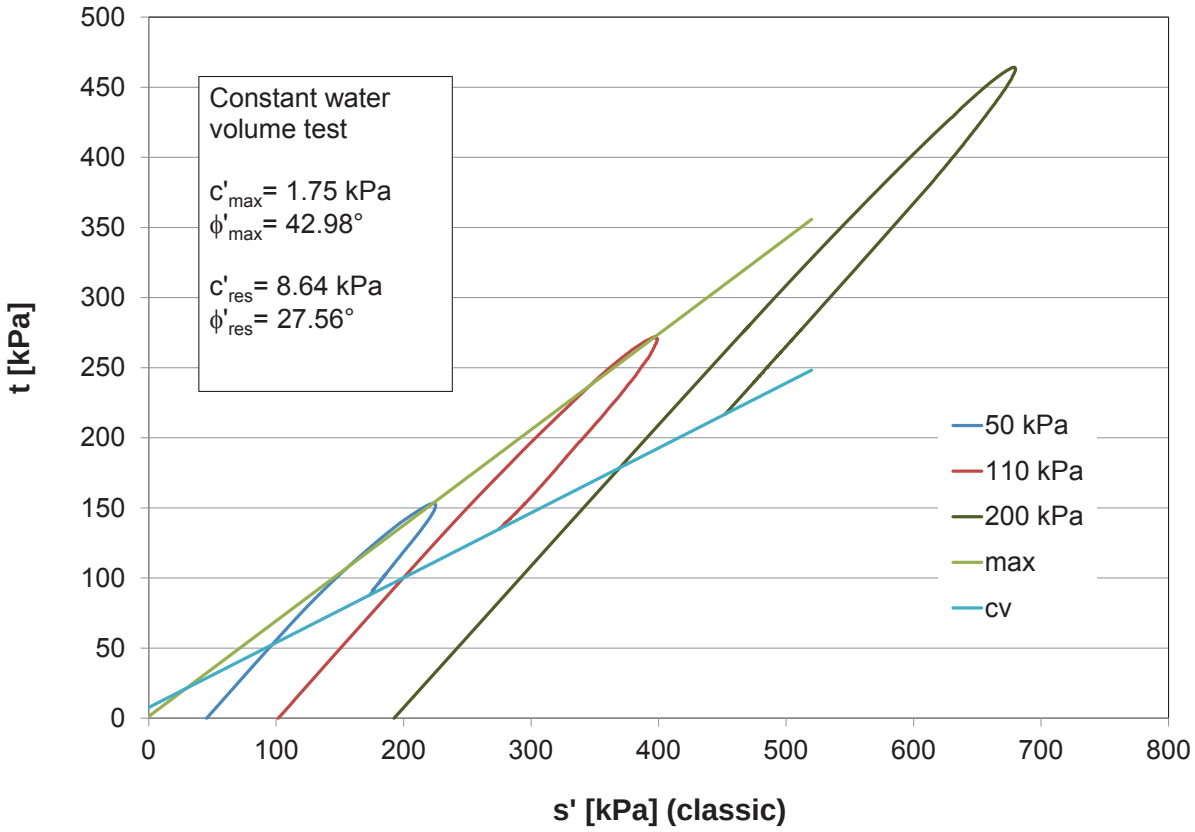
Constant water volume test
c'max= 1.75 kPa
ϕ'max= 42.98°
c'res= 8.64 kPa
ϕ'res= 27.56°
50 kPa
110 kPa
200 kPa
max
cv
t [kPa]
s' [kPa] (classic)
0
50
100
150
200
250
300
350
400
450
500
0
100
200
300
400
500
600
700
800

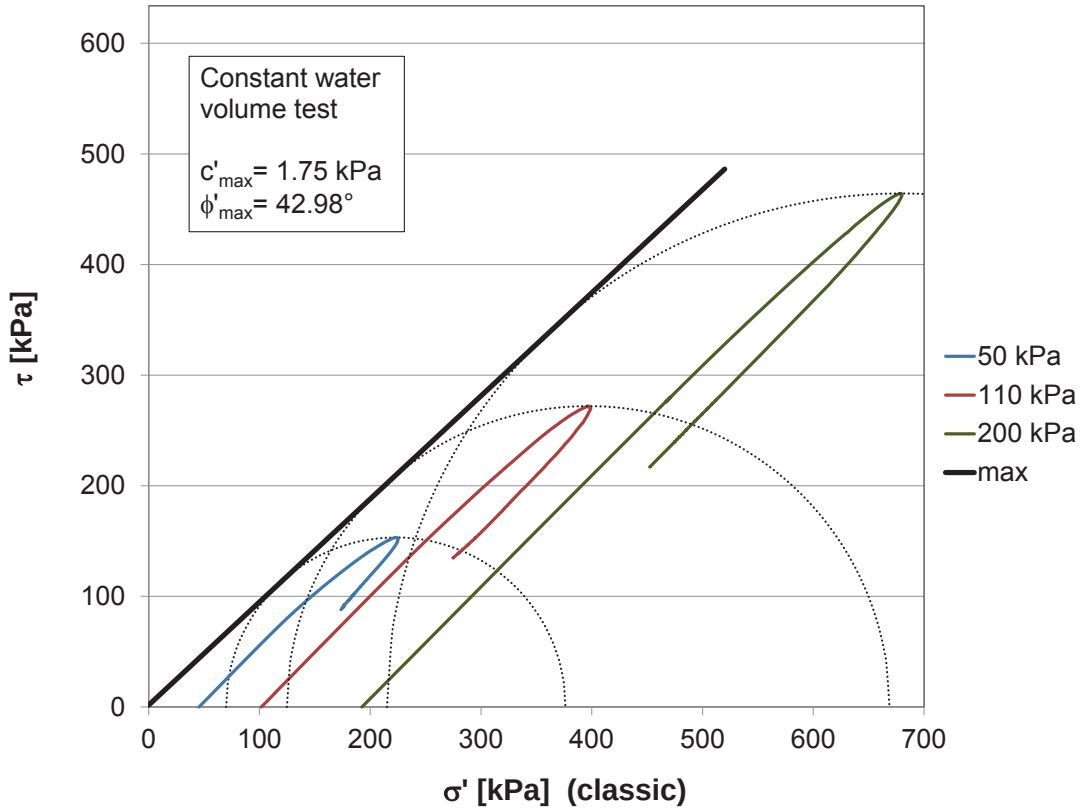
Constant water volume test
c'max= 1.75 kPa
ϕ'max= 42.98°
50 kPa
110 kPa
200 kPa
max
τ [kPa]
σ' [kPa] (classic)
0
100
200
300
400
500
600
0
100
200
300
400
500
600
700

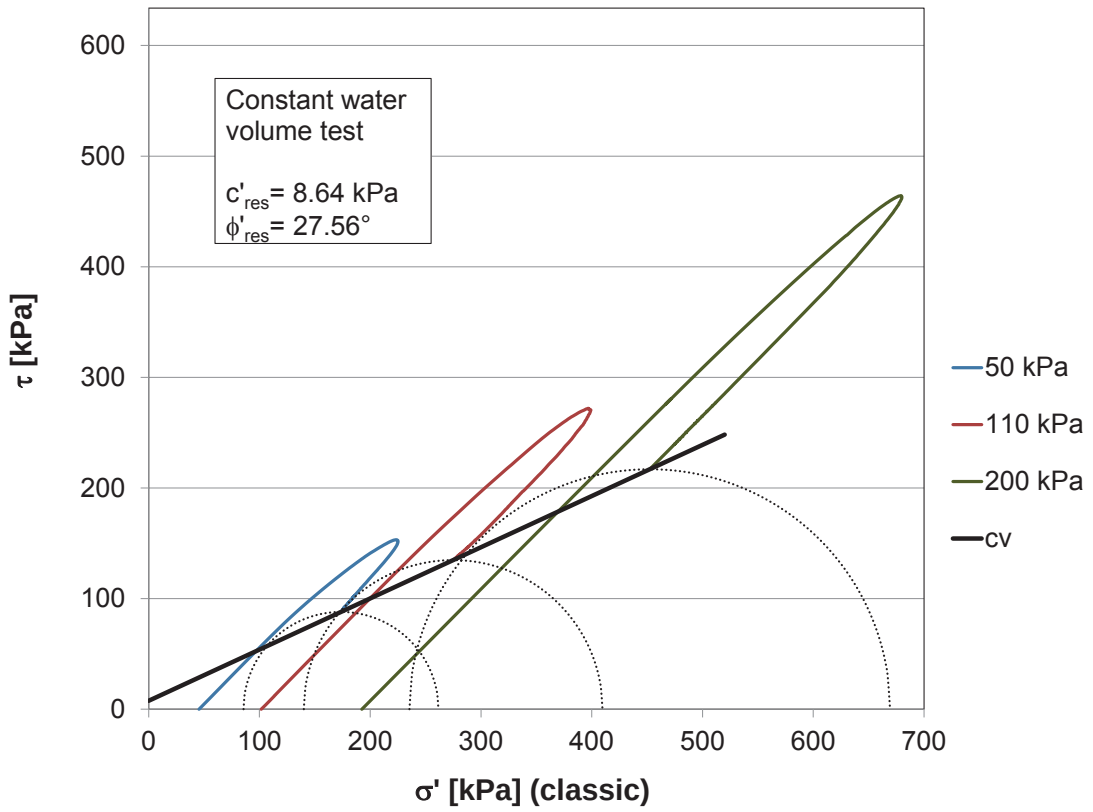
Constant water volume test
c'res= 8.64 kPa
ϕ'res= 27.56°
τ [kPa]
σ' [kPa] (classic)
50 kPa
110 kPa
200 kPa
cv
0
100
200
300
400
500
600
700

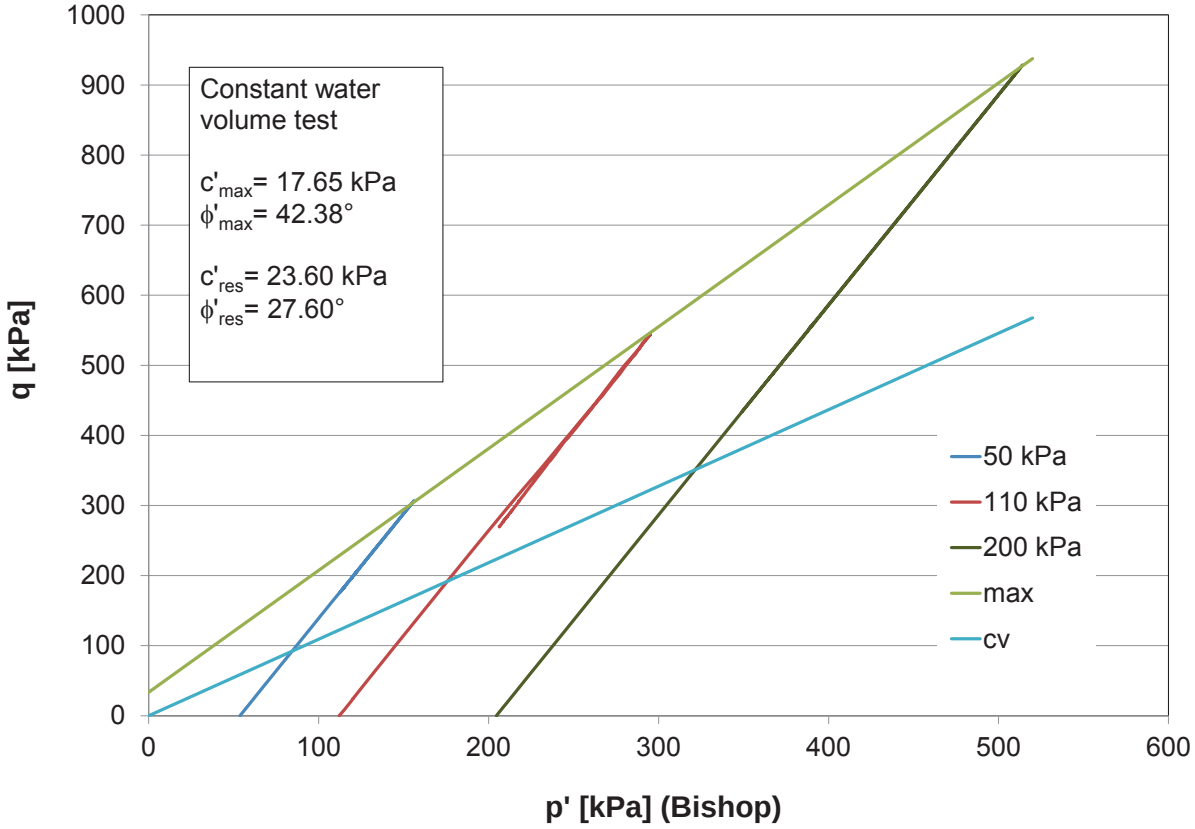
Constant water volume test
c'max= 17.65 kPa
ϕ'max= 42.38°
c'res= 23.60 kPa
ϕ'res= 27.60°
q [kPa]
p' [kPa] (Bishop)
50 kPa
110 kPa
200 kPa
max
cv
0
100
200
300
400
500
600
700
800
900
1000

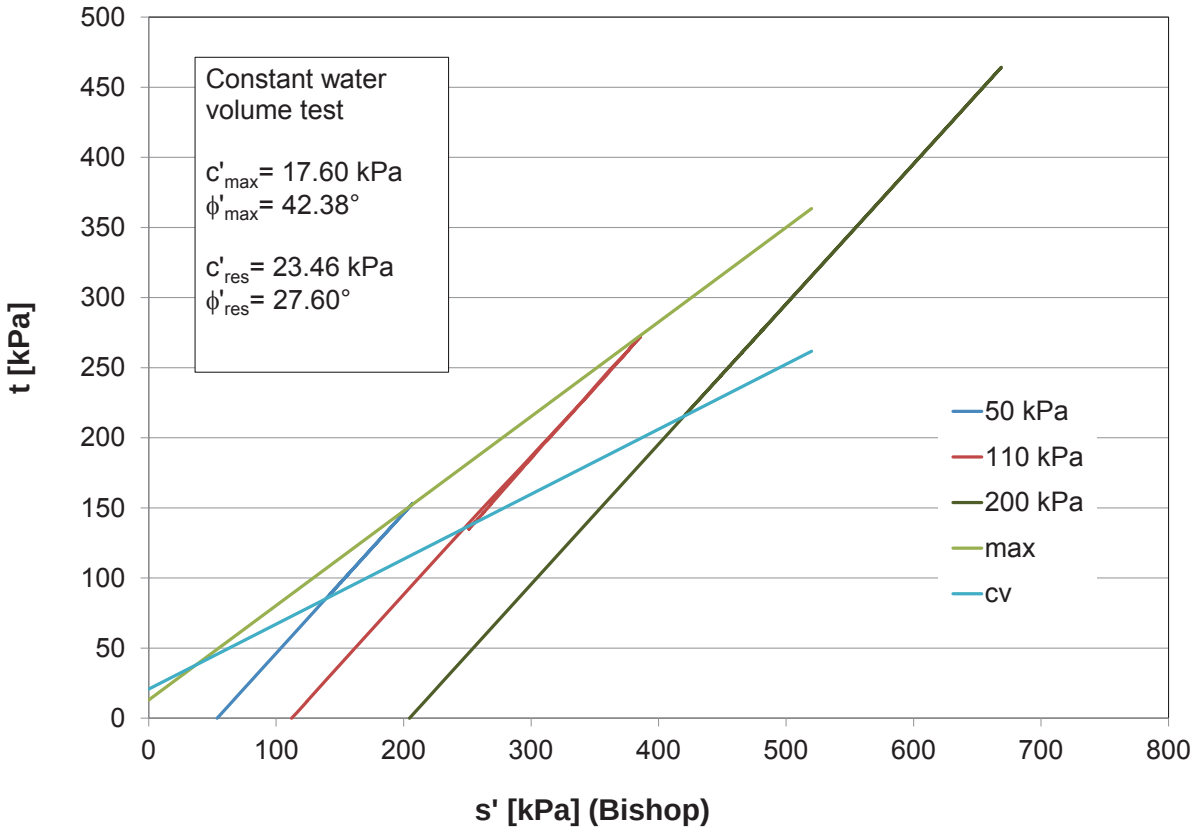
Constant water volume test
c'max= 17.60 kPa
ϕ'max= 42.38°
c'res= 23.46 kPa
ϕ'res= 27.60°
50 kPa
110 kPa
200 kPa
max
cv
t [kPa]
s' [kPa] (Bishop)
0
50
100
150
200
250
300
350
400
450
500
0
100
200
300
400
500
600
700
800

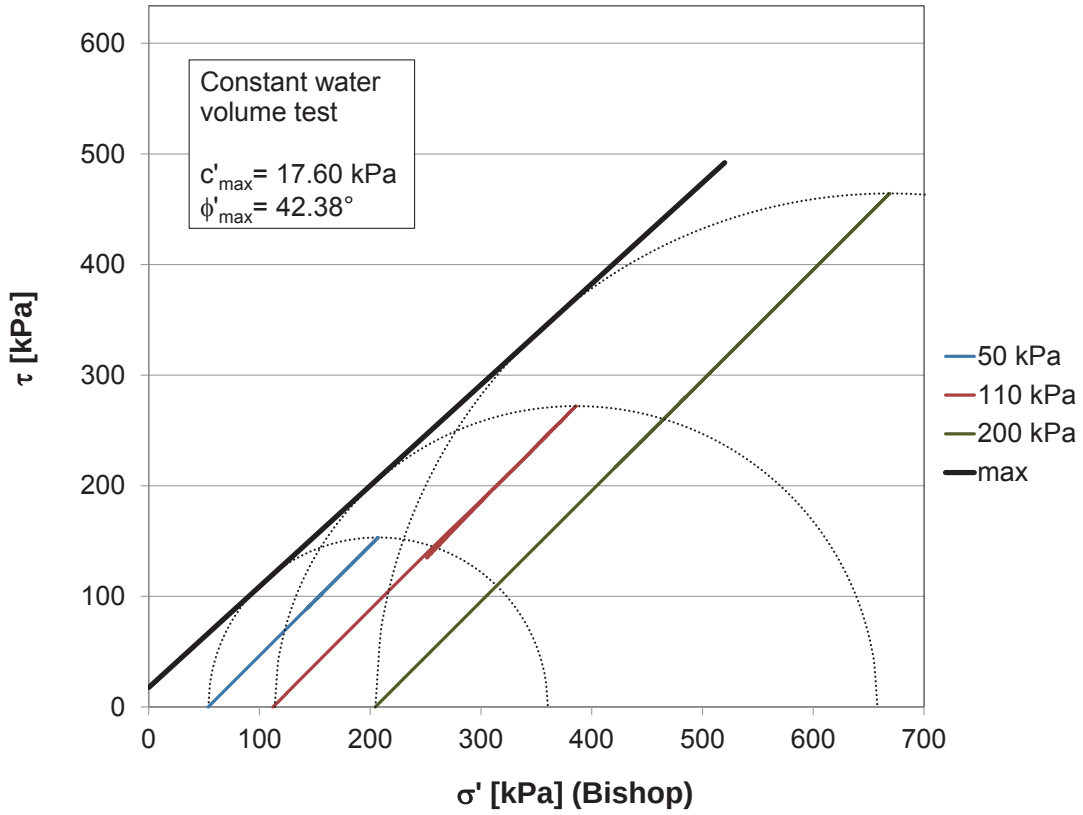
Constant water volume test
c'max= 17.60 kPa
ϕ'max= 42.38°
50 kPa
110 kPa
200 kPa
max
τ [kPa]
σ' [kPa] (Bishop)
0
100
200
300
400
500
600
0
100
200
300
400
500
600
700

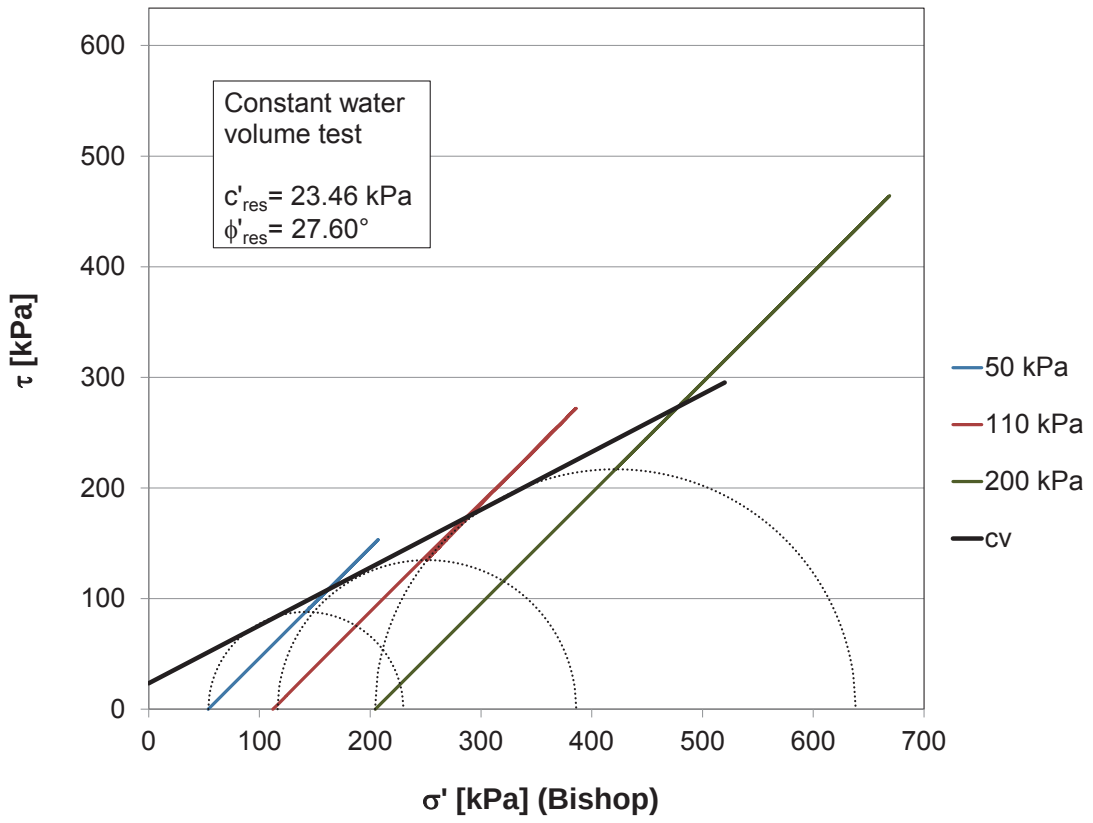
Constant water volume test
c'res= 23.46 kPa
ϕ'res= 27.60°
τ [kPa]
σ' [kPa] (Bishop)
0
100
200
300
400
500
600
700
50 kPa
110 kPa
200 kPa
cv

Appendix 5 Matlab routines

A5.1 Matlab routine to create HD videos from three cameras

```
% Script to create AVI videos from still images for several projects stored within a folder.
%   each project is taken with three cameras and the pictures of each
%   camera are stored at its corresponding folder.

% For the specific problem the folder structure is as follows:
% 1. Root_Folder %e.g. 'E:\Ferney'
%   1.1 Folder_containing_photos_of_all_projects %e.g. 'Photos_photogammetry'
%       1.1.1. Folder_of_project_1  %e.g.'wfm_10'
%           1.1.1.1 Folder_of_camera_A %e.g. 'Camera_A'
%           1.1.1.1 Folder_of_camera_B
%           1.1.1.1 Folder_of_camera_C
%
%   1.2 Folder_containing_generated_videos %e.g. 'Videos'
%       1.2.1. Folder_containing_all_three_videos_for_project_1
%
% Additionally the pictures were saved on BMP with the name '0_' +
% camera_name + sequence, e.g. 0_A106.BMP


% Coded at ETH Zurich by Ferney Morales, Nov-2012

RootFolder='E:\Ferney'; %Path of the root folder
PhotosFolder='Photos_photogammetry'; % Name of the folder containing the projects
VideosFolder='Videos'; % Name of the folder in which the videos will be saved
FileExt='BMP'; % Extension of the pictures.
FrameRate=50; % Changes the framerate of the video
Quality=80; % Change the quality of the video between 1-100 (default is 75)
ImRotate=180; % Degrees that the picture has to be rotate

Cam(1)='A'; % Name of the first camera
Cam(2)='B'; % Name of the second camera
Cam(3)='C'; % Name of the third camera
% Additional cameras can be used by adding terms to the Cam variable, e.g.
% Cam(4) till Cam(N), being N the total number of cameras used.
% Also if only 1 camera was used simple define Cam(1).

CamFolderName='Camera_'; % String before the name of the camera. This concatanated
with the name of the camera gives the name of the folder with the pictures

cd(strcat(RootFolder,'\',PhotosFolder)); %Sets the current folder to the photos Folder
ListProj = dir;    % List the projects inside the photos folder
isub = [ListProj(:).isdir]; %# returns logical vector
NameFolds = {ListProj(isub).name}'; % Takes the names of the folders
NameFolds(ismember(NameFolds,{'.','..'})) = []; % Erases the entries '.' and '..'
NumProj=size(NameFolds,1); % Total number of projects inside the root folder
Project=ListProj(3:size(ListProj,1)); % Saves the list of projects without '.' and '..'

for i=1:NumProj
   info=Project(i).name; % Takes the name of the current folder
```

```
   NewFolder=strcat(RootFolder,'\',VideosFolder,'\',info);
   cd(info); % Moves into the folder with the project
   if exist(NewFolder)==0 % Cero means the the folder doesn't exist yet.
         mkdir(NewFolder); %
   end
   for j=1:size(Cam,2) % Loops throughout all folders containing photos taken with different
cameras
      NameFilm=strcat(info,'_',CamFolderName,Cam(j));
      if exist(strcat(NewFolder,'\',NameFilm,'.avi')) == 0 % Executes the following code only if
the files doesn't exist
         cd(strcat(CamFolderName,Cam(j)))
         writerObj = VideoWriter(NameFilm,'Motion JPEG AVI'); %Other compression codecs
are avaiblable just type >>help VideoWriter
         writerObj.FrameRate=FrameRate; %Change the framerate
         writerObj.Quality=Quality; %Change the quality between 1-100 (default is 75)
         open(writerObj); % Opens the video file to work with
         listOfImages = dir(strcat('*.',FileExt)); % Creates a list of all the Images inside the
folder.
         for k = 1:25 %size(listOfImages,1) % Loops through all images in the current camera
folder
                  filename = strcat('0_',Cam(j),num2str(k),'.',FileExt); % Opens each picture
            [X, map] = imread(filename,FileExt); % Reads the image
            if imRotate <> 0
               X=imrotate(X,imRotate); % Rotates the image
            end
            txtInserter = vision.TextInserter(strcat(num2str(fix(k/FrameRate)),' days'));
            txtInserter.FontSize=50;
            txtInserter.Color=[255 255 255];
            J=step(txtInserter,X);
            F = im2frame(J, map); % Creates a frame from the read image
            writeVideo(writerObj,F); % Adds the taken frame into the video
         end
         close(writerObj); % Closes the video file
         movefile(strcat(NameFilm,'.avi'),NewFolder); % Moves the created video to its corre-
sponding folder
         tex=strcat({'video '},NameFilm,'.avi ',' has been processed');
         disp(tex)
         fprintf(strcat('video ',NameFilm,'.avi ',' has been processed'))
         cd ../
      end
   end
   cd ../
end
```

A5.2 Matlab routine for taking the hysteretic behavior of the SWRC into account

RootFolder='path_to_your_folder'; %Path of the root folder

NumAnalysis=3; %Total number of analyses to recover data from

AnalyList={'slope_1-2.0_H','slope_1-2.0_F','slope_1-2.0_W'}; % List with the name of the analyses

SlopeStabAIR=[]; % Variable which saves the information regarding slope stability of the air-side slope

SlopeStabWATER=[];% Variable which saves the information regarding slope stability of the water-side slope

FlowAna=[];% Variable which saves the information regarding flow analysis on the gauss points

Points=[1 2 3; 4 5 6; 7 8 9]; % Replace points_ids with a matrix full with the ID of the points of interest. Each row represents a test. In the default it takes info from points 1,2,3 from the first test (in this case 'slope_1-2.0_H'), points 4,5,6 from the second test ('slope_1-2.0_F') and point 7,8,9 from test 3 ('slope_1-2.0_W'). The number of rows of this matrix must be equal to the number of tests.

```
 for I=1:NumAnalysis
    AnalyNum=I;
    cd(strcat(RootFolder,'\',AnalyList{AnalyNum}))
    SlopeStabAIR=[];
    SlopeStabWATER=[];
    FlowAna=[];
    tic
    a=0;
    Stages = dir;    % List the stages analyzed
    isub = [Stages(:).isdir]; %# returns logical vector
    StagesList= {Stages(isub).name}';% Takes the names of the folders
    StagesList(ismember(StagesList,{'.','..'})) = []; % Erases the entries '.' and '..' from the
stages list
    NumStages=size(StagesList,1);% Amount of solved steps
    for i=1:NumStages %number of folders on each analysis. It's the same as the number of
analysis stages
            cd(strcat(RootFolder,'\',AnalyList{AnalyNum},'\',StagesList{i}))
        ListFold = dir;    % List the folders inside the folder
        isub = [ListFold(:).isdir]; %# returns logical vector
        NameFolds = {ListFold(isub).name}'; % Takes the names of the folders
        NameFolds(ismember(NameFolds,{'.','..'})) = []; % Erases the entries '.' and '..' from the
folders list
        NumFolds=size(NameFolds,1)-1;% Amount of solved steps (the entry 000 has no in-
formation of analysis, hence obviated

        if  (i==1 | i==4 | i==7 | i==10 | i==13 | i==16 | i==19)% (i==1 | i==4 | i==6 | i==9 | i==11 |
i==14 | i==16)
            time=csvread('time.csv',1,3,[1,3,NumFolds,3]);
            a=size(FlowAna,3);
```

```
        end

        %if i==1
        %     csvRangeGauss=[1,1, perl('NumRow.pl','gauss.csv')-1,10]; % Defines the range to
read the gauss points [for seep analyses]
        %end
        %if i==2
        %    csvRangeSlip=[1,1,125,1]; % Defines the range to read the slip surface
        %end
        %DummySlope=zeros(NumFolds,126);
        %DummyFlow=zeros(NumFolds,2503,10);
        for j=1:NumFolds;
           cd(NameFolds{j+1})

           if exist('slip_surface.csv')==2 % is an slope stability analysis
              wfm=csvread('slip_surface.csv',1,0);
                    %DummySlope(j,2:126)=csvread('slip_surface.csv',1,1,csvRangeSlip);
              %wfm=csv2struct('slip_surface.csv');
              %DummySlope=[NaN(size(wfm.SlipNum,1),1)        wfm.SlipNum        wfm.SlipFOS
wfm.SlipCenterX wfm.SlipCenterY wfm.SlipRadius wfm.SlipVolume wfm.SlipWeight];
           else % it's a flow analysis
              wfm=csvread('gauss.csv',1,0);
              %DummyFlow(j,2:2503,1:10)=csvread('gauss.csv',1,1,csvRangeGauss);
              %wfm=csv2struct('gauss.csv');
              %DummyFlow=[NaN(size(wfm.GaussPoint,1),1)                    wfm.GaussPoint
wfm.VolWaterContent      wfm.PoreWaterPressure      wfm.MatricSuction      wfm.XGradient
wfm.YGradient];
           end
           cd ..
           Dummy(1:size(wfm,1),1)=time(j);
           Dummy(1:size(wfm,1),2:size(wfm,2)+1)=wfm;
           if (i==2 | i==3| i==5 | i==6 | i==8 | i==9 | i==11  | i==12 | i==14 | i==15| i==17| i==18 |
i==20| i==21 )%(i==2 | i==3| i==5 | i==7 | i==8 | i==10 | i==12  | i==13 | i==15 | i==17| i==18 )

              if(i==2 | i==5 | i==8 | i==11 | i==14 | i==17 | i==20) % The analysis is on the air side
                 %SlopeStabAIR=[SlopeStabAIR;DummySlope];
                 SlopeStabAIR(:,:,j+a)=Dummy;
              else
                 %SlopeStabWATER=[SlopeStabWATER;DummySlope];
                 SlopeStabWATER(:,:,j+a)=Dummy;
              end
           else
              %DummyFlow(:,1)=time(j);
              %FlowAna=[FlowAna; DummyFlow];
              FlowAna(:,:,j+a)=Dummy;
           end
           clear Dummy wfm
        end
     end

     for n=1:NumAnalysis
        VolWC(:,n)=squeeze(FlowAna(FlowAna(:,2,2)==Points(AnalyNum,n),5,:)); % Volumetric
water content
```

```
        PWP(:,n)= squeeze(FlowAna(FlowAna(:,2,2)==Points(AnalyNum,n),6,:)); % Pore water pressure
    end
    FoS(:,1)=squeeze(min(SlopeStabAIR(:,3,:)));
    FoS(:,2)=squeeze(min(SlopeStabWATER(:,3,:)));
 cd ..

save(strcat(AnalyList{AnalyNum},'.mat'),'SlopeStabAIR','SlopeStabWATER',
‘FlowAna','VolWC','PWP','FoS','time' )
toc
clear  SlopeStabAIR SlopeStabWATER FlowAna

end
```